Comptes Rendus
de l'Académie des sciences

1873-7234 (electronic)

Mécanique

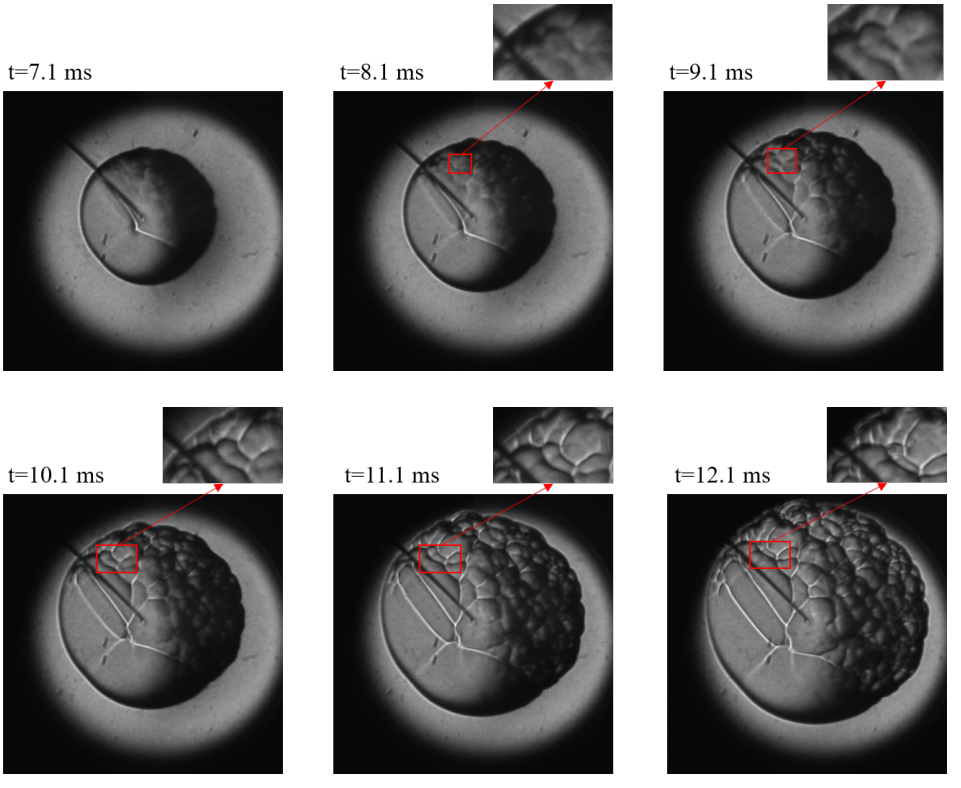

Volume 351, Special Issue S2, 2023

Special issue / *Numéro thématique*

Physical Science in Microgravity within the Thematic Group Fundamental and Applied Microgravity / *Sciences physiques en microgravité au sein du GDR Micropesanteur Fondamentale et Appliquée*

Guest editors / *Rédacteurs en chef invités*

Olga Budenkova, Catherine Colin, Guillaume Legros

Académie des sciences — Paris

INSTITUT DE FRANCE
Académie des sciences

CENTRE MERSENNE

Comptes Rendus

Mécanique

Objective of the journal

Comptes Rendus Mécanique is an internationally peer-reviewed electronic journal covering all areas of the discipline. It publishes original research articles, review articles, historical perspectives, pedagogical texts, and conference proceedings of unlimited length, in English or French. *Comptes Rendus Mécanique* is published according to a virtuous policy of diamond open access, free of charge for authors (no publication fees) as well as for readers (immediate and permanent open access).

About the journal

All journal's information, including the text of published articles, which is fully open access, is available from the journal website at https://comptes-rendus.academie-sciences.fr/mecanique/.

Author enquiries

For enquiries relating to the submission of articles, please visit this journal's homepage at https://comptes-rendus.academie-sciences.fr/mecanique/.

Contact

Académie des sciences
23, quai de Conti, 75006 Paris, France
Tel: (+33) (0)1 44 41 43 72
CR-Mecanique@academie-sciences.fr

Comptes Rendus
Mécanique
2023, 351, nº S2

Contents / *Sommaire*

Comptes Rendus
Mécanique
2023, Vol. 351, Special Issue S2, p. 1-2
https://doi.org/10.5802/crmeca.229

Physical Science in Microgravity within the Thematic Group Fundamental and Applied Microgravity / *Sciences physiques en microgravité au sein du GDR Micropesanteur Fondamentale et Appliquée*

Foreword

Catherine Colin [a] **and Guillaume Legros** [b]

[a] IMFT, Allée Camille Soula, 31400 Toulouse, France

[b] CNRS-ICARE / Univ. Orléans, 1C Avenue de la Recherche Scientifique, 45071 Orléans Cedex 2, France

Not yet published

As the editors of this special issue, we are delighted to introduce a selection of recent achievements associated with the French Research Network (*Groupement de Recherche*) on Fundamental and Applied Microgravity (GdR CNES/CNRS 2799). Last year marked the 30th anniversary of this group, making it the longest-standing GdR accredited by the *Centre National de la Recherche Scientifique* (CNRS). To open the 4th decade of our group, the *Comptes-Rendus Mécanique de l'Académie des Sciences* offered the invigorating opportunity of this special issue.

Over the past 30 years, a dedicated French aircraft has played a crucial role in evaluating theoretical and numerical investigations through experimental work conducted during parabolic flights to simulate microgravity conditions. From the initial *Caravelle* in the 90's to the current *Airbus A310*, three airplanes were specifically equipped to be full-time dedicated to parabolic flights. As highlighted in the first paper of this special issue, these facilities located on the French ground show—among others—the unfailing support of the French Space Agency (*CNES*) which we celebrate here.

Many processes are affected by gravity, and our understanding may be blurred by some gravitational effects. As an appealing illustration, the cover page displays a sequence of frames captured by a fast camera imaging the onset of an instability that propagates over the initially smooth sheet of an expanding premixed spherical flame. For sure, the directional feature of buoyancy makes it a serious trigger leading to the onset. So what if this trigger vanishes? Throughout a wide range of fields related to mechanics, the present issue compiles recent advances that pave the way to further understanding of fundamental processes, such as phase change or complex flows in the absence of gravity.

In the coming decade, space exploration that is clearly ambitioned by the major space agencies today also pushes new perspectives into our group. For this reason, our community now contributes at an international level to projects aiming at spacecraft safety or life sustainability. Papers related to fire safety or plant growth illustrate here these contributions.

Beyond these crucial issues, we also intend to celebrate a human adventure that a few generations of scientists strongly committed to. With this respect, we are deeply grateful to Christophe Delaroche, who retired one year ago after years serving as the Head of the Physical Sciences in

microgravity Department at CNES. We also express a moved homage to our colleague Professor Pierre Haldenwang who passed away two years ago after serving two terms as president of our group. We are convinced that Pierre's inspiring spirit will continue to guide our work for a long time. At the very least, the birth of our brand new website echoes this will:

https://gdr-mfa.fr/

Catherine Colin
Director of French Research Network on Fundamental and Applied Microgravity
France
colin@imft.fr

Guillaume Legros
Deputy director of French Research Network on Fundamental and Applied Microgravity
France
guillaume.legros@cnrs-orleans.fr

Comptes Rendus
Mécanique
2023, Vol. 351, Special Issue S2, p. 3-17
https://doi.org/10.5802/crmeca.144

Physical Science in Microgravity within the Thematic Group Fundamental and Applied Microgravity / *Sciences physiques en microgravité au sein du GDR Micropesanteur Fondamentale et Appliquée*

30 years of CNES parabolic flights for the benefit of the scientific community

Sébastien Rouquette[a]

[a] Human spaceflight experiment development department, CNES, 18 avenue Edouard Belin, F-31401 Toulouse Cedex 9, France
E-mail: Sebastien.Rouquette@cnes.fr

Abstract. Parabolic flights allow short microgravity investigations in Physical and Life Sciences, technology and instrumentation tests. The use of parabolic flights is complementary to other microgravity carriers, and preparatory to manned space missions onboard the International Space Station and other manned spacecraft, around the Earth or beyond, to the Moon for example.

The main advantages of parabolic flights for microgravity investigations are the short turn-around time, the relatively low cost, the flexibility of experimental approach, the possibility of direct intervention by investigators on board the aircraft during and between parabolas, and the possibility of modifying the experiment set-up between flights.

Keywords. Parabolic flights, CNES, Novespace, Microgravity, Weightlessness.
Published online: 13 January 2023

1. Introduction

1.1. *Sciences in weightlessness*

The aim of research in microgravity is to study phenomena that are usually hidden by Earth's gravity. Researchers therefore try to obtain data under microgravity conditions that are impossible to reproduce on Earth.

The experiments cover a wide range of topics: fundamental physics, physical sciences, life sciences, material sciences, sciences of the universe, technological experiments, tests of space devices and preparation for manned space missions.

There are several types of access to microgravity. From drop towers, sounding rockets and automated capsules to the International Space Station, these devices offer a wide variety of facilities to carry out science experiments (see Table 1). Of the five means of accessing weightlessness, only parabolic flights allow scientists to operate their own experiments (laboratory type instrumentation is most commonly used), without the need to automate, miniaturise or entrust them to operators such as astronauts, in a short time frame (typically about one year between the experiment proposal and its performance). In addition, during a parabolic flight, researchers can repeat their experiments many times and modify their parameters. Aircraft parabolic flights

Table 1. Comparison between microgravity platforms.

Mean	Duration of microgravity	Level of residual gravity	Payload capacity	Development duration and accessibility
Drop towers	4–9 s	10^{-5} g	165–225 kg dimension lower than $1.7 \times 0.6 \times 0.6$ m^3 automated	>6 months depending on complexity several campaigns a year
Parabolic flights	20–24 s	$\pm 10^{-2}$ g accuracy around the selected level between 0 g and 1 g for reduced gravity level	Several tons separated in racks laboratory hardware	Typically 6–12 months 5 campaigns a year (×10 experiments)
Sounding rockets	3–15 min	10^{-4} g	100 kg, diameter lower than 60 cm automated	>18 months variable availability
Capsules	15 days	10^{-5} g	Lower than 600 kg, dimension lower than $1.7 \times 1.7 \times 1.0$ m^3 automated space developed hardware	>18 months availability depending on current capsule development and availability (USA)
ISS	Up to year	10^{-5} g	Few kg automated space developed hardware	>18 months typically one call for experiments a year in France

repetitively provide 22 s of zero gravity and up to 35 s of reduced gravity (Martian or lunar gravity) during ballistic flight manoeuvres.

In this context, the parabolic flight offers great flexibility in the implementation of experiments at a low cost and with a large boarding capacity.

1.2. *History of the program*

The parabolic flight program in Europe was initiated by CNES astronauts Jean-François Clervoy and Jean-Pierre Haigneré, following the thesis presented by Jean-François Clervoy as part of his training as a test flight engineer, in 1984. The chosen aircraft was Caravelle serial number 234 belonging to the Flight Test Centre (CEV) of French general delegation of armament (DGA).

Shortly after the first scientific campaigns organised by CNES and CEV, CNES decided to entrust the management of the program to Novespace, a new private company subsidiary of Cnes, which has since retained responsibility for the program with the success that we know, on board 5 successive aircraft.

For these purposes, CNES, DLR (the German space agency) and ESA (the European space agency) have organised 170 campaigns since 1984, with several airplanes: CNES' Caravelle, NASA's KC-135, the Russian CTC Ilyushin IL-76-MDK, the Airbus A300 Zero-G and the A310. In addition, two Joint European Partial-g Parabolic Flight Campaigns were organised by ESA, CNES and DLR using the Airbus A300 Zero-G for experiments at reduced gravity levels, typically at Moon and Mars g levels [1, 2].

In 2014, CNES, DLR and ESA supported Novespace in the acquisition of the A310 "Konrad Adenauer", which was used to transport the German Chancellor and her government.

The excellent cooperation between the three agencies has ensured the success of the program to date.

Parabolic flights are therefore a superb example of European cooperation. They have become the world's leading reference in this activity, in the aircraft offering the largest volume in parabolic flight. They represent 30 years of continuous success.

For 30 years, the Zero-G aircraft, as they have been called since their inception, have been used to carry out research work in zero gravity. CNES, for its part, has carried out 65 parabolic flight campaigns, i.e. a total of around 200 flights, more than 200 different scientific experiments, resulting in thousands of high-level publications in all research disciplines and a large number of student researchers have obtaining their doctorate degree.

2. Gravity, weightlessness, microgravity . . . Let's clarify the concepts

Gravity is one of the fundamental interactions that govern our universe. It is in fact the attraction of bodies to each other due to their mass. This law applies to our Earth as well as to any other star.

Gravity is the feeling of this attraction on the surface of a planet. It is, for example, the force of gravity that acts on a human being when he or she touches the ground. Gravity is directed towards the centre of the Earth.

Weightlessness is the absence of feeling this force. It is therefore not at all the absence of attraction. It is a state reached by a body when the force of gravity has no obstacle to its action. Note that weightlessness is not the absence of gravity, but the absence of other forces that would oppose it. Indeed, a planet exerts its attraction over astronomical distances, which is why the Moon revolves around the Earth. It is captive in its field of attraction. The Sun holds the objects of the solar system under its influence billions of kilometres away.

On Earth, the effects of gravity are defined by weight. The effects of weight are felt due to the reaction of the Earth's ground and friction when falling (e.g. air or water friction). Weightlessness is therefore the state in which neither the reaction of a support nor friction is felt. It is therefore a state of free fall!

In the Zero-G aircraft, the particularity of parabolic flight makes it possible to create a situation of free fall lasting a few seconds. The absence of air friction inside the cabin creates a situation where we are freed from the sensation of weight. The aircraft and its occupants all fall along the same trajectory.

Nevertheless, perfect weightlessness situation does not really exist. In a parabolic flight, the fall is partly slowed by the air in the atmosphere. In space, on board space stations and spacecraft (in permanent free fall), weightlessness is also affected by factors such as radiation from the Sun, the pull of the Moon and even the shape of the Earth. Astronauts or scientists working on board Zero-G aircraft do not perceive these disturbances, but to take account of these factors, we generally speak of "microgravity", which translates in French to "micropesanteur".

3. Why do research in microgravity?

Research in microgravity tends to better understand structure and behaviour of matter and to prepare the medicine and technology of tomorrow.

To understand a phenomenon (chemical, physical, biological, physiological, etc.), we must try to decipher the mechanisms by which it functions under various conditions. Scientific studies carried out on Earth do not allow to highlight all the characteristics of a phenomenon, because gravity disturbs or masks certain aspects of it. Carrying out the same experiment in weightless conditions can give very different results. It is difficult to give a complete and wide view of the experiments that have been performed in parabolic flights. Bibliography tries to give a short sample of the latest studies.

Here are some examples of the objectives:

Physics of matter: Research on board parabolic flights tries to investigate the structure of matter and its modification at macroscopic or microscopic scales. Physics of fluid [3–6], physics of

granular media [7], test of principle of equivalence and atomic clocks [8], combustion [9,10]. . . . At the same time, analyses of fluid mechanics or plasma behaviour are used to find improvements in industry.

Medical research: Medical research in zero gravity is not only a field of study for the preparation of astronauts. Above all, it continues to shed light on the mechanisms of human physiology, even during short duration microgravity conditions. Parabolic flights offer a test platform to specifically study physiology or neurology, as cardiovascular adaptation, motor adaptation or environment perception perturbation [11–19]. Longer stays in a microgravity environment have effects on the human body that are very similar to those of ageing (loss of bone and muscle mass, degradation of arteries, etc.). The experiments carried out in this particular environment therefore frequently find applications in medicine on Earth in order to prevent and treat certain very terrestrial pathologies (osteoporosis, balance disorders, etc.).

Space technologies: The Zero-G aircraft also makes it possible to test the space technologies of the future. Indeed, the duration of microgravity makes it possible to deploy antennas or observe the behaviour of tanks such as those used on launchers or satellites as if they were in space [20]. It is also a training ground for European astronauts who are preparing to navigate, work and manipulate objects while floating. Similarly, some of the experiments that are carried out on the International Space Station are tested beforehand during parabolic flights.

Preparing for exploration: of course, research in microgravity also makes it possible to prepare for the great space journeys that human beings have dreamed of since time immemorial. Deciphering the mysteries of microgravity already makes it possible to design and prepare the long-term manned flights planned for the Moon and Mars in the coming decades.

4. The Zero-G aircraft, a unique laboratory

Studying certain phenomena can be complicated in conventional laboratories on the ground. To avoid some of the parasitic effects of gravity, many researchers use parabolic flights. Few means exist for conducting research in microgravity. The Zero G aircraft is the ideal laboratory. It is effectively the only manned access to microgravity on Earth (as opposed to capsules, towers or sounding rockets).

The scientific teams can interact directly with their equipment. This is a big difference from other means of accessing microgravity, where the experimental devices must be fully automated.

From an organisational point of view, the preparation time for an experiment is relatively short compared to other microgravity platforms, particularly the International Space Station (ISS). An experiment can be on board a parabolic flight in about 12 months, while the average time to reach the Space Station can be up to 5 years. With the Zero G, scientists benefit from a flexible and fast access tool to conduct cutting-edge research, without waiting years for results.

In addition, parabolic flight campaigns are less expensive than access to the ISS, with its imperatives in terms of safety, space requirements, availability of the astronaut, etc., is much more expensive (and restrictive) for scientists. In comparison, the Zero-G aircraft also offers the possibility of carrying larger experiments that are very difficult to send into orbit. Its experimental area, which is rather open, free of cables and other sensitive equipment, is over 200 m^3.

The overall microgravity time is also significant on a parabolic flight campaign (90 parabolas of 22 s).

The Zero-G aircraft (see Image 1) is a tool that offers many advantages for researchers thanks to its technical characteristics, its accessibility and its organisational aspects. A real avant-garde aerial space laboratory!

Image 1. Airbus Zero-g beginning microgravity phase. Picture taken by Alex Magnan during a demo flight. © Novespace.

United States, Russia and Ecuador have similar aircraft to the European Zero-G aircraft, in terms of cabin volume available for science experiments. The A310's activity is nevertheless much more intense than that of its peers and offers at least five campaigns slots a year provided by CNES, DLR and ESA.

Aircraft parabolic flights are a useful tool for performing short duration scientific and technological experiments in reduced gravity. Together with drop towers, sounding rockets, the International Space Station (ISS) and other manned and unmanned spacecraft, aircraft parabolic flights with the Airbus A310 Zero-G completes the set of flight research opportunities for European scientists.

The principal value of parabolic flights is to provide a flying laboratory in which the gravity level can be modified, producing, at a relatively low cost, scientific results for experiments operated by the scientists themselves and for which the microgravity duration and levels are adequate. Aircraft parabolic flights are the only flight opportunity beside ISS and Chinese spacecraft where medical research on human test subjects can be performed in weightlessness.

To summarize, the main advantages of parabolic flights for microgravity investigations are: the short turn-around time (typically about one year between the experiment proposal and its performance), the reliability of the campaign dates, the relatively low cost involved for ESA, CNES and DLR sponsored investigators, the flexibility of experimental approach (laboratory type instrumentation is most commonly used), the possibility of direct intervention by investigators on board the aircraft during and between parabolas, and the possibility of modifying the experiment set-up between flights. Other more detailed objectives are presented in [2].

5. CNES, specialist to support research

CADMOS (*Centre d'Aide au Développement des Activités en Micropesanteur et des Opérations Spatiales*), prepares and organises CNES parabolic flight campaigns.

This operational structure, based in Toulouse as part of CNES, helps scientists to prepare and conduct their experiments.

Its experts participate in the selection of experiments by giving an opinion on their technical feasibility. They design and develop complementary equipment if necessary. Its teams also manage the planning, safety aspects and procedures to be followed in flight to get the most out of the experiment. They accompany Novespace in the loading of the equipment and the conduct of the experiments on flight days.

Since the beginning of the CNES parabolic flight activity in 1989, CADMOS has hosted more than 200 different experimental studies, representing 1000 people involved and thousands of top scientific publications.

Over the last 12 years, CNES organized 24 campaigns and participated in four joint campaigns, with DLR and ESA. The total number of experiments tested in flight is 261, with a major contribution of Life sciences and Matter sciences. The average number of experiments onboard for a flight campaign is 10. Some research need a large amount of data, requiring several campaigns.

Most experiments conducted on microgravity research campaigns are proposed to an International Announcement of Opportunities and selected after a peer review. Proposals for microgravity experiments to be conducted during parabolic flights can be submitted at any time to ESA's Announcement of Opportunity and DLR proposals are peer reviewed on an annual basis.

On CNES side, flight campaigns enable the scientific programs of more than forty laboratories in France (Inserm, CNRS, universities, etc.) to be conducted. A call for experiment is announced on CNES Website. Experiments are selected by working groups including experts from outside CNES, who examine the scientific or technology merit of each one. This committee meets several times a year to study the numerous applications submitted in response to the annual calls launched by CNES.

After peer recommendation, the technical feasibility of the proposal is assessed and, upon positive assessment an experiment proposal is manifested for a specific campaign. ESA, CNES and DLR offer the opportunity of participating in the parabolic flights to selected investigators free of charge.

With these campaigns, France and Europe are at the forefront of scientific research in microgravity at international level.

6. Parabolic flight science campaigns

Each year, Novespace organises 5 to 6 flight campaigns on behalf of CNES, DLR and ESA. These campaigns take usually place from Bordeaux-Mérignac airport and involve between 10 and 15 experiments.

During each campaign, scientific and technology experiments prepared by research laboratories are flown on board the Airbus Zero-G.

6.1. *The course of the campaigns*

The experiments are selected, designed and tested at least 6 months in advance by the CNES thematic groups (see Figure 1 to have the repartition of thematics in CNES parabolic flights since 2009). Thus, fundamental or applied research projects, physiology/neurology, biology, fluid physics, astrophysics as well as technology experiments are flown. Some researchers fly regularly when their research projects require it.

As aircraft parabolic flights are considered to be test flights, particular precautions are taken to ensure that all operations during flights are conducted safely and that flying participants are adequately prepared for the repetitive high and low gravity environments. Prior to a campaign, Novespace provides support in the experiment equipment design and in all related safety aspects. All experiments to be performed and all equipment to be installed onboard the aircraft are reviewed from a structural, mechanical, electrical, safety and operational points of view by experts several months before a campaign. Technical visits are made to the experimenters' institutions to review equipment. A safety review is held one month before the campaign. During this review, the integration of all equipment is discussed, and the overall safety aspect of the campaign is assessed.

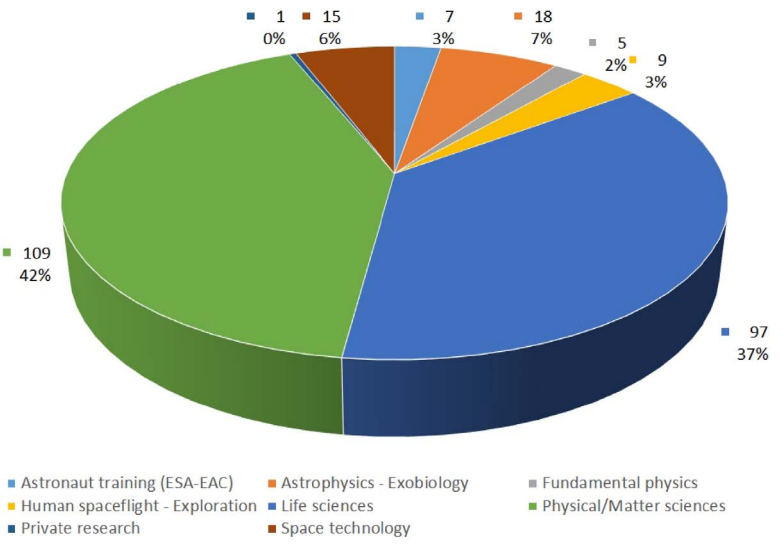

Figure 1. Overall repartition of thematics in CNES parabolic flights since 2009.

Image 2. Early morning flight preparation at Novespace. © S. Rouquette/CNES.

The campaign itself takes place over two weeks. The first week is devoted to the experiment preparation and loading into the aircraft. A final safety review visit is conducted on board the aircraft to verify that the experiments are ready for flight and that all safety requirements have been fulfilled.

Before the flights, a detailed briefing is given on the procedures to be followed during the flight and the safety standards to be respected. Everyone takes part: scientists, subjects, pilots, doctors, technicians, safety personnel and CNES managers.

Take-offs and landings are usually made at the Bordeaux airport, although other airports have been used in the past in Köln, Brussels, Paderborn, Dübendorf and Berlin. Parabolas are flown in dedicated air zones over the Gulf of Biscaye, the Mediterranean Sea, or Germany respectively.

Typically, three flights of 30 parabolas take place each morning on the Tuesday, Wednesday and Thursday, followed each time by a debriefing during which the needs and requests of investigators are reviewed and discussed (Image 2 shows the aircraft just before departure during a campaign).

All experimenters invited to participate in parabolic flights must pass a medical examination. During the flights, specialised personnel supervise and support the in-flight experiment operations. In addition, a Flight Surgeon participates in all flights to supervise the medical aspect of in-flight operations. Due to the alternation of flight phases of low and high gravity, parabolic flight participants might suffer from motion sickness. Therefore, prior to the flights, anti-motion sickness medication is made available upon request to flying participants.

After the campaign, parabolic flight investigators are requested to send a report with results of their experiments to the agencies.

7. The Airbus A310 Zero-G

7.1. *History*

Microgravity flights have been tested in France since 1946. It was the "*Direction Générale de l'Armement - Essais en vol*" that first tested aeronautical equipment in parabolic flight. It was onboard a Martinet NC-702, a twin-engine propeller plane. Its successor was the Caravelle F-ZACQ, which was in service from 1957 to June 1995. Its nickname was Caravelle Zero-G.

In 1989, CNES carried out a first campaign for space technology and scientific research onboard the Caravelle. The Caravelle carried out a total of 38 campaigns, i.e. 3770 parabolas or 24 hours of microgravity. One third of these campaigns were conducted by CNES.

In 1997, after three campaigns with the NASA KC-135 aircraft, Novespace acquired a new aircraft. It was an A300 registered F-BUAD, the third Airbus built by the manufacturer (in 1973) and only made test flights. It served for 18 years until 2014, when it reached its age limit. At the end of its service in 2014, it had flown more than 13,000 parabolas in 110 campaigns, including more than 30 campaigns for CNES.

In 2015, Novespace commissioned the Airbus A310 Zero-G to maintain a rhythm of 5 or 6 campaigns per year. It offers the same flight characteristics as the A300. The format of the standard flight campaigns is therefore based on the same model (3 flights of 30 parabolas).

For a complete overview of parabolic flights history in the word, refer to [21].

7.2. *An aircraft like no other*

The former "Chancellor Airbus" A310-304 (registered as "10 + 21") was delivered from aircraft manufacturer Airbus to East German airline Interflug on 24 June 1989 and was used by Interflug for East German government leaders and normal flight business until 1991. On 27 August 1991, the aircraft became the property of the German Air Force and was named "Konrad-Adenauer", after one of the Fathers of Europe and co-author of the Franco-German reconciliation.

Configured as a "VIP" aircraft; it was used for journeys and state visits by German Federal Chancellors and government ministers between 1993 and 2014. The A310 was stationed at the Cologne Bonn airport during its mission for the German Federal Ministry of Defence. Exactly 25 years after the initial handover, the "Konrad Adenauer" was handed over to its new owner, Novespace, on 24 of June 2014.

Converting the aircraft to a flying laboratory for weightless research is a symbol of Franco-German and European cooperation.

After a series of qualification flights in the summer of 2014 from the airport of Bordeaux-Mérignac, Lufthansa Technik in Hamburg overhauled the aircraft and converted it for use in parabolic flights. The certification process took place from July 2014 until Spring 2015 in agreement with the regulations of the European Aviation Safety Agency (EASA) and the French *Direction Générale de l'Aviation Civile* (DGAC).

Image 3. Crowded experimental zone during parabola. © S. Rouquette/CNES.

In excellent condition, perfectly maintained and with few flights to its credit, the aircraft, now registered as F-WNOV, passed from the status of a military aircraft yesterday to that of a laboratory aircraft today.

The aircraft was not modified in terms of airframe structural basis, wings, engine, hydraulic circuit, etc. It entirely remains in its basic configuration as parabolic flights are within the flight envelope of the aircraft. The Airbus A310 has approximately the same dimensions as the Airbus A300, except that it is shorter in length by about 5 m. However, as the seating accommodation in the Airbus A310 is slightly different from that of the Airbus A300 after modifications for parabolic flights, the cabin area and the interfaces for experiments are similar: approximately 20 m long by 5 m wide and 2.1 m high. This space is fully padded, equipped with handrails, vertical straps, seat racks, power units and light panels, allowing safe movement and scientific experiment interfaces (see Image 3 for an example of accommodation).

The Airbus A310 Zero-G has largest volume for parabolic flights in the world, in terms of passenger and experimental capacity Table 2 shows some technical characteristics of the A310 Zero-G aircraft.

The first scientific campaign took place in the April–May 2015 timeframe. The three main European space agencies CNES, ESA and DLR, which are the regular users of parabolic flights, decided to organise jointly a cooperative microgravity parabolic flight campaign to mark this beginning of a new era in microgravity and reduced gravity research. Twelve experiments, representing a mixed payload of physical and life sciences, have been conducted by investigators invited by the three agencies [2].

From May to November 2015, five more microgravity research campaigns were performed with the new Airbus A310 Zero-G: two campaigns each for ESA and CNES, and one for DLR. Research campaigns will continue at a rate of two campaigns for each of ESA and CNES per year, and one or two campaigns for DLR per year.

8. A synchronized piloting dance

Parabolic flights are performed in an aircraft that follows a flight profile alternating ascending and descending manoeuvres with intervening periods of level flight. It places the aircraft in unusual flight attitude with the pitch angle varying from 45° (nose up) to −45° (nose down), whereas for a conventional take-off it is lower than 20°. Each manoeuvre, called a parabola, put the aircraft and its occupants in free fall, giving up to 22 s of microgravity. A flight consists of a series of 30 parabolas, which represents about 10 minutes of cumulated microgravity.

Table 2. Characteristics of the Airbus A310 Zero-G.

Aircraft	Manufacturer serial number	498
	Two-engine	General Electric CF6-80
	Overall length	46.4 m
	Wingspan	43.9 m
	Fuselage diameter	5.64 m
	Total cabin volume	300 m^3
	Passenger doors	4
	Dimensions of front doors	1.80 × 1.06 m (H × W)
	Maximum mass	157 tons
	Based at	Bordeaux–Mérignac Internat. Airport, France
Experiment area	Dimensions	20 × 5 × 2.25 m (L × W × H)
	Volume	210 m^3
	Illumination	LEDs, continuous
	Accommodation	White padding on walls, floor and ceiling Nets at front and back
	Handrails	Rigid on sides, flexible on ceiling
Electrical	10 electrical panels	220 VAC, 50 Hz, (2 kVA + 3.5 kVA)
	Ground Fault Interrupt	Integrated in electrical panels
	Electrical power box	Integrated with plugs, fuse and emergency switch-off button, provided to experimenters
Mechanical	Experiment fixation	On rail tracks 503mm apart (identical to A300)
	Structural requirements	9 g/1.5 g (for/aft), 3 g (lateral), 4.2 g/7.3 g (up/down)
	Vent-line	4 ports, direct evacuation through fuselage skin
Data	Live data	3D acceleration, time reference, parabola n°, 3D position (GPS position)
	Distribution	On file post-flight

8.1. *Flight mechanics details*

An aircraft is flying considering four forces applied to its body and wings. Weight is driven by Earth gravity. Thrust is given by engines power. Drag is in the opposite direction of thrust because of the atmosphere resistance to the motion. Lift is also a consequence of air displacement around the wings that allows the aircraft to fly. Lift is oriented upward. During a stationary flight, forces equalise resulting in a straight uniform flight path.

To be in free fall, the forces must be cancelled out, except for the weight which cannot be changed.

Drag and thrust must be balanced so that their sum is zero.

The incidence will be reduced to zero by a steering action during the parabola to reduce incidence. Practically, pilot lowers the airflow incidence angle down to −3° relative to the wing profile (i.e. the air stream then comes from the upper face of the wing), where the lift force reduces to zero. The only remaining force is weight, which is the exact condition to create microgravity.

The microgravity environment is created in the Airbus A310 Zero-G flying the following manoeuvres:

- from steady horizontal flight, the aircraft climbs at 45° (pull-up) for about 20 s with accelerations between 1.8 and 2 g;
- the aircraft engine thrust is then significantly reduced for about 20 to 25 s to the point where it is only compensating for air drag (parabolic free fall);

Image 4. During the parabola. Pilots at the pitch axis (right), Roll axis (left), thrust (centre). © S. Rouquette/CNES.

Table 3. Main characteristics of a typical Zero-G parabola.

Altitude prior to the dish entry resource	6000 m
Speed prior to entering parabola resource	640 km/h (340 kt IAS)
Nose up angle at injection	45°
Parabolic injection altitude	7600 m
Parabolic injection point speed	460 km/h (250 kt IAS)
Parabola top altitude	8000 m
Parabola top speed	240 km/h (130 kt IAS)
Angle to dive at exit resource	45°
Weightlessness duration (0 g)	22 s ± 2 s
Weightlessness accuracy	±0.03 g
Weightlessness (heaviness at parabola entry/exit)	1.8 g
Total duration of parabolic manoeuvre (0 g)	74 s

- during the free fall phase, pitch angle varies from 45° nose up to 45° nose down;
- towards the end of the parabola, the aircraft is oriented in 45° nose-down attitude. It is pulled out of the trajectory and is accelerating at about 1.8 to 2 g for approximately 20 s, to come back to a steady level flight.

General flight parameters are given in Table 3.

8.2. *Three pilots in a row*

A high degree of piloting precision is required to operate a Zero G aircraft. Novespace currently has only seven highly qualified pilots who are experienced in this type of flight.

The Zero G aircraft is flown simultaneously by three pilots (Image 4). One pilot only handles the pitch (the nose-up or nose-down angle) to accurately follow the trajectory. Next to him, a second pilot handles the roll (keeping the wings horizontal) to prevent the aircraft from turning. A third pilot, seated behind them, manipulates the throttles to manage the engine power. He also monitors the flight parameters (alarms, temperatures, pressure, etc.).

To prevent the sun from bleaching out the instruments and to increase pilot concentration, the side windows of the cockpit are covered so that the pilots' view is concentrated on the central instrument panel.

In the pitch position, an additional control stick is attached to the control column for the parabolas (visible at the right of Image 4). It allows to act on the pitch axis without intervening in the roll axis. The pilot in charge of the roll has two small strings attached to the standard control column. It allows him to manage the roll without interfering with the action performed by the other pilot (the control columns of an aircraft are doubled, visible at the left of Image 4).

Accelerometers give each pilot a precise indication of the residual force along the corresponding flying axis. The main indicator is a vertical accelerometer that helps in controlling the pitch angle to maintain zero-g value.

Manoeuvres are separated by intervals of several minutes. Duration of these intervals between parabolas can be arranged prior to the flight such as to give enough time to investigators to change an experimental set-up. A typical flight lasts between two and half and three hours and includes 30 parabolas, in sets of five, with approximately two minutes intervals between parabolas and with four to six minutes between sets of parabolas. A parabalola typical profile is given in Figure 3. During the reduced gravity period, after a transitory phase of a few seconds, the residual accelerations sensed by experimental set-ups attached to the aircraft floor structure are typically in the order of 10^{-2} g, while for an experiment that is free-floated in the cabin, the levels can be improved to typically 10^{-3} g.

8.2.1. *"Pull up!"*

During the first phase, the aircraft is flying horizontally. The pilot prepares for the parabola by gradually increasing his speed to about 800 km/h, which is 640 km/h Indicated Air Speed (IAS), the maximum speed allowed for this type of aircraft.

Then, he gradually pitches the aircraft up to an angle of 45°. During this manoeuvre, known as the "pull up", gravity increases to 1.8 times the Earth's gravity level. The feeling of weight is greater. This is called hypergravity. This phase of flight lasts about 20 s.

8.2.2. *"Injection!"*

As the aircraft progressively climbs up to 45° nose up, the pilots will act together on their respective controls to place the aircraft on its ballistic trajectory. This moment is called the "injection". Practically, the pilot on the pitch axis lowers the airflow incidence down to −3° relative to the wing profile, and the pilot on the thrust axis adjust the engine power to equilibrate drag. The aircraft then follows a parabola. It is in a free fall conditions. The same applies to the passengers and instruments onboard.

While the aircraft is in full ascent, 3 pilots will act in concert on their respective controls (the stick for pitch and tilt of the wings, and the engine power control) in order to keep the aircraft on its ballistic trajectory.

An example of accelerometer data during a parabola is given in Figure 2: Example of a zero-g parabola. Horizontal axis shows duration since "injection". Parabola duration is 21.4 s. vertical axis gives remaining gravity level. Blue line indicates vertical acceleration (z axis, positive downward), green line stands for longitudinal acceleration (x axis, positive forward), red line is for roll axis (y axis, positive to the left).

8.2.3. *"Pull out!"*

About 22 s later, the aircraft is in a dive at 45° nose-down attitude. The pilot gradually straightens the aircraft. This is the end of the parabola. It is the "pull out resource". The passengers weigh 1.8 times their own weight again.

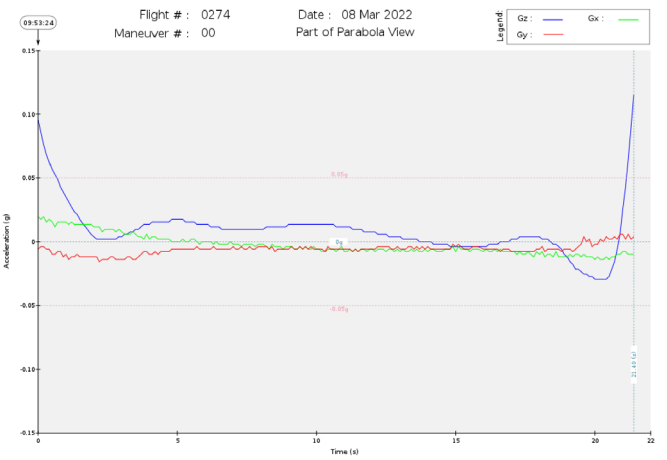

Figure 2. Example of a zero-g parabola. Horizontal axis shows duration since "injection". Parabola duration is 21.4 s. vertical axis gives remaining gravity level. Blue line indicates vertical acceleration (z axis, positive downward), green line stands for longitudinal acceleration (x axis, positive forward), red line is for roll axis (y axis, positive to the left).

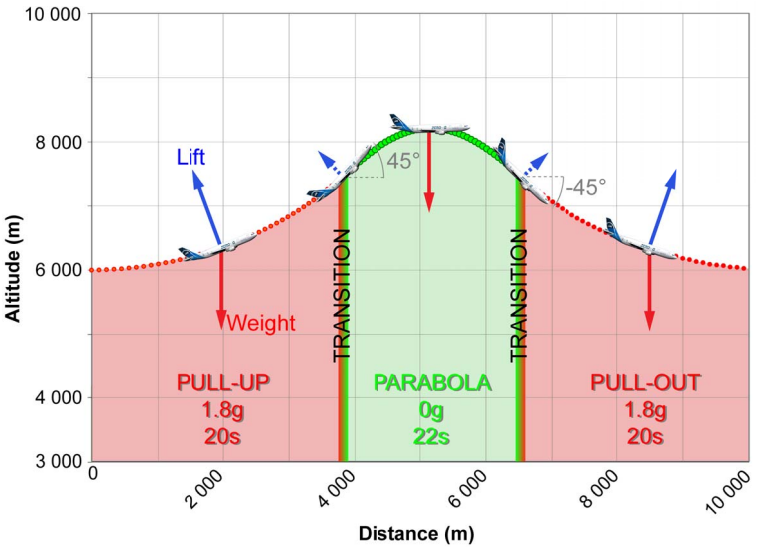

Figure 3. Parabola sequence in a distance/altitude view. Transition phases last for around 3 s. Angles depict the trajectory path relative to horizon. Actual angles of attack of the plane at injection point and pull-out are different due to wing setting angle.

8.2.4. *"Steady flight!"*

After 20 s, the aircraft returns to level flight. This is the "steady flight" phase. A two-minute delay is set between two parabolas, allowing the experimenters to prepare their experiments for the next parabola. The pilots repeat this flight sequence 30 times during the flight.

During the breaks between series, when the aircraft returns to a level flight, the pilots will execute turns, as well as for some of the experimental subjects. The researchers can take advantage of this stable flight phase to make adjustments to the experiments.

8.2.5. *After landing*

Back on the ground, researchers must record the data acquired and analyse their flight procedures. A debriefing takes place on the ground at the end of each flight. The aim is to make a collective assessment of the organisation and progress of the operations. . . .

The free fall duration is directly related to the velocity and the pitch angle at the injection. It is given by: $2 * V_i * \sin(A_i)/g$, where V_i is the velocity at injection point, A_i is the angle of trajectory relative to horizon at injection point, and g is the gravity acceleration.

The free fall duration can be improved by increasing one of these parameters. In fact, with the current aircraft (within its commercial aircraft family), the duration is already maximized with respect to the aircraft flight envelope. This aircraft will be used until at least 2030. In the future, another type of aircraft might be selected and certified. Based on its characteristics and performances, but also depending on the scientific need, parabolic flight program could evolve towards airborne means that we have to imagine tomorrow.

9. Conclusions

Since April 2015, the Airbus A310 Zero-G, the world largest airplane for reduced gravity research, is used in Europe for short duration microgravity investigations mainly by ESA, the French space agency CNES and the German Space Agency DLR. Parabolic flight campaigns are foreseen to continue at a rate of two campaigns per year for CNES and ESA and one up to two campaigns per year for DLR.

With this unique program, developed within an excellent cooperation between space agencies and Novespace, parabolic flights will continue to provide scientific and technical knowledge in the various scientific disciplines and technology fields that take advantage of the microgravity or reduced gravity. Together with drop towers, sounding rockets, the ISS and other manned and unmanned spacecraft, parabolic flights with the Airbus A310 Zero-G complete the set of flight research opportunities in reduced gravity for European scientists and researchers of other countries.

ESA website http://www.esa.int
CNES website http://www.cnes.fr
DLR website http://www.dlr.de
Novespace website http://www.novespace.fr.

Conflicts of interest

The author has no conflict of interest to declare.

References

[1] V. Pletser, S. Rouquette, U. Friedrich, J. F. Clervoy, T. Gharib, F. Gai, C. Mora, “The first European parabolic flight campaign with the Airbus A310 Zero-g”, *Microgravity Sci. Technol.* **28** (2016), p. 587-601.

[2] V. Pletser, S. Rouquette, U. Friedrich, J. F. Clervoy, T. Gharib, F. Gai, C. Mora, “European parabolic flight campaigns with Airbus A300 Zero-G: looking back at the A300 and looking forward to the A310”, *Adv. Space Res.* **56** (2015), no. 5, p. 1003-1013.

[3] B. Barry Elhadj, H. N. Yoshikawa, M. T. Fogaing, C. Kang, I. Mutabazi, “Critical modes of thermoelectric convection instabilities in a vertical slot”, *Microgravity Sci. Technol.* **33** (2021), no. 1, p. 1-9.

[4] A. Missaoui, E. Lacaze, A. Eremin, R. Stannarius, “Observation of backflow during the anihilation of topologocal defects in freely suspended smectic films”, *Crystals (2073-4352)* **11** (2021), no. 4, article no. 430.

[5] M. Noirhomme, A. Cazaubiel, E. Falcon, D. Fischer, Y. Garrabos, C. Lecoutre-Chabot, S. Mawet, E. Opsomer, F. Palencia, S. Pillitteri, N. Vandewalle, "Particle dynamics at the onset of the granular gas–liquid transition", *Phys. Rev. Lett.* **126** (2021), article no. 128002.

[6] M. Medale, D. Brutin, "Sessile drops in weightlessness: an ideal playground for challenging Young's equation", *NPJ Microgravity* **7** (2021), no. 1, p. 30-38.

[7] G. Bossis, O. Volkova, Y. Grasselli, A. Ciffreo, "The role of volume fraction and additives on the rheology of micron sized iron particles", *Front. Mater.* **6** (2019), p. 1-4.

[8] N. Mielec, M. Altorio, R. Sapam, D. Horville, D. Holleville, L. A. Sidorenkov, A. Landragin, R. Geiger, "Atom interferometry with top-hat laser beams", *Appl. Phys. Lett.* **113** (2018), article no. 161108.

[9] C. Chauveau, M. Birouk, F. Halter, I. Gökalp, "An analysis of the droplet support fiber effect on the evaporation process", *Int. J. Heat Mass Transf.* **128** (2019), p. 885-891.

[10] A. Guibaud, J.-M. Citerne, J.-L. Consalvi, J. L. Torero, O. Fujita, M. Kikuchi, P. V. Ferkul, N. Smirnov, G. Jomaas, B. Toth, S. Rouvreau, G. Legros, "Accessing the soot-related radiative heat feedback in a flame spreading in microgravity: optical designs and associated limitations", *Proc. Combust. Inst.* **38** (2021), no. 3, p. 4805-4814.

[11] P. Avan, H. Normand, F. Girauder, G. Gerenton, P. Denise, "Noninvasive in-ear monitoring of intracranial pressure during microgravity in parabolic flights", *J. Appl. Physiol.* **125** (2018), no. 2, p. 353-361.

[12] J. Bonnefoy, S. Ghislin, J. Beyrend, F. Coste, G. Calcagno, I. Lartaud, G. Gauquelin-Koch, S. Poussier, J.-P. Frippiat, N. Battista, "Gravitational experimental platform for animal models, a new platform at ESA's terrestrial facilities to study the effects of micro- and hypergravity on aquatic and rodent animal models", *Int. J. Mol. Sci.* **22** (2021), no. 6, article no. 2961.

[13] N. Boulanger, F. Buisseret, V. Dehouck, F. Dierick, O. White, "Motor strategies and adiabatic invariants: The case of rhythmic motion in parabolic flights", *Phys. Rev. E* **104** (2021), no. 2, article no. 024403.

[14] L. Bringoux, T. Macaluso, P. Sainton, L. Chomienne, F. Buloup, L. Mouchnino, M. Simoneau, J. Blouin, *Front. Physiol.* **11** (2020), article no. 377.

[15] A. Friedl-Werner, M.-L. Machado, C. Balestra, Y. Liegard, B. Philoxene, K. Brauns, A. C. Stahn, M. Hitier, S. Besnard, "Impaired attentional processing during parabolic flight", *Front. Physiol.* **12** (2021), article no. 675426.

[16] N. Goswami, O. White, A. Blaber, J. M. Evans, J. W. A. van Loon, G. Clément, "Human physiology adaptation to altered gravity environments", *Acta Astronautica* **189** (2021), p. 216-221.

[17] J. Hinkelbein, A. Ahlbäck, C. Antwerber, L. Dauth, J. DuCanto, E. Fleischhammer, C. Glatz, S. Kerkhoff, A. Mathes, T. Russomano, J. Schmitz, C. Starck, S. Thierry, T. Warnecke, "Using supraglottic airways by paramedics for airway management in analogue microgravity increases speed and success of ventilation", *Sci. Rep.* **11** (2021), no. 1, p. 1-8.

[18] A. J. H. Meskers, M. M. J. Houben, H. J. M. Pennings, G. Clément, E. L. Groen, "Underestimation of self-tilt increases in reduced gravity conditions", *J. Vestib. Res.* **31** (2021), no. 5, p. 345-352.

[19] L. Opsomer, F. Crevecoeur, J.-L. Thonnard, J. McIntyre, P. Lefèvre, "Distinct adaptation patterns between grip dynamics and arm kinematics when the body is upside-down", *J. Neurophysiol.* **125** (2021), no. 3, p. 862-874.

[20] F. Sanfedino, D. Alazard, G. Galvao-Adarme, I. Vivo-Martin, C. Chauffaut, E. Kassarian, L. Dubois, M. Rognant, H. Evain, "Autonomous navigation system for free floating experiments in parabolic flights", *IFAC-PapersOnLine* **54** (2021), no. 12, p. 61-67.

[21] F. Lehot, *Voler en apesanteur*, De Boeck Sup., 2020, ISBN 978-2-8073-2585-2.

Comptes Rendus
Mécanique
2023, Vol. 351, Special Issue S2, p. 19-40
https://doi.org/10.5802/crmeca.182

Physical Science in Microgravity within the Thematic Group Fundamental and Applied Microgravity / *Sciences physiques en microgravité au sein du GDR Micropesanteur Fondamentale et Appliquée*

Electric sampling of soot particles in spreading non-premixed flames: methodology and influence of gravity

Yutao Li[*, a], **Antoine Bordino**[b], **Augustin Guibaud**[c], **David Montero**[d], **Jean-Marie Citerne**[a], **Jean-Louis Consalvi**[e], **Jose Torero**[c] **and Guillaume Legros**[a, f]

[a] Institut Jean Le Rond d'Alembert/UMR CNRS 7190, Sorbonne Université, Paris F-75005, France

[b] Ecole Polytechnique, Palaiseau, France

[c] Department of Civil, Environmental and Geomatic Engineering, University College London, London WC1E6BT, UK

[d] Fédération de Chimie et Matériaux de Paris-Centre, Sorbonne Université, Paris F-75005, France

[e] Aix-Marseille Université, CNRS, IUSTI UMR 7343, 5 rue E. Fermi, 13013 Marseille, France

[f] CNRS-ICARE / Univ. Orléans, 1C Avenue de la Recherche Scientifique, 45071 Orléans Cedex 2, France

E-mails: yutao.li@sorbonne-universite.fr (Y. LI), antoine.bordino@polytechnique.edu (A. Bordino), a.guibaud@ucl.ac.uk (A. Guibaud), david.montero@sorbonne-universite.fr (D. Montero), jean-marie.citerne@sorbonne-universite.fr (J.-M. Citerne), jean-louis.consalvi@univ-amu.fr (J.-L. Consalvi), j.torero@ucl.ac.uk (J. Torero), guillaume.legros@sorbonne-universite.fr (G. Legros)

Abstract. Finer strategies of spacecraft fire mitigation require more experimental data related to fire detection. Fire detection systems developed on Earth rely massively on the optical detection of soot particles, which are present in the smoke. To detect the fire correctly, it is thus important to know how the optical properties of these particles are affected in reduced gravity. With different transport processes and increased residence time, soot in reduced gravity can be different from those produced at normal gravity. As their optical properties are related to their morphological properties, a better understanding about the evolution of soot particle morphology in flames under microgravity conditions is required. Within this context, a novel technique of soot sampling using electric field is applied to a spreading non-premixed flame at normal

* Corresponding author.

and micro-gravity. The soot particles sampled are observed subsequently under Transmission Electron Microscopy (TEM). Density, soot particle projected area, radius of gyration, fractal dimension, and primary particle size are extracted and the influence of gravity is investigated with the evolution of these morphological properties within the flame. Though the present study cannot be conclusive in itself, the similarity between the evolution of the optical density measured throughout the flame just before the electric perturbation required by the sampling technique and the evolution of the amount of soot deposited due to the electric perturbation along the sampling plates supports the future works that need to be devoted to further assess the consistency of the technique.

Keywords. Flame spread, Microgravity, Soot sampling, Soot morphology, Fire safety.

Funding. The authors feel grateful to the Centre National d'Etudes Spatiales (CNES) for its financial support under Contract No. 130615.

Electronic supplementary material. Supplementary material for this article is supplied as a separate archive available from the journal's website under article's URL or from the author.

Published online: 12 May 2023

1. Introduction

Fire safety is a major concern for space exploration [1]. As spaceflights transition from Low Earth Orbit (LEO) to deep space exploration, additional constraints challenge existing tools and protocols [2]. At the heart of the fire safety strategy, detection devices rely heavily on the detection of smoke produced by a fire-like diffusion flame. Discrimination from airborne dust is carried out through measurement of the scattering or ionization properties of soot particles, which are aggregates of impure carbon particles resulting from the incomplete combustion of hydrocarbons. However, little is known regarding the effect of reduced buoyancy flows on the soot particles' morphology and properties. Consequently, the investigation of smoke generated in a non-premixed flame in microgravity is crucial to prevent false alarms or, worse, the absence of alarm in a fire situation. In addition to these practical considerations, the tracking of soot particle formation, growth, and oxidation in reduced buoyancy presents fundamental benefits as these mechanisms can be captured with an elongated residence time, creating a new benchmark for numerical and theoretical models.

All existing smoke detectors on the International Space Station (ISS) today are designed and calibrated based on fire data from normal gravity experiments [3, 4]. The lack of data from microgravity experiments has led to detection accuracy difficulties. Trying to capture a fire signature as early as possible, Meyer et al. [5] analyzed particles generated in oxidative pyrolysis in microgravity and found that the particle dimensions were not significantly affected. However, this conclusion on oxidative pyrolysis contrasts with earlier findings regarding the size and morphology of soot particles produced in diffusion flames in microgravity. Due to the increase in residence time, more mature particles are retrieved and this makes the detection of fully-developed fire scenarios increasingly complex [6, 7]. Since the current smoke detectors on the ISS are based on light scattering, an investigation specific to the impact of gravity level on soot optical properties would be particularly relevant. The optimal situation is to perform straightforward measurements of soot particles using light scattering. However, microgravity soot particles suitable for investigation are difficult to generate. In addition, with space constraints in microgravity conditions, adding light scattering measurement equipment to experimental setups that produce soot particles is not easy. Therefore, studying the morphology of soot particles produced under microgravity can optimize the detection of soot particles by extracting their optical properties.

Non-intrusive optical techniques are available to investigate soot particle formation and evolution in situ without disturbing the flame. Such methods as Spectral Soot Emission (SSE) techniques [8], Laser-Induced Incandescence (LII) [9], light extinction [10], and light scattering [11] can lead to the evaluation of soot volume fraction, soot temperature, particle size, and aggregate morphology. Nevertheless, few optical techniques have been applied to flames in microgravity to study soot particle formation due to the constraints in equipment, timing, and volume. Reimann and Will [12] successfully applied the LII method to the study of soot formation in non-buoyant laminar jet diffusion flames in a drop tower experiment. Two-dimensional information on soot concentration and primary particle size in microgravity was obtained simultaneously, and the temperature field was measured by a 2-color emission pyrometer. It was shown that soot formation and oxidation change dramatically in microgravity, with the maximum flame temperature decreasing in the absence of buoyancy and the primary particle size doubling. Using another drop tower facility, Fujita and Ito [13] observed the soot agglomeration process in a jet diffusion flame using the Laser shadow method to evaluate the soot aggregates diameter and soot volume fraction. The size of soot aggregates was found to be much larger than that of a normal gravity flame, with the maximum size exceeding 100 μm. The size of soot agglomerates naturally increased with the distance from the burner outlet, following aging. It is likely that aggregates forming in such conditions can be conceived as aggregates of aggregates and show a hybrid-fractal character [14]. Such aggregates are called super-aggregates, and they exhibit multiple fractal dimensions. Considering the specificity of this soot particle morphology, there may be discrepancies between the real radiative properties of these particles and those calculated by simple, commonly used approximate light scattering models [15]. More recently, Guibaud et al. applied the implementation of the broadband modulated absorption/emission (B-MAE) technique to provide a mapping of soot temperature and volume fraction in a spreading flame during parabolic flights [16, 17]. These authors showed that the flow conditions, namely oxygen content, flow rate, and ambient pressure, affect the spreading rate and soot formation rate with dominant effects of oxygen content followed by pressure. However, this technique relies on particle size hypotheses regarding the dimensions of soot particles which the present study shows to be too limiting. All of these optical techniques are based on approximations regarding the optical properties of a soot-loaded atmosphere. Among the simplest absorption and diffusion assumptions commonly implemented, the Rayleigh approximation of the Mie theory provides simple calculations if the wavelength of the incoming light source is much larger than the particle size investigated. In typical flame conditions, the young soot particles as primary particles are near spherical with a size much smaller than the visible or near-infrared wavelength and they barely interact with each other. Therefore, they can be considered to be in the Rayleigh scattering approximation [18]. However, the mature soot particles as aggregates are usually beyond this limit in terms of dimensions and interactions, and other theories such as the Rayleigh–Debye–Gans for fractal aggregates (RDG-FA) approximation [18, 19] are better fit to the measurements. In microgravity, mature soot particles acting as microscopic fractal aggregates are more readily produced, casting doubt on the relevance of a Rayleigh approximation and supporting more elaborate assumptions. However, RDG and RDG-FA require additional information regarding the size, morphology, and fractal characteristics of the studied soot aggregates. Direct sampling of soot particles to collect data is then required to support the further development of optical diagnostics in reduced buoyancy environments.

To that end, Dobbins and Megaridis [20] implemented a thermophoretic sampling technique, now widely used to study the evolution of soot morphology and soot volume fraction in laminar diffusion flames [21–23]. In microgravity, Ku et al. [6] and Konsur et al. [24] performed the first thermophoretic sampling on a laminar diffusion flame in a drop tower experiment and analyzed the primary particle size and aggregate dimension with a Transmission Electron Microscope

(TEM). It was found that a longer residence time in microgravity enhanced soot formation and growth with an average primary particle size twice as large as that observed for soot formed at normal gravity. Following experiments aboard the space shuttle, Urban et al. [25] also performed soot sampling with the thermophoretic technique for laminar diffusion flame and outlined that soot primary particle size increases with distance from the burner, and that increasing ambient pressure tends to increase particle size. Although the results of the study using thermophoretic sampling in microgravity provide important and useful information about the morphology of soot collected in laminar diffusion flames, this sampling method is not fitted to spreading flames. The spreading flame over a solid fuel is a configuration closer to the real fire scenario. As the flame is always in movement, the thermophoretic sampling technique is difficult to apply in such a configuration. In addition, adding this sampling method requires adding quite a few additional devices, which is more difficult to implement in space-constrained microgravity experiments. Therefore, a special sampling technique is needed to study the soot particles formed by spreading flames in microgravity and to analyze their morphology.

To address this challenge, the present paper describes a novel particle sampling method that uses an electric field to sample soot particles on a brass plate both at normal and micro-gravity from a flame spreading on a cylindrical sample in an opposed-flow configuration. Introducing spatial resolution along the sample's axis, the evolution of soot particle morphology is tracked. Combining the ambitions of improving measurements from non-invasive optical diagnostics with the need to qualify the response of fire detection systems to soot particles being emitted at the trailing edge of the flame, the sampled soot particles are observed directly under a TEM and their morphological properties, namely density, particle projected area, radius of gyration, fractal dimension, and primary particles size distribution are extracted.

2. Initial observations and associated issues

Experiments have been conducted in microgravity and at normal gravity following the procedure detailed in Section 3, to highlight the effect of the gravity level on the flame from both macroscopic and microscopic perspectives. A diluted oxidizer stream consisting of 21% oxygen and 79% nitrogen flows at a rate of 150 mm/s in a combustion chamber, at an ambient pressure of 101.3kPa. Cylindrical wires, which consist of a 0.5 mm diameter Nickel-Chrome (NiCr) core coated with a 0.3 mm thick layer of Low-Density PolyEthylene (LDPE), are ignited under microgravity and normal gravity conditions, respectively. Once the flame is established, it propagates in an opposed flow configuration, as shown in Figure 1.

It can be seen that the gravity level impacts the condensed phase topology and the flame appearance at a macroscopic scale. In microgravity, the molten LDPE coating forms an axisymmetric bulb which pyrolyses at the flame leading edge upon heating from the flame (see Figure 1 (a)). At normal gravity, this bulb drips away on one side of the wire under its own weight (see Figure 1 (b)), affecting the spread rate, the pyrolysis, and breaking the symmetry of the flow to a certain extent. Furthermore, the flame is more stretched at normal gravity because of natural convection that accelerates the flow in the vicinity of the flame. In turn, this reduces the fuel residence time as compared to microgravity, according to the estimated characteristic flow time scale for the soot production in Section 4.1. This also affects soot formation, growth, oxidation, and radiative properties, and consequently changes the flame temperature and luminosity. The impact is such that the relatively slow flow conditions studied can lead to radiative quenching in microgravity, which is not observed at normal gravity.

These macroscopic observations have been documented in previous publications, using optical techniques that yield the fields of soot volume fraction and temperature. Yet, these quantitative measurements rely on a range of hypotheses regarding soot particles' dimensions and

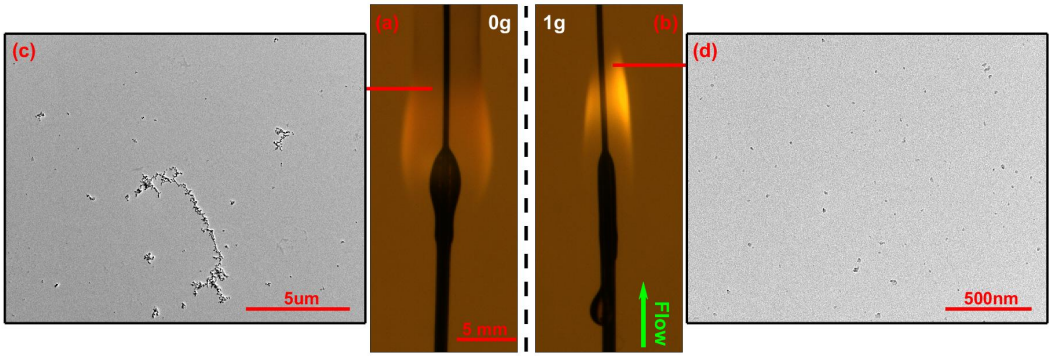

Figure 1. Illustration of the gravitational level impact on the flame appearance and the morphology of some soot particles sampled: (a)-(c) in microgravity; and (b)-(d) at normal gravity. The approximate locations of the soot sampling are represented by the end of the straight red solid lines on the imaging of the spreading flames (a) and (b). The smoking flame in microgravity (a) features large mature soot aggregates (c), that cannot be observed on the sampling (d) collected in the brighter flame at normal gravity (b).

morphology to solve the radiative transfer equation across the flame [16]. To assess the validity of these hypotheses, microscopic observations under TEM of particles sampled at the flame trailing edge are displayed for both microgravity and normal gravity in Figure 1 (c) and (d), respectively. The sampling is performed thanks to a novel methodology based on soot particle polarity, which is thoroughly described in Section 3. It can be noticed that the longer residence time in microgravity produces soot particles orders of magnitude larger than those sampled at normal gravity, and the more mature aggregates have a richer topology. This discrepancy clearly affects the quantitative results obtained with an optical setup, and also supports evidence of the need to adapt smoke detectors to the particle generated in a reduced-gravity environment.

In the following, the new sampling methodology is described and its relevance analysed before the morphological evolution of soot particles along the flame axis at both gravity levels is presented. Density, soot particle area, radius of gyration, fractal dimension, and primary soot particle are investigated as key parameters. The influence of gravity on the flame signature can then be documented using the above morphological properties.

3. Sampling with electric field

3.1. *Experimental setup*

The soot sampling method presented for the first time in this article has been designed to equip the Detection of Ignition And Mitigation Onboard for Non-Damaged Spacecrafts (DIAMONDS) rig described in detail in Ref. [26]. DIAMONDS can be handled on the ground to conduct experiments at normal gravity and, more distinctively, it can be boarded to the Novespace A310 ZeroG aircraft that operates parabolic flights to conduct experiments in reduced gravity. Each parabola provides 22 seconds of reduced gravity, aiming at zero acceleration in the referential of the aircraft with g-jitters lower than 0.05 g_0 (where $g_0 = 9.81\ m \cdot s^{-2}$).

DIAMONDS is built around a pressurized cylindrical combustion chamber with an inner diameter of 190 mm. A laminar oxidizer stream flowing parallel to the chamber's axis is established with a set oxygen content, pressure, and flow velocity within the ranges 0-21% in volume fraction, 50-150 kPa, and 0-300 mm/s, respectively. In the following, the conditions are set to 21%

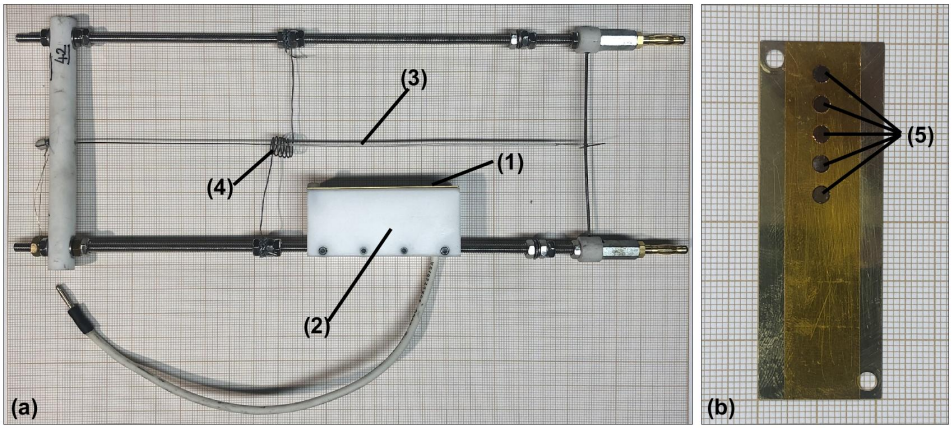

Figure 2. (a) Sample holder equipped with a brass plate (1). The brass plate is screwed to a PTFE beam (2) attached along the lower threaded rod of the sample holder. High voltage between the back of the plate and the NiCr core of the LDPE coated wire (3) that is connected to the threaded rod is supplied via a pin plug. The igniting Kanthal wire (4) can be seen; (b) Brass plate with TEM grids (5). The TEM grids are stuck to the plate with high-temperature adhesive tape.

oxygen content, 101.3 kPa and 150 mm/s. 150 mm-long NiCr-LDPE samples are attached on a sample holder along the chamber's axis, as illustrated in Figure 2 (a). Ignition, using an incandescent khantal wire rolled around the sample, can be controlled remotely once steady flow conditions are obtained to study flame spread. Depending on the position of the igniter, the flame can then spread with or against the flow. It has been reported that the flame could spread at a steady rate at both gravity levels under a wide range of counter-flow conditions [16, 17, 27, 28], while concurrent flame spread would continuously accelerate at normal gravity. As a result, this paper focuses on opposed-flow flame spread, and the igniter is located at the downstream edge of the sample.

The soot sampling technique relies on the electric field. With the help of the electric field, it is possible to manipulate the charged species in the flame. The most pronounced effect is the repeated collisions of ions with neighbouring neutral gases leading to a bulk fluid motion called ionic wind [29, 30], which has been evidenced under microgravity conditions [31]. Moreover, this conclusion was likewise verified under numerical models [32, 33]. The field of set amplitude and duration is generated between the metallic wire core, and a brass plate embedded into a PolyTetraFluoroEthylene (PTFE) beam, parallel to the wire and located 20 mm away from its axis. The boundary layer generated by the introduction of this additional element in the chamber can affect the flow downstream, but its action on the facing flame is limited. Assuming that the laminar boundary layer flow along the flat plate behaves according to the Blasius solution conditions, the thickness of the layer between the plate and the wire remains below 10 mm [34]. This is confirmed by observations of the unperturbed flame geometry, as shown in Figure 3 (a). The back of the brass plate is connected via a high voltage wire to an EMCO Q series DC high voltage generator located outside the combustion chamber. This device creates a tension up to 3 kV between the brass plate and the metallic core of the sample, which is electrically connected to the structure of the setup and acts as ground. The tension can be set for a duration prescribed by the operator. As the brass plate is charged by the generator, an electric field orthogonal to the sample's axis is generated between the brass plate, acting as the cathode, and the metallic

core, acting as the anode. The negatively charged particles of the flame caught in the field move towards the surface of the brass plate, creating an ionic wind rich in unoxidized soot particles. The particles then impact the surface of the brass plate, creating a shadow of the original flame. Similar to traditional thermophoretic sampling, the cold surface of the brass plate (compared to hot gas from the flame) serves an important purpose which is that it freezes heterogeneous reactions of the particles that are already captured. This chemical freezing action prevents changes in the soot morphology after the particles have impacted upon the cold surface [20].

The particles cannot be directly observed on the brass plate using TEM. To prevent the surface transfer and the associated degradation of the carbonaceous particles, TEM grids with a diameter of 3.05 mm are directly mounted on the central axis of the brass plate using high-temperature adhesive tape as shown in Figure 1 (b). The selected TEM grid is a copper grid with 300 square meshes covered with a film made of 5-6 nm pure carbon deposited on one side of the grid. These mesh grids have specific markers designed for quadrant location, including an asymmetrical mark in the rim and a center mark. It allows to identify their orientation at the time of the experiment and thus track the morphological evolution of soot particles at different positions along the vertical direction of the brass plate (see Figure 2 (b)). During the electric field activation, the particles are consequently deposited directly on the grids which can be detached with fine reverse action tweezers post-flight and brought to TEM for observation. Following observations from previous experiments in microgravity, five grids are regularly spaced from the top of the brass plate, with an inter-grid distance of 2mm.

Finally, all experiments are recorded by a JAI AT-140CL digital 12-bit tri-CCD camera equipped with a telecentric lens to limit the light collection to beams parallel to the optical axis. The camera images the spread at a rate of 39.06 fps on three 512x1396 pixel^2 CCD arrays, one for each of the broad green, blue, and red spectral bands. The resolution of the projected data is 72.6μm/pixel. A uniform backlighting consisting of a set of adjustable RGBW LEDs is alternately turned on and off as triggered by a pulse generator that also controls the camera acquisition. Doing so, a frame with backlighting follows one without. This strategy allows the effect of the soot sampling process on both the condensed coating and the smoke emissions to be captured.

3.2. *Sampling procedure and parameters*

To collect the soot particles produced in the flame after steady state spread conditions are reached in microgravity, sampling is performed at least 20 seconds after the hot wire ignition begins. Ignition is initiated before microgravity conditions are attained, to optimize the amount of time available for in-flight observations. Steady flame spread is defined as a situation where the flame front position progresses linearly, and the flame length and molten bulb volume are constant [35]. To capture particles from a range of positions within the flame, the electric field is generated once the flame faces the area covered by the TEM grids, which is indicated by horizontal lines on the visualization software to help the operator. Sampling onset is controlled manually because the flame spread rate varies based on the ambient condition.

The sampling sequence in microgravity is recorded in real-time by the tri-CCD camera images as shown in Figure 3 (a), (b) and (c), so the operator can track the evolution of the position of the flame relative to the brass plate. The positions of the five TEM grids are represented in yellow in the figure, and the dotted lines illustrate the upstream deformation position of LDPE, which can be assumed to correspond to the position where the solid fuel begins to pyrolyze and provide gaseous fuel.

During sampling (Figure 3 (b)), it can be noticed that the incandescent soot particles located within the flame and cold soot particles escaping from the trailing edge of the flame accelerate towards the brass plate immediately after the voltage is applied. At this point, it can be observed

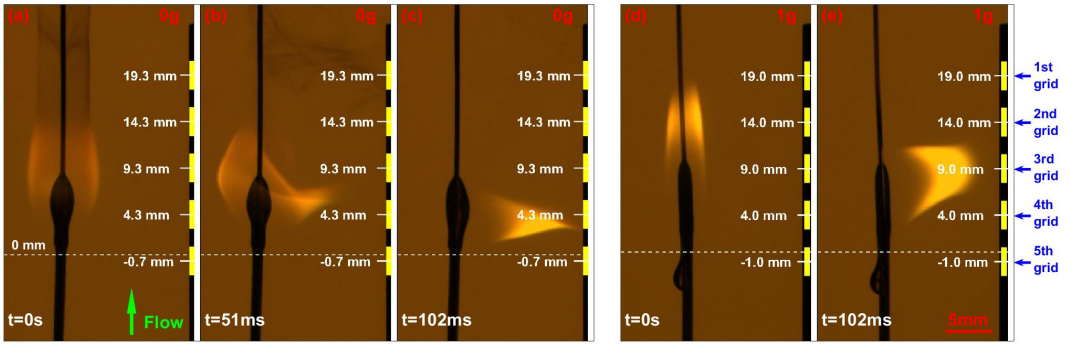

Figure 3. Sampling sequence in microgravity and normal gravity. The gravitational level is shown on the top right of the image and every TEM grid position is presented with a yellow rectangle. The horizontal dashed line indicates the upstream position of the LDPE deformation, which is set to z=0 mm (assumed to correspond to the position where the solid fuel begins to pyrolyze and provide gaseous fuel). The central position of each TEM grid along the vertical streamwise z-axis is then indicated with this origin as a reference. (a) and (d) are the last images before applying an electric field with t=0. (c) and (e) show maximal flame blending position under an electric field. (b) indicates how soot particles are moving toward the brass plate at the beginning of the sampling.

that soot particles in the gas phase move towards the nearest point on the brass plate. As such, one is inclined to anticipate that the position of the particles on the brass plate is tightly related to their initial position in the flame. As long as the electric field is sustained, the flame deforms towards the metal plate, as shown in Figure 3 (c). The flow rate appears to have a limited effect on the geometry of the flame, indicating that the ionic wind dominates the flow locally. The bright yellow aspect of the flame proves that soot particles are still generated when the voltage is on. It can be expected that soot particles produced in the presence of an electric field undergo a very different aging process compared to those collected in the initial sequence. It is also worth mentioning that the molten droplets are subjected to ionic forces and start to deform, with some spots of amorphous plastics being recorded on the TEM grids.

Voltage value and sampling duration are set in advance before each parabola flight. For effective sampling, it is necessary to ensure that sufficient soot can be collected on the TEM grids and that the quantity of soot particles is not too high to affect the subsequent TEM observation. From Figure 3 (b), it is found that at 51 ms after the application of the electric field, the soot to be sampled is still moving toward the brass plate, and the flame bends to the lowest point at 102 ms. Therefore, the sampling time should be at least 100 ms, so that the soot particles of interest have enough time to reach the brass plate. To ensure that enough soot can be sampled into the TEM grids, different sampling times of 100 ms, 300 ms, and 500 ms were investigated in microgravity under the same ambient conditions. It was observed that the soot particles on the TEM grid were already so dense at 300 ms that the amount of overlap prevented a straightforward analysis of the size and properties distribution, with more than 65% of the grid surface being covered by soot particles (versus 30% for a sampling period of 100 ms). A low sampling time of 100 ms is also preferred to minimize the amount of soot particles generated and aged in the electric field being sampled.

To minimize aging as the soot particles transit from their original location to the surface of the TEM grids, the particles should reach the brass plate as fast as possible. Three different voltage levels of 1.8 kV, 2.3 kV and 2.8 kV were carried out in microgravity with the same ambient

conditions. In the presence of a flow perpendicular to the sampling direction, the maximum bending angle of the flame was found to vary with the imposed voltage. The bending angles perpendicular to the flow direction were measured to be 18.1°, 7.1° and 4.8°, respectively. From the variation in the bending angle of the flame, it can be inferred that the flame bending is affected by both the ionic force generated by the voltage and the forced flow. The ionic force increases with the applied voltage and also increases the dominance of the ionic force against the forced flow. Meanwhile, it also appears that the particle sampling could be affected by the forced flow as particles move in the downstream region during sampling. In order to reduce this effect and let the particles reach the brass plate faster, the sampling voltage used in this paper is 2.8 kV.

At normal gravity, soot sampling relies on the same sampling parameters as in microgravity. Though there is no time constraint similar to parabolic flight, the flame cannot reach a steady state spread because of dripping. Soot sampling is then triggered when the flame passes the TEM grids to match the sampling position adopted in microgravity. As shown in Figure 3 (c) and (b), the spreading flame also bends toward the brass plat under the attracting electric field. However, due to the effect of natural buoyancy force, the bending is not as strong as in microgravity and reaches a maximum bending angle of 10.5°. The difference can be used to evaluate the force of the ionic wind and estimate the trajectory of the sampled soot particles.

The characteristic buoyancy-driven convective flow at normal gravity is provided by the momentum equation as:

$$U_{buoyancy} \approx \left(\frac{\triangle \rho}{\rho} g L \right)^{1/2} \tag{1}$$

where the density differences and the ambient density, $\triangle \rho$ and ρ respectively, can be considered to be similar [36]. At normal gravity, $g = 9.8 \mathrm{m}/s^2$ and a reported flame length $L_{f,1g} = 10.5$ mm give a buoyant flow velocity of 320 mm/s. Contrasting this value with the imposed forced flow of 150 mm/s in the combustion chamber, it can be concluded that the mixed convective flow velocity at normal gravity is then three times higher than it is in microgravity. Through the flame bending angle at different gravitational levels, it is possible to deduce the applied ionic force during the sampling. With the Boussinesq approximation, the natural buoyancy force can be determined by the following equation:

$$F_{buoyancy} = -g_0 \beta \rho_\infty (T - T_\infty) \tag{2}$$

Where T and T_∞ are the adiabatic flame temperature and the ambient temperature, respectively. With Gay-Lussac's law, the thermal expansion coefficient can be estimated as $\beta = 1/T$. As the flame bending angle is caused by forced flow, buoyant flow, and electric field, a simple force balance with the known buoyant force leads to an ionic force of $10.1 N/m^3$ during the 2.8 kV sampling.

With the same sampling voltage and duration, the sampling process at 1g is affected by natural convection, resulting in soot particles escaping from the flame to the brass plate with a different trajectory than under microgravity. Therefore, to investigate the influence of gravity levels on sooting properties, the following comparison is based on the overall evolution of different soot particle morphological properties along the flame axis, rather than a point-to-point comparison.

3.3. *TEM image acquisition*

The soot particles sampled on the TEM grids are observed under a JEOL JEM 1011 TEM, which is a tungsten hairpin 100kV electron microscope. The bright field images are acquired as tiff files on a CCD camera Gatan Orius SC 1000 A1 in 2672x4008 $pixel^2$. During observation, it is noticed

sample modification under electron beam revealed at least by soot vibration which limited the time of observation.

To follow the evolution of soot particle morphology along the wire axis, microscopic observations are performed at three positions on each grid. These three positions correspond to the central mesh and the two extreme meshes along the central axis. Since the sampled soot particles sizes fluctuate dramatically with the gravity level and the location of the observed grid position along the flame axis, the magnification of interest for the TEM observations varies accordingly from x400 to x60 000. The particles sampled at normal gravity cannot be observed at low magnification because their size is too small, while the massive soot aggregates collected in microgravity cannot be fully displayed at high magnification due to their excessive size. As a result, analyses are conducted over a range of magnifications.

In TEM, the observation range can be divided into low magnification below a x1200 magnification, and high magnification above. In the low magnification range, x400 images can show an entire mesh. It is used to verify whether the mesh has been damaged and whether the mesh is overloaded with soot particles. Also, it allows the quantitative analysis of the largest aggregates. A x1200 magnification can provide information about the aggregates that are too large to be fully visualized in the higher magnification images. At x5000 magnification, the particles generated at normal gravity begin to be clearly observed so that the images at this magnification can be applied to extract information on density, aggregate size, and certain large primary particle size, and to analyze the effects of gravity. The magnification between x5000 and x60 000 is then intended to extract information on primary particles.

4. Morphological properties analysis and discussion

As with all intrusive techniques, the samples are affected by the method used. The addition of an electric field to the flame can result in the inhibition or promotion of soot formation, and can alter the characteristics of soot deposition depending on the configuration of the experiment. Xie et al. [37] investigated the effect of direct and alternating current on soot formation for diffusion counter-current type flames. It was found that the residence time of charged soot precursors and charged soot particles in the flame could be altered by electric fields, which led to the large changes in soot formation observed in the experiments. In addition, Weinberg et al. [38] found that the electric field also modified the flow of charged species thus affecting the number of soot particles that acquired charge through the diffusion mechanism. Thus, both the size and the number of soot particles can be affected by the electric field. It is also important to consider that, if the suggestion about the cyclic participation of ions in the formation of PAHs and crystallites is correct, the ion pathway for soot formation is not excluded when soot sampling in an electric field [39, 40]. The above studies all show that the application of electric fields to flames is likely to have an impact on soot particle formation. Hence, the present soot sampling technique may affect soot formation.

In order to discriminate the investigated effect of gravity on soot particles from the unwanted effect of electric field on soot particles, the corresponding characteristic time needs to be appreciated. Different gravity level affects the natural convection and thus the soot residence time, and this characteristic flow time scale of the soot production process can be estimated as:

$$t_{res,s} \sim \frac{L_f}{u_\infty} \tag{3}$$

where u_∞ is the mixed convective flow velocity which includes the buoyant flow velocity and the forced flow velocity, and L_f is the visible flame length. The visible flame length in microgravity is $L_{f,0g}$ = 11.3 mm, hence its flow residence time for soot production is estimated as 75.5 ms.

In contrast, the residence time is 22.3 ms at normal gravity. Alternatively, it can be observed from Figure 3 (b) and (c) that the soot is moving toward the brass plate 51 ms after the activation of the electric field, while the flame is completely bent at t=102 ms. Therefore, the soot particles need to be fully collected in the time between 51 ms and 102 ms. Since the actual sampling time is not much smaller than the soot particle residence time for both gravity levels, it is likely that the electric field during the sampling process has an effect on soot particle formation for all sampling positions. As mentioned in Section 3.2, the flame is bent and pointed to the 3^{rd} (normal gravity) and 4^{th} (microgravity) grid sampling positions, respectively, due to the electric field. These positions are more severely affected by the electric field than the other sampling positions. The electric field is applied for a set time and these positions are affected by the bent flame for a longer time. As a result, the grids located at these positions are likely to collect more soot particles formed under the influence of the electric field.

As a result, the sampled soot particles are generated by the competition between the electric field force and buoyancy force, and the following discussion on the TEM measurements cannot directly conclude the sole effect between normal and micro-gravity. Since the sampling conditions (sampling voltage and sampling duration) applied at both gravity levels are the same, gravity remains the only variable in both cases. The discussion related to the effect of gravity on soot particles can still be carried out but in the context of the transient presence of the electric field. As the electric field is applied to the entire flame during the sampling process, it affects the overall generated soot particles in the flame under the same duration. To extract the influence of gravity on soot particles, it would be better to use the evolution of morphological soot particle properties along the flame axis through the comparison of the results obtained at normal and micro-gravity.

4.1. *Density of soot particle projected area*

With TEM images, the most intuitive results are the two-dimensional density of soot particles on the image and the projected area of each individual soot particle contributing to this density. As a result, the sampling procedure is designed as a trade-off between the need of statistical consistency, i.e. a significant number of particles sampled, and that of discrimination among the particles observed, i.e. a weak overlapping among the particles' projected area.

To extract the information on the density of soot particles on the image and the projected area of each individual soot particle, it is necessary to accurately identify the soot particles on the TEM images. The method of soot segmentation proposed by Sipkens and Rogak [41] is applied, which is built around a k-means clustering algorithm, and involves multiple steps of pre- and post-processing to denoise the images, enhance contrasts, and reconstruct the shapes of particles once the images have been binarized. This segmentation method has proven robust across almost all images, with a few cases of failures where the algorithm is unable to identify particles, due to the image being too noisy (which happened mainly with low magnification 1g-sampling images, where particles sizes rarely exceed a dozen pixels). In these latter cases, binarization was performed manually, while keeping the same image pre- and post-processing. In comparison, the Otsu thresholding method was much less efficient and tended to underestimate the binarization threshold, which led to aggregates being split into multiple parts. The k-means clustering tends on the other hand to overestimate this threshold a little, overestimating the area-equivalent diameter of individual aggregates by 2% on average [41]. With the generated binary masks, the density of soot particles is computed as the ratio of the total area of soot particles to the total area of the image and the individual soot particle projected area can be also obtained easily with the summation of all the detected areas for individual soot particle.

Figure 4 (a) shows the evolution of soot particles' projected area density over the grid observed by TEM as a function of the grid's position along the streamwise z-axis at both gravity levels. In

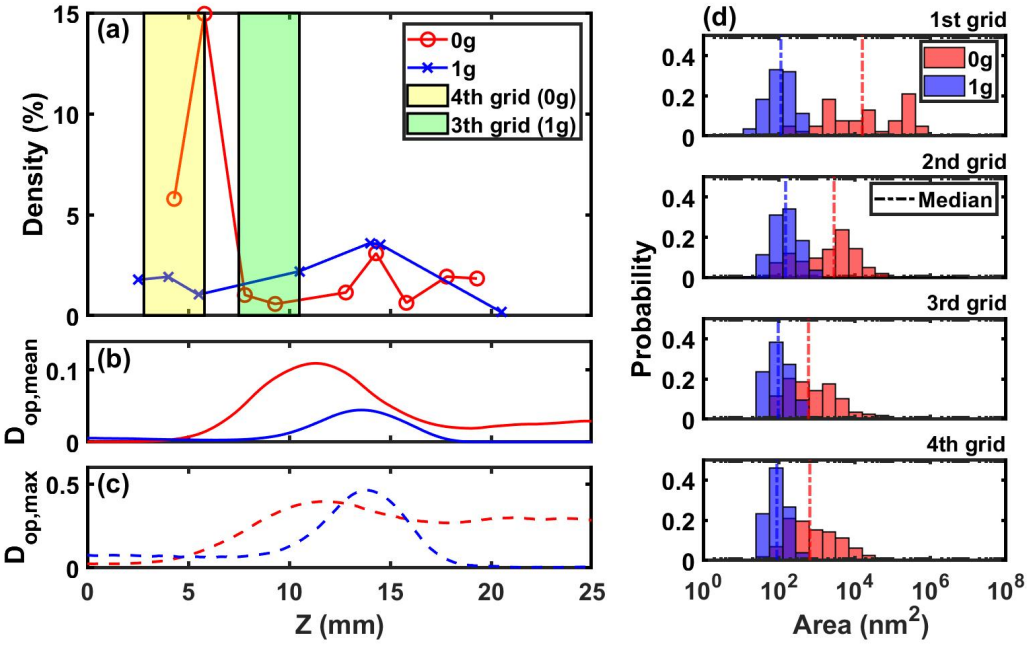

Figure 4. (a) Evolution along the streamwise coordinate z of the soot particle density over the sampling grid observed by TEM. The yellow and the green shaded areas indicate the 4th grid in microgravity and the 3rd grid in normal gravity, respectively. These areas represent the positions where the sampling is strongly impacted by the electric field. The corresponding positions of the different grids are also shown in Figure 3. (b) and (c) Evolutions with z of the mean and maximum optical density measured through the flame just before the electric perturbation and the subsequent sampling. (d) Distribution of the sampled soot particle's projected area over every grid.

microgravity, it can be noted that the density of the 4th grid is much higher than that of the other positions. From Figure 3 (c), it can be found that the flame bent and pointed to the 4th grid under the influence of the electric field. As described in Section 3.2 and at the beginning of Section 4, during the presence of the electric field, the flame points to this 4th grid position and continues to produce soot particles that affect the results, leading to a higher density of particles deposited on the grid at this sampling position. Nevertheless, the results from the other positions can still provide useful information regarding the difference in soot particles obtained at normal gravity and microgravity. Ignoring the 4th grid, i.e. the region represented by the yellow shaded region on Figure 4 (a), it is observed that the density tends to increase then decrease when analyzing meshes on the grids facing the flame from the leading to the trailing edge. Finally, the density gets constant on meshes located beyond the smoke point, i.e. the flame trailing edge.

At normal gravity, a very similar influence of the flame bent due to the electric field is also reported. This time, the flame bends and points slightly downstream, i.e. to the 3rd grid due. This downstream shift can be attributed to the buoyant force (as shown in Figure 3 (e)). Overall, the soot density increases, then decreases, and finally vanishes with the grid positions. Observing the meshes on the grid closest to the flame leading edge, the soot density is higher than that in microgravity. Interestingly, this trend is reversed on the meshes of the grid when moving towards the flame trailing edge. This observation correlates with a heavy smoke release by the non-buoyant flame which cannot be observed at normal gravity (as shown in Figures 3 (a) and (d)).

It also means that the obtained results can be projected to some extent to the evolution of the soot properties along the flame just before the electric field is applied.

To further assess this later statement, the optical density of the spreading flame can be extracted and compared with the density of the sampled soot particles on the grids. In earlier investigations, Guibaud et al [35] showed that the fields of local soot temperature and volume fraction can be extracted from the imaging of the flame shown in Figure 3. These authors especially evidenced that for the surrounding flow conditions investigated here, the flame produces a higher peak local soot volume fraction at normal gravity but a higher overall soot loading in microgravity. This is mainly attributed to the thermal expansion that makes the flame's peak diameter wider in microgravity while the residence time is enhanced [42].

The raw information processed by the diagnostics set by Guibaud et al is the field of optical density throughout the flame. Within the spectral range covered by the imaging, this optical density is highly dominated by the absorption of light by the soot particles. That being said, the relationship between the morphological features of the soot particles and their propensity to absorb light is complex and depends on many factors (e.g., the size and distribution of the soot particles). This will not be discussed in detail in this paper. However, it is of interest to assess the correlation between the distribution of optical density within the flame before it is perturbed by the electric field and the evolution with the grid's position of the soot particles' projected area density on the grid.

In brief, the integrated optical density through the flame can be extracted using the image of the flame with backlight, the following one without backlight, the image only with backlight (i.e. without any flame), and the one with only background noise (i.e. without any flame and without any backlight). On any pixel, their corresponding intensities captured by the camera are referred to as $I^{fl,on}$, $I^{fl,off}$, $I^{backlight}$, and I^{noise}, respectively. Based on the above information, the integrated optical density of the flame D_{op} can be evaluated as follows:

$$D_{op} = -log\left(\frac{I^{fl,on} - I^{fl,off}}{I^{backlight} - I^{noise}}\right) \tag{4}$$

For both flames in microgravity and at normal gravity, the data are extracted just before the electric field is set (i.e., Figure 3 (a) and Figure 3 (d), respectively). Then, the evolution along the streamwise coordinate z of the optical density $D_{op,mean}$ averaged over the flame width can be obtained (see Figure 4 (b)), together with that of the peak optical density $D_{op,max}$ (see Figure 4 (c)). Ignoring the upstream regions affected by the impact of the flame on the brass plate during the sampling process, an encouraging similarity between the evolutions of the optical density within the flame and the density of the soot particle's projected area on the grid can be observed. For the flame at normal gravity, both the maximum and mean optical densities peak around z=15 mm so does the density of the soot particles' projected area on the grid. In addition, all these densities vanish beyond the flame's trailing edge (z≈18 mm). For the flame in microgravity, the peaks of optical density (z≈1 1mm) and projected area one (z≈14 mm) are more separated. It is worth mentioning here that the sampling procedure has been primarily designed to evaluate the morphological features of soot, which in turn leads to relatively low levels of soot particles' projected area density on the grid. Consequently, it might be not curious that the trends of density displayed on the grids cannot discriminate levels of $D_{op,max}$ ranging from 0.4 at z≈11 mm to 0.35 at z>17 mm in microgravity (see Figure 4 (c)). Still, the plateau of density beyond the smoke point (z>17 mm) shown by both $D_{op,max}$ and $D_{op,mean}$ looks to be captured also on the higher two grids (z=18 mm and z=19 mm).

Finally, at the trailing end of the flame, both sets of information, i.e. the sampling and the optical ones show a crossover of the trends between both gravity levels. At z=16 mm (see Figure 4 (c)), the peak optical density gets lower at normal gravity than in microgravity.

Thus, though the present study cannot be conclusive in itself, the significant fit of the aforementioned profiles in the direction of the streamwise coordinate z supports the relevance of the sampling technique. It appears that the evolution along the streamwise coordinate z of the features extracted from the soot particles sampled on the TEM grids can represent to some extent the evolution of these features along the flame height just before the electric field perturbed the flame.

The distribution of soot particle projected area is reported to analyse the evolution of the size of soot particles along the brass plate. It can be found that the median projected area of the soot particles sampled in microgravity is much larger than that of soot particles at normal gravity at all grid locations. In addition, they follow different trends along the flame axis. In microgravity, the median value gradually shifts to larger area values from the grids facing the flame leading edge to the grids facing the flame trailing edge. In comparison, the median projected area of the soot particles remains stable at normal gravity. Since the 4^{th} grid is more severely affected by the electric field than the other sampling locations, particle area distribution is not further analysed. Starting from the 3^{rd} grid, a log-normal distribution is reported. This log-normal distribution breaks down at the 2nd grid facing the trailing edge of the flame, where a higher number of large particles is reported forming a bimodal distribution. Observing the 1^{st} grid, the largest particles are reported but no pattern can be extracted from the distribution. At normal gravity, the distribution does not vary much along the flame axis, and it always shows a log-normal type distribution. However, upon very careful observation and without considering the 3^{rd} grid position which is severely affected by the electric field, from the median and the maximum value of the particle area, it can be noticed that the particle area tends to increase first and then decrease along the direction from the leading to the trailing edge of the flame. The increase in the projected area can be explained by the formation and growth of the soot particles and the decrease is likely due to oxidation as the normal gravity flame training edge [43, 44]. According to the TEM image observation, most of the particles sampled at normal gravity are spherical primary particles, which contrasts with the fractal-like aggregates reported in microgravity. This difference is related to the discrepancy in residence time at normal and micro-gravity, allowing soot to mature in the absence of buoyant flow. According to Eq. (1), the residence time in microgravity is three times larger than at normal gravity given that the corresponding mixed convective flow is three times lower. With a shorter residence time of soot production, the soot particles sampled at normal gravity do not have enough time to become more mature under high temperatures and lack oxygen conditions as in microgravity. And these young and small soot particles are readily oxidized after contact with oxygen at the trailing edge of the flame [45], hence, it is more difficult to have smoke emission at normal gravity than in microgravity.

4.2. *Radius of gyration and fractal dimension*

The radius of gyration, R_g, and fractal dimension, D_f, are key features that drive the optical properties of soot aggregates from particle morphology [18, 46]. Intrinsically, they are parameters that can describe the overall size of the particle and its structure. R_g represents the overall size of the aggregate, while D_f informs on the chain-like (low values of D_f) or densely packed spherical (high values of D_f) internal structure [47]. Both are important properties to select the most suitable approximation for optical diagnostics and numerical simulations. Using the binarized TEM images enables the analysis of the gyration radius and fractal dimension. The radius of gyration is determined using a centroid approach, as described in [48], where R_g is computed as the root mean square distance of all the mass elements of aggregate to its center of mass.

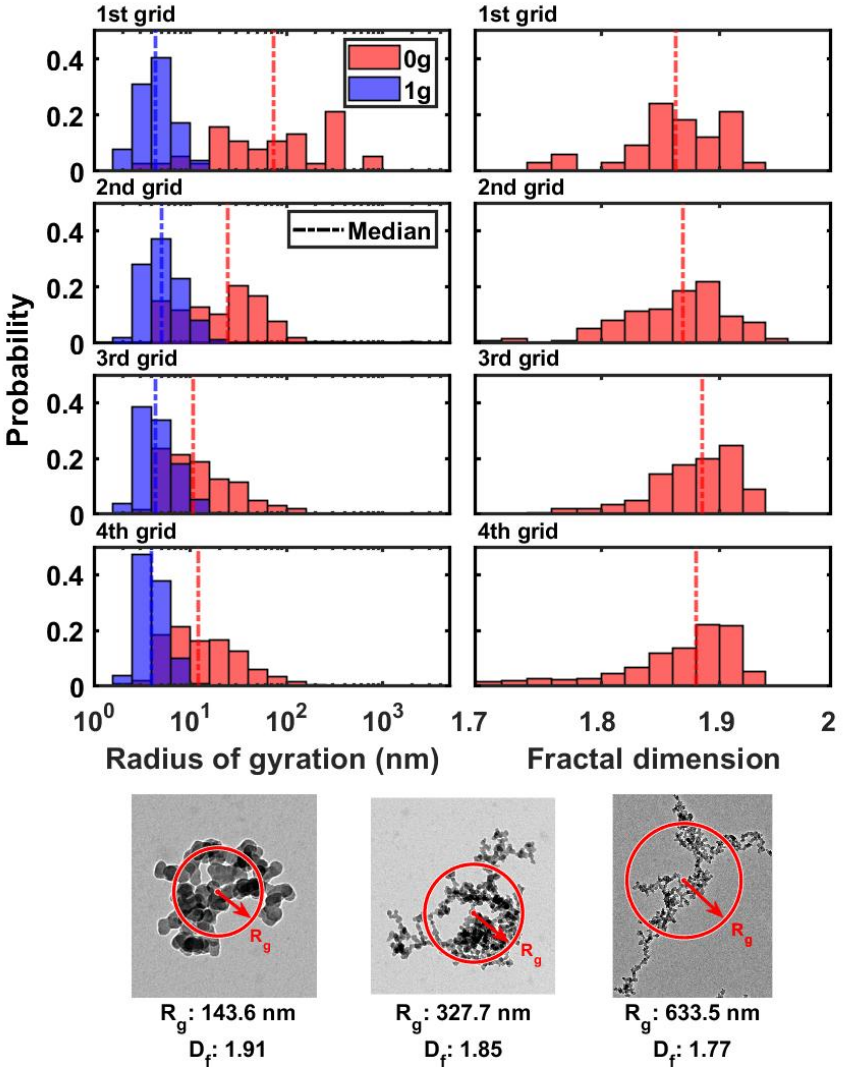

Figure 5. Evolution of radius of gyration distribution (left) and fractal dimension distribution (right), and three examples of the aggregates sampled with different radius of gyration and fractal dimension in microgravity (bottom).

The considered mass elements are the pixels composing the binary mask of the aggregate, each having a weight of 1. D_f is computed using a box counting method as:

$$D_f = -\lim_{a \to 0} \frac{ln(N(a))}{ln(a)} \tag{5}$$

where a represents the box size and $N(a)$ is the number of boxes needed to recover the aggregate binary mask. This method is limited by the resolution of TEM image [49]. If the studied soot particle takes up too few pixels, the precision drops as the range of potential box sizes is too limited. Therefore, only soot particles with a surface area above 500 pixels are analysed. According to the image resolution, particles with an area as small as 230 nm^2 can be processed.

Figure 5 shows the evolution of the radius of gyration and fractal dimension distribution along the brass plate. The radius of gyration follows the trend of the projected area distribution reported in Figure 4 at both gravity levels. R_g is much smaller at normal gravity than that in microgravity, with a median value remaining below 10 nm. In microgravity, soot particles sampled at each grid location can have much greater R_g, showcasing a median value as large if not larger than any of the particles sampled at normal gravity. Looking at particles on the 2nd grid which faces the trailing edge of the flame, the soot particles grow to a median size of 48 nm. This growth of the radius of gyration continues when processing the particles sampled on the 1st grid facing the smoke trail, which have a median size of 143 nm with a maximal size up to 695 nm. This evolution indicates that soot particles sampled in microgravity continue to mature and grow until they escape from the flame at the trailing edge of the flame. As mentioned previously, the soot particles are mainly small spherical primary particles at normal gravity. For those fractal-like soot aggregates in microgravity, the evolution of its structure can be tracked by the fractal dimension distribution. Overall, the mean value of the fractal dimension stays around 1.86 for all grids, but the distribution changes significantly. A more segregated distribution of fractal dimensions is reported in the 1st and 2nd grids, as shown in Figure 5. When following the sampling locations on the brass plate from the leading to the trailing edge of the flame, the median tends to move towards smaller fractal dimensions, which means that more particles transition to the chain-like branched aggregate. It is worth mentioning that the soot particles in the 4th grid, which are more severely affected by the electric field than the other sampling positions, display a different morphological structure and their distribution is more dispersed than on the other grids.

4.3. *Primary particle size distribution*

The purpose of the primary particle study is to identify the evolution of the primary particle size along the flame axis. Therefore, this necessarily leads to the development of a specific segmentation algorithm, which aims at identifying a majority of the primary particles. This allowed for faster treatment of a higher number of aggregates, which provided a good statistical correction to compensate for the missing particles.

This semi-automated method used three different features to segment primary particles. First, it makes use of the Circular Hough Transform (CHT) based algorithm, applied to the previously generated binary masks (as shown in Figure 6 (b)), to identify the particles on the contour of the aggregate (yellow circles on Figure 6 (a)). Then, the color gradients of the image are calculated to map all of the uniformly shaded areas of the aggregate which likely correspond to one primary particle (as shown in Figure 6 (c)). The center of each region is then computed and fed to the Center-Selected Edge Scoring (CSES) algorithm [50] which tries and fits a circle on the TEM image at this approximate location (blue circles in Figure 6 (a)). Finally, an entropy filter is applied to the image to highlight highly-textured areas (as shown in Figure 6 (d)), which are locations where a high number of overlapping particles is likely to be found, and the CSES algorithm is once again applied in this area to identify the primary particles (red circles on Figure 6 (a)).

This method is controlled by a set of operator-defined image-wide parameters, as experience showed that the optimal control parameters are the same for all aggregates in one TEM image. These parameters are:

- The particle radius range has to be adjusted when moving along the flame to accommodate for the evolution of soot maturity.
- The binarization threshold for both the gradient map and the entropy-filtered image mainly depends on the contrast and the overall quality of the image.

This method has given satisfying results on all images, both in microgravity and normal gravity, even though the gradient and entropy features require the aggregate to have a certain size to

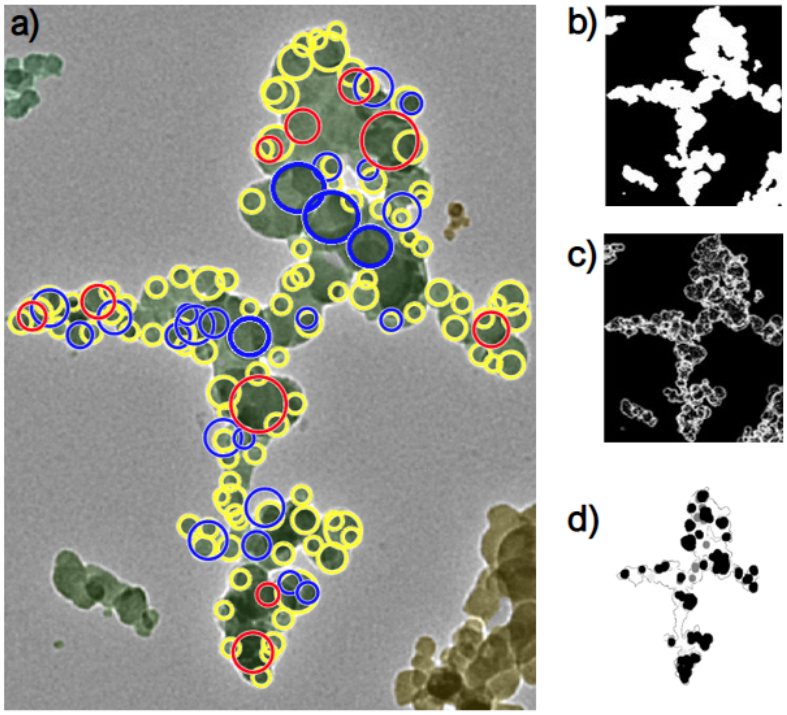

Figure 6. Primary particle segmentation process on one aggregate using three different features: (a) result of the primary particle segmentation, (b) binarization, (c) gradient map, and (d) entropy filtering.

be truly efficient. The number of segmented primary particles was at least 70% of the number of particles identified using an equivalent fully-manual method. The main limitations lie in the difficulty for the CSES algorithm to tell apart particles that overlap with a high number of others and to identify particles in large uniformly-shaded areas. Moreover, as it can be seen in Figure 6, a very small number of the drawn circles are erroneous, which requires manual cleaning. However, their influence on the overall measurements is negligible due to their statistically small number, and this problem is therefore a reasonable concession considering the great gain in efficiency of the method.

Figure 7 shows the evolution of the primary soot particle radius distribution along the flame axis at both gravity levels. Overall, the primary particles at normal gravity are smaller than those in microgravity and they are less than 10nm. This proximity to the radius of gyration of particles at normal gravity highlights the fact that the soot particles probed at normal gravity barely aggregate. Moving away from the grids closer to the flame leading edge, the primary particle size distribution at normal gravity shifts from a power-law to a log-normal type distribution and their size tends to increase first (2^{nd} grid) and then decrease slightly (1^{st} grid). In the beginning, the power-law type distribution is due to the particles nucleating and growing a radius between 2-4 nm [51]. As these particles continue to grow in the flame, their radius continues to grow to between 6-8 nm. At the grid position corresponding to the trailing edge of the flame, the distribution of soot primary particles is slightly skewed towards smaller particles because of the oxidation. In microgravity, the overall evolution of primary particle size distribution is very different from that in normal gravity and is more dispersed. The log-normal type distribution dominates from the 3^{rd} grid position onward. The primary soot particle radius distribution on the

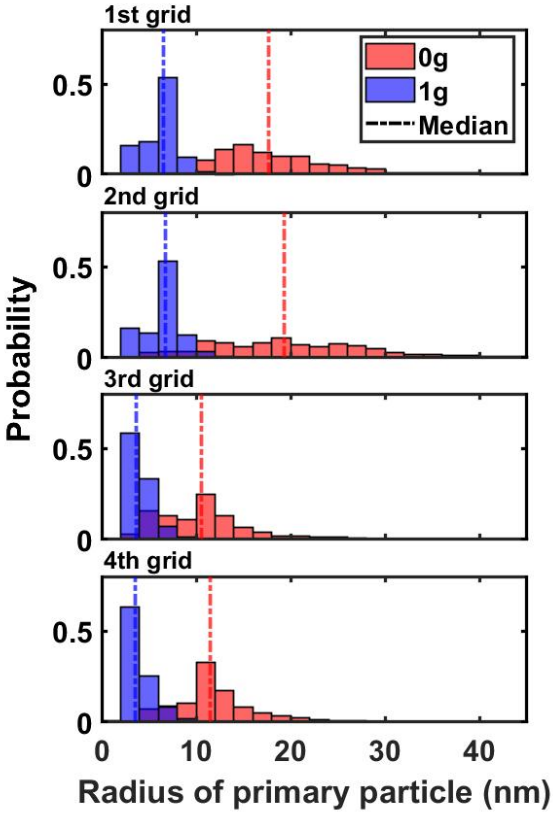

Figure 7. Evolution of primary particle radius distribution in microgravity and at normal gravity.

1st and 2nd grids facing the smoke-point transition are highly dispersed and the median particle size is larger than that on the 3rd and 4th grids facing the flame. However, a reduction in the median size of primary soot particles occurs between the 2nd and 1st grids, which is assumed to happen due to the oxidation process.

Going back to the investigation on optical approximations, the following size parameters need to be evaluated [18]:

$$x_p = \pi * d_{pp}/\lambda \tag{6}$$

where d_{pp} is the diameter of the primary particle and λ is the studied wavelength. It is commonly admitted that a value of x_p below 0.3 justifies the use of the Rayleigh limit of the Mie theory. In addition, another factor to be taken into account is the dispersion of the primary particle size, as the polydispersity of primary particles has been shown to play a significant effect on the radiative properties of soot [52–54]. Basically, the distribution of primary particle radius has a standard deviation between 15% and 25% of its mean value, which can be largely uniform depending on the particle size [55]. As has been emphasized previously, soot particles sampled using the sampling method presented in this paper are potentially affected to some extent by the electric field. Therefore, it is difficult to process soot particle morphological characteristics presented in this paper as absolute dimensions to validate any numerical model or the optical diagnostic method. However, the ambition of the present work is not to develop a new configuration that

could be supported by numerical endeavours trying to capture the complex action of the electric field on the spreading flame. Instead, the objective is to provide clues regarding how particle dimensions and morphology are affected by the absence of buoyant flow in a steady spread configuration. According to the primary particle radius obtained in the present work, the largest primary particle radius does not exceed 10nm at normal gravity, resulting in a $x_p < 0.3$ for the visible or near-infrared wavelength ($\lambda > 500$ nm). Yet, it can reach a maximum of 40 nm in microgravity, corresponding to an x_p of 0.5, as part of massive aggregates of a size similar to the wavelength of visible light. As such, it is reasonable to assume that individual primary particles approximate Rayleigh scattered particles at normal gravity but that this assumption fails in microgravity [55]. Yet, the standard deviation of the primary soot particle sampled at normal gravity for each grid is above 25% of its mean primary particle radius, raising questions about the impact of polydispersity on the measurements. In microgravity, the same standard deviation is higher than 30% of the mean value of radius for all the sampling positions, even reaching 51% at the 2nd grid. Hence, it could be anticipated that both its primary particle size and polydispersity pose a greater challenge than the case at normal gravity to estimate the optical properties [19].

5. Conclusion

The novel technique of soot sampling using an attracting electric field is applied to the flame spreading in an opposed flow over the LDPE coating of NiCr both at normal and microgravity. The main parameters of the sampling technique are the voltage applied and the time it is applied. Following the analysis, a shorter sampling time together with a higher sampling voltage lead to an appreciated trade-off between the need for visual discrimination among soot particles observed and the statistical consistency of the features extracted. The differences between microgravity and normal gravity sampling are identified as the experimental setup is operated at both gravity levels.

The sampled soot particles are observed under TEM. If the sampled soot particles are potentially affected by the electric field, keeping the sampling parameters constant under varying gravity field allows a relative investigation on the effect of buoyant flow on particles distributions. The effect of gravity on soot formation is explored by comparing the evolution of soot density, particle area, radius of gyration, fractal dimension and radius of primary particle at different locations of sampling grids located along the flame axis. In microgravity, the density of soot particles on grids facing the leading edge of the flame is lower than at normal gravity. Interestingly, this trend is reversed on grids facing the trailing edge of the flame, which correlates with a heavier smoke release reported for non-buoyant flames. Overall, soot particles sampled in microgravity are larger than those collected at normal gravity. In addition, the distributions of soot particle characteristics are different at both gravity levels: if a clear central peak can be identified at normal gravity, the distribution tends to be more complex in mircrogravity where increased dispersion is reported in the grids closer to the flame trailing edge. According to the TEM images, the soot particles sampled in microgravity show up as fractal-like aggregates while they are mainly spherical primary soot particles at normal gravity. The evolution of the soot aggregate structure in microgravity was tracked by its fractal dimension. According to the evolution of fractal dimension, the closer to the trailing edge of the flame, the more the soot tends to grow as chain-like branched aggregate. Looking then at the large and polydisperse primary particles sampled in microgravity, the limitation on the optical assumptions behind detection strategies of smoke detectors is highlighted. In contrast, particles sampled at normal gravity fall into the assumptions relevant to the Rayleigh limit of the Mie theory, as commonly implemented.

The present image-processing technique has potential for optimization, and further the 3-dimensional soot morphological properties could be obtained by electron tomography [56].

In addition, contrasting the present results with observations from other non-invasive experimental techniques [57,58] or results from steady spread numerical simulations [27,59] will refine the understanding of the effect of gravity on soot formation in spreading flames.

Conflicts of interest

The authors declare no competing financial interest.

Acknowledgments

The authors feel grateful to the Centre National d'Etudes Spatiales (CNES) for its financial support under Contract No. 130615. And the JEM1011 Microscope is part of FCMat, The Federation of Chemistry and Materials of Paris-Center (Sorbonne Université).

Supplementary data

Two videos of soot sampling in microgravity and at normal gravity, an original TEM image, and its results of primary particle size are provided as supplementary data.

References

[1] C. National Research, *Recapturing a Future for Space Exploration: Life and Physical Sciences Research for a New Era*, National Academies Press, 2011.

[2] A. Guibaud, G. Legros, J.-L. Consalvi, J. Torero, "Fire safety in spacecraft: Past incidents and Deep Space challenges", *Acta Astronaut.* **195** (2022), p. 344-354.

[3] R. Bukowski, G. W. Mulholland, *Smoke detector design and smoke properties. Volume 13*, National Bureau of Standards technical note, vol. 973, Department of Commerce, National Bureau of Standards, National Engineering Laboratory, Center for Fire Research, 1978.

[4] R. Bukowski, R. Peacock, J. Averill, T. Cleary, N. Bryner, P. Reneke, "Performance of Home Smoke Alarms, Analysis of the Response of Several Available Technologies in Residential Fire Settings", Tech. Report Technical Note (NIST TN) - 1455, National Institute of Standards and Technology, Gaithersburg, M.D., 2003.

[5] M. E. Meyer, D. L. Urban, G. W. Mulholland, V. Bryg, Z.-G. Yuan, G. A. Ruff, T. Cleary, J. Yang, "Evaluation of spacecraft smoke detector performance in the low-gravity environment", *Fire Saf. J.* **98** (2018), p. 74-81.

[6] J. C. Ku, D. W. Griffin, P. S. Greenberg, J. Roma, "Buoyancy-Induced Differences in Soot Morphology", *Combust. Flame* **102** (1995), no. 1, p. 216-218.

[7] H. Ito, O. Fujita, K. Ito, "Agglomeration of soot particles in diffusion flames under microgravity", *Combust. Flame* **99** (1994), no. 2, p. 363-370.

[8] M. Y. Choi, A. Hamins, G. W. Mulholland, T. Kashiwagi, "Simultaneous optical measurement of soot volume fraction and temperature in premixed flames", *Combust. Flame* **99** (1994), no. 1, p. 174-186.

[9] H. A. Michelsen, C. Schulz, G. J. Smallwood, S. Will, "Laser-induced incandescence: Particulate diagnostics for combustion, atmospheric, and industrial applications", *Prog. Energy Combust. Sci.* **51** (2015), p. 2-48.

[10] M. Y. Choi, G. W. Mulholland, A. Hamins, T. Kashiwagi, "Comparisons of the soot volume fraction using gravimetric and light extinction techniques", *Combust. Flame* **102** (1995), no. 1-2, p. 161-169.

[11] C. M. Sorensen, "Light Scattering by Fractal Aggregates: A Review", *Aerosol Sci. Technol.* **35** (2001), no. 2, p. 648-687.

[12] J. Reimann, S. Will, "Optical diagnostics on sooting laminar diffusion flames in microgravity", *Microgravity Sci. Technol.* **16** (2005), no. 1, p. 333-337.

[13] O. Fujita, K. Ito, "Observation of soot agglomeration process with aid of thermophoretic force in a microgravity jet diffusion flame", *Exp. Therm. Fluid Sci.* **26** (2002), no. 2-4, p. 305-311.

[14] W. Kim, C. M. Sorensen, D. Fry, A. Chakrabarti, "Soot aggregates, superaggregates and gel-like networks in laminar diffusion flames", *J. Aerosol Sci.* **37** (2006), no. 3, p. 386-401.

[15] R. Ceolato, L. Paulien, J. B. Maughan, C. M. Sorensen, M. J. Berg, "Radiative properties of soot fractal superaggregates including backscattering and depolarization", *J. Quant. Spectrosc. Radiat. Transfer* **247** (2020), article no. 106940.

[16] A. Guibaud, J.-M. Citerne, J.-L. Consalvi, G. Legros, "On the effects of opposed flow conditions on non-buoyant flames spreading over polyethylene-coated wires - Part 1: spread rate and soot production", *Combust. Flame* **221** (2020), p. 530-543.
[17] A. Guibaud, J.-M. Citerne, J.-L. Consalvi, G. Legros, "On the effects of opposed flow conditions on non-buoyant flames spreading over polyethylene-coated wires - Part 2: soot oxidation quenching and smoke release", *Combust. Flame* **221** (2020), p. 544-551.
[18] Ü. Ö. Köylü, G. M. Faeth, "Radiative Properties of Flame-Generated Soot", *J. Heat Transfer* **115** (1993), no. 2, p. 409-417.
[19] T. L. Farias, Ü. Ö. Köylü, M. d. G. Carvalho, "Range of validity of the Rayleigh—Debye-–Gans theory for optics of fractal aggregates", *Appl. Opt.* **35** (1996), no. 33, p. 6560-6567.
[20] R. A. Dobbins, C. M. Megaridis, "Morphology of flame-generated soot as determined by thermophoretic sampling", *Langmuir* **3** (1987), no. 2, p. 254-259.
[21] Ü. Ö. Köylü, C. S. McEnally, D. E. Rosner, L. D. Pfefferle, "Simultaneous measurements of soot volume fraction and particle size/microstructure in flames using a thermophoretic sampling technique", *Combust. Flame* **110** (1997), no. 4, p. 494-507.
[22] M. Kholghy, M. Saffaripour, C. Yip, M. J. Thomson, "The evolution of soot morphology in a laminar coflow diffusion flame of a surrogate for Jet A-1", *Combust. Flame* **160** (2013), no. 10, p. 2119-2130.
[23] M. L. Botero, N. Eaves, J. A. H. Dreyer, Y. Sheng, J. Akroyd, W. Yang, M. Kraft, "Experimental and numerical study of the evolution of soot primary particles in a diffusion flame", *Proc. Combust. Inst.* **37** (2019), no. 2, p. 2047-2055.
[24] B. Konsur, C. M. Megaridis, D. W. Griffin, "Fuel preheat effects on soot-field structure in laminar gas jet diffusion flames burning in 0-g and 1-g", *Combust. Flame* **116** (1999), no. 3, p. 334-347.
[25] D. L. Urban, Z.-G. Yuan, P. B. Sunderland, G. T. Linteris, J. E. Voss, K.-C. Lin, Z. Dai, K. Sun, G. M. Faeth, "Structure and soot properties of nonbuoyant ethylene/air laminar jet diffusion flames", *AIAA J.* **36** (1998), no. 8, p. 1346-1360.
[26] J.-M. Citerne, H. Dutilleul, K. Kizawa, M. Nagachi, O. Fujita, M. Kikuchi, G. Jomaas, S. Rouvreau, J. L. Torero, G. Legros, "Fire safety in space - Investigating flame spread interaction over wires", *Acta Astronaut.* **126** (2016), p. 500-509.
[27] A. Guibaud, J.-M. Citerne, J.-L. Consalvi, G. Legros, "Pressure Effects on the Soot Production and Radiative Heat Transfer of Non-Buoyant Laminar Diffusion Flames Spreading in Opposed Flow over Insulated Wires", *Combust. Flame* **222** (2020), p. 383-391.
[28] J.-L. Consalvi, A. Guibaud, A. Coimbra, J.-M. Citerne, G. Legros, "Effects of oxygen depletion on soot production, emission and radiative heat transfer in opposed-flow flame spreading over insulated wire in microgravity", *Combust. Flame* **230** (2021), article no. 111447.
[29] J. Lawton, "Electrical aspects of combustion", *Clarenton* (1969).
[30] S. Karnani, D. Dunn-Rankin, "Detailed characterization of DC electric field effects on small non-premixed flames", *Combust. Flame* **162** (2015), no. 7, p. 2865-2872.
[31] F. B. Carleton, F. J. Weinberg, "Electric field-induced flame convection in the absence of gravity", *Nature* **330** (1987), no. 6149, p. 635-636.
[32] M. Belhi, P. Domingo, P. Vervisch, "Direct numerical simulation of the effect of an electric field on flame stability", *Combust. Flame* **157** (2010), no. 12, p. 2286-2297.
[33] J. Hu, B. Rivin, E. Sher, "The effect of an electric field on the shape of co-flowing and candle-type methane–air flames", *Exp. Therm. Fluid Sci.* **21** (2000), no. 1-3, p. 124-133.
[34] H. Schlichting, J. Kestin, *Boundary layer theory*, vol. 121, Springer, 1961.
[35] A. Guibaud, J.-M. Citerne, J.-L. Consalvi, O. Fujita, J. L. Torero, G. Legros, "Experimental evaluation of flame radiative feedback: methodology and application to opposed flame spread over coated wires in microgravity", *Fire Technol.* **56** (2020), no. 1, p. 185-207.
[36] K. R. Sacksteder, "The implication of experimentally controlled gravitational accelerations for combustion science", *Proc. Combust. Inst.* **23** (1991), no. 1, p. 1589-1596.
[37] L. Xie, T. Kishi, M. Kono, "Investigation on the effect of electric fields on soot formation and flame structure of diffusion flames", *Proc. Combust. Inst.* **24** (1992), no. 1, p. 1059-1066.
[38] P. J. Mayo, F. J. Weinberg, "On the size, charge and number-rate of formation of carbon particles in flames subjected to electric fields", *Proc. R. Soc. Lond., Ser. A* **319** (1970), no. 1538, p. 351-371.
[39] A. B. Fialkov, "Investigations on ions in flames", *Prog. Energy Combust. Sci.* **23** (1997), no. 5-6, p. 399-528.
[40] H. F. Calcote, D. B. Olson, D. G. Keil, "Are ions important in soot formation?", *Energy Fuels* **2** (1988), no. 4, p. 494-504.
[41] T. A. Sipkens, S. N. Rogak, "Technical note: Using k-means to identify soot aggregates in transmission electron microscopy images", *J. Aerosol Sci.* **152** (2021), article no. 105699.
[42] G. Legros, A. Fuentes, S. Rouvreau, P. Joulain, B. Porterie, J. L. Torero, "Transport mechanisms controlling soot production inside a non-buoyant laminar diffusion flame", *Proc. Combust. Inst.* **32** (2009), no. 2, p. 2461-2470.
[43] Z. Li, L. Qiu, X. Cheng, Y. Li, H. Wu, "The evolution of soot morphology and nanostructure in laminar diffusion flame of surrogate fuels for diesel", *Fuel* **211** (2018), p. 517-528.

[44] M. L. Botero, Y. Sheng, J. Akroyd, J. Martin, J. A. H. Dreyer, W. Yang, M. Kraft, "Internal structure of soot particles in a diffusion flame", *Carbon* **141** (2019), p. 635-642.

[45] B. R. Stanmore, J.-F. Brilhac, P. Gilot, "The oxidation of soot: a review of experiments, mechanisms and models", *Carbon* **39** (2001), no. 15, p. 2247-2268.

[46] Ü. Ö. Köylü, G. M. Faeth, "Optical Properties of Soot in Buoyant Laminar Diffusion Flames", *J. Heat Transfer* **116** (1994), no. 4, p. 971-979.

[47] L. Liu, M. I. Mishchenko, W. P. Arnott, "A study of radiative properties of fractal soot aggregates using the superposition T-matrix method", *J. Quant. Spectrosc. Radiat. Transfer* **109** (2008), no. 15, p. 2656-2663.

[48] M. Altenhoff, S. Aßmann, C. Teige, F. J. T. Huber, S. Will, "An optimized evaluation strategy for a comprehensive morphological soot nanoparticle aggregate characterization by electron microscopy", *J. Aerosol Sci.* **139** (2020), article no. 105470.

[49] D. Lottin, D. Ferry, J.-M. Gay, D. Delhaye, F.-X. Ouf, "On methods determining the fractal dimension of combustion aerosols and particleclusters", *J. Aerosol Sci.* **58** (2013), p. 41-49.

[50] P. M. Anderson, H. Guo, P. B. Sunderland, "Repeatability and reproducibility of TEM soot primary particle size measurements and comparison of automated methods", *J. Aerosol Sci.* **114** (2017), p. 317-X326.

[51] B. Zhao, Z. Yang, J. Wang, M. V. Johnston, H. Wang, "Analysis of soot nanoparticles in a laminar premixed ethylene flame by scanning mobility particle sizer", *Aerosol Sci. Technol.* **37** (2003), no. 8, p. 611-620.

[52] G. Bushell, R. Amal, J. Raper, "The effect of polydispersity in primary particle size on measurement of the fractal dimension of aggregates", *Part. Part. Syst. Charact.* **15** (1998), no. 1, p. 3-8.

[53] J. Y. Yin, L. H. Liu, "Influence of complex component and particle polydispersity on radiative properties of soot aggregate in atmosphere", *J. Quant. Spectrosc. Radiat. Transfer* **111** (2010), no. 14, p. 2115-2126.

[54] N. Doner, F. Liu, "Impact of morphology on the radiative properties of fractal soot aggregates", *J. Quant. Spectrosc. Radiat. Transfer* **187** (2017), p. 10-19.

[55] Ü. Ö. Köylü, G. M. Faeth, T. L. Farias, M. d. G. Carvalho, "Fractal and projected structure properties of soot aggregates", *Combust. Flame* **100** (1995), no. 4, p. 621-633.

[56] K. Adachi, S. H. Chung, H. Friedrich, P. R. Buseck, "Fractal parameters of individual soot particles determined using electron tomography: Implications for optical properties", *J. Geophys. Res. Atmos.* **112** (2007), no. D14.

[57] A. Guibaud, J.-M. Citerne, J. M. Orlac'h, O. Fujita, J.-L. Consalvi, J. L. Torero, G. Legros, "Broadband modulated absorption/emission technique to probe sooting flames: Implementation, validation, and limitations", *Proc. Combust. Inst.* **37** (2019), no. 3, p. 3959-3966.

[58] J.-B. Renard, M. Francis, E. Hadamcik, D. Daugeron, B. Couté, B. Gaubicher, M. Jeannot, "Scattering properties of sands. 2. Results for sands from different origins", *Appl. Opt.* **49** (2010), no. 18, p. 3552-3559.

[59] A. Guibaud, J.-L. Consalvi, J. M. Orlac'h, J.-M. Citerne, G. Legros, "Soot production and radiative heat transfer in opposed flame spread over a polyethylene insulated wire in microgravity", *Fire Technol.* **56** (2020), no. 1, p. 287-314.

Comptes Rendus
Mécanique
2023, Vol. 351, Special Issue S2, p. 41-56
https://doi.org/10.5802/crmeca.174

Physical Science in Microgravity within the Thematic Group Fundamental and Applied Microgravity / *Sciences physiques en microgravité au sein du GDR Micropesanteur Fondamentale et Appliquée*

Investigation of cellular instabilities and local extinction for two-phase flames under microgravity conditions

Deniz Kaya Eyice *, [a, b, c], **Fabien Halter** [a, b], **Ahmet Yozgatlıgil** [c], **İskender Gökalp** [a, c] **and Christian Chauveau** [a]

[a] CNRS-INSIS, Institut de Combustion, Aérothermique, Réactivité et Environnement, Orléans, 45071, France

[b] Université d'Orléans, Orléans, 45100, France

[c] Department of Mechanical Engineering, Middle East Technical University, Ankara, 06800, Turkey

E-mails: deniz.kaya@cnrs-orleans.fr (D. Kaya Eyice), fabien.halter@cnrs-orleans.fr (F. Halter), ahmety@metu.edu.tr (A. Yozgatlıgil), iskender.gokalp@cnrs-orleans.fr (İ. Gökalp), christian.chauveau@cnrs-orleans.fr (C. Chauveau)

Abstract. The initial mechanism of cellular instabilities on the flame surface was investigated experimentally. Firstly, mono-dispersed ethanol droplets were created via the Wilson cloud principle in a spherical combustion chamber, and aerosol ethanol/air flame propagation was tracked under microgravity conditions. Schlieren images revealed that at the beginning of the cellular structure formation, dark spots formed linking to the signal loss in a density gradient. This phenomenon is assumed to be local extinction and quenching on the flame front due to either liquid droplets' presence or evaporation. To further investigate the observed phenomenon, stagnation flame experiments were performed for rich propane/air gaseous flames with isolated ethanol droplet injection. The evidence for the local extinction on the flame surface due to droplet passage was found via the Chemiluminescence method. The intrinsic instabilities were found to be triggered by the droplets in cases where the flame cannot recover its initial state.

Keywords. Two-phase combustion, cellular instabilities, local extinction, droplet-flame interaction, flame morphology, laminar flames.

Funding. The first author is supported by French Government Cotutelle Scholarship for her joint PhD studies between METU & Université d'Orléans and TÜBİTAK BİDEB 2211-C Scholarship.

Published online: 6 April 2023

* Corresponding author.

1. Introduction

Spray combustion occurs in various combustion applications, i.e., internal combustion engines, gas turbine combustion, liquid-fueled rockets, and burners. In these applications, strong spray/combustion interactions occur in the combustion chamber resulting in higher flame propagation speeds and flame instabilities compared to the gaseous flame at the same conditions [1–5].

Many experimental, theoretical, and numerical studies have been conducted to characterize the evaporation and combustion of droplets and their effects on a gaseous flame in different configurations. One of these configurations includes the presence of mono-sized and monodispersed droplet clouds due to the resemblance of spray combustion. Burgoyne and Cohen conducted the first study on mono-dispersed liquid aerosol flame with tetralin having 7-55 μm droplet size. [1]. They concluded that a brush-like flame structure was observed for the droplets larger than 10 μm. Mizutani and Nakjima reported that small kerosene droplets increased the burning velocity of propane more for lean flames than rich flames [2]. Hayashi and Kumagai used the Wilson cloud chamber method [6] to generate mono-sized droplets in a stagnant mixture [7, 8]. They created ethanol droplets with nearly 7 and 20 μm mean droplet sizes and reported that cellular flames were observed under microgravity at rich conditions for sufficiently large diameters. At the same time, the burning velocity increased under lean conditions. Atzler and co-workers also studied possible mechanisms of flame instabilities for iso-octane aerosol flames [9]. Their findings resulted in the observation of cellular instabilities with an increase in flame surface area and burning rate due to the change in the local equivalence ratio. Lawes et al. reported similar observations under microgravity conditions for iso-octane droplets [10]. Bradley et al. also observed flame surface wrinkling resulted in Darrieus–Landau and thermodiffusive instabilities due to the presence of large alcohol droplets, which may enter the reaction zone and significantly increase the fuel mass flux [11]. Thimothée et al. demonstrated that the gaseous ethanol-air flame was stable and smooth, as well as the aerosol flame with ethanol droplets fully vaporized in the pre-heating zone [12]. They also suggested a possible mechanism leading to the instabilities, including the heat sink phenomenon due to the heat taken by the droplet for vaporization from the flame field using water droplets as an inert medium [13]. They also correlated the topology of instabilities with the evaporation characteristics at different conditions under microgravity [14]. Renoux and co-workers extended the investigation under similar conditions by reporting a stability envelope for rich ethanol aerosol flames [15]. Spray-induced instabilities resulted from the perturbations on the flame front via surface area increase due to droplet passage.

Many studies mentioned above focused on the effect of liquid droplets on the flame propagation speed and morphology experimentally. In order to foresee the initiation of the change in flame parameters and structure, heat sink and local extinction phenomena are studied by many researchers for the interaction of the droplet and flame. Greenberg and co-workers theoretically predicted the onset of instabilities due to the heat loss from the flame zone for the evaporation of droplets via linear stability analysis [16, 17]. They reported that for richer conditions, droplets caused an increase in surface area and burning velocity while creating a heat sink, resulting in cellular structures [18]. They also developed an approach to understand how the amount of liquid fuel and the latent heat of vaporization affected the onset of instabilities causing flame extinction [19]. Han and co-workers also theoretically studied the sensitivity of spherical flame propagation and ignition to the finite rate of evaporation [20, 21]. They concluded that the flame structure was affected by droplet evaporation only by the heat absorbed for rich conditions. In contrast, local equivalence ratio change also had an impact on lean conditions. Recently, Li et al. reported the effects of heat loss from the flame to droplet for evaporation and Lewis number on

laminar planar flame propagation under droplet mists [22]. It was observed that for highly evaporative droplets, the flame propagation speed was decreased due to the heat sink on the flame zone [23]. Finally, numerical studies were performed by Nicoli and co-workers by performing DNS simulations of flame propagation in the presence of water droplets [24] and compared with microgravity experiments [25]. For larger droplet inter-distance, they reported the quenching in the flame zone due to the presence of water droplets, leading to the observation of Darrieus–Landau instabilities.

In the previous studies, the evidence of cellular instabilities caused by the presence of droplets was reported under microgravity conditions for aerosol ethanol flames via several optical diagnostics [12–15, 25–28]. However, there are very few experimental studies of the single droplet effect on the flame instabilities. In this study, the analogy between the aerosol flame and gaseous flame with a single droplet is investigated in order to understand the local extinction phenomenon resulting in flame instabilities. First, a qualitative analysis is performed from Schlieren images obtained in a zero-g environment at well-known and repeated conditions, reported by Renoux and co-workers [15], for spherically-expanding rich aerosol ethanol/air flames. Then, from the observation of the formation of local sinks and holes at the beginning of the cellular structures, the evidence of the local extinction phenomenon is investigated for rich propane/air gaseous stagnation flames at ground conditions with an isolated ethanol droplet injection.

2. Experimental

2.1. *Microgravity experiments: Spherically-expanding aerosol flame*

Microgravity experiments were performed during the parabolic flights of CNES Airbus A310 ZERO-G flight with aerosol spherical chamber configuration, given in Figure 1 (a), in order to observe cellular instabilities on the flame front due to the presence of droplets.

The experimental setup consists of two pressure-release-type chambers; an inner combustion chamber with 1 L volume and an outer high-pressure chamber with 11 L volume. The inner and outer chambers were filled with a premixed mixture and nitrogen for each experiment, respectively. There are eight evacuation valves inside the combustion chamber to evacuate the pressurized gases to the high-pressure chamber during the combustion to prevent the sudden release of pressure in the combustion chamber thanks to the high volume ratio between outer and inner chambers.

At the beginning of each set of experiments, the inner chamber was vacuumed and then filled with dry air and evaporated fuel via mass flow meters at the desired equivalence ratio and initial pressure. The amount of liquid fuel is adjusted with a liquid pump. Then, the fuel was fed to the preheater before feeding to the combustion chamber.

The fuel aerosol was created via the Wilson cloud chamber principle [29] by decreasing the pressure in the combustion chamber with the connection to an 0.5 L expansion vessel, leading to a temperature drop and finally, the condensation of the fuel. Thanks to the zero-g environment, mono-sized, uniformly distributed droplets could be maintained systematically inside the combustion chamber without settling to the bottom of the chamber. Then, the heterogeneous mixture was ignited via tungsten electrodes at the chamber's center. The distance between droplets, number of droplets, and droplet size was controlled by thermodynamic parameters such as initial pressure, $P_i = P_{ignition} + \Delta P$, equivalence ratio, ϕ, pressure drop, ΔP and duration of pressure drop, reported in Table 1 below. More details on the principle of aerosol creation can be found in the previous studies [12–15, 25–28].

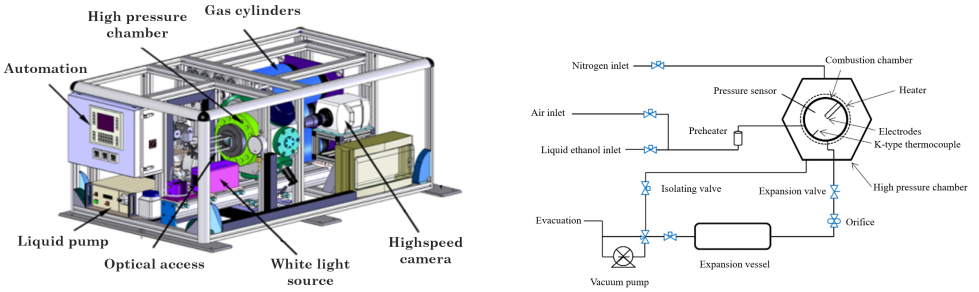

(a) (b)

Figure 1. (a) Experimental setup with Schlieren configuration. (b) The schematic of the aerosol chamber (AC).

The experimental configuration is presented in Figure 1. The combustion chamber was coupled with a laser-driven white light source (Energetiq LDLS 170 nm-2100 nm) and a high-speed camera, Phantom v1210 equipped with Nikon AF Micro-NIKKOR 105 mm lens. For imaging, 10,000 frames/s rate was used.

Experiments were performed with ethanol, C_2H_5OH as fuel and dry air (80% N_2, 20% O_2) at the conditions presented in Table 1 below. These conditions have been repeated in the previous studies by Renoux et al. [15, 26], and the characterization of the liquid phase has been done via several optical diagnostics. Therefore, the same droplet properties are assumed to be valid for this study.

Table 1. Experimental conditions performed in the aerosol chamber (AC) for spherically-expanding aerosol C_2H_5OH/air flames.

Condition	$P_{ignition}$ (MPa)	ϕ	ΔP (MPa)	$T_{ignition}$ (K)	a_{mean} (mm)	SMD (μm)	δ_L (mm)	Le_{eff}
AC-1	0.25	1.2	0.15	337	0.527±0.05	9.8±0.9	0.21	1.12
AC-2	0.33	1.3	0.12	341	0.596±0.05	8.3±0.9	0.19	1.10
AC-3	0.33	1.4	0.12	341	0.538±0.05	8.7±0.9	0.24	1.04
AC-4	0.30	1.1	0.20	339	0.497±0.05	9.9±0.9	0.18	1.19
AC-5	0.30	1.2	0.20	339	0.502±0.05	9.9±0.9	0.21	1.08
AC-6	0.35	1.0	0.25	335	0.468±0.05	9.6±0.9	0.18	1.31

2.1.1. *Optical diagnostics*

Schlieren technique was used to visualize the flame morphology for microgravity experiments. Two pairs of aligned transparent windows achieve optical access for the chamber. Two spherical lenses were replaced on the back and front of the chamber so that the light could penetrate as a sheet. In order to track the cellular structure, the distance between lenses was adjusted so that the darkness would be at the minimum level. Before the high-speed camera, a pinhole with a diameter of 0.7 mm was placed to focus the light.

During the parabolic flight, the pinhole was too sensitive to the changes in gravitational acceleration, and the opening was moved while g was changing. This situation caused unwanted darkness and visualization loss at several experimental conditions. Therefore, Schlieren images

are only used to obtain qualitative interpretations for the formation mechanisms of instabilities for the sake of certainty.

2.2. *Ground experiments: Stagnation flame*

Ground experiments were performed with a stagnation burner, given in Figure 2 (a), to observe the local extinction phenomenon due to the droplet passage through the flame front. Flame stabilization was achieved thanks to N_2 co-flow and the presence of an upper stagnation plate located 25 mm away from the burner outlet. A premixed mixture of air and fuel was fed to the system, and the mixture was ignited with an external igniter in the region between the stagnation plate and the burner outlet. Monodispersed isolated ethanol droplets with around 50 μm diameter were generated by a piezoelectric injector (Microdrop Technologies MDK-140). The frequency of the droplet injection was adjusted accordingly so there could not be any coagulations and close-distance droplets generated. The droplets were injected perpendicularly to the flame zone through a needle in which premixed gases carry them. The schematic of the stagnation burner is given in Figure 2 (a). Details of the stagnation flame burner can also be found in other studies [30], [26].

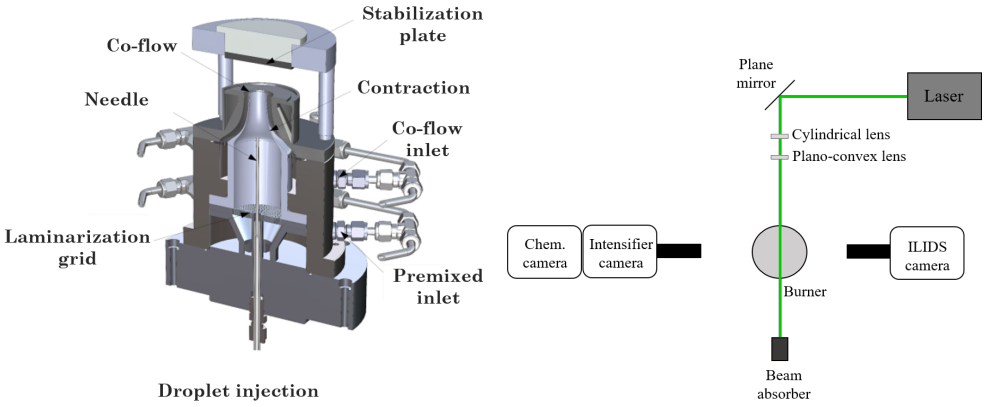

(a) (b)

Figure 2. (a) The schematic of the stagnation burner (SB) [31]. (b) Experimental configuration with ILIDS and Chemiluminescence.

Experimental configuration is represented in Figure 2 (b). The stagnation burner was coupled with a laser device, Coherent Verdi emitting at 532 nm, and a 2D laser sheet was created from a continuous laser beam with the help of one semi-cylindrical divergent lens (f2 = -25 mm) and one plano-convex lens (f2 = 500 mm). Two high-speed cameras, in addition to an intensifier, were used for visualization. The first camera, Phantom v1210 equipped with Sigma APO Macro 180 mm lens at the maximum opening, was utilized to measure the initial droplet size via ILIDS (Interferometric Laser Imaging for Droplet Sizing). A second camera, Phantom v1611 equipped with Sigma APO Macro 180 mm lens at the maximum opening, 38 mm extension system and 1:1 2x magnifier, was coupled with La Vision High-Speed IRO with 90 μs gate, in order to observe the changes in the flame front due to the droplet passage via Chemiluminescence. The cameras for ILIDS and Chemiluminescence had the same frame rate of 10,000 images per second. The camera acquisition sequence was triggered by a common trigger signal to align both cameras

and the intensifier in the time frame. 13.7 μm/px and 27.3 μm/px resolutions were obtained for Chemiluminescence and ILIDS cameras, respectively.

In this part of the study, experiments were performed with ethanol droplet as the liquid fuel and C_3H_8/air premixed gaseous flames at fuel-rich conditions, reported in Table 2 below.

Table 2. Experimental conditions performed in the stagnation burner (SB) for C_3H_8/air premixed stagnation flames with an ethanol droplet.

Condition	ϕ	d_0 (μm)	δ_L (mm)	Le_{eff}
SB-1	1.4	48.5	0.61	1.14
SB-2	1.3	51.9	0.46	1.18
SB-3	1.2	58.9	0.40	1.24
SB-4	1.1	55.4	0.39	1.31

2.2.1. *Optical diagnostics and image processing*

Interferometric Laser Imaging for Droplet Sizing (ILIDS) is utilized to obtain the initial droplet size. The high-speed camera used for ILIDS allows a good temporal resolution for the evolution of the droplet size by defocusing and capturing the interference fringe pattern of the droplet at each frame. By providing a high laser power, it is possible to increase the detection of fringes even if the droplet size is minimal since the ILIDS method is based on the reflected and the refracted rays visible on the droplet surface. In this study, 6 Watts laser power was used, enough to detect the droplet before reaching the flame zone. The number of fringes is computed for an individual droplet based on Discrete Fourier Transform (DFT) on the five vertical sections of the fringe pattern. With the help of peak intensities in Fourier space, the fringes is detected and computed. The fringe pattern for a droplet before reaching the flame zone is illustrated in Figure 3.

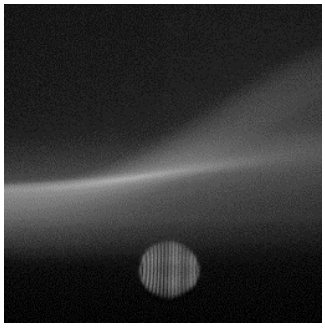

Figure 3. ILIDS image illustrating the droplet with 59 μm diameter injected to the flame front.

The droplet diameter based on the number of fringes is then calculated from the following relation [15];

$$d = N_{fringe}\frac{2\lambda}{\alpha}\left[cos(\theta/2) + \frac{m\,sin(\theta/2)}{\sqrt{m^2 - 2\,m\,cos(\theta/2) + 1}}\right]^{-1} \quad (1)$$

where d is the particle diameter, N_{fringe} is the number of fringes on the droplet, θ is the scattering angle (here, 90°), α is the collecting angle, λ is the laser wavelength (here, 532 nm) and m is the refractive index of the droplet. In this configuration, 3.46 μm/fringe resolution is obtained.

In order to observe the structural changes in the flame front, ILIDS is coupled with the flame luminosity measurements, Chemiluminescence. Direct measurement of the luminosity, which corresponds to the CO_2 radiation, is performed instead of using special band filters. It is known that with Chemiluminescence measurement, the integral signal along the sight of the line is captured, making it hard to observe small surface changes. The fuel was selected as propane and the high luminosity of propane can be captured by an intensifier with a low noise ratio so that the surface modifications can be captured during the post-processing of images. Chemiluminescence image of C_3H_8/air flame at ϕ =1.3 is given in Figure 4.

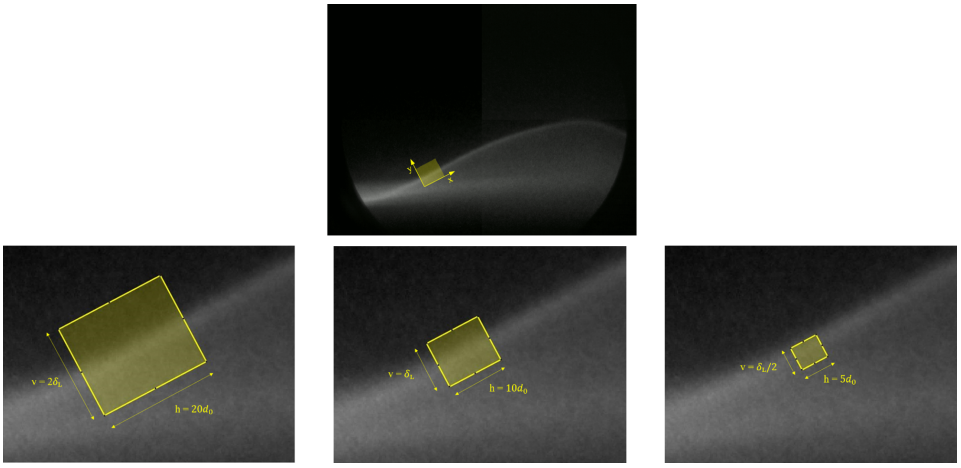

Figure 4. Chemiluminescence image of C_3H_8/air flame at ϕ =1.3 with the region of interest (yellow) having different sizes depending on the flame thickness and initial droplet size.

The local extinction phenomenon is investigated from Chemiluminescence images by creating a region of interest (ROI) in the droplet passage zone, as seen from Figure 4. The dimensions of the ROI are adjusted so that the horizontal distance is 20, 10, and 5 times the initial droplet size, d_0 and the vertical distance is 2, 1, and 0.5 times the flame thickness, δ_L. The ROI is also rotated by 28° to capture the signal loss from the perpendicular region to the flame. Two approaches are followed for region selection:

(1) The position of the ROI is kept constant at each frame.
(2) The position of the ROI is updated at each frame by changing its center according to the flame position. The flame position is updated for each image by calculating the position of the maximum intensity along a perpendicular line to the flame (y-axis) due to the fact that the flame oscillates slightly during the experiments. Then, the ROI is moved along the y-axis so that its center is aligned with the flame along the x-axis.

After positioning the ROI, the integral of the signal is computed for this region at each frame since it is expected to see a decrease in the signal when the droplet passes the flame zone. This phenomenon is also known as the local extinction phenomenon.

3. Results and Discussions

3.1. *Cellular instabilities on aerosol flame*

Renoux et al. performed the same experimental conditions, given in Table 1, with Mie scattering to determine the droplet position and inter-distance, with ILIDS to compute the droplet size and

with Shadowgraphy and Chemiluminescence to observe the flame morphology [15]. In this study, the morphology of the flame was determined via Schlieren method. In Figure 5, the comparison between Shadowgraphy, Chemiluminescence, and Schlieren images at the same condition are given. From these images, it can be interpreted that aerosol creation is successfully achieved, and the droplets are observed inside the combustion chamber without settling under a zero-g environment. While during the experiments of Renoux and co-workers (Figure 5 (a) and (b), homogeneous distribution of the droplets is observed, Schlieren image indicates that most of the droplets are near the top right corner of the chamber. This can be explained due to the movement of the plane, resulting in the movement of the droplets towards this side. Still, cellular structures can easily be observed under the reported conditions for qualitative interpretations.

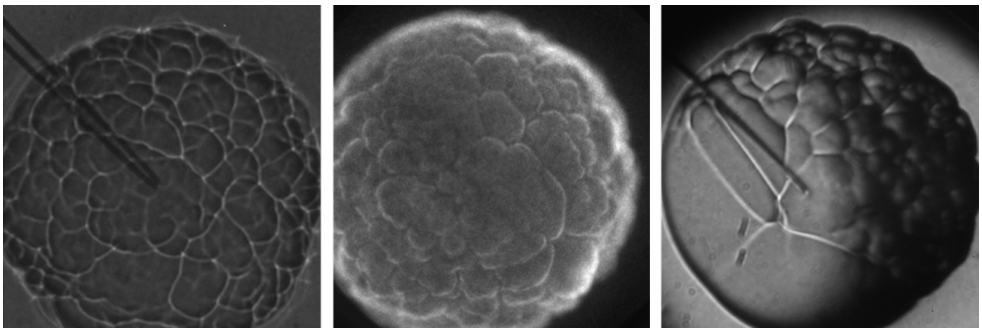

(a) (b) (c)

Figure 5. Comparison of (a) Shadowgraphy [15], (b) CH* Chemiluminescence [15] and (c) Schlieren images of equivalent flames and at a radius of 13.5 mm (aerosol ethanol/air flame at AC-1).

It is obviously seen that Shadowgraphy provides the clearest images for cell size detection. Renoux and co-workers reported the cell size distribution and stability envelope based on these images. However, as it is seen in Figure 5 (c), cell sizes are hard to detect with Schlieren method due to the sensitivity of the pinhole to the changes in gravitational acceleration during parabolic flight, resulting in shadows and darkness with a fixed position at the certain zones of the combustion chamber. Nevertheless, Schlieren method provides an additional information for the initiation of these cells, as it is the measurement of the first derivative of the flame field. In Figure 6, snapshots of the propagating flame can be seen in time for the condition of AC-1.

By focusing the wrinkles, first, the dark spots are observed, as in t=8.1 ms, indicating the loss of signal in the density gradient of the flame. Then, the extension of the flame surface can be seen as a lighter zone corresponding to the cellular cell formation. The dark spots and signal loss at the initiation of instabilities can be interpreted as the local hole structures due to the passage of liquid droplets and quenching in the flame zone, leading to the formation of the edges of cells. The same mechanism is observed for all performed conditions.

As pointed out in Renoux and co-worker's results, the droplets only act as a trigger on the development of the instabilities due to the fact that the wavenumbers related to droplet inter-distance are higher than the mode wavenumbers [15]. These instabilities then lead to intrinsic instabilities on gaseous flame. Therefore, it can be interpreted that the droplets act as obstacles that absorb heat from the flame zone for evaporation and cause local extinction on the flame surface by changing the flame properties locally.

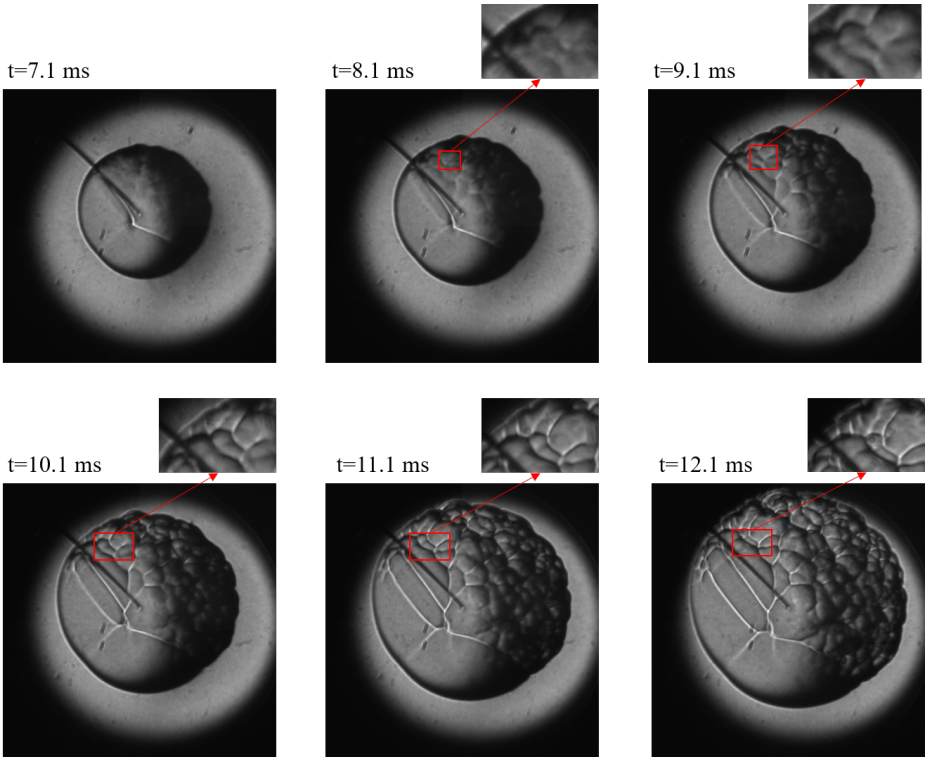

Figure 6. Formation of instabilities on the flame surface due to the presence of droplets (aerosol ethanol/air flame at AC-1).

3.2. *Local extinction due to droplet passage on stagnation flame*

The stagnation flame configuration with an isolated droplet injection is found to be very suitable for simplifying the physics and understanding the local extinction phenomenon deeply. These experiments were performed with a propane/air gaseous flame due to its high luminosity. Moreover, the Lewis number is slightly higher than the unity for rich propane/air flames, which tend to be prone to cellularities induced both by hydrodynamic and thermo-diffusive instabilities. Therefore, these flames are chosen to be good candidates for sensitivity to droplet passage. It is worth mentioning that the amount of premixed gas fed from the droplet injection tube was increased to create a flame surface with a little bump in order to increase the possibility of capturing the decrease in signal at the droplet injection point. It was done due to the fact that the camera captures the signal from the flame as a line integral of signals. Hence, if the signal is distributed to more areas, it will be easier to distinguish any change in a specific region. Since the curvature is negligible, the flame surface is still treated as flat.

The evaporation of an isolated ethanol droplet was investigated previously under premixed methane/air flame conditions, and it is found that 50 μm diameter is high enough to cross the flame front under elevated temperatures, regardless of the gas composition [30]. Hence, the droplet passage through the flame field and its effects on the flame structure can properly be observed under the fixed conditions, reported in Table 2. Additionally, Chemiluminescence experiments also showed that for fuel-rich propane/air flames, a perturbation occurs on the flame surface after the droplet passage. This perturbation, first, propagates with an increasing amplitude and then vanishes towards the edge of the flame. However, unlike spherically-expanding flames

at the similar flame conditions, the stagnation flames preserve its stable structure after a certain time from the droplet passage.

First, the decrease in collected signal from the flame surface when the droplet passes is computed. In order to achieve this, the summation of pixel values inside a specified region is calculated with two different approaches; with a constant position region of interest, given in Figure 7 and with an adaptive region of interest along with the flame position, shown in Figure 8 for ϕ=1.4 with d_0=48.5 μm. Although the decrease in the signal can be detected with both approaches, it is hard to distinguish from the former one due to the fact that the flame is oscillating during the experiment. Therefore, the adaptive approach is more suitable for capturing the percentage signal loss during the droplet passage since the baseline can be drawn to the flame position. For the adaptive ROI calculations, the total signal amount is normalized so that all cases can be compared.

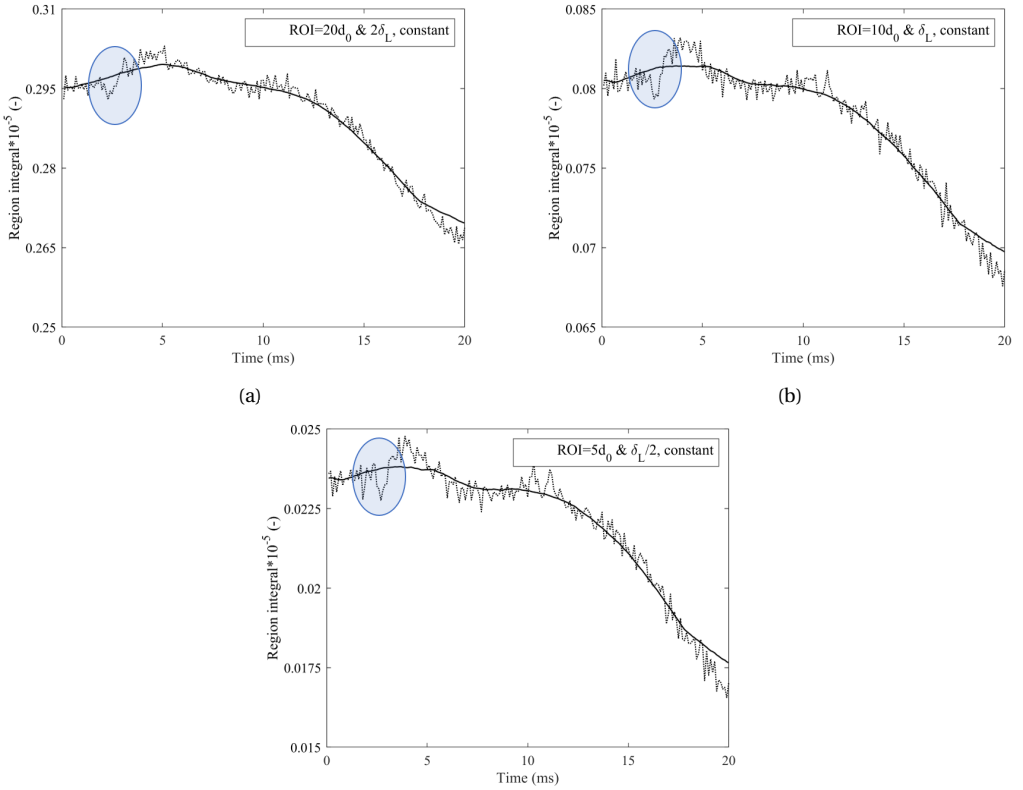

Figure 7. Change in integral of signal due to droplet passage (d_0=48.5 μm) at SB-1 with constant position ROI.

As it can be seen from Figure 8, the decrease in signal is observed between 2 to 6.6 ms, and the flame is recovered after the droplet passage. The decrease in the signal can directly be related to the droplet-flame interaction, where the droplet losses its mass due to evaporation. Since the fuel-rich cases do not contain excess oxygen in the flame zone, the droplet will not be oxidized. Hence, as the droplet takes heat from the flame, the luminosity and reactivity of the flame will decrease. For the droplet having 48.5 μm initial diameter, this time takes 1.7 ms. The recovery time takes almost 4.9 ms, which also depends on flame properties and the droplet's initial diameter and evaporation constant. The normalized signal values indicate 12%, 13.2%, and

15% signal loss during the droplet passage for the corresponding region of interest dimensions. For the smallest ROI, post-processing needs to be more accurate on the first detection of droplet passage so that the interaction point needs to be in the middle of the rectangle. Since the signal loss is very high compared to leaner cases, it can easily be determined for ϕ=1.4, which has the highest luminosity among the reported cases.

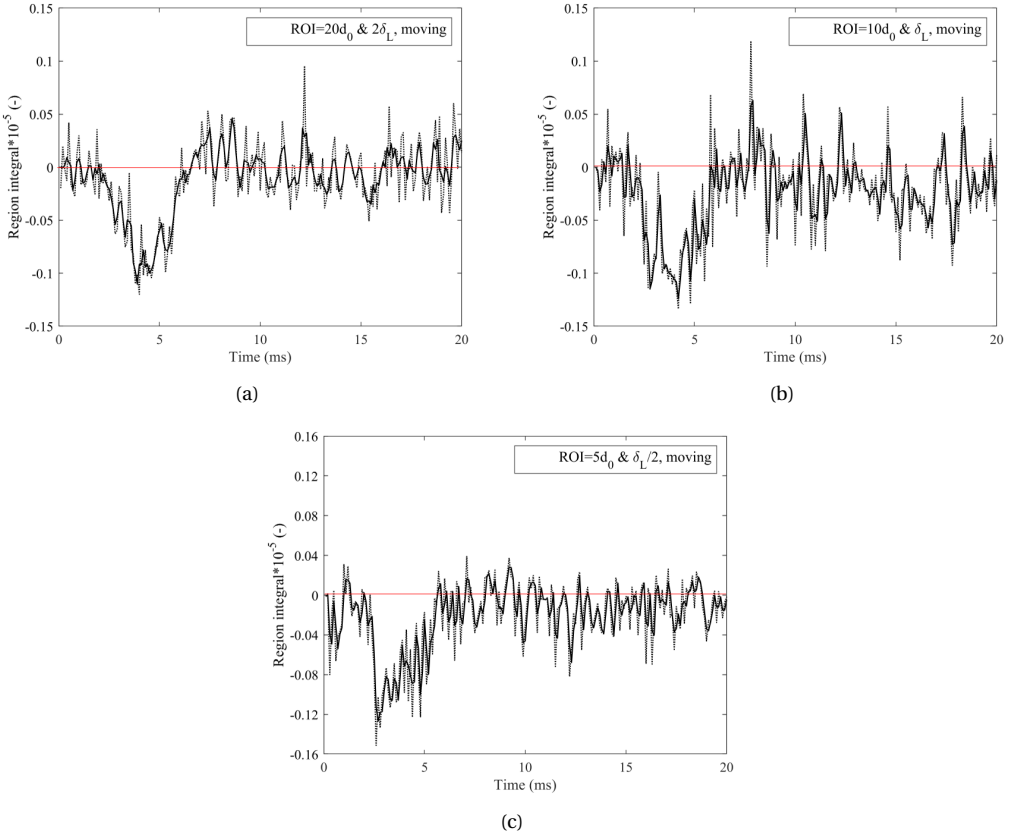

Figure 8. Change in integral of signal due to droplet passage (d_0=48.5 μm) at SB-1 with moving ROI.

Similar conclusions can be drawn for ϕ=1.3 in Figure 9, in which an average 10.71 % signal loss is detected between 2.2-5.5 ms. The recovery time for the flame, nearly 1.9 ms, is less than the richest case because when the flame condition is closer to stoichiometry, the flame is less prone to disturbances. Although the initial droplet diameter is slightly higher in SB-2 than in SB-1, heat loss duration differs by 0.3 ms due to the increased flame temperature, resulting in quicker evaporation.

At ϕ=1.2, the detection for signal loss can only be captured with the large ROI as 5.1 % on average during 3.6 ms, as given in Figure 10. The recovery time after extinction is calculated as 2.9 ms while the droplet crossing time is 0.7 ms, even though it is the largest droplet injected. The flame temperature for this case is nearly 75 K higher than ϕ=1.3 so that the droplet will evaporate more inside the preheating and reaction zones. As a result, gaseous ethanol will build up near to flame region, leading to more time to recover the flame itself.

In Figure 11, total signal inside ROI is given for ϕ=1.1. As can be seen clearly, it is almost impossible to detect signal loss with an adaptive ROI. However, from global computations, 1.8 %

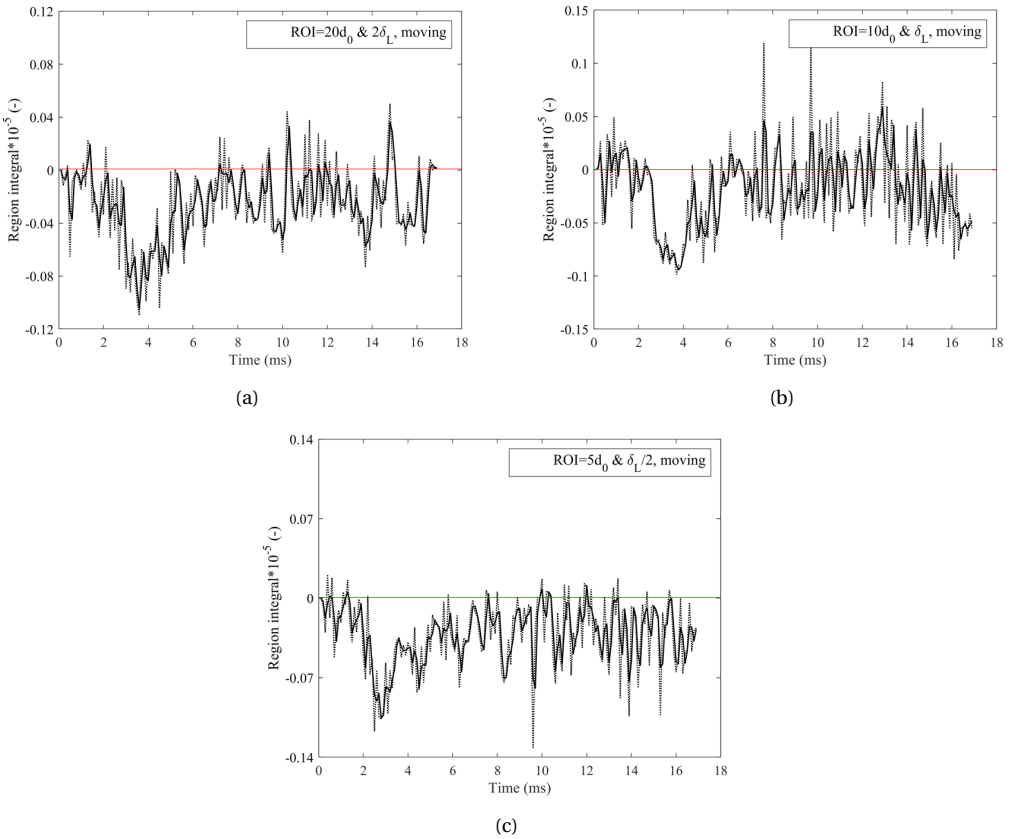

Figure 9. Change in integral of signal due to droplet passage (d_0=51.9 μm) at SB-2 with moving ROI.

signal loss can be reported for 0.5 ms. For near-to-stoichiometric cases, it is hard to distinguish the signal with a smaller region of interest. The first reason is that the luminosity of the flame will decrease when it becomes leaner. Secondly, leaner flames will be more stable, and they will be less sensitive to any changes.

In light of these results, the onset of instabilities and the effect of droplet passage from the flame surface are investigated. The reactive droplet takes heat from the flame front while passing, evaporating, and possibly burning, depending on the flame condition. This leads to local quenching on the flame zone. For fuel-rich propane/air flames, there is enough time for the flame to recover itself. However, for spherically-expanding aerosol ethanol/air flames, due to a high number of droplets with a small inter-distance, the flame surface will continually be disturbed without any time for recovery. Due to the evaporation of liquid fuel, the gaseous phase will be fed with more fuel thanks to the evaporated gas around the droplet. This concentration gradient locally changes the properties of flame, i.e., temperature, velocity, and diffusivity. The build-up of evaporated fuel may also cause an aperture on the flame field, which may lead to instabilities. The intrinsic instabilities are triggered by the presence of droplets in the cases where the flame cannot recover its initial state, and it locally extincts due to the heat sink effect from the presence of droplets, as observed for spherically-expanding flames. Additionally, the richer flames are more prone to local modifications, hence the recovery time is higher than the leaner flames.

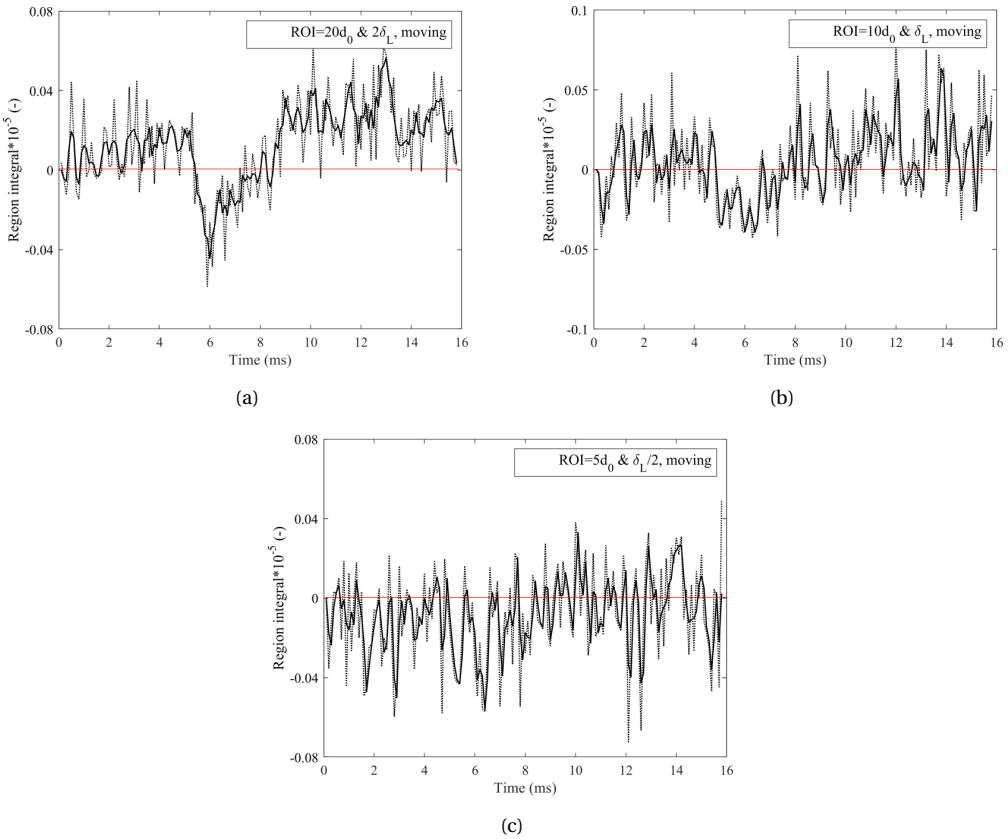

Figure 10. Change in integral of signal due to droplet passage (d_0=58.9 μm) at SB-3 with moving ROI.

4. Conclusion

The main purpose of this study is to investigate the flame/spray interactions. Accordingly, mechanism of cellular instability formation and the link between instabilities and local extinction are studied. In the first part of the study, spherically-expanding aerosol ethanol/air flame morphology is observed under microgravity via Schlieren method at well-established and reported conditions. Schlieren images revealed that at the initial phase of cellular structure formation, dark spots are observed linking to the signal loss in a density gradient. This phenomenon leads to a local extinction and quenching on the flame front due to either the presence or the evaporation of liquid droplets.

For further investigation of local extinction phenomenon, stagnation flame with a single droplet injection is examinated in the second part of the study. Rich propane/air flames are selected due to their high luminosity and sensitivity to disturbances, and their structure is captured via Chemiluminescence method. The droplet is selected as ethanol and tracked via ILIDS to determine its initial size. It is observed that the percentage signal loss due to the droplet passage is higher for richer cases, as well as the recovery time of the flame surface. The detection of signal loss can be achieved by changing the dimensions of the region of interest for richer cases. However, it is hard to detect the signal loss when the flame is close to the stoichiometry since it is less prone to disturbances. Although all the flames created at both flame configurations

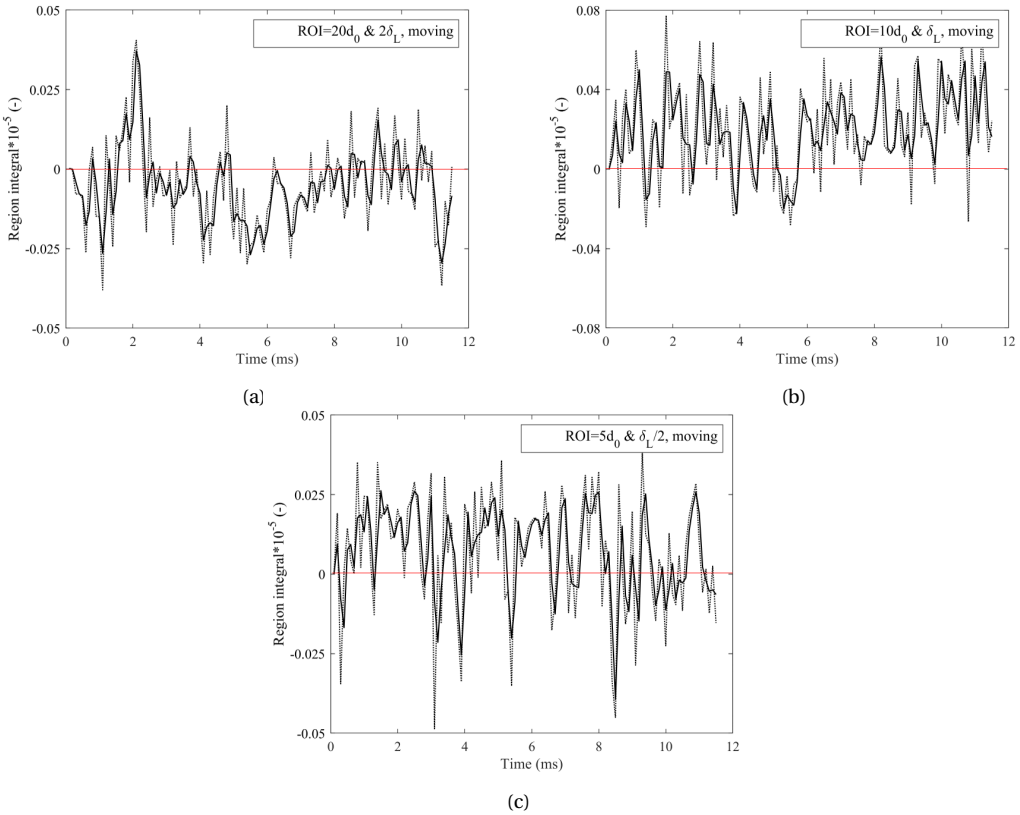

Figure 11. Change in integral of signal due to droplet passage (d_0=55.4 μm) at SB-4 with moving ROI.

are tend to be stable, the intrinsic instabilities are only triggered by droplets if the flame front is continuously fed with them, which is the case in spherically-expanding aerosol flames.

Conflicts of interest

The authors have no conflict of interest to declare.

Acknowledgments

The authors acknowledge CNES and CNRS for their financial and technical support for the parabolic flights.

References

[1] J. H. Burgoyne, L. Cohen, "The effect of drop size on flame propagation in liquid aerosols", *Proc. R. Soc. Lond., Ser. A* **225** (1954), no. 1162, p. 375-392.

[2] Y. Mizutani, A. Nakajima, "Combustion of fuel vapor-drop-air systems: Part II—Spherical flames in a vessel", *Combust. Flame* **20** (1973), no. 3, p. 351-357.

[3] D. R. Ballal, A. H. Lefebvre, "Flame propagation in heterogeneous mixtures of fuel droplets, fuel vapor and air", *Symposium (International) on Combustion* **18** (1981), no. 1, p. 321-328.

[4] G. D. Myers, A. H. Lefebvre, "Flame propagation in heterogeneous mixtures of fuel drops and air", *Combust. Flame* **66** (1986), no. 2, p. 193-210.

[5] H. Nomura, K. Izawa, Y. Ujiie, J. Sato, Y. Marutani, M. Kono, H. Kawasaki, "An experimental study on flame propagation in lean fuel droplet-vapor-air mixtures by using microgravity conditions", *Symposium (International) on Combustion* **27** (1998), no. 2, p. 2667-2674.

[6] C. T. R. Wilson, "On a method of making visible the paths of ionising particles through a gas", *Proc. R. Soc. Lond., Ser. A* **85** (1911), no. 578, p. 285-288.

[7] S. Hayashi, S. Kumagai, "Flame propagation in fuel droplet-vapor-air mixtures", *Symposium (International) on Combustion* **15** (1975), no. 1, p. 445-452.

[8] S. Hayashi, S. Kumagai, T. Sakai, "Propagation velocity and structure of flames in droplet-vapor-air mixtures", *Combust. Sci. Technol.* **15** (1977), p. 169-177.

[9] F. Atzler, F. X. Demoulin, M. Lawes, Y. Lee, N. Marquez, "Burning rates and flame oscillations in globally homogeneous two-phase mixtures (flame speed oscillations in droplet cloud flames)", *Combust. Sci. Technol.* **178** (2006), no. 12, p. 2177-2198.

[10] M. Lawes, Y. Lee, N. Marquez, "Comparison of iso-octane burning rates between single-phase and two-phase combustion for small droplets", *Combust. Flame* **144** (2006), no. 3, p. 513-525.

[11] D. Bradley, M. Lawes, S. Liao, A. Saat, "Laminar mass burning and entrainment velocities and flame instabilities of i-octane, ethanol and hydrous ethanol/air aerosols", *Combust. Flame* **161** (2014), no. 6, p. 1620-1632.

[12] R. Thimothée, C. Chauveau, F. Halter, I. Gökalp, "Characterization of cellular instabilities of a flame propagating in an aerosol", in *Proceedings of ASME Turbo Expo 2015: Turbine Technical Conference and Exposition*, American Society of Mechanical Engineer, 2015.

[13] R. Thimothée, C. Chauveau, F. Halter, I. Gökalp, "Experimental investigation of the mechanisms of cellular instabilities developing on spherical two-phase flames", *Combust. Sci. Technol.* **188** (2016), no. 11-12, p. 2026-2043.

[14] R. Thimothée, C. Chauveau, F. Halter, I. Gökalp, "Experimental investigation of the passage of fuel droplets through a spherical two-phase flame", *Proc. Combust. Inst.* **36** (2017), no. 2, p. 2549-2557.

[15] G. Renoux, F. Halter, C. Chauveau, "Experimental study of the morphology of two-phase flame instabilities in microgravity", *At. Sprays* **28** (2018), no. 10, p. 915-929.

[16] J. B. Greenberg, A. McIntosh, J. Brindley, "Instability of a flame front propagating through a fuel-rich droplet–vapour–air cloud", *Combust. Theory Model.* **3** (1999), no. 3, p. 567-584.

[17] J. B. Greenberg, "Propagation and extinction of an unsteady spherical spray flame front", *Combust. Theory Model.* **7** (2003), p. 163-174.

[18] J. B. Greenberg, A. C. McIntosh, J. Brindley, "Linear stability analysis of laminar premixed spray flames", *Proc. R. Soc. Lond., Ser. A* **457** (2001), no. 2005, p. 1-31.

[19] J. B. Greenberg, "Finite-rate evaporation and droplet drag effects in spherical flame front propagation through a liquid fuel mist", *Combust. Flame* **148** (2007), no. 4, p. 187-197.

[20] W. Han, Z. Chen, "Effects of finite-rate droplet evaporation on the ignition and propagation of premixed spherical spray flame", *Combust. Flame* **162** (2015), no. 5, p. 2128-2139.

[21] W. Han, Z. Chen, "Effects of finite-rate droplet evaporation on the extinction of spherical burner-stabilized diffusion flames", *Int. J. Heat Mass Transfer* **99** (2016), p. 691-701.

[22] Q. Li, H. Zhang, C. Shu, "Propagation of heterogeneous and homogeneous planar flames in fuel droplet mists", *Int. J. Multiphase Flow* **133** (2020), article no. 103452.

[23] Q. Li, H. Zhang, C. Shu, "Propagation of weakly stretched premixed spherical spray flames in localized homogeneous and heterogeneous reactants", *Phys. Fluids* **32** (2020), article no. 123302.

[24] C. Nicoli, P. Haldenwang, B. Denet, "Premixed flame dynamics in presence of mist", *Combust. Sci. Technol.* **191** (2019), no. 2, p. 197-207.

[25] R. Thimothée, C. Chauveau, F. Halter, C. Nicoli, P. Haldenwang, B. Denet, "Microgravity experiments and numerical studies on ethanol/air spray flames", *C. R. Méc. Acad. Sci. Paris* **345** (2017), no. 1, p. 99-116.

[26] G. Renoux, "Étude expérimentale de l'interaction goutte/flamme : propagation d'une flamme dans un aérosol en microgravité et passage d'une goutte à travers un front de flamme", PhD Thesis, Université d'Orléans, Orléans, France, 2020.

[27] R. Thimothée, "Caractérisation de la propagation d'une flamme dans un milieu diphasique (brouillards) en microgravité", PhD Thesis, Université d'Orléans, Orléans, France, 2017.

[28] M. Nassouri, "Caractérisation expérimentale de la propagation d'une flamme laminaire dans un milieu diphasique (brouillard) à haute pression et en microgravité", PhD Thesis, Université d'Orléans, Orléans, France, 2014.

[29] J. G. Wilson, *The principles of cloud-chamber technique*, Cambridge Monographs on Physics, Cambridge University Press, 2014.

[30] D. Kaya, G. Renoux, F. Halter, A. Yozgatlıgil, I. Gökalp, C. Chauveau, "Evaporation of a single ethanol droplet interacting with a premixed laminar CH_4/air flame", in *ICLASS 2021, 15$^{\text{th}}$ Triennial International Conference on Liquid Atomization and Spray Systems*, 2021.

[31] F. Thiesset, F. Halter, C. Bariki, C. Lapeyre, C. Chauveau, I. Gökalp, L. Selle, T. Poinsot, "Isolating strain and curvature effects in premixed flame/vortex interactions", *J. Fluid Mech.* **831** (2017), p. 618-654.

Comptes Rendus
Mécanique
2023, Vol. 351, Special Issue S2, p. 57-75
https://doi.org/10.5802/crmeca.149

Physical Science in Microgravity within the Thematic Group Fundamental and Applied Microgravity / *Sciences physiques en microgravité au sein du GDR Micropesanteur Fondamentale et Appliquée*

An engineering model for creeping flame spread over idealized electrical wires in microgravity

Alain Coimbra [a], Yutao Li [b], Augustin Guibaud [c], Jean-Marie Citerne [b], Guillaume Legros [d] and Jean-Louis Consalvi [a] *,

[a] Aix-Marseille Université, CNRS, IUSTI UMR 7343, 5 rue E. Fermi, 13013 Marseille, France

[b] Institut Jean le Rond d'Alembert/UMR CNRS 7190, Sorbonne Université, Paris F-75005, France

[c] Department of Civil, Environmental and Geomatic Engineering, University College London, London WC1 E6BT, UK

[d] ICARE/CNRS, 1C av. de la Recherche Scientifique, Orléans Cedex 1 45071, France

E-mails: alain.coimbra@univ-amu.fr (A. Coimbra), yutao.li@hotmail.com (Y. Li), a.guibaud@ucl.ac.uk (A. Guibaud), jean-marie.citerne@sorbonne-universite.fr (J.-M.. Citerne), guillaume.legros@cnrs-orleans.fr (G. Legros), jean-louis.consalvi@univ-amu.fr (J.-L. Consalvi)

Abstract. Flame spread over an insulated electrical wire is a major source of fire scenario in a space vehicle. In this work, an engineering model that predicts the creeping flame spread over cylindrical wires in microgravity is developed. The model is applied to interpret experimental data obtained in parabolic flights for wires composed by a 0.25 mm radius nickel-chromium (NiCr) metallic core coated by low-density polyethylene (LDPE) of different thicknesses ranging from 0.15 mm to 0.4 mm. The model relies on the assumption that, in the pyrolysis region, the NiCr and the LDPE are in thermal equilibrium. This assumption is supported by more detailed numerical simulations and the model reduces then to solving the heat transfer equations for both NiCr and LDPE in the pyrolysis region and in the region ahead of the flame front along with a simple degradation model for LDPE, an Oseen approximation of opposed oxidizer flow and an infinitely fast gas-phase chemistry. The flame spread rate (FSR) is controlled by two model parameters, which are measurable from intrinsic material and ambient gas properties: the convective flame heat flux transferred to the solid ahead from the flame front and the gaseous thermal heat length near the flame front. These parameters are then calibrated from experimental data for a given wire geometry and the calibrated model is validated against experimental data for other wire geometries and ambient conditions. The heat transfer mechanisms ahead of the pyrolysis front are investigated with a special emphasis on the LDPE thickness and the conductivity of the metallic core. In addition to NiCr, metallic cores of lower and higher conductivities are considered. The polymer is shown to be thermally thick for all tested wire geometries and core conductivities. The flame heat flux is found to dominate the heat transfer in the preheat zone where it applies. The core has

* Corresponding author.

nevertheless a significant impact in the heating of the LDPE with its contribution increasing with the core conductivity and when decreasing the LDPE thickness.

Keywords. Creeping flame spread, electrical wire, microgravity, low-density polyethylene, nickel-chromium core.

Published online: 10 March 2023

1. Introduction

In order to achieve the ambitious goals of manned deep space exploration in the near future, several safety issues aboard the spacecrafts must be resolved. Fire hazards in such confined environments are a threat to equipment integrity and even the safety of the astronauts. The main potential source of a fire in this situation is attributed to electrical malfunction. The insulation and jacket layers of wire and cable are made of plastic materials, which may release pyrolysis gases when heated by external sources or short-circuiting, supporting combustion. This common scenario of flame spread over polymer-coated electrical wires has motivated extensive research in both normal gravity [1–4] and microgravity [5–10].

Simplifying the in-flight configuration to a one dimensional academic problem, the analysis of steady state opposed flow flame spread over a vertical wire is key to understanding the flammability of solid fuels [11]. Flame spread over solid surfaces results from the heating process of the material ahead of the pyrolysis front. Heat transfers of multiple natures raise the unburnt solid from the ambient temperature up to the pyrolysis temperature at which the material starts to release gaseous fuel that is ignited by the flame, ensuring the spreading process [12]. The flame spread process can be viewed then as a series of piloted ignitions where the flame acts as both heating source and pilot [13].

Flame spread models and correlations have been proposed for steady-state opposed flame spread, denoted also as creeping flame spread [13]. Most notably, a model based on the heat balance ahead of the pyrolysis front in both thermally-thin and thick slabs has been proposed by de Ris [14]. In this approach, the heat transfer from the flame to the solid was obtained by solving the laminar boundary layer equation along with the infinitely fast gas-phase chemistry and Oseen approximations. The flame spread rate (FSR) could be then assessed and characterized based on measurable material and gas properties. It was nevertheless observed that this model largely overestimates the flame heat transfer and the corresponding FSR, owing to the assumption of infinitely fast kinetics, which is not satisfied at the flame leading edge. In this region, the relatively cold solid surface acts as a heat sink that produces local flame extinction, resulting in a complex flame attachment process [11].

In order to circumvent these difficulties and to provide an engineering analytical flame spread model, Delichatsios and co-workers reduced the flame heat transfer process to two properties, measurable from material and ambient gas properties, that characterize the creeping flame spread process: the convective heat flux per unit length, $E'_{gs,pr}$, from the flame to material near the pyrolysis front and the gaseous thermal length, L_g, generated by the opposed oxidizer flow [15]. In addition, they provide experimental methodology and methods for their determination. A heat balance equation and its corresponding methodology was first proposed for a flat burning surface [15], before being extended to cylindrical samples [16]. As compared to flat geometry, the cylindrical curvature was found to modify the heat balance by enhancing gas-to-surface heat transfer and by reducing the heated layer depth in the solid. This heat balance was also developed for a flat material undergoing a melting process [17].

A unique feature in the flame spread over electric wires is the presence of an inert, high thermal conductivity metallic core inside the flammable polymer coating. The presence of the

core is known to modify the heat transfer pattern, from the ignition, spread, extinction to the phase-change processes of the polymer insulation and emission of combustion products [4, 18]. It was shown that increasing the thermal conductivity of the core results in an increased FSR, but simultaneously increases the local extinction behavior due to increased heat losses in the the unburned zone [19]. This process is impacted however by several parameters, as the role of the metallic core as a heat sink or heat source is shown to be controlled by the wire material properties, geometry and ambient conditions, most of which are not well understood [4].

A detailed description of the heat transfer process in the case of a thermally-thin idealized electrical wire consisting of a metallic core and a LDPE coating has been provided by Konno et al. [20] and is displayed in Figure 1. The heat transfer to the virgin polymer upstream to the pyrolysis front is driven by both the flame heat flux and the heat transfer from the metallic core. As observed in the experiments of Guibaud et al. [21], the polymer is entirely consumed by the degradation process, leading to a diffusion flame that falls down to the bare wire at the trailing edge (See Figure 1). This induces a substantial heat flux from the flame to the bare wire, which is in turn conducted through the metallic core towards the pyrolysis zone, contributing in addition to the flame heat flux to pyrolyse the solid. A part of this flux is then transferred though the metallic core ahead of the pyrolysis zone.

The objective of this study is to predict creeping flame spread over idealized polymer coated metallic wires in microgravity. It will be shown how this complex heat transfer behaviour can be simplified if the pyrolysis can be treated as phase-change as assumed in the aforementioned heat balance flame spread models. An engineering heat balance flame spread model and an experimental procedure to determine the material properties characterizing the creeping flame spread over thin electrical wires are developed. The experiments made by Guibaud and co-workers on Nickel-Chrome (Nicr)/Low Density PolyEthylene (LDPE) electrical wires will be considered to determine these parameters and validate the model [21]. These experiments and assumptions for characterizing steady flame spread are described in Section 2. The flame spread model, governing equations and considered material and gas-phase properties will be subsequenty presented in Section 3. The results will be discussed in Section 4. The calibration of the model parameters is presented and validated against experimental data. Then, a study of the heat transfer mechanisms in the wire is discussed. Finally, Section 5 will be devoted to the conclusions and perspectives of this study.

2. Experimental methodology

The experimental procedure used to obtain the flame spread rate is briefly described in this section. Experiments in microgravity are conducted on the Detection of Ignition And Mitigation Onboard for Non-Damaged Sapcecrafts (DIAMONDS) rig, which is extensively described in Ref. [8, 22]. DIAMONDS was installed aboard the Novespace A310 ZeroG airplane, a facility that specifically operates parabolic flights. Every parabola provides a 22 s long sequence of microgravity with an accuracy level of $5{\cdot}10^{-2}$ g_0 ($g_0 = 9.81$ m/s^2). The experimental setup consists of a cylindrical combustion chamber with an inner diameter of 190 mm, where a laminar O_2/N_2 oxidizer flow can be established with a direction from the bottom to the top of the chamber. The flow conditions can be controlled with the oxygen content in volume fraction from 0-21%, the pressure from 50.7-121.6kPa and the flow velocity from 0-300 mm/s. The samples are cylindrical wires of length 150 mm, composed of a NiCr core coated by LDPE insulation. They were placed along the central axis of the chamber and parallel to the flow direction. LDPE has been used as coating of laboratory wires as an international target configuration to investigate flammability properties of electrical cables in both normal and microgravity conditions [4, 5, 23]. In these experiments, three core-to-wire radius ratios, R_c/R_s were tested: (i) 0.25/0.4 (Type#1),

(ii) 0.25/0.55 (Type#2) and (iii) 0.25/0.65 (Type#3), as summarized in Table 1. The core radius was kept unchanged and the LDPE thickness, δ_s, was varied. The cross sections area ratio, A_c/A_s, of Type#1 is about 2 and 2.63 times larger than those of Type#2 and Type#3, respectively. The samples were ignited using a hot Kanthal wire located at its upper end to initiate an opposed-flow flame spread.

Table 1. Configurations of NiCr core and LDPE insulations.

Type	R_c (mm)	R_s (mm)	δ_s (mm)	A_c/A_s
I	0.25	0.40	0.15	0.391
II	0.25	0.55	0.30	0.206
III	0.25	0.65	0.40	0.148

All experiments are recorded in using a JAI AT-140CL digital tri-CCD camera, equipped with a telecentric lens to restrict the light collection to beams parallel to the optical axis. A controlled uniform LED backlight is set on and off alternatively during the images acquisition in order to track the morphology of flame and LDPE droplet. Images are captured with a frame rate of 39.06fps over a 512x1396 pixels^2 CCD array in the red, green and blue spectral bans with a resolution of 72.6 μm, which can provide an entire view during the flame spread. FSR is determined by tracking the flame front using image without backlighting processing once a steady flame spread is reached. A detailed description can be found in Ref. [24]. According to the images with backlighting, the spreading over LDPE is characterized by the formation of a molten droplet whose, for the conditions investigated in the present study, volume increases first before reaching a steady value. The flame is assumed to spread at a steady rate once the dimensions of the molten insulation droplet, the visible flame length, and the rate of the flame front displacement reach a steady state value.

3. Flame spread model

3.1. *Model assumptions*

The model considers a flame spreading at a steady rate over a thin electrical wire composed by a metal core of radius R_c and a polymer coating of radius R_s. During steady-spread rate, the wire can be decomposed into four regions as illustrated in Figure 1. The region directly ahead of the pyrolysis front is referred to as the preheat zone and involves the heat transfer between the flame, the metallic core and the LDPE. This region is proceeded by the unburnt zone where the heating process is manly driven by conduction through the metallic core. The pyrolysis zone is located downstream the pyrolysis front followed by a bare metallic core as the polymer is completely burnt. The following assumptions are introduced:

(1) The polymer melting and the pyrolysis processes behave as phase changes occurring at temperatures $T_s = T_m$ and $T_s = T_p$, respectively.
(2) The polymer can expand or contract in the $r-$ direction.
(3) The pyrolysis front corresponds to the location at time t, $z_p(t)$, where the wire surface temperature reaches the pyrolysis temperature, T_p.
(4) In the pyrolyzing zone, the temperature of the polymer layer is maintained constant to $T = T_p$.
(5) In the pyrolyzing region, the metal core and the polymer layer become rapidly in thermal equilibrium. This assumption implies that the heat flux conducted from the bare metal

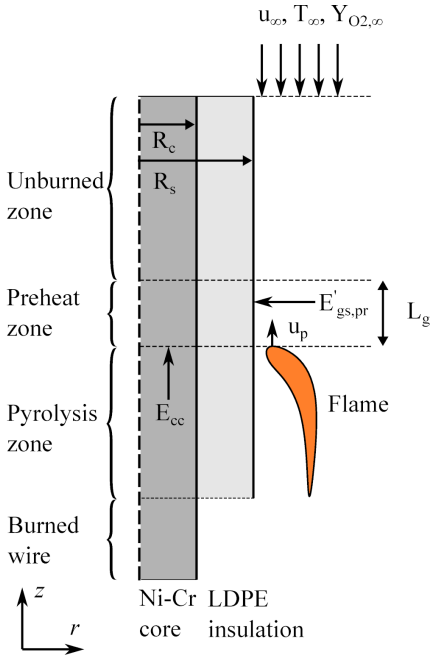

Figure 1. Scheme of the engineering flame spread model (not in scale). The distinction between the preheat and unburned zones is reproduced from the works of Konno et al. [20].

core toward the pyrolyzing region is completely transferred to the pyrolyzing polymer. Therefore, it does not affect the heat balance in the preheat region, and, in turn, the flame spread. The validity of this assumption has been assessed by using the CFD model described in detail in Refs. [21, 23, 25]. During these simulations, it was assumed that the pyrolyzing LDPE is at T_p, consistently with the assumption (4). The results are reported in Figure 2 that shows the evolution along the wire axis of the temperatures inside the metal core and LPDE for a simulation considering a LPDE/NiCr of Type#2 (see Table 1), an oxidizer composed of 21%-O_2/ 79%-N_2 flowing at a velocity of 150 mm/s and a pressure of 101 kPa. The same behavior has been observed for the other wire geometries and ambient conditions. The location z =0 corresponds to the pyrolysis front and the negative values of z to the region ahead of the pyrolysis front. The pyrolysing region is located between $z = 0$ and $z \approx 0.008$ m followed by the bare NiCr for $z > 0.008$ m. Figure 2 shows that the NiCr temperature reaches a peak at the location where the flame falls down to the bare metal core. This temperature decreases downstream and upstream the peak due to thermal diffusion. In the pyrolyzing region, it reaches rapidly the pyrolysis temperature, demonstrating that the assumption of thermal equilibrium between the LDPE and the NiCr is satisfied provided that assumption (4) holds.

(6) In the preheat zone, the radiative flux from the flame is balanced by the heat flux re-radiated by the solid surface. This assumption is sustained by numerical simulations [21, 23, 25].

(7) The opposed flow is modelled as an Oseen flow with a vertically uniform velocity, u_∞, parallel to the wire axis.

(8) The combustion kinetics is assumed to be infinitely fast with $F(kg) + s\ O_2 \rightarrow (1+s)Pr$.

(9) The cylindrical curvature enhances the convective heat transfer from the flame to the solid as compared to a flat slab and a corrective factor is introduced to account for this

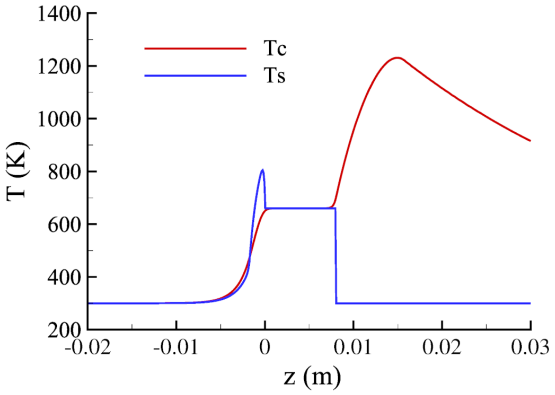

Figure 2. Evolution of LDPE, T_s, and NiCr, T_c, temperatures along the wire axis.

enhancement [16]. The convective heat power transferred from the flame to the polymer in the preheat region, $E_{gs,pr}$, can be estimated by using assumptions (6) to (8) [15, 16]:

$$E_{gs,pr} = 2\pi R_s \dot{q}''_{fl,c} L_g = 2\pi R_s E'_{gs,pr}. \tag{1}$$

In Eq. (1), L_g represents a gas-phase thermal diffusion length, i.e. the length over which the flame heat flux is applied. It is given by:

$$L_g = \frac{\alpha_g}{u_\infty} = \frac{k_g}{\rho_g c_g u_\infty}, \tag{2}$$

and $\dot{q}''_{fl,c}$ is the convective heat flux transferred from the flame to the solid. The diffusivity α is obtained from the conductivity, k_g, density, ρ_g, and heat capacity, c_g with the subscript g referring to gas properties. $E'_{gs,pr}$ is expressed as:

$$E'_{gs,pr} = \underbrace{\frac{\sqrt{\pi}\frac{L_g}{R_s}}{\ln\left(1+\sqrt{\pi}L_l/R_s\right)}}_{\mathrm{C}} \times \underbrace{k_g \frac{\left[B - r_f\right] L_v}{c_g}}_{E'_{gs,pr,flat}}. \tag{3}$$

$B = [Y_{O2,\infty}\Delta h_c/s - c_g(T_p - T_\infty)]/L_v$ is the mass transfer number, L_v the latent heat of gaseification, Δh_c the heat of combustion and $r_f = Y_{O2,\infty}/s$ the mass fuel-to-air ratio. $E'_{gs,pr}$ is composed of two contributions: the heat flux estimated for a flat slab, $E'_{gs,pr,flat}$, and a corrective factor to extend it to the cylindrical geometry, C. As discussed in the literature [15], the estimation of $E'_{gs,pr,flat}$ from the infinitely fast kinetics assumption leads to an overestimation of the heat flux from the flame to the unpyrolyzed polymer. For a given oxidizer composition, this property will be estimated from experiments for the Type#2 wire under a pressure of 101 kPa and will be applied to other wire and ambient conditions. The underlying assumption is:

(10) $E'_{gs,pr,flat}$ depends only of the oxygen concentration in the oxidizer, X_{O2} and, as a consequence, does not depend on the oxidizer flow rate, pressure, and wire geometry whose effects are captured through C and L_g.

The assumptions that the polymer pyrolysis can be assimilated to a vaporization process at constant pyrolysis temperature, T_p, (assumptions (1) and (3)) are the basis of the original formulations of the De Ris and Delichatsios flame spread models [14–16, 26] that serve as

strating point for the present study. However, they require further comments. First, analysis of the pyrolysis process of LDPE shows that it is more complex than a simple phase change [27]. Second, metallic core temperature measurements [28] have revealed that the metal core temperature does not exhibit the constant temperature behavior observed in Figure 2 in the pyrolysis region but increases continuously up to the peak. This suggests that the assumption of constant pyrolysis temperature in the polymer is questionable (see assumption (5)) and needs to be investigated in future works.

3.2. *Governing equations*

Based on the aforementioned assumptions, the axi-symmetric heat transfer equations and the corresponding boundary conditions for the LDPE coating and the NiCr core are given below. The assumption (3) defines the pyrolysis front as $z_p(t) = \underset{z}{max}\left(z|_{T_{s(R_s,z,t)=T_p}}\right)$ and the flame spread rate as:

$$u_p = \frac{dz_p(t)}{dt}. \tag{4}$$

The assumption (5) allows to simplify the problem by ignoring the heat flux transferred from the bare NiCr to the preheat zone and by reducing the computational domain to the pyrolysing zone, located for $z_p(t) - L_p \leq z \leq z_p(t)$, and the zone located ahead of the pyrolysis zone, $z > z_p(t)$, including the preheat zone and the unburned zone (see Figure 1). The pyrolysis length, L_p is assumed to be of 10 mm in accordance with experimental observations [29].

- For the LDPE: $R_c \leq r \leq R_s$
  - For $z \leq z_p(t)$:

$$T_s(r,z,t) = T_p \tag{5a}$$

  - For $z > z_p(t)$:

$$\frac{\partial \rho_s h_s}{\partial t} = \frac{1}{r}\frac{\partial}{\partial r}\left(r k_s \frac{\partial T_s}{\partial r}\right) + \frac{\partial}{\partial z}\left(k_s \frac{\partial T_s}{\partial z}\right) + \frac{1}{r}\frac{\partial}{\partial r}\left[\left(\int_{R_c}^{r} \frac{1}{\rho_s}\frac{\partial \rho_s}{\partial t} r dr\right)\rho_s h_s\right] \tag{5b}$$

for $T_s < T_m$ and $T_s > T_m$

$$0 = \frac{1}{r}\frac{\partial}{\partial r}\left(r k_s \frac{\partial T_s}{\partial r}\right) + \frac{\partial}{\partial z}\left(k_s \frac{\partial T_s}{\partial z}\right) - \dot{m}'''_m L_m \tag{5c}$$

for $T_s = T_m$ where $h_s = \int_0^{T_s} c_s dT$.

The third term in the right-hand side of Eq. (5b) represents the heat transfer associated with contraction or expansion of the material object. Equation (5c) describes the melting process.

The following boundary conditions are applied:

$$k_s \frac{\partial T_s}{\partial r} = \dot{q}''_{fl,c} \tag{6a}$$

For $r = R_s$ and $z_p \leq z \leq z_p + L_g$;

$$k_s \frac{\partial T_s}{\partial r} = h(T_\infty - T_s) \tag{6b}$$

For $r = R_s$ and $z \geq z_p + L_g$;

$$k_s \frac{\partial T_s}{\partial r} = k_c \frac{\partial T_c}{\partial r} \tag{6c}$$

For $r = R_c$ and $\forall\ z$;

$$\frac{\partial T_s}{\partial z} = 0 \tag{6d}$$

For $z \to \infty$;

$$T_s = T_p \tag{6e}$$

For $z < z_p - L_p$.
The convective coefficient h is computed as $h = k_g Nu/2R_s$, with $Nu = 0.32 + 0.155Re^{0.5}$ [30]. $Re = \rho_g u_\infty R_s/\mu_g$ is the Reynolds number with μ_g the kinematic viscosity.
The following initial conditions are also considered:

$$T_s(r, z, t = 0) = T_p \tag{7a}$$

For $z \leq z_p(t = 0)$;

$$T_s(r, z, t = 0) = T_\infty \tag{7b}$$

For $z > z_p(t = 0)$;

- For the NiCr: $0 \leq r \leq R_c$

$$\rho_c c_c \frac{\partial T_c}{\partial t} = \frac{1}{r}\frac{\partial}{\partial r}\left(r k_c \frac{\partial T_c}{\partial r}\right) + \frac{\partial}{\partial z}\left(k_c \frac{\partial T_c}{\partial z}\right) \tag{8}$$

The following boundary conditions are applied:

$$k_s \frac{\partial T_s}{\partial r} = k_c \frac{\partial T_c}{\partial r} \tag{9a}$$

For $r = R_c$ and $\forall\ z$;

$$\frac{\partial T_c}{\partial z} = 0 \tag{9b}$$

For $z \to \infty$;

$$\frac{\partial T_c}{\partial z} = 0 \tag{9c}$$

For $z = z_p - L_p$ and $\forall\ r$;
The initial condition is also applied:

$$T_c(r, z, t = 0) = T_\infty. \tag{10}$$

The heat transfer equations for the polymer and the metal core were solved in a coupled manner by using the finite volume method [31], a first-order backward Euler scheme for time integration and a second-order centered scheme for diffusion terms. The heat conductivity at the interface between LDPE and NiCr was computed with the harmonic mean to handle the large differences in conductivity between NiCr and LDPE [31].

A steady state flame front propagation was achieved approximately 1 s after the beginning of the simulations for all the wire geometries and ambient conditions, and an interval of $\Delta t = 1$ s between $t = 2$ and $t = 3$ s was used to capture the average spread rate from Eq. (4). A time step $\Delta t = 5.0 \times 10^{-5}$ s is used in all configurations. Multiplying or dividing this value by a factor of 10 was found to provide minor changes on the results. The spatial discretization is uniform, with a cell sizing of $\Delta z = 0.03$ mm and $\Delta r = 0.04$ mm. Multiplying or dividing these values by a factor of 2 was found to provide minor changes on the results.

3.3. *Material and gas phase properties*

The heat capacity, the melting temperature and the heat of melting of LPDE were obtained from differential scanning calorimetry. The evolution of the LDPE density with temperature was taken from literature [32] and it has been checked that the literature values at room temperature are equal to those measured in our experiments. The thermal conductivity of LPDE was measured using the transient line source method. These data are given in Table 2 for the LDPE and NiCr. The gas-phase density, heat capacity and conductivity are evaluated by assuming that the gas is air and by using a temperature evaluated as the average between the adiabatic flame temperature of ethylene in the investigated conditions and the ambient temperature.

Table 2. Thermal properties of the LDPE and Nickel-Chrome.

Property	LDPE	NiCr
Density (kg/m^3)	$\rho_s = 948.2$ for $T_\infty < T_s < T_m$	$\rho_c = 8670$
	$\rho_s = 948.2 - 0.94(T_s - T_\infty)$ for $T_m < T_s < T_p$	$\rho_c = 8670$
Heat capacity (J/kg/K)	$c_s = 0.2T^2 - 105.7T + 15773$ for $T_\infty < T_s < T_m$	$c_c = 440$
	$c_s = 3.4T + 1228.3$ for $T_m < T_s < T_p$	$c_c = 440$
Thermal conductivity	$k_v = 0.38$	$k_c = 17.4$
(W/m/K)	$k_m = 0.45$	$k_c = 17.4$
Heat of melting (J/kg)	$L_m = 101000$	—
Melting temperature (K)	$T_m = 384$	—
Pyrolysis temperature (K)	$T_p = 690$ [28]	—

4. Results and Discussion

4.1. *Calibration of the model parameters*

As previously discussed in the model assumption (9), the infinitely fast kinetics assumption led to a systematic overestimation of the heat flux transferred from the flame to the unpyrolyzed polymer [15]. A calibration procedure is performed to estimate the model parameters L_g and $E'_{gs,pr,flat}$. L_g is determined from its definition (Eq. (2)) and $E'_{gs,pr,flat}$ is calibrated by assuming that the geometry effects are modelled through the geometric correction C and the effects of the oxidizer flow rate and ambient pressure are captured solely through L_g. A consequence is that $E'_{gs,pr,flat}$ is expected to depend only on the oxygen concentration in the oxidizer, X_{O2}.

The calibration procedure consists in fitting the experimental spread rate for the Type#2 wire, a pressure of 101 kPa and an inflow velocity of 150 mm/s. The fitted values are reported in Table 3. As expected, $E'_{gs,pr,flat}$ increases with X_{O2}. It can be also observed that the fitted values represent 30% of the theoretical value given by Eq. (3) whatever X_{O2}. The quality of the fit is demonstrated in Figure 3.

4.2. *Flame spread rate*

The model along with the calibrated values of $E'_{gs,pr,flat}$ is applied to the other wire geometries and ambient pressures. Figure 4 shows the predicted FSR by the present model (referred to as Num. in the legend) as a function of X_{O2} for the Type#1, Type#2 and Type#3 wires. As expected from experimental observations in microgravity for electrical wires [20, 33], the FSR increases

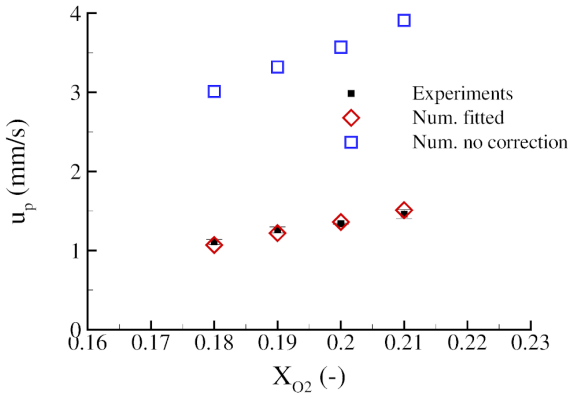

Figure 3. Spread rate as a function of X_{O2} for the Type#2 wire, an oxidizer velocity of 150 mm/s and a pressure of 101 kPa. The blue symbols represent the spread rate computed by using Eq. (3) whereas the red symbols represent that computed with the fitted $E'_{gs,pr,flat}$.

Table 3. Values of $E'_{gs,pr,flat}$ for the different values of X_{O2}.

X_{O2}	0.18	0.19	0.20	0.21
$\left[E'_{(gs,pr,flat)}\right]_{Calibrated}$ (W/m)	17.66	20.14	22.45	25.12
$\frac{\left[E'_{(gs,pr,flat)}\right]_{Calibrated}}{\left[E'_{(gs,pr,flat)}\right]_{Theoretical}}$	0.30	0.30	0.30	0.30

with X_{O2} for all the cases owing to an increase in flame temperature, which results in an increase of the flame heat flux transferred to the solid surface. This behavior is well captured by the model. The effect of wire geometry on the FSR is also well reproduced by the model. For a given X_{O2}, decreasing the wire diameter leads to an increase in the flame heat flux and, in turn, an increase in the FSR. This behavior was also observed in experiments involving black LDPE-coated copper wires [28].

Figure 4 compares also the experiments and the present predictions with the classical opposed-flow flame spread model proposed by Fernandez-Pello [13] and extended to cylindrical geometry in Ref. [34]. This model is referred to as CFP in Fig. 4 and ignores the heat transfer contribution of the metallic core. The flame spread velocity is given by:

$$u_p = 2C\frac{l_h\left(\dot{q}''_{fl,c}+\dot{q}''_{fl,r}-\dot{q}''_{rr}\right)}{\rho_s R_s\left[c_s(T_m-T_\infty)+L_m+c_s(T_p-T_m)\right]}-\text{func}\,(Da) \tag{11}$$

where Da is the Damkohler number and l_h is the solid heated length upstream of the flame front, taken equal to L_g to be consistent with our model. Da effects are neglected in accordance with the assumption of flame spread in the thermal regime whereas assumption (6) implies that $\dot{q}''_{fl,r} \approx \dot{q}''_{rr}$. The model has been slightly modified to include the contribution of the melting process and ρ_s and c_s are evaluated from the correlations of Table 2 at $\overline{T} = (T_m + T_\infty)/2$ before the melting and at $\overline{T} = (T_p + T_m)/2$ after the melting. Under these assumptions, Eq. (11) reduces

to the flame spread model proposed by Delichatsios et al. [16, 17] for cylindrical samples over a solid undergoing a melting process:

$$u_p = 2\frac{\frac{\sqrt{\pi}\frac{L_g}{R_s}}{ln(1+\sqrt{\pi}L_g/R_s)} \times E'_{gs,pr,flat}}{\rho_s R_s \left[c_s(T_m - T_\infty) + L_m + c_s(T_p - T_m)\right]} \tag{12}$$

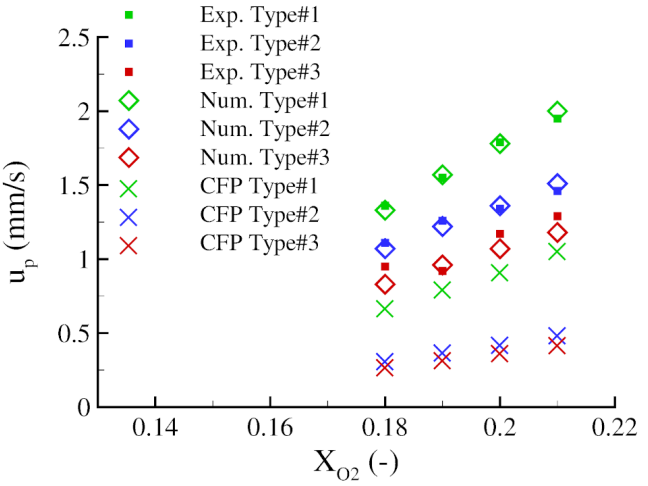

Figure 4. Spread rate as a function of X_{O2} for different wire geometries. The oxidizer velocity and the pressure are 150 mm/s and 101 kPa, respectively. The filled squared, the open diamonds and the crosses refer to the experiments, the present numerical model and the analytical model of Fernandez-Pello [13], respectively.

The CFM spread rates have been computed with the calibrated values of $E'_{gs,pr,flat}$ reported in Table 3. Figure 4 shows that the CFM model captures the trends, reproducing well the increase of u_p with X_{O2} and when decreasing the wire diameter. However, the spread rates predicted by the CFM model are significantly lower than those obtained experimentally, evidencing the contribution of the metallic core to the heat transfer to the LDPE.

The evolution of the FSR with X_{O2} is displayed for the Type#2 wire for different pressures in Figure 5. For a given oxygen concentration, the FSR slightly decreases while increasing the pressure due to an enhancement in the gas-phase density, ρ_g and, in turn, a reduction in L_g. This behaviour is well captured by the model. The good agreement between the model and the experiments for the different wire geometry and pressures supports the assumption (10).

4.3. *Heat transfer analysis*

Contours of temperature at steady spread rate for two LDPE thicknesses (Type#1 and Type#2 wires) are depicted in Figure 6. In this figure, the flame propagates from the bottom toward the top and the two heat fluxes as well as the preheat length, L_g, are indicated. The pyrolysis front is located at $z = 0$, and the vertical line shows the separation between the NiCr and LDPE.

The following conclusions may be drawn from analysis of Figure 6:

(1) The temperature gradients in the radial direction r observed in the LDPE coating in preheat as well as the unburned zones clearly suggest that the thermally-thin assumption, widely used in previous studies, is not valid (see Refs. [18, 20, 28] for example).

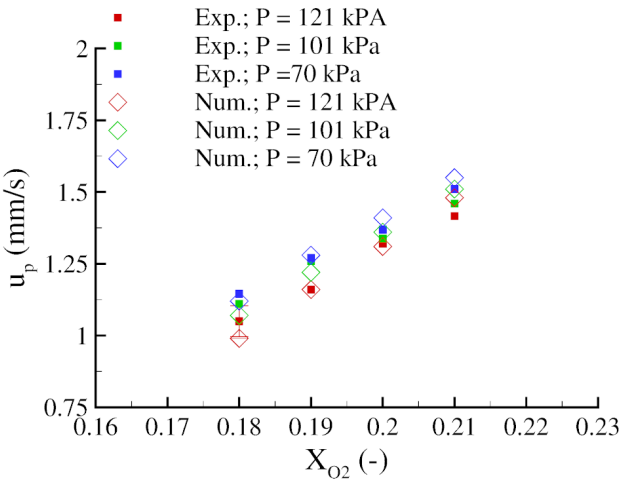

Figure 5. Spread rate as a function of X_{O2} for different pressures. The oxidizer velocity is 150 mm/s and the Type#2 wire is considered.

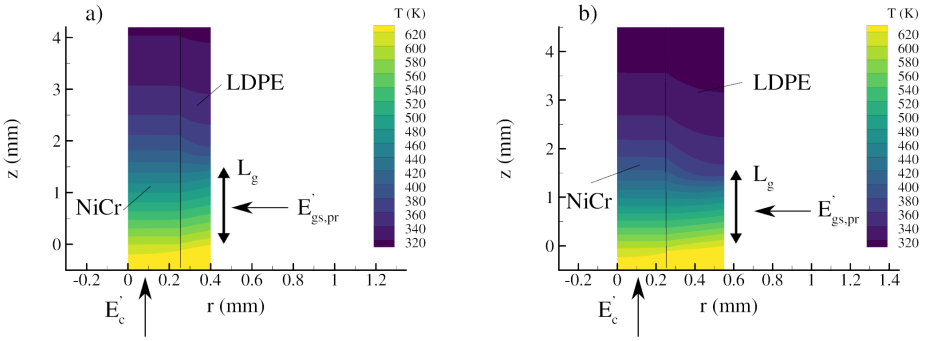

Figure 6. Temperature fields in the wire at steady state for (a) Type#1 and (b) Type#2. In both cases, the oxygen concentration and the pressure are 19 % and 101 kPa, respectively. The axis are not in the same scale.

(2) In the preheat zone, the surface temperature of LDPE is larger than that of NiCr. This behavior is observed for the other conditions. This suggests that, in this case, the heat transfer from the flame dominates in this region.

(3) The metallic core has a significant impact on the temperature field, and, therefore, on the FSR. In order to quantify this effect, simulations have been run by assuming that, on the one hand, the core is also LDPE with a conductivity significantly lower than NiCr ($k_s \approx 0.3W/m/K$, see Table 2) and, on the other hand, by considering iron (Fe) as the metal. Fe has a conductivity about four times higher than that of NiCr ($k_{Fe} = 58.1W/m/k$) [19]. Figures 7(b) and (c) show the temperature distribution at steady state for the Type #1 wire in the cases where the core is LDPE and Fe, respectively. A comparison with the temperature distribution for the NiCr Type #1 wire in Figure 6(a) illustrates clearly the role of metallic core and its conductivity. When pure LDPE is considered, the heating beyond the preheat zone ($z > L_g$) is negligible and the FSRs are substantially lower for all wire geometries, as shown in Figures 4 and 7(a). This behavior agrees with previous experimental observations [4]. When Fe is considered, the heating beyond the preheat

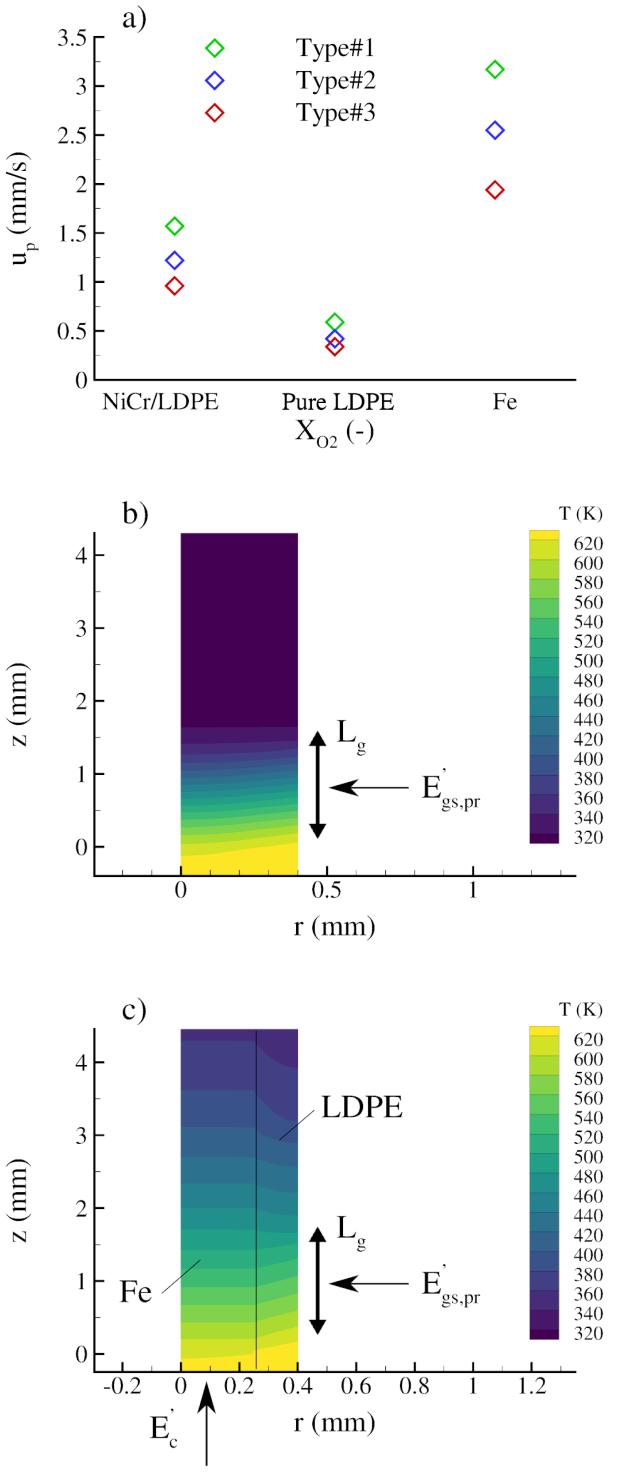

Figure 7. (a) Evaluation of the FSR for NiCr/LDPE and pure LDPE wires. (b) Temperature field for Type #1 pure LDPE wire. (c) Temperature field for Type #1 Fe/LDPE wire. The oxygen concentration and the pressure are 19 % and 101 kPa, respectively.

zone occurs over longer distances than for NiCr, resulting in higher spread rates (see Figure 7(a)).

(4) Let us first consider the effects of the wire geometry the case where the metallic core is made of NiCr. In the preheat zone, particularly at the vicinity of the flame front, temperature gradients observed in Figure 6 show that heat is transferred from the LDPE to the NiCr, i.e., the core acts as a heat sink for both depicted wire geometries. The heat balance in the preheat zone governs the flame extinction process, and this behavior could suggest that the metallic core has a role in this phenomena [28]. An opposite behavior is observed in the unburned zone with the heat being transferred from the metallic core to

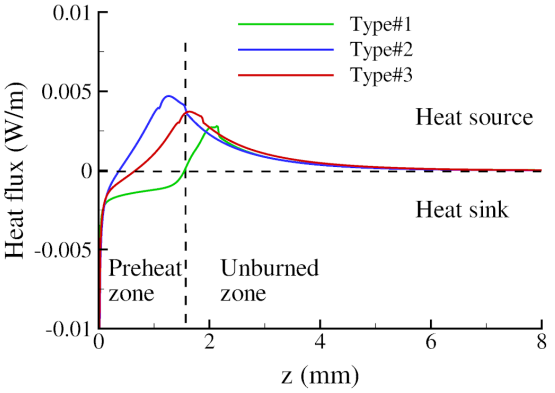

Figure 8. Conductive heat flux between the NiCr core and the LDPE coating, in W/m, in the preheat and unburned zones, for three wire geometries, along the wire length. The oxygen concentration and the pressure are 19 % and 101 kPa, respectively. Positive (negative) heat flux values denote heat transfer from the NiCr (LDPE) to the LDPE (NiCr), i.e., the core acts as a heat source (sink).

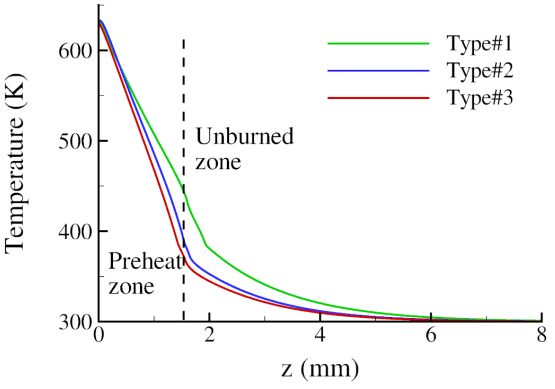

Figure 9. LDPE surface temperature, in *K*, in the preheat and unburned zones for a Nicr metallic core of Type #1. The oxygen concentration and the pressure are 19 % and 101 kPa, respectively.

the LDPE. The metallic core acts then as a heat source in this region, heating the LDPE before the preheat zone. A quantitative analysis of the heat transfer between the NiCr and LDPE along the wire length is shown in Figure 8. The pyrolysis front is at $z = 0$ and both preheat ($0 < z < L_g$) and unburned ($z > L_g$) zones are depicted. This figure illustrates the change of heat transfer direction between the preheat and the unburned zones. It also highlights the role of the LDPE thickness in the heat transfer between the LPDE and NiCr in the preheat zone. It appears that the length over which the NiCr core acts as a sink increases with decreasing LDPE thickness. For the thinner wire (Type #1), it acts as a heat sink over the entire preheat zone while, for the other wires, the length of the heat sink zone reduces. The role of the metallic core on the preheating process is further illustrated in Figure 9 which shows the elevation of LDPE surface temperature ahead of the flame front. The surface temperature increases as the coating thickness is reduced. For the thinner wire (Type #1), the surface temperature at the transition between the unburned and preheat zone exceeds the LDPE melting temperature. Let us investigate further the effects of the conductivity of the metallic core. In the case of pure LPDE, the conductive heat transfer in both r- and z-directions is negligible as indicated by the weak temperature gradients in Figure 7(b). On the other hand, Figure 10 compares the conductive heat transfer between the LDPE and the metallic core for Fe and NiCr for the thinnest Type #1 wire. The heat transfer exhibits a similar trend for both Fe and NiCr, with the core acting as a heat sink in the preheat zone and as a heat source in the unburned zone. However, the heat flux is conducted over a length significantly longer in the preheat zone in the case of Fe. This is confirmed by Figure 11 that shows that the heating process in the preheat zone is much more efficient for the Fe case, leading to a surface temperature of LDPE about about 486 K at the transition between the preheat and unburned zones.

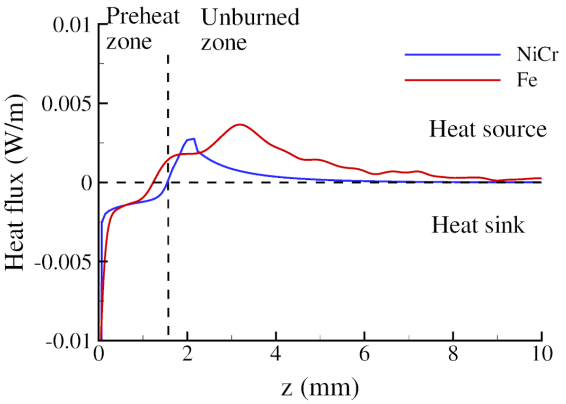

Figure 10. Conductive heat flux between the metallic core (Nicr or Fe) and the LDPE coating, in W/m, in the preheat and unburned zones, for Type #1 wire, along the wire length. The oxygen concentration and the pressure are 19 % and 101 kPa, respectively. Positive (negative) heat flux values denote heat transfer from the metallic core (LDPE) to the LDPE (metallic core), i.e., the core acts as a heat source (sink).

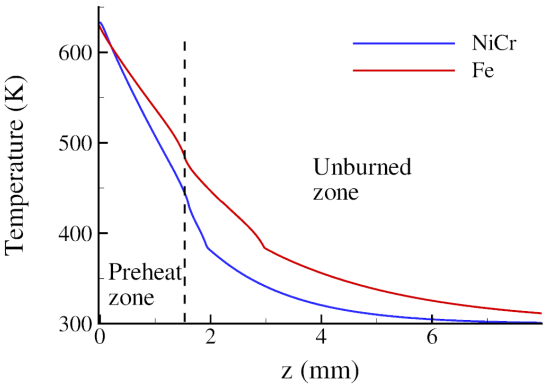

Figure 11. LDPE surface temperature, in K, in the preheat and unburned zones for a metallic core Type #1 made either of NiCr or Fe. The oxygen concentration and the pressure are 19 % and 101 kPa, respectively.

5. Conclusions

An engineering solution for a creeping flame spread model over idealized electrical wires composed of a NiCr metallic core and a LDPE coating in microgravity has been proposed and validated against experimental data obtained in parabolic flights. It has been shown that the heat transfer problem can be simplified by ignoring the heat flux from the bare metallic core and solving the coupled heat transfer equations for LDPE and NiCr in the pyrolysis zone and ahead of the pyrolysis front in conjunction with a simple phase-change based pyrolysis model for LDPE, an Oseen approximation of the flow and a infinitely fast chemistry for gas-phase combustion. The model reduces then to two parameters, the diffusive heat length and the heat conveyed from the flame to a flat surface, this latter depending only on the oxygen concentration in the oxidizer. The first parameters has been estimated from its definition whereas the second has been calibrated to match experimental flame spread rate as a function of the oxygen concentration for given wire geometry and ambient pressure and inflow velocity. The model with the calibrated parameters has been applied successfully to predict flame spread rates for other wire geometries and pressure conditions. A full validation of this model would require more experimental data on wire geometries and natures of the metallic core, which is a main perspective of this work.

The heat transfer mechanisms ahead of the pryolysis front have been investigated. The polymer has been shown to be thermally thick for all tested wire geometries. It has been showed that, in the preheat zone, the contribution of the flame flux dominate the LDPE heating process. In this region the metallic core can act as a heat sink or a heat source depending on the wire geometry. Upstream to the preheat zone, the metallic core behaves as a heat source whatever the wire geometry and the core conductivity. Its contribution to the heating process of the LDPE up to the pyrolysis temperature is enhanced with the core conductivity and as the LPDE thickness decreases.

Nomenclature

A	Cross section area, m^2
B	Mass transfer number
c	Heat capacity, $J/kg/K$
C	Corrective heat transfer factor for a cylindrical geometry
E_{cc}	Heat transferred in the metallic core, W
$E_{gs,pr}$	Heat transferred from the flame to the polymer, W
$E_{gs,pr,flat}$	Heat transferred from the flame to the polymer in a flat slab, W
h_s	Solid enthalpy, J/kg
k	Thermal conductivity, $W/m/K$
L_v	Latent heat of vaporization, J/kg
L_g	Preheat length, m
P	Pressure, Pa
$\dot{q}''_{fl,c}$	Convective heat flux transferred from the flame to the solid, W/m^2
$\dot{q}''_{r,c}$	Radiatiive heat flux transferred from the flame to the solid, W/m^2
$\dot{q}''_{rr}$	Surface re-radiation, W/m^2
r	Radial direction
r_f	Mass-to-fuel ratio
R	Radius, m
t	Time, s
T	Temperature, K
u	Velocity, mm/s
X_{O2}	Oxygen mole fraction
$Y_{O2,\infty}$	Oxygen mass fraction
z	Axial direction

Greek symbols

α	Thermal diffusivity, m^2/s
δ	Insulation thickness, mm
μ	Kinematic viscosity, $Pa.s$
ρ	Density, kg/m^3

Subscripts

c	Metallic core
g	Gas phase
m	Melting
p	Pyrolysis
s	Polymer
∞	Ambient conditions

Superscripts

'	Per meter
"	Per meter squared

Acronyms

FSR	Flame spread rate
LDPE	Low-density polyethylene
NiCr	Nickel-Chrome

Conflicts of interest

The authors declare no competing financial interest.

References

[1] Y. Nakamura, N. Yoshimura, T. Matsumura, H. Ito, O. Fujita, "Flame Spread over Polymer-Insulated Wire in Sub-Atmospheric Pressure: Similarity to Microgravity Phenomena", p. 17-27, Springer, 2008.

[2] L. Hu, Y. Zhang, K. Yoshioka, H. Izumo, O. Fujita, "Flame spread over electric wire with high thermal conductivity metal core at different inclinations", *Proc. Combust. Inst.* **35** (2015), no. 3, p. 2607-2614.

[3] Y. Kobayashi, X. Huang, S. Nakaya, M. Tsue, C. Fernandez-Pello, "Flame spread over horizontal and vertical wires: The role of dripping and core", *Fire Safety Journal* **91** (2017), p. 112-122, Fire Safety Science: Proceedings of the 12th International Symposium.

[4] X. Huang, Y. Nakamura, "A Review of Fundamental Combustion Phenomena in Wire Fires", *Fire Technol.* **56** (2020), p. 315-360.

[5] O. Fujita, M. Kikuchi, K. Ito, K. Nishizawa, "Effective mechanisms to determine flame spread rate over ethylene-tetrafluoroethylene wire insulation: Discussion on dilution gas effect based on temperature measurements", *Proc. Combust. Inst.* **28** (2000), no. 2, p. 2905-2911.

[6] A. Umemura, M. Uchida, T. Hirata, J. Sato, "Physical model analysis of flame spreading along an electrical wire in microgravity", *Proc. Combust. Inst.* **29** (2002), no. 2, p. 2535-2543.

[7] S. Takahashi, H. Takeuchi, H. Ito, Y. Nakamura, O. Fujita, "Study on unsteady molten insulation volume change during flame spreading over wire insulation in microgravity", *Proc. Combust. Inst.* **34** (2013), no. 2, p. 2657-2664.

[8] J.-M. Citerne, H. Dutilleul, K. Kizawa, M. Nagachi, O. Fujita, M. Kikuchi, G. Jomaas, S. Rouvreau, J. L. Torero, G. Legros, "Fire safety in space – Investigating flame spread interaction over wires", *Acta Astronautica* **126** (2016), p. 500-509, Space Flight Safety.

[9] A. Guibaud, J.-M. Citerne, J.-L. Consalvi, G. Legros, "On the effects of opposed flow conditions on non-buoyant flames spreading over polyethylene-coated wires – Part I: Spread rate and soot production", *Combust. Flame* **221** (2020), p. 530-543.

[10] M. Nagachi, F. Mitsui, J.-M. Citerne, H. Dutilleul, A. Guibaud, G. Jomaas, G. Legros, N. Hashimoto, O. Fujita, "Effect of Ignition Condition on the Extinction Limit for Opposed Flame Spread Over Electrical Wires in Microgravity", *Fire Technol.* **56** (2020), p. 149-168.

[11] I. S. Wichman, "Theory of opposed-flow flame spread", *Progress in Energy and Combustion Science* **18** (1992), no. 6, p. 553-593.

[12] R. F. McAlevy, R. S. Magee, "The mechanism of flame spreading over the surface of igniting condensed-phase materials", *Symposium (International) on Combustion* **12** (1969), no. 1, p. 215-227.

[13] F.-P. Carlos, "The solid phase", in *Combustion Fundamentals of Fire*, Academic Press Inc., 1994, p. 31-100.

[14] J. N. De Ris, "Spread of a laminar diffusion flame", *Symposium (International) on Combustion* **12** (1969), no. 1, p. 241-252.

[15] M. A. Delichatsios, "Creeping flame spread: Energy balance and application to practical materials", *Symposium (International) on Combustion* **26** (1996), no. 1, p. 1495-1503.

[16] M. A. Delichatsios, R. A. Altenkirch, M. F. Bundy, S. Bhattacharjee, L. Tang, K. Sacksteder, "Creeping flame spread along fuel cylinders in forced and natural flows and microgravity", *Proc. Combust. Inst.* **28** (2000), no. 2, p. 2835-2842.

[17] M. A. Delichatsios, "Relation of opposed flow (creeping) flame spread with extinction/ignition", *Combust. Flame* **135** (2003), no. 4, p. 441-447.

[18] S. Takahashi, H. Ito, Y. Nakamura, O. Fujita, "Extinction limits of spreading flames over wires in microgravity", *Combust. Flame* **160** (2013), no. 9, p. 1900-1902.

[19] Y. Konno, N. Hashimoto, O. Fujita, "Role of wire core in extinction of opposed flame spread over thin electric wires", *Combust. Flame* **220** (2020), p. 7-15.

[20] Y. Konno, N. Hashimoto, O. Fujita, "Downward flame spreading over electric wire under various oxygen concentrations", *Proc. Combust. Inst.* **37** (2019), no. 3, p. 3817-3824.

[21] A. Guibaud, J. L. Consalvi, J. M. Orlac'h, J.-M. Citerne, G. Legros, "Soot Production and Radiative Heat Transfer in Opposed Flame Spread over a Polyethylene Insulated Wire in Microgravity", *Fire Technol.* **56** (2020), p. 287-314.

[22] A. Guibaud, "Flame spread in microgravity environment : influence of ambient flow conditions", PhD Thesis, Sorbonne University, Paris, France, 2019, Thèse de doctorat dirigée par Legros, Guillaume et Consalvi, Jean-Louis, Mécanique Sorbonne université 2019, http://www.theses.fr/2019sorus129.

[23] A. Guibaud, J.-L. Consalvi, J.-M. Citerne, G. Legros, "Pressure effects on the soot production and radiative heat transfer of non-buoyant laminar diffusion flames spreading in opposed flow over insulated wires", *Combust. Flame* **222** (2020), p. 383-391.

[24] A. Guibaud, J.-M. Citerne, J.-L. Consalvi, O. Fujita, J. L. Torero, G. Legros, "Experimental evaluation of flame radiative feedback: methodology and application to opposed flame spread over coated wires in microgravity", *Fire Technol.* **56** (2020), no. 1, p. 185-207.

[25] J.-L. Consalvi, A. Guibaud, A. Coimbra, J.-M. Citerne, G. Legros, "Effects of oxygen depletion on soot production,

emission and radiative heat transfer in opposed-flow flame spreading over insulated wire in microgravity", *Combust. Flame* **230** (2021), article no. 111447.

[26] M. A. Delichastsios, "Exact Solution for the Rate of Creeping Flame Spread over Thermally Thin Materials", *Combustion Science and Technology* **44** (1986), no. 5-6, p. 257-267.

[27] A. Coimbra, J. Sarazin, S. Bourbigot, G. Legros, J.-L. Consalvi, "A semi-global reaction mechanism for the thermal decomposition of low-density polyethylene blended with ammonium polyphosphate and pentaerythritol", *Fire Safety Journal* **133** (2022), article no. 103649.

[28] Y. Konno, Y. Kobayashi, C. Fernandez-Pello, N. Hashimoto, S. Nakaya, M. Tsue, O. Fujita, "Opposed-Flow Flame Spread and Extinction in Electric Wires: The Effects of Gravity, External Radiant Heat Flux, and Wire Characteristics on Wire Flammability", *Fire Technol.* **56** (2020), p. 131-148.

[29] A. Guibaud, J.-M. Citerne, J.-L. Consalvi, O. Fujita, J. L. Torero, G. Legros, "Experimental Evaluation of Flame Radiative Feedback: Methodology and Application to Opposed Flame Spread Over Coated Wires in Microgravity", *Fire Technol.* **56** (2020), p. 185-207.

[30] Y. Sano, S. Nishikawa, "The Heat Transfer Coefficient of Fine Wires in Air Flow", *Chemical Engineering* **28** (1964), no. 4, p. 275-284.

[31] S. V. Patankar, *Numerical heat transfer and fluid flow*, Series on Computational Methods in Mechanics and Thermal Science, Hemisphere Publishing Corporation, 1980.

[32] J. E. Mark (ed.), *Physical Properties of Polymers Handbook*, second ed., Springer, 2007.

[33] Y. Kobayashi, K. Terashima, M. A. F. bin Borhan, S. Takahashi, "Opposed Flame Spread over Polyethylene Under Variable Flow Velocity and Oxygen Concentration in Microgravity", *Fire Technol.* **56** (2020), p. 113-130.

[34] M. Thomsen, C. Fernandez-Pello, X. Huang, S. Olson, P. Ferkul, "Buoyancy Effect on Downward Flame Spread Over PMMA Cylinders", *Fire Technol.* **56** (2020), no. 1, p. 247-269.

Comptes Rendus
Mécanique
2023, Vol. 351, Special Issue S2, p. 77-95
https://doi.org/10.5802/crmeca.146

Physical Science in Microgravity within the Thematic Group Fundamental and Applied Microgravity / *Sciences physiques en microgravité au sein du GDR Micropesanteur Fondamentale et Appliquée*

An approximate analytical model for the frequency response of evaporating droplets under a mixed feeding regime

Un modèle analytique approximatif pour la réponse en fréquence des gouttelettes d'évaporation sous un régime d'alimentation mixte

Kwassi Anani [a], Roger Prud'homme [*, b] and Mahouton N. Hounkonnou [c]

[a] Laboratory of Mathematical Modelling and Applications, Department of Mathematics, University of Lomé, 02 BP 1515 Lomé, Togo

[b] Jean Le Rond d'Alembert Institute, UMR 7190 CNRS, Sorbonne University, 4 place Jussieu, 75252 Paris Cedex 05

[c] University of Abomey-Calavi, International Chair in Mathematical Physics and Applications (ICMPA-UNESCO Chair) 072 B.P. 050 Cotonou, Republic of Benin

E-mails: kanani@univ-lome.tg (K. Anani), roger.prudhomme@sorbonne-universite.fr (R. Prud'homme), norbert.hounkonnou@cipma.uac.bj (M. N. Hounkonnou)

Abstract. This work is one of the analytical approaches to evaluate the evaporation frequency response of injected droplets, using the Heidmann analogy of a single droplet that is continuously fed with the same liquid fuel. Based on a linear analysis using the Rayleigh criterion, a dimensionless response factor is determined. The effects due to the variation of the heat transfer coefficient of the feeding process, as well as those due to the characteristic evaporation times and phase delay are analyzed. An abrupt increase of the response factor occurs, when a thermodynamic coefficient of the injected fuel takes certain specific values.

Résumé. Ce travail est l'une des approches analytiques pour évaluer la réponse en fréquence d'évaporation des gouttelettes injectées, en utilisant l'analogie de Heidmann i.e. d'une seule gouttelette alimentée en continu avec le même carburant liquide. Sur la base d'une analyse linéaire utilisant le critère de Rayleigh, un facteur de réponse sans dimension est déterminé. Les effets dus à la variation du coefficient de transfert de chaleur du processus d'alimentation, ainsi que ceux dus aux temps caractéristiques d'évaporation et au retard de phase sont analysés. Une augmentation brutale du facteur de réponse se produit, lorsqu'un coefficient thermodynamique du carburant injecté prend certaines valeurs spécifiques.

* Corresponding author.

Keywords. Combustion instability, Injection regime, Evaporation, Double confluent Heun equation, Transfer function.

Mots-clés. instabilité de combustion, régime d'injection, évaporation, équation de Heun à double confluence, fonction de transfert.

Published online: 20 February 2023

1. Introduction

Combustion instabilities are still nowadays a challenging area in combustion research, though their modeling and control have been investigated in many published works by various research teams during the past decades. These instabilities result from the coupling between acoustic waves and combustion. In confined devices, the coupling between acoustic field and heat or mass release at certain frequency levels may lead to engine failure or other catastrophic consequences [1, 2]. On the contrary, new blends of fuels can be engineered to undergo preferential instabilities leading to homogeneous combustion with higher efficiency [3]. Combustion instabilities can occur in both premixed and diffusion flames. The present study is concerned with subcritical diffusion flame models. In these latter, many causes were identified as being responsible for exciting or damping the mass release frequency response [4, 5]: period of ambient pressure oscillations that is closely related to the combustion chamber geometry, liquid fuel injection and atomization mechanisms with diverse boundary conditions, vaporization characteristic times that are obviously dependent on thermal convection and conduction processes, etc.

In comparison with other processes that take place inside the combustion chamber, the vaporization process has been pointed as the slowest [6], and hence may be the rate-controlling process. The evaporating mass frequency response of droplets to ambient pressure oscillations are generally computed by using classical droplet evaporation theories [3], on the basis of the Rayleigh criterion [7], by assuming simplifying assumptions. Many of the theoretical studies in the area are based on a single vaporizing droplet model as in [6, 8, 9]. Then, by means of numerical simulations, it is observed that the frequency response of spray droplets to ambient pressure oscillations can be considered as a statistical consequence of the vaporization characteristics of each individual droplet in the array. Among previous numerical works on vaporization frequency response of sprays, Tong and Sirignano [10] examined the effects of oscillating gas pressure and velocity on vaporization rates of continuously injected droplets during combustion instability. They concluded that self-sustained acoustical oscillations can occur in the combustor when vaporization is a controlling phenomenon. More recently, de la Cruz Garc'ıa et al. [11] investigated on the self-excited oscillations in a kerosene spray flame and concluded that the combustor stability strongly depends on the fuel distribution, degree of evaporation, and mixing before the main reaction zone. A progress has also been made in analytical modeling of vaporization frequency response of spray droplets. Haddad and Majdalani [12] provided a closed-form analytical solution for the transverse vorticoacoustic wave in a circular cylinder with headwall injection. Likewise, researchers have recently reported improved analytical models for spray combustion instability in diverse configurations as for example Greenberg and Katoshevski (see [13] and references therein).

One of the theoretical approaches for analyzing the evaporating mass frequency response to pressure oscillations of a spray of repetitively injected drops into a combustion chamber, can be considered from the Heidmann analogy of a spherical vaporizing droplet [14]. According to the Heidmann analogy, a single stationary spherical droplet represents this vaporizing spray of droplets. This mean droplet is a vaporizing droplet, continuously fed with the same liquid fuel, so that its volume is assumed to remain almost constant during the vaporization process. This

configuration consists of representing the spray of repetitively injected drops in the combustion chamber by a motionless mean droplet. The influence of spatial gas pressure and velocity variations, which are inherent to acoustic modes, are not taken into account with this approach, e.g. in the case of transverse acoustic modes to which the spray can be submitted, because this approach is focused on the behavior of droplets located at pressure anti-nodes. The single vaporizing droplet is continuously supplied at a stationary flow rate with the same liquid fuel. This classical model can permit to include most of the above-mentioned mechanisms that intervene in combustion instability phenomena, in a single theoretical analysis. Heidmann and Wieber first based their model on the hypothesis that, the mean spherical droplet summarizes the oscillatory rate of vaporization of an array of repetitively injected droplets in the combustion chamber [14]. However, they assumed an infinite thermal diffusivity of the liquid phase, therefore the mean droplet has a uniform temperature whatever the feeding process adopted.

This classical model was refined by Prud'homme et al. [15], especially at ONERA (the French Aerospace Laboratory) and within the framework of the research group GDR-MFA (Micropesanteur Fondamentale et Appliquée). This group leads a program on micro gravity in the field of engineering sciences with the assistance of the main research structures of the French State, namely the CNRS and the CNES. The present study is part of the celebration of the 30 years since the creation of this research group. During their first work, Prud'homme et al. [15] took into account a finite thermal diffusivity of the liquid, but the feeding process at the mean droplet center was assumed adiabatic, and the radial thermal convection term that appears in the energy equation of the liquid phase was neglected (pure conduction model). In [16], Anani and Prud'homme extended the study of this pure conduction model by taking into account the isothermal feeding process at the mean droplet center. More recently, an approximate analytical model has been realized by Anani et al. [17], where has been abandoned the simplifying assumption of negligible radial thermal convection effect inside the liquid phase. Nevertheless, only the two extreme cases of center injection that are the adiabatic and the isothermal feeding regimes were considered. Apart from this latter work, no analytical solution has been found nor any asymptotic study has been performed for intermediate injection cases, where the feeding regime at the mean droplet center is an intermediate case between the two extreme thermal forcing types.

Taking into account the mixed or generalized injection regime at the center of the mean droplet, this paper aims to contribute to the linear analysis of subcritical combustion instabilities by analytical approaches based on the mean spherical droplet configuration as in [17]. In Section 2, a brief description is given of the unperturbed state corresponding to the vaporization of the continuously fed spherical droplet in a stable environment. In Section 3, the linear analysis for harmonic perturbations in pressure is performed and a double confluent Heun equation (see [18]) is derived from the energy equation of the liquid phase. Then, an approximate analytical expression of the temperature field inside the mean droplet is obtained for the generalized or mixed injection regime and the mass response factor is defined. Results are discussed in Section 4. Throughout the discussion, comparisons are made with the results of other combustion instability models found in the literature that account for the vaporization of individual droplets injected into the spray. Finally, key results are recalled in the conclusions.

2. Description of the stabilized state

2.1. *Model assumptions*

Individual fuel droplets are repetitively injected into a subcritical combustion chamber such that the interaction between the droplets or between the droplets and the wall are negligible. Velocity-stabilized hypotheses are assumed as in [14], and an idealized physical configuration of a mean

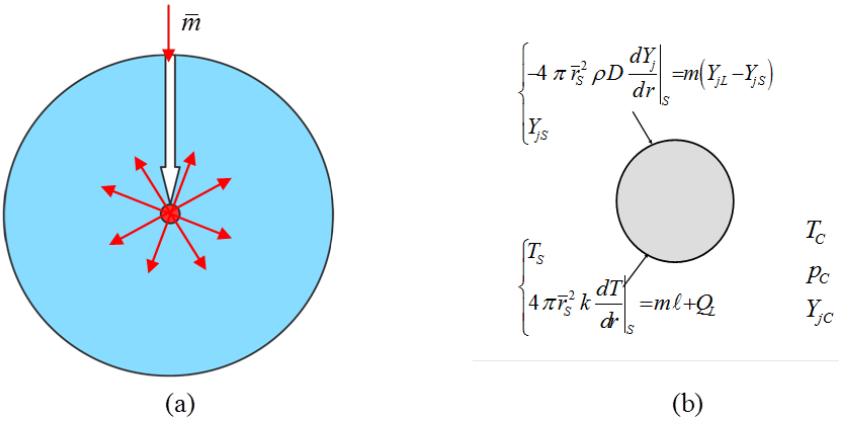

Figure 1. (a) The mean vaporizing droplet, continuously fed by a point source placed at its center. (b) Boundary conditions for the supplied droplet.

spherical droplet at rest in the combustion chamber, here represents the vaporizing spray of droplets. In the present model, the feeding is realized at some liquid-liquid heat transfer coefficient by using a source point placed at the spherical droplet center, in such a way that only radial thermal convection and conduction effects are taken into account inside the mean droplet during the process. This feeding process is now considered as a proper boundary condition, that is a mixed or a generalized feeding regime controlling the actual process of liquid fuel injection into the combustion chamber. Thus, the frequency response of individual drops in the spray is supposed to be summarized by the mean droplet, which is placed at a specific location in the combustion chamber (pressure anti-node and velocity node). As the instantaneous evaporating mass m of the mean droplet is continuously restored with the average mass flow rate $\overline{m}$ of the same fluid, an almost constant radius $\bar{r}_S$ is assumed for the vaporizing mean droplet during the process time. The choice of the Arithmetic Mean Diameter configuration for the mean droplet leads to conservation equations with fixed boundary conditions and is motivated by the analytical approach of the problem. From now on, all barred quantities denote mean values corresponding to the stabilized state, whereas all primed quantities will indicate relative perturbation quantities, i.e. $x' = (x - \bar{x})/\bar{x}$.

The feeding process is realized by using a point source placed at the droplet center in such a way that the local feeding rate is distributed throughout the droplet (see Figure 1(a)). Except for the radial thermal convection effect from the droplet center to its evaporation surface, any other convective transport or liquid recirculation phenomenon within the droplet will be assumed negligible. The thermal conductivity k_L, the density ρ_L and the specific heat c_L of the droplet will be treated as constant. The spherical shape of the mean droplet is maintained at every moment during the process, and the thermal dilatation of the liquid is negligible. At the mean droplet center, a mixed injection regime is considered, that is, the liquid fuel is injected into the droplet with a positive heat transfer coefficient h. The two extreme cases of this generalized boundary condition are the adiabatic feeding regime ($h = 0$), where a zero temperature gradient is assumed at the droplet center, and the isothermal feeding regime ($h = +\infty$), where the droplet center is kept at the constant temperature $\overline{T}_S$. This latter represents the mean value of T_S, the spatially uniform but time-varying temperature of the saturated vapor at the surface of the stabilized droplet.

Around the droplet surface, the gas phase evolves in a quasi-steady state. There is no gas diffusion into the droplet and equilibrium conditions are assumed at the droplet/gas interface for the stabilized state. Far from the mean droplet, the ambient environment of the chamber is at a constant subcritical temperature T_C and pressure p_C. These boundary conditions are shown on Figure 1(b), where subscripts L and l indicate the liquid phase while the round letter ℓ will be used throughout the document to denote the latent heat of vaporization per unit mass of liquid. The subscripts S and C refer respectively to the droplet surface and to the ambient conditions in the combustion chamber far from the droplet. The quantity Q_L designates the heat flux transferred to the liquid and D denotes the binary diffusion coefficient of the fuel vapor in air. The thermal conductivity and the density of the gas mixture around the droplet surface are respectively denoted by k and ρ. The gaseous mixture at the immediate vicinity of the droplet is made up of fuel species $j = F$ and of combustion products diluted species $j = A$ proceeding from the flame front at infinity. The mass fraction of species j is denoted by Y_j. For reason of simplicity, a mono-component droplet with only fuel species will be considered, that is $Y_{FL} = 1$ and $Y_{AL} = 0$.

Theoretical studies of the evaporating mass response of spray droplets to acoustic and/or velocity perturbations in combustors are mostly based on numerical simulations. But, even when assuming certain simplifying assumptions, analytical models that include more complex aspects of the problem are needed for providing deep insights in the vaporization frequency response. Nevertheless, both numerical and analytical models need to be confronted with appropriate experimental measurements and more detailed databases for validating the predictions. As stated in [19], specifications of an experimental design may include several regulations and measurement devices. Since the present theoretical study is based on the mean droplet configuration, experimental facility and methods similar to those described in [20] can provide tracks for some experiments. However, the problem is here considered only under its analytical aspect. As mentioned in the introduction, the mean droplet model can permit to include in a single theoretical analysis most of the mechanisms that intervene in spray combustion instability. The results obtained may then serve as references for full experimental and numerical simulations of sprays combustion instabilities, which will not necessarily need to rely on the simplifying assumptions adopted here.

The present model of a representative drop, continuously fed by a mass and thermal point source placed in its center, allows to include among other advantages, the possibility to formulate the boundary conditions with a heat transfer coefficient. But, unlike the classical adiabatic condition, the generalized boundary conditions do not ensure the regularity of the heat fluxes at the center. Even in the adiabatic feeding regime, the radial velocity of the liquid diverges at the center of the mean droplet, where its infinite value is counterbalanced by zero heat flux at the center. In all cases, in the adiabatic or mixed feeding regimes, the evaluation of the mass response factor depends only on the regularity of the temperature flux at the surface of the mean droplet, and this condition will be well verified here in all the different feeding regimes. Thus, using simplifying assumptions, the present study aims to provide regular approximate solutions, in order to investigate the effects of the heat transfer coefficient of the fuel injection process, on the frequency response of the vaporization.

2.2. *Evaporation characteristic times*

The residence time and the transfer time by thermal diffusion are the two characteristic times controlling heat transfer processes inside the stabilized mean droplet. The residence time of the continuously fed droplet replaces the notion of a free droplet lifetime in the present situation of almost constant volume and can be identified to the ratio $\bar{\tau}_v = \overline{M}/\overline{m}$. Here, $\overline{m}$ is the stationary feeding rate, while $\overline{M}$ represents the mean value of the actual mass M of the supplied droplet.

The transfer time by thermal diffusion process is identified to $\bar{\tau}_T = \bar{r}_S^2/\kappa_L$, where $\bar{r}_S$ is the average radius of the mean droplet and $\kappa_L = k_L/(\rho_L c_L)$ is the thermal diffusivity of the liquid. The timescale ratio $\theta = 9\bar{\tau}_v/\bar{\tau}_T = \bar{\tau}_v/\widetilde{\tau}_T$, where $\widetilde{\tau}_T = \bar{\tau}_T/9$, will be called the thermal exchange ratio or more briefly the exchange ratio from now on. It is of the same order of magnitude as $1/P_L$, where P_L is the Péclet number of the liquid phase. The coefficient 9, which appears in this ratio will lead hereafter to a more simple expression of the transfer function. It will be also kept for results comparison purposes with previous mean droplet models as in [16, 17]. During the vaporization process, instabilities related to intrinsic or external pressure oscillations can cause departure from the stabilized-state conditions and a linear analysis can be performed in the case of harmonic perturbations in pressure. A major characteristic time of the perturbed state of the mean droplet is the oscillation or wave period of the ambient pressure. The angular frequency of the harmonic oscillations in pressure will be denoted by ω. In [14], the mass response factor was studied over a wide range of flow conditions and the data was found to be correlated with some dimensionless parameter, that is the droplet lifetime or half lifetime normalized by the wave period. Likewise, in the present study, a reduced frequency u depending on the residence time $\bar{\tau}_v$ is defined as $u = 3\omega\bar{\tau}_v$.

2.3. *Equations for the stabilized state*

The mass balance of the mean evaporating droplet is written:

$$\frac{dM}{dt} = \overline{m} - m, \tag{1}$$

where $\overline{m}$ and m denote respectively the stationary flow of injection and the instantaneous flow of evaporation. In the unperturbed or stabilized state, equation (1) becomes: $dM/dt = 0$, implying $\overline{m} = m$ and $M = \overline{M}$. The instantaneous amount of heat Q_L penetrating into the droplet can be evaluated as:

$$Q_L = Q - m\ell = 4\pi\bar{r}_S^2 k_L \frac{\partial T_l}{\partial r}(r = \bar{r}_S,\, t), \tag{2}$$

where $T_l(r,\, t)$ is the droplet temperature at radial coordinate r and at time t, Q is the external gas heat flow and ℓ is the latent heat of vaporization per unit mass of the liquid. Equation (2) couples the gas and the liquid phase solutions at the droplet surface. Since both radial thermal convection and conduction data need to be appropriately included in the formulation of the energy conservation equation, the internal temperature $T_l \equiv T_l(r,\, t)$ verifies the following equation:

$$\rho_L c_L \frac{\partial T_l}{\partial t} + \rho_L c_L v_r \frac{\partial T_l}{\partial r} - \frac{k_L}{r}\frac{\partial^2 (rT_l)}{\partial r^2} = 0, \tag{3}$$

where v_r is the central injection velocity expressed as $v_r = \overline{m}/4\pi\rho_L r^2$ for $0 < r < \bar{r}_S$. Equation (3) is subject to a mixed boundary condition at the droplet center and to the Dirichlet boundary condition at the surface:

$$\begin{cases} \dfrac{\partial T_l}{\partial r}(r = 0, t) = \dfrac{h}{\bar{r}_S}\left(T_l(0,\, t) - \bar{T}_S\right), \\ T_l(\bar{r}_S,\, t) = T_S(t). \end{cases} \tag{4}$$

The parameter $h > 0$ in conditions (4) indicates the heat transfer coefficient. We recall that, $h = 0$ for the adiabatic injection regime and the boundary condition at the droplet center is reduced to $\partial T_l/\partial r = 0$ on $r = 0$, whereas $h = +\infty$ for the isothermal injection regime and the related condition at the droplet center becomes $T_l(0, t) = \overline{T}_S$. The mixed boundary condition at the droplet center can then be viewed as an idealized modeling of a preheated spray injection process. In liquid fuel injection processes, internal flow evaluations depend on inlet boundary conditions (see [21] and references therein). Some studies have shown that the reduction in kinematic viscosity resulting from fuel preheating improves the combustion and emissions performance of the

engine [22,23]. Now, in subcritical combustion systems, the two extreme cases bounding the possible range of real inlet liquid temperature fluxes are precisely the adiabatic and the isothermal feeding regimes. The adiabatic feeding regime at the mean droplet center can be related to an unheated spray feeding process, where the mean temperature $\overline{T}_A$ of the injected fuel is connected to standard conditions for temperature and pressure. On the contrary, the isothermal feeding regime can be brought closer to the process of injection of fuel at temperature $\overline{T}_S$. The latter is related to the liquid wet bulb temperature $\overline{T}_{WB}$ or to its boiling temperature $\overline{T}_B$, when $\overline{T}_{WB}$ estimate is unavailable (see [24]). Therefore, in an actual mixed injection process, the inlet fuel temperature may be stated between the extreme values that are $\overline{T}_A$ and $\overline{T}_S$. In brief, during the spray vaporization process, the corresponding rate of heat brought by the injected fuel to the array of droplets is here investigated by means of the heat transfer coefficient h.

Assuming the classical quasi-steady hypothesis of a local evaporation equilibrium at the surface of the mean droplet, the instantaneous mass vaporization rate can be evaluated as:

$$m = 2\pi\rho D r_S Sh^* \ln(1+B_M) = 4\pi \frac{k}{c_p} r_S Nu^* \ln(1+B_T), \tag{5}$$

where $B_M = (Y_{FS} - Y_{FC})/(1-Y_{FS})$ and $B_T = c_p(T_C - T_S)/(\ell + Q_L/m)$ represent respectively the mass and heat transfer numbers of Spalding, and c_p denotes the specific heat capacity of fuel vapor at constant pressure. The parameters ρ, k and D are here recalled as the density, the thermal conductivity and the binary diffusion coefficient of the mixture of vapor and ambient gas. The Nusselt and Sherwood numbers Nu^* and Sh^* were provided in the extended film model by Abramzon and Sirignano [25]. The saturated vapor pressure at the droplet surface is expressed as $p_{sat}(T_S) = \exp(a - b/(T_S - c))$, where a, b and c are coefficients related to the fuel thermophysical properties. The mole fraction X_{FS} of fuel species is connected to the saturated vapor pressure p_{sat} by the relation $p\,X_{FS} = p_{sat}(T_S)$, where $p = p_C$ is the ambient pressure. The mass fraction Y_{FS} of the vapor at the droplet surface can be expressed as a function of the mole fraction X_{FS} by:

$$Y_{FS} = \frac{\mathcal{M}_F}{\mathcal{M}_F X_{FS} + \mathcal{M}_A X_{AS}} X_{FS}, \tag{6}$$

with $\mathcal{M}_j$ denoting the molecular weight of species $j = A$ for combustion products diluted species, or $j = F$ for fuel species. Temperature and concentration values continually evolve in the gas phase and their averaged values can be respectively taken at some reference temperature $\overline{T} = T_S + A_r(T_C - T_S)$ and concentration $\overline{Y}_j = Y_{jS} + A_r(Y_{jC} - Y_{jS})$ with $A_r = 1/3$. Here, the Lewis number $Le = k/\rho D c_p$ is assumed equal to 1 and both Sh^* and Nu^* are equal to 2.

3. Linear analysis for harmonic perturbations

3.1. *Linear analysis of the liquid-phase*

In order to perform a linear analysis, each flow variable f is divided into steady and unsteady parts by writing $\Delta f = f - \bar{f}$, where $\bar{f}$ is the mean value, Δf is the absolute perturbation of the flow, and $f' = \Delta f/\bar{f}$ is the corresponding relative perturbation. Thus, the relative perturbation of the droplet temperature field is $T_l'(r,t) = [T_l(r,t) - \overline{T}_l(r,t)]/\overline{T}_l(r,t)$, and the linearized form of the heat flow penetrating into the droplet (see equation (2)) will read:

$$4\pi\,\bar{r}_S^2\, k_L \overline{T}_S \frac{\partial T_l'}{\partial r}(r=\bar{r}_S, t) = Q_L - \overline{Q}_L = Q_L = \Delta Q_L \tag{7}$$

since $\overline{Q}_L = 0$. The energy conservation equation (equation (3)) becomes in its perturbed form:

$$\frac{\partial(rT_l')}{\partial t} + \kappa_L\left(\frac{3\bar{r}_S}{\theta r}\frac{\partial T_l'}{\partial r} - \frac{\partial^2(rT_l')}{\partial r^2}\right) = 0, \tag{8}$$

where $\theta = \bar{\tau}_\nu / \bar{\tau}_T$ is the thermal exchange ratio as defined in Subsection 2.2. From equations (4), the boundary conditions at the perturbed state are deduced as:

$$\begin{cases} \dfrac{\partial T_l'}{\partial r}(r=0,t) = \dfrac{h}{\bar{r}_S} T_l'(0,t), \\ T_l'(\bar{r}_S, t) = T_S'. \end{cases} \tag{9}$$

In the case of harmonic perturbations in pressure of frequency ω, the relative perturbation of the flow variable f takes the form of $f' = \Delta f / \bar{f} = \widehat{f}(r)\mathrm{e}^{\mathrm{i}\omega t}$. The parameters as ambient pressure, temperature and heat transferred into the droplet are respectively perturbed as $p_C' = \widehat{p}_C \mathrm{e}^{\mathrm{i}\omega t}$, $T_l' = \widehat{T}_l(r)\mathrm{e}^{\mathrm{i}\omega t}$ and $\Delta Q_L = \Delta \widehat{Q}_L(r)\mathrm{e}^{\mathrm{i}\omega t}$. The perturbed form of the energy conservation equation (equation (8)) can now be written as follows:

$$\mathrm{i} r^2 \omega \widehat{T}_l + \frac{3\kappa_L \bar{r}_S}{\theta} \frac{d\widehat{T}_l}{dr} - \kappa_L r \frac{d^2\left(r\widehat{T}_l\right)}{dr^2} = 0. \tag{10}$$

Or by equivalence as:

$$\mathrm{i}\omega \bar{\tau}_T \xi \widehat{T}_l + \frac{1}{3\theta\xi}\frac{d\widehat{T}_l}{d\xi} - \frac{d^2\left(\xi\widehat{T}_l\right)}{d\xi^2} = 0, \tag{11}$$

where $\widehat{T}_l$ is rather written as a function of the reduced radius variable $\xi = r/\bar{r}_S$, with $0 < \xi < 1$. In connection with ξ, equations (9) expressing the boundary conditions in the mixed or generalized feeding regime will read:

$$\begin{cases} \dfrac{d\widehat{T}_l}{d\xi}(\xi=0) = \dfrac{h}{\bar{r}_S}\widehat{T}_0 \\ \widehat{T}_l(1) = \widehat{T}_S, \end{cases} \tag{12}$$

where $\widehat{T}_0$ is the temperature of the preheated liquid fuel injected at the droplet center.

We now consider the conjugate complex numbers

$$s_0 = (1+\mathrm{i})(\omega/2\kappa_L)^{1/2} \quad \text{and} \quad \bar{s}_0 = (1-\mathrm{i})(\omega/2\kappa_L)^{1/2},$$

obtained from equation (11) by using the two roots s_0 and $-s_0$ of the characteristic equation $\mathrm{i}\omega - \kappa_L s^2 = 0$, when neglecting the convective term $(3\kappa_L \bar{r}_S/\theta) d\widehat{T}_l/dr$. A solution of equation (11) subject to equations (12), can be sought in the form of $\xi\widehat{T}_l(\xi) = \mathrm{J}(\xi)\{1 - \cos[\bar{s}_0 \bar{r}_S \xi \exp(\mathrm{i}\arctan h)]\}$, with $\exp(\mathrm{i}\arctan h) = (\mathrm{i}h+1)/(h^2+1)^{1/2}$, where h is the heat transfer coefficient, J refers to a function to be determined and $\exp(\mathrm{i}\arctan h) = (\mathrm{i}h+1)/(h^2+1)^{1/2}$. Writing $S_0 = \bar{s}_0 \bar{r}_S \exp(\mathrm{i}\arctan h)$ and substituting the functions $\sin(S_0\xi)$ and $\cos(S_0\xi)$ in equation (11) by their truncated expansions of second order, that are $\sin(S_0\xi) \approx S_0\xi$ and $\cos(S_0\xi) \approx 1 - (S_0\xi)^2/2$, the expression $\xi\mathrm{J}$ should approximately verify the following double confluent Heun equation:

$$\frac{\xi^2 d^2(\xi\mathrm{J})}{d\xi^2} + \left(2\xi - \frac{3}{\theta}\right)\frac{d(\xi\mathrm{J})}{d\xi} - 2\bar{s}_0^2 \bar{r}_S^2 \frac{h(\mathrm{i}-h)}{h^2+1}\xi^2(\xi\mathrm{J}) = 0. \tag{13}$$

Now, using the notations of the Maple software, the solution of equation (13) can be expressed as $\mathrm{J}(\xi) = C_0 \exp[-3(\theta\xi)^{-1}]\mathrm{HeunD}(x_1, x_2, x_3, x_4, x)/\xi^{5/2}$, where C_0 is a constant to be determined and $\mathrm{HeunD}(x_1, x_2, x_3, x_4, x)$ is the double confluent Heun function. In this latter function, the variable x is expressed as function of ξ by $x = (\xi^2-1)/(\xi^2+1)$ and the four related parameters x_1, x_2, x_3 and x_4 are respectively given as:

$$\begin{aligned} x_1 &= 0, \\ x_2 &= -\left[\theta^2\left(h^2+1\right) - 9 - 9h^2 - 24uh(\mathrm{i}h+1)\theta\right]/4\theta^2\left(h^2+1\right), \\ x_3 &= -\left[9 + (9 - 24\mathrm{i}u\theta)h^2 - 24hu\theta\right]/2\theta^2\left(h^2+1\right) \\ \text{and } x_4 &= -\left[-\theta^2\left(h^2+1\right) - 9 - 9h^2 - 24uh(\mathrm{i}h+1)\theta\right]/4\theta^2\left(h^2+1\right). \end{aligned}$$

Here, the parameter $u = 3\omega\bar{\tau}_v$ is the reduced frequency of the ambient pressure as defined in the Subsection 2.2. The constant C_0 is determined by using the boundary condition at the mean droplet surface, $\widehat{T}_l(1) = \widehat{T}_S$. This leads to the expression of an approximate analytical solution of equation (11) as:

$$\widehat{T}_l(\xi) = \frac{\widehat{T}_S\left\{1-\cos\left[\bar{s}_0\bar{r}_S\xi\exp(\mathrm{i}\arctan h)\right]\right\}}{\left\{1-\cos\left[\bar{s}_0\bar{r}_S\exp(\mathrm{i}\arctan h)\right]\right\}\xi^{5/2}}\exp\left[\frac{3}{2\theta}\left(1-\frac{1}{\xi}\right)\right]\times\mathrm{HeunD}\left(x_1,x_2,x_3,x_4,\frac{\xi^2-1}{\xi^2+1}\right). \quad (14)$$

Except for the case where the temperature gradient is null at the droplet center ($h = 0$), the solution (14) presents an essential discontinuity at $\xi = 0$ once $h > 0$. Nevertheless, only the regularity condition at the droplet surface ($\xi = 1$) is needed for the calculation of the mass response factor and this condition is well verified by the equation (14).

The flow condition at the droplet surface (equation (7)) can be expressed as function of the reduced radius $\xi = r/\bar{r}_S$, and then be applied to the solution (14). This will lead to:

$$\Delta\widehat{Q}_L = -4\pi\bar{r}_S k_L \overline{T}_S \widehat{T}_S E(u,\theta,h), \quad (15)$$

where the function E is expressed with the parameters u, θ and h as:

$$E(u,\theta,h) = \frac{\bar{s}_0\bar{r}_S\exp(\mathrm{i}\arctan h)\sin\left[\bar{s}_0\bar{r}_S\exp(\mathrm{i}\arctan h)\right]}{\cos\left[\bar{s}_0\bar{r}_S\exp(\mathrm{i}\arctan h)\right]-1} - \frac{3}{2\theta}+\frac{5}{2}. \quad (16)$$

With $u = 3\omega\bar{\tau}_v$ and $\theta = \bar{\tau}_v/\widetilde{\tau}_T$, the calculations give $\bar{s}_0\bar{r}_S = (1-\mathrm{i})(3u/2\theta)^{1/2}$.

3.2. *The linearized equations of the gas phase*

The linearized equations for the liquid/gas interface were first presented in [15] and were used in [16,17]. Introducing the harmonic perturbations in the flow variables, the perturbed mass flow rate and ambient pressure respectively become $m' = \widehat{m}\mathrm{e}^{\mathrm{i}\omega t}$ and $p'_C = \widehat{p}_C\mathrm{e}^{\mathrm{i}\omega t}$. In consequence, the linearized equations were obtained from the stabilized state equations of the gas phase (see Subsection 2.3) as follow:

$$\widehat{m} = \alpha\frac{\mathrm{i}u}{1+\mathrm{i}u}\left(\bar{b}\widehat{T}_S - \widehat{p}_C\right), \quad (17)$$

and

$$\Delta\widehat{Q}_L = \overline{m}\bar{\ell}\left(\bar{a}\widehat{p}_C - \mu\widehat{T}_S\right). \quad (18)$$

The different coefficients involved in these equations were expressed as:

$$\bar{a} = \frac{\overline{T}_C}{\overline{T}_C-\overline{T}_S}\frac{\gamma-1}{\gamma}+\varphi, \quad \bar{b} = \frac{\overline{T}_S}{(\overline{T}_S-c)^2}b, \quad \mu = \frac{\overline{T}_S}{\overline{T}_C-\overline{T}_S} - \frac{2c}{\overline{T}_S-c}+\bar{b}\varphi$$

and

$$\alpha = \frac{\overline{B}_M}{(1+\overline{B}_M)\ln(1+\overline{B}_M)}\varphi, \quad \text{where} \quad \varphi = \frac{\overline{Y}_{AC}\overline{Y}_{FS}}{\overline{Y}_{AS}(\overline{Y}_{FS}-\overline{Y}_{FC})}\frac{\mathscr{M}_F}{\mathscr{M}_F\overline{X}_{FS}+\mathscr{M}_A\overline{X}_{AS}}.$$

The parameter γ denotes the constant isentropic coefficient, while the latent heat of vaporization per unit mass of the liquid is given by $\ell = bRT_S^2/\mathscr{M}_F(T_S-c)^2$, with R standing for the universal gas constant.

3.3. *Mass response factor*

The mean spherical droplet is assumed to be at rest in the combustion chamber and its velocity response can be neglected. Only the evaporating mass response due to the ambient acoustic forcing will here be considered. According to the Rayleigh criterion, the oscillations in pressure $p' = (p - \bar{p})/\bar{p}$ induces a perturbation in the evaporating mass flow rate $q' = (q - \bar{q})/\bar{q}$. The resulting mass response factor N can then be expressed as the ratio of the magnitude of the mass perturbation to that of the pressure perturbation:

$$N = \frac{\int_{V,t} q'(V,t)p'(V,t)\mathrm{d}t\mathrm{d}V}{\int_{V,t} (p'(V,t))^2\mathrm{d}t\mathrm{d}V}, \tag{19}$$

where the double integral is taken over the wave period of time t in the finite volume V. Considering now sinusoidal or harmonic oscillations that are uniform over a finite volume, the response factor N is reduced to $N = (|\widehat{q}|/|\widehat{p}|)\cos\phi$, where $|\widehat{q}|$ and $|\widehat{p}|$ stand for the modules of mass release q' and pressure p', and ϕ denotes the phase lag or i.e. the angle difference between q' and p'. Thus, in this case, a reduced mass response factor can be obtained as the real part of the mass transfer function $Z = \widehat{m}/(\alpha\widehat{p}_C)$. By using equations (15)-(18), the expression of the transfer function $Z \equiv Z(u,\theta,h)$ is obtained as:

$$Z(u,\theta,h) = \frac{\mathrm{i}u}{1+\mathrm{i}u}\frac{A+\theta E(u,\theta,h)}{B-\theta E(u,\theta,h)}, \tag{20}$$

where the involved thermodynamic coefficients $A = 3(\bar{a}\bar{b}-\mu)/\lambda$ and $B = 3\mu/\lambda$ depend on the fuel physical properties and are related to the ratio $\lambda = (c_L\overline{T}_S)/\bar{\ell}$. Then, the reduced mass response factor is the real part of the transfer function Z and will read:

$$\frac{N}{\alpha} = \Re(Z). \tag{21}$$

The reduced response N/α will be briefly called "response factor" or "mass response factor" in the rest of the paper. It includes phase lag relations since it becomes positive when the vaporization rate and the chamber pressure are either above or below their mean values, and negative when the vaporization rate and the chamber pressure are on the opposite sides of their means [7]. Moreover, the phase lag or angle difference ϕ between the vaporization rate and the chamber pressure, defined as the argument of the transfer function $\phi = \arg(Z)$, is proven to be insensitive to the chamber mean pressure magnitude [4]. Thus, the phase angle ϕ appears to be one of the key parameters for analyzing the mass frequency response due to ambient pressure oscillations.

4. Results and discussion

4.1. *General remarks*

The values $A = 10$ and $B = 100$ will be used for the thermodynamic coefficients A and B in all calculations and curves, since they correspond respectively to orders of magnitude of values encountered in the classical fuels [15]. The effects of the heat transfer coefficient h on the mass response factor were pointed out in a recent publication by the same authors (see [26]). Those results will be briefly recalled and if necessary improved in the following subsection. Then, the response factor will be analyzed in relation to the process characteristic times as highlighted in Subsection 2.2, and to the phase angle ϕ as defined in Subsection 3.3, and again to the influence of the value of the thermodynamic coefficient B.

In each diagram on Figures 2, 3, and 4, response factor curves are shown as function of the reduced frequency $u = 3\omega\bar{\tau}_v$ for a set of values of the exchange ratio θ. For a given value of the heat

transfer coefficient h, a quite large number of values of the exchange ratio θ are selected in order to illustrate a fairly wide range of curve profiles, among which the one related to a certain critical value of θ to be later deduced in this analysis. The diagrams are ranged in columns corresponding respectively to six different values of the heat transfer coefficient: $h = 0$ and $h = 0.1$ for Figure 2; $h = 1$ and $h = 1.05$ for Figure 3; $h = 10$ and $h = +\infty$ for Figure 4. As already mentioned, the extreme values ($h = 0$ and $h = +\infty$) are connected to the adiabatic and isothermal feeding regimes and the related curves are here illustrated for comparison purposes with previous results obtained in [17]. Among the other selected values of the heat transfer coefficient ($h = 0.1$; 1; 1.05; 10), the value $h = 1$ is a critical value and can be roughly considered with the three other intermediate values as representative of the main types of curve profiles obtained for h varying from 0 to $+\infty$.

4.2. *Effects of the heat transfer coefficient*

In [26], the evaporating mass response factor in a mixed injection regime has been analyzed in connection with the heat transfer coefficient h that controls this generalized feeding regime. The study has pointed out the following three main results.

First, it is noticeable that for $h = 0$ (Figures 2(a1), 2(a2) and 2(a3)), and for $h = +\infty$ (Figures 4(f1), 4(f2) and 4(f3)), the response factor curves seem very similar to those obtained respectively in the adiabatic and in the isothermal injection regimes, as discussed in [17]. In fact, calculations show that these curves are identical for a given value of the exchange ratio θ, since, when $h \to 0$,

$$E(u,\theta,h) \to \frac{\bar{s}_0 \bar{r}_S \theta \sin(\bar{s}_0 \bar{r}_S) + 2\theta \cos(\bar{s}_0 \bar{r}_S) - 3\cos(\bar{s}_0 \bar{r}_S) - 2\theta + 3}{\theta\,(1 - \cos(\bar{s}_0 \bar{r}_S))} = E(u,\theta,0). \tag{22}$$

While, as $h \to +\infty$,

$$E(u,\theta,h) \to -\frac{1}{2}\,\frac{2\theta s_0 \bar{r}_S \sin(s_0 \bar{r}_S) + 5\theta \cos(s_0 \bar{r}_S) - 3\cos(s_0 \bar{r}_S) - 5\theta + 3}{\theta\,(1 - \cos(s_0 \bar{r}_S))} = E(u,\theta,+\infty). \tag{23}$$

Thus, the expression of the function $E(u,\theta,h)$ in equation (16), coincides with those obtained in [17], for the calculation of the complex transfer function $Z(u,\theta,h)$ in the adiabatic and in the isothermal feeding regimes (respectively $h = 0$ and $h = +\infty$). Consequently, the results concerning the response factor curves in these two extreme regimes can be deduced as limiting cases from those of the present generalized injection regime. This kind of generalization has also been highlighted in a recent published paper (see [27]), where the mixed feeding regime was applied to a pastille-shaped droplet. Secondly, when the value of the heat transfer coefficient is fixed at one ($h = 1$), the corresponding response factor curves show intriguing fluctuations in their profiles, as it can be observed on Figures 3(c1), 3(c2) and 3(c3). If in addition, the value of the exchange ratio is chosen less than one ($\theta < 1$), that is for relatively small droplets, the fluctuations become straight chaotic as shown on Figure 3(c1). Nevertheless, these oscillations appear relatively reduced in amplitude compared to those obtained when the exchange ratio is much greater or equal to one ($\theta \geq 1$). In the latter case, the response factor curves show hyperbolic patterns with more higher peak values along the frequency axis. But, once the heat transfer coefficient differs slightly from one, almost all the corresponding curves tend to show more lower fluctuations in their profiles, even if h remains very close to one as for example $h = 1.05$ (see Figures 3(d1), 3(d2) and 3(d3)). The same behavior can be observed in the case where $h = 0.95$, case which is not illustrated with diagrams in the present paper. As comparison, a unity value of a heat transfer coefficient may characterize a heating from the flame towards the injection system through the chamber walls. According to [28], the radiative power is highly nonlinear and varies at the first order as the fourth power of the local instantaneous temperature. Likewise, in fuel injection processes, it may also be admitted that the evaporating mass frequency response

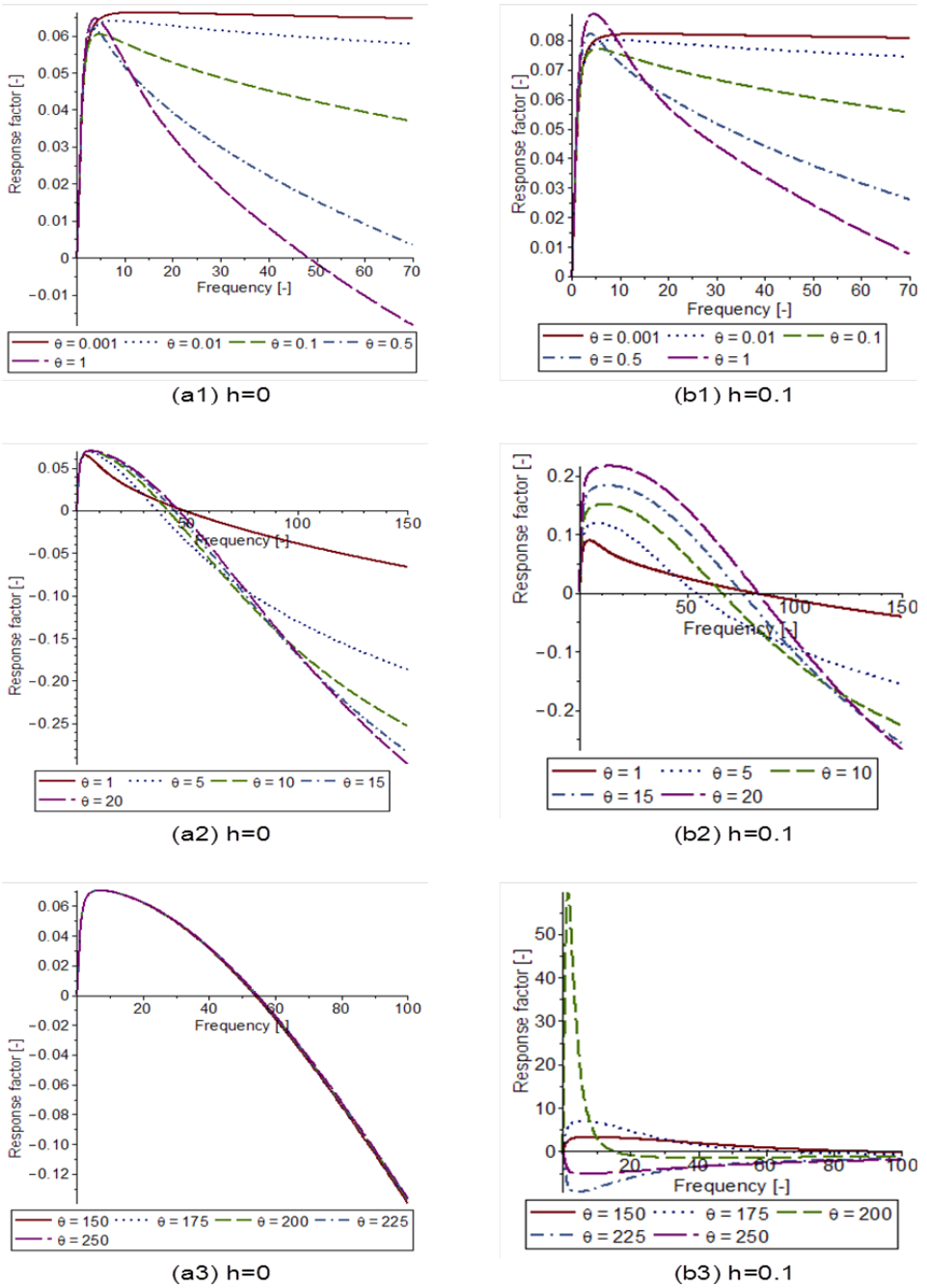

Figure 2. Mean droplet model with the thermodynamic coefficients $A = 10$ and $B = 100$: Variation of the reduced response factor N/α versus the dimensionless wave frequency u at various values of the non-dimensional exchange ratio θ and for the heat transfer coefficients $h = 0$ and $h = 0.1$.

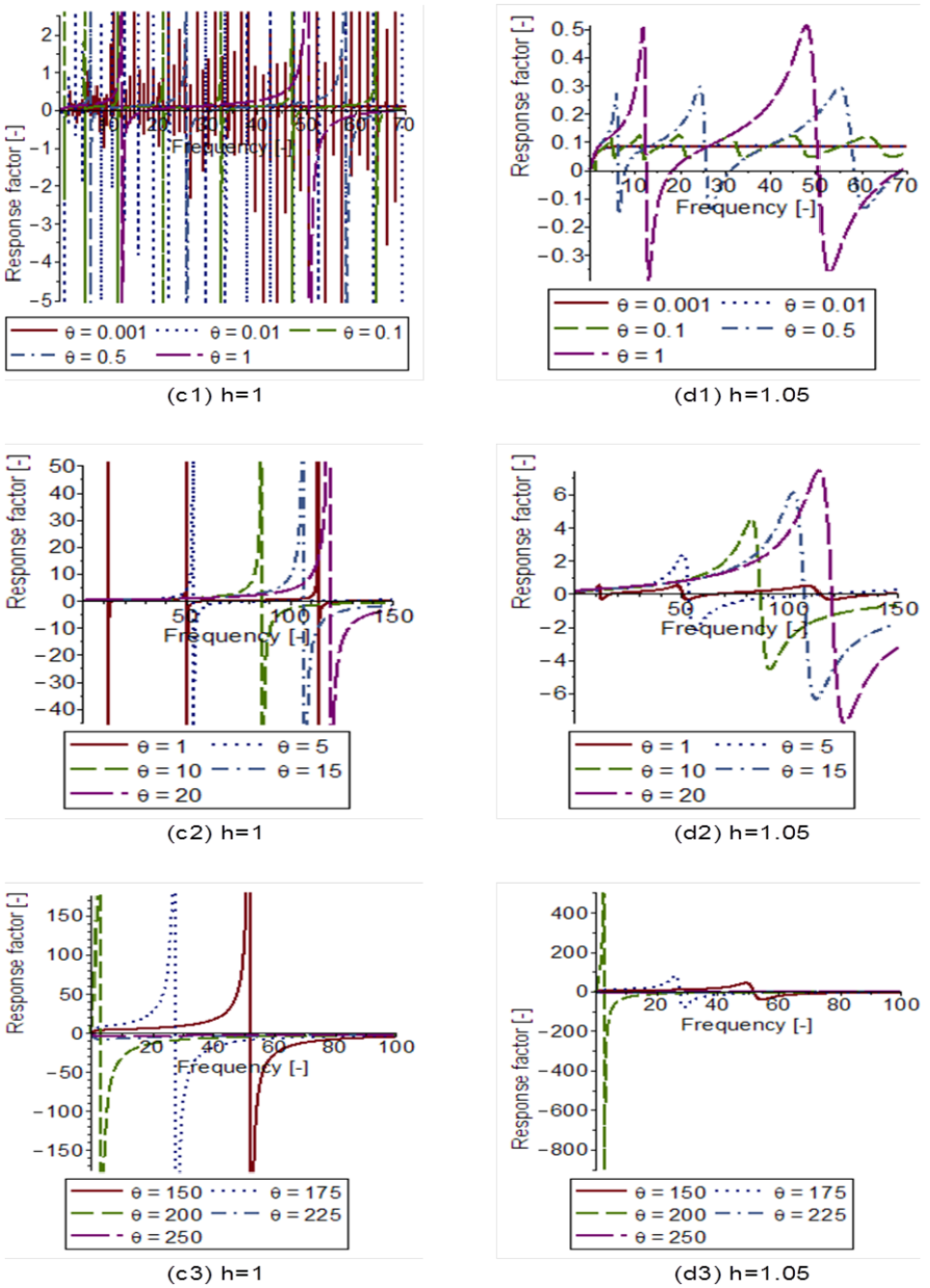

Figure 3. Mean droplet model with the thermodynamic coefficients $A = 10$ and $B = 100$: Variation of the reduced response factor N/α versus the dimensionless wave frequency u at various values of the non-dimensional exchange ratio θ and for the heat transfer coefficients $h = 1$ and $h = 1.05$.

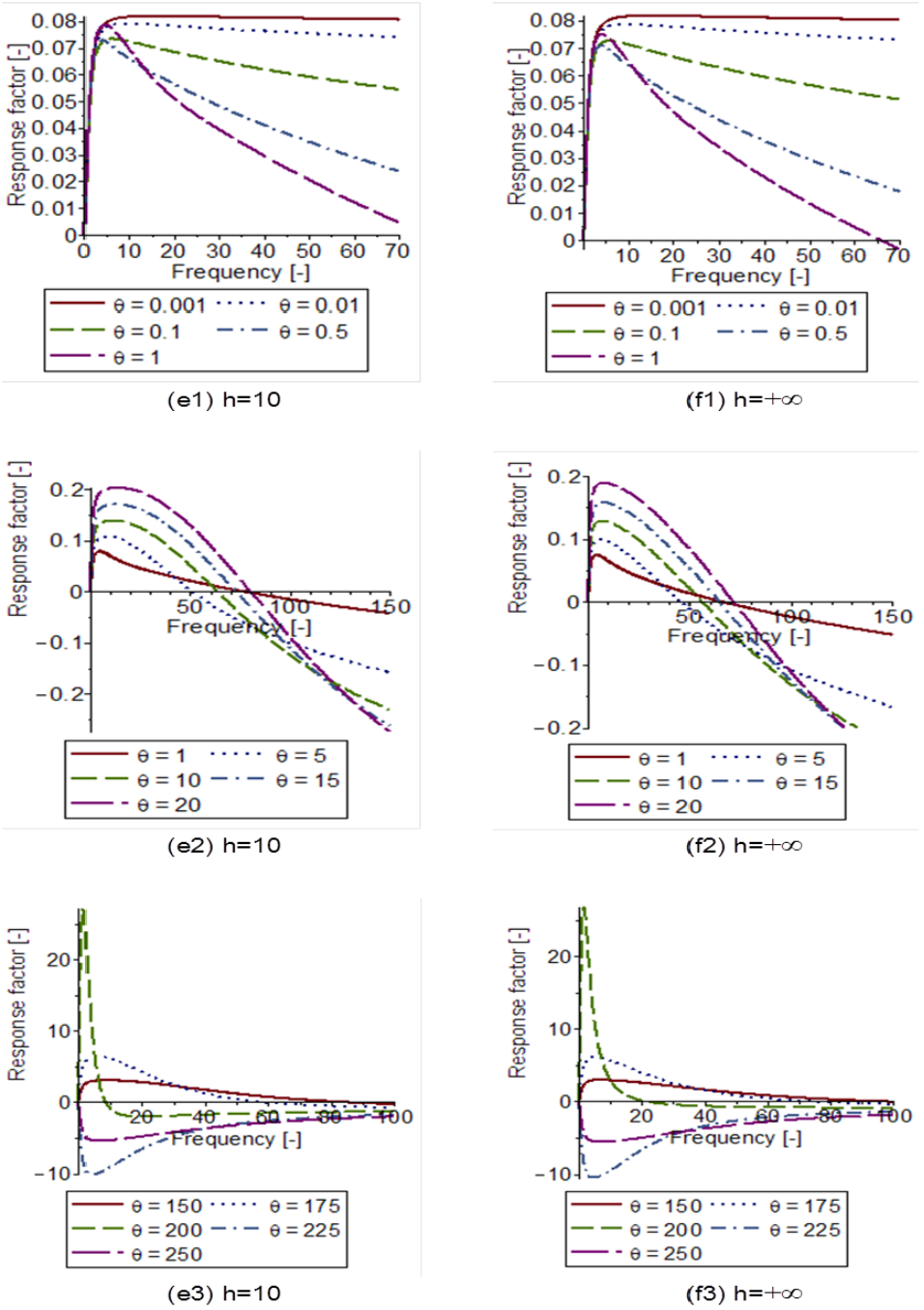

Figure 4. Mean droplet model with the thermodynamic coefficients $A = 10$ and $B = 100$: Variation of the reduced response factor N/α versus the dimensionless wave frequency u at various values of the non-dimensional exchange ratio θ and for the heat transfer coefficients $h = 10$ and $h = +\infty$.

of droplets and sprays can be strongly influenced near this specific value of the liquid-liquid heat transfer coefficient ($h = 1$). Thirdly, the mass response factor curves for relatively large values of the heat transfer coefficient ($h \geq 10$), seem to be very similar to those obtained in the isothermal injection regime ($h = +\infty$). Indeed, the convergence of the function $E(u,\theta,h)$ to $E(u,\theta,+\infty)$ together with that of the corresponding response factor $N/\alpha = \Re(Z)$ are proven to be asymptotic as h tends to $+\infty$. Thus, this convergence is approximately reached once the value of h is near 10, and the curves profiles on Figures 4(e1), 4(e2) and 4(e3) for $h = 10$ seem to be identical to those on Figures 4(f1), 4(f2) and 4(f3) for $h = +\infty$.

In brief, once the heat transfer coefficient becomes not null $h > 0$ in the injection process, high and nonlinear instabilities may appear in the vaporization frequency response of droplets and sprays. As highlighted in [29, 30] among others, the process of continuous supply of fuel to the chamber has been theoretically and experimentally identified as an important factor for producing or driving combustion instabilities.

4.3. *Effects of characteristic times and of the phase lag*

The vaporization response of a LOX droplet to oscillatory ambient conditions has been computed over a wide range of frequencies and the results were applied to prototypical cases pertinent to liquid rocket combustion instabilities [6]. It has been shown that the peak frequency for the computed response factor is correlated to the droplet lifetime. Indeed, as reported in [16, 17], the peak value of a response factor curve, whenever it exists, occurs at the same reduced frequency u_p that can be roughly evaluated about three. In mixed feeding regimes ($h > 0$) as well as in both extreme cases of adiabatic and isothermal injection regimes, the peak frequency value can be estimated at $u_p = 3\omega\bar{\tau}_v \approx 3$ (see among others, Figures 2(b1), 2(b2) for $h = 0.1$ and Figures 4(e1), 4(e2) for $h = 10$). This relation implies $\bar{\tau}_v \approx 1/\omega$, meaning that the injected liquid residence time $\bar{\tau}_v$ is at the same order of magnitude as the pressure oscillation period $1/\omega$. Now, the mean residence time $\bar{\tau}_v$ of a continuously fed droplet can be equated to the mean lifetime of free droplets in a spray. Therefore, whenever positive responses appear in the system, regardless of the value of the heat transfer coefficient $h \geq 0$, the vaporization rate can fully respond to the acoustic oscillations, only when the mean droplet lifetime is equal to the period of the ambient pressure oscillations.

It has also been anticipated that the well-known phase-lag model represents a key to a fundamental understanding of the evaporating mass frequency response to ambient pressure oscillations. Figure 5 shows phase angle curves ($\phi = \arg(Z)$), as functions of the reduced frequency $u = 3\omega\bar{\tau}_v$, for selected values of the exchange ratio θ. The curves are represented in a range of diagrams corresponding respectively to the same list of selected values of the heat transfer coefficient, namely $h = 0$; 0.1; 1; 1.05; 10 and $+\infty$, as retained for the illustration of the response factor curves. For $h = 0$, that is in the adiabatic feeding regime (see Figure 5(a)), phase angle curves collapse in a single line once $\theta \geq 1$, in accordance with the response factor curve profiles obtained on Figures 2(a1), 2(a2) and 2(a3). It is also remarkable that the cut-off frequency of this single curve, at which the phase angle cancels, is approximately equal to the peak frequency $u_p = 3\omega\bar{\tau}_v \approx 3$, where the vaporization rate oscillates in phase with the acoustic pressure ($\phi = 0$). In the adiabatic regime, a typical phase-angle curve starts from $\pi/2$ at the frequency $u = 0$, where the mass response is null, decreases rapidly to zero at the cut-off frequency u_p, where the response is maximal, and then decreases asymptotically to a negative value about $-\pi/3$, expressing thus a progressive damp of instability in the system. Likewise, the phase-angle curves for $h = 0.1$; 1 and 1.05 as shown on Figures 5(b), 5(c) and 5(d) are in agreement with the expectations. Indeed, when $h = 0.1$ (see Figure 5(b)), each corresponding response factor curve on Figures 2(b1), 2(b2) and 2(b3) shows for the selected value of the exchange ratio θ, a unique peak frequency u_p which

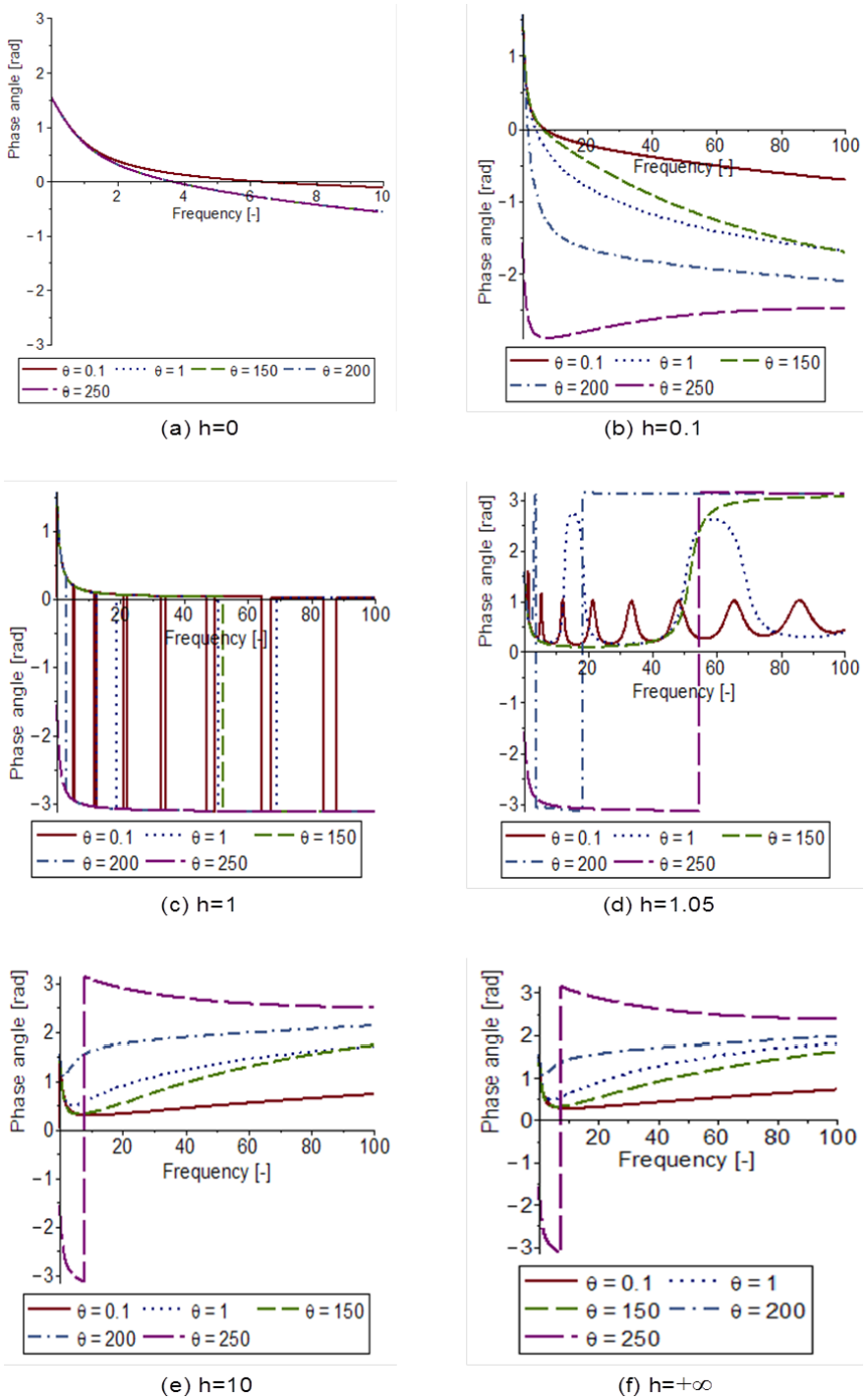

Figure 5. Mean spherical droplet model with the thermodynamic coefficients $A = 10$ and $B = 100$: variation of the phase lag ϕ versus the dimensionless wave frequency u at various values of the non-dimensional exchange ratio θ and for different value of the heat transfer coefficient h.

is relatively small. This leads to a reduced instability domain. A phase-angle curve on Figure 5(b) varies almost monotonously from the single peak frequency and remains inside a relatively limited range of values. On the contrary, except for $\theta = 250$, phase-angle curves for $h = 1$ and 1.05 as represented on Figures 5(c) and 5(d), exhibit many fluctuations even from the lower bound $-\pi$ to the upper bound π (see Figure 5(d) for $\theta = 200$). Those profiles are in accordance with their respective response factor curves, as shown on Figure 3.

The phase-angle curve profiles obtained on Figure 5(e) for $h = 10$ seem to be identical to those obtained in the isothermal feeding regime, i.e. on Figure 5(f) corresponding to $h = +\infty$. As mentioned in the subsection 4.2, this similitude is due to the asymptotic convergence of the response function, when h tends to $+\infty$. On the other hand, for $\theta = 250$, the phase-lag curve shows about the peak frequency u_p, an instantaneous change from the lower bound $-\pi$ to the upper bound π as it can be observed on Figures 5(e) and 5(f).

4.4. *Influence of a thermodynamic coefficient*

As they occur about a fixed value of the thermal exchange ratio ($\theta \approx 200$), the sharp changes noted in the response factor curve profiles on Figures 2(b3), 4(e3) and 4(f3) are not related to some particular values of the heat transfer coefficient, but rather to these specific values of θ. As in [17], those rapid changes in curve profiles around the reduced frequency $u_p \approx 3$, can be proven as depending on a specific value of θ, which is connected to the value of the fuel thermodynamic coefficient $B = 3\mu/\lambda$. In order to determine the threshold value θ_d of the thermal exchange ratio at which abrupt changes intervene in the curve profiles, the ratio $x = u/\theta = \omega\bar{\tau}_T/3$, may be particularly useful. Indeed, the thermal diffusion time $\bar{\tau}_T$ and the frequency of the oscillating wave ω do intervene in this ratio, but not the residence time $\bar{\tau}_v$. This ratio can then be assumed negligible at $u_p = 3\omega_p\bar{\tau}_{vp} \approx 3$, provided that the thermal transfer time by diffusion $\bar{\tau}_T$ is negligible compared either to the oscillation period $1/\omega_p$ or to the residence time $\bar{\tau}_{vp}$, since $1/\omega_p \approx \bar{\tau}_{vp}$ at the peak frequency u_p. Therefore, taking $h > 0$ and assuming u closer to u_p, the second-order truncated expansion of the transfer function $Z(u,\theta,h)$ in the neighborhood of $x = 0$ leads to the approximation:

$$Z(u,\theta,h) \approx \frac{\mathrm{i}u\left(A + \frac{\theta}{2} - \frac{3}{2}\right)}{(1+\mathrm{i}u)\left(B - \frac{\theta}{2} + \frac{3}{2}\right)}. \tag{24}$$

This expression does not depend anymore on the heat transfer coefficient h. In consequence, when the feeding process is controlled by a not null heat transfer coefficient ($h > 0$), the value of θ around which response factor curves exhibit the sharp peak at the frequency u_p, can be deduced from the approximation (24) by equating the denominator of Z to zero. Thus, $\theta_d = 2B+3 = 203$ for $B = 100$. Moreover, once the value of θ exceeds θ_d, one has $\Re(Z) \leq 0$ whenever $h > 0$, as it can be equally deduced from the same approximation (24). Therefore, the corresponding curves show only negative response for all frequencies as respectively shown on Figures 2(b3), 4(e3) and 4(f3) for $h = 0.1$; 10 and $+\infty$. As in [4, 31], many publications have highlighted that the rapid variations of fluid thermophysical properties near critical and supercritical processes, are the major factor contributing to abrupt changes in the vaporization frequency response. Now, when $h = 0$, i.e. in the adiabatic regime, the computations lead to the following approximation: $Z(u,\theta,0) \approx \mathrm{i}u(A-3)/[(1+\mathrm{i}u)(B+3)]$. In this case, as $B = 3\mu/\lambda > 0$, the denominator of the transfer function and hence that of the response factor cannot be canceled, even when $\theta \approx 200$. This explains the absence of abrupt changes in the profiles of the response factor curves, regardless of the values of the thermal exchange ratio θ and of the heat transfer coefficient h (see Figure 2(a3)).

5. Conclusions

By introducing a heat transfer coefficient in the liquid fuel injection process, this study has permitted to extend to a generalized feeding regime, the results of the pressure-coupled vaporization frequency response of spray droplets. The evaporating mass frequency response of a spray of repetitively injected droplets in the combustion chamber has been analyzed through the Heidmann analogy of a mean spherical droplet.

Using basic parameters in their dimensionless form, the effects of the liquid heat transfer coefficient and of the evaporation characteristic times, as well as those of the phase lag and of the thermal exchange ratio are found effective for driven or damped instabilities. It has been shown that, whenever positive responses appear in the system, the peak value is reached at a particular frequency, where the residence time of the mean droplet matches the period of the ambient pressure oscillations. Except for the cases where the heat transfer coefficient is closed to one, response factor curves exhibit a single maximal response at the peak frequency. This maximal response grows abruptly at the peak frequency if the thermal exchange ratio approaches a certain threshold value. The latter is shown to be equal to a simple affine function of a thermodynamic coefficient related to the injected fuel physical properties. Once this threshold value of the thermal exchange ratio is passed over, a factor curve shows only negative response for all frequencies, even in the case where the heat transfer coefficient is equal to one. The results are also found similar to those previously obtained in the adiabatic and isothermal feeding regimes. Indeed, mass response factors in such extreme cases of fuel injection are recovered as simple limit points.

On the theoretical level, the above-mentioned results may be beneficial for instability control in combustion processes and may also contribute to the modeling of liquid fuel propulsion systems as that of launcher engines for example. The dimensionless parameters provided by the linear analysis can be used to characterize the dynamic behavior of the vaporization process for a wide range of liquid fuels, especially when relatively large droplets are involved. Moreover, the present analytical approach may serve to improve the development of numerical codes, as for instance the Computational Fluid Dynamic (CFD) codes. However, this approximate analytical model based on the Heidmann analogy is still extendable to more complex configuration details.

References

[1] V. Nair, R. I. Sujith, "Multifractality in combustion noise: Predicting an impending instability", *J. Fluid Mech.* **747** (2014), p. 635-655.

[2] T. Pant, C. Han, H. Wang, "Computational investigations of the coupling between transient flame dynamics and thermo-acoustic instability in a self-excited resonance combustor", *Combust. Theory Model.* **23** (2019), no. 5, p. 854-884.

[3] S. Candel, D. Durox, T. Schuller, N. Darabiha, L. Hakim, T. Schmitt, "Advances in combustion and propulsion applications", *Eur. J. Mech. B Fluids* **40** (2013), p. 87-106.

[4] G. C. Hsiao, H. Meng, V. Yang, "Pressure-coupled vaporization response of n-pentane fuel droplet at subcritical and supercritical conditions", *Proc. Combust. Inst.* **33** (2011), p. 1997-2003.

[5] S. Lei, A. Turan, "Chaotic modeling and control of combustion instability due to vaporization", *Int. J. Heat Mass Transfer* **53** (2010), p. 4482-4494.

[6] W. A. Sirignano, J.-P. Delplanque, C. H. Chiang, R. Bhatia, "Liquid-propellant droplet vaporization: A rate controlling process for combustion instability", in *Liquid Rocket Engine Combustion Instability* (V. Yang, W. E. Anderson, eds.), Progress in Astronautics and Aeronautics, vol. 169, AIAA Publishers, Reston, 1994, p. 307-343.

[7] L. Magri, M. P. Juniper, J. P. Moeck, "Sensitivity of the Rayleigh criterion in thermoacoustics", *J. Fluid Mech.* **882** (2020), article no. R1.

[8] A. Duvvur, C. H. Chiang, W. A. Sirignano, "Oscillatory fuel droplet vaporization: Driving mechanism for combustion instability", *J. Propul. Power* **12** (1996), p. 358-365.

[9] L. Yuan, C. Shen, Z. Xinqiao, "Dynamic response of vaporizing droplet to pressure oscillation", *Heat Mass Transf.* **52** (2017), p. 711-723.

[10] A. Y. Tong, W. A. Sirignano, "Oscillatory vaporization of fuel droplets in an unstable combustor", *J. Propul. Power* **5** (1989), p. 257-261.
[11] M. d. l. C. García, E. Mastorakos, A. P. Dowling, "Investigations on the self-excited oscillations in a kerosene spray flame", *Combust. Flame* **156** (2009), p. 175-186.
[12] C. T. Haddad, J. Majdalani, "Transverse waves in simulated liquid rocket engines", *AIAA J.* **51** (2012), p. 591-605.
[13] J. B. Greenberg, D. Katoshevski, "Polydisperse spray diffusion flames in oscillating flow", *Combust. Theory Model.* **20** (2016), p. 349-372.
[14] M. F. Heidmann, P. R. Wieber, "Analysis of frequency response characteristics of propellant vaporization", Nasa technical note, NASA, 1966, https://ntrs.nasa.gov/api/citations/19670003840/downloads/19670003840.pdf.
[15] R. Prud'homme, M. Habiballah, L. Matuszewski, Y. Mauriot, A. Nicole, "Theoretical analysis of dynamic response of a vaporizing droplet to an acoustic oscillation", *J. Propul. Power* **26** (2010), p. 74-83.
[16] K. Anani, R. Prud'homme, "Theoretical analysis of thermal conduction effect on frequency response of a perturbed vaporizing spherical droplet", *Flow Turbul. Combust.* **98** (2017), p. 503-522.
[17] K. Anani, R. Prud'homme, M. N. Hounkonnou, "Dynamic response of a vaporizing spray to pressure oscillations: Approximate analytical solutions", *Combust. Flame* **193** (2018), p. 295-305.
[18] S. Y. Slavyanov, W. Lay, "The Heun class of equations", in *Special Functions: A Unified Theory Based on Singularities*, Oxford Mathematical Monographs, Oxford University Press, New York, 2000, p. 97-160.
[19] J. G. Lee, D. A. Santavicca, "Experimental diagnostics of combustion instabilities", in *Combustion instabilities in gas turbine engines: Operational Experience, Fundamental Mechanisms, and Modeling* (T. C. Lieuwen, V. Yang, eds.), Progress in astronautics and aeronautics, vol. 481, AIAA Publishers, Reston, 2005, p. 481-529.
[20] C. I. Sevilla-Esparza, J. L. Wegener, S. Teshome, J. I. Rodriguez, O. I. Smith, A. R. Karagozian, "Droplet combustion in the presence of acoustic excitation", *Combust. Flame* **161** (2014), p. 1604-1619.
[21] F. Laurén, J. Nordström, "Practical inlet boundary conditions for internal flow calculations", *Comput. Fluids* **175** (2018), p. 159-166.
[22] S. Bari, T. H. Lim, C. W. Yu, "Effects of preheating of crude palm oil (CPO) on injection system, performance and emission of a diesel engine", *Renewable Energy* **27** (2002), p. 339-351.
[23] S. Mondal, A. Mukhopadhyay, S. Sen, "Effects of inlet conditions on dynamics of a thermal pulse combustor", *Combust. Theory Model.* **16** (2012), p. 59-74.
[24] R. S. Miller, K. Harstad, J. Bellan, "Evaluation of equilibrium and non-equilibrium evaporation models for many droplet gas-liquid flow simulations", *Int. J. Multiphase Flow* **24** (1998), p. 1025-1055.
[25] B. Abramzon, W. A. Sirignano, "Droplet vaporization model for spray combustion calculations", *Int. J. Heat Mass Transfer* **32** (1989), no. 9, p. 1605-1618.
[26] K. Anani, R. Prud'homme, M. N. Hounkonnou, "Drop vaporization frequency response: an approximate analytical solution for mixed injection regimes", *Thermodynamics of Interfaces and Fluid Mechanics (TIFM)* **5** (2021), p. 1-11.
[27] R. Prud'homme, K. Anani, "Vaporization of an equivalent pastille", in *Fluid Mechanics at Interfaces 2: Case Studies and Instabilities* (R. Prud'homme, S. Vincent, eds.), ISTE/Wiley Publishers, London, 2022, p. 77-93.
[28] R. Gonçalves Dos Santos, M. Lecanu, S. Ducruix, O. Gicquel, E. Iacona, D. Veynante, "Coupled large eddy simulations of turbulent combustion and radiative heat transfer", *Combust. Flame* **152** (2008), p. 387-400.
[29] Y. Xu, M. Zhai, P. Dong, F. Wang, Q. Zhu, "Modeling of a self-excited pulse combustor and stability analysis", *Combust. Theory Model.* **15** (2011), p. 623-643.
[30] A. Kannan, B. Chellappan, S. Chakravarthy, "Flame-acoustic coupling of combustion instability in a non-premixed backward-facing step combustor: The role of acoustic-Reynolds stress", *Combust. Theory Model.* **20** (2016), p. 658-682.
[31] J. Ren, O. Marxen, R. Pecnik, "Boundary-layer stability of supercritical fluids in the vicinity of the Widom line", *J. Fluid Mech.* **871** (2019), p. 831-864.

Comptes Rendus
Mécanique
2023, Vol. 351, Special Issue S2, p. 97-113
https://doi.org/10.5802/crmeca.152

Physical Science in Microgravity within the Thematic Group Fundamental and Applied Microgravity / *Sciences physiques en microgravité au sein du GDR Micropesanteur Fondamentale et Appliquée*

Modelling physical processes in higher plants using leaf replicas for space applications

Modélisation de processus physiques de plantes supérieures à l'aide de répliques de feuilles pour des applications spatiales

Joanna Kuzma [a, b], **Lucie Poulet** [a], **Jean-Pierre Fontaine** [*, a] **and Claude-Gilles Dussap** [a]

[a] Université Clermont Auvergne, Clermont Auvergne INP, CNRS, Institut Pascal, F-63000, Clermont-Ferrand, 63000, France

[b] Centre National d'Etudes Spatiales (CNES), 31400 Toulouse, France

E-mails: joanna.kuzma@doctorant.uca.fr (J. Kuzma), Lucie.POULET@uca.fr (L. Poulet), j-pierre.fontaine@uca.fr (J.-P. Fontaine), C-Gilles.DUSSAP@uca.fr (C.-G. Dussap)

Abstract. In the future, higher plant cultivation will be a key component of Bioregenerative Life-Support Systems. This will require a deep understanding of phenomena that play an important role at the core of plant metabolism and of their interaction with the environment. Plants are complex organisms that must be studied with the use of leaf replicas. This enables the study of physical phenomena at the leaf surface, without biochemical or biological interactions nor genetic variability. To assess the influence of gravity, it is a necessary step to develop precise mechanistic models of plant behaviour in space. This review article presents the state-of-the-art of leaf replicas and concomitant phenomena, with a space gaze.

Résumé. À l'avenir, la culture de plantes supérieures sera un élément clé des systèmes de support de vie biorégénératifs. Cela nécessitera une compréhension approfondie des phénomènes qui jouent un rôle important au cœur du métabolisme des plantes et de leur interaction avec l'environnement. Les plantes sont des organismes complexes qui doivent être étudiés à l'aide de répliques de feuilles. Ceci permet l'étude des phénomènes physiques à la surface des feuilles, sans interactions biochimiques ou biologiques, ni variabilité génétique. Pour évaluer l'influence de la gravité, il est nécessaire de développer des modèles mécanistes précis du comportement des plantes dans l'espace. Cet article de synthèse présente l'état de l'art des répliques foliaires et des phénomènes concomitants, pour une application spatiale.

Keywords. Leaf replica, Transpiration, Energy balance, Life-support systems, Heat exchange, Biophysical phenomenon, Mechanistic modelling.

* Corresponding author.

Mots-clés. Réplique foliaire, Transpiration, Bilan énergétique, Systèmes de support de vie, Échange de chaleur, Phénomène biophysique, Modélisation mécaniste.

Published online: 6 March 2023

1. Introduction

The four pillars of life-support systems (LSS) are the provision of air, water, and food, as well as waste treatment [1, 2]. For long-duration space exploration missions, it will be necessary to recycle as much resources as possible and to grow food *in situ* [3]. Plants allow the supply of fresh vitamins and nutrients which will be lacking after many months in space [4, 5]. They also enable the recycling of oxygen and carbon into fresh nutrients and water sanitation through photosynthesis [6]. Moreover, it is well accepted that they contribute to the crew well-being [7].

Plants have grown in low Earth orbit [8, 9] for decades, but many challenges still remain before it will be possible to grow them sustainably for food production [10–13]. Since plants are reactive biological organisms, the elementary processes that govern their growth and development need to be thoroughly understood before they can reliably be grown on a larger scale in space and integrated within a bioregenerative LSS (BLSS) [12, 14]. This can be achieved with a mechanistic, multi-layer, and multi-scale (in space and time) approach to allow the development of knowledge-based models, which are prerequisites for implementing predictive models and run simulations out of the standard parametric range (e.g., in reduced gravity). For example, buoyancy-driven gas exchange at the leaf surface is altered in microgravity [15–18] and since it drives biomass and oxygen production [19], its understanding is crucial for plant growth in space.

Gas and heat exchange is largely dependent on leaf and plant canopy boundary layer thickness, which is a physical phenomenon linked to convective properties of the growth environment [17, 18, 20–22], which can be modelled independently of biological processes [23, 24]. It is influenced by airflow movements, which depend on forced and free convection—a result of buoyancy forces which therefore depends on gravity [17, 18]. Gas and heat exchange also depends on the plant stomata size and density, which are dependent on plant species and their growth environment [25–27].

The fact that plants present a genetic variability and are reactive systems [23,28,29] makes hard to study a given phenomenon independently from the others, in a controlled way. Therefore, leaf replicas have been developed and used to study strictly physical processes without influence of plant biological processes, particularly in the context of heat and mass exchange [21, 22, 30–45]. Most of the studied leaf replicas are made of metal and/or felt sheets and can incorporate pores to simulate stomata or resistors to study heat exchange. Their design depends on the hypotheses and research questions of the study.

The objective of this review is to provide an overview of the state-of-the-art of existing leaf replicas and their use to answer various questions pertaining to heat exchange and water transport across plants. A focus will be on the specific context of developing mechanistic models of plant gas exchange for applications in BLSS.

2. Challenges in using real plants

The high sensitivity of plants to their environment and their genetic variability makes it challenging to study their biophysical processes in spaceflight conditions, where volume and experiment opportunities are limited.

2.1. *Plants are reactive systems*

Plants need light (energy), water, carbon and nutrients and if these parameters are too far from optimal conditions, abiotic stress can appear [46]. Another source of stress can be the rapid changes in environmental physical parameters, such as temperature, light, or relative air humidity. The stress associated with these factors occurs within seconds to minutes of the parameter change and affects the metabolic processes of the plant which in consequence can lead to reduced yield [47].

According to [48] active suppression of growth is part of the plant survival strategies in response to adverse environments. The exact mechanisms, however, remain unknown, making it hard to take stress factors into consideration while modelling the growth or while computing for example the energy balance or transpiration rate.

Another factor which can affect the accuracy of the modelling is the plant morphology description. As it was highlighted in [49], the size and density of stomata can vary not only within the same plant species but also within the same plant if the environment conditions slightly vary. For example, small light or wind gradient can result in different stomatal densities between the leaves of a single plant. Moreover, the opening and closing of stomata is closely related to the time of day and to weather conditions [25, 50].

According to the plant needs, leaves can also modify the magnitude of absorbed solar radiation—incident, reflected, and transmitted—by orientating the leaves towards or against the sun and the wind [51]. As a consequence, untangling the biological and physical parameters is not simple.

2.2. *Sample size*

The estimation precision of the energy components or mass exchange between the environment and plants can also be affected by the variability of the collected samples, the variability of the process and the heterogeneity of environmental conditions. It was proven that light gradients across a growth chamber can cause significant differences in structure and physiology of the leaves [52]. These results highlight the fact that sample size may significantly affect the accuracy of ecophysiological trait estimates. To receive meaningful results, the sample size should be adjusted to the required confidence level and margin of error, as well as to the expected variation between individual results [53]. Taking all those factors into consideration, finding the optimal plant size sample is a challenge in spaceflight conditions where mass and volume are limited. Moreover, sample size might be limited by external factors like time, funding, or human capital.

One of the examples of a limited space and time are studies done in microgravity conditions—parabolic flights or outer space studies. Parabolic flight is one of the main sources of data on heat and mass exchange and boundary layer in microgravity, mainly because of its relatively low cost and availability, compared to studies in low Earth orbit. Additionally, most of the systems which were tested in space did not have the possibility to measure all of the previously mentioned parameters and phenomena on plants or leaf replicas because of the lack of humidity and/or temperature control [54]. In parabolic flight studies, the periodic evolution of the gravity level induces extra stresses to the plants. As described in the previous section, the influence of these stresses is not yet fully detailed and understood, and this might introduce confounded factors to the measurements.

Leaf replicas have been introduced in order to study physical processes occurring at the leaf level in steady and transient states, without the bias caused by environmental stress factors or genetic variability occurring on limited sample size. The collected data can be used for primary validation of predictive models describing these processes without biochemical interaction.

A model, which can accurately simulate physical processes, can later be extended or scaled to the whole canopy level [51].

3. Leaf replicas used in recent literature

Different types of replicas have been used to study physical processes within plants. Depending on the purpose, we identified three groups of replicas:

- Simple replicas made of one material (dry and wet),
- Complex replicas with simulated stomata,
- Replicas with internal heating.

The major topics analysed with replicas concerned the energy balance and transpiration rate and the boundary layer conductance. The symbols and notations, used later in this section, to present how leaf replicas can simplify the equations, are summarized in Table 1.

3.1. *Energy balance*

3.1.1. *Description of the biophysical phenomena*

The temperature of the environment is one of the major factors affecting almost all plant processes like photosynthesis, respiration, biosynthesis, membrane transport, transpiration and the volatilization of specific compounds [51]. Consequently, it is crucial to precisely understand its role in all processes.

Leaves absorb most of the short-wave radiation emitted by the sun (E_{photons}), from which small fractions are reflected, transmitted, or used in metabolic processes. As a result, plants developed mechanisms to dissipate the induced heat, to avoid getting overheated, so that these heat loss mechanisms are crucial for their survival. Heat is also given off as a side effect of photosynthesis through transpiration. The main components of plant energy balance are [55]:

- Emitting long-wave infrared radiation (E_{ray}),
- Convection heat transfer (E_{conv}),
- Latent heat transfer (E_{lat}).

All of the energy balance components are presented on the Figure 1.

During metabolic processes plants also produce some energy and during photosynthesis a certain amount of energy is consumed, however the amount of heat involved during these processes is relatively small compared to the processes mentioned above and is usually neglected in the calculations [51]. At steady state the conservation of energy implies that the sum of all these energy components is equal to zero, but even a small change in one of the components of the energy balance will cause a change in the leaf temperature. Mechanistic approaches to plant energy balance models have been described in [20, 24]. In general, the energy balance can be described using the following equation:

$$\frac{\mathrm{d}T_{\text{leaf}}}{\mathrm{d}t} = \frac{E_{\text{photons}} - E_{\text{ray}} - E_{\text{conv}} - E_{\text{lat}}}{Cp_{\text{leaf}}} \tag{3.1.1}$$

where Cp_{leaf}—the leaf specific heat capacity in $\mathrm{J{\cdot}K^{-1}}$.

For discrete light spectrum (like the ones in use on ISS), the amount of energy absorbed by the plants can be calculated using the equations described in [24]:

$$E_{\text{photons}} = I^{\max} N_A hc \sum_{i=\lambda_{\min}}^{\lambda_{\max}} \frac{\gamma_i}{\lambda_i} \tag{3.1.2}$$

Table 1. Summary of the symbols and notations.

Name	Symbol	Unit
Light velocity	c	$\mathrm{m{\cdot}s^{-1}}$
Molar air specific heat capacity at constant pressure	C_p	$\mathrm{J{\cdot}mol^{-1}{\cdot}K^{-1}}$
Liquid water specific heat capacity at constant pressure	$Cp_{\mathrm{H_2O}}$	$\mathrm{J{\cdot}kg^{-1}{\cdot}K^{-1}}$
Specific heat capacity of humid air	C_s	$\mathrm{J{\cdot}kg^{-1}{\cdot}K^{-1}}$
Specific heat capacity of i component	C_p^i	$\mathrm{J{\cdot}K^{-1}}$
Diffusion coefficient for water	$D_{\mathrm{H_2O}}$	$\mathrm{m^2{\cdot}s^{-1}}$
Heat diffusion coefficient	D_t	$\mathrm{m^2{\cdot}s^{-1}}$
Convection energy	E_{conv}	W
Latent energy	E_{lat}	W
Short-wave radiation energy	E_{photons}	W
Net longwave energy	E_{ray}	W
Gravitational acceleration	g	$\mathrm{m{\cdot}s^{-2}}$
Leaf conductance for water vapour	$G^{\mathrm{H_2O}}$	$\mathrm{mol{\cdot}m^{-2}{\cdot}s^{-1}}$
Boundary layer conductance for water	$g_{\mathrm{BL}}^{\mathrm{H_2O}}$	$\mathrm{mol{\cdot}m^{-2}{\cdot}s^{-1}}$
Stomatal conductance for water	$g_s^{\mathrm{H_2O}}$	$\mathrm{mol{\cdot}m^{-2}{\cdot}s^{-1}}$
Boundary layer conductance for heat transfer	$g_{\mathrm{BL}}^{\mathrm{heat}}$	$\mathrm{m{\cdot}s^{-1}}$
Planck constant	h	J·s
Height of plant chamber	H	m
Maximum light absorption rate	I^{max}	$\mathrm{mol{\cdot}s^{-1}}$
Incident shortwave radiation	I_s	$\mathrm{W{\cdot}m^{-2}}$
Heat capacity	k	$\mathrm{J{\cdot}m^{-2}{\cdot}K^{-1}}$
Heat transfer coefficient	k_t	$\mathrm{m{\cdot}s^{-1}}$
Leaf characteristic length	L	m
Leaf area	LA	$\mathrm{m^2}$
Water mass in the leaf	$m_{\mathrm{H_2O}}$	kg
Avogadro number	N_A	$\mathrm{mol^{-1}}$
Atmospheric pressure of the bulk air	P_{bulk}	Pa
Water partial pressure in bulk air	$p_{\mathrm{bulk}}^{\mathrm{H_2O}}$	Pa
Water partial pressure at the leaf surface	$p_{\mathrm{leaf}}^{\mathrm{H_2O}}$	Pa
Ideal gas constant	R	$\mathrm{J{\cdot}mol^{-1}{\cdot}K^{-1}}$
Temperature	T	K
Bulk air temperature	T_{bulk}	K
Bulk air velocity	V_{bulk}	$\mathrm{m{\cdot}s^{-1}}$
Forced convection velocity	V_{forced}	$\mathrm{m{\cdot}s^{-1}}$
Free convection velocity	V_{free}	$\mathrm{m{\cdot}s^{-1}}$
Short wave absorbance	α	-
Percentage of the wavelength	γ_i	-
Boundary layer thickness	δ	m
Emissivity	ε	-
Incident photon wavelength	λ_i	m
Air density	ρ	$\mathrm{kg{\cdot}m^{-3}}$
Water vapor molar density	$\rho_{\mathrm{mol,H_2O}}$	$\mathrm{mol{\cdot}m^{-3}}$
Stefan–Boltzmann constant	σ	$\mathrm{W{\cdot}m^{-2}{\cdot}K^{-4}}$
Water transpiration rate	$\varphi_{\mathrm{H_2O}}$	$\mathrm{mol{\cdot}s^{-1}}$
Water latent heat of vaporisation	Λ_{mol}	$\mathrm{J{\cdot}mol^{-1}}$
Subscript i refers to leaf, replica, black replica, white replica, dry replica, wet replica, heated replica respectively	i_{leaf}, i_{rep}, i_{black}, i_{white}, i_{dry}, i_{wet}, i_{heated}	-

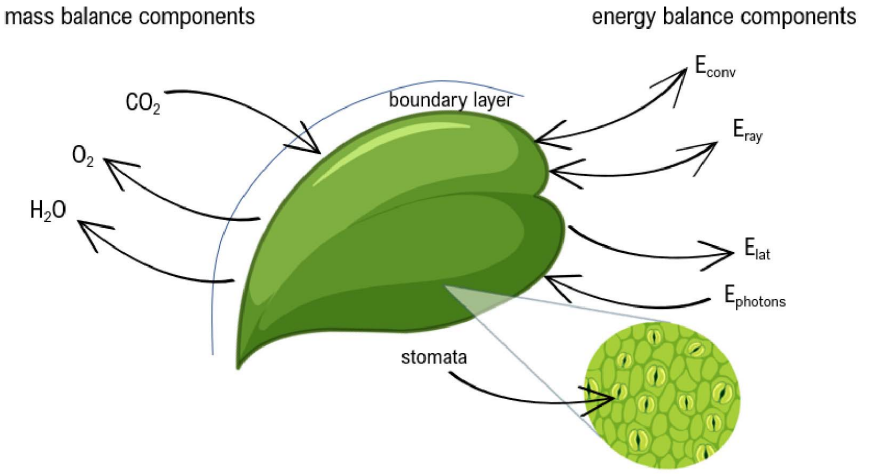

Figure 1. Leaf energy balance components.

where $I^{\max}$—maximum light absorption rate, N_A—Avogadro number, h—Planck constant, c—light velocity, $\lambda_{\min/\max}$—respectively the lowest and highest wavelengths of the light source, γ_i—percentage of the wavelength λ_i.

For continuous light spectrum (like the sun), the absorbed energy can be described as:

$$E_{\text{photons}} = \int_{\lambda_{\min}}^{\lambda_{\max}} \frac{I \cdot N_A hc}{\lambda} \, \mathrm{d}\lambda. \tag{3.1.3}$$

By assuming the plant canopy and the surroundings have similar emissivity, and according to the Stefan–Boltzmann law, the net radiation energy for the leaf can be calculated using following equation:

$$E_{\text{ray}} = \varepsilon\sigma(T_{\text{leaf}}^4 - T_{\text{bulk}}^4)LA \tag{3.1.4}$$

where ε—emissivity coefficient value usually between 0.94 and 0.99 for plants, σ—Stefan–Boltzmann constant, T_{leaf}—leaf temperature, T_{bulk}—bulk air temperature and LA—leaf area.

Although heat exchanged via transpiration is one of the main components of the energy balance, subsequent leaf cooling is a consequence of the stomatal opening required to sustain photosynthesis and leading to water evaporation through them, rather than a mechanism to control leaf temperature. Without latent energy loss however, the leaf temperature could rapidly rise to lethal level [56].

The latent heat flux can be calculated using the following equation:

$$E_{\text{lat}} = \Lambda_{\text{mol}} \varphi_{\text{H}_2\text{O}} \tag{3.1.5}$$

where Λ_{mol}—water latent heat of vaporisation and $\varphi_{\text{H}_2\text{O}}$—water transpiration rate.

Another component of plant heat balance is the convective heat transfer which is related to the air flow around the leaf. Heat and mass diffuse through the leaf boundary layers and are modelled by the boundary layer conductance [52]. It can be described with the following equation [24]:

$$E_{\text{conv}} = C_p k_t \frac{P_{\text{bulk}}}{RT_{\text{bulk}}}(T_{\text{leaf}} - T_{\text{bulk}})LA \tag{3.1.6}$$

where C_p—molar air specific heat capacity at constant pressure, P_{bulk}—atmospheric pressure of the bulk air, T_{leaf}—leaf surface temperature, LA—leaf area, k_t—heat transfer coefficient defined as a function of heat boundary layer thickness and heat diffusion coefficient:

$$k_t = \frac{D_t}{\delta} \tag{3.1.7}$$

where δ—boundary layer thickness D_t—heat diffusion coefficient.

Because of the phenomena described in this article appear in a gas phase—the Prandtl and Schmidt numbers are close to unity, the heat and mass boundary layers described here later, are assumed to be equal and named δ hereafter.

The boundary layer thickness can be calculated using following equation:

$$\delta = \frac{2}{\xi}\sqrt{\frac{\upsilon L}{V_{\text{bulk}}}} \tag{3.1.8}$$

where ξ—empirical coefficient, usually varying between 1–1.33, υ—air kinetic viscosity, L—leaf characteristic length, V_{bulk}—bulk air velocity.

Where bulk air velocity is defined in the following way:

$$V_{\text{bulk}} = V_{\text{free}} + V_{\text{forced}} \tag{3.1.9}$$

where V_{free}—free convection velocity, V_{forced}—forced convection velocity.

Free convection velocity is a function of gravity:

$$V_{\text{free}} = \sqrt{2gH\frac{\Delta\rho}{\rho}} \tag{3.1.10}$$

where g—gravitational acceleration, H—height of the chamber $\Delta\rho$—density gradient between the surface of the leaf and bulk air ρ—air density. Detailed description of this model can be found in [24].

For studies conducted in microgravity, the lack of natural convection must be considered, as it significantly affects the energy balance components [56]. The studies in microgravity will allow to understand this phenomenon and test the accuracy of the model.

3.1.2. *Associated replicas*

To study the energy balance of a leaf, many researchers used dry replicas (Table 2). The idea was to use a dry reference surface with properties (radiative and aerodynamic) similar to a real leaf and to place it in the same environment as a real plant or other replicas in order to assess the net energy flux due to light energy exchanges [31, 32]. The source of the energy provided to the replica was an external light source [32–34] or internal heating by using resistors [35, 36]. The use of dry replicas eliminates the latent heat term from the energy balance equations and thus enables their simplification; it also allows to remove from the equation most of the effects of the surrounding environment like for example long wave radiation.

Dry replicas were used to estimate the convective heat transfer in normal conditions—for different airflows [32, 38], leaf temperatures [35, 36], or gravity conditions [32, 33] without secondary effects of the stress on other energy balance components.

The shapes of the leaf replicas were usually mimicking the shape of real leaves tested in parallel, such as those of barley wheat, strawberry or sweet potato [31, 32, 36]. Dry replicas were made from copper [32], brass sheet [35], Perspex [36] or aluminium sheet [31, 34]. Scientists were searching for materials with optical properties close to the ones of real leaves [32, 35, 36].

Vialet-Chabrand and Lawson however have highlighted in [31] that the reference materials did not have exactly the same optical and thermal properties as real leaves, and this may introduce a bias in estimating the heat balance parameters. The authors suggested to directly include

Table 2. Summary of the energy balance studies done with replicas.

Studied phenomena	Type of replica	Reference	Tested parameters	Used sensors	Environment
Energy balance	Dry replica	[31]	Day/night transition	IR camera, thermocouples, light sensor	Controlled
	Pair of dry/wet replica	[32]	Wind speed, irradiance	Thermocouples	Controlled
		[33]	Gravity, wind speed	IR camera	Controlled
		[34]	Wind speed	Thermocouples, anemometer, scale	Controlled
	Heated replica/non heated replica	[35]	Wind speed	Thermocouples, anemometer	Controlled
		[36]	Wind speed, wind angle	IR camera, thermocouples, radiometer	Controlled
	Replica with stomata	[30]	Wind speed, humidity, irradiance, pores density	IR camera, thermocouples, heat flux sensor	Controlled
		[31]	Day/night transition	IR camera, thermocouples, light sensor	Controlled

differences in thermal and optical properties in the energy balance equations and predict the leaf thermal kinetics from a reference material instead of mimicking leaf properties [35]:

$$\frac{\mathrm{d}T^{\mathrm{leaf}}}{\mathrm{d}t} = \frac{Cp^{\mathrm{rep}}\frac{\mathrm{d}T^{\mathrm{rep}}}{\mathrm{d}t} - (E^{\mathrm{leaf}}_{\mathrm{photons}} - E^{\mathrm{rep}}_{\mathrm{photons}}) + (E^{\mathrm{leaf}}_{\mathrm{ray}} - E^{\mathrm{rep}}_{\mathrm{ray}}) + (E^{\mathrm{leaf}}_{\mathrm{conv}} - E^{\mathrm{rep}}_{\mathrm{conv}}) + E^{\mathrm{leaf}}_{\mathrm{lat}}}{Cp^{\mathrm{leaf}}} \tag{3.1.11}$$

The terms are as explained above. The superscript leaf is of the real leaf, the subscript rep for replica.

Another approach to simplify energy balance is by using dry and wet replicas with similar thermal capacity. Measuring the temperature difference between them in the same environmental conditions enables the computation of the latent heat flux from the wet replica. Indeed:

$$Cp^{\mathrm{rep}}\left(\frac{\mathrm{d}T^{\mathrm{dry}}}{\mathrm{d}t} - \frac{\mathrm{d}T^{\mathrm{wet}}}{\mathrm{d}t}\right) = (E^{\mathrm{dry}}_{\mathrm{photons}} - E^{\mathrm{wet}}_{\mathrm{photons}}) - (E^{\mathrm{dry}}_{\mathrm{ray}} - E^{\mathrm{wet}}_{\mathrm{ray}}) - (E^{\mathrm{dry}}_{\mathrm{conv}} - E^{\mathrm{wet}}_{\mathrm{conv}}) - (E^{\mathrm{dry}}_{\mathrm{lat}} - E^{\mathrm{wet}}_{\mathrm{lat}}) \tag{3.1.12}$$

The terms are as explained above. The superscript dry is of the dry replica, the subscript wet for wet replica.

Since the short-wave incoming radiation energy, the long-wave energy and the convection

energy are the same for both replicas, the equation can be derived only with the modelling of the latent energy flux:

$$Cp^{\text{rep}}\left(\frac{\mathrm{d}T^{\text{dry}}}{\mathrm{d}t}-\frac{\mathrm{d}T^{\text{wet}}}{\mathrm{d}t}\right)=E_{\text{lat}}^{\text{wet}} \tag{3.1.13}$$

By using replica with stomata together with dry replica it is possible to calculate the latent energy flux of the leaves with the specified size of stomata by applying Equation (3.1.13).

Heated replicas combained with not heated ones were used to calculate the convection energy. If the replica did not have an external source of energy (other than the heater in one of them) and if the temperature of the not heated one is equal to the temperature of the environment the Equation (3.1.12) can be simplified to:

$$Cp\frac{\mathrm{d}T^{\text{heated}}}{\mathrm{d}t}=-E_{\text{conv}}^{\text{heated}} \tag{3.1.14}$$

The terms are as explained above. The superscript heated is of the heated replica.

3.2. *Transpiration*

3.2.1. *Description of the biophysical phenomenon*

The transpiration rate (φ_{H_2O}) from the Equation (3.1.5) can be calculated using the following equation:

$$\varphi_{H_2O}=\Lambda_{\text{mol}}\frac{G^{H_2O}}{P_{\text{bulk}}}(p_{\text{leaf}}^{H_2O}-p_{\text{bulk}}^{H_2O})LA \tag{3.2.1}$$

where P_{bulk}—bulk air total pressure, $p_{\text{leaf}}^{H_2O}$—water partial pressure at the leaf surface, $p_{\text{bulk}}^{H_2O}$—water partial pressure in bulk air and LA—leaf area, G^{H_2O}—leaf conductance for water vapour defined as:

$$G^{H_2O}=\frac{g_{\text{BL}}^{H_2O}+g_s^{H_2O}}{g_{\text{BL}}^{H_2O}\cdot g_s^{H_2O}} \tag{3.2.2}$$

where $g_s^{H_2O}$—stomatal conductance for water and $g_{\text{BL}}^{H_2O}$—boundary layer conductance for water vapour, defined as a function of boundary layer thickness, where boundary layer thickness depends on the gravity. For the detailed equations, please refer to [24].

The leaf conductance for diffusion of water vapour depends on the stomatal and boundary layer conductance. The boundary layer conductance depends on their thicknes which depends on the gravity as it was described in Equations (3.1.8)–(3.1.10), so transpiration is another component which is strongly affected by a reduced or the absence of gravity and therefore needs to be studied.

3.2.2. *Associated replicas*

In the studies of transpiration rates, a few types of replicas have been used (see Table 3). The simplest approach was to use a wet replica together with a real leaf to determine the air water vapor resistance [22, 37].

When a wet replica was combined with a dry one, the resistance value could later be used to calculate the transpiration rate of the real leaf [34]. One of the early studies of the transpiration used two aluminium sheets, a bare one and one with a wet filter glued to it [34]. Both replicas had thermocouples sticked to the surface and were placed on a scale to measure the evaporation rate. The goal of the study was to determine the air water vapor resistance. Currently the simple wet replicas were mostly made from wet cloth or paper and placed on a supporting structure.

Table 3. Summary of the transpiration studies done with replicas.

Studied phenomena	Type of replica	Reference	Tested parameters	Used sensors	Environment
Transpiration rate	Wet replica combined with real leaf	[22]	Wind speed	IR camera, thermocouples, hygrometer	Controlled
		[37]	Gravity	IR camera, thermocouple, leaf porometer, hygrometer	Controlled
	Wet replica	[38]	Light intensity	IR camera	Controlled
	Pair of dry/wet replica	[34]	Wind speed	Thermocouples, anemometer, scale	Controlled
	Vessel with the perforated structure on the top	[39]	Pores size, pores density	Scale, humidity sensors	Controlled
		[40]	Pores size, pores density, pore geometry	Scale, anemometer, humidity sensor,	Controlled
		[41]	Pores size, pores density, leaf angle	Scale, thermocouples, anemometer, humidity sensor, pressure sensor	Controlled
	Replica with stomata	[30]	Wind speed, humidity, irradiance, pores density	IR camera, thermocouples, heat flux sensor	Controlled
		[31]	Day/night transition	IR camera, thermocouples, light sensor	Controlled

When they were compared with dry replicas it was possible to calculate the transpiration rate by applying equation:

$$\varphi_{H_2O} = \frac{Cp}{\Lambda_{mol}} \left(\frac{dT^{dry}}{dt} - \frac{dT^{wet}}{dt} \right) \tag{3.2.3}$$

The terms are as explained above.

The simple wet replica however, did not have pores, so the evaporation was not limited by them and it was similar to the evaporation from a free surface [34]. Hence, the evaporation energy from such replicas is overestimated compared to the one of a real leaf. To solve this problem another type of replica was developed. In the literature two types of replicas with artificial stomata are described. The first one consists of a petri dish or other small vessel with a micro-perforated foil, or a plate placed on it [39–41]. The main purpose of these studies was to investigate the influence of the size, the density, the shape of pores and the angle of the leaf on the evaporation

rate and relate it to the influence of stomata on leaf transpiration. The replicas were put on a scale or were weighted periodically [39–41] to measure the change in weight over time. This kind of setup allowed an accurate evaluation of the rate of evaporation, but the thermal and buffer properties of this type of replica are significantly different from those of real leaves. This is due to different surface areas, materials and thicknesses, flat shapes, not flexible structures, and greater heat capacities (due to the thick water layer in the vessel with water).

In order to solve this problem Schymanski *et al.* proposed another type of replica, which includes pores that are similar to stomata in terms of size [30]. This replica consists of a capillary filter paper glued onto aluminium tape with a water supplying tube and thermocouples sandwiched between the layers. On one side of the replica, the aluminium foil had artificial stomata with defined dimensions—similar in size to real stomata. The non-transpiring side was covered with black aluminium tape. The studies were conducted in a closed chamber and the evaporation rate was measured based on the parameters of the air coming in and out of the measurements area with the humidity sensor, anemometers, and thermocouples. The replica was tested for various humidity and wind speed conditions and with several pore densities. This setup allowed to study evaporation rate together with the energy balance. The replica was mainly developed to study the energy balance at steady state. This type of replica was slightly modified later by Vialet-Chabrand and Lawson to make measurements in dynamic conditions [31]. This replica was made of an aluminium plate which was covered by black tape with known absorbance and emissivity on non-transpiring side like in the previously described replica. The transpiring side of the leaf was covered with a felt fabric enclosed in a plastic microporous sheet, where pores had a known diameter depth and density. The felt sandwiched between the aluminium layers was saturated with water, so the only factors affecting the transpiration were the size and density of the pores and the environmental conditions (fluctuating light environment, wind speed or humidity). These factors together with the angle of the leaf facing the flow were studied in detail. This replica was studied together with two dry replicas of same absorbance but different emissivity. This allowed the calculation of every component of the leaf energy balance separately by measuring the difference in the temperature between all the replicas. The whole calculation procedure is described in [31].

3.3. *Boundary layer*

The boundary layer is a representation model of the thin layer of air that develops close to a leaf in presence of an air flow and where the physical parameters like velocity, temperature, H_2O and O_2 concentrations are modified by diffusion [57].

3.3.1. *Description of the biophysical phenomenon*

The boundary layer conductance for water ($g_{BL}^{H_2O}$) can be described using the following equation:

$$g_{BL}^{H_2O} = \frac{D_{H_2O}\rho_{mol,H_2O}}{\delta} \tag{3.3.1}$$

where: D_{H_2O}—diffusion coefficient for water, ρ_{mol,H_2O}—water vapor molar density, δ—boundary layer thickness, described with the Equation (3.1.8). For more details please, refer to [24].

It was shown in [22] that increased ventilation causes a reduction in the leaf boundary layer resistance. This phenomenon is quite significant in microgravity, where there is no free convection, and the thickness of the boundary layer goes to infinity if there is no forced convection [24]. A detailed description of the model of the boundary layer with the gravity as a parameter can be found in Poulet *et al.* [24].

3.3.2. *Associated replicas*

The experiments to study the boundary layer conductance can be divided into two groups (Table 4): experiments performed in a controlled, laboratory environment [22,30,31,33,35,36,44] and experiments in a natural environment—like field, forest or a greenhouse [21, 42–44].

Most of the experiments carried out in the field used a similar design for the leaf replica. They were made of highly polished brass sheets [21, 42, 44] or flexible Mylar1 sheet [43]. The shape and size of the replicas were adjusted to the shape and size of the average leaf of the studied plant or tree. In between the sheets or on the bottom part the heaters were glued. The heater was or isolated with enamel coating [21], or double-sided adhesive tape [42, 45] or glued with double-sided adhesive tape with epoxy resin [44], Sellotape [35] or moulded into the leaf replica [36]. The thermocouples were attached to the replica to measure the mean temperature of the replica surface and the dynamic of the temperature change. In the field experiments, replicas were attached to the real plant. In some studies, the replicas were used in pairs and were alternatively heated [42, 43] or one was heated and the other not [21, 44]. Similar replicas have been used to calculate the boundary layer conductance in controlled environment [35, 36, 44, 45]. In these tests, the main goal was to calculate the boundary layer conductance as a function of the leaf temperature and airflow [35, 36, 44, 45] and study the corelation between the boundary layer conductance and the angle of the wind [36]. The thickness and shape of the leaf were similar to the real leaves. In the experiment described by Schymanski *et al.* [30] the replica described in Section 3.2.2 was used, to test the leaf conductance as a function of wind speed and vapour pressure in steady state.

To simulate boundary layer parameters, Vialet-Chabrand and Lawson in [31] has proposed another approach (described as well in the Section 3.2.2). Using two dry replicas at the same time with identical thermal properties but covered with a different colour (black and white to differentiate their optical properties), allows to calculate heat boundary layer conductance in the dynamic conditions by applying equation below:

$$g_{\mathrm{BL}}^{\mathrm{heat}} = \frac{k\left(\frac{\mathrm{d}T^{\mathrm{white}}}{\mathrm{d}t} - \frac{\mathrm{d}T^{\mathrm{black}}}{\mathrm{d}t}\right) + I_s(\alpha^{\mathrm{black}} - \alpha^{\mathrm{white}}) - 2\sigma(\varepsilon^{\mathrm{white}} T^{\mathrm{white}^4} - \varepsilon^{\mathrm{black}} T^{\mathrm{black}^4})}{2\rho C_s (T^{\mathrm{white}} - T^{\mathrm{black}})} \tag{3.3.2}$$

where $g_{\mathrm{BL}}^{\mathrm{heat}}$—boundary layer conductance, I_s—incident shortwave radiation, α—short wave absorbance, ρ—air density, k—heat capacity of the replica, C_s—specific heat capacity of humid air.

The main goal of this experiment was to develop a procedure and model to calculate the stomatal conductance in transient regime by using replicas. A good understanding of the processes at the leaf level can pave the way to scaling up and modelling a whole canopy instead of single leaves by using mechanistic equations. The complexity of this topic is described in the next section.

4. Scaling-up gas exchange from the leaf to the canopy level with an energy balance

For the scaling-up of the physical phenomena from the leaf level to the canopy level, it is fundamental to determine among all the interactions within the plants, especially the ones that are strongly affected by the surroundings, as in most cases changing from one scale to another is not linear. For example, the prediction of canopy transpiration is different from the results which would be obtained by summing up individual leaf responses because each leaf significantly affects the surrounding environment by changing e.g., the wind speed, the irradiance, or the relative humidity. Therefore, the transpiration rate predicted for a canopy from a single leaf model would be overestimated. In addition, the change in irradiance is exponentially decreasing with

Table 4. Summary of the energy balance studies with replicas.

Studied phenomena	Type of replica	Reference	Tested parameters	Used sensors	Environment
Boundary layer conductance	Wet replica	[22]	Wind speed	IR camera, thermocouples, hygrometer	Controlled
	Pair of 2 dry replicas	[31]	Day/night transition	IR camera, thermocouples, light sensor	Controlled
	Pair of dry/wet replica	[33]	Gravity, wind speed	IR camera	Controlled
	Heated replica	[21]	Day/night transition, leaf position	IR camera, thermocouples, light sensor	Greenhouse
		[42]	Wind speed	IR camera, thermocouples, light sensor	Greenhouse
		[43]	Wind speed, time of the day	IR camera, thermocouples	Field experiment
		[44]	Wind speed	Thermocouples, humidity sensor, anemometer, scale	Field experiment, controlled
		[35]	Wind speed	Thermocouples, anemometer	Controlled
		[45]	Temperature gradient, wind speed	Thermocouples, cameras	Controlled
		[36]	Wind speed, wind angle	IR camera, thermocouples, radiometer	Controlled
	Replica with stomata	[30]	Wind speed, humidity, irradiance, pores density	IR camera, thermocouples, heat flux sensor	Controlled
		[31]	Day/night transition	IR camera, thermocouples, light sensor	Controlled

the leaf area index, and this significantly reduces the amount of light absorbed by the leaves which are not directly exposed to the sun [51].

The plant canopy generates a resistance to air movements, which in consequence reduces wind speed within the canopy and in turn lowers the boundary layer conductance of certain leaves, as compared to what would be expected based on a single leaf of similar dimension and submitted to the same environmental parameters. Transpiration also affects the local water vapour pressure around the leaf. When stomatal conductance increases, water vapour pressure around the leaves increases as well and therefore reduces transpiration (see Equation (3.2.1)). In consequence transpiration increases less than what would be expected from the increase in stomatal conductance alone [58].

A good model for scaling-up from leaf to the canopy level will be based on mechanistic processes that develop at a lower scale. Hence, it is necessary to determine mechanistic model of a single leaf behaviour under specific environmental conditions, and for that it is necessary to start with a leaf replica.

This approach will help to address the questions which still have not been completely answered, like for example: can we use a big leaf model to calculate gas exchange and energy balance of a whole plant? Or it is necessary to combine individual gas exchange of each leaf and their individual microclimate in the energy balance at the canopy level?

Answering these questions is mandatory for developing safe, reliable, and robust LSS based on plants and to reach a full control of them.

5. Conclusions—how can leaf replicas help us to fill the gap in modelling

Understanding physical processes behind stomatal conductance in space environment, linked to energy and mass balances through mechanistic models, should enable a better comprehension of plant gas exchange in greater details. To achieve this, it is crucial to quantify how the boundary layer thickness varies in changing conditions, like space, or fluctuating conditions associated to parabolic flights. Microgravity strongly affects the physical exchanges at the leaf surface, being the first step of a cascade of biological events that are a consequence of these out-of-range conditions. To achieve a detailed understanding of physical processes at the leaf surface, replicas are necessary. This will allow the development of safe and controllable life-support systems based on living organisms.

The integration of mechanistic models at the leaf level will have to be scaled at the whole canopy in order to use knowledge-based description of mass, heat and energy exchange instead of empirical models, that were not developed for closed or space environments. This is the path for the development of reliable higher plant chambers in space environments.

Conflicts of interest

Authors have no conflict of interest to declare.

Acknowledgements

The authors would like to acknowledge CNES and the MELiSSA Foundation for funding JK's PhD, in the frame of which this study was done.

The authors wish to thank deeply the reviewers for the time they spent on the review and the judicious comments they gave.

References

[1] M. K. Ewert, T. T. Chen, C. D. Powell, *Life Support Baseline Values and Assumptions Document*, 2022, NASA/TP-2015218570/REV2, NASA JSC. (English only) https://ntrs.nasa.gov/citations/20210024855.

[2] P. Eckart, "Fundamentals of life support systems", in *Spaceflight Life Support and Biospherics*, Springer, Netherlands, Dordrecht, 1996, p. 79-173.

[3] R. M. Wheeler, "Agriculture for space: people and places paving the way", *Open Agric.* **2** (2017), p. 14-32.

[4] G. D. Massa, J. T. Richards, L. E. Spencer, M. E. Hummerick, G. W. Stutte, R. M. Wheeler, G. L. Douglas, T. Sirmons, "Selection of leafy green vegetable varieties for a pick-and-eat diet supplement on ISS", in *45th International Conference on Environmental Systems ICES-2015-252, Bellevue, Washington, July*, 2015.

[5] C. M. Johnson, H. O. Boles, L. E. Spencer, L. Poulet, M. Romeyn, J. M. Bunchek, R. Fritsche, G. D. Massa, A. O'Rourke, R. M. Wheeler, "Supplemental food production with plants: a review of NASA research", *Front. Astron. Space Sci.* **8** (2021), article no. 734343.

[6] R. M. Wheeler, "Plants for human life support in space: from Myers to Mars", *Gravitat. Space Res.* **23** (2010), p. 25-36.

[7] R. Odeh, C. L. Guy, "Gardening for therapeutic people-plant interactions during long-duration space missions", *Open Agric.* **2** (2017), p. 1-13.

[8] D. M. Porterfield, G. S. Neichitailo, A. L. Mashinski, M. E. Musgrave, "Spaceflight hardware for conducting plant growth experiments in space: The early years 1960–2000", *Adv. Space Res.* **31** (2003), p. 183-193.

[9] G. D. Massa, R. M. Wheeler, R. C. Morrow, H. G. Levine, "Growth chambers on the International Space Station for large plants", *Acta Hortic.* **2** (2016), no. 1, p. 215-222.

[10] M. S. Anderson, D. Barta, G. Douglas, B. Motil, G. Massa, R. Fritsche, C. Quincy, M. Romeyn, A. Hanford, "Key gaps for enabling plant growth in future missions", in *AIAA SPACE and Astronautics Forum and Exposition*, American Institute of Aeronautics and Astronautics, Orlando, FL, 2017.

[11] E. Kordyum, K. H. Hasenstein, "Plant biology for space exploration – Building on the past, preparing for the future", *Life Sci. Space Res.* **29** (2021), p. 1-7.

[12] F. J. Medina, A. Manzano, A. Villacampa, M. Ciska, R. Herranz, "Understanding reduced gravity effects on early plant development before attempting life-support farming in the Moon and Mars", *Front. Astron. Space Sci.* **8** (2021), article no. 729154.

[13] L. Poulet, K. Engeling, T. Hatch, S. Stahl-Rommel, Y.-A. Velez Justiniano, S. Castro-Wallace, J. Bunchek, O. Monje, M. Hummerick, C. L. M. Khodadad, L. E. Spencer, J. Pechous, C. M. Johnson, R. Fritsche, G. D. Massa, M. W. Romeyn, A. E. O'Rourke, R. W. Wheeler, "Large-scale crop production for the Moon and Mars: current gaps and future perspectives", *Front. Astron. Space Sci.* **8** (2022), article no. 733944.

[14] L. Poulet, J.-P. Fontaine, C.-G. Dussap, "Plant's response to space environment: a comprehensive review including mechanistic modelling for future space gardeners", *Bot. Lett.* **163** (2016), p. 337-347.

[15] Y. Kitaya, M. Kawai, J. Tsuruyama, H. Takahashi, A. Tani, E. Goto, T. Saito, M. Kiyota, "The effect of gravity on surface temperature and net photosynthetic rate of plant leaves", *Adv. Space Res.* **28** (2001), p. 659-664.

[16] Y. Kitaya, H. Hirai, T. Shibuya, "Important role of air convection for plant production in space farming", *Biol. Sci. Space* **24** (2010), p. 121-128.

[17] D. M. Porterfield, "The biophysical limitations in physiological transport and exchange in plants grown in microgravity", *J. Plant Growth Regul.* **21** (2002), p. 177-190.

[18] O. Monje, G. W. Stutte, G. D. Goins, D. M. Porterfield, G. E. Bingham, "Farming in space: Environmental and biophysical concerns", *Adv. Space Res.* **31** (2003), p. 151-167.

[19] E. Peiro, A. Pannico, S. G. Colleoni, L. Bucchieri, Y. Rouphael, S. De Pascale, R. Paradiso, F. Gòdia, "Air distribution in a fully-closed higher plant growth chamber impacts crop performance of hydroponically-grown lettuce", *Front. Plant Sci.* **11** (2020), article no. 537.

[20] S. J. Schymanski, D. Or, "Wind increases leaf water use efficiency", *Plant Cell Environ.* **39** (2016), p. 1448-1459.

[21] K. Kimura, D. Yasutake, A. Yamanami, M. Kitano, "Spatial examination of leaf-boundary-layer conductance using artificial leaves for assessment of light airflow within a plant canopy under different controlled greenhouse conditions", *Agric. For. Meteorol.* **280** (2020), article no. 107773.

[22] Y. Kitaya, J. Tsuruyama, T. Shibuya, M. Yoshida, M. Kiyota, "Effects of air current speed on gas exchange in plant leaves and plant canopies", *Adv. Space Res.* **31** (2003), p. 177-182.

[23] S. J. Schymanski, D. Or, M. Zwieniecki, "Stomatal control and leaf thermal and hydraulic capacitances under rapid environmental fluctuations", *PLoS One* **8** (2013), article no. e54231.

[24] L. Poulet, C.-G. Dussap, J.-P. Fontaine, "Development of a mechanistic model of leaf surface gas exchange coupling mass and energy balances for life-support systems applications", *Acta Astronaut.* **175** (2020), p. 517-530.

[25] O. Monje, B. Bugbee, "Radiometric method for determining canopy stomatal conductance in controlled environments", *Agronomy* **9** (2019), article no. 114.

[26] G. Thakur, S. Schymanski, I. Trebs, K. Mallick, M. Suils, O. Eiff, E. Zehe, "Bridging the gap between leaf surface and

the canopy air space: Leaf size matters for heat transfer resistance at canopy-scale", in *EGU General Assembly 2022, Vienna, Austria, 23–27 May 2022, EGU22-4268*, 2022.

[27] C. Amitrano, Y. Rouphael, A. Pannico, S. De Pascale, V. De Micco, "Reducing the evaporative demand improves photosynthesis and water use efficiency of indoor cultivated lettuce", *Agronomy* **11** (2021), article no. 1396.

[28] F. E. Rockwell, N. M. Holbrook, A. D. Stroock, "The competition between liquid and vapor transport in transpiring leaves", *Plant Physiol.* **164** (2014), p. 1741-1758.

[29] S. Vialet-Chabrand, T. Lawson, "Thermography methods to assess stomatal behaviour in a dynamic environment", *J. Exp. Bot.* **71** (2020), p. 2329-2338.

[30] S. J. Schymanski, D. Breitenstein, D. Or, "Technical note: An experimental set-up to measure latent and sensible heat fluxes from (artificial) plant leaves", *Hydrol. Earth Syst. Sci.* **21** (2017), p. 3377-3400.

[31] S. Vialet-Chabrand, T. Lawson, "Dynamic leaf energy balance: deriving stomatal conductance from thermal imaging in a dynamic environment", *J. Exp. Bot.* **70** (2019), p. 2839-2855.

[32] Y. Kitaya, M. Kawai, J. Tsuruyama, H. Takahashi, A. Tani, E. Goto, T. Saito, M. Kiyota, "The effect of gravity on surface temperatures of plant leaves: Effect of gravity on leaf temperatures", *Plant Cell Environ.* **26** (2003), p. 497-503.

[33] A. Tokuda, Y. Kitaya, H. Hirai, H. Hashimoto, Y. Inatomi, "Effects of gravity on stem sap flow and water and heat exchange in the leaves of sweetpotato", *Int. J. Microgravity Sci. Appl.* **35** (2018), no. 3, p. 350302-1-350302-6.

[34] A. S. Thom, "The exchange of momentum, mass, and heat between an artificial leaf and the airflow in a wind-tunnel", *Q. J. R. Meteorol. Soc.* **94** (1968), p. 44-55.

[35] J. Grace, F. E. Fasehun, M. Dixon, "Boundary layer conductance of the leaves of some tropical timber trees", *Plant Cell Environ.* **3** (1980), p. 443-450.

[36] G. Wigley, J. A. Clark, "Heat transport coefficients for constant energy flux models of broad leaves", *Bound.-Layer Meteorol.* **7** (1974), p. 139-150.

[37] H. Hirai, Y. Kitaya, "Effects of gravity on transpiration of plant leaves", *Ann. N. Y. Acad. Sci.* **1161** (2009), p. 166-172.

[38] A. Tokuda, Y. Kitaya, H. Hirai, "Development of a simple thermal method for measuring sap flow in plants for space experiments", *Biol. Sci. Space* **32** (2018), p. 17-21.

[39] M. A. Zwieniecki, K. S. Haaning, C. K. Boyce, K. H. Jensen, "Stomatal design principles in synthetic and real leaves", *J. R. Soc. Interface* **13** (2016), article no. 20160535.

[40] I. P. Ting, W. E. Loomis, "Diffusion through stomates", *Am. J. Bot.* **50** (1963), p. 866-872.

[41] J. N. Cannon, W. B. Krantz, F. Kreith, D. Naot, "A study of transpiration from porous flat plates simulating plant leaves", *Int. J. Heat Mass Transf.* **22** (1979), p. 469-483.

[42] N. Katsoulas, A. Baille, C. Kittas, "Leaf boundary layer conductance in ventilated greenhouses: An experimental approach", *Agric. For. Meteorol.* **144** (2007), p. 180-192.

[43] V. J. Stokes, M. D. Morecroft, J. I. L. Morison, "Boundary layer conductance for contrasting leaf shapes in a deciduous broadleaved forest canopy", *Agric. For. Meteorol.* **139** (2006), p. 40-54.

[44] A. J. Brenner, P. G. Jarvis, "A heated leaf replica technique for determination of leaf boundary layer conductance in the field", *Agric. For. Meteorol.* **72** (1995), p. 261-275.

[45] M. Kitano, H. Eguchi, "Buoyancy effect on forced convection in the leaf boundary layer", *Plant Cell Environ.* **13** (1990), p. 965-970.

[46] G. R. Cramer, K. Urano, S. Delrot, M. Pezzotti, K. Shinozaki, "Effects of abiotic stress on plants: a systems biology perspective", *BMC Plant Biol.* **11** (2011), article no. 163.

[47] H. Kollist, S. I. Zandalinas, S. Sengupta, M. Nuhkat, J. Kangasjärvi, R. Mittler, "Rapid responses to abiotic stress: priming the landscape for the signal transduction network", *Trends Plant Sci.* **24** (2019), p. 25-37.

[48] H. Zhang, Y. Zhao, J.-K. Zhu, "Thriving under stress: How plants balance growth and the stress response", *Dev. Cell* **55** (2020), p. 529-543.

[49] S. H. Eckerson, "The number and size of the stomata", *Bot. Gaz.* **46** (1908), p. 221-224.

[50] R. M. Wheeler, A. H. Fitzpatrick, T. W. Tibbitts, "Potatoes as a crop for space life support: effect of CO_2, irradiance, and photoperiod on leaf photosynthesis and stomatal conductance", *Front. Plant Sci.* **10** (2019), article no. 1632.

[51] H. Lambers, F. S. Chapin, T. L. Pons, "The plant's energy balance", in *Plant Physiological Ecology*, Springer, New York, NY, 2008, p. 225-236.

[52] F. Valladares, S. J. Wright, E. Lasso, K. Kitajima, R. W. Pearcy, "Plastic phenotypic response to light of 16 congeneric shrubs from a panamanian rainforest", *Ecology* **81** (2000), p. 1925-1936.

[53] M. Pérez-Llorca, E. Fenollosa, R. Salguero-Gómez, S. Munné-Bosch, "What is the minimal optimal sample size for plant ecophysiological studies?", *Plant Physiol.* **178** (2018), p. 953-955.

[54] P. Zabel, M. Bamsey, D. Schubert, M. Tajmar, "Review and analysis of over 40 years of space plant growth systems", *Life Sci. Space Res.* **10** (2016), p. 1-16.

[55] S. L. Ustin, S. Jacquemoud, "How the optical properties of leaves modify the absorption and scattering of energy and enhance leaf functionality", in *Remote Sensing of Plant Biodiversity* (J. Cavender-Bares, J. A. Gamon, P. A. Townsend, eds.), Springer International Publishing, Cham, 2020, p. 349-384.

[56] L. Poulet, J.-P. Fontaine, C.-G. Dussap, "A physical modeling approach for higher plant growth in reduced gravity environments", *Astrobiology* **18** (2018), p. 1093-1100.
[57] H. Schlichting, K. Gersten, "Fundamentals of boundary-layer theory", in *Boundary-Layer Theory*, Springer, Berlin, Heidelberg, 2017, p. 29-49.
[58] P. G. Jarvis, K. G. McNaughton, "Stomatal control of transpiration: scaling up from leaf to region", in *Advances in Ecological Research*, vol. 15, Elsevier, 1986, p. 1-49.

Comptes Rendus
Mécanique
2023, Vol. 351, Special Issue S2, p. 115-123
https://doi.org/10.5802/crmeca.196

Physical Science in Microgravity within the Thematic Group Fundamental and Applied Microgravity / *Sciences physiques en microgravité au sein du GDR Micropesanteur Fondamentale et Appliquée*

Bending effects distorting axisymmetric capillary bridges. Generalized Young–Laplace equation and associated capillary forces

Distorsion des ponts capillaires axisymétriques due aux effets de flexion. Équation de Young-Laplace généralisée et forces capillaires associée

Olivier Millet[*, a] **and Gérard Gagneux**[a]

[a] LaSIE, UMR-CNRS 7356, Université de La Rochelle, avenue Michel Crépeau,17042 La Rochelle cedex 1, France

E-mails: olivier.millet@univ-lr.fr (O. Millet), gerard.maryse.gagneux@gmail.com (G. Gagneux)

Abstract. This study proposes a theoretical contribution to the problem of the various distortions affecting axisymmetric capillary bridges, due to gravity or to bending effects linked to the Gaussian curvature. We deduce a clear hierarchization of effects between various reference configurations and put in a prominent position an exact first integral for the Young–Laplace equations, classical or generalized. These relationships are taken advantage of to obtain the theoretical expression of the varying inter-particle force, quantified effects of flexural strength. Finally, we establish a generalization of the classical "gorge method" to calculate accurately the capillary force of a profile subjected to distorsion due to bending when the gravity effects are negligible or not taken into account.

Résumé. Cette étude propose une contribution théorique au problème des distorsions affectant les ponts capillaires axisymétriques, dues à la gravité ou aux effets de flexion liés à la courbure gaussienne. Nous en déduisons une hiérarchisation claire de ces effets pour différentes configurations de référence et nous mettons en évidence une intégrale première exacte pour les équations de Young–Laplace, classiques ou généralisées. Ces relations sont mises à profit pour obtenir une expression théorique de la force capillaire, tenant compte des effets de flexion, qui n'est plus constante. Enfin, nous établissons une généralisation de la "gorge method" classique pour calculer avec précision la force capillaire d'un doublet capillaire soumis à une distorsion due aux effets de flexion lorsque les effets de la gravité sont négligeables ou non pris en compte.

Keywords. Distortion of capillary bridges, Mean and Gaussian curvatures impact, Generalized Young–Laplace equation, Bending effects.

* Corresponding author.

Mots-clés. Distorsion des ponts capillaires, Courbure moyenne et courbure gaussienne, Équation de Young–Laplace généralisée, Effets de flexion.

2020 Mathematics Subject Classification. 49N45, 53A10, 58E12, 74F10, 74G05, 74G15.

Published online: 21 September 2023

1. Introduction

It is well known that the constant mean curvature surfaces, highly studied, are obtained by minimizing the only surface tension energy at fixed volume, the constant corresponding to the Lagrange multiplier [1–6]. Implicitly, this means that the Gaussian curvature (or the total curvature) is not taken into account and that therefore, the bending energy is disregarded or a priori considered as having negligible effects compared to the effects of surface tension[1] [8–14].

Admittedly, the spherical or distorted water drops, freely evolving in the air, exactly agree with this simplifying assumption. However, this result is not valid when the drop, or any capillary bridge, is subjected to contact boundary conditions. In that case, the bending energy can be directly linked to an integral on the boundaries using Gauss–Bonnet theorem and must be taken into account. Let us quote that in the modeling of fluid membranes, an energy of the same type containing the Gaussian curvature is introduced (see for example [15]).

This study proposes a theoretical contribution to the problem of the various distortions affecting axisymmetric capillary bridges, due to gravity or to bending effects linked to the Gaussian curvature, in order to establish a structured and practical framework for experimentation and numerical approach [16]. We deduce a clear hierarchization of effects between various reference configurations. In Sections 3 and 4, we put in a prominent position an exact first integral for the Young–Laplace equations, classical or generalized. These relationships, which are actually total energy conservation laws, are taken advantage of to obtain the theoretical expression of the varying inter-particle force, quantified effects of flexural strength. When considering the only bending effects, the method allows to easily obtain a parameterization of the profile by generalizing together a Delaunay formula related to constant mean curvature surfaces [17], and the resolution method of the Young–Laplace equation as an inverse problem developed in [18–23].

Moreover, we establish an original generalization of the classical "gorge method", based on energy conservation principle, to calculate accurately the capillary force of a profile subjected to distorsion due to bending when the gravity effect is negligible or not taken into account.

2. The generalized Young–Laplace equation with gravity

In this work, we assume that the shape of the capillary surfaces remains axisymmetric in the deformations.

The strong distorsions of capillary bridges for which the bending effects, bending the interface[2], may be modeled by an additional curvature-related term: the introduction of C_K, a multiplier coefficient of the Gaussian curvature K, at the dimension of a force and standing for the bending stress. Under appropriate boundary conditions, the shape of a capillary interface between two fluids is then described by the so-called generalized Young-Laplace equation, involving both mean and Gaussian curvatures. Structurally analogous to the Gullstrand equation of

[1] The principal curvatures are intrinsically the two eigenvalues of the shape operator, the Gauss curvature being its determinant and the mean curvature is its trace [7].

[2] Bending the interface, i.e. changing its curvature, in a first approach.

geometrical optics[3], the resulting equation, at the upward vertical measurement x linked to the value Δp_0 at $x = 0$, comes in the following form [24–26]:

$$\gamma\left(\frac{1}{\rho_c}+\frac{1}{N}\right)+C_K\frac{1}{\rho_c\, N}=\Delta p_0-\Delta\rho\; g x, \tag{1}$$

where the force C_K divided by the area $\rho_c N$ stands for the bending stress, ρ_c and N for the principal radii of curvature (evaluated algebraically, positively when the curvature is turned into the interior of the capillary bridge) and the pressure deficiency is Δp_0 at $x = 0$.

Thenceforth, a major difficulty is to estimate the influence of C_K on two determinant data: the modified contact angles and the spontaneous curvature $\frac{\Delta p_0}{\gamma}$ at $x = 0$ after distortion.

It is also reported [27] that in electro-capillarity, at the nanoscale, the presence of electric fields leads to an extra stress term to be added in the Young–Laplace equation.

The length $\frac{|C_K|}{\gamma}$ that occurs in the generalized Young–Laplace equation allows in a certain way to assess the relative importance of bending effects (a typical scale of tension versus bending). In particular, for this purpose, the smallness or not of the dimensionless number $\frac{|C_K|}{2\gamma Y^*}$ appears significant, Y^* being the gorge radius of the distorted bridge. In the form $\frac{\pi|C_K|}{2\pi\gamma Y^*}$, this number appears as the quotient of the contributions of the bending and liquid surface tension forces at the distorted bridge neck. Strictly speaking, the formulas obtained retain the value $\frac{\pi|C_K|}{2\pi\gamma Y^*-\Delta p_0\pi Y^{*2}}$ as the most accurate criterion, taking then into account the contribution of the hydrostatic pressure.

By placing oneself out of gravity for a simple illustration, it appears that the bending effects will be of little importance when the dimensional number $\frac{|C_K|}{2\gamma Y^*}$ is small compared to 1, i.e. since y^* or the characteristic length of the capillary bridge is of the order of a few millimeters. This effect will be enhanced for synclastic capillary bridge surfaces[4] for which the meridian in concave, so that y^* is larger than for anticlastic surfaces[5]. Hence, the common horizontal axis nodoid with convex upper meridian is certainly sensitive to bending effects. In the modeling of membranes and vesicles [15], when the thickness of the fluid membrane is of the order of a few micrometers or even less, the contribution of the bending energy may become important.

In the case of minimal surfaces such as catenoids[6] where the mean curvature is zero, the Gaussian curvature has the specificity of being determined by the direct relationship at established equilibrium:

$$\frac{1}{\rho_c\, N}=-\frac{1}{{\rho_c}^2}=\frac{1}{C_K}\Delta p_0, \tag{2}$$

Δp_0 being here an unknown spontaneous value to be identified by the data of an additional boundary condition. This implicit unknown value, a priori non-zero, would highlight the significant interest in considering the bending effects after experimental verifications in microgravity to inter in the framework of Eq. (2).

[3]It must be noted that, in respect of certain theoretical issues, a capillary bridge may be considered as an optic system because it is composed of two interfaces [24]. In particular, the Gullstrand equation of geometrical optics involves the gravitational bending angle of light for finite distance. It presents also strong correspondances with geometrical approachs to gravitational lensing theory in the astrophysical context.

[4]Synclastic surfaces are those in which the centres or curvature are on the same side of the surface (dome-shape or elliptic surface). The Gaussian curvature is everywhere strictly positive; for examples among the Delaunay constant mean curvature surfaces of revolution (see *in* [18] a synoptic table for identifying the capillary bridges of revolution): a portion of unduloid, catenoid or nodoid with concave upper meridian, the axis of the bridge being horizontal.

[5]Anticlastic surfaces are those in which the centers of curvature are located on opposing sides of the surface (saddle shape or hyperbolic surface for the confined liquid). The Gaussian curvature is then everywhere strictly negative; for example: a portion of unduloid, catenoid, nodoid, or sphere with convex upper meridian, the axis of the bridge being horizontal.

It is then not mathematically correct to say without further information that a nodoid is an anticlastic surface.

[6]Surface with strictly negative Gaussian curvature and therefore, a priori, really subject to bending effects.

3. Analytical evaluation of weak capillary distortions by gravity effects

3.1. *Generalized Young–Laplace equation for axisymmetric vertical liquid bridge*

As a benchmark to be used for comparative purposes, consider, first in the classical theory, an axisymmetric vertical liquid bridge (i.e. the $x-$ axis is vertical and Δp_0 is the pressure difference through the interface at the neck level $x = 0$). I is an open interval on which we can define by Cartesian representation, say $x \to y(x)$, a portion of the Delaunay roulette strictly containing the convex profile of the bridge considered without taking into account the gravity (a zero or low gravity environment) [18]. So the shear stress is zero in the y direction and at first, we place ourselves in the relevant cases in which $y"(0) > 0$.

Taking then, if necessary into account the effects of gravity, *via* an over-pressure [19, 28, 29], results conventionally in the modified nonlinear differential equation for the distorted profile $x \to Y(x)$, according to the volumic mass densities difference between the liquid and the surrounding fluid

$$\Delta\rho = \rho_{int} - \rho_{ext}$$

a quantitated balance between the surface tension and gravity forces:

$$\frac{Y''(x)}{\left(1+Y'^2(x)\right)^{3/2}} - \frac{1}{Y(x)\sqrt{1+Y'^2(x)}} = -\frac{\Delta p_0}{\gamma} + \frac{g\,\Delta\rho}{\gamma}x =: H + Bx\,,\ x \in I. \tag{3}$$

In (3), the only parameter of the disturbance is the apparent density $\Delta\rho = \rho_{int} - \rho_{ext}$. The bridge fluid is not necessarily completely embedded in the surrounding fluid as for a wall-bound pendant drop without frictional contact constraints on the low boundary, possibly strongly distorting[7]. In continuum mechanics, this equation is obtained in the absence of motion when gravity is the only body force present. It is counterintuitive that the sign and the order of magnitude of the Gaussian curvature do not come into consideration for defining the distorted shape of the free capillary surface. This implicitly assumes that bending effects are neglected and that we are *de facto* limited here to studying rather moderate distortions. The question of bending and its impact on the deformation will be thoroughly discussed below.

3.2. *A first integral of the Young–Laplace equation for distorted bridges with gravity*

We still find ourselves in the framework and notations of the previous subsection, concerning essentially any bridge with strictly negative Gaussian curvature K (the product of the two principal curvatures). The free surface is then saddle shaped, precisely the case mainly concerned by the bending effects.

It is particularly proposed to provide a theoretical justification for an extension of the conventional gorge method in order to evaluate the interparticle capillary force under gravitational perturbation at the neck level as a special case of an energy conservation principle. Unlike the situation of axisymmetric bridges with constant mean curvature, the capillary force is no longer constant at all points of the distorted profile. The analytic expression of the interparticle force $\mathscr{F}_{cap}(x)$ is given with exactness at the generic level x; it can be used by direct calculation from observed data and takes into account the gravitational forces versus the upward buoyancy forces. For other approaches, we can consult the Russian authors about low-gravity fluid mechanics [30].

First, we introduce (X^*, Y^*) the coordinates of the moved neck (i.e. the point such that $Y(X^*) = Y^*$, $Y'(X^*) = 0$) and the two branches x^+ and x^- of Y^{-1} in the set-theoretical sense,

[7] See in [10, Figure 15 p. 780], a stable pendent water drop in a bath of castor oil exhibiting inflection on the profile, also neck and bulge (artificial low gravity: $\Delta\rho = 39\ kg/m^3$).

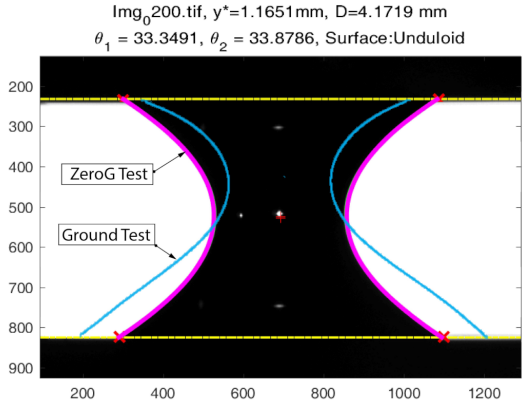

(a) Capillary bridge of pure water between two parallel planes of glass. Distorsion observed due to Earth gravity in comparison with the same experiment done without gravity (zeroG experiment) during a parabolic flight campaign with CNES and Novespace.

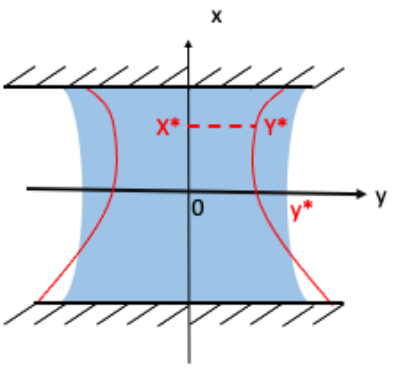

(b) Paramaterization adopted.

Figure 1. Distorded capillary bridge and paramaterization adopted.

respectively defined on $\{x \geq X^*\}$ and $\{x \leq X^*\}$, subsets of the vertical $x-$ axis, in the Cartesian coordinate system linked to the neck level of the distorted bridge (Figure 1).

Keep in mind that the capillary bridge profile loses its symmetry: the gravitational perturbation modifies the localization of the contact points and hence, also the domain of definition for the modified nonlinear differential Young-Laplace equation; the associated boundary value problem does not admit locally symmetric solutions that are physically relevant.

Due to gravity, the mass of water is displaced toward the lower solid.

Moreover, the upper boundary of the liquid thus slides over a wetted part of the solid, while the lower part spreads over a dry part, which should substantially affect the resulting values of the wetting angles. As it is well known, the observed contact angle hysteresis depends on whether the liquid is advancing or receding on the surface. Let us add that the capillary phenomena are known to be highly sensitive to all types of microscopic non-uniformity (canthotaxis effects). The main result is stated as follows:

Result 1. *Whatever the shape taken by the distorted axisymmetric bridge due to gravity, we have in relation to the case where the effects of gravity are neglected, the following relationship which is a generalization of an energy conservation principle:*
along each concerned branch of the profile, the two following functional expressions are constant and equal, at the dimension of a force.

For any $x \geq X^*$,

we have:

$$\mathscr{F}^+ = 2\pi\gamma\left(\frac{Y(x)}{\sqrt{1+Y'^2(x)}} + \frac{H}{2}Y^2(x) + B\int_{Y^*}^{Y(x)} x^+(y)\,y\,dy\right) \tag{4}$$

and, if $x \leq X^*$,

$$\mathscr{F}^- = 2\pi\gamma\left(\frac{Y(x)}{\sqrt{1+Y'^2(x)}} + \frac{H}{2}Y^2(x) + B\int_{Y^*}^{Y(x)} x^-(y)\,y\,dy\right). \tag{5}$$

Moreover, the common value is

$$\begin{aligned}\mathscr{F}^+ = \mathscr{F}^- &= 2\pi\gamma Y^* + \pi\gamma H {Y^*}^2 \\ &= -\pi\Delta p_0 {Y^*}^2 + 2\pi\gamma Y^*.\end{aligned}$$

Proof. The key to understanding how to get this first integral is to rewrite locally the modified nonlinear differential Young–Laplace equation (3) in the following local form, separately in the two branches related to $\{x \geq X^*\}$ and $\{x \leq X^*\}$, H being rigorously evaluated as the mean curvature at the neck of the distorted bridge:

$$-\frac{1}{Y}\frac{d}{dY}\frac{Y}{\sqrt{1+Y'^2}} = H + B\, x^{\pm}(Y). \tag{6}$$

Hence, by quadrature, quantities $\mathscr{F}^+$ and $\mathscr{F}^-$ are constant respectively on $\{x \geq X^*\}$ and $\{x \leq X^*\}$; write $\mathscr{F}^+ = C^+$ and $\mathscr{F}^- = C^-$.

A continuity argument at (X^*, Y^*) implies

$$C^+ = C^- = 2\pi\gamma Y^* + \pi\gamma H {Y^*}^2.$$

The demonstration lends itself to various easy generalizations, especially when a surface inflection exists and the Gaussian curvature changes sign. These analytical expressions are generalizations of formulas obtained in [18, equation (14)], and used in several other works [31–33]. □

4. Generalized Young–Laplace equation with Gaussian curvature at strong distortions

4.1. *A generalization of an exact energy invariant related to strongly distorted bridges*

In the case of strong capillary distortions, the meridian $x \to Y(x)$ of an axisymmetric capillary bridge is given by the generalized Young–Laplace equation (1) taking then into account simultaneously the combined effects of gravity and flexure, that can be rewitten as:

$$\begin{aligned}\frac{Y''(x)}{\left(1+Y'^2(x)\right)^{3/2}} - \frac{1}{Y(x)\sqrt{1+Y'^2(x)}} - \frac{C_K}{\gamma}\frac{Y''(x)}{Y(x)\left(1+Y'^2(x)\right)^2} \\ = -\frac{\Delta p_0}{\gamma} + \frac{g\,\Delta\rho}{\gamma}x \;=: H + Bx\;,\; x \in I.\end{aligned} \tag{7}$$

It must be borne in mind that for very distorted profiles, the surface tension γ may be surface temperature and curvature-dependent, which severely complicates the mathematical treatment. It follows the specified formulation, with suitably dimensioned coefficients c_T and c_J, c_K ([26, equation (27) p. 9] here, interfacial tension equals local Gibbs free energy per non-planar surface area for chemically pure fluids):

$$\gamma = \gamma_0 + c_T T + c_J\left(\frac{1}{\rho_c} + \frac{1}{N}\right) + c_K\frac{1}{\rho_c N}.$$

The qualitative results elaborated in the framework of the constant mean curvature theory are essentially based on the existence of an exact invariant (in fact, a first integral for the second order nonlinear differential equation which reveals the conservation of the total energy of the free surface). With minor adaptations, they are immediately applicable to the situation where the Gaussian curvature and bending effects are taken into account. Indeed, as we will see, we still highlight in this case a first integral for the generalized Young–Laplace equation by limiting ourselves to a presentation concerning essentially any bridge with strictly negative Gaussian curvature.

It is possible to deduce from Eq. (7) a generalization of an exact energy invariant related to strongly distorted bridges taking into account Gauss curvature and gravity. We then have the following result:

Result 2. *For the spontaneous but a priori unknown value of H, the generalized Young–Laplace equation can be rewritten, with the previous notations, in the differential form:*

$$-\frac{1}{Y}\frac{d}{dY}\left(\frac{Y}{\sqrt{1+Y'^2}}-\frac{C_K}{2\gamma}\frac{1}{1+Y'^2}\right)=H+Bx^{\pm}(Y). \tag{8}$$

Hence, along each concerned branch of the strongly distorted profile, the two following functional expressions are constant and equal, at the dimension of a force. Moreover, we have for any $x \geq X^*$, (X^*, Y^*) being the coordinates of the moved neck,

$$\mathscr{F}^{+}_{C_K}=2\pi\gamma\left(\frac{Y(x)}{\sqrt{1+Y'^2(x)}}-\frac{C_K}{2\gamma}\frac{1}{1+Y'^2(x)}+\frac{H}{2}Y^2(x)+B\int_{Y^*}^{Y(x)}x^{+}(y)ydy\right) \tag{9}$$

and, if $x < X^*$,

$$\mathscr{F}^{-}_{C_K}=2\pi\gamma\left(\frac{Y(x)}{\sqrt{1+Y'^2(x)}}-\frac{C_K}{2\gamma}\frac{1}{1+Y'^2(x)}+\frac{H}{2}Y^2(x)+B\int_{Y^*}^{Y(x)}x^{-}(y)ydy\right). \tag{10}$$

By highlighting a continuous connection at the neck, the common value is

$$\begin{aligned}\mathscr{F}^{+}_{C_K}=\mathscr{F}^{-}_{C_K}&=2\pi\gamma Y^*-\pi C_K+\pi\gamma HY^{*2}\\&=-\pi\Delta p_0 Y^{*2}-\pi C_K+2\pi\gamma Y^*,\end{aligned}$$

Proof. The proof of this result is very similar to those of Result 1 and is left to the reader. It results from quadrature of Eq. (8) and then a continuity argument at the neck Y^*. □

4.2. *The special case of only bending effects without gravity*

It is interesting to note that when considering the only bending effects (i.e. $C_K \neq 0, B = 0$), then for any axisymmetric capillary bridge, the interparticle capillary force

$$\mathscr{F}^{cap}_{C_K}=2\pi\gamma\left(\frac{Y}{\sqrt{1+Y'^2}}-\frac{C_K}{2\gamma}\frac{1}{1+Y'^2}+\frac{H}{2}Y^2\right) \tag{11}$$

is constant at all points of the profile. It constitutes a generalization of [18, Proposition 1] on the conservation of the total energy of the liquid bridge free surface.

The evaluation of $\mathscr{F}^{cap}_{C_K}$ at the gorge radius Y^* leads to a generalization of the classical "gorge method"[8]:

$$\mathscr{F}^{cap}_{C_K}=2\pi\gamma Y^*-\pi C_K+\pi\gamma HY^{*2}.$$

As explicited at the beginning of the paper, this exact formula allows to assess the relative importance of bending effects linked to C_K. Of course equivalently, this expression may be evaluated at one or the other triple line. More generally, the capillary force may be calculated at any point of the profile of the capillary bridge according to

$$\mathscr{F}^{cap}_{C_K}=2\pi\gamma Y(x)\cos\Theta(x)-\pi C_K\cos^2\Theta(x)+\pi\gamma HY^2(x)$$

where $\Theta(x)$ is the easily calculable angle made by the tangent vector to the meniscus with the $x-$axis at the generic point $(x, Y(x))$. It constitutes a generalization of the classical "gorge method" only valid when the bending effects are negligible or not taken into account.

[8]The "gorge method" (see for instance [4]) consists in calculating at the gorge Y^* the first integral of Young–Laplace equation or of generalized Young–Laplace equation (11) which is directly linked to the capillary force.

5. Conclusions

In this work, we have studied distorsion of capillary bridges due to bending effects and gravity. The true shape of the static bridge surfaces can be described by parametric equations, generalizing Delaunay formulas. Moreover, we showed that the related generalized Young–Laplace boundary value system can be solved as an inverse problem from experimental data for the unknown parameters identification.

On the other hand, we have establish generalized energy conservation laws than enable to obtain theoretical expressions of the varying inter-particle force, quantified effects of flexural strength. These expressions, involving the Gaussian curvature and gravity effect, constitute a generalization of the classical "gorge method" to calculate accurately the capillary force of a profile subjected to weak or strong distorsions.

It must of course be kept in mind that conduct such a predictive modeling for the motion of the contact lines by gravity and flexure effects is a problem considerably more difficult than to model the static distorted case, observed *in situ*. The isomorphic structure between the Gullstrand and generalized Young–Laplace equations may be thought to allow experimenters to consider a capillary bridge as an optical system. Although the two physical phenomena seem a priori disjoined but intellectually close, it could be deduced new practices for curvature measurements and fast, effective parameters identification. Nevertheless, the combined effect of volume, bending and axial gravity on the axisymmetric liquid bridge stability is a broad research subject to explore. The considerations on the numerical treatment of the distortion problem are given here as an indication of a research direction necessary to the advancement of the topic.

Conflicts of interest

The authors have no conflict of interest to declare.

Acknowledgements

The authors would like to express their sincere gratitude to the French National Centre for Space Studies (CNES) for having supported this work.

References

[1] P. G. de Gennes, "Wetting: statics and dynamics", *Rev. Mod. Phys.* **57** (1985), no. 3, p. 827-863.
[2] J. P. Gras, J. Y. Delenne, M. S. El Youssoufi, "Study of capillary interaction between two grains: A new experimental device with suction control", *Granul. Matter* **15** (2013), no. 1, p. 49-56.
[3] R. E. Johnson, R. H. Dettre, D. A. Brandreth, "Dynamic contact angles and contact angle hysteresis", *J. Colloid Interface Sci.* **62** (1977), no. 2, p. 205-212.
[4] G. Lian, C. Thornton, M. J. Adams, "A theoretical study of the liquid bridge forces between two rigid spherical bodies", *J. Colloid Interface Sci.* **161** (1993), no. 1, p. 138-147.
[5] F. M. Orr, L. E. Scriven, A. P. Rivas, "Pendular rings between solids: meniscus properties and capillary force", *J. Fluid Mech.* **67** (1975), no. 104, p. 723-742.
[6] C. D. Willett, S. A. Johnson, M. J. Adams, J. P. Seville, "Chapter 28 Pendular capillary bridges", in *Granulation*, Handbook of Powder Technology, vol. 11, Elsevier, 2007, p. 1317-1351.
[7] P. G. Ciarlet, "An Introduction to Differential Geometry. Differential geometry: theory and applications", Series in contemporary applied mathematics, vol. 9, p. 1-93, Series in contemporary applied mathematics, World Scientific, 2008.
[8] J. C. Berg, *An introduction to interfaces colloids: the bridge to nanoscience*, World Scientific, 2010.
[9] S. R. Brown, "Fluid flow through rock joints: the effect of surface roughness", *J. Geophys. Res. Solid Earth* **92** (1987), p. 1337-1347.

[10] R. Finn, "Capillary surface interfaces", *Notices Am. Math. Soc.* **46** (1999), no. 7, p. 770-781.
[11] E. Giusti, G. H. Williams, *Minimal surfaces and functions of bounded variation*, Monographs in Mathematics, vol. 80, Birkhäuser, 1984.
[12] A. de Lazzer, M. Dreyer, H. J. Rath, "Particle-surface capillary forces", *Langmuir* **15** (1999), no. 13, p. 4551-4559.
[13] A. D. Rey, "Capillary models for liquid crystal fibers, membranes, films, and drops", *Soft Matter* **3** (2007), no. 11, p. 1349-1368.
[14] R. N. Wenzel, "Surface roughness and contact angle", *J. Phys. Chem.* **53** (1949), no. 9, p. 1466-1467.
[15] U. Seifert, "Configurations of fluid membranes and vesicles", *Adv. Phys.* **46** (1997), no. 1, p. 13-137.
[16] E. Hartmann, "G^2 interpolation and blending on surfaces", *Vis. Comput.* **12** (1996), no. 4, p. 181-192.
[17] C. H. Delaunay, "Sur la surface de révolution dont la courbure moyenne est constante", *J. Math. Pures Appl.* **6** (1841), p. 309-315.
[18] G. Gagneux, O. Millet, "Analytic Calculation of Capillary Bridge Properties Deduced as an Inverse Problem from Experimental Data", *Transp. Porous Med.* **105** (2014), no. 1, p. 117-139.
[19] G. Gagneux, O. Millet, B. Mielniczuk *et al.*, "Theoretical and experimental study of pendular regime in unsaturated granular media", *Eur. J. Environ. Civ. Eng.* **21** (2016), no. 7-8, p. 840-853.
[20] H. N. G. Nguyen, O. Millet, G. Gagneux, "Exact calculation of axisymmetric capillary bridge properties between two unequal-sized spherical particles", *Math Mech Solids* **24** (2019), no. 9, p. 2767-2784.
[21] H. N. G. Nguyen, O. Millet, G. Gagneux, "Liquid bridges between a sphere and a plane-classification of meniscus profiles for unknown capillary pressure", *Math Mech Solids* **24** (2019), no. 10, p. 3042-3060.
[22] H. N. G. Nguyen, O. Millet, G. Gagneux, "On the capillary bridge between spherical particles of unequal size: analytical and experimental approaches", *Contin. Mech. Thermodyn.* **31** (2019), no. 1, p. 225-237.
[23] H. N. G. Nguyen, O. Millet, C. Zhao, G. Gagneux, "Theoretical and experimental study of capillary bridges between two parallel planes", *Eur. J. Environ. Civ. Eng.* (2020), p. 1-11.
[24] M. A. Rodriguez-Valverde, M. A. Cabrerizo-Vilchez, R. Hidalgo-Alvarez, "The Young–Laplace equation links capillarity with geometrical optics", *Eur. J. Phys.* **24** (2003), no. 2, article no. 159.
[25] L. Boruvka, A. W. Neumann, "Generalization of the classical theory of capillarity", *J. Chem. Phys.* **66** (1977), no. 12, p. 5464-5476.
[26] J. Gaydos, L. Boruvka, Y. Rotenberg *et al.*, "The Generalized Theory of Capillarity", in *Applied Surface Thermodynamics* (A. W. Neumann, J. K. Spelt, eds.), Surfactant science series, vol. 63, Marcel Dekker, 1996, p. 1-52.
[27] J. W. Van Honschoten, N. Brunets, N. R. Tas, "Capillarity at the nanoscale", *Chem. Soc. Rev.* **39** (2010), no. 3, p. 1096-1114.
[28] P. G. De Gennes, F. Brochard-Wyart, D. Quéré, "Capillarity and gravity", in *Capillarity and Wetting Phenomena*, Springer, 2004, p. 33-67.
[29] B. Mielniczuk, O. Millet, G. Gagneux *et al.*, "Characterisation of pendular capillary bridges derived from experimental data using inverse problem method", *Granul. Matter* **20** (2018), no. 1, article no. 14.
[30] A. D. Myshkis, V. G. Babskii, N. D. Kopachevskii *et al.*, *Low-gravity fluid mechanics*, Springer, 2012.
[31] G. Gagneux, O. Millet, "An analytical framework for evaluating the cohesion effects of coalescence between capillary bridges", *Granul. Matter* **18** (2016), no. 2, article no. 16.
[32] H. N. G. Nguyen, C. F. Zhao, O. Millet *et al.*, "An original method for measuring liquid surface tension from capillary bridges between two equal-sized spherical particles", *Powder Technol.* **363** (2020), p. 349-359.
[33] H. N. G. Nguyen, C. F. Zhao, O. Millet *et al.*, "Effects of surface roughness on liquid bridge capillarity and droplet wetting", *Powder Technol.* **378** (2021), p. 487-496.

Comptes Rendus
Mécanique
2023, Vol. 351, Special Issue S2, p. 125-137
https://doi.org/10.5802/crmeca.200

Physical Science in Microgravity within the Thematic Group Fundamental and Applied Microgravity / *Sciences physiques en microgravité au sein du GDR Micropesanteur Fondamentale et Appliquée*

A direct relation between bending energy and contact angles for capillary bridges

Une relation directe entre l'énergie de flexion et les angles de contact pour les ponts capillaires

Olivier Millet [a] **and Gérard Gagneux** *, [a]

[a] LaSIE, UMR-CNRS 7356, Université de La Rochelle, avenue Michel Crépeau, 17042 La Rochelle cedex 1, France.

E-mails: olivier.millet@univ-lr.fr, gerard.maryse.gagneux@gmail.com

Abstract. The didactic object of these developments on differential geometry of curves and surfaces is to present fine and convenient mathematical strategies, adapted to the study of capillary bridges. The common thread is to be able to calculate accurately in any situation the bending stress over the free surface, represented mathematically by the integral of the Gaussian curvature over the surface (called the total curvature) involved in the generalized Young–Laplace equation. We prove in particular that the resultant of the bending energy is directly linked to the wetting angles at the contact line.

Résumé. L'objet didactique de ces développements basés sur la géométrie différentielle des courbes et des surfaces est de présenter des stratégies mathématiques adaptées à l'étude des ponts capillaires. Le fil conducteur est de pouvoir calculer avec précision, dans n'importe quelle situation, la contrainte de flexion de la surface libre d'un pont capillaire, représentée mathématiquement par l'intégrale de courbure de Gauss (courbure totale) de la surface libre intervenant dans l'équation de Young–Laplace généralisée. Nous établissons en particulier un résultat très général suivant lequel la résultante de l'énergie de flexion est directement liée aux angles de mouillage au niveau de la ligne de contact.

Keywords. Distortion of nonaxisymmetric capillary bridges, Mean and Gaussian curvatures impact, Euler characteristic, Generalized Young–Laplace equation, Bending effects, Fenchel's theorem in differential geometry, Gauss–Bonnet Theorem, Geodesic curvature, Bending stress, Influence of the contact angles.

Mots-clés. Distorsion des ponts capillaires non axisymétriques, impact des courbures moyennes et gaussiennes, caractéristique d'Euler, équation de Young–Laplace généralisée, effets de flexion, théorème de Fenchel en géométrie différentielle, théorème de Gauss–Bonnet, courbure géodésique, contrainte de flexion, influence des angles de contact.

2020 Mathematics Subject Classification. 49N45, 53A10, 58E12, 74F10, 74G05, 74G15, 53Z05.

Manuscript received 13 July 2022, revised 8 February 2023 and 23 May 2023, accepted 24 May 2023.

* Corresponding author.

1. Introduction

Under boundaryless manifold condition, the most common formulation of the Gauss–Bonnet integration theorem indicates that for a spherical drop or a soap bubble without contact, with or without bump, the integral of the Gaussian curvature[1] over the surface, proportional to the bending energy, is invariant if one bends and deforms the surface (this value is a topological invariant).

Indeed, according to the Gauss–Bonnet integration theorem, for a closed free surface, the energy contribution of the Gaussian curvature during deformation is directly proportional to the Euler constant (see Eq. (2)), and therefore is constant as long as the topology of the surface, described by the Euler characteristic of the surface, does not change [1], and can be ignored when determining the shape of such a membrane.

This has probably favored the in-depth study of constant mean curvature surfaces, excluding gravity effects [2–8]. In the case of capillary bridges, the presence of contact surfaces does not allow this simplification (the total geodesic curvature of the boundary is to be taken into account to apply the Gauss–Bonnet integration theorem) and makes it a priori necessary to take into account the Gaussian curvature, to establish a hierarchy of the various configurations with regard to the bending effects and to introduce the generalized Young–Laplace equation. Some other works proposed a general law for continuum media with interface or a derivation of thermo balance equation for systems with interface [9]. A second order thermodynamical approach has been used to model surface tension of bubbles leading to a generalization of Young–Laplace theory [10], but without involving the Gaussian curvature of the interface.

In this work, we present various results and complementary strategies of mathematical analysis that can be applied to concrete capillary bridges problems, concerning in a new way, the Gauss–Bonnet and Fenchel's theorems to establish various analytical formulas easy to use for capillary bridges. In a first step, we will focus on surfaces of revolution (circular boundaries, which makes these cases much easier, especially for the explicit calculation of the total geodesic curvatures of the boundaries, rarely possible in practice by the integral calculus). We prove that, in the general case including particular axisymmetric capillary bridges, the resultant of the bending energy is directly linked to the wetting angles at the contact line. We also highlight the determining parameters and their respective influence in the bending energy and its variation.

Then the approach is extended to the rather delicate modelling of nonaxisymmetric capillary bridges distortions. The key to achieving generalization is a direct consequence of the Fenchel's theorem in differential geometry which avoids a lot of dead-end integration calculations. These developments relate to surfaces of revolution on the basis of an unit speed reparameterization (or by arc length) for a regular curve, in this case, the semi-meridian. For detailed presentations of the subject, the reader may refer to [11, p. 161-164], [12, p. 161-162] and also to [13, 14].

2. Generalized Young–Laplace equation and associated

The generalized Young–Laplace equation concerns the strong distortions for which the bending effects are modeled by an additional curvature-related term involving the Gaussian curvature K though a multiplier coefficient C_K which has the dimension of a force and stands for the bending stress [15–17]. According to generalized Young–Laplace equation, the downward vertical measurement x in relation with the value Δp_0 at $x = 0$ (a spontaneous unknown value), may be linked to the mean an Gaussian curvature according to [7, 8, 16, 18, 19]:

$$\gamma\left(\frac{1}{\rho_c}+\frac{1}{N}\right)+C_K\frac{1}{\rho_c\,N}=\Delta p_0-\Delta\rho\;g\,x, \tag{1}$$

[1] The product of the main curvatures.

where C_K has a dimension of a force[2]. Therefore the term $C_K/\rho_c N$ stands *via* a pressure for the local bending stress, where ρ_c and N denote the principal radii of curvature (evaluated algebraically, positively when the curvature is turned into the interior of the capillary bridge). Finally, Δp_0 is the pressure deficiency at $x = 0$ and $\Delta\rho$ the difference of the densities between the fluid and the gas.

It is assumed that the different cefficients, implicit unknown a priori, as Δp_0, resulting from the final equilibrium, have been previously identified *in situ* from exprerimental data, by solving a linear system, well posed and numerically stable (for example, thanks to a first integral and a principle of conservation) [20–22], [23–28].

It is extremely noteworthily [29], that this strongly nonlinear differential equation is mathematically isomorphic (the same structure) but with different variables and physical units, to the Gullstrand equation of geometrical optics, which relates the optic power P'_{op} of a thick lens (in diopters, the reciprocal of the equivalent focal length) to its geometry and the properties of the media. For example, the superficial tension γ is equivalent to the refractivity $\frac{n_1}{n_2} - 1$, where n_i is a refractive index, C_K is analogous to the expression $-(\frac{n_1}{n_2} - 1)^2 \frac{n_2}{n_1} d$, d the lens thickness and Δp_0 corresponds to P'_{op}.

Shear or free energy problems and the longitudinal bending stress of ship hulls have an analogy with the subject [30–34]. The mathematical modeling and simulations of the petroleum engineering are also concerned by this theoretical topic, in order to obtain for media with periodic microstructure an "equivalent" macroscopic representation, by some statistical or homogenization methods [35, Chapter 1].

The bending stress over the free surface Σ may be represented in the following integral form, at the dimension of a force:

$$\mathscr{E}_{bending\,stress} = C_K \int_\Sigma K \, d\Sigma,$$

where K is the Gaussian curvature of the free surface Σ, intrinsic value, in particular independent of the choice of the unit normal vector, and the nondimensional integral is the total curvature[3].

Concerning the capillary tension forces, by term by term integrating over the free surface Σ the generalized Young–Laplace equation, we have for example the relationship between various forces:

$$\gamma \int_\Sigma \left(\frac{1}{\rho_c} + \frac{1}{N} \right) d\Sigma = -C_K \int_\Sigma K \, d\Sigma + \int_\Sigma \left(\Delta p_0 - \Delta\rho \; g x \right) d\Sigma,$$

with the particular situation:

$$\gamma \int_\Sigma \left(\frac{1}{\rho_c} + \frac{1}{N} \right) d\Sigma = -C_K \int_\Sigma K \, d\Sigma + \Delta p_0 \text{ area } (\Sigma)$$

when neglecting gravity effects.

This would allow to have a reasoned opinion on the relative importance of the bending forces; according to an objective criterion, either by relative value or by intrinsic value.

3. Homotopic surfaces, Euler characteristic and Gauss–Bonnet theorem

3.1. *General theory*

Recall that the Euler characteristic (or Euler–Poincaré characteristic) is a topological invariant, an integer that describes, according to precise axiomatic principles, the shape or a structure of a topological space regardless of how it is bent according to the formula: number of

[2] C_K results from the physics at the interface molecular scale. Its sign a priori depends on the dynamics of the wetting (advancing or recessing wetting angle) and on the value of the wetting angle (see Eq. (7)).

[3] For example, the total curvature of the catenoid whose axis is of infinite length is -4π, the total curvature of the sphere of radius r is 4π and the torus 0.

vertices−number of edges+ number of faces with the property of invariance by homeomorphy. It is commonly denoted by χ or $\chi(M)$. As examples for surfaces in homological algebra, we have $\chi(M) = 2$ for a sphere, $\chi(M) = 4$ for two spheres (not connected), $\chi(M) = 0$ for a torus and $\chi(M) = -2$ for a two-holed torus.

To speak very figuratively, quite approximately, the Euler–Poincaré characteristic is an integer, invariant when the size and the shape of a geometrical object change by an effect of a "plastic" deformation.

This invariance property makes it a providential tool in the context of this study on the bending effects, associated to the Gauss–Bonnet theorem, a deep relationship between surfaces in differential geometry, connecting the Gaussian curvature of a surface to its Euler characteristic.

The Euler characteristic of the right cylinder is zero, thus so is that of the cylinder with one or two boundaries. These following free surfaces with two circular boundaries and whose meridian is an arc of Delaunay roulette are considered topologically equivalent (same common topological genus), because it is possible to continuously move one to obtain the other: portion of concave or convex, catenoid or unduloid (the right cylinder being the transition case). Accordingly, these axisymmetric surfaces have in common the same Euler characteristic, in this case, the value zero. It is the same for their continuous axisymmetric smooth deformations by distorting effect of bending or gravity [19, 36].

The Gauss–Bonnet theorem is reputed to be one of the most profound and elegant results of the study of surfaces [1, 11, 13, 37]. It has no surprisingly many applications in Physics. It is used in sectors of activity where the problems of bending beams surely arises (civil engineering, naval architecture, shell theory to predict the stress and the displacement arising in an elastic shell, [37–40], etc...).

In fact, it unexpectedly links two completely different ways of studying a surface: one geometric, the other topological. Indeed, for any compact, boundaryless two-dimensional Riemannian manifold Σ, the integral of the Gaussian curvature K over the entire manifold with respect to area measure is 2π times the Euler characteristic of Σ, also called the Euler number of the manifold, i.e.

$$\int_{\Sigma} K \, d\Sigma = 2\pi\chi(\Sigma). \tag{2}$$

For example, for a sphere Σ of radius R in $\mathbb{R}^3$, it comes:

$$\int_{\Sigma} K \, d\Sigma = \frac{1}{R^2} 4\pi R^2 = 4\pi \text{ and here } \chi(\Sigma) = 2 \tag{3}$$

Suppose now that M is a compact two-dimensional Riemannian manifold with a boundary δM and let k_g the signed geodesic curvature of δM. Then, in nondimensional writing,

$$\int_{M} K \, dM + \int_{\delta M} k_g ds = 2\pi\chi(M). \tag{4}$$

We recall that the geodesic curvature k_g, of an arbitrary curve at a point P on a smooth surface, is defined as the curvature at P of the orthogonal projection of the curve onto the plane tangent to the surface at P and we have:

$$k_g = k\cos\theta_g, \tag{5}$$

where θ_g is the angle between the osculating plane of C and the tangent plane Q at point P, which corresponds to the local contact angle for capillary bridges wetting a plane surface. In particular, when the curve C representing δM is a circle of radius R, we have $k = \frac{1}{R}$ and therefore:

$$\int_{\delta M} k_g ds = 2\pi\cos\theta_g \tag{6}$$

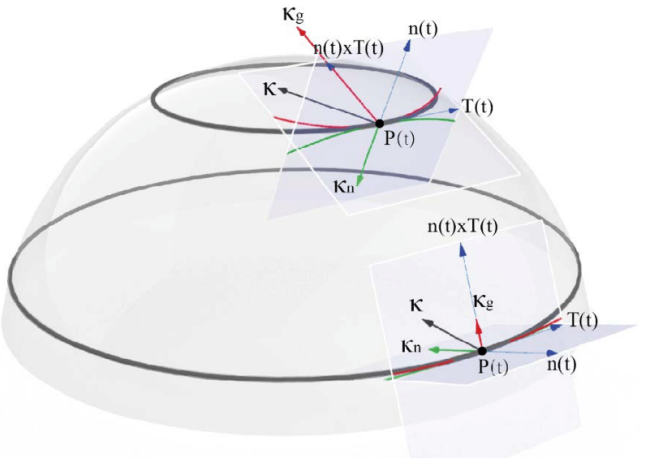

Figure 1. Representation of the geodesic curvature.

3.2. *Application to droplets and capillary bridges*

As explained in the introduction, the case of a spherical droplet (closed surface) of radius R has no interest, as the contribution of the Gaussian curvature is directly proportional to the Euler constant $\chi(M)$ whose value $\chi(M) = 2$ for a sphere[4]. In that case, relation (4) gives no supplementary information, as no wetting area exists.

Let us consider now the case of a spherical droplet lying on a plane surface as represented on Fig. 2(a). The application of Gauss–Bonnet theorem leads to calculate both contributions in the right hand side of equation (4). The first one is directly link the external surface area of the spherical cap representing the droplet and is equal to $2\pi(1-\cos\alpha)$, where α is the opening angle (Fig. 2(a)). The contribution of the geodesic curvature is equal to $2\pi\cos\theta$, according to (6), since the contact line is circular and the droplet lies on a plane surface (2(a)). In that case, (4) leads to the obvious and known geometric relation $\theta = \alpha$. For a droplet lying on the sphere, as the wetted surface is not plane, the geodesic curvature is $k_g = \frac{1}{r_c}\cos\theta_g$ with $\theta_g \neq \theta$. In that case, the Gauss–Bonnet theorem leads to the relation $\theta_g = \frac{\pi}{2} - \delta$.

For axisymmetric capillary bridges whose contact lines are circles, typically capillary bridges between two parallel planes (Fig. 3), we obtain a general expression of the bending stress for a surface of revolution[5]

$$\mathscr{E}_{bending\ stress} = C_k \int_M K\, dM = -2\pi C_k\,(\cos\theta_1 + \cos\theta_2)\,, \tag{7}$$

with here the Euler characteristic $\chi(M) = 0$ and when the total geodesic curvature at the boundaries is $2\pi(\cos\theta_1 + \cos\theta_2)$ according to (6).

For symmetric profiles with $\theta_1 = \theta_2 = \theta$, we obtain a relationship between the contact angle θ and the bending stress:

$$\theta = \arccos \frac{\displaystyle\int_M -K\, dM}{4\pi}.$$

[4] $\chi(M) = 1$ for a half-sphere or a cap.

[5] We have denoted θ_1 and θ_2 the upper and lower contact angles assumed to be constant. In the case of a plane wetted surface, θ_g corresponds to the wetting angle θ.

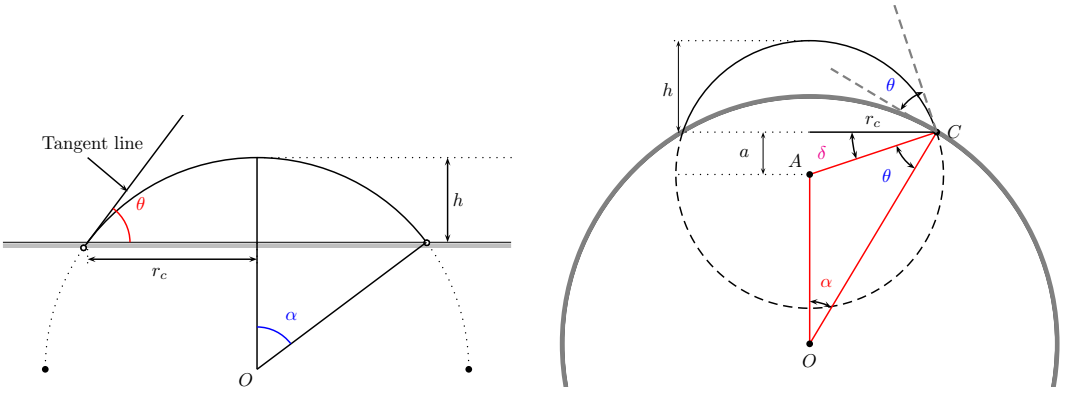

(a) Representation of a droplet on a plane surface. **(b)** Representation of a droplet on a sphere.

Figure 2

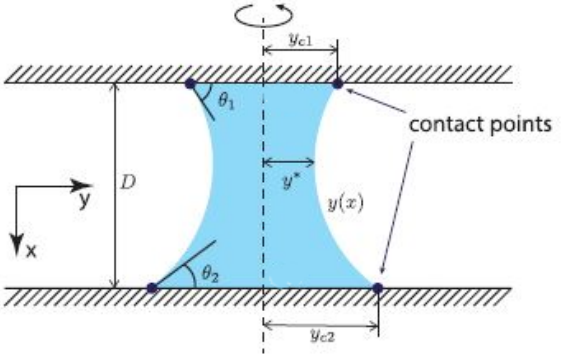

Figure 3. Capillary bridge between two parallel planes.

Coming back to (7) with the same contact angle θ, the relative finite variation of the bending stress, as function of the contact angle θ, is then given by the formula:

$$\frac{\delta\left(\mathscr{E}_{bending\,stress}\right)}{\mathscr{E}_{bending\,stress}} = -\tan\theta\,\delta\theta\ ,\ \theta \neq \frac{\pi}{2}. \tag{8}$$

In summary, it should be kept in mind that the value of the bending stress depends, besides physical constants, only on the observed values of the contact angles, whereas these angles result in part implicitly from the final equilibrium of the device.

In the general case of capillary bridges, using the classification and the associated parameterization of [20], the Gauss–Bonnet theorem leads to a supplementary relation linking the geometric properties of the capillary bridge. In the particular case of a catenoid[6], where the parameterization of the meridian is given by

$$y(x) = y^* \cosh\left(\frac{x}{y^*}\right),$$

y^* denoting the gorge radius (Fig. 3), we may obtain an explicit and useful relation between between θ, y^* and the length D of the capillary bridge.

[6]Transition between unduloid or nodoid shape.

In the next, we want to generalize these expressions in any situation, for capillary bridges with non necessarily circular contact lines in non-axisymmetric cases (this is the case for instance when coalescence of capillary bridges occurs [21]).

3.3. *The prevaling roles of the contact angles values and of the convexity/nonconvexity of the boundaries.*

For didactic purposes, we mainly limited ourselves to the detailed case of axisymmetric capillary bridges to show the interest of the simultaneous use of the Gauss–Bonnet formula and of the topological notion of Euler characteristic to evaluate the importance of the bending stress. The obtained result clearly shows in an explicit way, the major role of the contact angles values after distortion effects, eventually distinct (Eqs. (7) and (8)). Therefore, all the factors determining the contact angle have consecutively an influence on the bending stress (surface roughness and heterogeneity, influence of gravity, contact angle hysteresis [4, 30, 41–43]).

It is well known that the contact angle value is determined by the balance between adhesive and cohesive forces on the rigid supports. As the tendency of a drop to spread out over a flat, solid surface increases, the contact angle decreases. Thus, the contact angle provides an inverse measure of wettability. In this context, the case of the right cylinders is still a borderline case.

A contact angle less than $\frac{\pi}{2}$ (low contact angle) usually indicates that wetting of the surface is very favorable, and the fluid will spread over a large area of the surface. Contact angles greater than $\frac{\pi}{2}$ (high contact angle) generally mean that wetting of the surface is unfavorable. It should be quoted that a certain number of terms of the generalized Young–Laplace equation are spontaneous values, resulting from instantaneous equilibrium, and are therefore implicit unknowns. This is a difficulty for the mathematical resolution of this nonlinear differential boundary problem.

In addition, the Fenchel's theorem sheds light on the importance of the convexity or the nonconvexity of the outer edges in calculating exactly the value of the total curvatures.

Consequently, even a limited displacement of the surface boundary can modify the bending stress, by local modifications of the contact angles or affecting the local curvature of the outline curve and then, the total geodesic curvature. The contact angle hysteresis can also be significant.

4. The aim and effective convenience of the arc length reparameterization strategy

The generalization of expression (7) for non necessarily circular contact lines and possibly non closed will be performed using Fenchel's theorem based on an unit speed reparameterization (or by arc length) of the contact line to calculate the total geodesic curvature.

4.1. *Surface of revolution*

The rather paradoxical aspect of this method is that it is only very rarely easy to get in practice an explicit calculation formula. However, it leads to general quantitative results in the form of analytical formulas very easy to use from the experimental data, via a very convenient expression of the Gaussian curvature of a surface of revolution (the speed and acceleration vectors are then orthogonal).

To illustrate what we are talking about, let us consider a smooth curve of the half-plan $\{y > 0, z = 0\}$ parametrized by the arc length. The surface of revolution resulting in $\mathbb{R}^3$ from the rotation of the curve around the x-axis, ψ being the angle of rotation, is parametrized by:

$$M\big((s,\psi)\big) = \big(x(s),\ y(s)\cos\psi,\ y(s)\sin\big(\psi\big)\big)\ \ 0 \le \psi \le 2\pi, 0 \le s \le L.$$

As the meridian portion is parameterized by arc length, we have *ipso facto* the following remarkable and convenient relations and convenient expressions for angular (in radians) and trigonometric values as well as for the Gaussian curvature of the surfaces of revolution:

$$x'^2 + y'^2 = 1 \text{ at any point,} \tag{9}$$

and therefore, by differentiating, the orthogonality relationship

$$x'x'' + y'y'' = 0,$$

that is to say that $T.\frac{dT}{ds} = 0$ where the dot denotes the scalar product of $\mathbb{R}^3$ and where $T(s) = \frac{dM(s)}{ds}$ is the unit tangent vector to the curve $M(s) = M(s,0)$.

The Gaussian curvature K of the surface of revolution has then the very convenient expression (see [13, p. 162, eq. (9)]):

$$K(s,\theta) = -\frac{y''(s)}{y(s)}.$$

In this context, the expression of the mean curvature H of a surface of revolution is less attractive (see [13, p. 162, eq. (11)]).

A remarkable illustrative example of the arc length reparameterization strategy is the determination of the axisymmetric surfaces of constant Gaussian curvature[7]. We consider then the classical differential equation, linear, of the second order, homogeneous:

$$y''(s) + Ky(s) - 0,\ 0 \le s \le L,$$

with the three following cases: $K < 0$, $K = 0$, $K > 0$. Then, introducing the general form of the corresponding solutions in y, we consider the resulting differential equations

$$x'^2 = 1 - y'^2, 0 \le s \le L \tag{10}$$

resulting from (9).

Moreover, φ being the angle that the tangent to the profile curve makes with the x-axis, we have the following relationships:

$$sin\varphi = \frac{y'(s)}{\sqrt{x'^2(s) + y'^2(s)}}, \text{i.e. } \sin\varphi = y'(s) \text{ and } \cos\varphi = x'(s).$$

To compute the global bending stress in this context, we have to consider succesively:

$$\mathscr{E}_{bending\,stress} = C_k \int_M K\, dM = C_k \int\int -\frac{y''(s)}{y(s)}\, y(s)\, d\psi ds$$

and therefore

$$C_k \int\int -y''(s)\, d\psi ds = -2\pi C_k \left(y'(L) - y'(0)\right)$$

so that

$$\mathscr{E}_{bending\,stress} = -2\pi(C_k\left(\sin\left(\varphi(L)\right) - \sin\left(\varphi(0)\right)\right),$$

φ being the angle that the tangent to the profile curve makes with the $x-$axis, the axis of rotation.

Let us quote that this case of a surface of revolution around x-axis may correspond to a capillary bridge between two parallel planes at $x = 0$ and $x = L$. With the notation of Fig. 3, we have $\varphi(L) = \pi/2 - \theta_1$ and $\varphi(0) = \theta_2 - \pi/2$ and we recover the general expression (7) for axisymmetric capillary bridges.

[7] Problem studied more extensively by Gaston Darboux 1890. Among the solutions, surfaces are found that look like a hyperboloid.

4.2. *The conclusive Fenchel's theorem for the general case*

In the case of non circular contact lines, for instance portions of an ellipse, the parameterization involves elliptic integrals, rarely possible to explain in practice, so that the parameters would have to be sought numerically (spline interpolation) [44, 45]. This computational difficulty is overcame by knowing the Fenchel's theorem [13, 46], which shows the complementarity of the three methods leading to a generalization of expression (7) for possibly non convex or even non closed contact lines.

To well illustrate the interest of Fenchel's theorem associated with the theorems of Gauss and Bonnet, let us consider a reparameterization by arc length of the curve Γ.

4.2.1. *Close plane curve*

According to Fenchel's theorem[8] (1929), the value of the total curvature

$$\int_\Gamma k(s)\,ds$$

of any smooth closed space curve Γ is at least 2π, *i.e* $\int_\Gamma k(s)\,ds \geq 2\pi$. The equality holds if and only if the curve is a convex plane curve. In other words, the average curvature of a closed convex plane curve equals $2\pi/L$, where L is the length (the perimeter) of the curve[9].

By the Fenchel's theorem, without calculation of primitive functions, often tedious or ineffective, we deduce directly, for any closed convex plane curve Γ (i.e. the curve is the boundary of a convex set in the Euclidean plane), that

$$\int_\Gamma k(s)\,ds = 2\pi.$$

This case is certainly the most encountered in practice when the boundaries of the capillary bridge (the contact lines) are two closed plane convex curves, not necessarily circular. We then recover expression (7) which is still valid in this more general case[10]:

$$\mathscr{E}_{bending\,stress} = C_k \int_M K\,dM = -2\pi C_k\,(\cos\theta_1 + \cos\theta_2)\,. \tag{11}$$

In the case of a closed nonconvex plane curve, we are led to conclude by defining of the notion of the winding index, a topological argument, in what follows.

4.2.2. *Open plane curve*

Let us give some classical preliminary elements of differential geometry related to smooth boundaries of surfaces, parametrized by arc length. The curvature of a plane curve parametrized by arc length is the rate of turning of the tangent line with respect to an *ad hoc* frame along the curve.

Let $\varphi(s)$ be the angle of inclination of the unit tangent vector $T = T(s)$ with respect to a fixed frame of reference, for instance $x-$axis. Considered then as a rate of turning for the tangent line when one moves along the curve at unit speed, the curvature $k(s)$ becomes

$$k(s) = \frac{d\varphi}{ds}(s) = \varphi'(s).$$

---

[8] The Fary–Milnor theorem concerning the total curvature of the knotted closed curves does not seem appropriate for the subject of this study.

[9] For a given arc of a plane curve, the local average curvature quantifies the ratio of the change in inclination of the tangent to the curve over the arc length.

[10] When the wet solid surface is not plane, relation (11) involves θ_{g1} and θ_{g2} which corresponds to θ_1 and θ_2 to within a constant linked to the geometry of the wet solid interface.

It follows that the total curvature of a smooth curve C is then given by the formula depending only of the initial and final states:

$$\int_C k(s)\,ds = \varphi(ending) - \varphi(starting), \text{(in radians)}. \tag{12}$$

For a piecewise smooth curve parametrized by arc length, then we need to deal with the exterior angles at the corners according to the orientation of the curve in the turning motion. However, up to now, to our knowledge such capillary bridges with non convex or open contact line have are not considered in literature.

5. The general case and its implementation

In the general cases of nonaxisymmetric capillary bridges between two supports, possibly of distinct natures, the method remains applicable in principle. The difficulty is not conceptual in dealing with the general case but rather calculative. We must then, in any given case, engage in a delicate exercise in differential and analytical geometries to explicitly calculate the total signed geodesic curvature of the boundaries by the classical methods of analytical geometry.

5.1. *The calculation procedure is as follows*

At any point P of the border liquid-solid, one considers the tangent plane in P to the free surface (that supposes an adequate local regularity). One then considers the orthogonal projection of each edge into this tangent plane. The curvature in P of the projected curve is then calculated, what introduces the important role of the cosine of the local contact angle and leads to expression (5) of the the curvature k which related related to the geodesic curvature k_g at P by the relationship:

$$k_g = k\cos\theta_g$$

where θ_g is linked to the local contact angle θ to within a constant depending on the geometry of the wet solid surface. When it is plane, θ_g corresponds to the wetting angle θ, that will be considered in the next to simplify the developments.

When the contact angle is constant on the considered contact surface, we have the particularly simple relationship:

$$\int_{\Gamma_i} k_g(s)ds = cos\theta \int_{\Gamma_i} k(s)\ ds.$$

5.2. *The special situation of heterogeneous contact surfaces*

When the contact angles are separately variable on each of the contact surfaces, i.e. $\theta = \theta_1(M)$ and $\theta = \theta_2(M)$ according to the physical conditions of the two surfaces (non ideal smooth surfaces), the integral along each boundary, corresponding to the total geodesic curvature, in fact, of the kind

$$\int_{\Gamma_i} cos\theta_i(M(s))\ k(s)\ ds, \tag{13}$$

is more complicated to calculate with computational prediction of wetting (at our knowledge, an open problem for the probably most realistic case). The use of a mean theorem would likely be imprecise (effects of surface roughness).

5.3. *The general case of homogeneous contact surfaces*

When multiplied by the coefficient $(-C_K)$ at the dimension of a force, the dimensionless integral of these curvature values along the reunion of the two contact edges gives finally the value of the resulting bending stress by the Fenchel's theorem (the cornerstone of the method).

The three possible scenarios then arise according to the geometry of the boundaries (closed plane convex or nonconvex curves) are the following, the surfaces having in common, without loss of generality, the same Euler characteristic, in this illustrative case, the value zero.

By introducing the contact angles θ_1 and θ_2 (in radians) on each outline of contact surfaces, we proved that, at least theoretically, the wettability being evaluated, here, by constant contact angles, separately on each contact support.

Case 1: The boundaries are two closed plane convex curves. Then,

$$\mathscr{E}_{bending\,stress} = C_k \int_M K\, dM = -2\pi C_k\ (\cos\theta_1 + \cos\theta_2)\,.$$

Case 2: The boundaries are two closed plane curves, one convex and the other nonconvex. Then,

$$\mathscr{E}_{bending\,stress} = C_k \int_M K\, dM = -C_k\ (2k_1\pi\cos\theta_1 + 2\pi\cos\theta_2)\,,$$

the observed integer k_1, $k_1 \geq 2$, being the winding number of the nonconvex curve (the winding index in algebraic topology).

Case 3: The boundaries are two closed disjoint plane curves, nonconvex. Then,

$$\mathscr{E}_{bending\,stress} = C_k \int_M K\, dM = -C_k\ (2k_1\pi\cos\theta_1 + 2k_2\pi\cos\theta_2)\,,$$

k_1 and k_2 being the integers, ≥ 2, winding numbers of the curves, observed and known *in situ*.

In the rather theoretical case, where the value of the Euler characteristic is non-zero, it should be necessary to write:

$$\mathscr{E}_{bending\,stress} = C_k \int_M K\, dM = 2\pi\chi(M) - C_k\ (2k_1\pi\cos\theta_1 + 2k_2\pi\cos\theta_2)\,.$$

It must be emphasized that, when the contact angles are separately variable on each of the contact surfaces according to the physical conditions of the two surfaces (non ideal smooth surfaces), the integral along each boundary, corresponding to the total geodesic curvature of the plane and closed boundaries, seems a serious difficulty to explain. The question might interest specialists in differential geometry.

6. Conclusion

The developments obtained here for surfaces of revolution and their generalization to more general surfaces representing the shape of capillary bridges, result from concepts in differential geometry and geometric analysis with applications to Lagrangian Mechanics, without resorting to differential calculus and integral calculus. The methods of Euler's characteristic, associated to the Gauss–Bonnet–Binet theorem and the strongly complementary Fenchel's theorem apply immediately to the cases of the nonaxisymmetric surfaces, with explicit, easy-to-use, results formulations.

We proved that in the general way, the value of the bending stress depends, besides physical constants, only on the observed values of the contact angles, whereas these angles result in part implicitly from the final equilibrium of the device. Therefore, all the factors determining the contact angle have an influence on the bending stress (surface roughness and heterogeneity, influence of gravity, contact angle hysteresis.

It would be interesting to reconsider, in taking into account these new results concerning the bending effects, the important role of the contact curves geometry and the Gauss–Bonnet and Fenchel theorems, an analytical framework for reassessing the cohesion effects of coalescence between saddle shaped capillary bridges [21]. Finally, by creating a support material having a nonconvex region with high wettability and a complementary region with very low wettability, the experimenter could illustrate the theory by experimentation.

Conflicts of interest

The authors have no conflict of interest to declare.

Acknowledgments

The authors would like to express their sincere gratitude to the French National Centre for Space Studies (CNES) for having supported this work. They also thank Antoine Moreau (LaSIE) and Marc Medale (IUSTI) for valuable discussions.

References

[1] H.-H. Wu, "Historical development of the Gauss-Bonnet theorem", *Sci. China, Ser. A* **51** (2008), no. 4, p. 777-784.
[2] R. Finn, "Capillary surface interfaces", *Notices Am. Math. Soc.* **46** (1999), no. 7, p. 770-781.
[3] G. Gagneux, O. Millet, B. Mielniczuk, M. S. El Youssoufi, "Theoretical and experimental study of pendular regime in unsaturated granular media", *Engineering* **21** (2017), no. 7-8, p. 840-853.
[4] P.-G. de Gennes, F. Brochard-Wyart, D. Quere, *Capillarity and gravity. In Capillarity and Wetting Phenomena*, Springer, 2004.
[5] E. Giusti, *Minimal surfaces and functions of bounded variation*, Monographs in Mathematics, vol. 80, Birkhäuser, 1984.
[6] F. M. Orr, L. E. Scriven, A. P. Rivas, "Pendular rings between solids: meniscus properties and capillary force", *J. Fluid Mech.* **67** (1975), no. 4, p. 723-742.
[7] F. Sauvigny, "Surfaces of prescribed mean curvature $H(x, y, z)$ with one-to-one central projection onto a plane", *Pac. J. Math.* **281** (2016), no. 2, p. 481-509.
[8] F. Sauvigny, "Solution of boundary value problems for surfaces of prescribed mean curvature H (x, y, z) with 1–1 central projection via the continuity method", *Lith. Math. J.* **58** (2018), no. 3, p. 320-358.
[9] F. Dell'Isola, A. Romano, "On the derivation of thermomechanical balance equations for continuous systems with a nonmaterial interface", *Int. J. Eng. Sci.* **25** (1987), no. 11-12, p. 1459-1468.
[10] F. Dell'Isola, H. Gouin, P. Seppecher, "Radius and surface tension of microscopic bubbles by second gradient theory", *C. R. Acad. Sci., Paris, Sér. II, Fasc. b* **320** (1995), no. 5, p. 211-216.
[11] M. P. do Carmo, *Selected papers*, Springer, 2012.
[12] M. P. do Carmo, *Differential geometry of curves and surfaces*, Prentice Hall, 1976.
[13] M. P. do Carmo, *Differential Geometry of Curves and Surfaces*, Prentice Hall, 1976, ISBN: 0-13-212589-7.
[14] A. Gray, E. Abbena, S. Salamon, *Modern differential geometry of curves and surfaces with Mathematica*, Textbooks in Mathematics, CRC Press, 2017.
[15] L. Boruvka, A. W. Neumann, "Generalization of the classical theory of capillarity", *J. Chem. Phys.* **66** (1977), no. 12, p. 5464-5476.
[16] J. Gaydos, L. Boruvka, Y. Rotenberg, P. Chen, A. W. Neumann, "The Generalized Theory of Capillarity", in *Applied Surface Thermodynamics*, Surfactant science series, vol. 63, Marcel Dekker, 1996, p. 1-52.
[17] L. Scholtès, P.-Y. Hicher, F. Nicot, B. Chareyre, F. Darve, "On the capillary stress tensor in wet granular materials", *Int. J. Numer. Anal. Methods Geomech.* **33** (2009), no. 10, p. 1289-1313.
[18] Ch. . Delaunay, "Sur la surface de révolution dont la courbure moyenne est constante", *J. Math. Pures Appl.* **6** (1841), p. 309-315.
[19] D. N. Mazzone, G. I. Tardos, R. Pfeffer, "The effect of gravity on the shape and strength of a liquid bridge between two spheres", *J. Colloid Interface Sci.* **113** (1986), no. 2, p. 544-556.
[20] G. Gagneux, O. Millet, "Analytic Calculation of Capillary Bridge Properties Deduced as an Inverse Problem from Experimental Data", *Transp. Porous Med.* **105** (2014), no. 1, p. 117-139.

[21] G. Gagneux, O. Millet, "An analytical framework for evaluating the cohesion effects of coalescence between capillary bridges", *Granul. Matter* **18** (2016), no. 2, article no. 16.
[22] B. Mielniczuk, O. Millet, G. Gagneux, M. S. El Youssoufi, "Characterisation of pendular capillary bridges derived from experimental data using inverse problem method", *Granul. Matter* **20** (2018), no. 14, p. 1-13.
[23] H. N. G. Nguyen, C.-F. Zhao, O. Millet, G. Gagneux, "An original method for measuring liquid surface tension from capillary bridges between two equal-sized spherical particles", *Powder Technol.* **363** (2020), p. 349-359.
[24] H. N. G. Nguyen, O. Millet, G. Gagneux, "Exact calculation of axisymmetric capillary bridge properties between two unequal-sized spherical particles", *Math. Mech. Solids* **24** (2019), no. 9, p. 2767-2784.
[25] H. N. G. Nguyen, O. Millet, G. Gagneux, "Liquid bridges between a sphere and a plane - classification of meniscus profiles for unknown capillary pressure", *Math. Mech. Solids* **24** (2019), no. 10, p. 3042-3060.
[26] H. N. G. Nguyen, O. Millet, G. Gagneux, "On the capillary bridge between spherical particles of unequal size: analytical and experimental approaches", *Continuum Mech. Thermodyn.* **31** (2019), no. 1, p. 225-237.
[27] H. N. G. Nguyen, O. Millet, C.-F. Zhao, G. Gagneux, "Theoretical and experimental study of capillary bridges between two parallel planes", *European Journal of Environmental and Civil Engineering* **26** (2022), no. 3, p. 1198-1208.
[28] H. N. G. Nguyen, C.-F. Zhao, O. Millet, A. P. S. Selvadurai, "Effects of surface roughness on liquid bridge capillarity and droplet wetting", *Powder Technol.* **378** (2021), p. 487-496.
[29] M. A. Rodríguez-Valverde, M. A. Cabrerizo-Vílchez, R. Hidalgo-Álvarez, "The Young–Laplace equation links capillarity with geometrical optics", *Eur. J. Phys.* **24** (2003), no. 2, article no. 159.
[30] O. Carrier, D. Bonn, "Contact angles and the surface free energy of solids", in *Droplet, Wetting and evaporation*, Academic Press Inc., 2015, p. 15-23.
[31] O. Millet, A. Hamdouni, A. Cimetière, "Justification du modèle bidimensionnel non linéaire de plaque par développement asymptotique des équations d'équilibre", *C. R. Acad. Sci., Paris, Sér. II, Fasc. b* **324** (1997), no. 6, p. 349-354.
[32] O. Millet, A. Cimetière, A. Hamdouni, "An asymptotic elastic-plastic plate model for moderate displacements and strong strain hardening", *Int. J. Non-Linear Mech.* **22** (2003), no. 3, p. 369-384.
[33] Y. Okumo, Y. Takeda, M. Mano, T. Okada, *Design of ship hull structures: a practical guide for ingineers*, Springer, 2009.
[34] C. Quilliet, "Depressions at the surface of an elastic spherical shell submitted to external pressure", *Phys. Rev. E* **74** (2006), no. 4, article no. 046608.
[35] G. Gagneux, M. Madaune-Tort, *Analyse mathématique de modèles non linéaires de l'ingénierie pétrolière*, Mathématiques et applications, vol. 22, Springer, 1995.
[36] A. D. Myshkis, V. G. Babskii, N. D. Kopachevskii, L. A. Slobozhanin, A. D. Tyuptsov, *Low-gravity fluid mechanics*, Springer, 2012.
[37] P. G. Ciarlet, *An Introduction to Differential Geometry*, Springer, 2005.
[38] A. Hamdouni, K. Elamri, C. Vallée, O. Millet, "Compatibility of large deformations in nonlinear shell theory", *Eur. J. Mech. A Solids* **17** (1998), no. 5, p. 855-864.
[39] A. Hamdouni, O. Millet, "Classification of thin shell models deduced from the nonlinear three-dimensional elasticity. Part II: the strongly bent shells", *Arch. Mech.* **55** (2003), no. 2, p. 177-219.
[40] A. Hamdouni, O. Millet, "An asymptotic non-linear model for thin-walled rods with strongly curved open cross-section", *Int. J. Non-Linear Mech.* **41** (2006), no. 3, p. 396-416.
[41] J. Hure, B. Roman, J. Bico, "Wrapping an adhesive sphere with an elastic sheet", *Phys. Rev.* **106** (2011), no. 17, article no. 174301.
[42] J. W. van Honschoten, N. Brunets, N. R. Tas, "Capillarity at the nanoscale", *Chem. Soc. Rev.* **39** (2010), no. 3, p. 1096-1114.
[43] Y. J. Wang, S. Guo, H.-Y. Chen, P. Tong, "Understanding contact angle hysteresis on an ambient solid surface", *Phys. Rev.* **93** (2016), no. 5, article no. 052802.
[44] E. Hartmann, "G^2 interpolation and blending on surfaces", *Visual Comput.* **12** (1996), no. 4, p. 181-192.
[45] M. M. Mesmoudi, L. De Floriani, P. Magillo, "Discrete curvature estimation methods for triangulated surfaces", in *Applications of Discrete Geometry and Mathematical Morphology* (U. Köthe, A. Montanvert, P. Soille, eds.), Springer, 2012, p. 28-42.
[46] R. A. Horn, "On Fenchel's theorem", *Am. Math. Mon.* **78** (1971), p. 380-381.

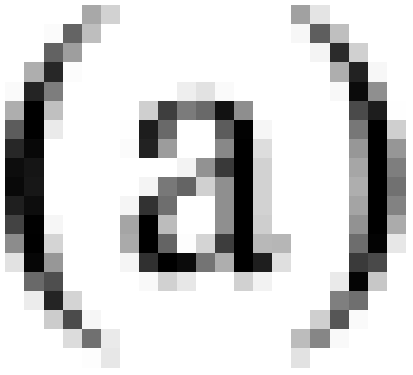
(a)

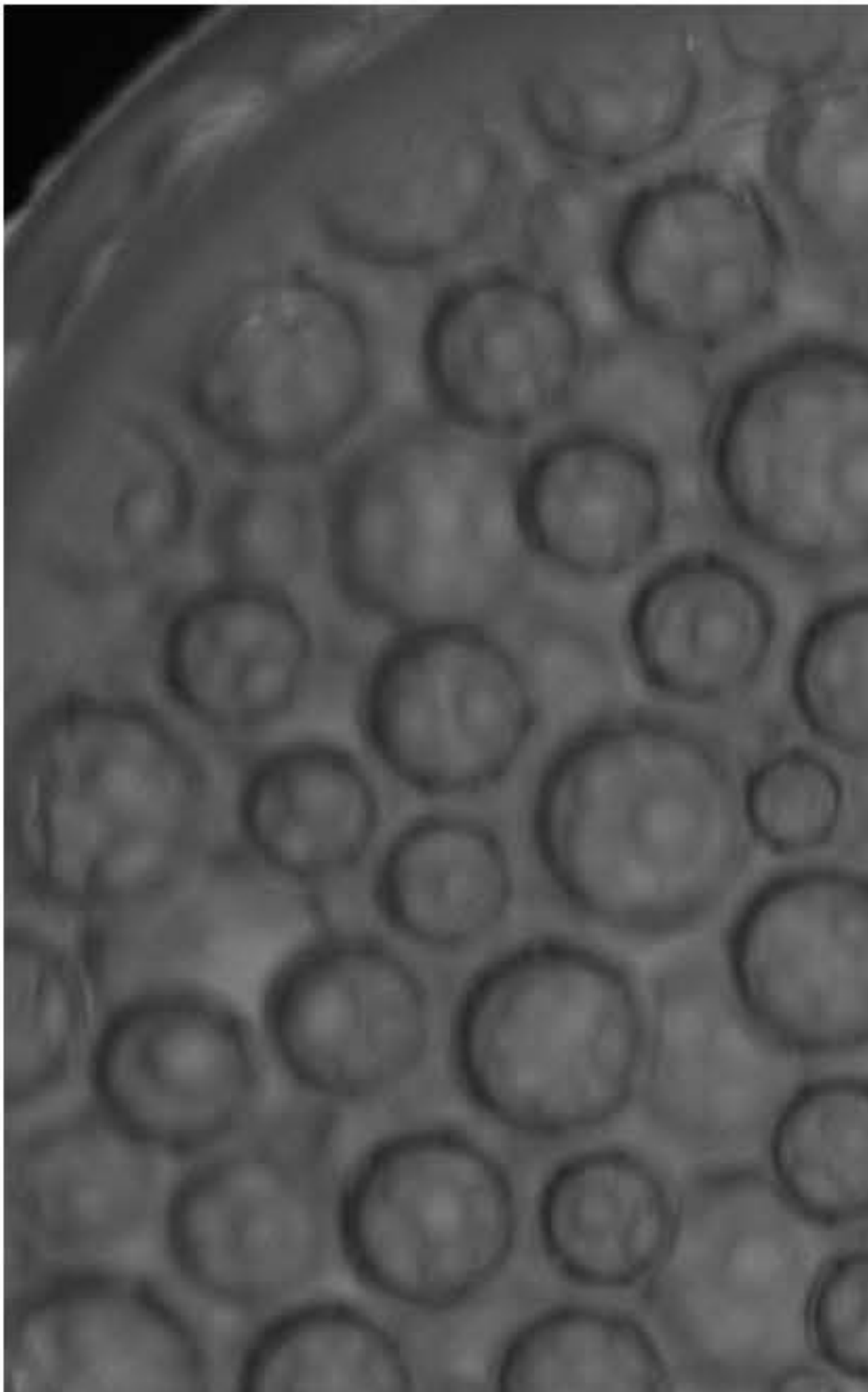

(a)

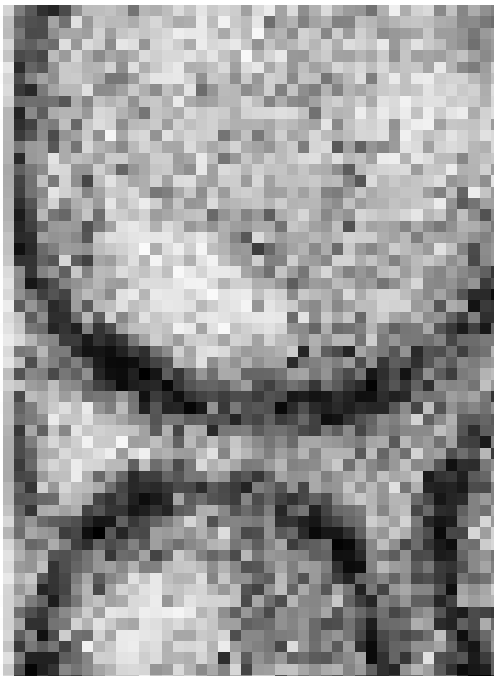

1. flux

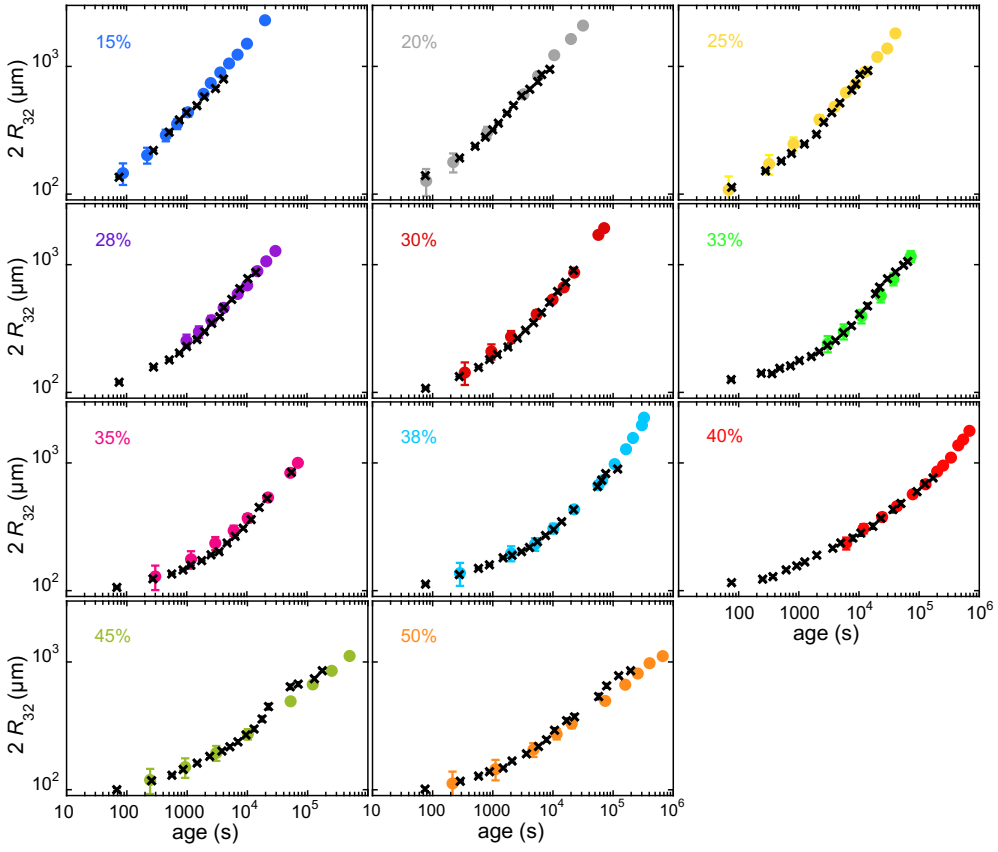

[h]

ISS data: Sauter m

Conclusion

Extracting the bubble size distribution from images of a foam surface is difficult and full of pitfalls. We have

To investigate whether the coarsening dynamics of the foam structure in the bulk is the same as at the sampl

The cuboid shape and the "point-in / point-out" illumination and light detection geometry of our setup are fa

Using the theory of diffuse light transport we derive an analytic expression relating the transport mean free p

In conclusion, the tools provided by the ISS module are efficient and well adapted to foams in the context of a

*Conflicts of interest The authors have no conflict of interest to declare.

*Acknowledgements We acknowledge funding by ESA and CNES (via the projects "Hydrodynamics of Wet F

10

I. Cantat, S. Cohen-Addad, F. Elias, F. Graner, R. Höhler, O. Pitois, F. Rouyer, A. Saint-Jalmes, *Foams: Structu*

L. J. Gibson, M. F. Ashby, *Cellular solids*, 2nd ed., Cambridge University Press, 1997.

W. W. Mullins, "The statistical self-similarity hypothesis in grain growth and particle coarsening", *J. Appl. Phys.*

P. Taylor, "Ostwald ripening in emulsions", *Adv. Colloid Interface Sci.* **75** (1998), no. 2, p. 107-163.

P. Born, M. Braibanti, L. Cristofolini, S. Cohen-Addad, D. J. Durian, S. U. Egelhaaf, M. A. Escobedo-Sánchez, R

Y. Wang, S. J. Neethling, "The relationship between the surface and internal structure of dry foam", *Colloids Sur*

H. C. Cheng, R. Lemlich, "Errors in the measurement of bubble-size distribution in foam", *Ind. Eng. Chem. Fun*

D. J. Durian, D. A. Weitz, D. J. Pine, "Multiple Light-Scattering Probes of Foam Structure and Dynamics", *Scie*

T. Gaillard, M. Roché, C. Honorez, M. Jumeau, A. Balan, C. Jedrzejczyk, W. Drenckhan, "Controlled foam gener

S. Cohen-Addad, R. Höhler, Y. Khidas, "Origin of the slow linear viscoelastic response of aqueous foams", *Phys.*

A. van Der Net, L. Blondel, A. Saugey, W. Drenckhan, "Simulating and interpretating images of foams with comp

A. M. Kraynik, D. A. Reinelt, F. van Swol, "Structure of random foam", *Phys. Rev. Lett.* **93** (2004), no. 20, artic

"Kolmogorov–Smirnov test", in *Encyclopedia of Mathematics*, 2010, http://encyclopediaofmath.org/index.php?titl

R. Höhler, S. Cohen-Addad, D. J. Durian, "Multiple light scattering as a probe of foams and emulsions", *Curr. C*

J. H. Li, A. A. Lisyansky, T. D. Cheung, D. Livdan, A. Z. Genack, "Transmission and Surface Intensity Profiles in

P. D. Kaplan, A. D. Dinsmore, A. G. Yodh, D. J. Pine, "Diffuse-transmission spectroscopy: A structural probe of

P. A. Lemieux, M. U. Vera, D. J. Durian, "Diffusing-light spectroscopies beyond the diffusion limit: The role of ba

A. Ishimaru, *Wave propagation and scattering in random media. Volume 1 - Single scattering and transport theory*

D. J. Durian, "Influence of boundary reflection and refraction on diffusive photon transport", *Phys. Rev. E* **50** (1

F. Morin, R. Borrega, M. Cloitre, D. J. Durian, "Static and dynamic properties of highly turbid media determined

J. D. Jackson, *Classical electrodynamics*, 2nd ed., John Wiley & Sons, 1975.

H. Hoballah, "Disproportionnement, Structure et Rheologie d'une Mousse Aqueuse", PhD Thesis, Université de M

G. H. Weiss, J. M. Porrà, J. Masoliver, "The continuous-time random walk description of photon motion in an iso

M. U. Vera, A. Saint-Jalmes, D. J. Durian, "Scattering optics of foam", *Appl. Opt.* **40** (2001), no. 24, p. 4210-421

H. Hoballah, R. Höhler, S. Cohen-Addad, "Time Evolution of the Elastic Properties of Aqueous Foam", *J. Phys.*

Comptes Rendus
Mécanique
2023, Vol. 351, Special Issue S2, p. 163-182
https://doi.org/10.5802/crmeca.148

Physical Science in Microgravity within the Thematic Group Fundamental and Applied Microgravity / *Sciences physiques en microgravité au sein du GDR Micropesanteur Fondamentale et Appliquée*

Mechanical characterization of core-shell microcapsules

Kaili Xie [a] **and Marc Leonetti** [*, b]

[a] Univ. Bordeaux, CNRS, LOMA, UMR 5798, F-33400 Talence, France

[b] Aix Marseille Univ, CNRS, CINaM, Marseille, France

E-mails: kaili.xie@u-bordeaux.fr (K.Xie), marc.leonetti@univ-amu.fr (M. Leonetti)

Abstract. Core-shell configurations are ubiquitous in nature such as in the form of bacterial and cells. Inspired by this, microcapsules are designed with actives as the cores surrounded by thin shells. They not only play an increasing role as artificial models for understanding dynamic behaviors of biological cells in flows, but are also becoming a fundamental class of artificial vehicles at the heart of drug delivery and release in applications. The mechanical properties of the shells are of great importance in this context. Here, we review recent experimental and theoretical characterizations of microcapsules, focusing on the soft and deformable particles with liquid cores. We begin by exploring the concept and fabrication of artificial microcapsules, followed by a discussion of different methods on the mechanical characterization of the shell.

Keywords. capsule, vesicle, RBC, interfaces, interfacial rheology, encapsulation, polymers.
Published online: 6 April 2023

1. Introduction

In nature, core-shell particles are commonly found in various forms such as bacteria and cells [1], with scales ranging from a few nanometers up to several millimeters (Figure 1). The shell encloses and protects the core material from the surrounding environment, while also mediates core-environment interactions through well defined and controllable pathways for the substance transfer and exchange. Recently, synthetic microcapsules have attracted increasing attention in food, cosmetics, and biomedicine applications [2–4]. Research has primarily focused on encapsulation techniques, development of shell materials, and assembly strategies for different purposes [5–8]. One of the most promising use of synthetic microcapsules is the delivery of drugs under controllable release [9]. Actives can be loaded into the microcapsules and then transferred to the target sites. External stimuli, such as pH values [10], temperatures [11], or stresses [12–14] are often considered as the effective strategies to release the contents through permeability changes or mechanical degradation of the shell. The design of functional microcapsules for

* Corresponding author.

specific purposes requires the well-controlled and known shell properties such as the structure and mechanical properties.

The determination of the shell mechanical properties is essential for investigating the stability of microcapsules against the external forces, e.g., shear and stretch. A sufficiently robust shell is required when the microcapsules are used as microscale reactors [15]. For example, the encapsulated catalysts or enzymes have to be protected from degradation, and retained within the microcapsules during mixing. The shell rupture in contrast may be desired as a pathway for efficient and rapid release of the core materials when the microcapsules flow and deform in the fluid medium [14, 16]. The tuning of the shell properties is correlated to the preparation process of the microcapsules [6, 17].

There are various techniques to probe the mechanical properties of the shell of microcapsules. This review aims to summarize the principles behind these approaches as well as the conditions of their utilization. In what follows, we begin the concept of microcapsules and their shell deformation. Following this, we cover different methods for the determination of the shell properties, for a single microcapsule, from both the local and global deformations. In this review, we intend to provide a summary of the most recent developments on liquid-core microcapsule characterizations which are accessible in laboratory measurements. An in-depth analysis is beyond the scope of this review article.

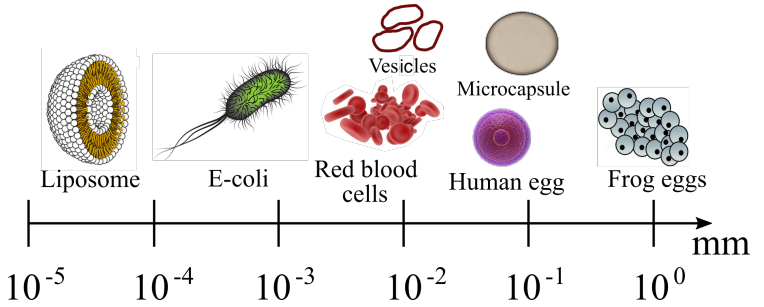

Figure 1. Scale overview of various core-shell configurations in nature (adapted from Ref. [18]).

2. Microcapsules: concept and shell assembly

A wide range of capsule systems has been developed and investigated for various aims in different communities. There is probably no clear boundary among them regarding the definition. However, it is generally accepted that a microcapsule has a core material which is surrounded or coated with a continuous shell [19]. The core-shell configuration is hence the primary nature of microcapsules. Depending on the purposes, the core materials can be liquid, solid, and even gas (hollow microcapsules). In most cases, the shell is solid and it generally has a thickness much smaller than the dimension of the microcapsule. The formation of the shell can be achieved by cross-linking or physical bonding [2]. The process of preparing the microcapsules is called encapsulation. In this review, we limit our focus on the deformable microcapsules with a liquid content and a thin elastic or viscoelastic shell. This type of microcapsules is often considered as a simple physical model for understanding the dynamic behaviours of biological cells, for example Red Blood Cells (RBCs) in the blood circulation [20–23].

Microcapsules tend to be confused with other deformable particles, such as RBCs [24], polymersomes [25], and vesicles [26] due to their resemblance [27]. We here briefly clarify their differences in terms of the shell structure and mechanical properties. Vesicles have a membrane that

consists of a lipid bilayer. RBCs have a spectrin network beneath a lipid bilayer with anchored membrane proteins. This shell also called membrane has a shear resistance [28] (Figure 2a, b). The lipid bilayers are incompressible, and thus the membrane surface area is often considered as constant in deformation [29–31] even in the case of large deformation [32,33]. The membrane is more likely to bend rather than to be compressed or stretched [34]. Note that the lipid bilayers in the membrane of vesicles is fluid and the two monolayers can slide over each other. The physical properties of polymersomes are close to lipid layers but with a high two-dimensional shear viscosity. A striking difference between vesicles and capsules is the emergence of vortices at the membrane of vesicles [35,36]. Associated to this material property, microcapsules have a reference state different from vesicles.

The composite capsule shell (Figure 2c) has elastic and viscous resistances against the shear and dilation deformations. The deformation occurs through stretching the shell at the cost of elastic energy. The bending resistance is often neglected when studying the overall deformation of microcapsules. However, it does play an important role in the local modulation of the shape such as wrinkling or folding as evoked previously [18,37]. Conveniently, the mechanical properties of microcapsules can be tunable by controlling the polymerization process which can be handled precisely using microfluidics [6].

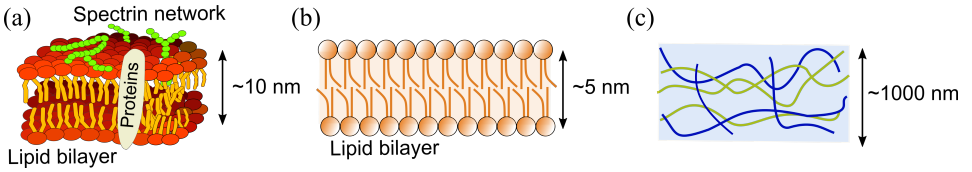

Figure 2. Illustration of the membrane/shell structures of (a) red blood cells, (b) vesicles, and (c) microcapsules.

There are various well developed methods for assembling the shell of microcapsules [2]. However, if we limit ourselves to the microcapsules with fluid cores wrapped by elastic shells, the assembly process can, in general, be classified into two categories: polymerization/cross-linking [38] and interaction bonding [39,40]. Two steps are generally involved: the formation of droplets by emulsification, and the shell assembly at the droplets interfaces. By stirring the emulsion the monomers migrate to the water/oil interface and polymerize. The droplets are stabilized avoiding coalescence for example. The degree of interface polymerization significantly affects the shell mechanical properties. Typical examples are nylon capsules [41], polysiloxane microcapsules [42], and albumin microcapsules [17]. If oppositely charged polyelectrolytes exist in the immiscible phases, the shell can be formed by interaction bonding such as electrostatic adsorption [6,7] and H-bonding [5,40]. The layer-by-layer (LbL) technique is introduced to precisely tailor the structure and mechanical properties of the shell of the microcapsules. Additional details on this subject can be found in recent review paper [2].

3. Shell deformation of microcapsules

From the mechanical point of view, it is more interesting to understand how the shell of a microcapsule undergoes deformation. Indeed, the deformability of the shell closely depends on the assembly process during the microcapsule fabrication. Regarding the mechanical behaviours, several constitutive laws had been proposed in the past decades [1]. The proper constitutive law for a certain type of capsules could be chosen by a combination of experimental and numerical investigations [43].

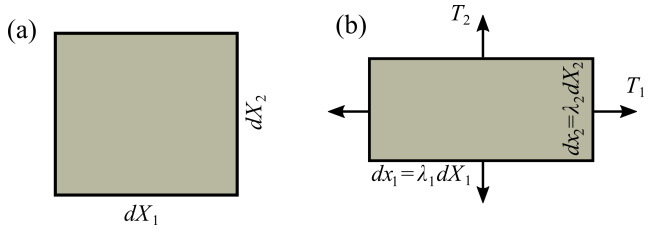

Figure 3. An element of 2D membrane in deformation. (a) Reference shape. (b) Deformed shape with extension ratios λ_1 and λ_2 under the principal tensions T_1 and T_2.

As mentioned above, the thickness of the shell is much smaller than the capsule size, typically smaller than 10% of the capsule radius. The transverse shear stress vanishes across the thickness of the shell allowing the use of a two-dimensional elasticity framework. The bending resistance is often neglected [1, 44], but essential if surface wrinkling or buckling instabilities appear [18, 37]. The shell can thus be treated as a two-dimensional membrane (Figure 3 and Figure 4), associated to the constitutive laws or the laws of behaviours. In this framework, when stretched or compressed, the membrane only undergoes in-plane deformation. The tension tensor $\boldsymbol{T}$ can be decomposed into two principal directions associated to two eigenvalues T_1 and T_2 (Figure 3). The deformation is simply related with two principal extension ratios by $dx_1 = \lambda_1 dX_1$, $dx_2 = \lambda_2 dX_2$. Constitutive laws give the stress-strain relationship [43, 45, 46] beginning by the most classic one, the generalized Hooke model:

$$T_1^{GH} = \frac{G_s}{1-\nu_s}\frac{\lambda_1}{\lambda_2}\left[\lambda_1^2 - 1 + \nu_s\left(\lambda_2^2 - 1\right)\right], \tag{1}$$

where ν_s is the surface Poisson's ratio, G_s the surface shear elastic modulus. The unit is the N/m or Pa·m. Indeed, $G_s = Gh = Eh/2(1+\nu_s)$, where G, h, and E are the bulk shear modulus, the thickness, and the bulk Young modulus (Pa), respectively. In order to recall that the non-linearities are preserved in the strain-stress tensor, the term *generalized* is preferred to distinguish from the linearized Hooke model:

$$T_1^{H} = \frac{G_s}{1-\nu_s}\left[\lambda_1^2 - 1 + \nu_s\left(\lambda_2^2 - 1\right)\right]. \tag{2}$$

The corresponding expressions for T_2 can be obtained by interchanging the roles of indices 1 and 2 in the following equations. In the limit of small deformations (linear regime), all the elastic models reduce to the Hooke model.

If the membrane material exhibits a strain-softening property, e.g., rubber-like or gelled material, a neo-Hookean law (NH) is given by

$$T_1^{NH} = \frac{G_s}{\lambda_1\lambda_2}\left[\lambda_1^2 - \frac{1}{\lambda_1^2\lambda_2^2}\right]. \tag{3}$$

The NH law can be used to model the behaviour of an infinitely thin membrane that is volume incompressible and isotropic, but it may not work well to model the area-incompressible membrane [1]. A general expression of NH law is referred to as the Mooney–Rivilin (MR) law,

$$T_1^{MR} = \frac{G_s}{\lambda_1\lambda_2}\left(\lambda_1^2 - \frac{1}{\lambda_1^2\lambda_2^2}\right)\left[\Psi + \lambda_2^2(1-\Psi)\right], \tag{4}$$

where Ψ is a coefficient ranging between 0 and 1. When $\Psi = 1$, it reduces to the NH law. The use of Ψ intends to compensate the area dilation by the corresponding thinning of the membrane in deformation.

Another law often used to model the strain-hardening material, such as RBCs membrane, is proposed by R. Skalak et al. [47],

$$T_1^{SK} = \frac{G_s}{\lambda_1\lambda_2}\left[\lambda_1^2\left(\lambda_1^2-1\right)+C\lambda_1^2\lambda_2^2\left(\lambda_1^2\lambda_2^2-1\right)\right], \tag{5}$$

where $C = \nu_s/(1-\nu_s)$ is the tuning parameter concerning the membrane area incompressibility. For example, the RBC membrane has a lipid bilayer which is almost area incompressible but easy to shear. In this case, the coefficient should be $C \gg 1$. However, in simulation, C is often equal to 1 or 10 due to numerical constraints with sometimes a global penalization of the area. Also, as for all elastic models, the membrane fluidity of RBCs is lost.

These elastic laws will show differences in the membrane behaviour as soon as it undergoes moderate deformation. Detailed comparisons can be found in the references [19, 43, 44, 46]. The investigation of the overall deformed shape and the dynamics (stationary shape, oscillations, and tumbling, etc.) has been largely performed by neglecting the bending energy. In fact, these motions lead to deformations that exhibit an order of magnitude of the particle size. The bending tension scales as B/R^2, while the in-plane elastic tension scales as G_s, where $B = Eh^3/[12(1-\nu_s^2)]$ is the bending modulus and R is the capsule radius. The ratio of these tensions is proportional to $(h/R)^2 << 1$; typically, $h \approx 100$ nm and $R \approx 50\,\mu$m for a capsule made of chitosan for example. The bending energy has to be taken into account when the local patterns, such as wrinkles or folds, appear [48].

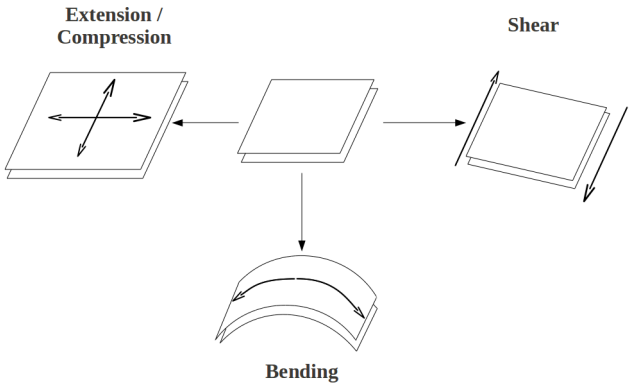

Figure 4. The microcapsule shell deformations: dilation, shear and bending resistances.

4. Mechanical characterization

The determination of the mechanical properties of individual capsules is interesting to represent the diversity of shell properties, and further to point a guide to optimize the synthetic process. In this section, we summarize the characterization methods which have been validated for liquid-core capsules, including plate-plate compression, local indentation, aspiration, and flow-induced deformation.

4.1. *Compression*

A straightforward way to deform a spherical capsule is to apply forces on the capsule by compression [49, 50] (see Figure 5). This can be achieved by using two parallel planes in which the forces

and moving distance are simultaneously measured. Such technique can be traced back to as early as 1932 when Cole studied the surface forces of sea urchin eggs [51]. Later, well controlled plate-plate compression systems have been established: see notably the works of the group of Zhibing Zhang [52]. The capsule can be compressed at a speed as low as a few micrometers per second with a force range from μN to N. Smaller capsule (in microscale) is also accessible to be compressed. Imaging with the high resolution camera allows to detect the quasi-static profile of the deformed capsule. Multiple views make it possible to understand the origin of shell bursting during compression [53].

In experiments, the measuring force monotonically increases with the compression [53, 54]. For small deformation (approximately below 5% deformation), the Reissner model [55] illustrates the linear force-displacement relationship for a hollow capsule under compression. Lytra et al. [56] recently extended the Reissner model for capsule deformation up to 50%,

$$F = \frac{4Eh^2}{\sqrt{3\left(1-\nu^2\right)}}\frac{\delta}{a} + \pi\frac{4Eh}{a^2}\delta^3 \tag{6}$$

where h is the shell thickness, a is the radius of undeformed capsules, δ is half the value of the distance change between the two plates. There are only two unknown parameters: the Young's modulus E (unit: Pa) and the Poisson's ratio ν of the shell. Generally, for polymeric capsule ν is supposed to be close to 0.5 for the sake of simplicity (see further). By fitting the experimental data using Equation (6), the elastic modulus can be measured reliably even for a liquid-core capsule [57]. For gellan gum microcapsules, this technique yields to measure the shell Young's modulus ranging from 10 kPa to 50 kPa, depending on the concentration of gellan gum [57].

However, for large deformation a more sophisticated mechanical analysis has to be conducted. Its derivation was originally performed by Feng and Yang [58]. Properties such as the shear modulus and the dilation modulus can then be determined by combining the experimental and numerical results [19, 53]. Capsules prepared by crosslinking human serum albumin (HSA) with alginate [53] are found to have a surface shear modulus of $G_s = 4.4$ N/m for a thickness of 68 μm and $G_s = 1.6$ N/m for a thickness of 30 μm. If the Poisson's ratio is assumed to be 0.5, the Young's modulus is obtained around $E = 3G_s/h = 0.18 \pm 0.02$ MPa.

Since liquid-core capsules are often immersed into another fluid, it is worth to note that low squeezing speed is preferred during compression to ensure that the equilibrium state is achieved, and to avoid flow effect in each step. Nevertheless, the constant application of the force, particularly for longer periods of time, will induce mass exchange between the interior and exterior of the capsule, and further change the deformation response. Therefore, the osmotic change has to be avoided by careful preparation of the microcapsules and choice of compression speed. Another limit of the plate-plate compression method is that it may not be applicable for small shell thickness (e.g., $h < 1$ μm) of capsules as they tend to break during compression even for small deformation.

Figure 5. Side-view images of a capsule under the axial compression in a saline solution. After removing the top plate, the capsule has returned to its undeformed shape. Adapted from Ref. [54].

4.2. *Indentation*

Another technique similar to the plate-plate compression is deforming microcapsule by the use of an atomic force microscope (AFM). Differently, AFM indentation can apply a smaller force ranging from pN to μN, which makes it possible to manipulate on much softer microcapsules [59]. AFM has been established in various measurements such as topography, adhesion [60], and interface rheology [61]. One of the advantages of AFM is that it can directly measure the deformation (indentation displacement) and the force response with high resolution. A typical measurement procedure can be summarized as: 1) selection of a cantilever with suitable stiffness and tip size; 2) cantilever calibration; 3) approaching the tip towards the capsule and measuring the curve of force *versus* displacement; 4) analysis of the force-indentation curve with the appropriate model.

Regarding the capsule size and AFM tip type, there are two typical measurement strategies: colloidal probe (Figure 6a) and sharp probe (Figure 6b). Both methods can induce from a small to large deformation of the capsule shell. However, here we only summarize the small deformation region from which we can extract the mechanical properties of the capsule shell. The indentation is much smaller than the capsule initial size.

A simple measurement was performed by Dubreuil et al. [62] using a home-made colloidal probe on multi-layer polyelectrolyte microcapsules. The force was observed to increase linearly with the indentation up to 100 nm (Figure 7). The loading speed of the AFM tip seems to have no effect on the force-displacement curve at least up to the speed of 200 nm/s. In the linear regime, the deformation of the capsule is reversible for several loading and unloading cycles. The slope of the linear curve, k, can be linked to the capsule shell property, i.e. Young's modulus E by

$$k = \xi \frac{Eh^2}{a} \tag{7}$$

where h is the shell thickness, a is radius of the capsule, and ξ is a coefficient that depends on the Poisson's ratio ν, presenting the form $\xi = 1/[(1+\nu)\sqrt{6(1-\nu)}]$ for pure shear deformation; and $\xi = 1/[(1\text{-}\nu)\sqrt{6(1+\nu)}]$ for pure stretch deformation. The shear deformation may occur for the capsules assembled using the layer-by-layer (LbL) method due to sliding between adjacent layers in deformation. However, in most cases both shear and stretch deformations are likely to happen, and it is difficult to distinguish one from the other. If the Poisson's ration is taken as $\nu = 0.5$, the coefficient ξ then ranges between 0.38 and 0.67, which is within the same order of magnitude.

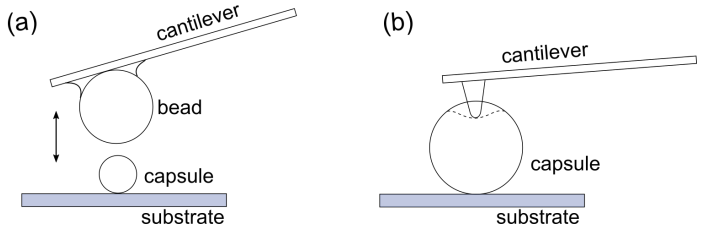

Figure 6. Schematic of indentation on the microcapsule performed by using atomic force microscope. (a) The capsule has a dimension smaller or similar to that of the colloidal on the probe. The different sizes of the beads can be glued onto the cantilever. (b) The AFM tip is much smaller than the capsule dimension.

As mentioned above, the value of the Poisson's ratio ν is generally unknown except the case of albumin capsules where the value 0.4 was determined [43]. However with a close kind of capsules $\nu = 0.5$ was also proposed using a different technique proving that it is still a challenge [63]. Note that some polymer gels such as polyacrylamide have a smaller Poisson's ratio much closer

to $\nu = 0.3$ [64, 65]. Finally, some caution is needed when considering the value of the Poisson's ratio even for cases in which we only wish to determine an approximate order of magnitude of the Young's modulus. Extracting the slope of the force-displacement curve gives the Young's modulus of the capsule shell (Equation (7)). As the indentation is small in the case of colloidal probe measurement, this method is similar to the plate-plate compression in the region of small deformation; Equation (7) has a reduced-order form of the Reissner model (without the second term on the right side of Equation (6)) [66, 67]. In literature, using this method, it is found that the sodium poly(styrene sulfonate)/poly(allylamine hydrochloride) (PSS/PAH) capsules have a value of Young's modulus in a range of 1.5-1.8 GPa [62].

The second measurement method is using a sharp AFM tip which has an effective radius much smaller than the capsule size. The indentation depth is generally only 1∼2% of the microcapsule dimension. Thus, it can be approximated to the case of a probe deforming a flat membrane. The Hertz model, taking into account the geometries of the object and the AFM tip, describes the relationship between the force and deformation,

$$F = \frac{4E}{3\left(1-\nu^2\right)}\sqrt{a^*}\Delta^{3/2} \tag{8}$$

where $1/a^* = 1/a_t + 1/a_s$, and a_t and a_s are the radius of the AFM tip and capsule, respectively. Δ is the indentation depth. An elastico-adhesion model, Johnson–Kendal–Roberts (JKR) model [68], can be used to better describe the force curves for the cases where adhesion between the AFM tip and the sample is significant. A crucial point of using the sharp AFM tip measurement is to ensure the local deformation of the shell, avoiding the overall nonlinear capsule deformation.

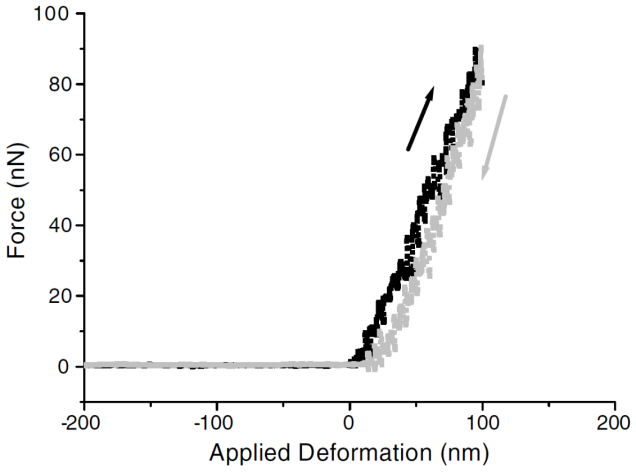

Figure 7. Force-displacement curve in the small-deformation regime for a PSS/PAH capsule [62]. The black curve corresponds to the loading process while the gray one is the unloading process.

The AFM technique is usually limited to thin microcapsule shells. The stiffness selection of the AFM tip is essential to have a high sensitivity. Similar to the plate-plate compression, AFM measurments are often performed in a liquid environment in which the movement of capsule, such as sliding, should be prevented. The effect of dynamic flow should be reduced as much as possible during manipulation. Measurements using the colloidal probe may be less sensitive to local membrane heterogeneities, as the probe size is comparable to the capsule size, unlike

the case of where sharp probes are used. A more recent work [69] compared the results of Young's modulus measurements by AFM nanoindentation and compression test for melamine-formaldehyde (MF) microcapsules. The obtained data showed that both methods give similar results within the standard deviation.

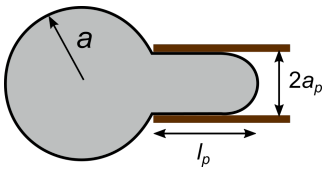

Figure 8. Illustration of micropipette aspiration on a microcapsule. The suction pressure is well controlled by using a precise pressure transducer.

4.3. *Micropipette aspiration*

Micropipette aspiration is a technique often used to obtain physical properties of biological cells as well as artificial capsules. A micropipette or capillary with a few micrometers in diameter is used to aspirate an elastic capsule with controlled pressure ΔP. A portion of the capsule shell goes into the micropipette with a aspiration length l_p (see Figure 8). The shell is assumed to be homogeneous and incompressible, with a elastic Young's modulus E. In the elastic regime, the shape of the deformed capsule can be linked with the shell mechanical properties by [70, 71]

$$\Delta P = \alpha E \frac{l_p}{a_p}, \tag{9}$$

where a_p is the radius of the micropipette, α is the coefficient related to the sizes of capsule and micropipette, and is given by $\alpha = \beta_1[1-(a_p/a)^{\beta_3}]/3$. The constants $\beta_1 = 2.01$ and $\beta_3 = 2.12$ were obtained numerically by Zhou et al. [72]. A course estimation of the coefficient can also be taken, $\alpha \approx 1$ [73]. The bending rigidity and the stretching elasticity can be deduced with a sophisticated model developed by Henriksen & Ipsen [74].

The pressure control is essential in this aspiration technique. A precise pressure transducer, e.g. microfluidic pump, is preferred but it is usually costly. Hydrostatic pressure offers a simple and low-cost way to adjust the suction pressure by changing the relative height between the micropipette head and the reservoir [71].

A close configuration is the *pendant* capsule, a technique called elastometry [37, 75]. A pendant drop is put at the end of a capillary embedded in an immiscible solvent. The chemical reaction between reactants in both phases takes place at the interface. When the stationary state is reached, a small suction is applied to change the shape slightly. wrinkles appear in the part of the membrane under compression. The measurement of the wavelength is a mean to evaluate the bending modulus independently.

4.4. *Characterization by non local stress: hydrodynamic flow*

The hydrodynamic flows provide conceptually different approaches to deform microcapsules. The flow strength is tunable by using different viscosities of the external liquids and the flow rates, i.e., shear rate and extensional rate. This approach can be performed in the linear and nonlinear regimes of deformations. The first one allows the determination of elastic moduli using analytical developments. Thanks to accurate numerical codes [76–81], the nonlinear regime allows to fit the

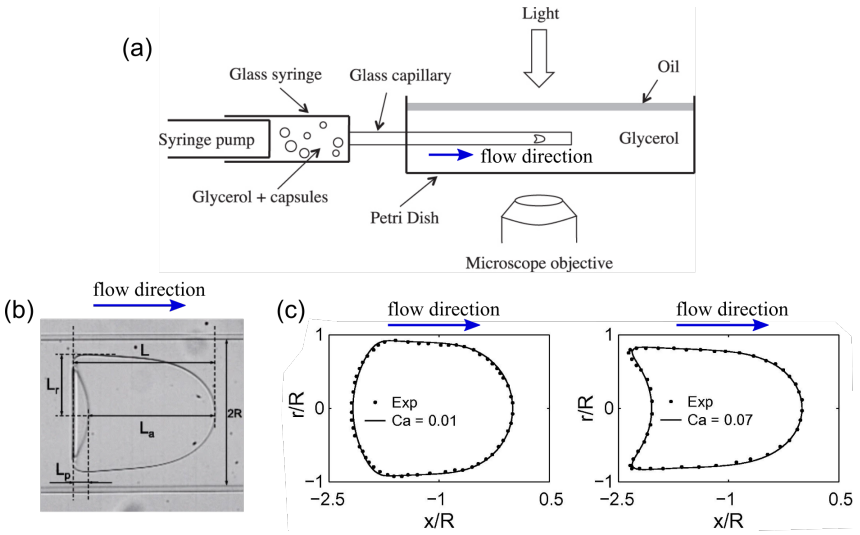

Figure 9. Microcapsules characterization in the confined flow. (a) Schematic of the experimental setup (from Ref. [88]). (b) The profile of a deformed microcapsule in the capillary flow (from Ref. [89]). L, L_a, L_p and L_r are the geometric parameters which can be extracted from the image. R is the radius of the channel. (c) Comparison of the experimental (dotted line) and numerical (continuous line) profiles (from Ref. [63]).

experimental curves to deduce the elastic moduli in a large range of deformations, and it also can help to determine the constitutive law of the membrane material. One advantage of flow is its ability to perform the measurements automatically in batch [63, 82], prefiguring applications on a production line and live analysis. Another advantage is its ability to explore the nonlinear regime and to provide new insights on the constitutive laws. However, as the capsule is free, the role of a mismatch between internal and external densities due to the fabrication or the required application becomes important. Using microgravity is an efficient tool to separate the contributions of gravity from flow. Here, we discuss the main and easily accessible approaches which can be achieved by microfluidic techniques [83, 84].

For a liquid-core capsule deformed in an external viscous flow, the jump of viscous traction across the shell is the driving force that deforms the capsule, and is equal to the load on the shell [1]. The shape of the capsule thus results from the mechanical equilibrium at the interface (a coupling relation) associating the hydrodynamic stresses and the tensions in the shell (Figure 10c).

In experiments, the external viscosity is generally high which leads to a Reynolds number Re that is much smaller than 1: $Re = \rho U a/\eta$, where ρ is the external fluid density, U the typical velocity, η the external fluid viscosity, and a the radius of the capsule. With $\rho \approx 10^3\,\mathrm{kg/m^3}$, $U \approx 1\,\mathrm{mm/s}$, $a \approx 100\,\mu\mathrm{m}$ and $\eta \approx 100\,\mathrm{mPa{\cdot}s}$, we can obtain $Re \approx 10^{-3}$. Thus, experiments are often performed in the Stokes regime where the theory has been well established [85, 86]. Thanks to the boundary integral method [87], accurate numerical models have been developed. In the regime of small deformation, all the surface elastic models are equivalent. Otherwise, the deformation is closely related to the constitutive laws of the shell material. This is a challenge that can only be solved by numerical investigations.

4.4.1. *Confined flow*

The confined flow, also called channel flow, is usually achieved by injecting the diluted microcapsules suspension through a small size channel [63, 88–90] (see Figure 9). The cross section of the channel can be round, square, or rectangular. The static shape of the capsule in the confined flow is associated with the size ratio of the capsule to the channel and the flow strength. If the microcapsule has a dimension smaller than the channel size, its shape is only slightly deformed. However, if the size of the microcapsule is comparable to the size of the channel, or even bigger, the shape becomes bullet-like or parachute-like depending on the flow rate (Figure 9c).

The mechanical properties of the microcapsule are obtained by using an inverse analysis method, a technique developed by the BMBI group [63, 91, 92]. The basic idea is to compare the profiles of deformed capsules from the numerical model and the experimental measurement. The initial shape of the microcapsule is assumed to be spherical with a radius a. When it is deformed in the channel, the geometric parameters L, L_a, L_p, and L_r can be measured using image processing, where $L_p = L - L_a$. The confinement ratio is defined as the size of the capsule to the dimension of the channel, a/R. The velocity of the capsule, v, is experimentally measured by a video recording. In the numerical calculation, a constitutive law is selected to model the deformation of the microcapsules in the confined flow. At steady state, the velocity and the shape of the deformed capsule only depend on the confinement ratio a/R and capillary number $Ca = \eta U/G_s$, where η is the viscosity of the external fluid, U is the mean unperturbed velocity of the external liquid, and G_s is the surface shear modulus of the capsule shell.

From the numerical calculation, a database is first created, containing the geometric characteristics L/a, L_a/a, L_r/a and the velocity ratio v/U as function of a/R and Ca. In experiments, the confinement ratio value a/R and the geometric lengths L/a, L_a/a and L_r/a are measurable. By comparing the confinement ratio and geometric lengths from the numerical and the experimental results (where the shape should be very similar within a tolerance), then the Ca and v/U can be known from the database. The shear elastic modulus is given by,

$$G_s = \frac{\eta U}{Ca}. \tag{10}$$

More detailed procedures are recommended to read the references [63, 88, 89, 91]

This method has the capability to measure the mechanical properties of capsules in a high throughput with the advantage of being easily performed using a microfluidic chip. However, the appropriate elastic model to describe the capsule shell deformation has to be chosen primarily. For some types of capsules, the shell materials are complex and the constitutive law is unknown. Experimental and numerical work for determining the shell model have to be done before using this method [43].

4.4.2. *Shear flow*

Shear flow is another approach to deform the microcapsule. A high aspect ratio channel or the Couette device are often used to generate the shear flow field (see Figure 10a,b). The hydrodynamic stresses are created by the established flow fields of the interior and exterior of the capsule. The steady-state deformation of the capsule is defined as $D_\infty = (L-S)/(L+S)$, where L and S are semi-major and semi-minor axis lengths of the deformed capsule, respectively. In the small deformation regime, an asymptotic solution has been proposed by D. Barthès-Biesel and co-authors [1, 44],

$$D_\infty = \frac{5}{2(c+1)} \frac{2+\nu_s}{1+\nu_s} \frac{\eta\dot{\gamma}a}{G_s} \tag{11}$$

where for the shear flow the constant $c = 1$, ν_s the surface Poisson's ratio, G_s the surface shear elastic modulus, and $\dot{\gamma}$ is the shear rate.

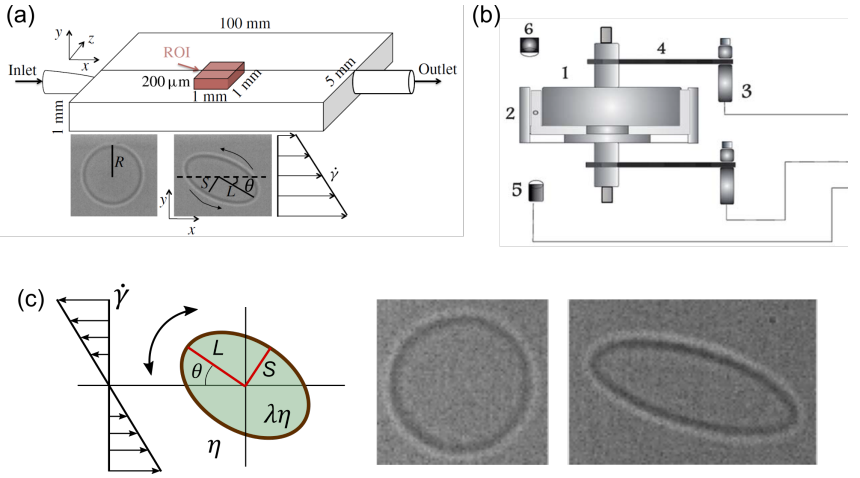

Figure 10. Microcapsule deformation in shear flow. (a) Approximately linear shear flow (ROI) in a high aspect ratio channel (from Ref. [43]). (b) Schematic of the Couette-like rheoscope. 1—inner cylinder, 2—outer cylinder, 3—motor drive unit, 4—belts, 5—microscope objective, 6—light source. (from Ref. [42]). (c) The microcapsule aligned and deformed in the shear flow. The viscosity ratio between the interior and exterior is λ. Images are from Ref. [43].

The steady-state deformation (Equation (11)) of the capsule in shear flow has been verified by various experimental investigations. For instance, H. Rehage and co-authors [42,93,94] measured the rheological properties of polysiloxane microcapsules using a rheoscope setup (Figure 10b). S. Joung et al. [95] used a similar rheoscope to extract the properties of composite microcapsules. de Loubens and co-authors [43, 96] have reported that HSA capsules show different mechanical properties depending on the degree of the shell crosslinking. Higher crosslinking gives rise to a larger value of the Young's modulus of the shell.

The measurement here is limited within the small deformation regime (generally $D_\infty \leq 5\%$ for the steady-state deformation). The shear elastic modulus is extracted by plotting the deformation *versus* the shear rate for individual capsules. However, the dynamics of the capsule in shear flow are complex. The deformation may exhibit oscillation due to swinging, tumbling, or tank-treading motions [1, 95, 96]. In practice, it is better to prevent such complex behaviors when measuring the shell mechanical properties.

4.4.3. *Extensional flow*

The extensional flow is simpler than the shear flow as no tank-treading exists and as the capsule stays at the centre during a sufficient time to reach stationary deformations. The original setup that produces such flow field is the four-roll mill device developed by G. Taylor [97] (Figure 11). The flow field is considered as two-dimensional as no liquid flows vertically, $[v_x, v_y, v_z] = [\dot{\varepsilon}x, -\dot{\varepsilon}y, 0]$, where $\dot{\varepsilon}$ is the extensional rate. The extensional rate can be accurately controlled by changing the rotation speed of the four rolls. At the center of the flow, the velocities $v_x = v_y = v_z = 0$, which is called stagnation point. The field of extensional rate around the stagnation point is roughly constant [6, 17, 82]. To ensure the capsules are exposed to a homogeneous extensional field, they are generally stabilized near the stagnation point in the flow.

Chang & Olbricht [41] are probably the first to use the four-roll mill device to deform synthetic millimetric capsules. The steady-state deformation D_∞ was plotted as a function of various flow

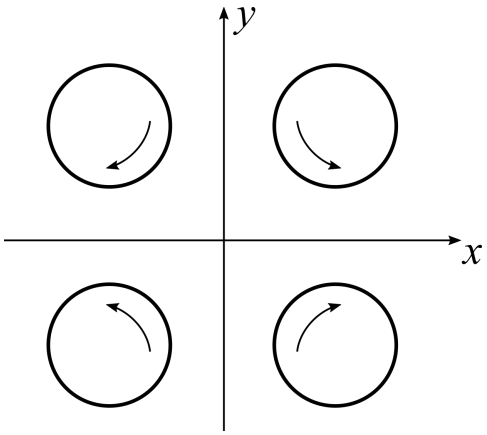

Figure 11. Schematic of the top view of the four-roll mill. The extensional flow field is generated in the center.

strain rates G. It was found that the deformation is linearly related to the strain rate, $D_\infty = 25/2[\eta GR/(Eh)]$, where R is the radius of the capsule, E is the Young's modulus, and h is the thickness of the capsule shell. Fitting the experimental data gives the mechanical property Eh of the shell which is considered as the two-dimensional modulus, i.e. surface Young's modulus. Compared to the plate-plate compression, the values of surface Young's modulus from the extensional flow measurement are slightly higher, but they are within the same order, between 0.1-0.4 N/m for the case of the nylon capsules.

Microfluidics has been recently used to create the extensional flow field to deform capsules [6, 17, 84, 98]. The extensional rate $\dot{\varepsilon}$ is easily adjustable by the flow rate. A diluted microcapsules suspension is injected into the extensional flow chip through a syringe. Individual microcapsules pass the stagnation point and deform. The steady-state deformation is achieved by stabilizing the capsule near the stagnation point for a long enough period of time (Figure 12a).

Equation (11) also gives the prediction of capsule deformation in the extensional flow in the linear regime (deformation $D_\infty \leq 0.1$), where the constant $c = 0$. For a uniform and incompressible shell material with Poisson's ratio $\nu_s = 0.5$, the Equation (11) can be rewritten as,

$$G_s = \frac{25}{6}\frac{\sigma R}{D_\infty}. \tag{12}$$

Note that the Equation (12) has the same formula with the reduced order of the prediction used in the work of Chang & Olbricht [41]. Figure 12b illustrates the linear relationship of the deformation *versus* flow stress $\sigma = \eta\dot{\varepsilon}$. The capsule with a stiffer shell needs a larger flow stress to be able to be deformed. By using the Equation (12) to fit the experimental measurement, it gives the surface shear elastic modulus G_s. The bulk Young's modulus E of the shell can then be correlated by $Eh = 2G_s(1+\nu_s) = 3G_s$.

For capsules assembled by interface complexation of chitosan and ammonium phosphatidic fatty acid (PFacid) [6, 18, 82], the Young's modulus $E \approx 6.5$ MPa. Whereas, for nylon capsules the membrane Young's modulus is around 0.1 MPa, an order of magnitude lower [41]. The surface shear modulus for chitosan capsules is invariant to the capsule size; while for HSA capsules, it is observed to increase several orders of magnitude with the capsule size (Figure 12c). The differences are due to the different kinetics of the membrane formation. In the time scale of chitosan membrane assembly (from minutes to hours), the concentrations of chitosan and the opposite-charge surfactant both are sufficient. The membrane growth of the chitosan capsules

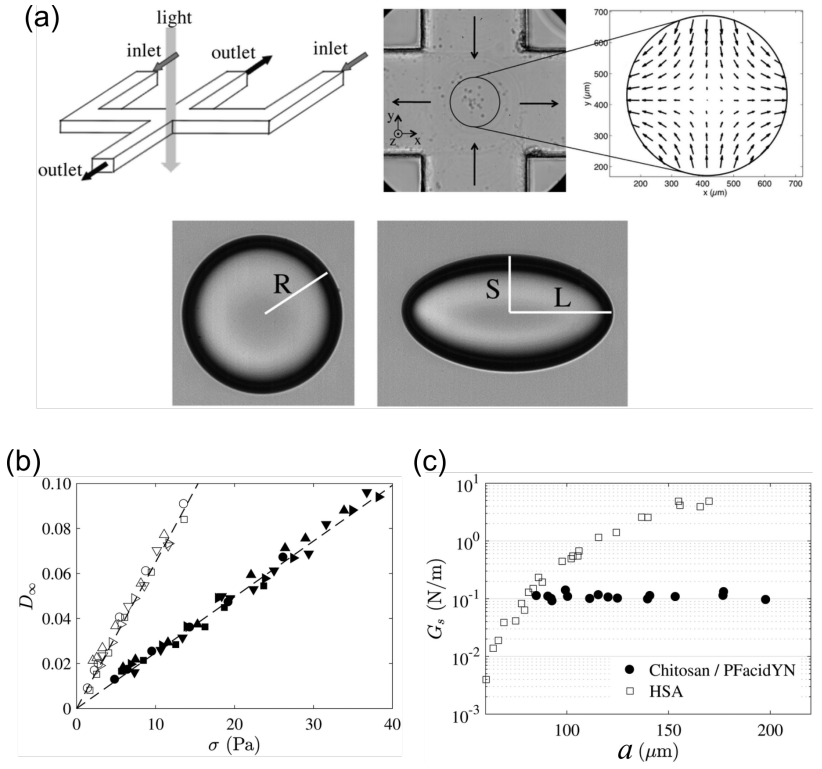

Figure 12. Microcapsule deformation in a planar extensional flow. (a) The extensional flow setup. Two opposite flow meet at the center of the chamber (stagnation point), followed by flowing away towards the two outlets. The capsule is deformed at the stagnation point. (b) The steady-state deformation D_∞ linearly increases with the hydrodynamic stress $\sigma = \eta\dot{\varepsilon}$. Two batches of capsules (radius 102 μm) are shown here. These two batches of capsules were prepared using different concentrations of chitosan and surfactant (ammonium phosphatidic fatty acid). The different slopes show different G_s values: 0.17 N/m for the closed symbols, and 0.065 N/m for open symbols. (c) Surface shear modulus G_s *versus* the capsule radius for the batch of chitosan and HSA capsules. The Young's modulus for chitosan capsules is $E \approx 6.5$ MPa. (adapted from Ref. [6])

is predominately governed by the diffusion of the surfactant where the thickness of the capsule shell scales with time with a power of 1/2 [6, 7, 39]. In contrast, the HSA molecules are adsorbed onto the surface and crosslinked for HSA capsules. The surface concentration of HSA increases with the capsule size. This gives rise to higher crosslinking degree in the membrane for larger size capsule, and consequently results in larger elasticity (i.e. surface shear modulus).

When the flow stress is high enough, the capsule is deformed without reaching a steady-state deformation. The capsule breaks and releases the encapsulated content [14]. The critical breakup of capsule closely depends on the surface shear modulus when this one is larger than 0.1 N/m. While, for the small value of G_s, the critical breakup stress seems to have weak dependence of the surface shear modulus (Figure 13). In breakup, the chitosan capsules [14] with high G_s exhibit an elastic-like breakage where the irregular shape is observed. Fluorescent imaging confirms that the membrane discontinuity leads to the irregular shape in the breakup process.

Compared to the shear flow, the extensional flow results in simpler capsule motion dynamics, without the observation of more complex dynamics such as tank-treading, swinging, and

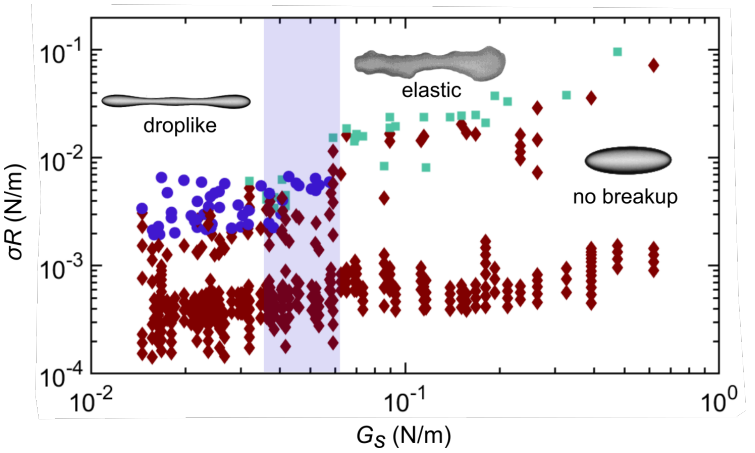

Figure 13. Phase diagram of capsule breakup in the extensional flow. The symbols ♢, ○ and □ denote no breakup, drop-like behavior (breakup) and elastic behavior of capsules (solid-like breakup also called breakage), respectively. σ is the viscous stress, R here is the radius of capsule, and G_s is the surface shear modulus. The shaded region indicates the transition zone between drop-like and elastic behaviors breakup. Inset images are the typical shapes observed. (from Ref. [14])

tumbling [42, 96, 99]. The final deformation of the capsule in flow is stable. However, it has some limits during the experimental operation. One of the difficulties is that it requires rapid adjustment of the capsule position in flow as a small perturbation will bring the capsule away from the stagnation point. Moving out of a certain size of observation window [6, 17], the extensional rate $\dot{\epsilon}$ will significantly drop due to the walls, which should be avoided in experiments. To ensure long observation times, a computer control with fast image acquisition and processing is therefore needed, keeping the capsule near the stagnation point [100].

4.5. *Characterization by non local stress: electric field*

Another method avoiding the contact between a probe and a capsule membrane is to apply an external electric field to induce the membrane deformation. It is well known that vesicles [101–103] and droplets [104, 105] deform in DC and AC electric fields. A protocol has recently been proposed to measure surface viscosities in such systems by imaging the relaxation of the shape in an electric field [106]. Contrary to membranes of vesicles and polymersomes, the capsule membrane may be not electrically insulated, for example the albumin membrane. However, if the internal and external fluids have different conductivities and permittivities, it becomes possible to deform the capsules using the electric field [107–109]. This opens a new route to characterize the membrane properties as used in vesicles. A potentially high advantage of the use of an electric field is the control of the location of analysis by flow, and it is also accessible to achieve high throughput of analysis.

5. Conclusion & Outlook

The core-shell microcapsules are becoming the focus in many interdisciplinary research. The mechanical properties of microcapsules are essential not only for the fundamental studies of their dynamic behaviors in flow but also for the different purposes in applications.

In this review, we have discussed the principles of different methods for characterizing microcapsules with thin shells, i.e with a thickness at least ten times smaller than the capsule radius. In this limit, the framework of two-dimensional elasticity can be used. In the linear regime, there are three independent parameters: the Young modulus, the Poisson's ratio, and the thickness. It is generally more convenient to use the surface shear modulus, the Poisson's ratio, and the bending modulus. Due to the difficulty in evaluating the Poisson's ratio, some authors have used the area dilation modulus K. Some shells also exhibit a viscoelastic response as observed in droplets [110], which leads to more difficult analysis by adding two additional parameters: the surface shear and dilational viscosities. On the basis of flow method and three different kinds of analysis [96,111,112], the shear surface viscosity has been determined with an order of magnitude which seems reasonable at the leading order. A drawback is the necessity to know the constitutive law. Unfortunately, the understanding of the nonlinear behavior (constitutive law) of shells is still a challenge even in the simplest case, i.e. purely elastic shell. Finally, two kinds of key studies would improve our understanding of the mechanics of shells. First, a cross-analysis comparing the results of the different techniques on the same capsules is still lacking. It prevents from defining their limits and their ranges of validity as in cell mechanics [113]. Second, a comparison with the mechanics of flat membranes measured by surface rheology tools should allow to decipher what is a matter of capsule (finite volume, curvature) from the general process of polymerization.

Conflicts of interest

The authors declare no competing financial interest.

Dedication

The manuscript was written through contributions of all authors. All authors have given approval to the final version of the manuscript.

Acknowledgments

M. L. thanks CNES and ANR (ANR-18-CE06-0008-01) for financial support and access to microgravity. The authors thank Zaiyi Shen and Pedro M. Resende for the careful reading of the manuscript.

References

[1] D. Barthès-Biesel, "Motion and deformation of elastic capsules and vesicles in flow", *Annu. Rev. Fluid Mech.* **48** (2016), p. 25-52.

[2] M. G. Bah, H. M. Bilal, J. Wang, "Fabrication and application of complex microcapsules: A review", *Soft Matter* **16** (2020), no. 3, p. 570-590.

[3] E. Assadpour, S. M. Jafari, "Advances in spray-drying encapsulation of food bioactive ingredients: From microcapsules to nanocapsules", *Annual review of food science and technology* **10** (2019), p. 103-131.

[4] B. Kupikowska-Stobba, D. Lewińska, "Polymer microcapsules and microbeads as cell carriers for in vivo biomedical applications", *Biomater. Sci.* **8** (2020), no. 6, p. 1536-1574.

[5] J. Dupré de Baubigny, C. Trégouët, T. Salez, N. Pantoustier, P. Perrin, M. Reyssat, C. Monteux, "One-step fabrication of ph-responsive membranes and microcapsules through interfacial h-bond polymer complexation", *Sci. Rep.* **7** (2017), no. 1, article no. 1265.

[6] K. Xie, C. De Loubens, F. Dubreuil, D. Z. Gunes, M. Jaeger, M. Leonetti, "Interfacial rheological properties of self-assembling biopolymer microcapsules", *Soft matter* **13** (2017), no. 36, p. 6208-6217.

[7] R. Chachanidze, K. Xie, H. Massaad, D. Roux, M. Leonetti, C. de Loubens, "Structural characterization of the interfacial self-assembly of chitosan with oppositely charged surfactant", *Journal of Colloid and Interface Science* **616** (2022), p. 911-920.
[8] Z. Jiang, S. Zhao, M. Yang, M. Song, J. Li, J. Zheng, "Structurally stable sustained-release microcapsules stabilized by self-assembly of pectin-chitosan-collagen in aqueous two-phase system", *Food Hydrocolloids* **125** (2022), article no. 107413.
[9] V. Kudryavtseva, S. Boi, J. Read, R. Guillemet, J. Zhang, A. Udalov, E. Shesterikov, S. Tverdokhlebov, L. Pastorino, D. J. Gould *et al.*, "Biodegradable defined shaped printed polymer microcapsules for drug delivery", *ACS Appl. Mater. Interfaces* **13** (2021), no. 2, p. 2371-2381.
[10] D. R. Thakare, G. Schaer, M. Yourdkhani, N. R. Sottos, "Fabrication of pH-responsive monodisperse microcapsules using interfacial tension of immiscible phases", *Soft Matter* **16** (2020), no. 22, p. 5139-5147.
[11] M. Ina, A. P. Zhushma, N. V. Lebedeva, M. Vatankhah-Varnoosfaderani, S. D. Olson, S. S. Sheiko, "The design of wrinkled microcapsules for enhancement of release rate", *Journal of colloid and interface science* **478** (2016), p. 296-302.
[12] Y. Xu, Y. Shen, T. C. T. Michaels, K. N. Baumann, D. Vigolo, Q. Peter, Y. Lu, K. L. Saar, D. Vella, H. Zhu *et al.*, "Deformable and Robust Core-Shell Protein Microcapsules Templated by Liquid–Liquid Phase-Separated Microdroplets", *Advanced Materials Interfaces* **8** (2021), no. 19, article no. 2101071.
[13] B. C. Leopércio, M. Michelon, M. S. Carvalho, "Deformation and rupture of microcapsules flowing through constricted capillary", *Sci. Rep.* **11** (2021), no. 1, article no. 7707.
[14] R. Chachanidze, K. Xie, J. Lyu, M. Jaeger, M. Leonetti, "Breakups of Chitosan microcapsules in extensional flow", *Journal of Colloid and Interface Science* **629** (2023), p. 445-454.
[15] D. Lensen, D. M. Vriezema, J. C. M. van Hest, "Polymeric microcapsules for synthetic applications", *Macromolecular bioscience* **8** (2008), no. 11, p. 991-1005.
[16] A. Le Goff, B. Kaoui, G. Kurzawa, B. Haszon, A.-V. Salsac, "Squeezing bio-capsules into a constriction: deformation till break-up", *Soft matter* **13** (2017), no. 41, p. 7644-7648.
[17] C. De Loubens, J. Deschamps, M. Georgelin, A. Charrier, F. Edwards-Lévy, M. Leonetti, "Mechanical characterization of cross-linked serum albumin microcapsules", *Soft matter* **10** (2014), no. 25, p. 4561-4568.
[18] K. Xie, "Instabilities of microcapsules in flow: breakup and wrinkles", PhD Thesis, Ecole Centrale Marseille, France, 2019.
[19] C. Pozrikidis, *Modeling and simulation of capsules and biological cells*, Chapman & Hall/CRC Mathematical and Computational Biology, Chapman & Hall/CRC, 2003.
[20] J. B. Freund, "Numerical simulation of flowing blood cells", *Annu. Rev. Fluid Mech.* **46** (2014), p. 67-95.
[21] Z. Shen, A. Farutin, M. Thiébaud, C. Misbah, "Interaction and rheology of vesicle suspensions in confined shear flow", *Phys. Rev. Fluids* **2** (2017), no. 10, article no. 103101.
[22] T. W. Secomb, "Blood flow in the microcirculation", *Annu. Rev. Fluid Mech.* **49** (2017), p. 443-461.
[23] P. Balogh, P. Bagchi, "Direct numerical simulation of cellular-scale blood flow in 3D microvascular networks", *Biophys. J.* **113** (2017), no. 12, p. 2815-2826.
[24] A. Viallat, M. Abkarian, *Dynamics of blood cell suspensions in microflows*, CRC Press, 2019.
[25] M. Dionzou, A. Morere, C. Roux, B. Lonetti, J. D. Marty, C. Mingotaud, P. Joseph, D. Goudouneche, B. Payre, M. Léonetti, A. F. Mingotaud, "Comparison of methods for the fabrication and the characterization of polymer self-assemblies: what are the important parameters?", *Soft Matter* **12** (2016), p. 2166-2176.
[26] H.-G. Döbereiner, "Properties of giant vesicles", *Current Opinion in Colloid & Interface science* **5** (2000), no. 3-4, p. 256-263.
[27] P. M. Vlahovska, T. Podgorski, C. Misbah, "Vesicles and red blood cells in flow: From individual dynamics to rheology", *C. R. Physique* **10** (2009), no. 8, p. 775-789.
[28] P. B. Canham, "The minimum energy of bending as a possible explanation of the biconcave shape of the human red blood cell", *J. Theor. Biol.* **26** (1970), no. 1, p. 61-81.
[29] Z. Shen, T. M. Fischer, A. Farutin, P. M. Vlahovska, J. Harting, C. Misbah, "Blood crystal: emergent order of red blood cells under wall-confined shear flow", *Phys. Rev. Lett.* **120** (2018), no. 26, article no. 268102.
[30] G. Boedec, M. Leonetti, M. Jaeger, "3D vesicle dynamics simulations with a linearly triangulated surface", *J. Comput. Phys.* **230** (2011), no. 4, p. 1020-1034.
[31] W. Helfrich, "Elastic Properties of Lipid Bilayers: Theory and Possible Experiments", *Z. Naturforsch., C, J. Biosci.* **28** (1973), no. 11-12, p. 693-703.
[32] Z. H. Huang, M. Abkarian, A. Viallat, "Sedimentation of vesicles: from pear-like shapes to microtether extrusion", *New J. Phys.* **13** (2011), no. 3, article no. 035026.
[33] G. Boedec, M. Jaeger, M. Leonetti, "Sedimentation-induced tether on a settling vesicle", *Phys. Rev. E* **88** (2013), no. 1, article no. 010702.
[34] E. A. Evans, "Bending resistance and chemically induced moments in membrane bilayers", *Biophys. J.* **14** (1974), no. 12, p. 923-931.

[35] G. Boedec, M. Jaeger, M. Leonetti, "Settling of a vesicle in the limit of quasispherical shapes", *J. Fluid Mech.* **690** (2012), p. 227-261.
[36] G. Coupier, A. Farutin, C. Minetti, T. Podgorski, C. Misbah, "Shape diagram of vesicles in Poiseuille flow", *Phys. Rev. Lett.* **108** (2012), no. 17, article no. 178106.
[37] S. Knoche, D. Vella, E. Aumaitre, P. Degen, H. Rehage, P. Cicuta, J. Kierfeld, "Elastometry of deflated capsules: Elastic moduli from shape and wrinkle analysis", *Langmuir* **29** (2013), no. 40, p. 12463-12471.
[38] M.-C. Andry, F. Edwards-Lévy, M.-C. Lévy, "Free amino group content of serum albumin microcapsules. III. A study at low pH values", *International journal of pharmaceutics* **128** (1996), no. 1-2, p. 197-202.
[39] D. Z. Gunes, M. Pouzot, M. Rouvet, S. Ulrich, R. Mezzenga, "Tuneable thickness barriers for composite o/w and w/o capsules, films, and their decoration with particles", *Soft Matter* **7** (2011), no. 19, p. 9206-9215.
[40] J. Dupré de Baubigny, P. Perrin, N. Pantoustier, T. Salez, M. Reyssat, C. Monteux, "Growth mechanism of polymer membranes obtained by H-bonding across immiscible liquid interfaces", *ACS Macro Lett.* **10** (2021), no. 2, p. 204-209.
[41] K.-S. Chang, W. L. Olbricht, "Experimental studies of the deformation of a synthetic capsule in extensional flow", *J. Fluid Mech.* **250** (1993), p. 587-608.
[42] I. Koleva, H. Rehage, "Deformation and orientation dynamics of polysiloxane microcapsules in linear shear flow", *Soft Matter* **8** (2012), no. 13, p. 3681-3693.
[43] C. De Loubens, J. Deschamps, G. Boedec, M. Leonetti, "Stretching of capsules in an elongation flow, a route to constitutive law", *J. Fluid Mech.* **767** (2015).
[44] E. Lac, D. Barthès-Biesel, N. A. Pelekasis, J. Tsamopoulos, "Spherical capsules in three-dimensional unbounded Stokes flows: effect of the membrane constitutive law and onset of buckling", *J. Fluid Mech.* **516** (2004), p. 303-334.
[45] D. Barthès-Biesel, "Capsule motion in flow: Deformation and membrane buckling", *C. R. Physique* **10** (2009), no. 8, p. 764-774.
[46] D. Barthès-Biesel, A. Diaz, E. Dhenin, "Effect of constitutive laws for two-dimensional membranes on flow-induced capsule deformation", *J. Fluid Mech.* **460** (2002), p. 211-222.
[47] R. Skalak, A. Tozeren, R. P. Zarda, S. Chien, "Strain energy function of red blood cell membranes", *Biophys. J.* **13** (1973), no. 3, p. 245-264.
[48] S. Knoche, J. Kierfeld, "Buckling of spherical capsules", *Phys. Rev. E* **84** (2011), no. 4, article no. 046608.
[49] A. Ghaemi, A. Philipp, A. Bauer, K. Last, A. Fery, S. Gekle, "Mechanical behaviour of micro-capsules and their rupture under compression", *Chemical Engineering Science* **142** (2016), p. 236-243.
[50] F. Risso, M. Carin, "Compression of a capsule: Mechanical laws of membranes with negligible bending stiffness", *Phys. Rev. E* **69** (2004), no. 6, article no. 061601.
[51] K. S. Cole, "Surface forces of the Arbacia egg", *Journal of Cellular and Comparative Physiology* **1** (1932), no. 1, p. 1-9.
[52] A. Rehor, L. Canaple, Z. Zhang, D. Hunkeler, "The compressive deformation of multicomponent microcapsules: Influence of size, membrane thickness, and compression speed", *Journal of Biomaterials Science, Polymer Edition* **12** (2001), no. 2, p. 157-170.
[53] M. Carin, D. Barthès-Biesel, F. Edwards-Lévy, C. Postel, D. C. Andrei, "Compression of biocompatible liquid-filled HSA-alginate capsules: Determination of the membrane mechanical properties", *Biotechnology and bioengineering* **82** (2003), no. 2, p. 207-212.
[54] E. Häner, M. Heil, A. Juel, "Deformation and sorting of capsules in a T-junction", *J. Fluid Mech.* **885** (2020).
[55] E. Reissner, "Stresses and small displacements of shallow spherical shells. I", *Journal of Mathematics and Physics* **25** (1946), no. 1-4, p. 80-85.
[56] A. Lytra, V. Sboros, A. Giannakopoulos, N. A. Pelekasis, "Modeling atomic force microscopy and shell mechanical properties estimation of coated microbubbles", *Soft Matter* **16** (2020), no. 19, p. 4661-4681.
[57] Y.-H. Huang, F. Salmon, A. Kamble, A. X. Xu, M. Michelon, B. C. Leopércio, M. S. Carvalho, J. M. Frostad, "Models for the mechanical characterization of core-shell microcapsules under uniaxial deformation", *Food Hydrocolloids* **119** (2021), article no. 106762.
[58] W. W. Feng, W.-H. Yang, "On the Contact Problem of an Inflated Spherical Nonlinear Membrane", *J. Appl. Mech.* **40** (1973), no. 1, p. 209-214.
[59] M. P. Neubauer, M. Poehlmann, A. Fery, "Microcapsule mechanics: From stability to function", *Advances in colloid and interface science* **207** (2014), p. 65-80.
[60] K. Xie, A. Glasser, S. Shinde, Z. Zhang, J.-M. Rampnoux, A. Maali, E. Cloutet, G. Hadziioannou, H. Kellay, "Delamination and wrinkling of flexible conductive polymer thin films", *Advanced Functional Materials* **31** (2021), no. 21, article no. 2009039.
[61] Z. Zhang, V. Bertin, M. Arshad, E. Raphael, T. Salez, A. Maali, "Direct measurement of the elastohydrodynamic lift force at the nanoscale", *Phys. Rev. Lett.* **124** (2020), no. 5, article no. 054502.
[62] F. Dubreuil, N. Elsner, A. Fery, "Elastic properties of polyelectrolyte capsules studied by atomic-force microscopy and RICM", *Eur. Phys. J. E* **12** (2003), no. 2, p. 215-221.
[63] T. X. Chu, A.-V. Salsac, E. Leclerc, D. Barthès-Biesel, H. Wurtz, F. Edwards-Lévy, "Comparison between measure-

ments of elasticity and free amino group content of ovalbumin microcapsule membranes: discrimination of the cross-linking degree", *Journal of colloid and interface science* **355** (2011), no. 1, p. 81-88.

[64] J. Cappello, V. d'Herbemont, A. Lindner, O. Du Roure, "Microfluidic in-situ measurement of Poisson's ratio of hydrogels", *Micromachines* **11** (2020), no. 3, p. 318.

[65] Y. Li, Z. Hu, C. Li, "New method for measuring Poisson's ratio in polymer gels", *Journal of applied polymer science* **50** (1993), no. 6, p. 1107-1111.

[66] M. Pretzl, M. P. Neubauer, M. Tekaat, C. Kunert, C. Kuttner, G. Leon, D. Berthier, P. Erni, L. Ouali, A. Fery, "Formation and mechanical characterization of aminoplast core/shell microcapsules", *ACS Appl. Mater. Interfaces* **4** (2012), no. 6, p. 2940-2948.

[67] M. D. Biviano, L. J. Böni, J. D. Berry, P. Fischer, R. R. Dagastine, "Viscoelastic characterization of the crosslinking of β-lactoglobulin on emulsion drops via microcapsule compression and interfacial dilational and shear rheology", *Journal of colloid and interface science* **583** (2021), p. 404-413.

[68] K. L. Johnson, K. Kendall, A. D. Roberts, "Surface energy and the contact of elastic solids", *Proceedings of the royal society of London. A. mathematical and physical sciences* **324** (1971), no. 1558, p. 301-313.

[69] A. Aniskevich, V. Kulakov, O. Bulderberga, P. Knotek, J. Tedim, F. Maia, V. Leisis, D. Zeleniakiene, "Experimental characterisation and modelling of mechanical behaviour of microcapsules", *Journal of Materials Science* **55** (2020), no. 27, p. 13457-13471.

[70] G. R. Plaza, T. Q. P. Uyeda, Z. Mirzaei, C. A. Simmons, "Study of the influence of actin-binding proteins using linear analyses of cell deformability", *Soft Matter* **11** (2015), no. 27, p. 5435-5446.

[71] B. González-Bermúdez, G. V. Guinea, G. R. Plaza, "Advances in micropipette aspiration: applications in cell biomechanics, models, and extended studies", *Biophys. J.* **116** (2019), no. 4, p. 587-594.

[72] E. H. Zhou, C. T. Lim, S. T. Quek, "Finite element simulation of the micropipette aspiration of a living cell undergoing large viscoelastic deformation", *Mech. Adv. Mater. Struct.* **12** (2005), no. 6, p. 501-512.

[73] D. P. Theret, M. J. Levesque, M. Sato, R. M. Nerem, L. T. Wheeler, "The Application of a Homogeneous Half-Space Model in the Analysis of Endothelial Cell Micropipette Measurements", *J. Biomech. Eng.* **110** (1988), no. 3, p. 190-199.

[74] J. R. Henriksen, J. H. Ipsen, "Measurement of membrane elasticity by micro-pipette aspiration", *Eur. Phys. J. E* **14** (2004), no. 2, p. 149-167.

[75] J. Hegemann, S. Knoche, S. Egger, M. Kott, S. Demand, A. Unverfehrt, H. Rehage, J. Kierfeld, "Pendant capsule elastometry", *Journal of colloid and interface science* **513** (2018), p. 549-565.

[76] J. Walter, A.-V. Salsac, D. Barthès-Biesel, P. Le Tallec, "Coupling of finite element and boundary integral methods for a capsule in a Stokes flow", *Int. J. Numer. Methods Eng.* **83** (2010), no. 7, p. 829-850.

[77] G. Boedec, M. Leonetti, M. Jaeger, "Isogeometric FEM-BEM simulations of drop, capsule and vesicle dynamics in Stokes flow", *J. Comput. Phys.* **342** (2017), p. 117-138.

[78] Y. Sui, Y.-T. Chew, P. Roy, H.-T. Low, "A hybrid method to study flow-induced deformation of three-dimensional capsules", *J. Comput. Phys.* **227** (2008), no. 12, p. 6351-6371.

[79] S. B. Q. Tran, Q. T. Le, F. Y. Leong, D. V. Le, "Modeling deformable capsules in viscous flow using immersed boundary method", *Phys. Fluids* **32** (2020), no. 9, article no. 093602.

[80] J. Ma, L. Xu, F.-B. Tian, J. Young, J. C. S. Lai, "Dynamic characteristics of a deformable capsule in a simple shear flow", *Phys. Rev. E* **99** (2019), no. 2, article no. 023101.

[81] W. R. Dodson, P. Dimitrakopoulos, "Dynamics of strain-hardening and strain-softening capsules in strong planar extensional flows via an interfacial spectral boundary element algorithm for elastic membranes", *J. Fluid Mech.* **641** (2009), p. 263-296.

[82] M. Maleki, C. de Loubens, K. Xie, E. Talansier, H. Bodiguel, M. Leonetti, "Membrane emulsification for the production of suspensions of uniform microcapsules with tunable mechanical properties", *Chemical Engineering Science* **237** (2021), article no. 116567.

[83] G. Kaufman, R. Boltyanskiy, S. Nejati, A. R. Thiam, M. Loewenberg, E. R. Dufresne, C. O. Osuji, "Single-step microfluidic fabrication of soft monodisperse polyelectrolyte microcapsules by interfacial complexation", *Lab on a Chip* **14** (2014), no. 18, p. 3494-3497.

[84] C. Tregouët, T. Salez, C. Monteux, M. Reyssat, "Microfluidic probing of the complex interfacial rheology of multilayer capsules", *Soft matter* **15** (2019), no. 13, p. 2782-2790.

[85] D. Barthès-Biesel, J.-M. Rallison, "The time-dependent deformation of a capsule freely suspended in a linear shear flow", *J. Fluid Mech.* **113** (1981), p. 251-267.

[86] D. Barthès-Biesel, H. Sgaier, "Role of membrane viscosity in the orientation and deformation of a spherical capsule suspended in shear flow", *J. Fluid Mech.* **160** (1985), p. 119-135.

[87] C. Pozrikidis *et al.*, *Boundary integral and singularity methods for linearized viscous flow*, Cambridge Texts in Applied Mathematics, Cambridge University Press, 1992.

[88] J. Gubspun, C. de Loubens, R. Trozzo, J. Deschamps, M. Georgelin, F. Edwards-Lévy, M. Leonetti, "Perturbations of the flow induced by a microcapsule in a capillary tube", *Fluid Dynamics Research* **49** (2017), no. 3, article no. 035501.

[89] J. Gubspun, P.-Y. Gires, C. de Loubens, D. Barthès-Biesel, J. Deschamps, M. Georgelin, M. Leonetti, E. Leclerc, F. Edwards-Lévy, A.-V. Salsac, "Characterization of the mechanical properties of cross-linked serum albumin microcapsules: effect of size and protein concentration", *Colloid. Polym. Sci.* **294** (2016), no. 8, p. 1381-1389.
[90] F. Risso, F. CollÉ-Paillot, M. Zagzoule, "Experimental investigation of a bioartificial capsule flowing in a narrow tube", *J. Fluid Mech.* **547** (2006), p. 149-173.
[91] X.-Y. Wang, A. Merlo, C. Dupont, A.-V. Salsac, D. Barthès-Biesel, "A microfluidic methodology to identify the mechanical properties of capsules: comparison with a microrheometric approach", *Flow* **1** (2021).
[92] C. Quesada, C. Dupont, P. Villon, A.-V. Salsac, "Diffuse approximation for identification of the mechanical properties of microcapsules", *Mathematics and Mechanics of Solids* **26** (2021), no. 7, p. 1018-1028.
[93] A. Walter, H. Rehage, H. Leonhard, "Shear-induced deformations of polyamide microcapsules", *Colloid. Polym. Sci.* **278** (2000), no. 2, p. 169-175.
[94] H. Rehage, M. Husmann, A. Walter, "From two-dimensional model networks to microcapsules", *Rheologica acta* **41** (2002), no. 4, p. 292-306.
[95] S. Joung, M. Song, D. Kim, "Synthetic capsule breakup in simple shear flow", *Phys. Fluids* **32** (2020), no. 11, article no. 113603.
[96] C. De Loubens, J. Deschamps, F. Edwards-Lévy, M. Leonetti, "Tank-treading of microcapsules in shear flow", *J. Fluid Mech.* **789** (2016), p. 750-767.
[97] G. I. Taylor, "The formation of emulsions in definable fields of flow", *Proc. R. Soc. Lond. A* **146** (1934), no. 858, p. 501-523.
[98] J. Deschamps, V. Kantsler, E. Segre, V. Steinberg, "Dynamics of a vesicle in general flow", *Proc. Natl. Acad. Sci. USA* **106** (2009), no. 28, p. 11444-11447.
[99] H. Noguchi, "Swinging and synchronized rotations of red blood cells in simple shear flow", *Phys. Rev. E* **80** (2009), no. 2, article no. 021902.
[100] M. Vona, E. Lauga, "Stabilizing viscous extensional flows using reinforcement learning", *Phys. Rev. E* **104** (2021), no. 5, article no. 055108.
[101] M. Kummrow, W. Helfrich, "Deformation of giant lipid vesicles by electric fields", *Phys. Rev. A* **44** (1991), no. 12, p. 8356-8360.
[102] R. Dimova, K. A. Riske, S. Aranda, N. Bezlyepkina, R. L. Knorr, R. Lipowsky, "Giant vesicles in electric fields", *Soft matter* **3** (2007), no. 7, p. 817-827.
[103] R. Dimova, N. Bezlyepkina, M. D. Jordö, R. L. Knorr, K. A. Riske, M. Staykova, P. M. Vlahovska, T. Yamamoto, P. Yang, R. Lipowsky, "Vesicles in electric fields: Some novel aspects of membrane behavior", *Soft Matter* **5** (2009), no. 17, p. 3201-3212.
[104] O. Vizika, D. A. Saville, "The electrohydrodynamic deformation of drops suspended in liquids in steady and oscillatory electric fields", *J. Fluid Mech.* **239** (1992), p. 1-21.
[105] J. R. Melcher, G. I. Taylor, "Electrohydrodynamics: a review of the role of interfacial shear stresses", *Annu. Rev. Fluid Mech.* **1** (1969), no. 1, p. 111-146.
[106] H. A. Faizi, R. Dimova, P. M. Vlahovska, "A vesicle microrheometer for high-throughput viscosity measurements of lipid and polymer membranes", *Biophys. J.* **121** (2022), no. 6, p. 910-918.
[107] R. B. Karyappa, S. D. Deshmukh, R. M. Thaokar, "Deformation of an elastic capsule in a uniform electric field", *Phys. Fluids* **26** (2014), no. 12, article no. 122108.
[108] S. Puri, R. M. Thaokar, "Study of dependence of elasticity on the microstructure of microcapsules using electro-deformation technique", *Colloids and Surfaces A: Physicochemical and Engineering Aspects* **569** (2019), p. 179-189.
[109] S. Das, R. M. Thaokar, "Large-deformation electrohydrodynamics of an elastic capsule in a DC electric field", *J. Fluid Mech.* **841** (2018), p. 489-520.
[110] J. Gounley, G. Boedec, M. Jaeger, M. Leonetti, "Influence of surface viscosity on droplets in shear flow", *J. Fluid Mech.* **791** (2016), p. 464-494.
[111] T. Lin, Z. Wang, R. Lu, W. Wang, Y. Sui, "A high-throughput method to characterize membrane viscosity of flowing microcapsules", *Phys. Fluids* **33** (2021), no. 1, article no. 011906.
[112] T. Lin, Z. Wang, W. Wang, Y. Sui, "A neural network-based algorithm for high-throughput characterisation of viscoelastic properties of flowing microcapsules", *Soft Matter* **17** (2021), no. 15, p. 4027-4039.
[113] P.-H. Wu, D. R.-B. Aroush, A. Asnacios, W.-C. Chen, M. E. Dokukin, B. L. Doss, P. Durand, A. Ekpenyong, J. Guck, N. V. Guz *et al.*, "Comparative study of cell mechanics methods", *Nature methods* **15** (2018), no. 7, p. 491-498.

Comptes Rendus
Mécanique
2023, Vol. 351, Special Issue S2, p. 183-197
https://doi.org/10.5802/crmeca.159

Physical Science in Microgravity within the Thematic Group Fundamental and Applied Microgravity / *Sciences physiques en microgravité au sein du GDR Micropesanteur Fondamentale et Appliquée*

A new experimental set-up for aerosol stability investigations in microgravity conditions

Charles Graziani [a], Mathieu Nespoulous [a], Renaud Denoyel [a], Stephan Fauve [b], Christian Chauveau [c], Luc Deike [d] and Mickaël Antoni [*, a]

[a] Aix-Marseille Univ, CNRS, MADIREL, Marseille, France

[b] LP ENS-Paris, France

[c] CNRS–ICARE, University Orléans, France

[d] MAE/HMEI, Princeton University, USA

E-mails: charles.graziani@univ-amu.fr (C. Graziani), mathieu.nespoulous@univ-amu.fr (M. Nespoulous), renaud.denoyel@univ-amu.fr (R. Denoyel), fauve@lps.ens.fr (S. Fauve), christian.chauveau@cnrs-orleans.fr (C. Chauveau), ldeike@princeton.edu (L. Deike), m.antoni@univ-amu.fr (M. Antoni)

Abstract. The temporal and spatial evolution of dispersed media is a fundamental problem in a wide range of physicochemical systems, such as emulsions, suspensions and aerosols. These systems are multiphasic and involve compounds of different densities. They are therefore subject to the influence of gravity which determines the sedimentation rate of their dispersed phase. This effect can be dominant and prevent a detailed study of the phenomena occurring between the constituents themselves, such as the coalescence of drops in emulsions, the evaporation of droplets or the flocculation in suspensions. In this context, the Centre National d'Etudes Spatiales (CNES) has recently supported the development of a new instrument to produce populations of droplets, a few micrometers in radius, under controlled conditions with the objective of allowing a detailed study of their properties in microgravity conditions. The principle of this instrument is to generate, by a fast compression/expansion of air, populations of water droplets and to track their evolution by optical scanning tomography in transmission mode within a volume of approximately 2 mm^3. Parabolic flight experiments have shown the possibility to generate and accurately follow the evolution of populations of several hundred droplets for more than 20 s. The first experimental results show that it is possible to study their evaporation kinetics or their motion when imposing von Karman swirling flows. This work is part of the AEROSOL project of DECLIC-EVO supported by CNES and aims to help the understanding of cloud microphysics which remains a critical open problem in the context of global warming.

Keywords. Droplets, Microgravity, Microscopy, Tomography, von Karman swirling flow.

Published online: 22 March 2023

* Corresponding author.

1. Introduction

An aerosol is a multiphase system in which at least one of the phases is in a dispersed form. These phases can be liquid or solid and their simultaneous evolution within the surrounding gas involves mechanisms at the molecular and macroscopic scales. Like emulsions or nanofluids, aerosols are dispersions with large exchange surfaces which give them specific physico-chemical properties, making them central to fundamental and applied fields. Aerosols can be of natural or anthropogenic origin. Fog, dust, clays, forest exudates are natural examples while smog, fine particles produced by internal combustion engines or building heating devices are all anthropogenic.

Aerosols are complex media, sensitive to temperature and pressure conditions, sometimes chemically active. They are naturally subject to the influence of gravity, which determines the settling speed of the particles they contain [1, 2]. Aerosols are used in the pharmaceutical [3] and cosmetic industries (inhalers, sprays) [4] in metallurgy (spray drying) [5] and in agriculture (pesticides) [6]. From an academic point of view, they are still the subject of intense research activity. The description of their evolution is for example a major issue in climatology, especially for the understanding of cloud microphysics [7–9]. This problem motivated CNES to support the development of a new experimental facility for conducting experiments in parabolic flight conditions (Figure 1).

A relevant study of cloud microphysics requires well controlled conditions, especially in temperature and pressure. In clouds, droplets are made of water and constitute metastable systems produced by a rapid condensation (actually liquefaction) in a gaseous medium in which the relative humidity is sufficiently high. Despite their small size, cloud droplets are subject to the acceleration of the earth's gravity field. Their limiting velocity in the atmosphere was measured more than 70 years ago with values typically between 1 cm/s and 100 cm/s for radii ranging between 1 and 100 μm [10]. Other measurements carried out under well controlled experimental conditions (20 °C, 1 atm, 50% relative humidity) show that droplets of 80 μm diameter exhibit a drainage velocity that reaches 150 cm/s [11]. Empirical laws have been proposed and give values in good coherence with these observations and with Stokes law when the diameter of the drops becomes lower than 50 μm [2]. Measurements have confirmed these settling velocities and demonstrated the key contribution of gravity in the evolution of aerosols.

In the context of cloud microphysics, this raises the question of scale separation. The characteristic times associated with the interaction between water droplets, such as coalescence, can be very short when compared to those associated with gravity. When droplets radii reach few micrometers, gravity becomes dominant and complicates studies of their mutual interactions. Performing experiments in microgravity is therefore essential for a detailed understanding of the mechanisms governing the evolution of aerosols. The reduced gravity of parabolic flights has the great advantage of decoupling buoyancy from capillary phenomena and, in the case of aerosols, of making possible an original description of the interaction mechanisms involved in a droplet population. In such conditions, it becomes indeed possible to measure the damping time of the flows created during the aerosol formation or the evolution of the droplet size distribution.

The aerosols investigated hereafter consist of populations of water droplets with radius of a few micrometers evolving in air. They are thus assimilable to fogs. From an experimental point of view, the air used is not inseminated with solid particles[1]. The one used in the experiments is not purified and therefore naturally contains particles favouring heterogeneous nucleation.

[1]The possibility of performing such experiments has been considered with, for example, hydrophobic magnetic micro-particles that could be collected by applying a magnetic field. But this would imply additional devices and further require complex cleaning protocols that would probably affect the overall repeatability of the experiments.

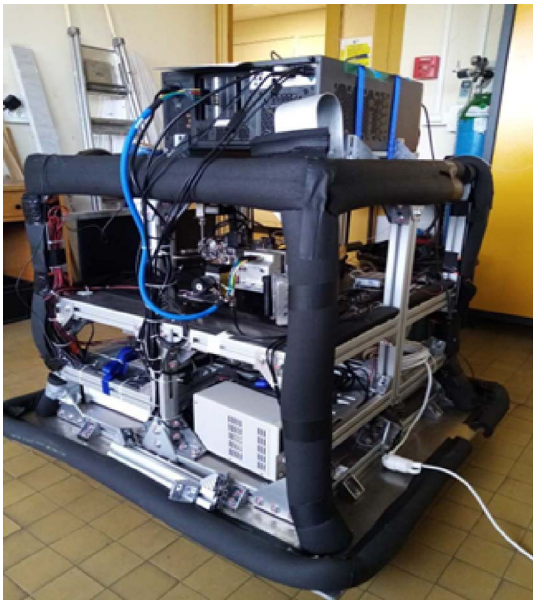

Figure 1. Overall view of the rack used for the parabolic flight experiments.

This is the reason why the term "aerosol" will be used hereafter to designate the populations of droplets under consideration. Investigations on such a "canonical" family of aerosols is seen here as essential to improve the understanding of their physical properties. The main goal here is the production of aerosols sufficiently stable for the realization of reference experiments to bring new elements in the understanding of (i) the dynamics of evaporation/condensation of droplet populations, (ii) the coalescence of droplets in turbulent flows, (iii) the influence of relative humidity in nucleation phenomena.

Three parabolic flight campaigns have been carried out, all aiming at validating the technical options implemented and at establishing the good feasibility of the experiments. So far, they demonstrated the possibility of producing populations of droplets by a protocol involving a fast compression of the air followed by a fast expansion (see Sections 2 and 5) and validated aerosol observability by optical tomographic microscopy. The key point here was to ensure that the fast flows created by the compression/expansion sequence were damped over times smaller than the driving times of the physical phenomena governing the evolution of the aerosol when evolving in microgravity. The continuous phase being air, the appearance of long-lasting transient regimes was to be feared. Such behaviors would have been incompatible with an analysis by optical tomographic microscopy due to coherence loss between successive tomographic images. Preliminary estimates based on the numerical integration of a simplified model (a hard sphere with given initial velocity evolving in a continuous viscous phase) suggested damping times of the order of a few seconds. But this basic model was not accounting for important parameters such as the multiplicity of neighboring droplets, the finite geometry of the experimentation chamber (Figure 2), the pressure difference used for the expansion, etc. The parabolic flight experiments conducted in the frame of this work allowed to validate the dimensioning of the different elements of the equipment as well as the protocols to be implemented for the creation of the aerosols. They also evidenced typical damping times which turn out to be shorter than few seconds. Beyond these times, aerosols show up as droplet populations whose movements are only due to the residual acceleration of the flight conditions and not to the initial compression/expansion

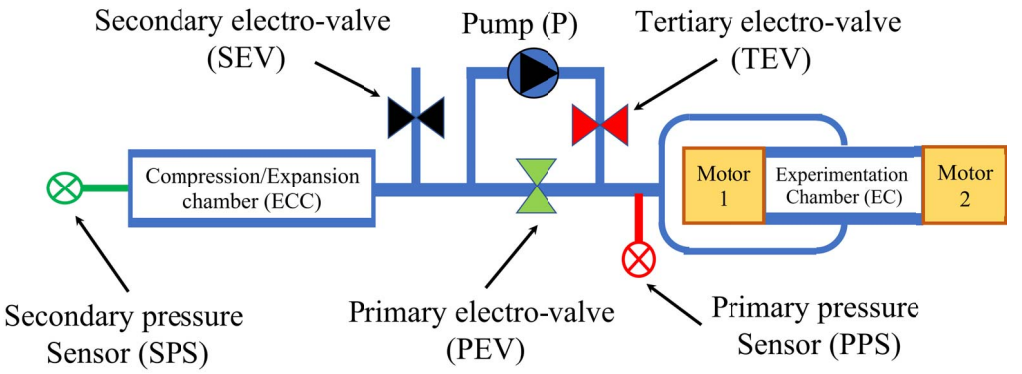

Figure 2. Schematic view of the experimental set-up.

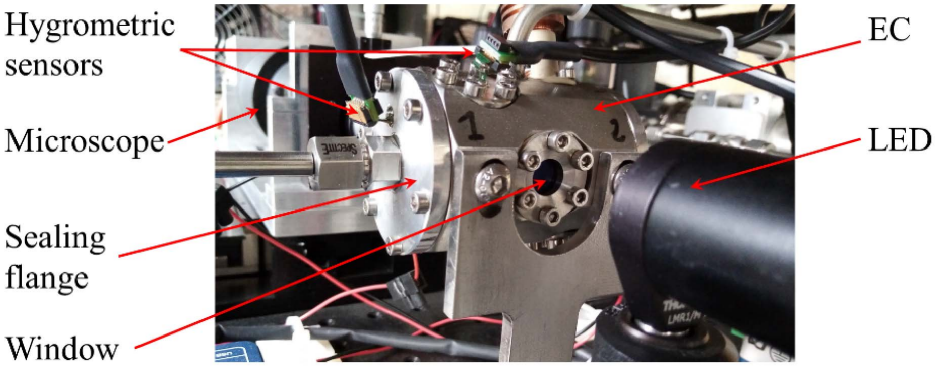

Figure 3. Photograph of the EC assembly. LED (foreground), EC (foreground), microscope (background). In this picture the motors used for von Karman swirling flow generation are not mounted.

procedure. Sequences of about 15 s of reduced gravity were carried out during which the aerosols present a good stability thus allowing to track the evolution of several hundreds of droplets.

2. Experimental cell and aerosol production protocol

Aerosols are produced from moist air with a pneumatic circuit consisting of two chambers (Figure 2): a cylindrical experimentation chamber (EC, diameter 3 cm, height 6 cm) inside which droplets are generated and an compression/expansion chamber (ECC, volume of about 170 cm^3) acting alternatively as a gas reservoir or an expansion tank (Figures 2 and 3). EC and ECC are initially at room temperature and pressure. They both contain air which may or may not be saturated with water. A membrane pump is used to circulate the air from the ECC into the EC. Then, by means of a system of valves, a fast expansion between the EC and the ECC is achieved. This expansion leads to a temperature drop inside the EC, which results in a decrease of the equilibrium saturation vapour pressure. An excess of water vapor is created that condensates into micron-sized droplets by nucleation [12–14].

Each experiment follows the same protocol: (i) closure of all valves, (ii) opening of TEV, (iii) starting up the pump for pressure increase in the EC up to a target value, (iv) closure of

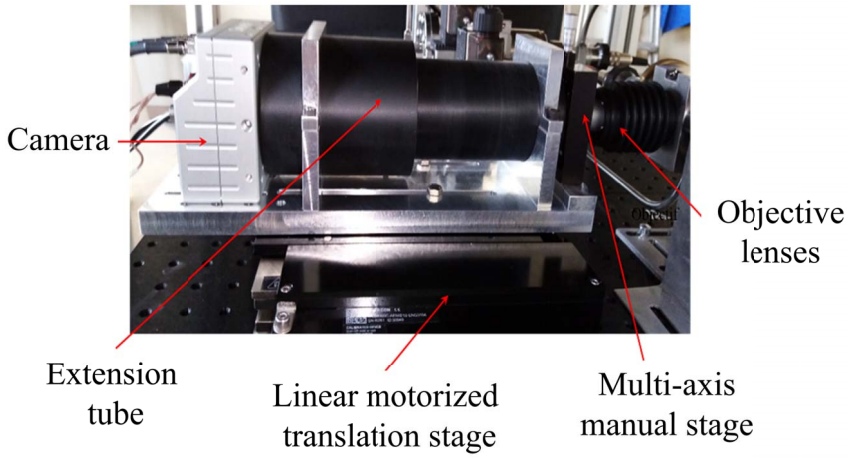

Figure 4. View of the microscope and optical tomography system.

TEV, (v) few seconds delay for temperature relaxation, (vi) opening of PEV for air expansion and droplet formation, (vii) scanning tomography with image recording. The interest of this protocol is to maintain temperature and pressure in the EC before and after droplet formation almost constant and thus to avoid the implementation of an accurate thermal control of the whole set up which would be, from an instrumental point of view, highly challenging. This protocol takes only a few seconds and has the great advantage of limiting heat transfers especially with the walls of both EC and ECC.

A temperature measurement device composed of a type K thermocouple driven by an Agilent 34972A LXI is implemented inside the EC. The pressure inside the EC and the ECC are recorded with two pressure sensors (KELLER PAA-33X). A hygrometric sensor is mounted inside the EC (Sensirion SEK-SHT35). It also gives the temperature which allows a redundancy of the measurements. All the above sensors are placed at selected locations to provide measurements as accurate as possible without being too intrusive.

3. Optical tomography microscopy and imaging technique

Optical tomography microscopy in transmission mode is used to observe the droplets once formed and to track their evolution. This technique consists of acquiring images with a microscope with moving object plane. It has the advantage of enabling analyses in the visible spectrum and, in the particular case of optically transparent droplet populations as the ones investigated here, to allow in-depth analyses. The acquisition of tomographic scanning sequences allows a 3D reconstruction and thus a precise follow-up of the evolution of droplets over time. This technique is well known and has been for long used in medical fields [15–17] and, more recently, to describe emulsions [18, 19]. An Optronis CP70-1HS-MC-1900 grabbing camera is used and mounted on a motorized translation stage (Figure 4). It allows a frequency acquisition up to 2000 fps in full frame that ensures reasonable coherence between all successive images. The microscope traveling distance is 2 mm with travel speed up to 10 mm/s. A tomographic shot (i.e. a single scan forwards or backwards) therefore lasts 0.2 s and generates 400 images of about 1 Mb each. The distance between two successive images is typically 5 μm. Tomography is applied perpendicularly, at ±1 mm on both sides of the symmetry axis of the EC and almost at its center. The overall analyzed area corresponds to a volume of about 2 mm^3.

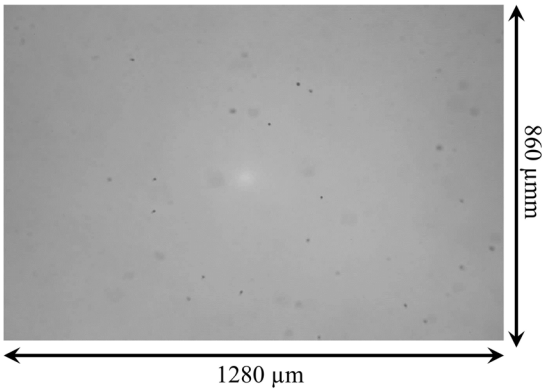

Figure 5. Typical image of a population of droplets. Droplet show up as black spots.

Images are encoded on 8 bits and correspond to a field of view of 1280 μm by 860 μm (Figure 5). They all present a sufficient contrast (on at least 128 gray levels) for reliable post-processing. Vignetting may remain despite the optical quality and the collimation of the incident light beam. It is eliminated by subtracting a reference image acquired before the aerosol formation. The identification of the droplets and their location in the images is performed by thresholding predetermined gray levels (about ten). An image of the contours generated by each droplet is then obtained (Figure 6). The spherical geometry of the droplets and the fact that they are distant from each other produces typical circular contours, which is very helpful for the accuracy and CPU time effort of image post-processing. The principle of the imaging technique is to first detect the location of the center of each of the contours (Figure 6(b) and (d)), regardless of whether the corresponding droplet is focused or not, and then to construct, from the set of the centers of all the droplets and all the images of a given scanning shot, the individual optical axis of each droplet (Figure 7). The quality of the optics and image contrasts allows the detection of droplets with a radius down to 2 μm.

Optical axis are processed one by one in a way to determine the droplet location in the scanning direction. This process is iterated for all the droplets (Figure 8). Optical axis construction requires coherence between consecutive images and thus an aerosol evolving on slow characteristic times when compared to those of the image acquisition system. This constraint is not satisfied right after droplet formation because of the fast flows generated by the initial expansion. As these flows decay after a few seconds (see below), sequences of several tens of thousands of coherent images are produced and therefore usable for post processing. Figure 7 represents all the optical axes for a single tomographic sequence. It shows hundreds of optical axes and illustrates the accessible precision of the analyses. This imaging technique is further used to obtain 3D representations (Figure 11).

The identification of the optical response produced by each droplet leads to optical axes of length depending upon their diameter. The larger the radius of droplets, the longer their optical axis. Figure 8 illustrates this fact in a representation showing the radius obtained from the optical response of each droplet. When the working plane of the microscope is in the vicinity of a droplet location, the measured apparent radius reaches a minimum value. This property is used in the last phase of the image analysis procedure to estimate the radii of the droplets. The apparent radius of a given droplet is obtained from the value at half-height of the radial average of the gray levels of its optical response. This radius is larger when droplet is out of focus and minimal when it is in focus (Figure 8(b)). Its actual radius is finally computed from the minimum of a quadratic

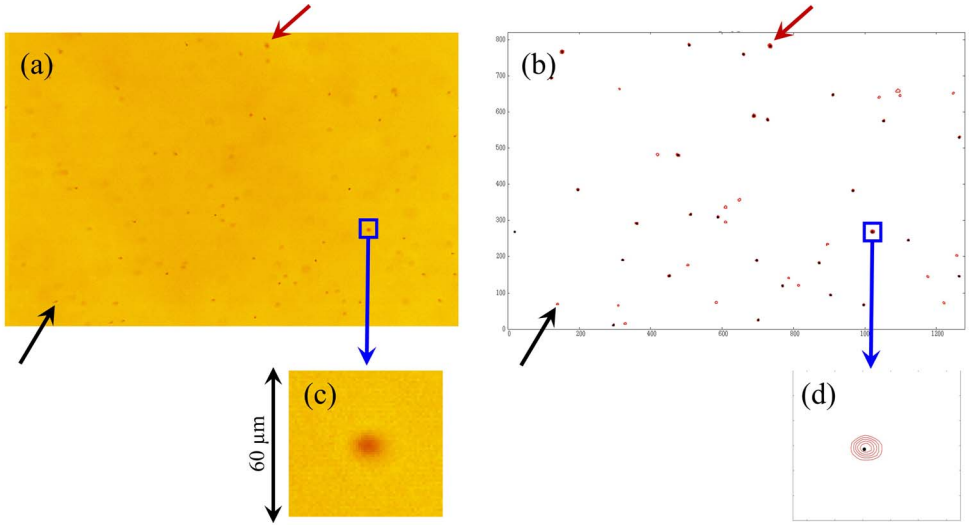

Figure 6. Image after background subtraction (a) and after treatment (b). The black and red arrows indicate two droplets and their signature after treatment. (c) and (d) correspond to a zoom on a droplet and both illustrate the gray levels produced by a droplet of about 10 µm in diameter. The black point is the center position obtained when averaging over all the contours.

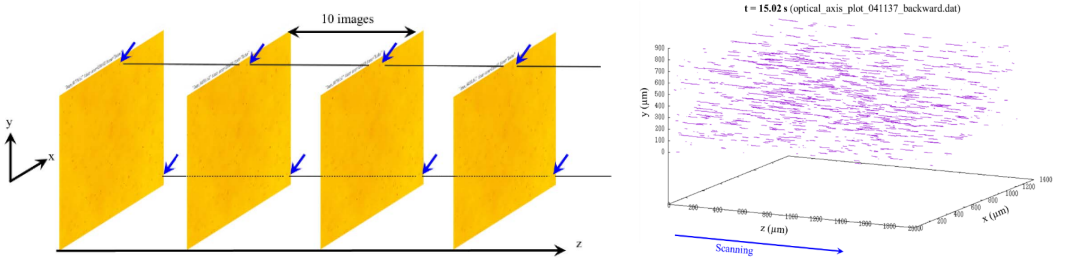

Figure 7. Left : Schematic illustration of droplet tracking. The two horizontal lines correspond to the optical trajectory of two droplets indicated by the blue arrows. The decimation of 10 images is used. The actual distance (resp. time interval) between each image of this figure is thus about 50 µm (resp. 5 ms). The coordinates (x, y) are in the plane of the images and z indicates the position of the microscope working plane. Right: Treated tomographic sequence. The orientation of the optical axes along the z the direction is a signature of the aerosol stability and good image coherence.

fitting of all the apparent radii when running along its optical axis. At this minimum contrast is the sharpest. Beside droplet radius, this procedure also determines the location of the droplet along its optical axis. This technique may however be too rough regarding to the comparatively large fluctuations shown Figure 8(b). Accurate measurements of droplet size distributions will therefore require further efforts and most likely the implementation of refined techniques such as FFT-based analysis.

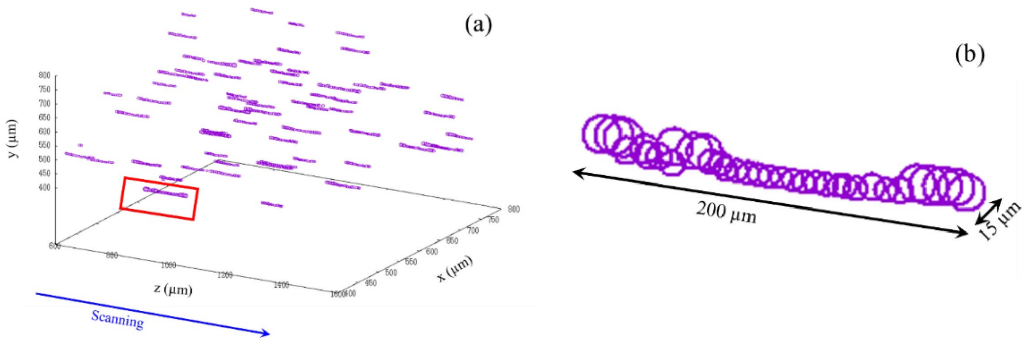

Figure 8. (a) Zoom into the domain $400 < x < 800$ (μm), $400 < y < 800$, $600 < z < 1600$ (μm) of Figure 7. The apparent radii of the droplets are shown as circles. (b) Evolution of the apparent radius of the droplet in the red frame of (a) as a function of the position of the working plane.

4. Set up for von Karman swirling flows and droplet coalescence investigations

The EC is equipped with two coaxial counter-rotating rotors consisting of smooth flat disks of 29 mm diameter facing each other. They're used to generate a von Karman swirling flow within the EC [20–22]. When activating the rotors, the air close to the disks is driven radially outward by the centrifugal force. This generates an axial flow toward the disks along their axis and a recirculation along the opposite direction along the EC lateral boundary. Therefore, a radially inward flow is generated in the midplane between the disks such that there is a stagnation point at the center of the EC. It is expected that the droplets, being subject there to the azimuthal velocity shear, are driven by the air flow and accumulate in the vicinity of this stagnation point. The main interest of setting the droplets in motion in such a flow is to force them closer to each other. Such experiments are actually expected to help to understand coalescence of droplets within clouds [23] as they will give access to the evolution of the density (actually the liquid fraction) and the mean size of the droplets in the vicinity of the stagnation point. Investigations of the influence of the properties of the von Karman swirling flows (VKSF), that can involve more or less turbulent regimes depending on the Reynolds number, are also planned.

The motion of the rotors is achieved with two FAULHABER servomotors (4221G 024EXTH) equipped with an encoder (IE3-2024) each controlled by a motion controller (MC5005 S RS) allowing regulation of the rotation frequency (motors are shown in Figure 2 but not in Figure 3). Rotors are both attached to a relay magnetically driven by a motion transmitter connected to the motors allowing rotation frequencies in the range 1 to 75 Hz. The sealing is obtained by a flange which separates the relay from the EC and thus from the outside. Magnetic neodymium segmental arc magnets provide the magnetic coupling. The main advantage of this configuration is that it allows for optimal sealing since no direct drive shaft has to be used.

5. Ground experiments

Ground experiments are essentially aimed at qualifying and understanding the response of experimental devices and to ensure control of experimental conditions in terms of pressure, temperature and relative humidity. For all experiments presented in this section, initial pressure and temperature are ambient ones while relative humidity (H) ranges between 2% and 96%. The aerosol formation protocol (Section 2) and the optical tomography analysis are synchronized, which allows for a fast triggering of all devices (actually with a single "click"). This is necessary

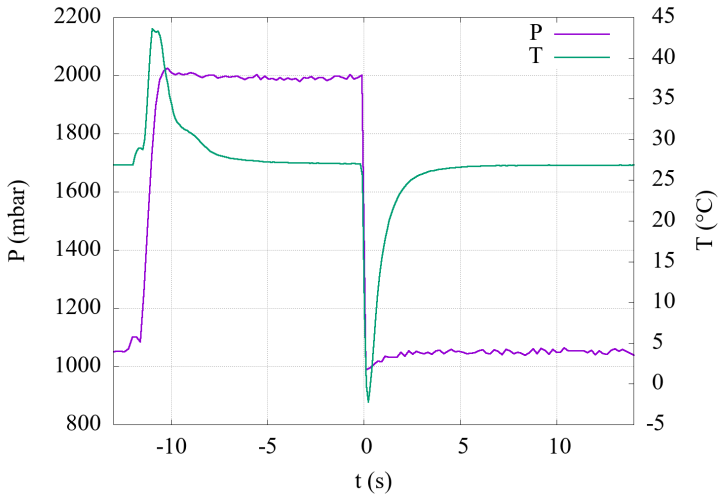

Figure 9. Evolution of pressure and temperature as a function of time inside the EC. Reference time $t = 0$ is set at the opening of the PEV (step (vi)).

because of the fast gravity drainage of the droplets and, for parabolic flights, the limited duration of the microgravity periods.

Figure 9 displays the pressure and temperature evolution when producing an aerosol with a target pressure of 2000 mbar. Reference time ($t = 0$) is set at the opening of PEV (step (vi)). As expected, two jumps in both temperature and pressure obviously associated to step (iii) and (vi) show up. Temperature relaxes back to its initial value sufficiently fast for both steps which confirms that air, within the EC, keeps close to its initial value despite droplet formation. In other words, forming droplets is not expected to yield significant heat transfers with the boundary conditions (in particular the walls of EC). It is therefore reasonable to assume that aerosol production can be achieved, at first approximation, under quasi-isothermal conditions.

The typical temperature relaxation time, t_{relax}, as a function of relative humidity H is plotted in Figure 10 for 108 experiments and four target pressures (2000, 2100, 2200 and 2300 mbar). t_{relax} is defined as the time required for the system to recover 95% of its initial temperature after step (vi). This figure shows that the higher the relative humidity, the higher the relaxation time. This is a straightforward consequence of the larger thermal heat capacity of water loaded air. The increasing trend of t_{relax} as a function of H is therefore consistent with thermodynamics and a straightforward consequence of the fact that equilibration time of a system increases with its thermal capacity. The set of experiments of Figure 10 also provides fundamental information about droplet formation. Image analysis (not shown here) indicates indeed that within the pressure ranges investigated here, no droplets are formed when $H < 40\%$. It also appears that the overall number of droplets (resp. the typical radius of the droplets) increases (resp. reduces) when increasing the target pressure. This turns also consistent with thermodynamics but, droplets getting drained very fast due to buoyancy forces, reliable quantitative investigations are not possible.

6. Microgravity preliminary results

All the results presented in this section were obtained from three CNES parabolic flight campaigns carried out in October 2020, March 2021 and March 2022 in Bordeaux on board the Airbus

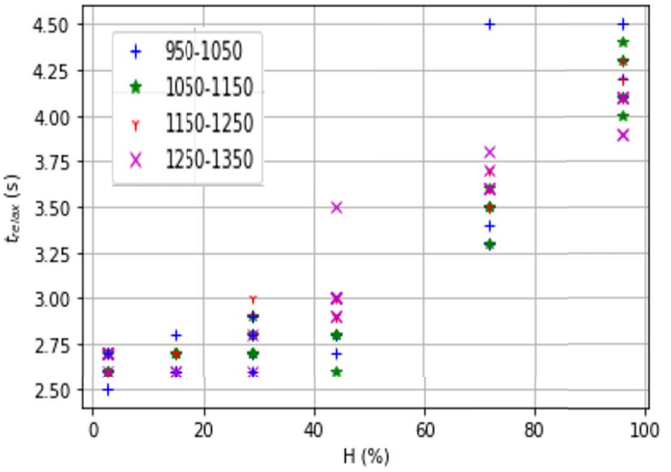

Figure 10. Time required for temperature stabilization after expansion as a function of H. The legend indicates the target pressure range in mbar at step (iii) (compression phase). For these experiments, temperature is 24 °C ± 2 °C.

A310 0G managed by Novespace. Aerosol formation follows the same protocol as for ground experiments. The pressure in the EC is well controlled and fixed at 1 atm. It is thus slightly higher than that of the cabin. The conditions in temperature are determined by the temperature in the cabin and are thus not controlled. It tends to increase as the experiments are carried out but remains within the range of 18 and 28 °C, over the duration of each flight. This temperature drift obviously results from the activity of the people and the numerous experiments running onboard. Given the precision of the measurements and the way experiments are planned for each parabola sequence, this problem is not expected to significantly affect the accuracy of the experimental results.

The first fundamental question that experiments had to answer was the possibility of producing aerosols and to verify that they were stable enough to maintain coherence between the tomographic images for relevant image post-processing. All experiments have clearly demonstrated the possibility of producing droplets. The continuous phase being air, fast turbulent transient regimes occur right after expansion (step (vi)). This makes tomographic microscopy analysis potentially ineffective, as image coherence is essential. Fortunately, it turns out that the rapid flows created by the initial expansion are damped out within typically 4 to 7 s. Beyond this time, droplets exhibit small amplitude movements only due to the residual acceleration of the parabolic flight conditions. Periods of about 15 s of reduced gravity are thus accessible during which their evolution can be studied under scientifically relevant conditions. Figure 11 shows an example of a 3D reconstruction of a single tomographic shot and illustrates the achieved level of precision.

Tomographic shots are processed one by one to identify each individual droplet. This process is iterated to investigate the properties of the droplet populations generated for each experiment. Figure 12 shows the evolution of their number (N) as a function of time for four replica experiments and two values of relative humidity: water saturated (H = 100%) and sub-saturated (H = 70%). The expansion phase starts at t = 0 and is operated at the very beginning of the parabola microgravity phase. The gray shaded area indicates the time period within which image reconstruction quality is poor due to the lack of coherence between successive images. Here, it lasts for typically 7 s. Beyond this time, water-saturated experiments show droplets persisting

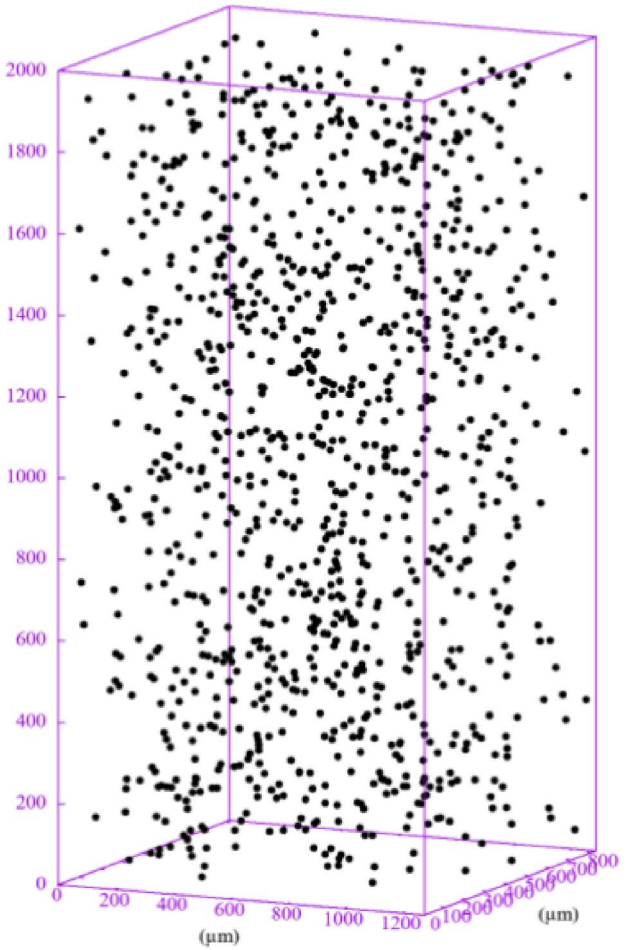

Figure 11. 3D reconstruction of an aerosol. Droplets are black spots. Their radius is multiplied by a factor 10 for visibility. About 24 h CPU are necessary for such a reconstruction on a basic work-station. This experiment was performed in the CNES 59th parabolic flight campaign (parabola 57, September 2020) with an EC of 4 cm diameter and 4 cm height.

for the remaining duration of the parabolas while they have all disappeared after typically 11 s when $H = 70\%$ [24,25].

These results clearly demonstrate the possibility to measure the number of formed droplets in microgravity conditions. This is an essential condition for assessing the feasibility of aerosol investigations over longer periods of time. They further indicate that evaporation of droplets in the sub-saturated regime is a very fast phenomenon as it takes place in less than 0.1 s. Such investigations could for sure complete the very rich literature focused on the evaporation of sessile droplets in microgravity [26–28]. Furthermore, fundamental questions such as how quickly droplet populations evaporate as relative humidity conditions change or the precise number of droplets (e.g. liquid fraction) remaining after expansion become quantitatively accessible. But Figure 12 raises practical questions that have yet to be resolved. The experiments show indeed poor reproducibility. Broader ensemble of data have to be collected to reduce the statistical variability of probing a small volume. Another explanation could be associated to unexpected differences, up to couple of seconds, in the duration of step (v) of aerosol formation. This problem

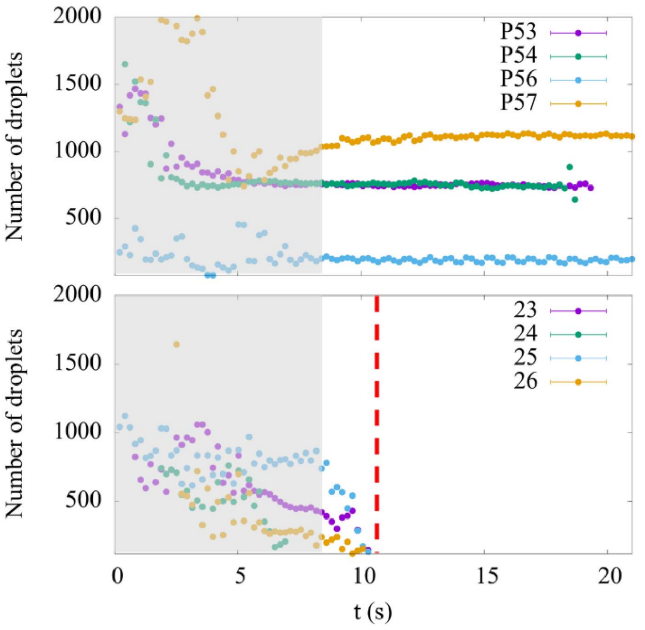

Figure 12. Evolution of the number of droplets as a function of time for target pressure 2000 mbar and temperature 22 °C. Top: $H = 100\%$. Bottom $H = 70\%$. The gray shaded area corresponds to the transient evolution phase. Vertical red dashed line indicates evaporation time. For parabolas P53 and P54 microgravity duration was shorter than expected. These experiments were performed in the CNES 59th parabolic flight campaign (September 2020). For both figures, EC diameter is 4 cm and height 4 cm.

results from the lack of precise synchronization in the operation of the pump (for pressure increase in the CE) and the valves opening/closing (for aerosol formation). The consequences of this uncontrolled delay are most likely differences in the pressure drop during aerosol formation and thus modified heat exchanges from one experiment to another. This instrumental problem has been solved and forthcoming parabolic flight experiments are expected to show a significantly improved reproducibility.

Parabolic flights have demonstrated that it is possible to generate stable aerosols only subject to the residual acceleration of flight conditions (Figure 11). Another fundamental point to check here is the ability of the rotor device presented in Section 4 to generate a VKSF within the EC and to set the overall aerosol in motion. The rotors have a smooth surface (not equipped with blades) and the question is whether it is possible or not to make droplets move and, if set in motion, to determine the time required for the establishment of a VKSF. Tuning parameter is the rotation frequency (noted f hereafter) imposed on the rotors. In practice, it is not possible to have a global view of this flow as only a very limited volume in the vicinity of the center of the EC is analyzed (Section 3). But, in view of its structure, this volume is expected to contain the stagnation point in the vicinity of which the droplets are expected to gather. This phenomenon is unfortunately not observable in the experiments because the periods of microgravity are too short and the positioning of the rotors most likely lack of precision. Still, the droplets, once formed, can be used as tracers. The analyzed area being in the center of the EC, it is reasonable to consider that the VKSF is established in the whole EC once they're set in motion (actually transported by the VKSF).

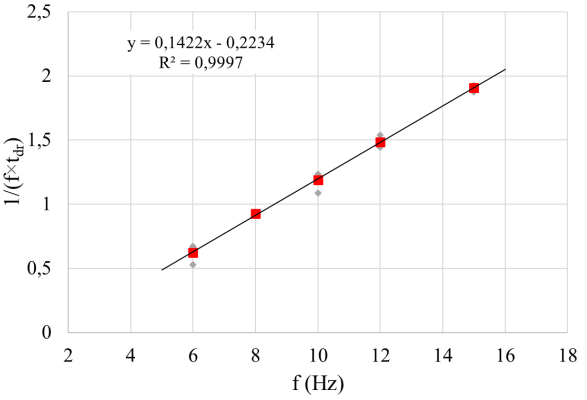

Figure 13. $1/(f \times t_{\mathrm{dr}})$ as a function of rotation frequency f. Five replica experiments are achieved for each experiment (small gray diamonds). The red squares are the average value for each replica series.

The experiments are focused on the measurement of the drag time (t_{dr}) corresponding to the time lag between rotor activation and droplet transport by the VKSF. The protocol is similar to that of Section 2 with the following additional step: after 7 s of an ongoing parabola, as the droplets are at rest, the rotors are activated. The drag time t_{dr} is evaluated by a direct observation of the movement of the droplets. Its value is determined when they appear to exhibit a coherent motion over a distance larger than 100 μm. Such movements are easy to identify by eye and cannot be the consequence of residual acceleration. Results are plotted in Figure 13 and indicate that $1/(f \times t_{\mathrm{dr}})$ increases linearly with f in the investigated frequency range ($6 \leq f \leq 15$ Hz). It extrapolates down to zero for $f \approx 1.5$ Hz which is consistent with the fact that no motion is observed for the duration of the parabolas when $f < 4$ Hz. This corresponds to a Reynolds number of the order 400 ($Re = 2\pi f R^2/n$, where $\upsilon \approx 1.5 \times 10^{-5}$ m^2·s^{-1}, is the kinematic viscosity of air and $R \approx 1.45$ cm the rotor radius) for which it is known that the first instabilities of the VKSF take place. For smaller values the flow is laminar and the motion develops on a diffusive time scale $(2R)^2/n \sim 60$ s after the rotors are set into motion. This turns longer than the duration of the parabolas. No flow is therefore observable.

7. Conclusions

The developments carried out within this work for the study of the populations of water droplets in microgravity required the implementation of specific instrumental techniques. Parabolic flight experiments were performed to verify their relevance. For the formation of the droplets, a protocol consisting of compressing and then expanding the air in a cylindrical experimentation cell was implemented. This protocol is short enough to assume droplet production to be a quasi-isothermal process. Preliminary parabolic flight experiments have established the possibility to quantitatively describe droplet populations under microgravity conditions. The flows generated by the initial expansion fade away in few seconds. Beyond this time, as residual acceleration is small, the droplets are almost at rest. Optical microscopy tomography in transmission mode is used to reconstruct the droplet populations in 3D and to follow their evolution in time over more than 15 s of microgravity. As the thermodynamic conditions are controlled, the evaporation dynamics of large droplets can be investigated. This work also shows how droplets can be set in motion by creating a von Karman flow. The instrumental developments will be continued in the next

future. Important improvements remain to be undertaken for the control of the relative humidity and the thermal regulation of all the elements containing the air used for the droplet formation.

Conflicts of interest

Authors have no conflict of interest to declare.

Acknowledgements

Authors gratefully thank CNES, in particular Christophe Delaroche and Laurent Arnaud, CNRS and Région Provence-Alpes-Côte d'Azur for important financial support, ESA—European Space Agency, within the project ESA/EVAPORATION (ESA Contract Number 4000129506/20/NL/PG) and Yvan CECERE from MADIREL for technical support.

References

[1] R. Gunn, G. D. Kinzer, "The terminal velocity of fall for water droplets in stagnant air", *J. Meteorol.* **6** (1949), no. 4, p. 243-248.
[2] A. C. Best, "Empirical formulae for the terminal velocity of water drops falling through the atmosphere", *Q. J. R. Meteorol. Soc.* **76** (1950), no. 329, p. 302-311.
[3] N. Davidson *et al.*, "Measurement of the Raman spectra and hygroscopicity of four pharmaceutical aerosols as they travel from pressurised metered dose inhalers (pMDI) to a model lung", *Int. J. Pharm.* **520** (2017), no. 1-2, p. 59-69.
[4] I. Márquez-Sillero, E. Aguilera-Herrador, S. Cárdenas, M. Valcárcel, "Determination of parabens in cosmetic products using multi-walled carbon nanotubes as solid phase extraction sorbent and corona-charged aerosol detection system", *J. Chromatogr. A.* **1217** (2010), no. 1, p. 1-6.
[5] K. Du, H. Xie, G. Hu, Z. Peng, Y. Cao, F. Yu, "Enhancing the thermal and upper voltage performance of Ni-rich cathode material by a homogeneous and facile coating method: spray-drying coating with Nano-Al_2O_3", *ACS Appl. Mater. Interfaces* **8** (2016), no. 27, p. 17713-17720.
[6] V. Caratelli, G. Fegatelli, D. Moscone, F. Arduini, "A paper-based electrochemical device for the detection of pesticides in aerosol phase inspired by nature: A flower-like origami biosensor for precision agriculture", *Biosens. Bioelectron.* **205** (2022), article no. 114119.
[7] U. Lohmann, L. Rotstayn, T. Storelvmo, A. Jones, S. Menon, J. Quaas, A. M. L. Ekman, D. Koch, R. Ruedy, "Total aerosol effect: radiative forcing or radiative flux perturbation?", *Atmos. Chem. Phys.* **10** (2010), no. 7, p. 3235-3246.
[8] B. N. Holben, D. Tanré, A. Smirnov, T. F. Eck, I. Slutsker, N. Abuhassan, W. W. Newcomb, J. S. Schafer, B. Chatenet, F. Lavenu, Y. J. Kaufman, J. V. Castle, A. Setzer, B. Markham, D. Clark, R. Frouin, R. Halthore, A. Karneli, N. T. O'Neill, C. Pietras, R. T. Pinker, K. Voss, G. Zibordi, "An emerging ground-based aerosol climatology: aerosol optical depth from AERONET", *J. Geophys. Res.* **106** (2001), no. D11, p. 12067-12097.
[9] L. A. Remer, R. G. Kleidman, R. C. Levy, Y. J. Kaufman, D. Tanré, S. Mattoo, J. V. Martins, C. Ichoku, I. Koren, H. Yu, B. N. Holben, "Global aerosol climatology from the MODIS satellite sensors", *J. Geophys. Res.* **113** (2008), no. D14, article no. D14S07.
[10] R. A. Bagnold, *The Physics of Blown Sand and Dust and Desert Dunes*, William Morrow, New-York, 1942.
[11] R. Gunn, G. D. Kinzer, "The terminal velocity of fall for water droplets in stagnant air", *J. Meteorol.* **6** (1949), p. 243-248.
[12] Y. Vilsanen, R. Strey, H. Reiss, "Homogeneous nucleation rates for water", *J. Chem. Phys.* **99** (1993), p. 4680-4692.
[13] A. Dillmann, G. E. A. Meier, "A refined droplet approach to the problem of homogeneous nucleation from the vapor phase", *J. Chem. Phys.* **94** (1991), p. 3872-3884.
[14] R. Miller, R. J. Anderson, J. L. Kassner, D. E. Hagen, "Homogeneous nucleation rate measurements for water over a wide range of temperature and nucleation rate", *J. Chem. Phys.* **78** (1983), p. 3204-3211.
[15] S. R. Arridge, "Optical tomography in medical imaging", *Inverse Probl.* **15** (1999), no. 2, p. R41-R93.
[16] S. R. Arridge, J. C. Schotland, "Optical tomography: forward and inverse problems", *Inverse Probl.* **25** (2009), no. 12, article no. 123010.
[17] U. S. Kamilov, I. N. Papadopoulos, M. H. Shoreh, A. Goy, C. Vonesch, M. Unser, D. Psaltis, "Learning approach to optical tomography", *Optica* **2** (2015), no. 6, p. 517-522.
[18] M. Schmitt, S. Limage, D. O. Grigoriev, J. Krägel, V. Dutschk, S. Vincent-Bonnieu, R. Miller, M. Antoni, "Transition from spherical to irregular dispersed phase in water/oil emulsions", *Langmuir* **30** (2014), no. 16, p. 4599-4604.

[19] M. Schmitt, S. Limage, R. Denoyel, M. Antoni, "Effect of SPAN80 on the structure of emulsified aqueous suspensions", *Colloids Surf. A* **521** (2017), p. 121-132.
[20] P. J. Zandbergen, D. Dijkstra, "Von Karman swirling flows", *Annu. Rev. Fluid Mech.* **19** (1987), no. 1, p. 465-491.
[21] S. Douady, Y. Couder, M.-E. Brachet, "Direct observation of the intermittency of intense vorticity filaments in turbulence", *Phys. Rev. Lett.* **67** (2007), no. 8, p. 983-986.
[22] R. Labbé, J.-F. Pinton, S. Fauve, "Study of the von Karman flow between coaxial corotating disks", *Phys. Fluids* **8** (1996), p. 914-922.
[23] L. Dufour, R. Defay, "Thermodynamics of clouds", *Bull. Am. Meteorol. Soc.* **46** (1965), no. 10, p. 674-676.
[24] Y.-Y. Su, R. E. H. Miles, Z.-M. Li, J. P. Reid, J. Xu, "The evaporation kinetics of pure water droplets at varying drying rates and the use of evaporation rates to infer the gas phase relative humidity", *Phys. Chem. Chem. Phys.* **20** (2018), p. 23453-23466.
[25] N. R. Devlin, K. Loehr, M. T. Harris, "The importance of gravity in droplet evaporation: A comparison of pendant and sessile drop evaporation with particles", *AIChE J.* **62** (2016), p. 947-955.
[26] D. Brutin, Z.-Q. Zhu, O. Rahli, J.-C. Xie, Q.-S. Liu, L. Tadrist, "Sessile drop in microgravity: creation, contact angle and interface", *Microgravity Sci. Technol.* **21** (2009), p. 67-76.
[27] Z.-Q. Zhu, D. Brutin, Q.-S. Liu, Y. Wang, A. Mourembles, J.-C. Xie, L. Tadrist, "Experimental investigation of pendant and sessile drops in microgravity", *Microgravity Sci. Technol.* **22** (2010), p. 339-345.
[28] M. Brandenbourger, H. Caps, Y. Vitry, S. Dorbolo, *Microgravity Sci. Technol.* **29** (2017), p. 229-239.

Comptes Rendus
Mécanique
2023, Vol. 351, Special Issue S2, p. 181-200
https://doi.org/10.5802/crmeca.147

Physical Science in Microgravity within the Thematic Group Fundamental and Applied Microgravity / *Sciences physiques en microgravité au sein du GDR Micropesanteur Fondamentale et Appliquée*

Conception of a compact flow boiling loop for the International Space Station- First results in parabolic flights

Paul Chorin [a], Antoine Boned [a], Julien Sebilleau [*, a], Catherine Colin [*, a], Olaf Schoele-Schulz [b], Nicola Picchi [b], Christian Schwarz [c], Balazs Toth [c] and Daniele Mangini [d]

[a] Institut de Mécanique des Fluides de Toulouse - Université de Toulouse - CNRS-INPT-UPS, Allée Camille Soula - 31400 Toulouse - France

[b] Airbus Defence and Space GmbH Claude-Dornier-Straße 88090- Immenstaad Germany

[c] European Space Agency ESTEC TEC-MMG Keplerlaan 1, PO Box 299 NL-2200 AG Noordwijk, The Netherlands

[d] cosine Remote Sensing BV Warmonderweg 14, 2171 AH Sassenheim, The Netherlands

E-mails: paul.chorin@toulouse-inp.fr (P. Chorin), antoine.boned@etu.toulouse-inp.fr (A. Boned), julien.sebilleau@imft.fr (J. Sebilleau), catherine.colin@imft.fr (C. Colin), olaf.schoele-schulz@airbus.com (O. Schoele), nicola.picchi@airbus.com (N. Picchi), christian.schwarz@esa.int (C. Schwarz), balazs.toth@esa.int (B. Toth), danymangini@msn.com (D. Mangini)

Abstract. The design of a pipe flow boiling experiment for the International Space Station is proposed, taking into account typical weight, power consumption and size constraints. The effect of singularities such as elbows upstream the test section is investigated. Velocity profiles downstream two elbows, measured by Particle Image Velocimetry are in good agreement with numerical simulation and allow to determine a specific distance (decay length) downstream the elbows for which the velocity profile recover its axisymmetry. From these results a breadboard is designed and tested in parabolic flights. Care has been taken to generate boiling downstream the decay length. Two-phase bubbly flow is observed with 2 perpendicular high-speed cameras in the test section and a symmetry of the bubble distribution in the pipe is verified for different gravity conditions when the bubbles are created after the decay length.

Keywords. Flow boiling, microgravity, Dean Vortex, Flow visualisation, bubbly flow.

Published online: 27 February 2023

* Corresponding authors.

1. Introduction

Gas-liquid and vapor-liquid flows are present in a wide variety of applications: vapor generator in thermal, nuclear or solar power plants for electricity production, transport of crude oil and natural gas mixture through long pipelines in petroleum industry. The chemical industries have utilized gas-liquid contactors to increase interfacial heat and mass transfers in absorption, stripping and distillation processes involving two-phase flow through complex geometries. Phase change in liquid-vapor systems is also beneficial for cooling of hot surfaces in steel industry or for the thermal management of electronic components. Two-phase flows are also present in space applications with the thermal control of the cryogenic upper stage tanks of the launchers, the chill-down of supplied lines by cryogenic liquid before engine re-ignition, thermal control of electronic components in satellites with loop heat pipes. Space exploration will also need the development and control of two-phase systems for energy production, propulsion of launchers, waste water treatment, operating in microgravity conditions but also in Moon or Mars gravity. Two-phase flow with phase change, boiling, condensation are complex phenomena, which combine heat and mass transfers, hydrodynamics, and interfacial phenomena. Furthermore, gravity affects the fluid dynamics and may lead to unpredictable performances of thermal management systems. From the 1960s onwards, the space industry has faced classic technical problems that stimulated the development of two-phase flow research at microgravity conditions. Among these are the predictions of flow pattern, pressure drop, heat transfer including critical heat flux and void fraction in thermo hydraulic systems. Beyond the design of space systems, reduced gravity two-phase flows can address some fundamental questions, which remain unsolved. On earth, due to the contrast of densities between the liquid and the vapor, the flow dynamics is often controlled by the gravitational force. As the gravity is suppressed, a new balance comes into play between inertial, viscous and interfacial forces so that the mechanics which govern the interactions between phases drastically changes. Low gravity conditions are particularly favorable to the emergence of surface tension as dominating force whose role is often small at 1g conditions except in microfluidic devices. Studies performed in the 1990s and early 2000s mainly concerned gas-liquid adiabatic flows, with the determination of the flow patterns and transitions [1–7], the measurements of void fraction or phase velocities [8], pressure drop [5, 7, 9]. From the beginnings of the 2000s the number of flow boiling experiments in tubes increased. Several results were reported on the detailed characterization of flow pattern and heat transfer coefficient including critical heat flux with different refrigerants R113, FC72, HFE7000, HFE7100 [10–20]. Several review articles have been published sumarising the main results: [5, 10, 12, 21–23]. Most of these experiments were performed in parabolic flights. However parabolic flights have some limitations due to g-jitter, that can affect the flow behavior at low mass flux. The time limitation of about 20s of microgravity is also too short to reach a steady state at low mass flux or a thermal equilibrium in metallic tubes. This observation has motivated the international space agencies to consider the opportunity to carry out flow boiling experiments on board the International Space Station.

A team of Japanese researchers developed the TPF (Two-Phase Flow) experiment in the KIBO module with the support of Japanese Space Agency JAXA. This experiment was operated onboard the International Space Station(ISS) during from July 2017 to March 2018, and from February 2019 to July 2019. Two series of flow boiling experiments with n-Perfluorohexane in a 4mm diameter tube were conducted in a metallic copper tube and in a transparent glass tube coating by a gold deposite. The data are under evaluation with a special care to the estimation of the heat losses for a precise evaluation of heat transfer [24].

An American experiment Flow Boiling and Condensation Experiments (FBCE) was launched to the ISS in August 2021. Flow boiling of n-Perfluorohexane in saturated conditions is under investigation in a rectangular channel of dimensions 114.6 mm heated length, 2.5 mm width, and

5 mm height. Two phase flows pattern, heat transfer and critical heat flux are studied. Results of ground experiments with a similar set-up are reported by the authors [25].

Europe is also considering the development of a two-phase flow loop to study flow boiling and condensation on board the ISS. The objective of this experiment would be to increase the range of studied parameters by comparison to the previous experiments and also to improve the diagnostics, with local time resolved measurements of the heat transfer, void fraction, wall and interfacial shear stresses and a careful characterization of the flow structure by high-speed video recording. The challenge for performing a flow boiling experiment in the ISS is to be able to implement the loop in a limited space with a limited power available. This motivated the European Space Agency to support a specific study to evaluate the implementation of a flow boiling loop with a test section consisting of a tube of 6 mm diameter in the European Drawer Rack 2 (EDR2). This study was performed in collaboration between the Institute of Fluid Mechanics of Toulouse and Airbus Defence and Space in Friedrichshaffen with the support of the European Space Agency. Due the space limitation, the distance between singularities (as elbows) and the test section is of course limited and a careful analysis has to be performed to insure that the flow will recover its axisymmetry in the test section where heat transfer, void fraction and wall shear stress are measured.

The second section of the manuscript is a detailed description of the context of the implementation of the loop: size of the container, power available, weight limitation which led to a first design of the loop. The single-phase flow hydrodynamics downstream 2 elbows is investigated by PIV measurements and by direct numerical simulations. The comparison of experimental and numerical results is presented and discussed in Section 3. In Section 4, a design of the two-phase flow loop for the ISS is proposed. This set-up has been operated on ground and in a parabolic flight campaign with microgravity and partial gravity conditions. In Section 5, some experimental results on the effect of gravity on the bubbly flow hydrodynamics are presented and discussed and the axisymmetry of the bubbly flow is checked.

2. Design of the experimental setup

The experimental setup, called CoSmo (compact small scale convection loop) aims to study the effects of gravity on the flow pattern and associated heat transfer in convective flow boiling in a tube of 6 mm internal diameter. As the CoSmo breadboard is designed for a typical accommodation on-board the ISS, taking EDR2 as a reference, it has to fulfil several constraints in terms of mass, dimension, power consumption (both to heat the fluid and to power the acquisition systems), cooling power (to condensate the fluid before the entrance of the pump) and has to be operated in a specific temperature range. Table 1 summarizes these constraints for the CoSmo breadboard.

Within the operational temperature range and power consumption constraint, n-perfluorohexane has been chosen as working fluid. Its moderate saturation temperature allows to work at various pressures (T_{sat} = 37.7°C at P = 0.5 Bar and T_{sat} = 68.9°C at P = 1.5 Bar) and of its low latent heat (L_v = 88 kJ.kg^{-1}) avoids too much power consumption for the boiling process. The density and dynamic viscosity of the liquid at 1 bar are ρ_l= 1619 kg.m^{-3} and μ_l=4.53 10^{-4} Pa.s, respectively. With this fluid, the range of parameters that can be achieved in the CoSmo breadboard are given in the Table 2.

It can be noticed that the maximum mass flux (G = 150 kg.m^{-2}.s^{-1}) remains smaller but not so far from the value G = 200 kg.m^{-2}.s^{-1} where inertial effects become dominant compared to gravity effects [15]. The range of vapor quality allows to study the main flow patterns encountered in convective boiling namely bubbly, slug, churn and annular flows. In addition to the power

Table 1. Maximum values of the CoSmo breadboard dimension, weight, power consumption, cooling power and operational temperatures for possible accommodation in the EDR2.

Parameter	Constraints
Dimension (mm)	720x900x400
Mass (kg)	50
Power consumption (W)	1030
Cooling (W)	1030
Operational temperatures (°C)	27-69

Table 2. Parameters range in the CoSmo breadboard.

Parameter	minimum value	maximum value
Mass flux G (kg.m^{-2}.s^{-1})	20	150
Thermodynamic vapor quality x	0.01	0.80
Pressure P (Bar)	0.5	1.5
Subcooling (K)	0	10

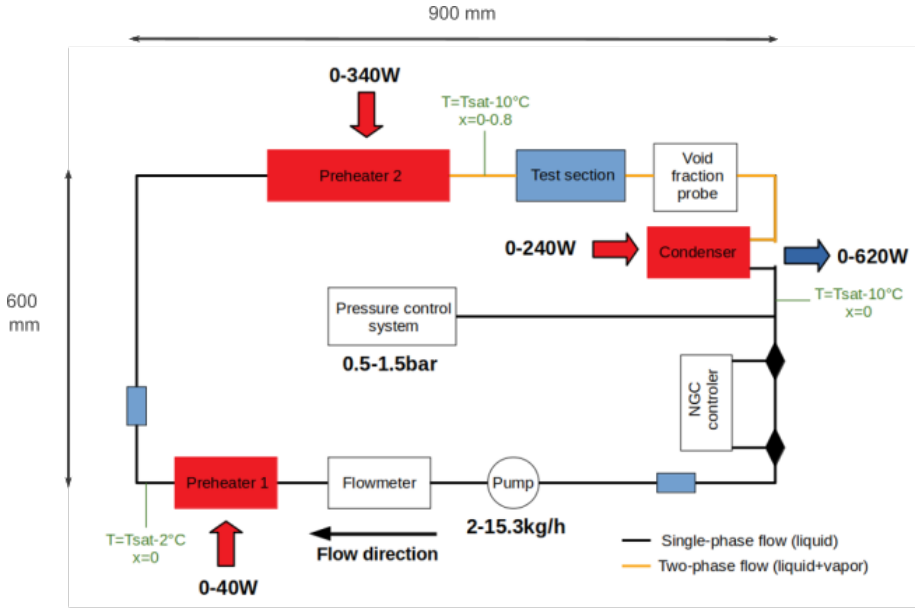

Figure 1. Scheme of the CoSmo breadboard.

consumption constraint, the CoSmo breadboard is also limited in its size. According to these constraints the typical scheme of the CoSmo breadboard is given in the Figure 1.

As one can see, the loop consists in two main part: a monophasic one from the condenser to the preheater 2 and a diphasic part (from the preheater 2 to the condenser) where the experiment on convective boiling is performed. Because of the dimension constraints, several elbows are present in the loop and we decided to keep a monophasic flow before the entrance of the Preheater 2, in order to avoid a liquid/vapor stratification in the elbows between the 2 preheaters.

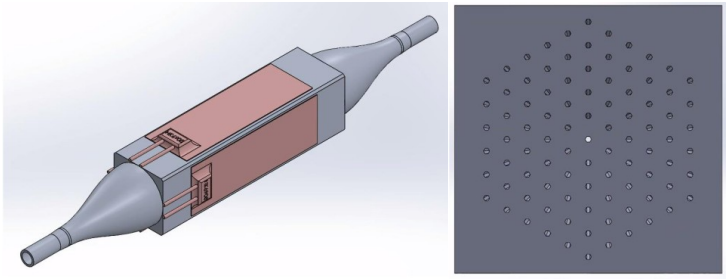

Figure 2. Scheme of the preheater 1 geometry and section.

At the outlet of the condenser, the fluid temperature is fixed at $T_{sat} - 10°C$ to avoid any cavitation in the pump. Due to the constraint of the maximum length (900 mm) it was not possible to vaporize all the fluid to the desired quality in preheater 2. Thus another preheater (preheater 1) was added after the flowmeter to heat up the fluid to $T_{sat} - 2°C$. This preheater has to be carefully designed in terms of length and heat flux to be able to reach the desired temperature with a sufficiently low heat flux to avoid boiling incipience. The maximum heat flux before the boiling inception was estimated thanks to the correlation of Frost and Dzakowic [26]:

$$\Delta T_{ONB} = T_p - T_{sat} = \sqrt{\frac{8\sigma \overset{\circ}{q} T_{sat}}{\lambda_L \rho_V h_{LV}} Pr_L} \tag{1}$$

where T_p is the wall temperature, σ the surface tension, λ_L the liquid thermal conductivity, ρ_V the vapor density, Pr_L the Prandtl number based on the liquid properties and $\overset{\circ}{q}$ the applied heat flux. Combining the Frost and Dzakovic correlation and the theoretical Nusselt number for laminar flow in tubes allows to determine the minimum length of heated tube to reach the desired temperature at the outlet of preheater 1. Unfortunately the calculated length was too large to be accommodated within the dimension restriction. Thus a specific design similar to a honeycomb structure was developed to allow to reach the desired temperature in a small length. The scheme of the preheater is illustrated in Figure 2. This preheater was manufactured thanks to a metallic 3D printing process and the heat is provided by four flat MINCO heating elements on its surface. Even if the flow is supposed to be monophasic between the two Preheaters, the elbows perturb the flow and can give rise to Dean vortices that break the axisymmetry of the flow in the preheater 2. It can result in undesired segregation of vapor bubbles in the bubbly flow regime. Thus the monophasic flow and the minimum length to retrieve an axisymmetric flow in the test section has to be studied prior the building of the CoSmo breadboard. This has been done both with numerical simulation and PIV measurements that are presented in the next section.

3. Single-phase flow qualification

As mentioned in the previous section, prior to the building of the CoSmo breadboard, the monophasic flow in the loop has to be studied to ensure that the flow at the entrance of the test section is axisymmetric and avoids bubble segregation in the bubbly flow regime. As the preheater 2 and the test section are downstream two elbows, a secondary flow induced by the curvature of the elbows can develop and break the axisymmetry. This secondary flow known as Dean vortices has been studied since the 1870's by Thomson [27–29]. Monophasic flows in curved pipes are parametrized with the pipe-to-curvature radii ratio $\delta = \frac{r}{R}$ (r being the pipe radius and R the radius of curvature of the pipe) and the Reynolds number $Re = \frac{2U_x r}{\nu}$ (U_x being the mean

flow velocity and ν the viscosity) and the secondary flow is generally parametrized thanks to the Dean number $D = Re\sqrt{\delta}$. Even if numerous studies have been devoted to classify the secondary flow with the Dean number, the decay length (minimum length to recover an axisymmetric flow after the curved part) has received less attention and the results mainly concern a U-bend [30–33]. Thus, to assess the proposed geometry for the CoSmo breadboard, both numerical simulations with OpenFOAM and PIV measurements have been performed to ensure that the flow at the entrance of the test section remains axisymmetric for the mass fluxes of interest $G \leq 150$ kg.m^{-2}.s^{-1} that corresponds to Reynolds numbers $Re \leq 2063$. According to Spedding et al. [34], with $\delta = 0.01$ which is the value proposed for the CoSmo breadboard the critical Reynolds number for transition to turbulence is $Re_c = 4838$ and thus a laminar flow is expected.

3.1. *Numerical simulations*

The numerical simulations have been performed with OpenFOAM using the simpleFoam solver that is adapted for laminar flows. The Semi-Implicit Method for Pressure Linked Equations (SIMPLE) algorithm is used for the pressure-velocity coupling. The gradient and laplacian terms are evaluated by central differencing scheme and the divergence terms by an upwind-biased scheme. All the spatial derivatives are second-order accurate. For each time step during the transient regime up to the converged steady state, the residuals fall below 10^{-8}. As the middle plane of the bend is a symmetry plane of the flow, only the upper half of the pipe is considered which enables to reduce the mesh size by a factor two. Thus, a symmetry condition on all variables is consequently set as a boundary condition for the middle plane. Within these parameters, the simulation have been tested on a single elbow configuration, depicted in Figure 3 **(a)**, that has been studied both numerically [35] and experimentally [36] for $Re = 700$ and $\delta = \frac{1}{6}$.

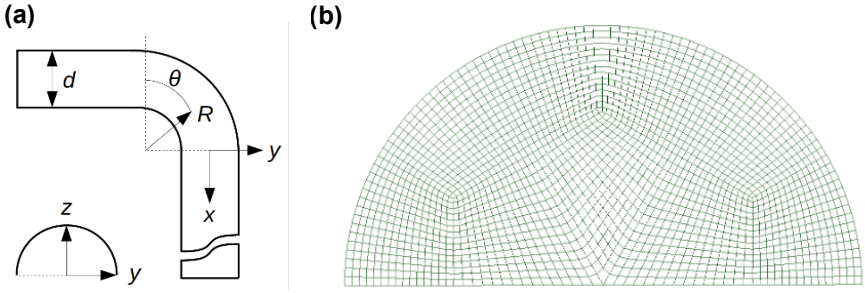

Figure 3. **(a)**: Scheme of the elbow and typical notation, **(b)**: mesh used in the simulation.

To prevent any disturbance at the entrance of the elbow, a small straight pipe of length 5d is added upstream the bend entrance. At the entrance of this 5D length pipe, a fully developed laminar velocity profile is imposed. A grid convergence is applied in this situation and it appears that a mesh with $N_{sect} = 8100$ cells per section and $N_{ax} = 12$ sections along the pipe per length of 6 mm (one pipe diameter) is sufficiently fine to obtain converged results. Figure 4 shows comparison of our results with those from literature at several positions in the elbow (i.e. at different θ values).

As one can see, a pretty good agreement is found with the experiments and previous numerical analysis. Numerical simulations were then performed on the CoSmo breadboard geometry from the entrance of the first elbow to the straight pipe at the exit of the second elbow to measure the flow profile and the decay length. The results are provided with the one obtained with the PIV measurements later in the text.

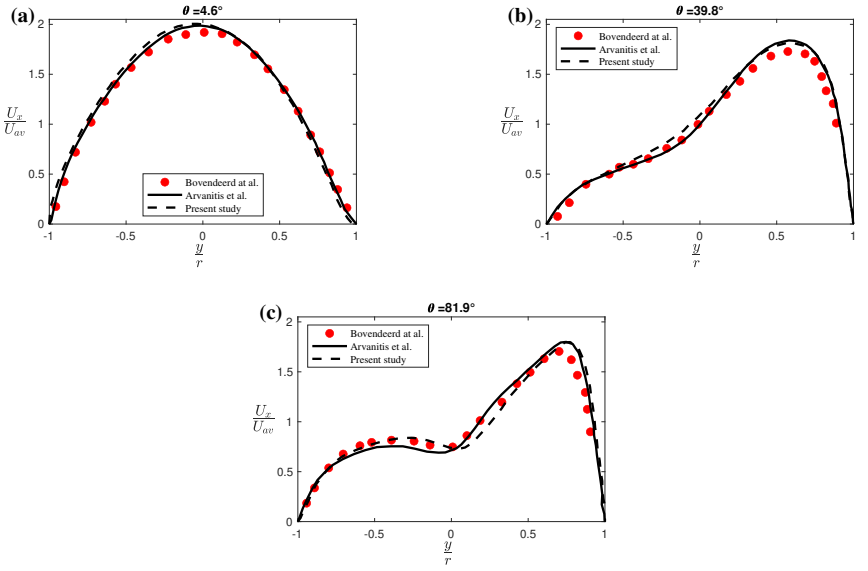

Figure 4. Comparison of the numerical results with the literature at position: **(a)**: $\theta = 4.6°$, **(b)**: $\theta = 39.8°$ and **(c)**: $\theta = 81.9°$.

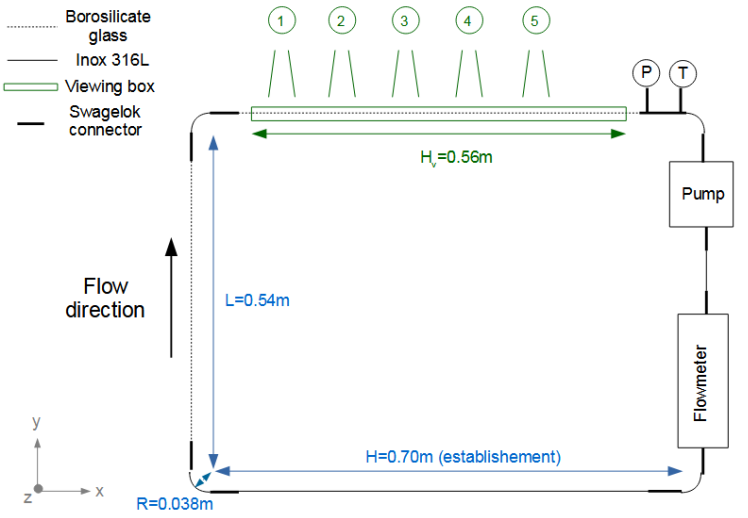

Figure 5. Scheme of the experimental setup used for PIV measurements.

3.2. *PIV measurements*

To perform PIV measurement in a tube of 6 mm inner diameter, a specific test loop, with the same dimensions as the CoSmo breadboard, has been developed and is illustrated in Figure 5. To avoid severe optical distorsions linked to the small diameter of the tube, the measurement section is made of a tube in borosilicate glass inside a rectangular viewing box whose walls are also in borosilicate. Then, using an aqueous solution of potassium thiocyanate as working fluid

(and for filling the viewing box) allows to match the refractive index of the fluid and the glass [37] and to perform PIV measurement in both the horizontal and vertical middle plane of the tube. The borosilicate glass (from Schott) has a refractive index close to 1.47. Then to achieve index matching we use an aqueous solution with 64% of potassium thiocyanate in mass. According to Agrawal et al. [38] this solution has a density of 1384 kg.m^{-3} and a kinematic viscosity of 1.78 10^{-6} m^2.s^{-1}. As this fluid is corrosive, great care has been taken in the choice of the materials used in this loop. To achieve a Reynolds number up to $Re = 2000$ with this loop, an Iwaki MDG-M4 gear pump was chosen and the mass flow rate was measured with a Coriolis Bronkhorst M15 flowmeter. The PIV measurement were performed with a PCO DIMAX camera with a maximal resolution of 2000x2000 and the measurement plane was illuminated with Nd-Yag laser (532nm wavelength) of maximal 20W power. An optic device (from LaVision) generates a laser sheet 120μm thick and 3.2cm wide. The particles used as tracers were particles of glass covered with silver (average diameter 10μm, density 1400kg/m^3 close to the one of the fluid). Four Reynolds numbers ($Re = 500$, $Re = 1000$, $Re = 1500$ and $Re = 2000$) were tested and Bazus displacement bench allowed to move both the camera and laser to explore several locations as depicted in Figure 5.

3.3. *Decay length*

Figures 6, 7 and 8 present comparisons between the PIV measurements and the numerical results for several axial positions for $Re = 1000$, $Re = 1500$ and $Re = 2000$ respectively. The results for $Re = 500$ are not presented because both experiments and numerical simulations give a fully developed profile (i.e. Poiseuille flow) at the entrance of the viewing box.

As one can see, the numerical results and the PIV measurements gives very close results for $Re = 1000$ and $Re = 1500$ and the flow recovers an axisymmetry at a given distance downstream the second elbow allowing to measure a decay length L_d. The decay length is defined as the length downstream the second elbow at which the flow recovers its axisymmetry corresponding to a maximum of the velocity profile located at a distance of the tube axis smaller than 0.05 d, d being the tube diameter. For $Re = 2000$, the experiments shows a flow profile that appears flatter than the one predicted by the numerical simulations. This may results from a transition to turbulence in our experiments while the simulations were performed for a laminar regime. Nevertheless, the flow profile still recovers an axisymmetry downstream the second elbow and still allows to measure the decay length.

This decay length for both PIV measurements and numerical simulation is presented in Table 3. As one can see the good agreement between PIV measurements and numerical simulations is confirmed except for $Re = 2000$ (due to the transition to turbulence mentioned before). Theses values are of interest for the development of the CoSmo breadboard as having an axisymmetric flow to avoid bubble segregation in bubbly flow regime is a scientific requirement for the study of convective boiling under various gravity conditions.

Table 3. Decay length values from PIV measurements and from numerical simulations.

Re	L_d (cm) from PIV	L_d (cm) from numerics	$\frac{L_d}{d}$ from PIV	$\frac{L_d}{d}$ from numerics
500	14	13	23	22
1000	24	28	40	46
1500	51	46	85	77
2000	19	>60	32	>100

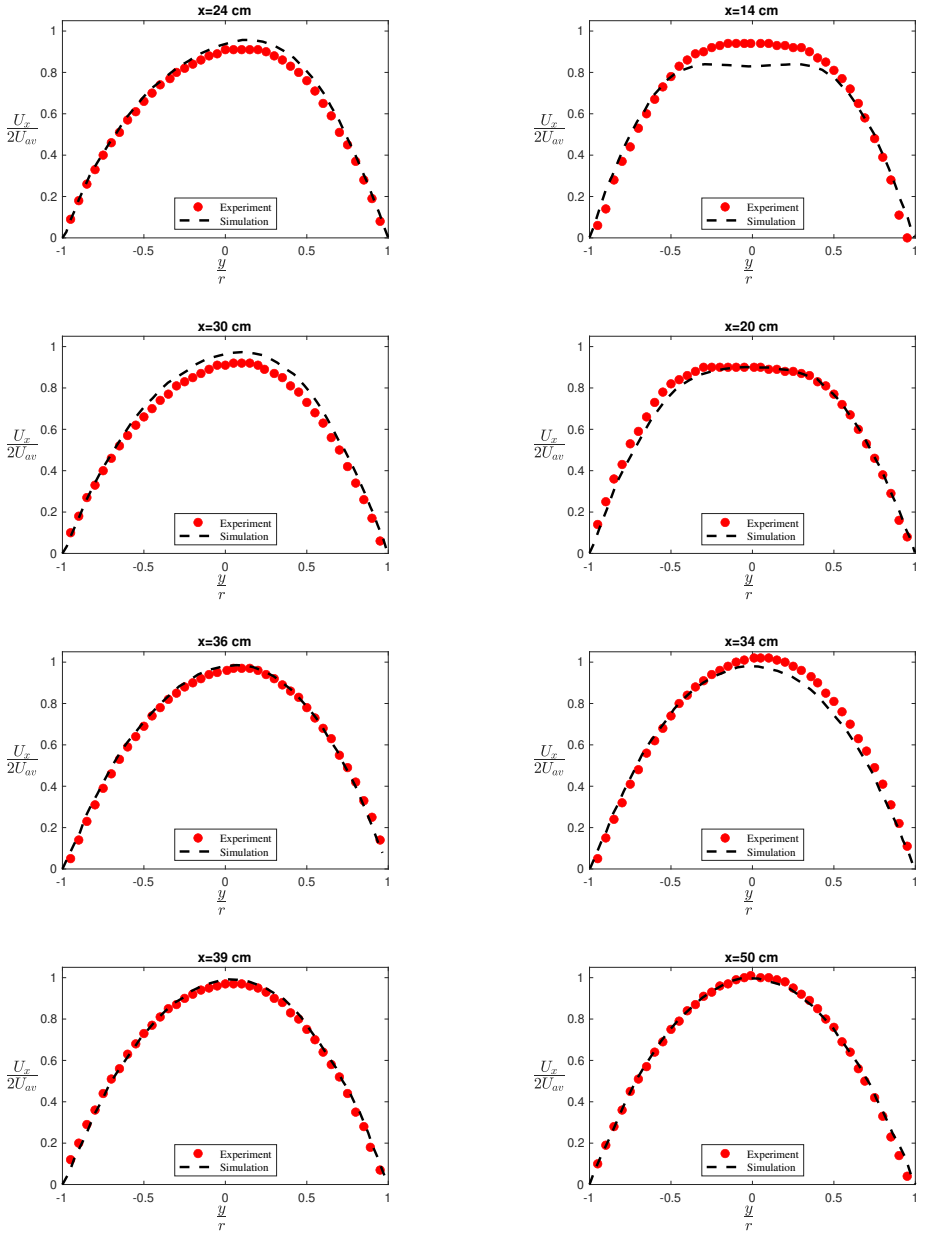

Figure 6. Comparison between the PIV measurement and the numerical simulation for $Re = 1000$ at various axial location. Left plots present experiments and simulations in the horizontal mid plane while right plots present experiments and simulations in the vertical mid plane.

4. Implementation of the CoSmo breadboard in parabolic flight and qualification

4.1. *Description of the CosMo loop*

Based on the previous results on the flow qualification downstream the elbows, a design of the CoSmo breadboard (Figure 9) with a 6mm inner diameter tube has been proposed. The size,

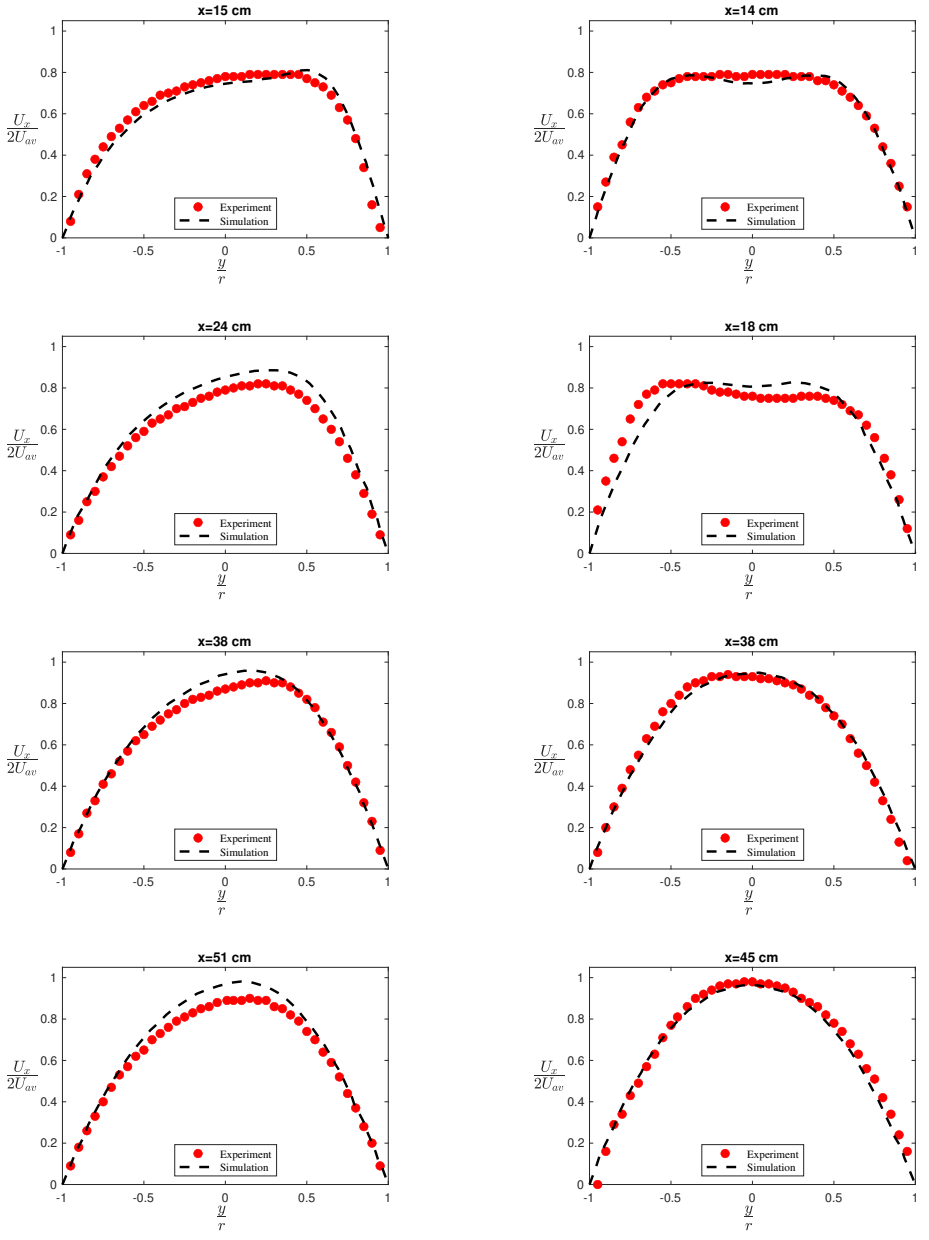

Figure 7. Comparison between the PIV measurement and the numerical simulation for $Re = 1500$ at various axial location. Left plots present experiments and simulations in the horizontal mid plane while right plots present experiments and simulations in the vertical mid plane.

weight and power consumption are compatible with an implementation in typical ISS payload racks, i.e EDR2 (see Table 1). In order to check the functionality of the loop in a microgravity environment, we first implemented it in a dedicated rack to participate to a parabolic flight campaign onboard the Airbus ZeroG Aircraft. The loop consists of a micro-annular gear pump

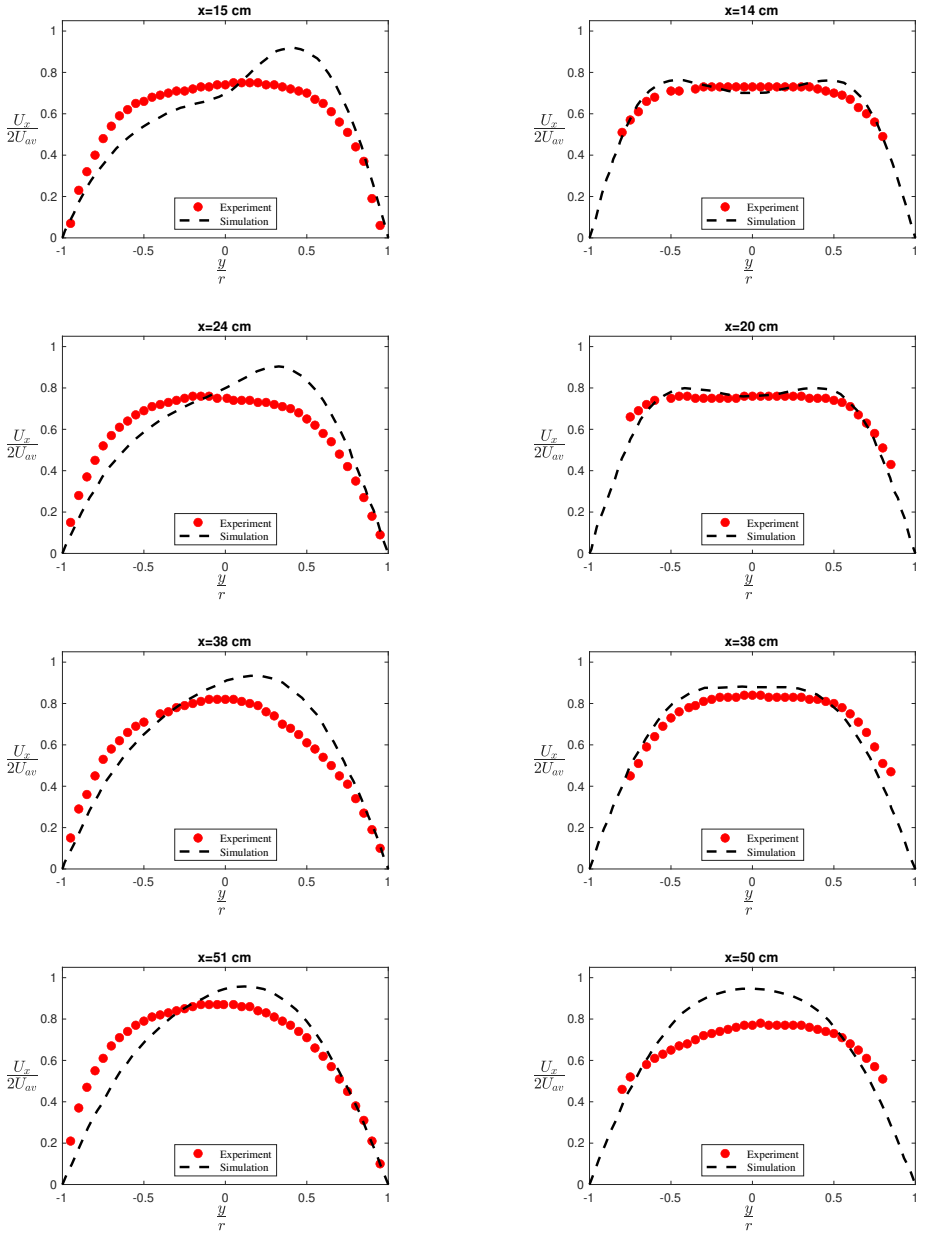

Figure 8. Comparison between the PIV measurement and the numerical simulation for $Re = 2000$ at various axial location. Left plots present experiments and simulations in the horizontal mid plane while right plots present experiments and simulations in the vertical mid plane.

model mzr-7265 from HNP Mikrosysteme operating with mass flux G up to 150 kg.m^{-2}.s^{-1}, a Coriolis flowmeter Bronkhorst M14, the preheater 1 (Figure 2), a straight line between the 2 elbows at the bottom part, the preheater 2 dowstream the second elbow, the test section, a void fraction probe, a condenser. The part of the loop between the preheaters 1 and 2 is the same as

the one of the loop for PIV measurements (Figure 5). The preheater 2 is a copper tube of 320 mm length, 6 mm inner-diameter and 10 mm outer-diameter with spiral grooves of 1mm depth. Due to size constraint, the length of the Preheater 2 has to be limited. The tube is heated by 3 wires (length 500 mm, diameter 1 mm) from Thermocoax, spiral rolled around an extruded copper cylindrical tube, providing each a maximal power of 110 W, allowing to reach a quality x up to 0.8. Each of the wire can be supplied independently, mentioned as PH2.1, PH2.2, PH2.3. For experiments at low quality values, especially for bubbly flow regimes, only the third wire farthest from the elbow (PH2.3) was used to let the flow recover its axisymmetry before nucleating the bubbles. PH2.1 is located between 7 cm and 18 cm downstream the elbow, PH2.2 from 18 cm to 29 cm and PH2.3 from 29 cm to 40 cm. For higher qualities values and the highest mass fluxes, the 3 wires were used. At the outlet of the test section, the two-phase flow enters the condenser composed of a cold plate with parallel mini channels. It is condensed and cooled down to a temperature of 10°C below the saturation temperature. On the external surface of the cold plate, 8 Thermo-Electric Coolers (TEC RC12-9 from Marlow) allow to extract a power up to 620 W. Series of fins (or heat sink) are placed above the TEC. Fans located above the fins allow to significantly increase the thermal dissipation. The pressure in the loop is set between 0.5 bar and 1.5 bar by a pressure control system designed and built by Airbus DS. The PCS consists of a metal membrane bellow that separates the fluid loop side chamber and the gas side chamber; the fluid side is assumed incompressible, therefore, its pressure can be controlled by regulating the pressure on the gas side. In order to avoid the need for a gas reservoir, the gas side chamber of the PCS is connected to a Diaphragm pump that can suck or inject air in the gas chamber. For laboratory and parabolic flight experiments, the experimental setup was placed vertically. The axis of the Preheater 2 and the test section was aligned with residual gravity, perpendicular to the floor (both in laboratory and in the aircraft).

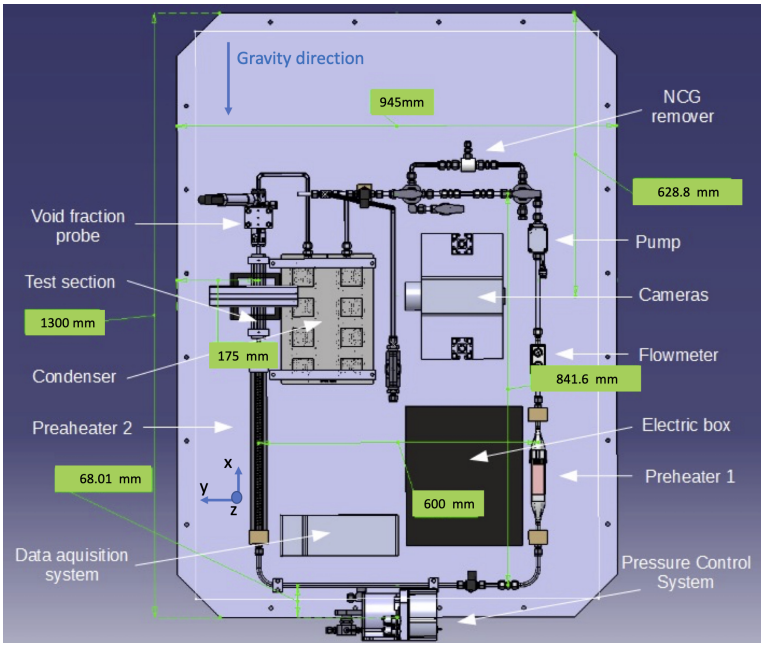

Figure 9. Scheme of the CoSmo loop for the parabolic flight campaigns.

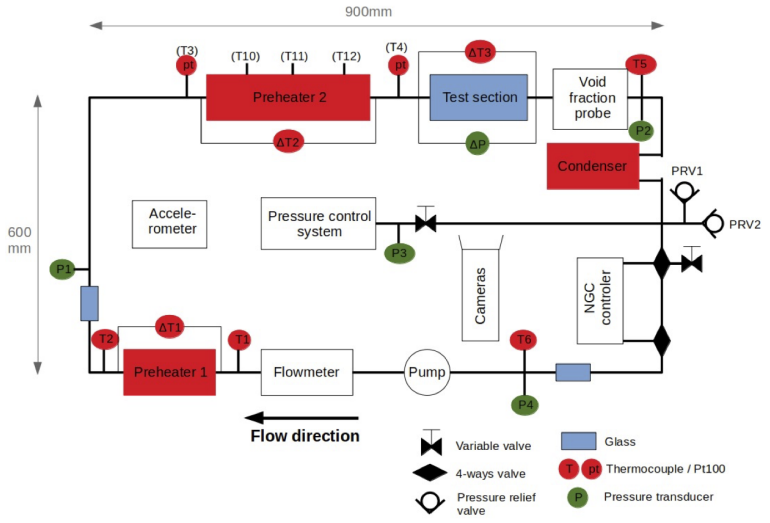

Figure 10. Location of thermocouples, pressure transducers in the CoSmo loop.

4.2. *Measurement technics*

Several Type K thermocouples and Pt100 probes are located all along the loop to measure the fluid temperature (T1 to T6), and the wall temperature of the preheater 2 (T10 to T12) (see Figure 10). Two Differential type T thermocouples allows to measure temperature difference along the 2 preheaters, for a precise thermal balance. Thanks to these thermocouples it was possible to quantify the heat losses and to measure the quality x at the entrance of the test section as described in [15]. The pressure at different locations in the loop (P1 to P4) is measured with four absolute pressure transducers (Keller 0-5 bars) and the pressure drop in the test section by a differential pressure transducer Validyne. An accelerometer is also used to record the residual acceleration along the 3 axis of the Aircraft during the flight. The void fraction probe, is a capacitance probe giving an averaged value of the capacitance of the liquid-vapor mixture which can be related to the void fraction after experimental or numerical calibration. Description of this probe can be found in [15]. All the measurements are acquired by the Data Acquisition system Ni-DAQ Compact Rio and recorded on a laptop. An interface for the control of the loop and the data acquisition, has been developed using Labview software.

4.3. *Test section and flow visualizations*

The test section is used for the visualizations of the two-phase flow and to assess the axisymmetry, especially in the bubbly flow regime. This test section is adiabatic and 12 cm long. It is a borosilicate glass tube of 6mm inner diameter and 8 mm outer diameter surrounded by a rectangular glass box. Two cameras PCO 1200 HS (16bit gray scale images size of 1280x401pixels with a spatial resolution of 30 pixels/mm and a frame rate of 400Hz) are used to film the flow in two perpendicular planes. The two cameras are placed one above the other and a mirror reflects one of the views. Camera 2 recorded images of the flow in the plane (x,y) in Figure 9 and Camera 1 in the plane (x,z) in Figure 9. Two backlights are placed on the opposite side of the cameras for homogenous and parallel backward illumination. They allow to have a good contrast in the images and to ease the detection of the bubble contours. The visualization box is filled with glycerin to reduce optical distortion. The index of refraction of the glycerin and

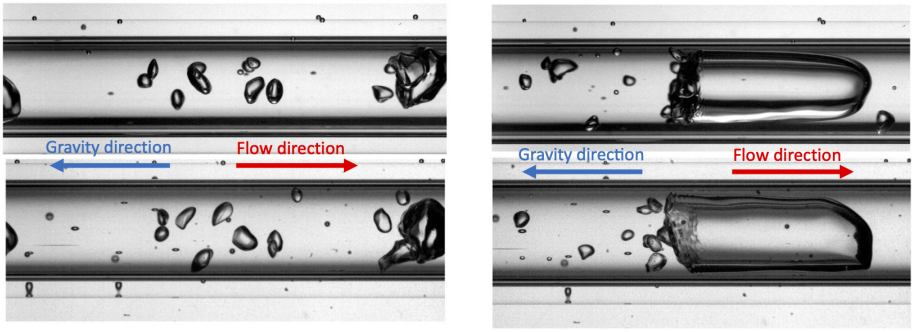

Figure 11. Flow visualization in earth gravity with the 2 perpendicular cameras (top camera 1, bottom camera 2): left bubbly flow G=20kg/m^{-2}.s^{-1} and x=0.01, right slug flow G=80 kg/m^{-2}.s^{-1}, x=0.06.

the glass are the same and equal to 1.47 and the index of refraction of the fluid FC72 is 1.23. The optical distortion was measured with a grid target of points regularly spaced of 0.125 mm. No distortion was observed in the area between -2 and +2mm from the pipe axis. Nevertheless, optical distorsion was observed very close to inner wall of the tube. It is visible on the images with the black bands in the vicinity of the inner wall. Synchronized images of the two cameras are acquired with the Cameware software on a computer. An example of bubbly flow and slug flow visualisation is given Figure 11.

4.4. *Parabolic flights*

For the parabolic flight campaign, the experimental set-up was accommodated into 2 racks: one containing the fluid loop and electronics in a double containment (Rack 1) and one is the “control Rack” (Rack 2) containing the electrical supplies and 3 computers for data and image acquisitions. It is operated by three people (see Figure 12). The 76th ESA Parabolic Flight Campaign took place in Paderborn (Germany) from 25th to 30th June 2021, with 3 flights of 31 parabolas each. It was a partial gravity campaign with 31 parabolas in microgravity, 31 parabolas in Moon gravity (0.16g) and 31 parabolas in Mars gravity (0.38g). The periods of partial gravity were at least 20 s long. Experiments were performed with 3 mass fluxes G=50, 100 and 150 kg/m^{-2}.s^{-1}, corresponding to liquid Reynolds numbers Re_l of about 650, 1300 and 2000, respectively and qualities x up to 0.4.

5. First results of the parabolic flight campaign

The main objective of this parabolic flight campaign was to assess the axisymmetry of the two-phase flow in the test section in microgravity conditions. Unfortunately, for this campaign, only PH2.1 the first part of the Preheater 2 worked, due to an electrical failure. The single-phase flow recovered its axisymmetry only at the end of PH2.1 for G= 50 kg/m^{-2}.s^{-1}. It means that for the mass fluxes G= 100 and 150 kg/m^{-2}.s^{-1}, the bubbles were produced in the preheater 2 at a distance from the elbow where the single-phase flow did not recover its axisymmetry. From the flow visualisations with the two perpendicular cameras, the radial distribution of the bubbles was investigated and compared to some results obtained on ground. Another target for this parabolic flight campaign, was to point out the influence of the residual gravity on the bubbly flow.

Figure 12. Operators during pre-flight preparation in front of the control rack (Rack 2), in the background the experimental rack (Rack 1); interior of the AirZero-G A310 aircraft.

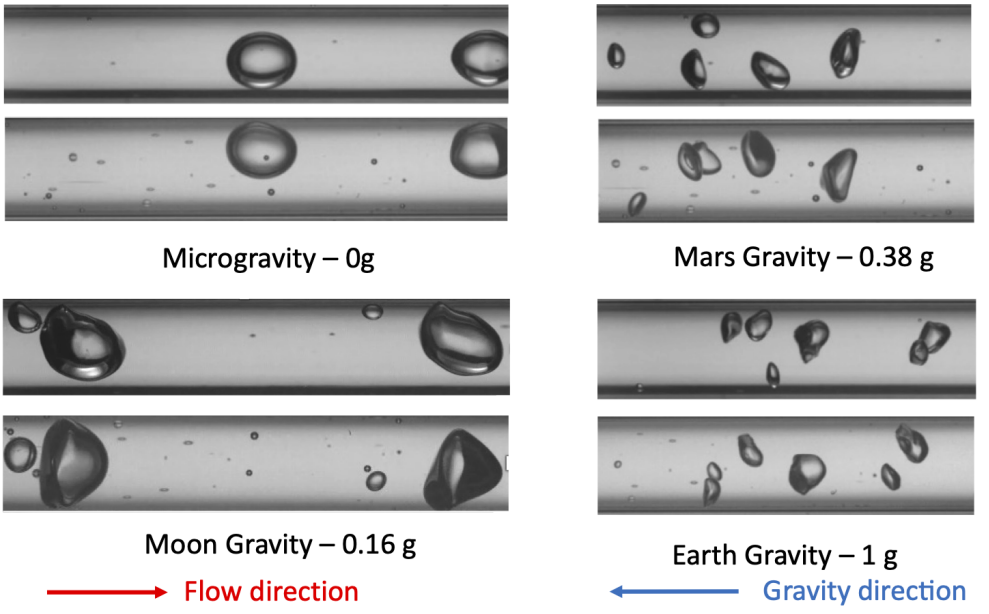

Figure 13. Flow visualizations with the 2 cameras for G=100 kg/m^{-2}.s^{-1} and x=0.01 for different gravity levels: microgravity (0g), Moon gravity (0.16g), Mars gravity (0.38g), Earth gravity (1g).

5.1. *Gravity effect on bubble size distribution*

Interesting results were obtained concerning the effect of the gravity on the flow structure, especially in bubbly flows as shown in Figure 13 and in the video: https://www.esa.int/Enabling_Support/Space_Engineering_Technology/Just_add_bubbles_for_cooler_future_spacecraft.
Small bubbles are formed in the Preheater 2, and we can remark that the bubble sizes and

shapes are very sensitive to gravity. In microgravity and Moon gravity, the bubble sizes are larger than in Mars and Earth gravity. This is due to two effects. The sizes of the bubbles detaching from the wall of Preheater 2 are larger, since the bubbles are mainly detached by the shear of the flow and not by the buoyancy force, at least in microgravity. Moreover the rate of coalescence of the bubbles is higher in microgravity, as reported in previous studies [2, 15]. These 2 effects lead to larger bubble sizes. Bubbly flows in Mars gravity and earth gravity do not look very different. The bubble sizes and the bubble deformations are similar. It seems that a threshold in the gravity level between Moon and Mars, leads to a different behavior of the bubbly flow. We can see that in microgravity, the bubbles are spherical and they have a rectilinear trajectory. Even in Moon gravity, a small deformation of the bubbles can be seen. The deformation and oscillation of the bubbles are linked to their relative velocity due to buoyancy, which leads to detachment of eddies in their wake. These preliminary results concerning the effect of partial gravity (Moon and Mars) on the two-phase flow dynamics are of great interest and show that the flow structure cannot be predicted easily by interpolation of results obtained both in microgravity and earth gravity.

5.2. *Bubble radial distribution in the tube*

In order to check the axisymmetry of the two-phase flow, some experiments were performed on ground in vertical upward bubbly flow and during the parabolic flight campaign. On ground experiments, nucleate boiling was generated in the last part of the preheater 2 PH2.3 at 3 mass fluxes G=50, 100 and 150 kg/m^{-2}.s^{-1}. As mentioned previously for parabolic flight experiments, only PH2.1 was utilized. To analyse the bubble distributions in the tube, the power was limited in the preheater 2 and the quality x was lower than 0.01, to have a limited number of bubbles to ease the bubble detection and to avoid overlapping of several bubbles. The images of the 2 cameras are processed using Matlab software following the different steps (see Figure 14): starting from the raw image (a), substraction of a background image without bubble (b), enlightening of the bubbles (c), binarization (d), bubble filling (e), morphological opening (f), contour detection (g).

The space resolution of the cameras is 30 pixels/mm. From the contour of the bubble it is possible to determine the position of the center of gravity of the bubbles: longitudinal (x) and lateral (y) coordinates, their equivalent diameter (diameter of a disk with the same area). During the parabolic flight campaign, the bubble sizes were much larger in microgravity and in Moon gravity and too few bubbles are observed in the test section during the parabolas, to obtain a converged bubble lateral distribution after image processing. Thus, only the results concerning converged values of the mean bubble position and its RMS value for the experiments performed in Mars gravity are presented in Figure 15 and the radial distributions were calculated for a population of 700 bubbles. The mean lateral positions (y and z) of the bubbles in the tube and their rms values are reported in Table 4. We can see a slight asymmetry of the bubble distribution, which is confirmed by the mean values of the lateral position especially for the camera 2 for G=150 kg/m^{-2}.s^{-1}. Camera 2 has taken the images in the plane of the elbows, which is the most affected by the Dean vortices. Despite the use of PH2.1 in these experiments, it is interesting to see that for the lowest mass fluxes G=50 and 100 kg/m^{-2}.s^{-1}, the asymmetry of the distribution is not critical.

On ground experiments, in vertical upward flow, the third part of the prehater 2 PH2.3 was used. In this configuration, vapor bubbles are mostly produced at a distance 35 to 40 cm downstream the elbow, for which the single-phase flow has almost recovered its axisymmetry. The equivalent diameters of the bubbles ranged from 0.3 mm to 1.8 mm. About 2000 bubbles were detected in the processed images. The distributions of lateral position of the bubbles (y) on the 2 cameras are displayed in Figure 15. Bubbles are distributed quite in a homogeneous way over the pipe cross section. The mean distance is for most of the runs lower than 0.1 mm from the axis.

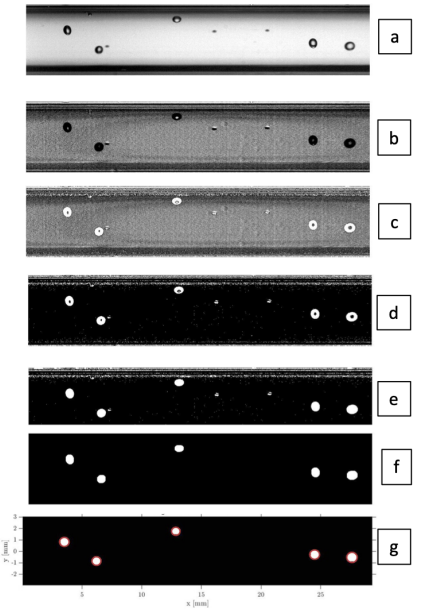

Figure 14. Different steps of image processing.

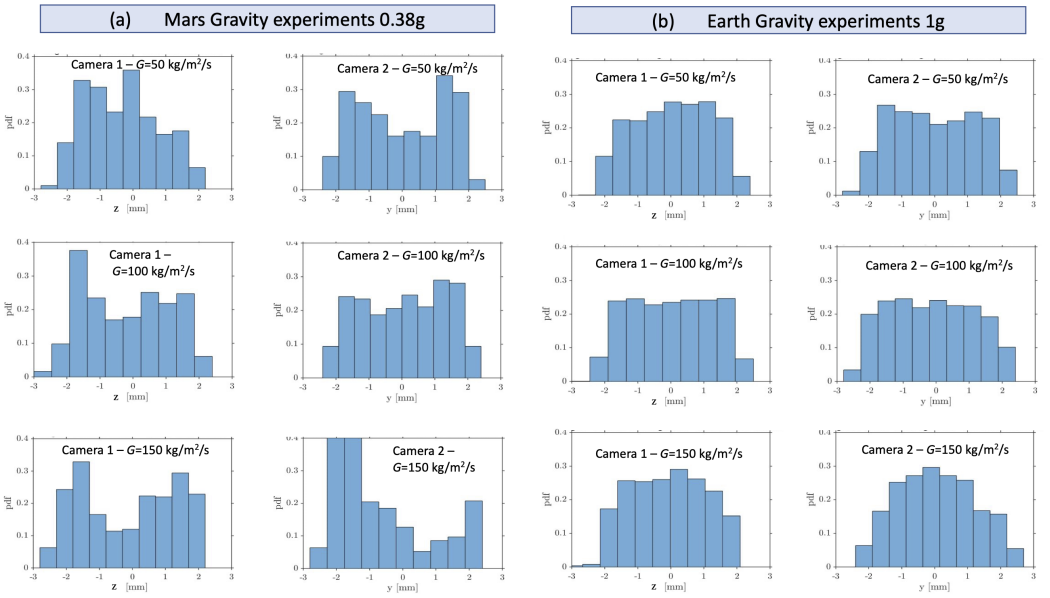

Figure 15. Bubble lateral distributions measured from the images of the 2 cameras: **(a)**: parabolic flight experiments in Mars Gravity 0.38g, **(b)**: Ground experiments in normal gravity 1g.

Thus the bubble distributions can be considered as axisymmetric for bubbles formed in the preheaters at least 29 cm downstream the second elbow. Despite the limited length of the Preheater 2, for all the flow rates, the bubble lateral distributions are symmetrical, which validates the design of the CoSmo breadboard.

Table 4. Bubble distribution.

			cam 1	cam 1	cam 2	cam 2
G(kg/m^2/s)	Preheater 2	Gravity Level	mean pos.	rms pos.	mean pos.	rms pos.
50	PH2.1	0.38g	-0.32 mm	1.1 mm	0.0061 mm	1.3mm
100	PH2.1	0.38g	-0.19 mm	1.2 mm	0.069 mm	1.3 mm
150	PH2.1	0.38g	-0.11 mm	1.4 mm	-0.69 mm	1.4mm
50	PH2.3	1g	0.035 mm	1.1 mm	-0.004 mm	1.2mm
100	PH2.3	1g	0.029 mm	1.2 mm	-0.15 mm	1.3 mm
150	PH2.3	1g	-0.068 mm	1.1 mm	0.066 mm	1.2mm

6. Conclusion

In the frame of a project of the European Space Agency, a small scale flow boiling loop CoSmo has been designed in collaboration between the Institute of Fluid Mechanics of Toulouse and Airbus/ Defence and Space. Aiming at a potential implementation on-board the International Space Station, CoSmo has to fulfil typical size, power consumptions and weight constraints. The presence of singularities as elbows in the hydraulic circuit perturbes the flow hydrodynamics by creating Dean vortices and a strong flow asymmetry downstream the elbows. This perturbation is damped by viscous effects and after a decay length the flow recovers its axisymmetry. The objective of this study was to characterize the decay of the flow perturbation after two elbows both by PIV measurements and numerical simulations. The decay lengths obtained from numerical simulation and experiments are in good agreement for different flow Reynolds numbers Re_l equal to 500, 1000, 1500. For Re_l= 2000, the experimental value of the decay length is much smaller than the numerical one, probably because of the transition to a turbulent flow. From these results a design of the CoSmo loop was proposed. A preheater between the second elbow and the test section was composed of 3 heating parts to generate bubble vaporisation. For bubbly flows very sensitive to flow asymmetry, the downstream part of the preheater PH2.3 has to be used. The other parts of the preheater PH2.1 and PH2.2 can be used for flow with higher quality (slug flow or annular flows) less sensitive to the secondary flow downstream the elbows. The CoSmo loop was used to assess the axisymmetry of the bubble distributions in the test section thanks to 2 high-speed video cameras taken images in two perpendicular planes. Experiments were performed on ground in vertical upward flow and in partial gravity during a parabolic flight campaign. During the flight campaign only the preheater PH2.1 worked and a asymmetry of the bubble distribution was observed for the highest mass flux G=150 kg/m^{-2}.s^{-1}. For ground experiments, the preheater PH2.3 was used and the distribution of the bubbles was found symmetrical in the 2 planes for the 3 flow rates. For future experiments the test section will be replaced by a heated tube to study heat transfer coefficient in flow boiling. The CoSmo loop will allow to implement different test section and measurement techniques such as a sapphire tube using Pt 100 probes [15, 39] or temperature sensitive paint [19].

Conflicts of interest

The authors declare no competing financial interest.

Dedication

The manuscript was written through contributions of all authors. All authors have given approval to the final version of the manuscript.

Acknowledgments

Airbus DS and IMFT have been supported by the European Space Agency through the Invitation to Tender AO/1-9380/NL/KML. IMFT would like also to thank the french space agency CNES through the GDR "Micropesanteur Fondamentale et Appliquée" for additionnal support.

Supplementary data

Supporting information for this article is available on the ESA website.

References

[1] A. E. Dukler, J. A. Fabre, J. B. McQuillen, R. Vernon, "Gas-liquid flow at microgravity conditions: Flow patterns and their transitions", *Int. J. Multiphase Flow* **14** (1988), no. 4, p. 389-400.

[2] C. Colin, J. A. Fabre, A. E. Dukler, "Gas-liquid flow at microgravity conditions–I. Dispersed bubble and slug flow", *Int. J. Multiphase Flow* **17** (1991), no. 4, p. 533-544.

[3] L. Zhao, K. S. Rezkallah, "Gas-liquid flow patterns at microgravity conditions", *Int. J. Multiphase Flow* **19** (1993), no. 5, p. 751-763.

[4] W. S. Bousman, J. B. McQuillen, L. C. Witte, "Gas-liquid flow patterns in microgravity: Effects of tube diameter, liquid viscosity and surface tension", *Int. J. Multiphase Flow* **22** (1996), no. 6, p. 1035-1053.

[5] C. Colin, J. A. Fabre, J. McQuillen, "Bubble and slug flow at microgravity conditions: state of knowledge and open questions", *Chem. Eng. Commun.* **141-142** (1996), no. 1, p. 155-173.

[6] K. S. Rezkallah, "Weber number based flow-pattern maps for liquid-gas flows at microgravity", *Int. J. Multiphase Flow* **22** (1996), no. 6, p. 1265-1270.

[7] J.-f. Zhao, J. C. Xie, H. Lin, W. R. Hu, A. V. Ivanov, A. Y. Belyaev, "Experimental studies on two-phase flow patterns aboard the Mir space station", *Int. J. Multiphase Flow* **27** (2001), no. 11, p. 1931-1944.

[8] K. J. Elkow, K. S. Rezkallah, "Void fraction measurements in gas-liquid flow under $1g$ and μ conditions using capacitance sensors", *Int. J. Multiphase Flow* **23** (1997), no. 5, p. 815-829.

[9] L. Zhao, K. S. Rezkallah, "Pressure drop in gas-liquid flow at microgravity conditions", *Int. J. Multiphase Flow* **21** (1995), no. 5, p. 837-849.

[10] O. Haruhito, "Microgravity Heat Transfer in Flow Boiling", in *Advances in Heat Transfer*, vol. 37, Elsevier, 2003, p. 1-76.

[11] H. Zhang, I. Mudawar, M. M. Hasan, "CHF model for subcooled flow boiling in Earth gravity and microgravity", *Int. J. Heat Mass Transfer* **50** (2007), no. 19-20, p. 4039-4051.

[12] G. P. Celata, G. Zummo, "Flow boiling heat transfer in microgravity: recent progress", *Multiph. Sci. Technol.* **21** (2009), no. 3, p. 187-212.

[13] C. Baltis, G. P. Celata, M. Cumo, L. Saraceno, G. Zummo, "Gravity Influence on Heat Transfer Rate in Flow Boiling", *Microgravity Sci. Technol.* **24** (2012), no. 3, p. 203-213.

[14] H. Ohta, S. Baba, "Boiling Experiments Under Microgravity Conditions", *Exp. Heat Transf.* **26** (2013), no. 2-3, p. 266-295.

[15] M. Narcy, E. de Malmazet, C. Colin, "Flow boiling in tube under normal gravity and microgravity conditions", *Int. J. Multiphase Flow* **60** (2014), p. 50-63.

[16] S. Luciani, D. Brutin, C. Le Niliot, O. Rahli, L. Tadrist, "Flow Boiling in Minichannels Under Normal, Hyper-, and Microgravity: Local Heat Transfer Analysis Using Inverse Methods", *J. Heat Transfer* **130** (2008), no. 10, article no. 101502.

[17] C. Konishi, H. Lee, I. Mudawar, M. M. Hasan, H. K. Nahra, N. R. Hall, J. D. Wagner, R. L. May, J. R. Mackey, "Flow boiling in microgravity: Part 2 – Critical heat flux interfacial behavior, experimental data, and model", *Int. J. Heat Mass Transfer* **81** (2015), p. 721-736.

[18] Y. Zhang, B. Liu, J.-f. Zhao, Y. Deng, J. Wei, "Experimental Study of Subcooled Flow Boiling Heat Transfer on a Smooth Surface in Short-Term Microgravity", *Microgravity Sci. Technol.* **30** (2018), no. 6, p. 793-805.

[19] M. T. Lebon, C. F. Hammer, J. Kim, "Gravity effects on subcooled flow boiling heat transfer", *Int. J. Heat Mass Transfer* **128** (2019), p. 700-714.

[20] M. T. Lebon, C. F. Hammer, J. Kim, "Using a modified single-phase model to predict microgravity flow boiling heat transfer in the bubbly flow regime", *Exp. Heat Transf.* **34** (2021), no. 5, p. 474-492.

[21] J.-f. Zhao, "Two-phase flow and pool boiling heat transfer in microgravity", *Int. J. Multiphase Flow* **36** (2010), no. 2, p. 135-143.

[22] M. Narcy, C. Colin, "Two-phase flow in microgravity with and without phase change: recent progress and future prospects", *Interfacial Phenom. Heat Transf.* **3** (2015), no. 1, p. 1-17.

[23] C. Konishi, I. Mudawar, "Review of flow boiling and critical heat flux in microgravity", *Int. J. Heat Mass Transfer* **80** (2015), p. 469-493.

[24] K. Inoue, H. Ohta, H. Asano, O. Kawanami, R. Imai, K. Suzuki, Y. Shinmoto, T. Kurimoto, S. Matsumoto, "Heat Loss Analysis of Flow Boiling Experiments Onboard International Space Station with Unclear Thermal Environmental Conditions (2nd Report: Liquid-vapor Two-phase Flow Conditions at Test Section Inlet)", *Microgravity Sci. Technol.* **33** (2021), no. 5, article no. 57.

[25] V. S. Devahdhanush, S. J. Darges, I. Mudawar, H. K. Nahra, R. Balasubramaniam, M. M. Hasan, J. R. Mackey, "Flow visualization, heat transfer, and critical heat flux of flow boiling in Earth gravity with saturated liquid-vapor mixture inlet conditions – In preparation for experiments onboard the International Space Station", *Int. J. Heat Mass Transfer* **192** (2022), article no. 122890.

[26] V. P. Carey, *Liquid-Vapor Phase-Change Phenomena: An Introduction to the Thermophysics of Vaporization and Condensation Processes in Heat Transfer Equipment*, 2 ed., CRC Press, 2018.

[27] W. R. Dean, "XVI. Note on the motion of fluid in a curved pipe", *The London, Edinburgh, and Dublin Philosophical Magazine and Journal of Science* **4** (1927), no. 20, p. 208-223.

[28] W. R. Dean, J. M. Hurst, "Note on the motion of fluid in a curved pipe", *Mathematika* **6** (1959), no. 1, p. 77-85.

[29] S. A. Berger, L. Talbot, L. S. Yao, "Flow in Curved Pipes", *Annu. Rev. Fluid Mech.* (1983), p. 461-512.

[30] K. C. Cheng, F. P. Yuen, "Flow Visualization Studies on Secondary Flow Patterns in Straight Tubes Downstream of a 180 deg Bend and in Isothermally Heated Horizontal Tubes", *J. Heat Transfer* **109** (1987), no. 1, p. 49-54.

[31] J. A. Fairbank, R. M. C. So, "Upstream and downstream influence of pipe curvature on the flow through a bend", *Int. J. Heat Fluid Flow* **8** (1987), no. 3, p. 211-217.

[32] J. T. Ault, K. K. Chen, H. A. Stone, "Downstream decay of fully developed Dean flow", *J. Fluid Mech.* **777** (2015), p. 219-244.

[33] A. Pantokratoras, "Steady laminar flow in a 90° bend", *Adv. Mech. Eng.* **8** (2016), no. 9, p. 1-9.

[34] P. L. Spedding, E. Benard, G. M. Mcnally, "Fluid Flow through 90 Degree Bends", *Dev. Chem. Eng. Mineral Process.* **12** (2004), no. 1-2, p. 107-128.

[35] K. D. Arvanitis, D. Bouris, E. Papanicolaou, "Laminar flow and heat transfer in U-bends: The effect of secondary flows in ducts with partial and full curvature", *Int. J. Therm. Sci.* **130** (2018), p. 70-93.

[36] P. H. M. Bovendeerd, A. A. V. Steenhoven, F. N. V. D. Vosse, G. Vossers, "Steady entry flow in a curved pipe", *J. Fluid Mech.* **177** (1987), p. 233-246.

[37] R. Budwig, "Refractive index matching methods for liquid flow investigations", *Exp. Fluids* **17** (1994), no. 5, p. 350-355.

[38] Y. K. Agrawal, R. Sabbagh, S. Sanders, D. S. Nobes, "Measuring the Refractive Index, Density, Viscosity, pH, and Surface Tension of Potassium Thiocyanate (KSCN) Solutions for Refractive Index Matching in Flow Experiments", *J. Chem. Eng. Data* **63** (2018), no. 5, p. 1275-1285.

[39] P. O. Ayegba, J. Sebilleau, C. Colin, "Hydrodynamics of vertical upward and downward flow boiling in a millimetric tube", *Int. J. Multiphase Flow* **153** (2022), article no. 104120.

Comptes Rendus
Mécanique
2023, Vol. 351, Special Issue S2, p. 219-231
https://doi.org/10.5802/crmeca.142

Physical Science in Microgravity within the Thematic Group Fundamental and Applied Microgravity / *Sciences physiques en microgravité au sein du GDR Micropesanteur Fondamentale et Appliquée*

In situ experiments in microgravity and phase-field simulations of the lamellar-to-rod transition during eutectic growth

Silvère Akamatsu [a], Sabine Bottin-Rousseau [a], Melis Şerefoğlu [b], Victor T. Witusiewicz [c], Ulrike Hecht [c] and Mathis Plapp [*, d]

[a] Sorbonne Université, CNRS-UMR 7588, Institut des NanoSciences de Paris, case courrier 840, 4 place Jussieu, 75252 Paris Cedex 05, France

[b] Department of Metallurgical and Materials Engineering, Marmara University, Maltepe, İstanbul, Turkey

[c] Access e.V., Intzestr. 5, 52072 Aachen, Germany

[d] Laboratoire de Physique de la Matière Condensée, CNRS, Ecole Polytechnique, Institut Polytechnique de Paris, 91120 Palaiseau, France

E-mails: silvere.akamatsu@insp.jussieu.fr (S. Akamatsu), bottin@insp.jussieu.fr (S. Bottin-Rousseau), mserefoglukaya@gmail.com (M. Şerefoğlu), v.vitusevych@access-technology.de (V. T. Witusiewicz), u.hecht@access-technology.de (U. Hecht), mathis.plapp@polytechnique.edu (M. Plapp)

Abstract. In recent experiments on the solidification of the binary eutectic alloy succinonitrile-(D)camphor carried out on board of the International Space Station (ISS), a transition from rod to lamellar patterns was observed for low growth velocities. The transition was interpreted in terms of a competition between a propagative instability of lamellae and a drift induced by a transverse temperature gradient. Phase-field simulations of a symmetric model alloy support this scenario: for a fixed transverse temperature gradient, the transition from rods to lamellae occurs for a critical composition at fixed velocity, and for a critical velocity at fixed composition. Since the alloy and control parameters used in experiments and simulations are different, our results strongly suggest that this morphological transition is generic for eutectic alloys.

Keywords. Solidification, Eutectic alloys, In situ experiments, Modeling, Microgravity, Pattern formation.

Published online: 8 February 2023

* Corresponding author.

1. Introduction

Experiments on crystal growth and solidification in microgravity have a long tradition [1–12]. The main reason is that the growth of any crystal from melt or solution is accompanied by concentration and/or temperature gradients, and, on ground, the concomitant density gradients create convective motion of the fluid. This complicates the analysis of the growth process and makes a precise control of the growth conditions difficult. Experiments in reduced gravity thus offer a unique possibility to obtain data which can be compared to theories and mathematical models without convection. Examples of such studies in solidification science include benchmark data on dendritic and cellular growth in dilute binary alloys [1,9,10], as well as experiments on eutectic solidification [12].

In addition to such "planned" benchmark data, microgravity experiments can also reveal new effects that would be masked by convection under terrestrial conditions. One example is the recent observation of oscillatory growth modes in cellular solidification [9] that were predicted by numerical simulations [13], but never observed in experiments under terrestrial conditions. In the present contribution, we report on another phenomenon that is difficult to observe on the ground in large samples: the transition from lamellar to rod eutectic growth upon a change of solidification velocity.

A binary eutectic alloy exhibits a temperature T_E in its phase diagram at which the liquid can be in equilibrium with two distinct solids of different compositions. Alloys with a composition sufficiently close to the concentration C_E of the eutectic liquid directly freeze into a two-phase solid. The volume fractions of the two solid phases are approximately fixed by thermodynamics through the lever rule. The spatial organization of the two phases in the bulk solid results from a spontaneous pattern-formation process at the solid-liquid interface. An interplay between diffusion of chemical species in the liquid and capillary effects leads to the emergence of various coupled-growth patterns.

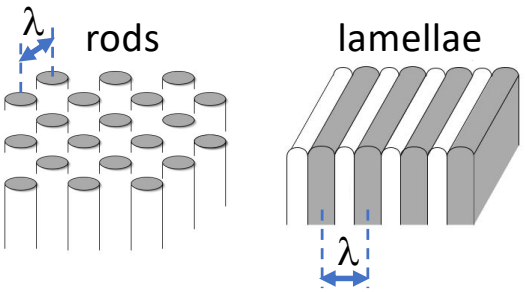

Figure 1. Rod-like and lamellar patterns (schematics). λ: interphase spacing.

The most common coupled-growth patterns are alternating lamellae of the two phases, and rods of the minority phase in a matrix of the majority phase. They are typically obtained during directional solidification, that is, by pulling an alloy sample toward the cold part of a fixed temperature gradient at a fixed velocity V. The standard theory of eutectic growth, formulated by Jackson and Hunt [14], predicts that the characteristic length scale of both lamellae and rods, λ_{JH}, varies as the geometric mean of the diffusion length $l_D = D/V$ (where D is the chemical diffusion coefficient in the liquid), and the capillary length d_0, which is proportional to the surface energy of the solid-liquid interfaces. As a consequence, the product $\lambda_{JH}^2 V$ is constant. It is also commonly stated that lamellae are favored over rods if the volume fractions of the two phases are comparable, whereas rods form for strongly different volume fractions. In this context, the

two relevant variables that control eutectic morphologies are the concentration and the scaled spacing $\Lambda = \lambda/\lambda_{JH}$. Previous studies of morphologies and instabilities have been analyzed in terms of these quantities [15–20].

The above considerations also imply that a dynamic transition between lamellae and rods is expected only when the volume fraction of the solid phases changes with space and/or time, as could indeed happen in the presence of macrosegration [21]. Such a transition has been observed in phase-field simulations in which the average concentration can be controlled at will [20].

It came thus as a great surprise that a transition from rods to lamellae was observed both in microgravity and ground experiments after a velocity jump [22, 23]. Indeed, according to the scaling theory outlined above, a change of the velocity should change the overall scaling length, but not the morphology.

A tentative explanation of this observation had to take into account several known facts. First, in phase-field simulations it was observed that the transition from lamellae to rods proceeds in a propagative manner: the instability starts at lamella terminations, and one rod after another "pinches off" from the lamella [20]. Second, directional solidification experiments often present a residual transverse temperature gradient which makes the patterns drift laterally when observed along the growth direction [24]. The transition between morphologies could therefore result from the balance between a propagative instability and a lateral drift of the microstructures.

Here, we present the experimental data together with preliminary phase-field simulations which support this scenario. The simulations are carried out for various compositions, transverse temperature gradients, and velocities, and it is shown that a transition from rods to lamellae can be triggered both by increasing the volume fraction of the minority phase, and by lowering the velocity. Whereas no quantitative agreement between experiments and simulations is reached, the simulation data clearly bear out the proposed scenario for the lamella-to-rod transition.

The remainder of this article is structured as follows: we first present the experimental observations made with the Transparent Alloys (TA) apparatus onboard the International Space Station (ISS) in section 2. Then, we outline the tentative interpretation of these observations in section 3. Results of phase-field simulations are presented in section 4, followed by conclusions in section 5.

2. Experiments

2.1. *Methods*

The succinonitrile-(d)camphor (SCN-DC) system ($T_E = 38.3$ °C; $C_E = 13.9$ mol%) [25] is a well-known model transparent eutectic alloy for in situ solidification studies [26–29]. It solidifies into nearly pure SCN and DC crystal phases that grow nonfaceted from the melt. The small volume phase fraction of the DC solid phase $\eta \approx 0.24$ favors the formation of DC rods in an SCN matrix. The constant $\lambda_{JH}^2 V = 10.2 \pm 1.5$ μm$^3 s^{-1}$ has been estimated in Ref. [27]. Eutectic alloys were prepared with purified SCN and DC. For microgravity experiments, the alloy was contained in a rectangular cartridge with optically flat fused-silica walls (Hellma). We shall define an **xyz** reference frame with **z** being the main solidification axis, **x** the lateral axis parallel to the isotherms, and **y** the transverse axis perpendicular to **x** and **z**. The useful-space dimensions of the samples were 6 mm along **x**, 1 mm along **y** (sample thickness), and 70 mm along **z**.

The TA apparatus (Qinetiq Space, Antverp, Belgium) was designed under the supervision of the European Space Agency (ESA), based on the same method as that presented in Ref. [30]. It has been installed in the Microgravity Science Glovebox (MSG) facility onboard the ISS. The TA setup permits to impose an axial temperature gradient G of about 50 ± 10 Kcm^{-1} in the region of the growth front for regular directional solidification (DS), and to control a transverse gradient

so that the isotherms could be tixted about the **x** axis (tilted-DS configuration; Fig. 2). The tilt angle ϕ was actually set to $-6.2 \pm 0.3^{\circ}$. With no tilt ($\phi = 0$), the two straight (when averaged over a long distance) contact lines of the solid-liquid interface with the sample walls (those lines are parallel to the **x** axis) are located at the same z coordinate. By setting $\phi \neq 0$, those two lines remain parallel to each other, but their **z** positions are different. The term of "foremost contact line" will designate the contact line that lies at the larger z value. For solidification, the sample was pulled at a well-controlled velocity V (between 0.007 and 0.04 μms^{-1}) along **z** toward the cold part. Real-time observation was performed from the exterior with a long-distance optics at a fixed, oblique incidence (in the **xz** plane), with an oblique-view angle θ_{opt} set to $43.6 \pm 0.3^{\circ}$ about **y**. The optical system delivers dark-field images of the solidification pattern with sharp contrast between the bright DC phase and the dark SCN matrix [30]. Astigmatism due to plane diopters was partly corrected (Lambda-X, Nivelles, Belgium). With the help of elementary numerical processing, good-quality images with a 1:1 aspect ratio were obtained over about 2/3 of the sample thickness. During microgravity experiments, partially automatized TA operations were remotely controlled by telescience from the operation center (E-USOC, Madrid, Spain). Experiments were carried out following a standard protocol: partial directional melting; directional solidification at constant velocity during long period of times (thus reaching a steady-state regime) separated by stepwise V changes (or "jumps"). Morphological changes over time scales ranging from a few minutes to tens of hours were monitored continually. Importantly, no convection motion was observed in the liquid. More technical details can be found in Ref. [22], and references therein.

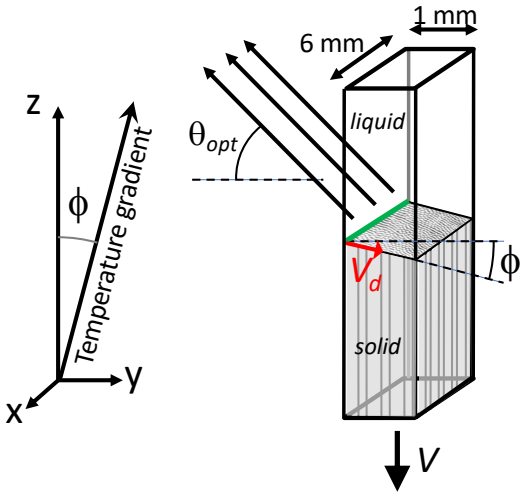

Figure 2. Principle of the tilted-DS method. In green: foremost contact line. Red arrow: drifting direction of the coupled-growth pattern. Symbols: see text.

2.2. *Results*

In order to obtain reference observations in a microgravity environment, regular-DS experiments –that is, with no measurable tilt of the isotherms– were performed. A decreasing-velocity program was operated, starting with $V = 0.04$ μms^{-1}, and ending with $V = 0.007$ μms^{-1}. The alloy was solidified for about 150 hours at the latter velocity. Rod-like patterns made of domains with local hexagonal order, separated by topological defects were observed over the explored V range, in

agreement with previous observations on ground [28, 29]. In practice, after a downward velocity jump, many rods were eliminated (the average spacing was below the rod elimination threshold). At constant velocity, a slow transverse stretching of the pattern, hence a continual increase of the rod spacing, was observed. It was due to a slight forward curvature of the envelope of the growth front (mean radius of curvature: 9-10 mm). This instrumental effect is determined by a deformation of the isotherms, which originates from the different thermal conductivities of the media in presence (glass walls, liquid and solid alloy), both on ground [28], and in microgravity [22]. At long times, the increase of the rod spacing was eventually balanced by rod splitting events. The quasi steady-state distribution of the spacing then roughly extended between the rod elimination threshold λ_{el} on the low-λ side, and the rod-splitting threshold λ_{sp} on the large-λ side. The average spacing λ_{av} was close to λ_{JH}. The stretching effect also provoked a progressive alignment of the hexagons, mostly with dense rows tending to align parallel or perpendicular to the sample walls. Short lamellae were observed at the lowest velocity, close to subboundaries, and in contact with the sample wall (Fig. 3a).

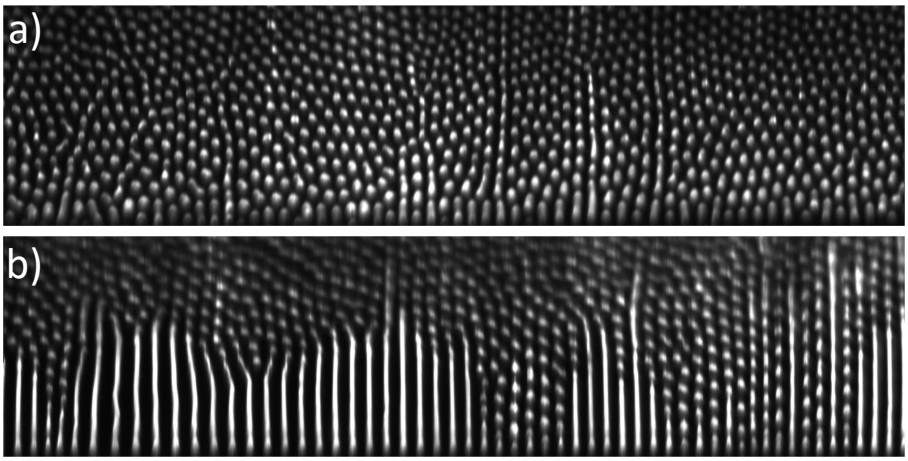

Figure 3. Coupled-growth patterns (eutectic SCN-DC alloy) during DS experiments in microgravity at a low pulling velocity ($V = 0.007\ \mu\text{ms}^{-1}$). a) Regular DS. b) Tilted-isotherm DS. The foremost contact line with the sample wall is at the bottom of the image. Vertical dimension: 500 μm (the upper part of the image was slightly off focus, and is not shown here).

Using the tilted-isotherm configuration, with a fixed inclination of the main axis of the temperature gradient by an angle ϕ from the axis **z**, a global drift of the coupled-growth pattern was imposed along the transverse direction **y**. That tilted-DS strategy was used in a previous study (with another transparent eutectic alloy) to propagate a periodic lamellar pattern at the expense of a labyrinth-like pattern [24]. Here, a similar effect – a lateral drift of the pattern – permitted to establish a long-lived coexistence between a pre-existing rod-like pattern and a fresh lamellar domain. Let us review the main stage of that process. We measured the global drift velocity V_d, and confirmed that its component along the **y** axis was approximately equal to $V\tan\phi$, according to the geometry of the system, with the rods growing essentially perpendicular to the average front envelope. New rods appeared by splitting at the foremost contact line (Fig. 2). At $V = 0.04\ \mu\text{ms}^{-1}$, no lamellae formed. An efficient alignment of the hexagon domains normal to the sample walls was observed. Long lamellae were observed at low velocity ($V = 0.007\ \mu\text{ms}^{-1}$) after relatively long rod-elimination transient, during which the alignment of the hexagons in the

initial situation was, however, essentially preserved. At that velocity, short, wavy lamellae in the core of the pattern were unstable, breaking up into rods on both ends before reaching a length larger than, say, two or three times the inter-rod spacing in the surrounding pattern. In contrast, straight lamellae that appeared at the foremost contact line were observed to elongate perpendicular to the sample wall. The longest ones were reaching about 500 μm at the ending time of the experiment. A large, stable lamellar pattern was thus growing at the expense of the initial rod-like pattern. This experiment provides, in other words, a clear evidence of a coexistence of dynamically metastable rod-like and lamellar patterns in the form of large domains with uniform morphological features – in contrast to mixed, transient patterns observed previously in directionally solidified eutectic alloys in bulk containers [21, 31, 32] and in confined-geometry samples [33].

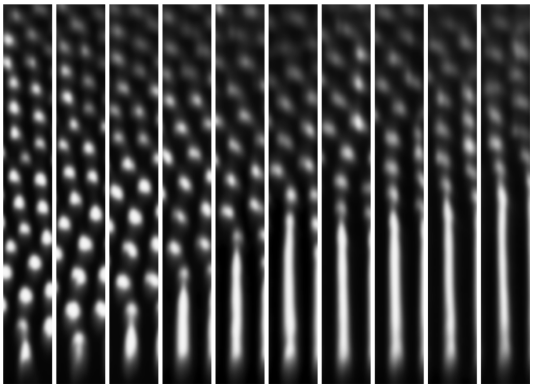

Figure 4. Series of ten successive snapshots showing the time evolution (from left to right) of a single lamella (detail). Same experiment as in Fig. 3b. Time interval between the images: 9 hours 36 minutes. Horizontal dimension of each panel: 60 μm.

Remarkably, the growth rate of the lamellar domain was significantly slower than V_d. The mechanism at play is illustrated in Fig. 4, which shows the evolution of a single lamella within the domain. It can be seen that the lamella formed via the elongation of a rod that was initially located at the foremost contact line. In the first stages, the rod elongated and split several times, until it started to elongate more durably. From that moment, the end of the new lamella in contact with the sample wall remained stable over the whole duration of the experiment. In contrast, the free end (or termination) underwent a repeated breakup, thus emitting new rods that drifted at the velocity V_d once included in the surrounded hexagon pattern. Each breakup event was preceded, and followed by an undulating instability. This scenario is schematically represented in Fig. 5.

3. Tentative interpretation

The experimental observations reported above, together with the results of previous numerical simulations, indicate a possible scenario for the transition from a rod to a lamellar pattern. The "natural" pattern is rod-like, in the sense that the evolution of an extended system from a "random" (that is, largely uncontrolled) initial state of the crystallization front will produce a rod pattern. In the presence of a transverse temperature gradient, lamellae can then grow starting at the sample wall. Such lamellae are subject to two antagonistic effects: (i) the drift induced by the misalignment between the temperature gradient and the sample wall, together with the fact that the lamellae remain "anchored" to the sample wall, leads to an elongation of the lamellae, and (ii) the pinch-off instability at the lamella termination leads to the creation of new rods and thus to a

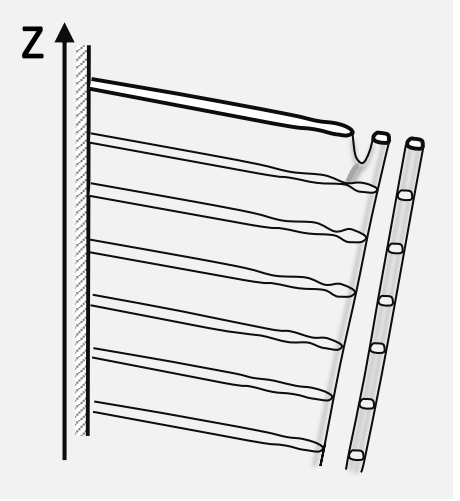

Figure 5. Scheme of the competition between lateral drift and propagating breakup of a lamella of the minority phase. The newly formed rod grows along the direction of the temperature gradient, which is tilted with respect to the sample wall.

shortening of the lamella. If the drift velocity is larger than the propagation velocity of the lamella breakup, the lamellae grow, and could fill the entire system if the duration of the experiment was long enough. In the opposite case, the lamellae can never grow to an appreciable size.

The crucial point is therefore the comparison between the drift velocity and the propagation velocity of the lamella breakup instability. Whereas the former can be linked to the structure of the thermal field, the latter is an intrinsic property of the eutectic system and cannot easily be determined. In the following section, we report on preliminary phase-field simulations which shed some light on this point.

4. Phase-field simulations

We performed three-dimensional phase-field simulations using the model developed in Ref. [34] and the code that has been used in previous simulations of eutectic systems [19, 20, 24, 35]. Our first goal is to confirm the scenario outlined above, and to investigate whether it is generic. For this purpose, it is advantageous to choose alloy and control parameters that lead to efficient numerical calculations, without seeking to reproduce quantitatively the SCN-DC system.

As in previous studies, we use a phase diagram that is completely symmetric with respect to an exchange of the two solid phases α and β, and which has parallel liquidus and solidus lines for the solid-liquid equilibria, and vertical solvus lines. We use a scaled composition variable $c = C - C_E/(C_\beta - C_\alpha)$, where C_E, C_α, and C_β are the concentrations of the liquid and the two solid phases at the eutectic temperature T_E. The nominal volume fractions of the two solid phases are related to the initial composition of the liquid c_0 by $\eta_\alpha = 0.5 - c_0$ and $\eta_\beta = 0.5 + c_0$. As usual, we define three characteristic lengths: the diffusion length $l_D = D/V$, the thermal length $l_T = m\Delta C/G$, and the capillary length $d_0 = \gamma T_E/(L|m|\Delta C)$, with γ the solid-liquid surface free energy (assumed equal for both solid-liquid interfaces), L the latent heat, m the liquidus slope, and $\Delta C = C_\beta - C_\alpha$. The characteristic spacing $\lambda_{JH} \sim \sqrt{l_D d_0}$. The spatial resolution of the phase-field model is set by the thickness W of the diffuse interfaces. We fixed the ratio $l_T/d_0 = 4000$ and simulated two different velocities, corresponding to $l_D/d_0 = 1000$ and $l_D/d_0 = 2000$, respectively;

in the following, we will refer to these two sets as the "fast" and the "slow" velocities. The interface thickness was set to $W/d_0 = 10.826$; this yields $\lambda_{JH} \approx 20\,W$ and $\lambda_{JH} \approx 30\,W$ for the fast and slow velocities, respectively, which is in the range where the phase-field model is well converged. A multi-grid algorithm was employed to achieve both a good resolution of the interface and an efficient treatment of the long-range diffusion field; the grid spacing in the interface region was chosen as $\Delta x = 0.8\,W$. Growth with a transverse temperature gradient is simulated by choosing the thermal field

$$T(x, y, z, t) = T_E + G\left(z + y\sin\phi - V\,t\right), \tag{1}$$

where $z = 0$ is defined by the position of the eutectic isotherm at the colder side of the sample ($y = 0$) at $t = 0$. The simulation is started with a disordered initial condition, that is, a solid that is a random mixture of domains in a proportion that corresponds to the lever rule.

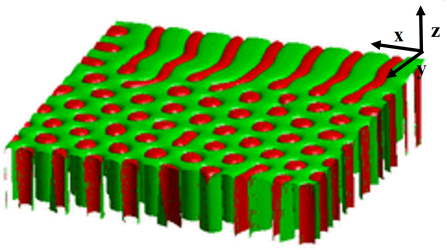

Figure 6. Three-dimensional view of a mixed pattern for $c_0 = 0.16$ and $\phi = 4°$.

Without a transverse temperature gradient ($\phi = 0$), the simulations yield disordered rod patterns that evolve slowly in time by local geometric rearrangements. With $\phi \neq 0$, the patterns depend on the liquid composition c_0. A three-dimensional view of the simulation cell (of lateral section $160 \times 160\,W$) for $\phi = 4°$ is shown in Fig. 6. Here, for better viewing, the foremost contact line (at $y = 0$) is at the rear of the image; the global tilt of the eutectic front can clearly be distinguished. Fig. 7 displays top views of the crystallization front for three different compositions ($c_0 = 0.15$, 0.16, and 0.17, respectively) at three different times, all for $\phi = 4°$ and for the faster velocity. The morphology at long times clearly depends on c_0. For $c_0 = 0.15$, lamellae start to grow at the foremost contact line, elongate across the sample, essentially without pinchoff events, and fill the entire sample at the end of the simulation. A zigzag instability occurs, so that the lamella are not straight. Stable zigzag patterns have been observed both in experiments [36] and in simulations [19] when the lamellar spacing exceeds approximately $1.2\,\lambda_{JH}$. In the present experiments, zigzag patterns are observed locally as transient structures [22]; their stability in the simulations in Fig. 7 is possibly due to the small sample size. For $c_0 = 0.16$, lamellae start to grow, but pinchoff occurs at their terminations. The balance between drift and pinchoff seems to depend on the local spacing; some parts of the lamellar front advance well while others lag behind. The rods that have been created by pinchoff events form a regular triangular lattice without defects. Finally, for $c_0 = 0.17$, one can distinguish short "pieces" of lamellae at the foremost contact line, but they never grow longer than about one interrod spacing.

Some particular features of the runs, such as the occurrence of the zigzag instability for $c_0 = 0.15$, the fact that certain lamellae are connected to the sample wall whereas others exhibit a gap, or the inhomogeneous dynamics of the lamellar front, certainly depend on the details of the random initial condition. Nevertheless, it is clear that there is a transition between a lamellar and rod final state for $c_0 \approx 0.16$ (which corresponds to $\eta_\alpha \approx 0.34$) for the tilt angle of $\phi = 4°$.

We repeated similar series of runs for the slower velocity. The average interrod and interlamellar spacing was larger, following the $V^{-1/2}$ scaling. However, a clear departure from scaling occurs,

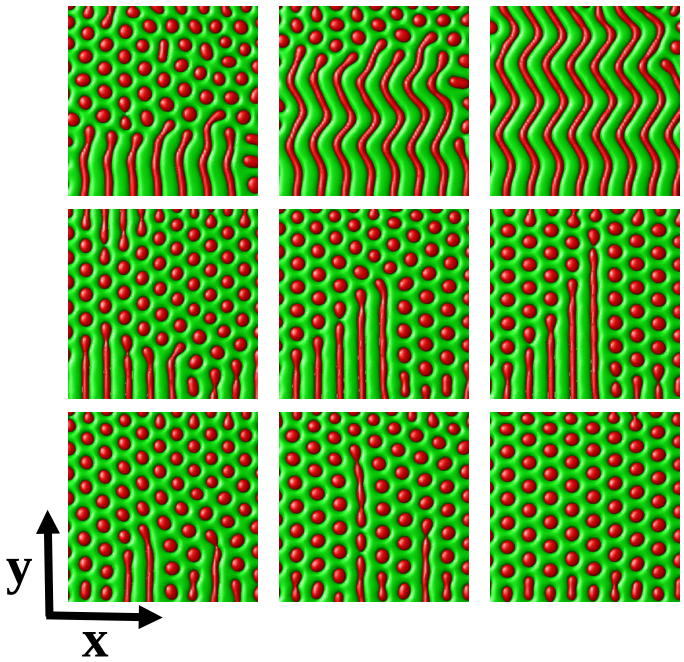

Figure 7. Top views of samples with different composition, at different times. Top row: $c_0 = 0.15$. Middle row: $c_0 = 0.16$. Bottom row: $c_0 = 0.17$. Left, middle and right columns: three times corresponding to solidification distances of 4.8, 9.6 and 14.4 times the lateral system size, respectively. The tilt angle is $\phi = 4°$.

in that the transition between the two morphologies happens for a much lower volume fraction of the minority phase, around $\eta_\alpha \approx 0.25$ ($c_0 \approx 0.25$).

Since the critical volume fraction for the transition from rods to lamellae decreases with decreasing velocity, for a fixed composition (at least in the range between the two critical compositions determined for high and low velocity), there must exist a critical velocity below which the creation of lamellae becomes favored. This is in qualitative agreement with the experimental observations. Furthermore, we performed simulations for different values of the tilt angle. The drift velocity of the rods increased with increasing tilt, and the transition between rods and lamellae occurred for increasing tilt angle at fixed composition and velocity, in agreement with the observations in the experiments of Ref. [22].

The breakup of lamellae can be studied in more detail by performing simulations of single lamellae without a transverse temperature gradient. To this end, a single lamella of spacing 32 W (close to λ_{JH}) is placed in an elongated simulation box with zero-gradient Neumann boundary conditions for all fields on all lateral walls. To trigger the lamella breakup, a small piece of the lamella is removed on one end of the box as illustrated in Fig. 8a; the newly created lamella termination then retracts and forms a round bulbous shape. For $c_0 = 0.26$ (Fig. 8b), this shape remains stationary and no further evolution occurs. For higher concentrations (Figs. 8c, d, and e for $c_0 = 0.27, 0.28$, and 0.29, respectively), successive pinchoff events occur at regular time intervals and create elongated rods. The propagation velocity was determined by dividing the interrod distance by the time interval between pinchoffs; it increases linearly with the distance

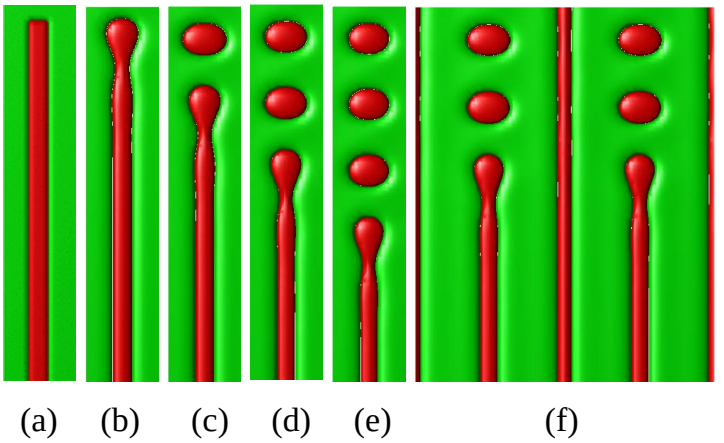

Figure 8. Top views of lamella breakup at the slow velocity without tilt ($\phi = 0°$). (a) initial condition, (b) $c_0 = 0.26$, (c) $c_0 = 0.27$, (d) $c_0 = 0.28$, (e) $c_0 = 0.29$, (f) $c_0 = 0.28$, with neighboring intact lamellae. Snapshots (b) to (f) are all taken after the same solidification distance of 10 lamellar spacings. The lamella termination is stable in (b), whereas lamella breakup is in progress in snapshots (c) to (f).

from the threshold composition ≈ 0.26. A similar transition occurs when the velocity is varied at fixed composition: the lamellar termination is stable below a critical velocity, but unstable above, and the breakup propagation velocity increases linearly with the distance from this velocity threshold.

Since the zero-gradient Neumann boundary conditions are equivalent to a plane of mirror symmetry, the simulations discussed so far correspond to a simultaneous breakup of an infinity of lamellae into a rectangular array of rods. Since such a geometry is never observed in the experiments, we performed several simulations with two lamellae to test the influence of the boundaries on the breakup dynamics. As an example, Fig. 8f shows a simulation cell where the lamella with the termination is placed between two unperturbed lamellae (for a better view of the morphology, two copies of the simulation cell are displayed next to each other). The intact lamellae develops tiny undulations but remain stable, whereas the breakup of the lamella termination proceeds with the same velocity as before.

Besides on velocity and composition, the breakup propagation velocity as well as the critical values for composition and velocity also depend on the lamellar spacing, and possibly on the transverse temperature gradient. For a full quantitative understanding of the morphology transition, these dependencies would need to be studied in detail, but this is outside of the scope of the present work.

5. Conclusion

The results of experiments and phase-field simulations presented here indicate a possible mechanism for the transition from rods to lamellae in directional solidification of eutectic alloys when the velocity is decreased.

The centerpiece of the argument is a competition between the propagative breakup of lamellae and a lateral drift of lamella terminations, starting at one side wall of the sample, which is

driven by a transverse temperature gradient. The phase-field simulations have revealed that for a fixed velocity, there is a critical volume fraction above which the replacement of the rod by a lamellar pattern takes place, and that this critical composition depends on the velocity. As a corollary, for a fixed composition there exists a critical velocity below which the growth of lamellae is favored. Note that this also implies that the transition can happen both ways, from rods to lamellae or from lamellae to rods, for decreasing and increasing velocity, respectively. It can also be triggered by a change in tilt angle.

Since the alloy phase diagram and the control parameters differ between experiments and simulations, these results indicate that this scenario is generic. For a more quantitative understanding, it is necessary to obtain more information on the propagative instability of lamellae as a function of lamellar spacing, volume fraction, and pulling velocity. It should be mentioned that this instability is clearly distinct from the Rayleigh–Plateau instability of a liquid jet [37] or diffusive instabilities of one-dimensional solid structures [38], since these instabilities do not have a threshold: a liquid jet or a solid cylinder is always unstable under the action of capillarity. In contrast, eutectic lamellae are stable for extended composition and velocity ranges. Furthermore, the transition might also be influenced by crystallographic effects (interface anisotropy), as recently evidenced for example in Ref. [39]. Phase-field simulations are clearly a promising tool to obtain more data on these questions.

An interesting perspective for experiments in microgravity would be to solidify a sample in which the liquid composition varies in space; this could be achieved by melting a solid sample that contains a carefully prepared concentration gradient. While this would be a "one-shot experiment" because the concentration gradient would decrease in the course of the experiment by diffusion in the liquid, it could still provide valuable insights on the lamella-to-rod transition since in this setting the transition occurs on a shorter time scale than in the experiments described here. Preparations for this kind of experiment are currently ongoing.

Conflicts of interest

The authors declare no competing financial interest.

Dedication

The manuscript was written through contributions of all authors. All authors have given approval to the final version of the manuscript.

Acknowledgments

This work has been supported by the Centre National d'Etudes Spatiales (CNES), France, via the Groupement de recherche (GDR) Micropesanteur Fondamentale et Appliquée (MFA) of the French Centre National de la Recherche Scientifique (CNRS).

References

[1] M. E. Glicksman, M. B. Koss, E. A. Winsa, "Dendritic Growth Velocities in Microgravity", *Phys. Rev. Lett.* **73** (1994), no. 4, p. 573-576.

[2] L. A. Tennenhouse, M. B. Koss, J. C. LaCombe, M. E. Glicksman, "Use of microgravity to interpret dendritic growth kinetics at small supercoolings", *J. Cryst. Growth* **174** (1997), p. 82-89, 10th American Conference on Crystal Growth/9th International Conference on Vapor Growth and Epitaxy, VAIL, CO, AUG 04-09, 1996.

[3] J. C. LaCombe, M. B. Koss, V. E. Fradkov, M. E. Glicksman, "Three-dimensional dendrite-tip morphology", *Phys. Rev. E* **52** (1995), no. 3, p. 2778-2786.
[4] M. B. Koss, J. C. LaCombe, L. A. Tennenhouse, M. E. Glicksman, E. A. Winsa, "Dendritic growth tip velocities and radii of curvature in microgravity", *Metall. Mater. Trans. A* **30** (1999), p. 3177-3190.
[5] J. J. Favier, J. P. Garandet, A. Rouzaud, D. Camel, "Mass-transport phenomena during solidification in microgravity – Preliminary results of the 1st MEPHISTO flight experiment", *J. Cryst. Growth* **140** (1994), p. 237-243.
[6] B. Drevet, H. Nguyen-Thi, D. Camel, B. Billia, M. D. Dupouy, "Solidification of aluminium-lithium alloys near the cell/dendrite transition-influence of solutal convection", *J. Cryst. Growth* **218** (2000), no. 4-5, p. 419-433.
[7] D. J. Jarvis, O. Minster, "Metallurgy in space", in *Solidification and Gravity IV* (R. Roósz, M. Rettenmayr, Z. G'ácsi, eds.), Materials Science Forum, vol. 508, Univ Miskolc, Mat & Met Engn Fac, Phys Met & Metalforming Dept; Hungarian Acad Sci, Res Grp Mat Sci; NASA MSFC; HAS, Mickolc Comm; Hungarian Space Off; Assoc Hungarian Foundries, Trans Tech Publications, 2006, 4th International Conference on Solidification and Gravity, Miskolc Lillafured, HUNGARY, SEP 06-09, 2004, p. 1-18.
[8] J. P. Garandet, G. Boutet, P. Lehmann, B. Drevet, D. Camel, A. Rouzaud, J. J. Favier, G. Faivre, S. Coriell, J. I. D. Alexander, B. Billia, "Morphological stability of a solid-liquid interface and cellular growth: Insights from thermoelectric measurements in microgravity experiments", *J. Cryst. Growth* **279** (2005), no. 1-2, p. 195-205.
[9] N. Bergeon, D. Tourret, L. Chen, J.-M. Debierre, R. Guérin, A. Ramirez, B. Billia, A. Karma, R. Trivedi, "Spatiotemporal Dynamics of Oscillatory Cellular Patterns in Three-Dimensional Directional Solidification", *Phys. Rev. Lett.* **110** (2013), article no. 226102.
[10] D. Tourret, J.-M. Debierre, Y. Song, F. L. Mota, N. Bergeon, R. Guérin, R. Trivedi, B. Billia, A. Karma, "Oscillatory cellular patterns in three-dimensional directional solidification", *Phys. Rev. E* **92** (2015), no. 4, article no. 042401.
[11] G. Salloum-Abou-Jaoude, H. Nguyen-Thi, G. Reinhart, R. H. Mathiesen, G. Zimmermann, D. Voss, "Characterization of Motion of Dendrite Fragment by X-Ray Radiography on Earth and under Microgravity Environment", *Materials Science Forum* **790-791** (2014), p. 311-316.
[12] M. Plapp, S. Bottin-Rousseau, G. Faivre, S. Akamatsu, "Eutectic solidification patterns: Interest of microgravity environment", *Comptes Rendus Mécanique* **345** (2017), no. 1, p. 56-65, Basic and applied researches in microgravity – A tribute to Bernard Zappoli's contribution.
[13] M. Plapp, M. Dejmek, "Stability of hexagonal solidification patterns", *Eur. Phys. Lett.* **65** (2004), no. 2, p. 276-282.
[14] K. A. Jackson, J. D. Hunt, "Lamellar and Rod Eutectic Growth", *Transactions of the Metallurgical Society of AIME* **236** (1966), p. 1129-1142.
[15] K. Kassner, C. Misbah, "Similarity laws in eutectic growth", *Phys. Rev. Lett.* **66** (1991), no. 4, p. 445-448.
[16] K. Kassner, C. Misbah, "Spontaneous parity-breaking transition in directional growth of lamellar eutectic structures", *Phys. Rev. A* **44** (1991), no. 10, p. 6533-6543.
[17] A. Karma, A. Sarkissian, "Morphological instabilities of lamellar eutectics", *Metall. Mater. Trans. A* **27** (1996), p. 635-656.
[18] M. Ginibre, S. Akamatsu, G. Faivre, "Experimental determination of the stability diagram of a lamellar eutectic growth front", *Phys. Rev. E* **56** (1997), p. 780-796.
[19] A. Parisi, M. Plapp, "Stability of lamellar eutectic growth", *Acta Mater.* **56** (2008), no. 6, p. 1348-1357.
[20] A. Parisi, M. Plapp, "Defects and multistability in eutectic solidification patterns", *Europhysics Letters* **90** (2010), article no. 26010.
[21] S. Liu, J. H. Lee, R. Trivedi, "Dynamic effects in the lamellar-rod eutectic transition", *Acta Mater.* **59** (2011), no. 8, p. 3102-3115.
[22] S. Bottin-Rousseau, V. T. Witusiewicz, U. Hecht, J. Fernandez, A. Laveron-Simavilla, S. Akamatsu, "Coexistence of rod-like and lamellar eutectic growth patterns", *Scr. Mater.* **207** (2022), article no. 114314.
[23] M. Şerefoğlu, S. Bottin-Rousseau, S. Akamatsu, "Lamella-rod pattern transition and confinement effects during eutectic growth", *Acta Mater.* **242** (2023), article no. 118425.
[24] M. Perrut, A. Parisi, S. Akamatsu, S. Bottin-Rousseau, G. Faivre, M. Plapp, "Role of transverse temperature gradients in the generation of lamellar eutectic solidification patterns", *Acta Mater.* **58** (2010), no. 5, p. 1761-1769.
[25] V. T. Witusiewicz, L. Sturz, U. Hecht, S. Rex, "Thermodynamic description and unidirectional solidification of eutectic organic alloys: I. Succinonitrile-(D)camphor system", *Acta Mater.* **52** (2004), p. 4561-4571.
[26] M. Şerefoğlu, R. E. Napolitano, "On the selection of rod-type eutectic morphologies: Geometrical constraint and array orientation", *Acta Mater.* **56** (2008), no. 15, p. 3862-3873.
[27] S. Akamatsu, S. Bottin-Rousseau, M. Perrut, G. Faivre, V. T. Witusiewicz, L. Sturz, "Real-time study of thin and bulk eutectic growth in succinonitrile-(D)camphor alloys", *J. Cryst. Growth* **299** (2007), no. 2, p. 418-428.
[28] M. Perrut, S. Akamatsu, S. Bottin-Rousseau, G. Faivre, "Long-time dynamics of the directional solidification of rodlike eutectics", *Phys. Rev. E* **79** (2009), no. 3, article no. 032602.
[29] M. Perrut, S. Bottin-Rousseau, G. Faivre, S. Akamatsu, "Dynamic instabilities of rod-like eutectic growth patterns: A real-time study", *Acta Mater.* **61** (2013), p. 6802-6808.

[30] S. Bottin-Rousseau, M. Perrut, C. Picard, S. Akamatsu, G. Faivre, "An experimental method for the in situ observation of eutectic growth patterns in bulk samples of transparent alloys", *J. Cryst. Growth* **306** (2007), p. 465-472.

[31] V. Trnovcová, P. P. Fedorov, C. Bàrta, V. Labas, V. A. Meleshina, B. P. Sobolev, "Microstructure and physical properties of superionic eutectic composites of the LiF–RF_3 (R 5 rare earth element) system", *Solid State Ionics* **119** (1999), no. 1-4, p. 173-180.

[32] M. Neuroth, K. Recker, F. Wallrafen, "Investigations on the directional solidification of the eutectic LiF–$LiBaF_3$", *Zeitschrift für Kristallographie - Crystalline Materials* **209** (1994), no. 4, p. 295-302.

[33] M. Şerefloğlu, S. Bottin-Rousseau, S. Akamatsu, G. Faivre, "Dynamics of rod eutectic growth patterns in confined geometry", in *The 3rd International Conference on Advances in Solidification Processes 7–10 June 2011, Rolduc Abbey, Aachen, The Netherlands*, IOP Conference Series: Materials Science and Engineering, vol. 27, IOP Science, 2012.

[34] R. Folch, M. Plapp, "Quantitative phase-field modeling of two-phase solidification", *Phys. Rev. E* **72** (2005), no. 1, article no. 011602.

[35] M. Şerefloğlu, R. E. Napolitano, M. Plapp, "Phase-field investigation of rod eutectic morphologies under geometrical confinement", *Phys. Rev. E* **84** (2011), article no. 011614.

[36] S. Akamatsu, S. Bottin-Rousseau, G. Faivre, "Experimental evidence for a zigzag bifurcation in bulk lamellar eutectic growth", *Phys. Rev. Lett.* **93** (2004), no. 17, article no. 175701.

[37] L. Rayleigh, "Instability of Jets", *Philos. Mag.* **36** (1878), p. 4.

[38] F. A. Nichols, W. W. Mullins, "Surface-(Interface-) and volume-diffusion contributions to morphological changes driven by capillarity", *Transactions of the Metallurgical Society of AIME* **233** (1965), no. 10, p. 1840-1848.

[39] S. Khanna, S. K. Aramanda, A. Choudhury, "Role of Solid–Solid Interfacial Energy Anisotropy in the Formation of Broken Lamellar Structures in Eutectic Systems", *Metall. Mater. Trans. A* **51** (2020), p. 6327-6345.

Comptes Rendus
Mécanique
2023, Vol. 351, Special Issue S2, p. 233-247
https://doi.org/10.5802/crmeca.145

Physical Science in Microgravity within the Thematic Group Fundamental and Applied Microgravity / *Sciences physiques en microgravité au sein du GDR Micropesanteur Fondamentale et Appliquée*

Equiaxed growth of interacting Al–Cu dendrites in thin samples: a phase-field study at copper concentrations relevant for practical applications

Croissance équiaxe de dendrites Al–Cu en interaction dans des échantillons minces: une étude de champ de phase à des concentrations de cuivre pertinentes pour des applications pratiques

Tong Zhao Gong [a], **Ahmed Kaci Boukellal** [b], **Yun Chen** [a] **and Jean-Marc Debierre** *, [c]

[a] Shenyang National Laboratory for Materials Science, Institute of Metal Research, Chinese Academy of Sciences, Shenyang, Liaoning, 110016, P. R. China

[b] IMDEA Materials Institute, Getafe, Madrid, Spain

[c] Aix-Marseille Université, CNRS, Université de Toulon, IM2NP UMR 7334, 13397 Marseille, France

E-mails: tzgong15s@imr.ac.cn (T. Z. Gong), boukellalahmed@gmail.com (A. K. Boukellal), chenyun@imr.ac.cn (Y. Chen), Jean-marc.debierre@im2np.fr (J.-M. Debierre)

Abstract. We perform three-dimensional phase-field simulations of equiaxed solidification in Al–Cu thin samples. Purely diffusive conditions are considered in order to describe systems where convection and gravity effects can be neglected. The use of a parallel adaptive finite element algorithm introduced recently [Gong *et al.*, *Comput. Mater. Sci.* **147** (2018) p. 338-352] allows us to reach the domain of copper concentrations used in practical applications ($c \geq 3$ wt% Cu). We compare the present results with those of a previous study which was restricted to lower copper concentrations ($c \leq 2$ wt% Cu) [Boukellal *et al.*, *Materialia* **1** (2018) p. 62-69] due to the use of a finite difference code. In the fast dendritic growth regime, our results confirm that the

* Corresponding author.

dimensionless growth length Λ is independent of the copper concentration and the average separation distance between the dendrite nuclei. The new data obtained at higher copper concentrations lead to a more accurate estimate of Λ. Physical arguments are developed to specify the meaning of Λ and the grounds of the scaling law Λ = cst. Comparisons with available experimental results of the literature give additional support to this scaling law.

Résumé. Nous réalisons des simulations de type champ de phase tri-dimensionnel de la solidification equiaxe dans les échantillons minces d'Al–Cu. Des conditions purement diffusives sont considérées pour décrire des systèmes où la convection et la gravité peuvent être négligées. L'utilisation d'un algorithme parallèle adaptatif de type éléments finis proposé récemment [Gong *et al.*, *Comput. Mater. Sci.* **147** (2018) p. 338-352] nous permet d'atteindre le domaine des concentrations en cuivre utisées dans les applications pratiques ($c \geq 3$ wt% Cu). Nous comparons nos résultats à ceux d'une étude antérieure qui, en raison de l'utilisation d'un code de différences finies, était restreinte à des concentrations de cuivre plus faibles ($c \leq 2$ wt% Cu) [Boukellal *et al.*, *Materialia* **1** (2018) p. 62-69]. Dans le régime de croissance dendritique rapide, nos résultats confirment que la longueur de croissance adimensionnée Λ est indépendante de la concentration du cuivre et de la distance moyenne séparant les germes dendritiques. Les nouveaux résultats obtenus aux concentrations plus élevées conduisent à une estimation plus précise de Λ. Des arguments physiques sont développés pour préciser la signification de Λ et les fondements de la loi d'échelle Λ = cst. La comparaison avec les résultats expérimentaux disponibles dans la litérature scientifique apporte une confirmation supplémentaire de cette loi d'échelle.

Keywords. Metals and alloys, Solidification, Solute diffusion, Grain structure, Phase-field, Microgravity.

Mots-clés. Métaux et alliages, Solidification, Diffusion des solutés, Structure des grains, Champ de phase, Microgravité.

Published online: 13 January 2023

1. Introduction

The isotropic physical properties of industrial metallic parts, such as cast engine blocks are usually obtained by using equiaxed solidification processes. Many materials employed in related applications belong to the large family of aluminum alloys [1, 2], like the numerous variants of Al–Cu alloys that have been studied quite intensively over the last decades [3]. Since the final properties of such parts largely depend on the multigrain structure that is formed during their fabrication, predicting and controlling the interactions between two grains that grow toward each other is one of the key points of the equiaxed solidification processes.

Scaling laws that govern the grain growth and the grain–grain interactions in diffusive conditions were recently proposed in reference [4] (hereafter denoted as BEA). These laws are thought to be of practical relevance because they can be extrapolated to predict the dynamics of equiaxed dendrites in materials containing higher copper concentrations c_0, which are not easy to simulate directly. However, it is still reasonable to question the validity of such extrapolations because it is well known that the selection of the dendrite tip velocity and curvature is affected by the undercooling and thus by c_0 in a nontrivial way [5]. In the present study, phase-field simulations in three dimensions are performed to explore copper concentrations higher than the ones originally used in BEA. This is made possible by implementing the finite element algorithm with an adaptive space mesh introduced in reference [6] (hereafter denoted as GEA).

In the literature about Al–Cu solidification, many of the reported phase-field studies are either for directional solidification [7–9] or for solidification at constant applied undercooling [10]. The case of solidification with a constant cooling rate, as we consider here, is less commonly encountered [4, 11]. In Al–Cu alloys, heat diffuses much faster than mass. Moreover, the latent heat released at the solid–liquid interface of the growing dendrite is easily evacuated through the highly conducting crucible walls [12]. A frozen temperature approximation is thus adopted in the model. The resulting problem is, nonetheless, far from being trivial since the sample temperature is steadily decreased in time, which provokes a drift of the undercooling that drives

solute diffusion. Our model being purely diffusive, is directly suitable to describe experiments in micro-g environments.

In Section 2, we introduce the phase-field model that is used to simulate this process. The constitutive physical equations are discussed together with the corresponding phase-field equations, and their implementation in the numerical code is described. The present numerical results are given in Section 3 and they are used to test growth scaling laws previously obtained in BEA. Physical arguments are developed in Section 4 to justify these scaling laws. Finally, Section 5 summarizes our main conclusions and strategies to compare simulations to experiments performed both on earth and in micro-g conditions are evoked.

2. Phase-field model

2.1. *Physical equations*

We consider an aluminum alloy of average copper concentration c_0. The partition coefficient $k < 1$ and the liquidus slope $m < 0$, so $m(k-1) > 0$. At the liquidus temperature $T = T_0$, which corresponds to the average alloy concentration, the phase diagram imposes

$$c_0 = (T_0 - T_M)/m, \tag{1}$$

where T_M is the melting temperature of Al. In the reference frame where the material is at rest, the copper diffusion equation reads

$$\frac{\partial c(\vec{r},t)}{\partial t} = D\nabla^2 c, \tag{2}$$

where $c(\vec{r},t)$ is the copper concentration at location $\vec{r}$ and time t, and D is the solute diffusion coefficient that will be assumed zero in the solid phase (one-sided model). In addition, two local equations must be verified at any interface point. The first one expresses solute conservation and it imposes the interface normal velocity,

$$V_n = -D\left(\frac{\partial c}{\partial r}\right)_\ell, \tag{3}$$

the derivative being taken on the liquid (ℓ) side, in the direction perpendicular to the solid–liquid interface. The second one is the Gibbs–Thomson equation that expresses local thermodynamic equilibrium and that reads in terms of temperatures,

$$T_i = T_M + mc_i - \frac{\Gamma}{\rho} - \frac{V_n}{\mu}. \tag{4}$$

In this equation, ρ is the average radius of curvature, μ the linear kinetic coefficient, and the Gibbs–Thomson constant Γ is related to the chemical capillary length d_0 through

$$d_0 = \frac{\Gamma}{m(k-1)c_0}. \tag{5}$$

In the present case, solidification results from uniform cooling at a constant rate $R = 0.5$ K/min. Then the interface temperature $T_i = T_0 - Rt$, and we obtain the Gibbs–Thomson equation in terms of concentrations,

$$U_i^* = \frac{c_i - c_0}{(1-k)c_0} = -\frac{d_0}{\rho} - \beta_{\text{kin}} V_n + \frac{Rt}{m(k-1)c_0}, \tag{6}$$

where $\beta_{\text{kin}} = 1/[m(k-1)c_0\mu]$ is the kinetic coefficient in factor of the interface velocity. In the following, we will use the notation

$$\Theta(t) = -\frac{Rt}{m(k-1)c_0} \tag{7}$$

for the negative undercooling, which decreases in time as a result of the sample cooling.

2.2. *Phase-field equations*

Instead of the usual phase-field $-1 \leq \varphi \leq 1$, we use the preconditioned phase-field

$$\psi = \sqrt{2}\tanh^{-1}(\varphi) \tag{8}$$

that was shown to increase numerical precision for a given mesh size [13]. A number of recent phase-field studies confirmed that quantitative results are obtained when using the preconditioned phase-field [4,6,14–17]. We adopt the quantitative phase-field model introduced by Karma *et al.* to simulate the solidification of diluted alloys [18, 19]. The evolution equation for ψ is

$$\begin{aligned}\tau(\vec{n})[1-(1-k)\Theta]\frac{\partial\psi}{\partial t} &= W(\vec{n})^2(\nabla^2\psi - \sqrt{2}\varphi|\vec{\nabla}\psi|^2) \\ &+ \sqrt{2}[\varphi - \lambda(1-\varphi^2)(U+\Theta)] + \sum_{i=x,y,z} W_0^2\partial_i\left[(\vec{\nabla}\psi)^2 a_s\frac{\partial a_s}{\partial(\partial_i\psi)}\right],\end{aligned} \tag{9}$$

where $\vec{n}$ is the unit vector along the normal to the solid–liquid interface. The anisotropy function a_s of the interface width, $W(\vec{n}) = W_0 a_s(\vec{n})$, is taken to be that of the surface free energy, with W_0 the diffuse interface width. For Al–Cu alloys, the solid–liquid interface is rough at the atomic scale, so the kinetic coefficient β_{kin} can be set to zero for the low solidification velocities considered here. In practice, this is ensured by imposing two conditions. The first is that the anisotropic relaxation time $\tau(\vec{n}) = \tau_0 a_s^2(\vec{n})$ and the second that the constant λ that couples the non-dimensional concentration field U to the phase-field is equal to $(75/47)D\tau_0/W_0^2$ [20]. Since $W_0 = \xi d_0$ is adjusted by varying the numerical parameter ξ, this fixes $\tau_0 = (47\sqrt{2}/120)(d_0^2/D)\xi^3$. We follow the usual convention where lengths are scaled by W_0 and times by τ_0. The resulting non-dimensional evolution equation for ψ is then

$$\begin{aligned}a_s^2[1-(1-k)\Theta]\frac{\partial\psi}{\partial t} &= a_s^2(\nabla^2\psi - \sqrt{2}\varphi|\vec{\nabla}\psi|^2) \\ &+ \sqrt{2}[\varphi - \lambda(1-\varphi^2)(U+\Theta)] + \sum_{i=x,y,z}\partial_i\left[(\vec{\nabla}\psi)^2 a_s\frac{\partial a_s}{\partial(\partial_i\psi)}\right],\end{aligned} \tag{10}$$

where the crystal cubic anisotropy reads

$$a_s = (1-3\epsilon_4) + 4\epsilon_4(n_x^4 + n_y^4 + n_z^4), \tag{11}$$

with n_x, n_y, n_z are the three components of $\vec{n}$ and ϵ_4 the anisotropy strength [21]. As in the case of directional solidification, the imposed undercooling $\Theta(t)$ is also introduced on the left hand side of this equation to prevent the kinetic coefficient β_{kin} from deviating in time from its imposed value (zero here) [19]. The non-dimensional concentration field U is related to the physical concentration field c through

$$U = \frac{f_U(\varphi)c - c_0}{(1-k)c_0}, \tag{12}$$

with

$$f_U(\varphi) = \frac{2}{(1+k)-(1-k)\varphi}. \tag{13}$$

This is the diffuse interface version of the physical definition given in Equation (6): in the liquid phase, $\varphi = -1.0$, so $f_U(\varphi) = 1.0$.

As solute diffusion is neglected in the solid (one-sided model), a corrective solute current

$$\vec{j}_{at} = \frac{W_0}{2\sqrt{2}}c_0(1-k)[1+(1-k)U]\frac{1-\varphi^2}{\sqrt{2}}\frac{\partial\psi}{\partial t}\vec{n} \tag{14}$$

is introduced in the concentration evolution equation in order to counterbalance the excess of solute trapping and other spurious corrections due to the finite interface thickness W_0 [18, 19]. The non-dimensional evolution equation for U then reads [6]

$$\begin{aligned}[(1+k)-(1-k)\varphi]\frac{\partial U}{\partial t} &= [1+(1-k)U]\frac{1-\varphi^2}{\sqrt{2}}\frac{\partial \psi}{\partial t} \\ &+\vec{\nabla}\cdot\left\{D^*(1-\varphi)\vec{\nabla}U\right\} \\ &+\vec{\nabla}\cdot\left\{[1+(1-k)U]\frac{1-\varphi^2}{2}\frac{\partial \psi}{\partial t}\frac{\vec{\nabla}\psi}{|\vec{\nabla}\psi|}\right\},\end{aligned} \tag{15}$$

where

$$D^* = \frac{D\tau_0}{W_0^2}. \tag{16}$$

2.3. *Implementation*

In the present work, we very closely follow the numerical implementation described in GEA. The finite element method, together with parallel computing with multiple processors using distributed memory based on MPI protocol, is employed to solve the phase-field (PF) equations (10) and (15). The code is developed based on the open source package of deal.II (Differential Equations Analysis Library) [22]. For PF simulations, a sufficiently fine mesh is necessary to get quantitative results but this usually leads to very low computing efficiency when c_0 is increased. Since the PF varies steeply across the interface but remains constant in the bulk solid and liquid phases, an adaptive mesh refinement/coarsening algorithm is thus preferable to accelerate the calculations. With this mesh adaptation we obtain a non-uniform computational mesh with refined elements in the interface layer while grid elements are coarser in the bulk phases. As a result, the number of grid points automatically increases during the dendrite growth. The dimensionless minimum grid size in the interface layer is set to $(\Delta x)_{\min} = 0.78$, and the maximum grid size in the bulk liquid and solid phases $(\Delta x)_{\max} = 8(\Delta x)_{\min}$. Time is discretised using the implicit Euler method with the dimensionless time step $\Delta t/\tau_0 = 0.1$. More detailed information about this procedure can be found in the documentation of deal.II [23] and our previous work [6].

The advantage of using GEA algorithm is evidenced in Figure 1, where the number of grid points in the adaptive mesh is estimated at time when the tip velocity reaches a maximum and is compared with the the finite difference method used in BEA, where a uniform mesh was adopted. Obviously, using the adaptive mesh results in a substantial drop in the grid points number. The grid number gain is already 2 times for a two percent copper concentration but it greatly increases at higher concentrations because the number of mesh points continues to increase as the cube of copper concentration in the finite-difference code, while it slowly decreases in the adaptive mesh code. This is the reason why simulations at copper concentrations higher than 2 percent were not considered in [4]. In addition, the grid refinement algorithm we use does not pose serious overhead problems since the computing time required for grid refinement takes a very small proportion of the total calculation time (less than five percent) [24]. Comparisons of the numerical results obtained by both algorithms were made for $c_0 = 2$ wt% Cu. As seen below (for instance in Figures 4 and 6), we obtained very similar results from the two codes. This confirmed that the two implementations are compatible and are very likely to be free of numerical artifacts.

The main physical parameters of the Al–Cu alloys are listed in Table 1. For the partition coefficient k and the liquidus slope m, we use the average values $k = 0.14$ and $m = -2.6$ K/wt% Cu taken from [25]. Closer looks at the phase diagrams of diluted alloys indicate that the liquidus and solidus lines are usually curved, even at small solute concentrations c_0 [26]. However, as shown recently, taking into account the variations of k and m with c_0 does not significantly affect

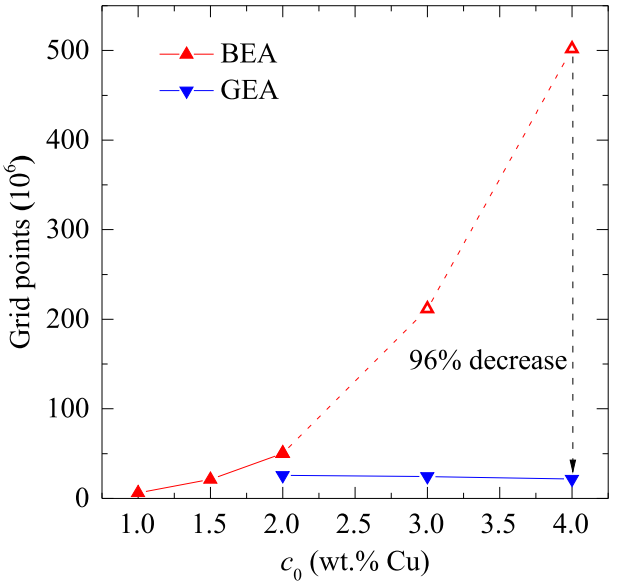

Figure 1. Comparison at the maximum tip velocity $V = V_m$ of the number of grid points in the 3D PF simulations between BEA using uniform mesh and a finite difference scheme and GEA using adaptive mesh and a finite element scheme. $L = 1000$ μm. The dotted portion of the BEA curve is extrapolated from the size of the numerical domains used with $c_0 \leq 2$ wt% Cu. The reduction factor in grid points of GEA compared with BEA is 49%, 86% and 96%, respectively for $c_0 = 2$, 3, and 4 wt% Cu.

Table 1. Physical parameters of the Al–Cu alloys considered in the simulations.

Symbol	Physical parameter	Value	Unit
D	Copper diffusion coefficient in the liquid	3000.0	$\mu m^2/s$
T_M	Aluminum melting temperature	933.0	K
c_p	Aluminum specific heat at melting temperature	2.8×10^{-12}	$J/K/\mu m^3$
c_0	Copper concentration	1.0–4.0	wt% Cu
ϵ_4	Crystal cubic anisotropy	0.01	–
Γ	Gibbs–Thomson coefficient	0.236	K·μm

the scaling growth laws for the copper concentrations considered here [27]. The accuracy of the present algorithm is mainly conditioned by the minimum grid spacing used to mesh the region near the solid–liquid interface [6]. To ensure comparable accuracy for the two concentrations considered (3 and 4 wt% Cu), we use the same interface width, $W_0 = 1.0$ μm, which results in the same interface grid size, $(\Delta x)_{\min} = 0.78$ μm in both cases. As seen in Equation (5), the capillary length is smaller at higher concentrations. The convergence numerical parameter $\xi = W_0/d_0$ is thus set to 28.4 and 37.9, respectively. For $c_0 = 4$ wt% Cu, a convergence test with ξ showed that variations of a small percentage are expected when ξ is further decreased. Moreover, for the finite difference algorithm used in BEA, convergence with W_0 was found to be satisfactorily reached for comparable ξ values [4]. The time step is set to $0.1\tau_0$, that is 5.248×10^{-4} s and 6.998×10^{-4} s for $c_0 = 3$ and 4 wt% Cu, respectively.

The initial value for the preconditioned phase field is $\psi(\vec{r}) = R_0 - r$, with R_0 the radius of the spherical solid seed and r the distance from point $\vec{r}$ to the seed center. The initial value of

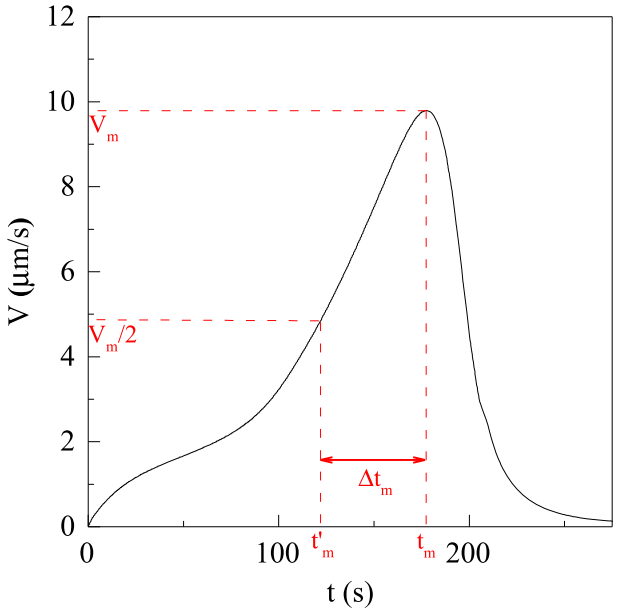

Figure 2. Dendrite tip velocity V as a function of time. $c_0 = 4.0$ wt% Cu and $L = 1000$ μm.

the rescaled solute concentration field is $U(\vec{r}) = 0$. Mirror (no-flux) conditions are constantly imposed at all the domain boundaries. Thus, it is sufficient to simulate a quarter of the whole sample plane xz, for instance, $x \geq 0$ and $z \geq 0$. For the same reason, only one half of the sample thickness is necessary, for instance, $y \geq 0$. Altogether, we only simulate an eighth of the sample and complete it by applying symmetries; the origin of the numerical domain is thus the center of the solid. Due to the no-flux boundary conditions, mirror dendrites develop and progress toward the reference dendrite from the right and from above, causing dendrite-dendrite collisions after some time. The dimensions $L \times L \times H$ of the simulated physical domains are the same as in BEA, i.e., $L = 800.0, 1000.0, 1200.0$ μm and $H = 100.0$ μm. They are chosen to reproduce the geometry of recent experiments using thin samples in order to visualize dendritic growth by real-time X-ray imaging [4, 12].

3. Growth scaling law

Figure 2 shows a typical curve for the dendrite tip velocity as a function of time that is obtained in our simulations. In BEA, we proposed to characterize such curves by the maximum velocity, $V = V_m$, and by the time Δt_m necessary for the tip to accelerate from $V_m/2$ to V_m (see Figure 2). It was shown in [4, 11] that this fast growth regime corresponds to a crossover between free growth (before the inflexion point) during which the initial globular nuclei basically develop primary dendritic arms, to early growth during which the interactions between two opposite dendrites develop with the increasing overlap of their diffusion fields (after the inflexion point). The grain morphological evolution from an initial spherical seed to the final coarsened dendrite with developed sidebranches is shown in Figure 3. Owing to the drastic increase of the computing resources needed at the late solidification stage when the secondary arms develop, the simulations are ended before late ripening, as the one shown in BEA, is reached.

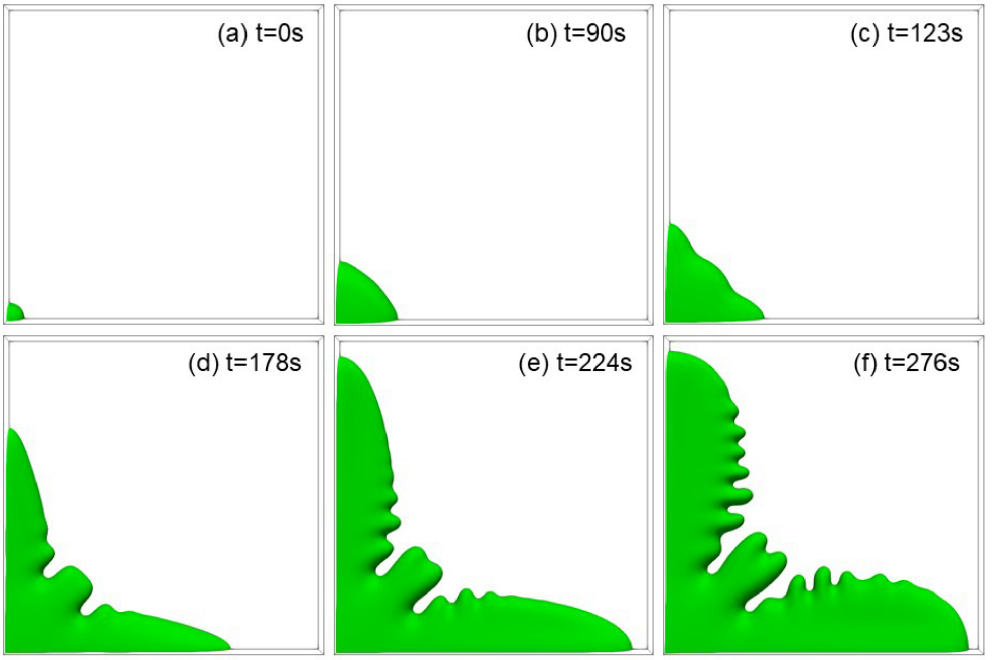

Figure 3. Snapshots showing the growth of a dendrite simulated in a thin domain of size $1000 \times 100 \times 1000$ μm^3 ($\psi = 0$ isosurfaces are represented). Perspective views are shown to give a better 3D impression: (a) initial condition, (b) slow growth, (c) fast growth, (d) end of the fast growth ($V = V_m$), (e) early ripening, (f) ongoing ripening. $c_0 = 4.0$ wt% Cu.

The numerical values of V_m and Δt_m obtained in the present study are shown in Table 2, together with the ones obtained in BEA at lower copper concentrations. For the latter ones, the dimensionless length

$$\Lambda = \frac{L_m}{L} = \frac{V_m \Delta t_m}{L}, \tag{17}$$

was found to be roughly a constant, $\Lambda = \text{cst}$ [4]. The value $\Lambda \simeq 0.546$ was quoted in BEA but a recent reanalysis of the original data rather gave the value $\Lambda \simeq 0.550$ that will be used hereafter [27].

Figure 4 represents the dimensionless length Λ as a function of the dimensionless variable

$$\sigma = \frac{c_0}{c_0^*} + \frac{L - L^*}{L^*}. \tag{18}$$

This variable expresses both the concentration dependence of Λ through the ratio c_0/c_0^* and its domain size dependence through the group $L/L^* - 1$, where c_0^* and L^* are two reference quantities that are respectively taken equal to 1 wt% Cu and 1000.0 μm here. In Figure 4, the Λ data are grouped by triplets corresponding to a given value of c_0 and increasing values of L. Concerning the evolution of Λ with L, one obtains different behaviors for the different triplets (globally increasing, globally decreasing, strongly nonuniform). This suggests that, on average, Λ does not vary significantly with L, as already remarked in BEA. Concerning the evolution of Λ with c_0, if each triplet is replaced by a single point placed at the triplet average coordinates, one again observes no obvious dependence on c_0. Thus, it is a very good approximation to consider that Λ is roughly equal to a dimensionless constant, as in BEA. A simple average of the Λ estimates obtained for all the concentrations and all the system sizes roughly gives 0.539, which is very close

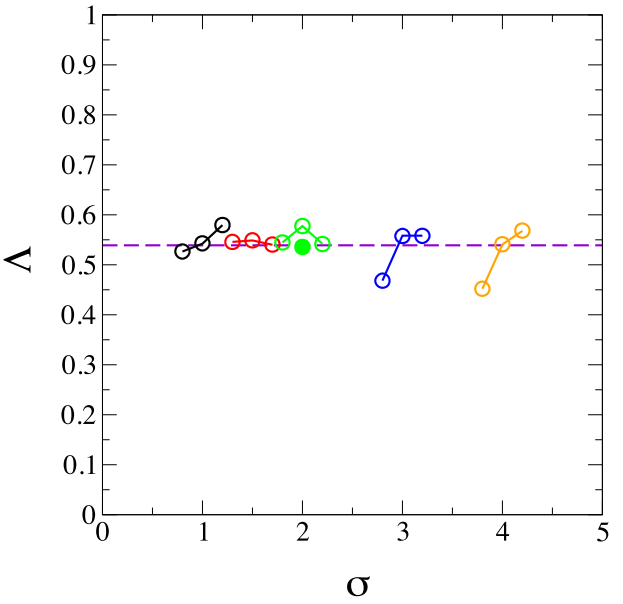

Figure 4. Dimensionless growth length $\Lambda = L_m/L$ as a function of the dimensionless variable $\sigma = (c_0/c_0^*) + (L - L^*/L^*)$ ($c_0^* = 1$ wt% Cu and $L^* = 1000.0$ μm). Each color corresponds to a triplet of data obtained at a given c_0 and for increasing values of L. The filled circle results from a simulation using the present parallel adaptive code for $c_0 = 2$ wt% Cu and $L = 1000.0$ μm and the empty circle just above is the corresponding result found in BEA with a finite difference code.

Table 2. Numerical estimates of $V_m(c_0, L)$, and $\Delta t_m(c_0, L)$ obtained in BEA and in the present study at different copper concentrations c_0 and for different numerical domain length L. Also given is the growth length Δx_m defined later in Equation (20).

	c_0 (wt% Cu)	L (μm)	V_m (μm/s)	Δt_m (s)	Δx_m (μm)
BEA	1.0	800.0	16.52	25.50	303.00
		1000.0	25.74	21.09	397.00
		1200.0	33.12	21.00	540.00
	1.5	800.0	12.13	36.00	327.00
		1000.0	20.38	26.94	410.00
		1200.0	31.14	20.83	473.00
	2.0	800.0	9.610	45.35	333.00
		1000.0	15.67	36.86	432.00
		1200.0	24.77	26.24	504.00
Present	2.0	1000.0	16.63	32.21	415.00
	3.0	800.0	7.440	50.35	293.56
		1000.0	12.18	45.79	443.75
		1200.0	18.90	35.42	522.60
	4.0	800.0	6.010	60.18	286.07
		1000.0	9.790	55.28	416.69
		1200.0	15.00	45.48	514.67

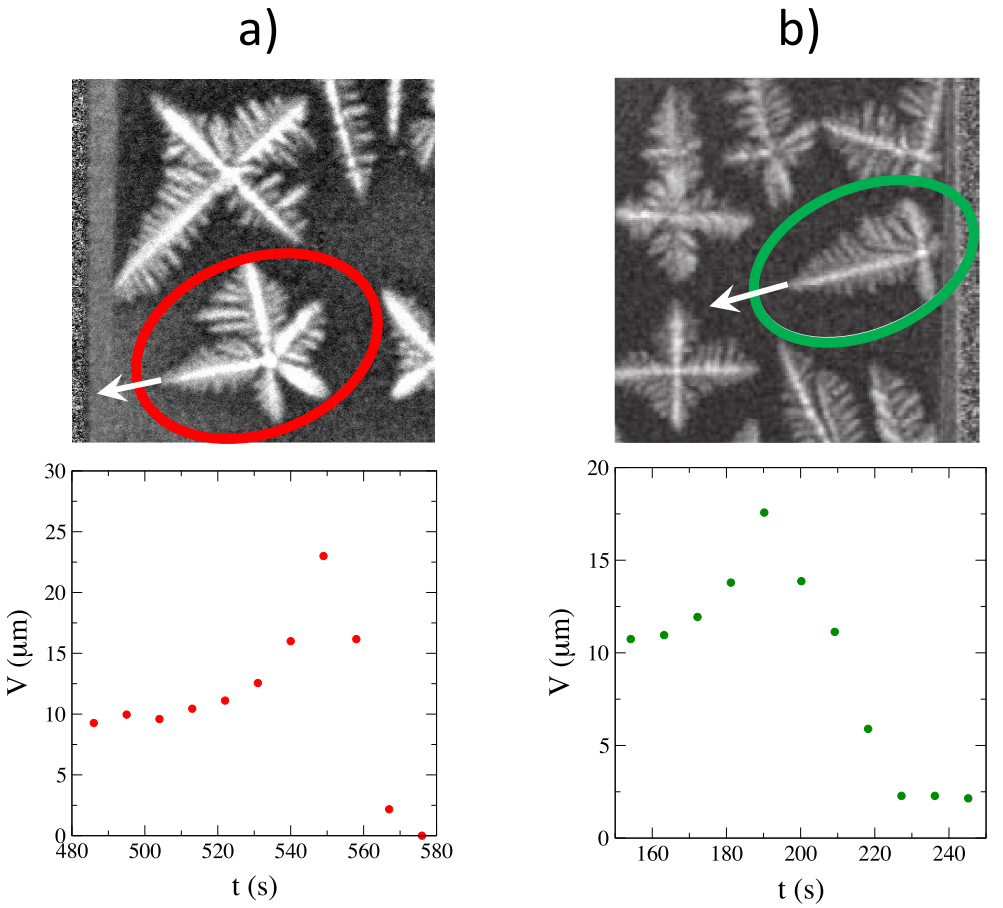

Figure 5. Two experimental examples of dendritic interactive growth in Al–4 wt% Cu samples (top row). The sample sections represented are both 3×3 mm^2 in size. The reference dendrites are encircled and, in each case, an arrow indicates the growth direction of the dendrite tip that is observed. The corresponding tip growth velocities are represented as functions of time (bottom row): (a) adapted from Ref. [4], and (b) adapted from Ref. [11].

to the value 0.550 obtained for the lower copper concentrations c_0. This result definitely confirms the scaling law

$$\Lambda = \text{cst} \simeq 0.539. \tag{19}$$

It is to be noted that the initial condition imposed to the concentration field U in the present work ($U = 0$) differs from the one imposed in BEA (solid–liquid equilibrium condition). Our results thus confirm that no significant influence of the initial condition can be detected, as it was already the case in reference [27].

As illustrated in Figure 5, direct comparison with experiments at 4 wt% Cu is possible for a few cases that have been recently described in the literature [4, 11]. In these experimental situations, little gravity effects are expected. The experimental results for the dimensionless length Λ are reported in Table 3. In this table, the first entry corresponds to the situation shown in Figure 5a: this case is very comparable to the present simulations because a single dendrite arm grows toward the crucible boundary. The second table entry corresponds to a more complicated situation shown in Figure 5b: several dendrites simultaneously grow toward each other. The free

Table 3. Dimensionless ratio $\Lambda = (V_m \Delta t_m)/L$ estimated from two experiments at copper concentration $c_0 = 4.0$ wt% Cu.

Ref.	Λ
[4]	0.549
[11]	0.533–0.648

distance ahead of the reference dendrite (that is encircled in the figure), may be taken with respect to the cross-shaped dendrite that sits in the bottom left corner of the figure or to the elongated slanted dendrite that grows from below in between them. These two choices explain the interval reported in the last entry of Table 3. In both cases, the experimental results are in good agreement with the estimate $\Lambda \simeq 0.539$ predicted by the present study.

4. Physical justification of the scaling law for the growth length

The main result of the previous section is that the dimensionless growth length Λ remains constant when c_0 and L vary in an extended range of values. A simple justification of this result can be provided by simple considerations, some of which were already mentioned in BEA. To proceed, it is useful to switch to a simple physical quantity related to the dendrite tip position, $x_{\rm tip}(t)$. An alternative growth length is obtained by integrating the tip velocity, $V(t)$ over a given time interval. We consider again the time interval $[t'_m, t_m]$ during which the tip velocity increases from $V_m/2$ to V_m. The corresponding growth length,

$$\Delta x_m = \int_{t'_m}^{t_m} V(t)\, \mathrm{d}t = x_{\rm tip}(t_m) - x_{\rm tip}(t'_m), \tag{20}$$

corresponds to the growth of the dendrite tip during the crossover regime already discussed in the previous section. Figure 6 shows the time evolution of $x_{\rm tip}$ for a given copper concentration and three different values of the domain length L. It is obvious from this figure that the three curves can be rescaled to a common master curve by rescaling the time (see below) and rescaling the tip position by L. The natural scaling variable for the tip position is thus $x_{\rm tip}/L$, so we expect that the scaled alternative growth length

$$\chi = \Delta x_m / L \tag{21}$$

is a constant. One can object that, instead of $x_{\rm tip}/L$, a better choice for the scaling variable would be $(x_{\rm tip} - R_0)/(L - R_0)$, where R_0 is the radius of the initial solid nucleus. Although this choice is more rigorous, it would not modify χ by much because L is always much larger than R_0 here.

We now return to BEA, where it was shown that a universal law relates the scaled velocity

$$Y = (2V - V_m)/V_m \tag{22}$$

to the scaled time

$$X = (t - t'_m)/\Delta t_m, \tag{23}$$

with $\Delta t_m = t_m - t'_m$. For these scaled coordinates one obtained a universal curve $Y(X)$ that could be parametrized by a fourth-order polynomial, $Y = A_1 X + A_2 X^2 + A_3 X^3 - A_4 X^4$. The four prefactors A_{1-4} were obtained by a numerical fit to the data points. The area $\mathscr{A}$ below the universal curve $Y(X)$ is given by

$$\mathscr{A} = \int_0^1 Y\, \mathrm{d}X = \frac{2}{L_m} \int_{t'_m}^{t_m} V(t)\, \mathrm{d}t - 1 = \frac{2}{L_m} \Delta x_m - 1, \tag{24}$$

with $L_m = V_m \Delta t_m$. Using (21), one finally sees that

$$\Lambda = \frac{L_m}{L} = \frac{2\chi}{\mathscr{A} + 1}. \tag{25}$$

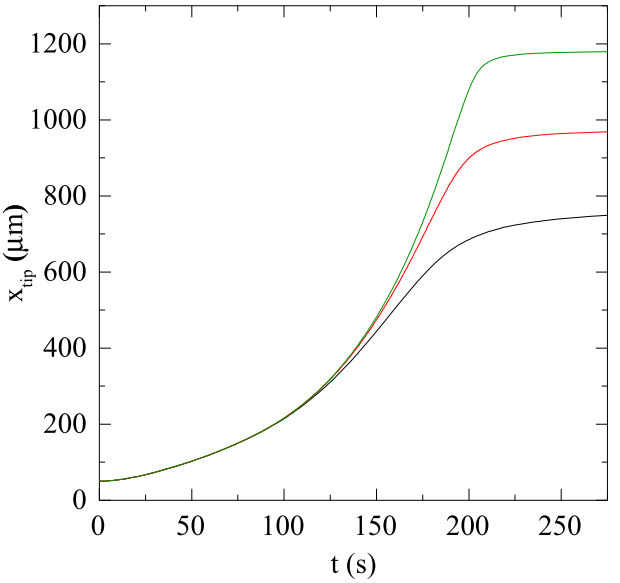

Figure 6. Tip position x_{tip} as a function of time t. Increasing curves correspond to increasing values of L (800.0, 1000.0, 1200.0 μm). $c_0 = 4.0$ wt% Cu.

This is indeed equivalent to the scaling relation $\Lambda = \text{cst}$, provided that our physical argument that χ is a constant is justified. Figure 7 shows our simulation data for χ versus σ. They do confirm with a good accuracy that χ is a constant $\simeq 0.411$. Using the $A_{1\text{–}4}$ coefficients obtained in BEA, one can estimate that the area $\mathscr{A} \simeq 0.5057$. Combining both results, one finally obtains

$$\Lambda = \frac{2\chi}{\mathscr{A}+1} \simeq 0.546, \tag{26}$$

a value that is very close to the estimate 0.539 obtained in the previous section. To summarize this section, the scaling law $\Lambda = \text{cst}$ can be shown to result from a simple physical scaling argument, $\Delta x_m / L = \text{cst}$, relating the growth length Δx_m during the crossover regime to the total available free growth distance L.

5. Summary and conclusion

In summary, the scaling law $\Lambda = \text{cst}$ predicted in BEA has been tested for the dimensionless length $\Lambda = L_m / L$, where $L_m = V_m \Delta t_m$ is a length related to the increase of the dendrite tip velocity in the fast growth regime, and L is half the average distance between dendritic nuclei, related to the volume density of the nuclei in the sample. New simulation results have been obtained at higher copper concentrations that are used in industrial applications. This has been made possible by using a parallel adaptive finite element algorithm. A careful analysis of the data has confirmed that, within numerical errors, Λ is indeed a constant, thus confirming that it shows no concentration and no dendrite density dependence. Physical arguments have been developed to justify this scaling law.

A few remarks can be formulated in conclusion. The addition of thermodynamic effects, like thermal fluctuations or concentration dependence of the phase diagram, was recently considered [27]. There again, the scaling laws predicted in BEA were found to be very robust against these effects. The combination of these results with the ones of the present study thus conveys an impression of great robustness for the proposed scaling relation. Confinement effects are necessarily present for the thin experimental samples considered here through numerical simulations.

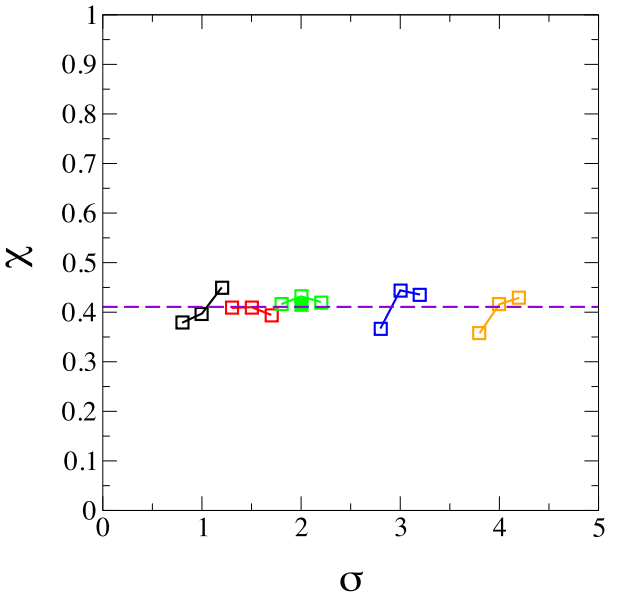

Figure 7. Dimensionless alternative growth length $\chi = \Delta x_m / L$ as a function of the dimensionless variable $\sigma = (c_0/c_0^*) + (L - L^*/L^*)$ ($c_0^* = 1$ wt% Cu and $L^* = 1000.0$ µm). Each color corresponds to a triplet of data obtained at a given c_0 and for increasing values of L. The filled square results from a simulation using the present parallel adaptive code for $c_0 = 2$ wt% Cu and $L = 1000.0$ µm and the empty square slightly above is the corresponding result found in BEA with a finite difference code.

Quantifying these effects would be important to generalize the present results to a wider class of experimental situations corresponding to different confinement levels. As discussed above, in the experimental studies of equiaxed solidification the situation generally differ from the simplified geometry assumed in the present simulations. The main differences are that more than two dendrites simultaneously interact, their respective orientations are not correlated, and their relative separation distances vary from one experimental case to the other. It would be interesting in the future to test dendritic interactions in a more statistical way by performing simulations at larger scales and by analyzing a sufficiently large number of different cases. In a wider context, it would be very instructive to test the possibility to extend the present scaling laws to other alloys. Indeed, the growth dynamics may substantially depend on materials characteristics as surface energy anisotropies that can vary either in strength or in crystal symmetries (or both). Recent results obtained for AlGe alloys that, in addition to the four-fold anisotropy of Al–Cu, also display a six-fold anisotropy show that this alloy would probably be a good candidate to conduct such tests [28, 29]. The present phase-field code models solidification of Al–Cu in purely diffusive conditions. In ground experiments this is very seldom the case because gravity may induce convection in the liquid, solute accumulation at the sample bottom, and grain buoyancy or grain sedimentation [30]. To compare simulations to experiments, two approaches are thus possible: either perform experiments in microgravity conditions or refine the phase-field models to include gravity effects. Both approaches are currently explored.

Conflicts of interest

Authors have no conflict of interest to declare.

Acknowledgments

We would like to thank CNES. This work was supported by the Youth Innovation Promotion Association CAS, and China Postdoctoral Science Foundation (Grant No. 2021TQ0335).

References

[1] S. S. Miller, L. Zhuang, J. Bottema, A. J. Wittebrood, P. De Smet, A. Haszlar, A. Viregge, "Recent development in aluminium alloys for the automotive industry", *Mater. Sci. Eng. A* **280** (2000), p. 37-49.

[2] J. G. Kaufman, E. L. Rooy, *Aluminum Alloy Castings: Properties, Processes and Applications*, AMS International, Materials Park, OH, 2004.

[3] L. F. Mondolfo, *Aluminum Alloys: Structure and Properties*, Butterwoths, London, 1976, 693-758 pages.

[4] A. K. Boukellal, J.-M. Debierre, G. Reinhart, H. Nguyen-Thi, "Scaling laws governing the growth and interaction of equiaxed Al–Cu dendrites: A study combining experiments with phase-field simulations", *Materialia* **1** (2018), p. 62-69.

[5] P. Pelcé, *New Visions on Form and Growth: Fingered Growth, Dendrites, and Flames*, Oxford University Press, New York, 2004.

[6] T. Z. Gong, Y. Chen, Y. F. Cao, X. H. Kang, D. Z. Li, "Fast simulations of a large number of crystals growth in centimeter-scale during alloy solidification via nonlinearly preconditioned quantitative phase-field formula", *Comput. Mater. Sci.* **147** (2018), p. 338-352.

[7] A. Badillo, C. Beckermann, "Phase-field simulation of the columnar-to-equiaxed transition in alloy solidification", *Acta Mater.* **54** (2006), p. 2015-2026.

[8] G. Boussinot, M. Apel, "Phase field and analytical study of mushy zone solidification in a static thermal gradient: From dendrites to planar front", *Acta Mater.* **122** (2017), p. 310-321.

[9] A. J. Clarke, D. Tourret, S. D. Imhoff, P. J. Gibbs, K. Fezzaa, A. Karma, "Microstructure selection in thin-sample directional solidification of an Al–Cu alloy: In situ X-ray imaging and phase-field simulations", *Acta Mater.* **129** (2017), p. 203-216.

[10] F. Li, W. Zhi-Ping, Z. Chang-Sheng, L. Yang, "Phase-field model of isothermal solidification with multiple grain growth", *Chin. Phys. B* **18** (2009), p. 1985-1991.

[11] Y. Chen, D. Z. Li, B. Billia, H. Nguyen-Thi, X. B. Qi, N. M. Xiao, "Quantitative phase-field simulation of dendritic equiaxed growth and comparison with in situ observation on Al–4 wt.% Cu alloy by means of synchrotron X-ray radiography", *ISIJ Int.* **54** (2014), p. 445-451.

[12] A. Bogno, H. Nguyen-Thi, G. Reinhart, B. Billia, J. Baruchel, "Growth and interaction of dendritic equiaxed grains: In situ characterization by synchrotron X-ray radiography", *Acta Mater.* **61** (2013), p. 1303-1315.

[13] K. Glasner, "Nonlinear preconditioning for diffuse interfaces", *J. Comput. Phys.* **174** (2001), p. 695-711.

[14] J.-M. Debierre, R. Guérin, K. Kassner, "Crystal growth in a channel: Pulsating fingers, merry-go-round patterns, and seesaw dynamics", *Phys. Rev. E* **88** (2013), article no. 042407.

[15] N. Bergeon, D. Tourret, L. Chen, J.-M. Debierre, R. Guérin, R. Ramirez, B. Billia, A. Karma, R. Trivedi, "Spatiotemporal dynamics of oscillatory cellular patterns in three-dimensional directional solidification", *Phys. Rev. Lett.* **110** (2013), article no. 226102.

[16] J. Ghmadh, J.-M. Debierre, J. Deschamps, M. Georgelin, R. Guérin, A. Pocheau, "Directional solidification of inclined structures in thin samples", *Acta Mater.* **74** (2014), p. 255-267.

[17] A. K. Boukellal, A. K. Sidi Elvalli, J.-M. Debierre, "Equilibrium and growth facetted shapes in isothermal solidification of silicon: 3D phase-field simulations", *J. Cryst. Growth* **522** (2019), p. 37-44.

[18] A. Karma, "Phase-field formulation for quantitative modeling of alloy solidification", *Phys. Rev. Lett.* **87** (2001), article no. 115701.

[19] B. Echebarria, R. Folch, A. Karma, M. Plapp, "Quantitative phase-field model of alloy solidification", *Phys. Rev. E* **70** (2004), article no. 061604.

[20] A. Karma, W. J. Rappel, "Quantitative phase-field modeling of dendritic growth in two and three dimensions", *Phys. Rev. E* **57** (1998), p. 4323-4349.

[21] J. J. Hoyt, M. Asta, A. Karma, "Method for computing the anisotropy of the solid-liquid interfacial free energy", *Phys. Rev. Lett.* **86** (2001), p. 5530-5533.

[22] W. Bangerth, D. Davydov, T. Heister, L. Heltai, G. Kanschat, M. Kronbichler, M. Maier, B. Turcksin, D. Wells, "The deal.II Library, Version 8.4", *J. Numer. Math.* **24** (2016), p. 135-141.

[23] W. Bangerth, "Reference document for deal.II" (2016-03-15), https://www.dealii.org/developer/doxygen/deal.II/Tutorial.html.

[24] M. Kronbichler, W. Bangerth, "The step-22 tutorial program" (2022-06-23), https://www.dealii.org/current/doxygen/deal.II/step_22.html#Results.

[25] R. Hultgren, P. R. Desai, D. T. Hawkins, M. Gleiser, K. K. Kelley, *Selected Values of the Thermodynamic Properties of Binary Alloys*, American Society for Metals, Metals Park, OH, 1973, 151-153 pages.
[26] H. Okamoto, *Phase Diagrams for Binary Alloys*, 2nd ed., ASM International, Materials Park, OH, 2010.
[27] A. K. Boukellal, M. Rouby, J.-M. Debierre, "Tip dynamics for equiaxed Al–Cu dendrites in thin samples: Phase-field study of thermodynamic effects", *Comput. Mater. Sci.* **186** (2021), article no. 110051.
[28] M. Becker, S. Klein, F. Kargl, "Free dendritic tip growth velocities measured in Al–Ge", *Phys. Rev. Mater.* **2** (2018), article no. 073405.
[29] M. Becker, L. Sturz, D. Bräuer, F. Kargl, "A comparative in situ X-radiography and DNN model study of solidification characteristics of an equiaxed dendritic Al-Ge alloy sample", *Acta Mater.* **201** (2020), p. 286-302.
[30] H. Nguyen-Thi, A. Bogno, G. Reinhart, B. Billia, R. H. Mathiesen, G. Zimmermann, Y. Houltz, K. Löth, D. Voss, A. Verga, F. de Pascale, "Investigation of gravity effects on solidification of binary alloys with in situ X-ray radiography on earth and in microgravity environment", *J. Phys. Conf. Ser.* **327** (2011), article no. 012012.

Comptes Rendus
Mécanique
2023, Vol. 351, Special Issue S2, p. 231-244
https://doi.org/10.5802/crmeca.140

Physical Science in Microgravity within the Thematic Group Fundamental and Applied Microgravity / *Sciences physiques en microgravité au sein du GDR Micropesanteur Fondamentale et Appliquée*

The effect of confinement on thermal convection and longitudinal macrosegregation in directionally solidified dilute succinonitrile–camphor alloy

L'effet du confinement sur la convection thermique et la macroségrégation longitudinale pendant la solidification dirigée d'un alliage dilué succinonitrile–camphre

Fatima L. Mota [*, a, b], **Luis M. Fabietti** [b, c, d], **Nathalie Bergeon** [a] **and Rohit Trivedi** [b]

[a] Aix Marseille Univ, Université de Toulon, CNRS, IM2NP, Marseille, France

[b] Iowa State Univ, Dept Mat Sci & Engn, Ames, IA 50010, USA

[c] Universidad Nacional de Córdoba, Facultad de Matemática, Astronomía, Física y Computación, Ciudad Universitaria, 5000 Córdoba, Argentina

[d] Instituto de Física Enrique Gaviola, CONICET, Córdoba, Argentina

E-mails: fatima.mota@im2np.fr, fatima.lisboa-mota@im2np.fr (F. L. Mota), fabietti@famaf.unc.edu.ar (L. M. Fabietti), nathalie.bergeon@im2np.fr (N. Bergeon), rohit.trivedi@gmail.com, trivedi@iastate.edu (R. Trivedi)

Abstract. Directional solidification experiments were conducted in a succinonitrile–0.24 wt% camphor alloy with an emphasis on the planar front interface temperature dynamics using different sample thicknesses. The interface temperature was found to depend significantly on the thickness due to non-negligible convection effects in the thicker samples. The results were interpreted with the help of an order of magnitude analysis and a boundary layer model, which permitted estimation of the solute macrosegregation profile. The experiments and corresponding analyses performed in this work constitute an experimental characterization of convection effects as a function of sample thickness.

* Corresponding author.

Résumé. Des expériences de solidification dirigée ont été menées dans un alliage succinonitrile–0,24% en poids de camphre en se concentrant sur la dynamique de la température de l'interface du front plan en utilisant différentes épaisseurs d'échantillons. La température d'interface s'est avérée dépendre de manière significative de l'épaisseur en raison d'effets de convection non négligeables dans les échantillons plus épais. Les résultats ont été interprétés à l'aide d'une analyse d'ordre de grandeur et d'un modèle de couche limite, qui ont permis d'estimer le profil de macroségrégation du soluté. Les expériences et les analyses correspondantes réalisées dans ce travail constituent une caractérisation expérimentale des effets de convection en fonction de l'épaisseur de l'échantillon.

Keywords. Directional solidification, Planar interface dynamics, Convection, Succinonitrile–camphor binary system, Solute boundary layer.

Mots-clés. Solidification dirigée, Dynamique des interfaces planes, Convection, Système binaire succinonitrile–camphre, Couche limite solutate.

Published online: 5 January 2023

1. Introduction

Macrosegregation, i.e. the non-homogeneous macroscopic distribution of alloy components in the solidified casting, can significantly deteriorate the mechanical properties and the processing characteristics of the material. While macrosegregation can usually be kept within acceptable margins, it is desirable to control and minimize it in order to improve and optimize the product quality and process efficiency [1–4]. The metallurgical industry typically faces difficulties in the production of materials free from macrosegregation. Several processes can contribute to the existence of segregation such as long-range diffusion, liquid flow due to shrinkage, melt convection, solid deformation and transport of solid grains/fragments. Natural convection in the melt disturbs the homogeneity of processing conditions in bulk samples and, hence, microstructure formation [5–8]. Two ways are available to get rid of this natural convection in the melt during experiments: under low-gravity conditions or using thin-samples to limit the extent of convection through confinement.

Directional solidification techniques permit study of situations ranging from metal casting to model experiments on interface pattern selection and dynamics [9–11]. It has long been recognized that it is convenient to introduce length scales in the theoretical analysis and modeling of alloy solidification. Two of them can be defined by considering steady-state solidification with planar front: the solutal diffusion length l_s given by the ratio D_L/V, with D_L the solute diffusion coefficient in the melt and V the pulling velocity; and the thermal diffusion length $l_T = (k-1)m_L C_0/kG$, with k the solute partition coefficient, m_L the *liquidus* slope, C_0 the nominal concentration and G the thermal gradient. The use of thin-sample geometries, where the distance between specimen walls is smaller than, or comparable to, the characteristic microstructure spacing, makes easier the comparison to two-dimensional theories and numerical calculations. This is in part justified by the fact that the solutal diffusion length is typically much larger than the sample thickness [12]. The geometrical confinement imposed in thin-samples is a way to influence the solidification microstructures formation.

Studies on eutectic growth have shown that there is a decisive influence of geometrical constraints on the array geometry, and morphologies in thin specimens vary between the two extreme limits of perfectly circular rods and completely lamellar structures with several distorted rod geometries in between [13, 14]. Confinement can trigger a transition from rods to lamellae, even for growth conditions and alloy compositions where rods would be the preferred morphology in extended systems [15]. The confinement effect on dendritic and cellular microstructures has been extensively studied both experimental and numerically [12, 16–28]. It has already been proven that sample thickness has an influence on cellular branches [29–35] and cell-dendrite transition [36] in directional solidification of binary alloys; the physical reason being that the thickness is shorter than the solutal diffusion length at low velocities [37]. Liu *et al.* [38] and

Athreya *et al.* [16] experimental and numerically studied the effect of dimensionality on microstructures in directional solidified succinonitrile-salol alloys. They were studying the role of confinement in dendritic growth and found that its effects became important when the container size is on the order of the primary dendrite spacing.

In contrast, very little information is available on finite-size effects on the planar front temperature during directional solidification of binary alloys. If local equilibrium conditions at the interface are satisfied and growth is controlled by diffusion, the planar interface temperature at steady-state corresponds to the *solidus* temperature at the nominal alloy concentration C_0. However, convection in the liquid can be present during growth and makes the steady-state temperature at the front deviate from the *solidus* temperature. For a given thermal gradient G, there are two critical experimental parameters playing a role on the convection effects: the growth rate and the sample thickness. The convection effects can be made negligible by increasing the growth rate or reducing the sample thickness. Since low velocities are required to maintain a stable planar front during growth, the only choice is to check if the thickness is small enough to make convection effects negligible. The effect of crucible diameter reduction on the convection and macrosegregation has been raised during directional solidification of Pb–Sb alloys [39, 40]. The solutal profiles obtained during plane front solidification are clearly not those expected from a diffusive mass transport. Their segregation pattern indicates extensive convection and mixing during directional solidification. The extent of macrosegregation, however, shows a systematic decrease with the decreasing crucible diameter. So, the intensity of convection decreases while the crucible diameter decreases.

Since the pioneering work of Burton, Prim and Slichter (BPS) [41], simplified models for predicting the longitudinal macrosegregation during crystal growth have been developed by considering the general non-stationary diffusion problem within a zone of extent δ in front of the interface, with a melt of spatially uniform composition outside this diffusion layer [42]. Karma *et al.* [43] (KRFT) assumed a non-constant interface velocity, and their model reduces to the previous ones only in the case of both the concentration field and interface velocity being constant. When no convection effects are present in the melt, the purely diffusive limit is found, equivalent to Warren and Langer model [44], which physically corresponds to a boundary layer thickness much larger than the solutal diffusion length l_s. In the case of convection effects being present, in the limit of an infinite sample length, the melt composition remains constant and equal to the alloy composition, which is equivalent to the well-known segregation equation developed by BPS [41]. In KRFT model, the composition in the solid C_s is governed by the non-dimensional boundary layer thickness $\Delta_{\mathrm{KRFT}} = \delta V / D_L$: the limiting case of diffusive growth occurs when $\Delta_{\mathrm{KRFT}} \to \infty$ where $C_s = C_0$; and complete mixing in the liquid occurs when $\Delta_{\mathrm{KRFT}} \to 0$ where $C_s = kC_0$. The KRFT model is then an improvement of the previous models of macrosegregation, and its basic equations, initially developed for peritectic systems, can be easily adapted to interpret the growth of other binary alloys with a planar solid–liquid interface.

An order of magnitude analysis (OMA) was developed by Camel and Favier [45, 46] for a two-dimensional rectangular solidification system with the growth planar interface parallel to the gravity vector g. They assumed: negligible convective heat flow (low Prandtl number), adiabatic upper and lower walls, laminar regime (convection not too strong), two-dimensional fluid velocity field and steady fluid motion, a Newtonian fluid and transport properties independent of the temperature and concentration. Their technique consists in non-dimensionalizing the equations of the problem, taking into account the expected variable variations. Then, the non-dimensional coefficients are compared and their order of magnitude evaluated. Different regimes can be defined as a function of the non-dimensional numbers, Grashof–Schmidt $GrSc = \beta_T g Z^4 / \upsilon D_L$ and Péclet $Pe = VZ/D_L$, where β_T is the thermal expansion coefficient, Z is the smallest sample dimension between height (H) and length (L) of the confined liquid zone, υ is the kinematic

viscosity, and D_L is the diffusion coefficient in the liquid. The corresponding limiting lines can be drawn in a diagram that permits analysis of the segregation behavior as a function of the problem's data (Figure 7 of [45] or Figure 4 of [46]). A variety of Péclet number definitions can be found in the literature, the main difference between them lies in the underlying assumptions about solute transport. The authors choose to use the structural definition previously given, where the characteristic length of the system is related to the Bridgman growth configuration.

For a sample of infinite length L (aspect ratio $A = L/H$ much higher than 1), two different regimes can be distinguished: a convective–diffusive boundary layer regime where the dominant driving force is the thermal buoyancy driven convection; and a diffusive boundary layer regime where the dominant driving force is the solute rejection at the interface. The convecto-diffusive transition is found when the maximum fluid flow velocity becomes of the order of the diffusion rate imposed by solidification (i.e. the growth rate) [47]. The transition is given by:

$$Gr\,Sc = Pe^4 \quad \text{if } \{Pe > 5 \text{ and } Gr\,Sc > 625\} \tag{1}$$

$$Gr\,Sc = 125\,Pe \quad \text{if } \left\{ \frac{1}{A} < Pe \text{ and } \frac{125}{A} < Gr\,Sc < 625 \right\}. \tag{2}$$

For a sample of finite length, there is an additional limited diffusion regime where solute diffusion extends over the whole liquid length ($Pe < 1/A$ and $Gr\,Sc < 125/A$). Looking at (1) and the definitions of Pe and $Gr\,Sc$, for a given thermal gradient G on Earth ($g = 9.81$ m/s^2), the convecto-diffusive transition depends only on the pulling rate V. However, in the region defined by (2), dependence is seen on the pulling rate V and the smallest dimension of the sample.

There is a good qualitative agreement between this analysis and experimental results obtained during solidification of metallic alloys and semiconductors (Figure 4 of [46]). In order to get rid of convection effects, one can rather increase the pulling rate or decrease the sample thickness. Based on the previous equations, for a given pulling rate V and thermal gradient G, the critical dimension limiting the transition between convective–diffusive boundary layer and diffusive boundary layer regimes can be estimated using the relation:

$$H_c = \left(\frac{125 V \upsilon}{\beta_T g G} \right)^{\frac{1}{3}}. \tag{3}$$

The OMA described above was developed for the solidification of a doped metal or semiconductor in a simplified horizontal Bridgman crystal growth configuration. These kind of materials have a low Prandtl number (Pr), which means that the thermal diffusion is very quick in comparison to the momentum transport diffusion. However, as evidenced in their work, there is a wide range of control parameters where solute convective transport occurs, while heat transfer remains mainly conductive. For example, for an aluminum (Al)–0.4 wt% copper (Cu) alloy, whose thermal diffusion length is one order of magnitude higher than the solutal diffusion length, one may have a solutal diffusion-controlled growth if the experiments are performed in reduced gravity. The comparison between the obtained laws of the OMA and experimental literature results did not concern any organic material that, in general, presented Prandtl numbers higher than 1. In the present work, the validity of this OMA will be tested for the organic transparent alloy succinonitrile (SCN)–camphor ($Pr \approx 20$). This transparent organic analog behaves like metallic alloys concerning solidification and its main advantages are: transparency to visible light, so that *in situ* and real time observation of the interface can be made by classical optical techniques; and low melting temperature (≈58 °C), which simplifies the design of the Bridgman furnace. Based on the material properties (Table 1) and the imposed experimental conditions (described in later sections), one would have solidification controlled by solutal diffusion. But it will be shown that there is a range of parameters for which it is not the case. In that way, thin-sample directional solidification experiments with stable planar front growth were realized with different sample thicknesses.

The experimental data were further interpreted using a boundary layer model of planar interface dynamics allowing to access quantitatively the effect of convection [43].

2. Experimental procedure

The SCN was purified by distillation under vacuum followed by zone refining as in previous works [48]. The purity was characterized by the freezing range (0.003 °C) which corresponds to 99.9998%. Camphor was sublimated under vacuum from the 98% commercial product. An alloy of 0.24 wt% camphor composition was prepared inside the glovebox under the protection of high-purity nitrogen. Nitrogen atmosphere was preferred over argon because previous studies have shown that the addition of argon provides a dilute solute with SCN [49, 50].

For the directional solidification experiments, the liquid alloy was introduced into rectangular thin sandwiched glass cells (4 × 300 mm) of different thicknesses (from 12.5 to 200 μm) inside the glovebox under high-purity nitrogen atmosphere. Two additional cells, identical to the sample cells, were also prepared with pure SCN and eutectic composition (23.6 wt% camphor). These additional cells were placed on the two sides of the sample cell, and the three-cell assembly was placed in the temperature gradient stage for stabilization. The hot and cold baths were maintained at 97 and 3.5 °C, respectively, yielding a nominal thermal gradient of 78 °C/cm based on the pure SCN and eutectic positions and their respective known temperatures (58.08 and 37.7 °C [51]). The gradient measurement was double checked using a sample similar to those used in directional solidification experiments but filled with a K-type thermocouple and pure SCN. The gradient was measured by pushing the thermocouple into the hot zone one centimeter and pulling it out at a velocity of 2.5 μm/s. This allowed the measured position of the thermocouple to be related to the sampled temperature by time. The measured gradient, 74 °C/cm, was the result of a linear fit of the temperature–distance relationship. The samples were then directionally solidified at a constant pulling velocity V for a long time until the presence of steady-state growth was established. The evolution of interface position with time was measured and the interface temperature was determined from its position knowing the pure SCN position and the thermal gradient.

3. Results and discussion

The binary alloy, SCN–0.24 wt% camphor, was solidified by pulling through a fixed thermal gradient. The planar solid–liquid interface can be destabilized by increasing the velocity, thus giving rise to cellular or dendritic microstructures. The critical velocity V_c leading to the transition from a planar to a cellular front can be calculated using the Mullins–Sekerka linear stability analysis [52], $V_c = kGD_L/(k-1)m_L C_0$, and is equal to 0.48 μm/s (material properties given in Table 1). Although, the main focus of this work was on planar front temperature (V should be lower than V_c), some directional solidification experiments were performed with a pulling rate higher than V_c ($V = 1$ μm/s) using samples of thicknesses between 25 and 100 μm. Under these experimental conditions, the morphological instability appeared at the interface after the initial transient, and cellular patterns were obtained in steady-state growth (Figure 1). For $V = 1$ μm/s, the solutal diffusion length (270 μm) is higher than the sample thickness leading to effects on cellular branches. As previously reported in the literature [16, 35, 38], the confinement has an effect on the primary spacing λ, defined as the distance between the cell center and its closest neighbors. The characteristic microstructure spacing, which is higher or comparable to the distance between specimen walls, decreases with the increase of thickness. In order to keep a stable planar front till steady-state growth, a pulling rate of 0.3 μm/s ($\ll V_c$) was chosen in the following experiments.

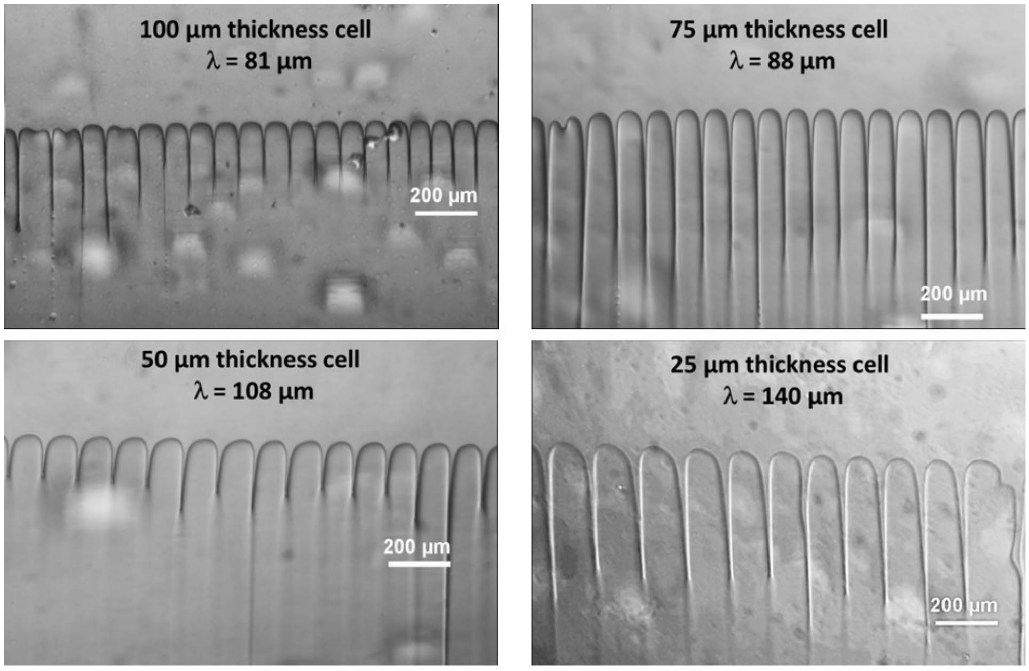

Figure 1. Steady-state growth morphology of SCN–0.24 wt% camphor alloy directionally solidified at $V = 1$ µm/s and $G = 78$ °C/cm in samples of different thicknesses. The sample thickness and the primary spacing (λ) are given in each picture.

Table 1. Properties of succinonitrile and succinonitrile–0.24 wt% camphor alloy.

Thermal expansion coefficient (β_T) [53]	7.85×10^{-4} K^{-1}
Solutal expansion coefficient (β_c) [54]	1.73×10^{-4} wt%$^{-1}$
Kinetic viscosity (υ) [55]	2.6 mm^2/s
Liquidus slope (m_L) [56]	−1.365 K/wt%
Liquidus temperature (T_L) [56]	57.7 °C
Solidus temperature (T_s) [51]	53.5 °C
Solute partition coefficient (k) [51]	0.07
Solute diffusion coefficient in the liquid (D_L) [56]	270 µm^2/s
Thermal diffusion coefficient (D_{th}) [56]	1.15×10^5 µm^2/s

The sample thicknesses were selected based on the universal diagram developed by Camel and Favier [45, 46], reproduced in Figure 2 for the Péclet (*Pe*) and Grashof–Schmidt (*Gr Sc*) ranges used in this work. In the definition of the *Pe* number used by these authors, Z is the smaller of the dimensions between the height and length of the confined liquid region. In thin-samples, the thickness (or height) is much lower than the length, and is then used as the characteristic dimension of the system to estimate *Pe* number. For the experimentally applied thermal gradient $G = 78$ °C/cm, several red dashed lines were drawn in Figure 2, which represent constant pulling rate with increasing sample thickness H along the line. Applying (3) with $V = 0.3$ µm/s, a critical dimension of 117 µm was found, corresponding to the transition between convecto-diffusive and diffusive regimes. Given this critical value, different sample thicknesses (H) were selected

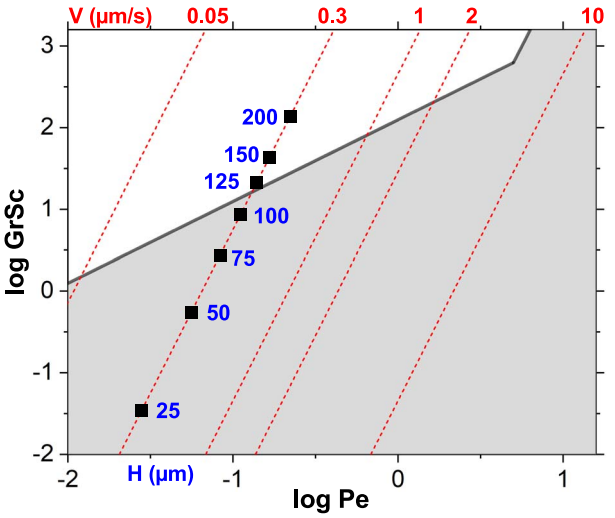

Figure 2. Grashof–Schmidt versus Péclet number diagram [45, 46], where the white region corresponds to convective–diffusive boundary layer regime and the grey shaded region correspond to diffusive boundary layer regime. The red dashed lines represent constant pulling velocity V. The square markers represent different sample thickness H.

to perform directional solidification experiments, evidenced by the different markers over the $V = 0.3$ μm/s line in Figure 2.

For some of the samples directionally solidified at $V = 0.3$ μm/s, the interface broke up before reaching a steady state with a temperature below the theoretical *solidus* temperature. This happened in the samples with thicknesses 12.5, 25 and 50 μm. The most likely reason was the presence of a meniscus, which deformed the interface and shifted the threshold of critical velocity to a lower value [57, 58]. Furthermore, a linear relationship between the break time and the sample thickness was observed. The interface position data as function of time were manipulated in order to obtain the interface velocity and the solid composition at the interface. The constitutional supercooling criterion [59, 60] assumes that any perturbation at the flat interface will grow if $G - m_L G_c < 0$, where G_c is the concentration gradient in the liquid at the interface. This criterion was fulfilled for thicknesses lower than 75 μm, as evidenced by the evolution of the concentration gradient in the liquid at the interface (Figure 3). These results are in agreement with the previous findings of De Cheveigné *et al.* [57]. They found that the meniscus affects a distance of about 50 μm, which is of the order of the sample thickness range over which the threshold pulling rate is seen to vary.

Figure 4(a) shows the evolution of the planar front interface temperature for samples of different thicknesses (higher than 50 μm), directionally solidified at $V = 0.3$ μm/s and $G = 78$ °C/cm. There was a non-negligible effect of the thickness on steady-state temperature. The criterion applied to stop the experiments was that the difference between the interface temperature was not visible for a period of time higher than 30 h. The thermal diffusivity in organic alloys is several orders of magnitude higher than the solute diffusivity (D_{th} and D_L, respectively, in Table 1), which means that heat diffusion is much faster than solute diffusion. Thus, slow solute diffusion is often the limiting physical process and the solute diffusion length $l_s = D_L/V$ is the most important scale (or in the time scale, $t_s = D_L/V^2$). For the SCN–0.24 wt% camphor alloy solidified at $V = 0.3$ μm/s, $l_s = 900$ μm and $t_s = 0.83$ h, which means that 30 h of *plateau* are more than 30 times longer than this limiting time scale. The planar front temperature found for the sample

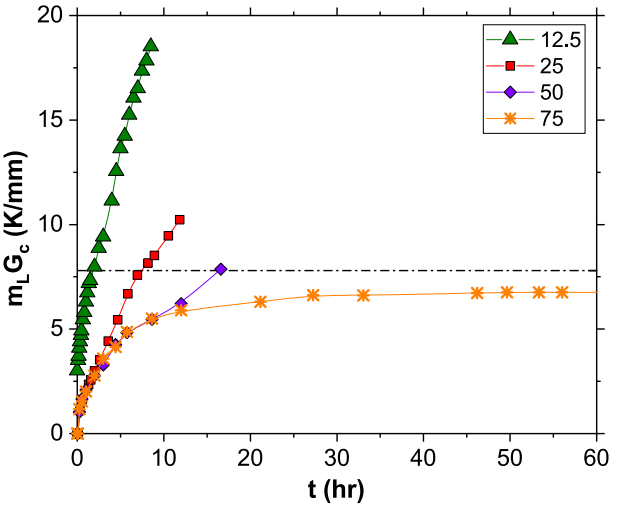

Figure 3. Concentration gradient in the liquid at the interface, $m_L G_c$, as function of time t for the SCN–0.24 wt% camphor alloy solidified at $V = 0.3$ μm/s and $G = 78$ °C/cm in thin-samples of different thicknesses.

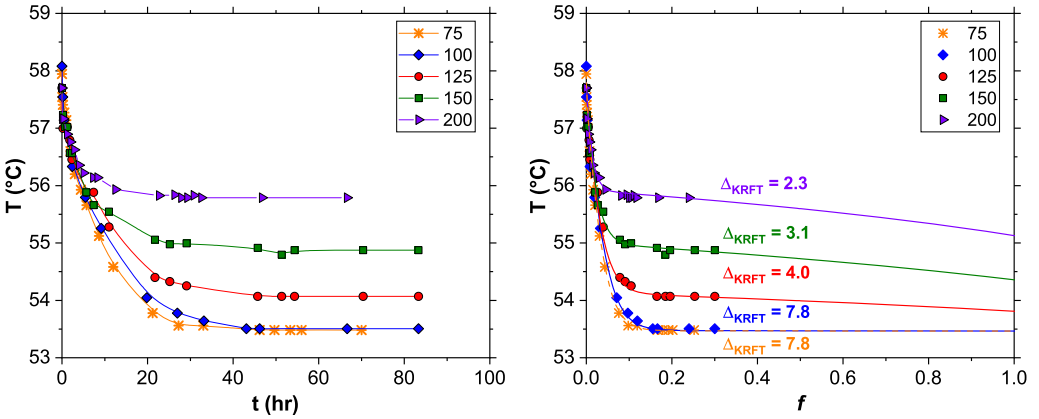

Figure 4. Planar interface temperature T as function of (a) time t and (b) solidified fraction f, for a SCN–0.24 wt% camphor alloy directionally solidified at $V = 0.3$ μm/s and $G = 78$ °C/cm in samples of different thicknesses. The curves in (b) correspond to the calculated profiles using KRFT model [43] with different Δ values.

of thickness 100 μm (53.5 °C) is in good agreement with the previously reported *solidus* temperature T_s [51]. Teng and Liu [56] measured the steady-state planar interface temperature during directional solidification of a SCN–0.35 wt% camphor alloy on 200 μm thick samples, and found a steady-state temperature of 55.7 °C. The result obtained in this work for a sample of thickness 200 μm (55.8 °C) also highlights the reproducibility of the results: a slightly higher temperature was measured for a slightly lower concentration, as theoretically predicted by the phase diagram [51].

These results can be further interpreted using a boundary layer model of transient planar interface dynamics. Considering the growth of only one solid phase, the basic equations of the KRFT model [43] were used to fit the experimental data of the planar interface temperature

Table 2. Non-dimensional boundary layer thickness using KRFT model [43] and OMA analysis [45,46,61], and relative importance of solutally driven flow [62] defined by the ratio V_c/V_T.

Sample thickness (μm)	Δ_{KRFT}	Δ	$\Delta_{KRFT,c}$	V_c/V_T
75	7.8	1.00	1.00	14.4
100	7.8	1.00	1.00	8.1
125	4.0	0.83	0.98	3.6
150	3.1	0.48	0.95	0.8
200	2.3	0.20	0.90	0.1

(Figure 4(b)). The calculations were realized assuming a sample length of 725 mm in the model, but the solidified fraction f in Figure 4(b) was calculated as the ratio between the solidified length Vt and the experimental sample length L = 300 mm. All these experiments were performed with the same control parameters (C_0, G and V), the only difference being the sample thickness. Considering an infinite sample length ($L \gg l_s$ = 900 μm), different Δ_{KRFT} values were used to fit the experimental data which increased with decreasing sample thickness (Table 2). This means that the boundary layer decreases with sample thickness, and becomes of the same order as the diffusion layer for the highest thickness. It should be mentioned that the curves for the 100 and 75 μm thickness samples were labeled with Δ_{KRFT} = 7.8, but any value of Δ higher than 7.8 leads to similar results, which in turn correspond to those of the Warren and Larger model [44]. This means that this value of Δ_{KRFT} is slightly higher than the threshold at which convection effects become negligible.

As previously mentioned, the experiments were stopped after about 100 h of solidification because the interface was not moving, at least for the last 30 h, so steady-state was considered to have been reached. However, the model curves show that this was the case only for the 100 and 75 μm thickness samples (Figure 4(b)). In all the other experiments, the interface was still moving but at a very slow drifting rate (<0.15 °C/day), that it was very difficult to see, if not impossible, within the experimental error. For example, based on the KRFT model results,the planar interface temperature of the 125 μm thick sample would take at least another 47 days to reach the *solidus* temperature. It would be exceedingly difficult to perform a solidification experiment during such a long period of time. One of the advantages of the model is that it allows the experimental data to be extrapolated and, consequently, the results to be better interpreted.

The segregation profiles could be calculated using the KRFT model [43] (Figure 5). In the limiting case of diffusive growth (dashed line), the solute distribution can be divided into three regions, i.e. initial transient, steady state growth and the final transient region. The complete mixing in the liquid is traduced by a convex profile (dotted line). For intermediate values of Δ_{KRFT}, the S-shaped segregation profiles are very different from the two boundary profiles. The calculated profiles soon deviate from the diffusion profile, thus illustrating the blocking of the pure diffusion profile over a finite distance ahead of the interface. However, even for the highest sample thickness, 200 μm, the complete mixing is still a long way off. Sample thickness does indeed have a non-negligible effect on the longitudinal macrosegregation.

In their order and magnitude analysis, Camel and Favier [45, 46] also included a solute boundary layer δ (or $\Delta = \delta V/D_L$), which can be determined as function of the problem data. With this parameter, boundary layer models can be used to discuss longitudinal segregation: in a diffusive regime Δ = 1; in a convective–diffusive regime $\Delta = 125(Pe/GrSc)$ (Figure 5 of [46]). The Δ values were estimated based on Figure 2 for the studied thicknesses (Table 2), and they are quite different from those used in the KRFT model (Figure 4b and Δ_{KRFT} in Table 2). However, as discussed in detail by Camel and Favier [61], the Δ_{KRFT} values should not be compared directly

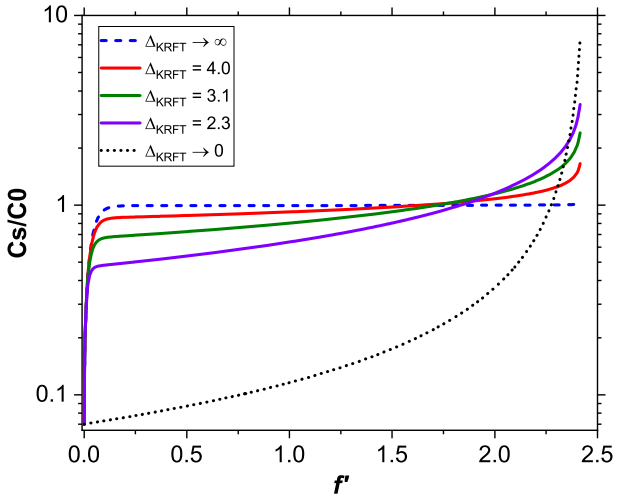

Figure 5. Segregation profiles calculated using KRFT model [43] with different Δ_{KRFT} values as function of the solidified fraction f'. f' is the ratio of the solidified length to the sample length used in the model. SCN–0.24 wt% camphor alloy, $V = 0.3$ µm/s and $G = 78$ °C/cm.

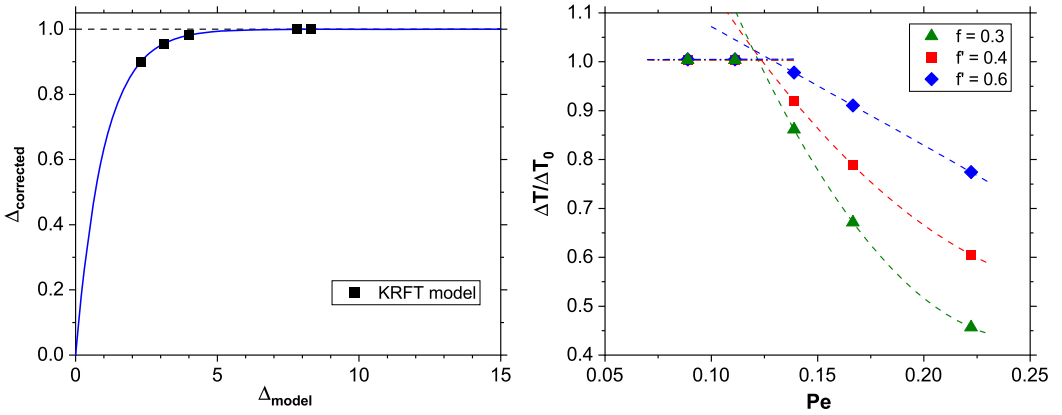

Figure 6. (a) Correction of the non-dimensional boundary layer thickness used in models like KRFT [43]. (b) Dimensionless undercooling ($\Delta T/\Delta T_0$) as a function of Péclet number (Pe) for different solidified fractions f.

with those arising from the boundary layer Δ, but they should be corrected $\Delta_{KRFT,c} = 1 - e^{-\Delta_{KRFT}}$ (Figure 6(a)). Even if there is still a difference between the corrected values $\Delta_{KRFT,c}$ and the boundary layer Δ (Table 2), both results underline that there is a sample thickness between 100 and 125 µm corresponding to the dominant transport mode transition.

A weakness of the OMA developed by Camel and Favier [45, 46] is that the relative importance of solutally driven flow is not estimated. Garandet and Alboussiere [62] proposed to estimate this relative importance, at the scale of the boundary layer thickness, using the ratio of the solute-driven [$V_c(\delta)$] and thermally [$V_T(\delta)$] driven natural convection flow velocities:

$$\frac{V_c(\delta)}{V_T(\delta)} = \frac{\beta_c G_c}{\beta_T G}\left(\frac{\Delta}{Pe}\right)^2 \tag{4}$$

with β_c the solutal expansion coefficient and G_c the composition gradient at the interface ($G_c = VC_0(1-k)/D_L k$). The solute driven fluid flow was at most, of the same order for the smaller thicknesses, meaning that solutal convection dominated thermal convection, in contrast to the highest thicknesses (Table 2). For 125 μm, the solutal convection appeared to be dominant, but the effects of thermal convection cannot be neglected, as evidenced by the previous analyses.

The effect of thickness can also be analyzed by representing dimensionless undercooling as function of Péclet number (Figure 6(b)). The dimensionless undercooling was estimated using the relation:

$$\frac{\Delta T}{\Delta T_0} = \frac{T_L - T}{T_L - T_S} \tag{5}$$

where T_L and T_S are the *liquidus* and *solidus* temperatures for SCN–0.24 wt% camphor, respectively 57.7 and 53.5 °C, and T is the interface temperature. The green triangles in Figure 6(b) correspond to the experimental data; experiments were stopped after 100 h of solidification which corresponds to a solidified fraction of $f \approx 0.3$. The red squares and blue diamonds correspond to f' equal to 0.4 and 0.6, respectively, and could be represented using the boundary layer model results. For solidified fractions higher than 0.6, the segregation profiles have a strong effect of the sample end and the final transient, leading to a rapid decrease in the interface temperature (Figure 5). This was the reason why solidified fractions higher than 0.6 were not compared with the experimental results. Two different regions can be distinguished: one where the dimensionless undercooling is constant and does not depend on f; and another where the dimensionless undercooling depends on Pe and also on f. The existence of these two different regimes is an evidence of the change in the dominant transport mode. Tendency curves were plotted for each data-set and for each of the regions. For each data-set, the tendency curves of the two regions intersect at $Pe \approx 0.12$, corresponding to a thickness $H \approx 112$ μm. This value is very close to the estimated using the order and magnitude analysis of Camel and Favier [45, 46] ($H_c = 117$ μm).

4. Conclusion

The effect of sample thickness on interface stability and cell/dendrite shape during directional solidification had already been examined in the literature. However, the effect of thickness on the interface temperature during steady-state planar front growth had not been studied. In this work, directional solidification experiments were performed on a succinonitrile–0.24 wt% camphor alloy using sample thicknesses between 75 and 200 μm. The imposed experimental conditions, pulling rate $V = 0.3$ μm/s and thermal gradient $G = 78$ °C/cm, were set in order to keep a planar front throughout the experiment. The temperature of the planar front was found to depend on the sample thickness. The experiments were stopped after 100 h of solidification because the interface temperature was not changing in several consecutive measurements, so steady-state growth was considered to have been reached. The experimental results were analyzed using a boundary layer model of transient planar interface dynamics. In some experiments, in particular, those with sample thickness higher than 125 μm, the interface was still moving when they were stopped, but at such a slow rate that it was not possible to notice it visually. An order and magnitude analysis allowed to realize that for a given growth velocity and thermal gradient, there is a critical Péclet number (equivalent to thickness) above which convection effects became non-negligible. This critical thickness was estimated to be 117 μm, which is in good agreement with that estimated based on the experimental and boundary layer model results (112 μm). The experimental results and the respective analyses showed that above a given thickness, another mechanism besides diffusion was activated, that contributed to the solute removal in front of the interface. This mechanism is associated with convection of thermal origin. The results found in this work provide experimental proof of the effect of thickness on macrosegregation profiles during planar front directional solidification.

Conflicts of interest

The authors declare no competing financial interest.

Dedication

The manuscript was written through contributions of all authors. All authors have given approval to the final version of the manuscript.

Acknowledgments

The authors gratefully acknowledge fruitful discussions with B. Billia. The authors express their gratitude to CNES and NASA (through Grant no. NNX12AK54G) for the support received in the scientific projects MISOL3D (Microstructures de SOLidification 3D) and DSIP (Dynamical Selection of Interface Patterns).

References

[1] J. Li, M. H. Wu, A. Ludwig, A. Kharicha, "Simulation of macrosegregation in a 2.45-ton steel ingot using a three-phase mixed columnar-equiaxed model", *Int. J. Heat Mass Transfer* **72** (2014), p. 668-679.

[2] E. J. Pickering, C. Chesman, S. Al-Bermani, M. Holland, P. Davies, J. Talamantes-Silva, "A comprehensive case study of macrosegregation in a steel ingot", *Metall. Mater. Trans. B* **46** (2015), p. 1860-1874.

[3] K. V. S. Rao, "Experimental studies on microstructure evolution and macro segregation during upward directional solidification of lead–tin alloys", *Proc. Mater. Sci.* **5** (2014), p. 1224-1230.

[4] M. Chatelain, M. Albaric, D. Pelletier, V. Botton, "Solute segregation in directional solidification: Scaling analysis of the solute boundary layer coupled with transient hydrodynamic simulations", *J. Cryst. Growth* **430** (2015), p. 138-147.

[5] M. E. Glicksman, S. R. Coriell, G. B. Mcfadden, "Interaction of flows with the crystal–melt interface", *Annu. Rev. Fluid Mech.* **18** (1986), p. 307-335.

[6] S. H. Davis, "Hydrodynamic interactions in directional solidification", *J. Fluid Mech.* **212** (1990), p. 241-262.

[7] M. D. Dupouy, D. Camel, J. J. Favier, "Natural-convection in directional dendritic solidification of metallic alloys. 1. Macroscopic effects", *Acta Metall.* **37** (1989), p. 1143-1157.

[8] H. Nguyen-Thi, G. Reinhart, B. Billia, "On the interest of microgravity experimentation for studying convective effects during the directional solidification of metal alloys", *C. R. Méc.* **345** (2017), p. 66-77.

[9] W. Kurz, D. J. Fisher, *Fundamentals of Solidification*, Trans Tech Publications, New Hampshire, USA, 1998.

[10] M. Cross, H. Greenside, *Pattern Formation and Dynamics in Nonequilibrium Systems*, Cambridge University Press, Cambridge, 2009.

[11] J. A. Dantzig, M. Rappaz, *Solidification*, EPFL Press, Lausanne, 2009.

[12] S. Gurevich, A. Karma, M. Plapp, R. Trivedi, "Phase-field study of three-dimensional steady-state growth shapes in directional solidification", *Phys. Rev. E* **81** (2010), article no. 011603.

[13] M. Serefoglu, R. E. Napolitano, "On the selection of rod-type eutectic morphologies: Geometrical constraint and array orientation", *Acta Mater.* **56** (2008), p. 3862-3873.

[14] V. T. Witusiewicz, U. Hecht, S. Rex, "Fibrous eutectic growth in succinonitrile–neopentylglycol–(D)camphor–aminomethylpropanediol alloys for thin and bulk sample geometry", *Acta Mater.* **65** (2014), p. 360-372.

[15] M. Serefoglu, R. E. Napolitano, M. Plapp, "Phase-field investigation of rod eutectic morphologies under geometrical confinement", *Phys. Rev. E* **84** (2011), article no. 011614.

[16] B. P. Athreya, J. A. Dantzig, S. Liu, R. Trivedi, "On the role of confinement on solidification in pure materials and binary alloys", *Philos. Mag.* **86** (2006), p. 3739-3756.

[17] N. F. Dean, A. Mortensen, M. C. Flemings, "Steady-state cellular solidification of Al–Cu reinforced with alumina fibers", *Metall. Mater. Trans. A* **26** (1995), p. 2141-2153.

[18] L. M. Fabietti, J. A. Sekhar, "Planar to equiaxed transition in the presence of an external wetting surface", *Metall. Mater. Trans. A* **23** (1992), p. 3361-3368.

[19] L. M. Fabietti, J. A. Sekhar, "Quantitative microstructure maps for restrained directional growth", *J. Mater. Sci.* **29** (1994), p. 473-477.

[20] J. D. Hunt, S. Z. Lu, "Numerical modeling of cellular and dendritic array growth – spacing and structure predictions", *Mater. Sci. Eng. A* **173** (1993), p. 79-83.

[21] J. H. Jeong, N. Goldenfeld, J. A. Dantzig, "Phase field model for three-dimensional dendritic growth with fluid flow", *Phys. Rev. E* **64** (2001), article no. 041602.
[22] L. X. Liu, J. S. Kirkaldy, "Systematics of thin-film cellular dendrites and the cell-to-dendrite transition in succinonitrile salol, succinonitrile acetone and pivalic acid ethanol", *J. Cryst. Growth* **140** (1994), p. 115-122.
[23] S. Z. Lu, J. D. Hunt, "A numerical-analysis of dendritic and cellular array growth – the spacing adjustment mechanisms", *J. Cryst. Growth* **123** (1992), p. 17-34.
[24] M. Plapp, M. Dejmek, "Stability of hexagonal solidification patterns", *Europhys. Lett.* **65** (2004), p. 276-282.
[25] J. A. Sekhar, R. Trivedi, "Development of solidification microstructures in the presence of fibers or channels of finite width", *Mater. Sci. Eng. A* **114** (1989), p. 133-146.
[26] A. Semoroz, S. Henry, M. Rappaz, "Application of the phase-field method to the solidification of hot-dipped galvanized coatings", *Metall. Mater. Trans. A* **31** (2000), p. 487-495.
[27] D. Shangguan, J. D. Hunt, "In situ observation of nonfaceted cellular growth in a narrow channel", *Metall. Trans. A* **22** (1991), p. 1683-1687.
[28] R. Trivedi, H. Miyahara, P. Mazumder, E. Simsek, S. N. Tewari, "Directional solidification microstructures in diffusive and convective regimes", *J. Cryst. Growth* **222** (2001), p. 365-379.
[29] M. A. Eshelman, V. Seetharaman, R. Trivedi, "Cellular spacings—I. Steady-state growth", *Acta Metall.* **36** (1988), p. 1165-1174.
[30] S. H. Han, R. Trivedi, "Primary spacing selection in directionally solidified alloys", *Acta Metall. Mater.* **42** (1994), p. 25-41.
[31] J. S. Kirkaldy, "Spontaneous evolution of microstructure in materials", *Metall. Trans. A* **24** (1993), p. 1689-1721.
[32] L. X. Liu, J. S. Kirkaldy, "Relationship between free and forced velocity or cellular dendrites", *Scr. Metall. Mater.* **29** (1993), p. 801-806.
[33] L. X. Liu, J. S. Kirkaldy, "Systematics of pattern parameters in steady-state solidification of succinonitrile-salol, succinonitrile-acetone and pivalic acid-ethanol", *Scr. Metall. Mater.* **28** (1993), p. 1029-1034.
[34] L. X. Liu, J. S. Kirkaldy, "Thin-film forced velocity cells and cellular dendrites. 1. Experiments", *Acta Metall. Mater.* **43** (1995), p. 2891-2904.
[35] K. Somboonsuk, J. T. Mason, R. Trivedi, "Interdendritic spacing. 1. Experimental studies", *Metall. Trans. A* **15** (1984), p. 967-975.
[36] P. Kurowski, C. Guthmann, S. Decheveigne, "Shapes, wavelength selection, and the cellular-dendritic transition in directional solidification", *Phys. Rev. A* **42** (1990), p. 7368-7376.
[37] B. Billia, H. Jamgotchian, H. N. Thi, "Influence of sample thickness on cellular branches and cell-dendrite transition in directional solidification of binary alloys", *J. Cryst. Growth* **167** (1996), p. 265-276.
[38] S. Liu, M. Suk, L. Fabietti, R. Trivedi, "The effect of dimensionality on microstructures in directionally solidified SCN-Salol alloys", in *Solidification Processes and Microstructures: A Symposium in Honor of Wilfried Kurz* (M. Rappaz, C. Beckermann, R. Trivedi, eds.), Minerals, Metals & Materials Soc., Pittsburgh, PA, 2004, p. 211-218.
[39] J. Chen, P. K. Sung, S. N. Tewari, D. R. Poirier, H. C. de Groh, "Directional solidification and convection in small diameter crucibles", *Mater. Sci. Eng.* **357** (2003), p. 397-405.
[40] J. Chen, S. N. Tewari, G. Magadi, H. C. de Groh, "Effect of crucible diameter reduction on the convection, macrosegregation, and dendritic morphology during directional solidification of Pb-2.2 wt pct Sb alloy", *Metall. Trans. A* **34** (2003), p. 2985-2990.
[41] J. A. Burton, R. C. Prim, W. P. Slichter, "The distribution of solute in crystals grown from the melt. Part I. Theoretical", *J. Chem. Phys.* **21** (1953), p. 1987-1991.
[42] J. J. Favier, "Macrosegregation. 2. A comparative-study of theories", *Acta Metall.* **29** (1981), p. 205-214.
[43] A. Karma, W. J. Rappel, B. C. Fuh, R. Trivedi, "Model of banding in diffusive and convective regimes during directional solidification of peritectic systems", *Metall. Mater. Trans. A* **29** (1998), p. 1457-1470.
[44] J. A. Warren, J. S. Langer, "Prediction of dendritic spacings in a directional-solidification experiment", *Phys. Rev. E* **47** (1993), p. 2702-2712.
[45] D. Camel, J. J. Favier, "Thermal-convection and longitudinal macrosegregation in horizontal bridgman crystal-growth. 1. Order of magnitude analysis", *J. Cryst. Growth* **67** (1984), p. 42-56.
[46] D. Camel, J. J. Favier, "Thermal-convection and longitudinal macrosegregation in horizontal bridgman crystal-growth. 2. Practical laws", *J. Cryst. Growth* **67** (1984), p. 57-67.
[47] J. J. Favier, "Recent advances in bridgman growth modeling and fluid-flow", *J. Cryst. Growth* **99** (1990), p. 18-29.
[48] L. Strutzenberg, "Plane front dynamics and pattern formation in diffusion controlled directional solidification of alloys", PhD Thesis, Iowa State University, 2004.
[49] T. Taenaka, H. Esaka, S. Mizoguchi, H. Kajioka, "Equilibrium phase diagram of succinonitrile-camphor system", *J. Japan Inst. Metals Mater.* **52** (1988), p. 491-494.
[50] M. A. Chopra, M. E. Glicksman, N. B. Singh, "Dendritic solidification in binary-alloys", *Metall. Trans. A* **19** (1988), p. 3087-3096.

[51] F. L. Mota, L. M. Fabietti, N. Bergeon, L. L. Strutzenberg, A. Karma, B. Billia, R. Trivedi, "Quantitative determination of the solidus line in the dilute limit of succinonitrile-camphor alloys", *J. Cryst. Growth* **447** (2016), p. 31-35.

[52] W. W. Mullins, R. F. Sekerka, "Stability of a planar interface during solidification of a dilute binary alloy", *J. Appl. Phys.* **35** (1964), p. 444-451.

[53] J. C. LaCombe, J. L. Oudemool, M. B. Koss, L. T. Bushnell, M. E. Glicksman, "Measurement of thermal expansion in liquid succinonitrile and pivalic acid", *J. Cryst. Growth* **173** (1997), p. 167-171.

[54] M. Schraml, F. Sommer, B. Pur, W. Kohler, G. Zimmermann, V. T. Witusiewicz, L. Sturz, "Measurement of non-isothermal transport coefficients in a near-eutectic succinonitrile/(d)camphor mixture", *J. Chem. Phys.* **150** (2019), article no. 204508.

[55] Q. Li, C. Beckermann, "Modeling of free dendritic growth of succinonitrile-acetone alloys with thermosolutal melt convection", *J. Cryst. Growth* **236** (2002), p. 482-498.

[56] J. Teng, S. Liu, "Re-determination of succinonitrile (SCN)-camphor phase diagram", *J. Cryst. Growth* **290** (2006), p. 248-257.

[57] S. Decheveigne, C. Guthmann, M. M. Lebrun, "Cellular instabilities in directional solidification", *J. Phys.* **47** (1986), p. 2095-2103.

[58] L. M. Fabietti, V. Seetharaman, R. Trivedi, "The development of solidification microstructures in the presence of lateral constraints", *Metall. Trans. A* **21** (1990), p. 1299-1310.

[59] J. W. Rutter, B. Chalmers, "A prismatic substructure formed during solidification of metals", *Can. J. Phys.* **31** (1953), p. 15-39.

[60] W. A. Tiller, K. A. Jackson, J. W. Rutter, B. Chalmers, "The redistribution of solute atoms during the solidification of metals", *Acta Metall.* **1** (1953), p. 428-437.

[61] D. Camel, J. J. Favier, "Theoretical-analysis of solute transport regimes during crystal-growth from the melt in an ideal czochralski configuration", *J. Cryst. Growth* **61** (1983), p. 125-137.

[62] J. P. Garandet, T. Alboussiere, "Bridgman growth: modelling and experiments", *Prog. Cryst. Growth Character. Mater.* **38** (1999), p. 73-132.

Comptes Rendus
Mécanique
2023, Vol. 351, Special Issue S2, p. 263-272
https://doi.org/10.5802/crmeca.172

Physical Science in Microgravity within the Thematic Group Fundamental and Applied Microgravity / *Sciences physiques en microgravité au sein du GDR Micropesanteur Fondamentale et Appliquée*

On species separation in n-component mixture under microgravity

Mehdi Mojtabi [a], **Marie-Catherine Charrier-Mojtabi** [b] **and Abdelkader Mojtabi*** [b]

[a] SUPii Mécavenir. Puteaux, Ile-de-France, France

[b] Université de Toulouse, I.M.F.T. UMR CNRS/INP/UPS, 31400 Toulouse, France

E-mails: m.mojtabi@mecavenir.com (M. Mojtabi), marie-catherine.mojtabi@univ-tlse3.fr (M.-C. Charrier-Mojtabi), mojtabi@imft.fr (A. Mojtabi)

Abstract. Recently, we proved that it was possible to significantly increase the importance of the species separation for binary mixtures, under microgravity, using forced convection obtained by a uniform translational displacement of the horizontal isothermal walls of the cell maintained at T_h and T_c respectively, with $\Delta T = T_h - T_c$.

The present work is an extension of the study performed by Mojtabi (2020) with various mixtures, from binary to n-component mixtures. An application with a ternary mixture was presented. The mixture of tetralin, isobutyl benzene, n-dodecane with respectively 0.8–0.1–0.1 mass fractions was studied experimentally in weightlessness.

Keywords. Thermo-diffusion, Species separation, Soret effect, Microgravity, Forced convection, Multicomponent mixtures.

Published online: 2 March 2023

1. Introduction

In the gravity field or under microgravity, pure thermo-diffusion leads to very weak species separation. To increase the species separation in the presence of gravity, many authors use thermo-gravitational diffusion in vertical or inclined columns (TGC) [1–4]. The flow velocity strongly depends on the temperature difference, ΔT, imposed between the two walls facing each other, and also on the distance, H, between the walls. An optimum species separation cannot be obtained in relation to ΔT and H simultaneously. We can obtain an optimum which is only a function of H for a fixed ΔT or as a function of ΔT for a fixed H, Mojtabi [5].

* Corresponding author.

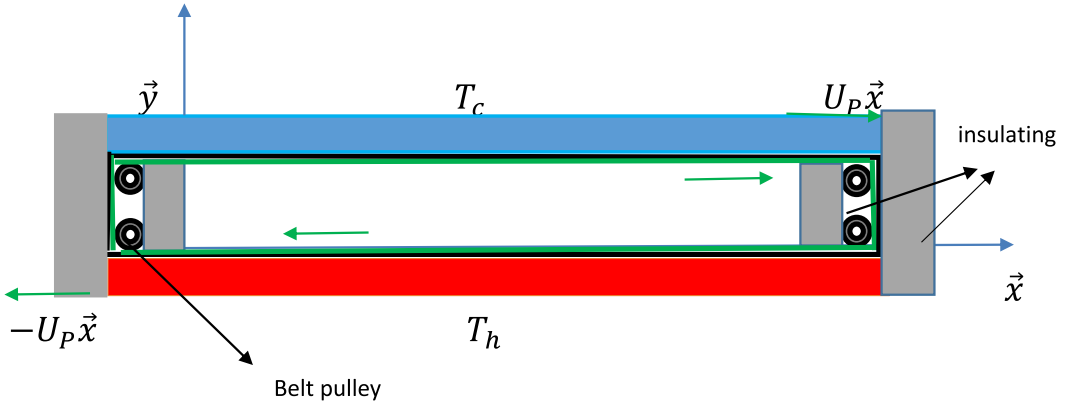

Figure 1. Schematic diagram of the rectangular cavity.

Studies on ternary mixtures are more recent. Experiments were conducted recently in the International Space Station (ISS) to measure the thermodiffusion coefficients of the ternary mixture tetralin, isobutyl benzene and n-dodecane [6, 7].

Mutschler and Mojtabi [8] studied numerically and theoretically the Soret driven convection in a horizontal porous layer saturated by n-components, with an application to a ternary hydrocarbon mixture composed of tetralin, isobutyl benzene, n-dodecane.

Recently, Mojtabi [9] showed that it is possible to significantly increase the importance of species separation for binary mixtures, in microgravity, using forced convection obtained by a uniform translational displacement of the isothermal walls maintained at T_h and T_c respectively, with $\Delta T = T_h - T_c$. In this new configuration, the species separation is several orders of magnitude greater than the one obtained in thermo-gravitational columns (TGC). The author verified that it is possible to carry out experiments, in microgravity, in order to measure directly the thermodiffusion coefficients of a binary mixture.

The present work is an extension of the study performed by Mojtabi [9] with various mixtures, from binary to n-component mixtures. An application with a ternary mixture was presented. The mixture of tetralin, isobutyl benzene, n-dodecane with respectively 0.8–0.1–0.1 mass fractions was studied experimentally in weightlessness. The geometry is a rectangular cavity. An analytical solution was obtained using the parallel flow approximation. The parameters leading to the optimal species separation for tetralin and n-dodecane were calculated. The analytical results were corroborated by direct numerical simulations (Comsol Multiphysics software).

2. Mathematical formulation

We considered a rectangular cavity of large aspect ratio $B = L/H$, where H is the thickness of the cavity along the y axis and L is the length along the x axis. The cavity is filled with a multicomponent mixture of density ρ and dynamic viscosity μ. The two walls $x = 0$ and $x = L$ are adiabatic and impermeable. The two other walls $y = 0$ and $y = H$ are kept at constant and uniform temperature T_h and T_c respectively and move at two opposite but constant imposed velocities $(-U_P\vec{e}_x, U_P\vec{e}_x)$ (see Figure 1).

The Boussinesq approximation is assumed to be valid. Thus, the thermo-physical properties of the multicomponent mixture are constant, except for the density in the buoyancy term, which varies linearly with the temperature and the mass fraction of $(n-1)$ components of the fluid mixture:

$$\rho = \rho_0 \left(1 - \beta_T (T - T_0) - \sum_{k=1}^{n-1} \beta_{C_k} (C_k - C_{0k}) \right), \tag{1}$$

where β_T and β_{C_k} are respectively the thermal expansion coefficient of the mixture and the mass expansion coefficients of $(n-1)$ components of mass fraction C_k with $k = 1,\ n-1$. The mass flux density vector of each constituent is defined as follows:

$$\vec{J}_k = -\rho_0 \sum_{j=1}^{n-1} (D_{kj} \nabla C_j + D'_{T,k} \nabla T), \quad k = 1, n-1. \tag{2}$$

The parameters D_{kj} is the mass diffusion coefficient of species k in species j and $D'_{T,k}$ the thermodiffusion coefficients of species k. They are defined as follows:

$$D'_{T,k} = F(C_k) D_{T,k}.$$

The functions $F(C_k)$ verify: $F(C_k = 0) = 0$ and $F(C_k = 1) = 0$.

We assumed that the variations of the mass fraction in the vicinity of C_{0k} remain small:

$$F(C_k) \approx F(C_{0k}).$$

Most of the authors use the hypothesis: $F(C_{0k}) = C_{0k}(1 - C_{0k})$ where C_{0k} is the mass fraction of species k at the initial state of the mixture.

The dimensional equations governing the forced convection flow of a multi-component fluid, in microgravity, are given by:

$$\begin{cases} \nabla \cdot \vec{V} = 0 \\ \rho_0 \left(\dfrac{\partial}{\partial t} \vec{V} + \vec{V} \cdot \nabla \vec{V} \right) = -\nabla P + \mu \nabla^2 \vec{V} \\ \dfrac{\partial T}{\partial t} + \vec{V} \cdot \nabla T = \alpha \nabla^2 T \\ \dfrac{\partial C_k}{\partial t} + \vec{V} \cdot \nabla C_k = \displaystyle\sum_{j=1}^{j=n-1} (D_{kj} \nabla^2 C_j + \nabla \cdot (D'_{T,k} \nabla T)) \quad \text{with } k = 1, n-1, \end{cases} \tag{3}$$

where $\vec{V}$ is the velocity field, inside the rectangular cavity, induced by the walls $y = 0$ and $y = H$ moving at constant velocity $-U_P \vec{e}_x$ and $U_P \vec{e}_x$ respectively, where α is the thermal diffusivity and μ is the dynamic viscosity of the n-components fluid.

The corresponding dimensional boundary conditions are:

$$\begin{cases} x = 0, L\colon \vec{V} = 0; \dfrac{\partial T}{\partial x} = 0, \displaystyle\sum_{j=1}^{j=n-1} D_{kj} \frac{\partial C_j}{\partial x} = 0, k = 1, n-1 \quad \forall y \in [0, H] \\ y = 0, H\colon \vec{V} = -Up\vec{e}_x, Up\vec{e}_x, T = T_h, T_c; \displaystyle\sum_{j=1}^{j=n-1} D_{kj} \frac{\partial C_j}{\partial y} + D'_{T,k} \frac{\partial T}{\partial y} = 0, \quad k = 1, n-1 \ \forall x \in [0, L]. \end{cases} \tag{4}$$

3. Analytical solution in the case of shallow cavity

In the case of a shallow cavity $B \gg 1$ the parallel flow approximation, used by many previous authors [10], is considered. The streamlines are all parallel to the x axis throughout the cavity except for the vicinity of the insulated walls $x = 0$ and $x = L$, which gives:

$$\vec{V}_b = U_b(y) \vec{e}_x. \tag{5}$$

The temperature and mass fraction profiles can then be written as the sum of a term defining a linear variation along x and another term giving the distribution along y:

$$\begin{cases} T_b = bx + g(y) \\ C_{bk} = m_k x + f_k(y) \quad \forall k = 1, n-1. \end{cases} \tag{6}$$

The constants b and m_k represent the temperature and mass fraction gradients along the x direction respectively. The constant b is zero due to constant temperatures imposed on the walls $y = 0$, H. By replacing in the system of Equations (3), the velocity, the temperature and the mass fractions by their expression in the Equations (5) and (6) we obtain the following simplified equations

$$\begin{cases} \dfrac{\partial^3 U_b}{\partial y^3} = 0 \\ \dfrac{\partial^2 T_b}{\partial y^2} = 0 \\ m_k U_b - \displaystyle\sum_{j=1}^{j=n-1} (D_{kj} \nabla^2 C_{bj} + \nabla \cdot (D'_{T,k} \nabla T_b)) = 0. \end{cases} \tag{7}$$

For weak separations, the last equation of the system (7) is written:

$$m_k U_b - \sum_{j=1}^{j=n-1} (D_{kj} \nabla^2 C_{bj} + C_{k0}(1 - C_{k0}) D_{T,k} \nabla^2 T_b) = 0. \tag{8}$$

By using the boundary conditions (4), we deduce the expressions of the temperature field and the velocity field:

$$\begin{cases} T_b = T_C - \dfrac{(T_H - T_C) y}{H} \\ U_b = \dfrac{U_P (2y - H)}{H}. \end{cases} \tag{9}$$

We obtained for the mass fraction the following result in matrix form:

$$\begin{aligned} [C_{bk}] \; = \; & [m_k] x - \left(\int \left(\int U_p \, \mathrm{d}y \right) \mathrm{d}y \right) [D_{kj}]^{-1} [m_j] \\ & + [D_{kj}]^{-1} \left[D_{T,j} (T_H - T_C) C_{j0} (1 - C_{j0}) \left(\frac{y}{D_{kj} H} + \frac{1}{2 D_{kj}} \right) \right] + C_{k0}, \quad k = 1, n-1. \end{aligned} \tag{10}$$

The different mass fraction gradients were obtained assuming that the mass flux associated with each components k through any cross-section of the rectangular cavity perpendicular to the x-axis is equal to zero:

$$\int_0^H \left(U_b C_{bk} - \left([D_{kj}] \frac{\partial C_{bj}}{\partial x} + \left[D_{T,k} C_{k0} (1 - C_{k0}) \frac{\partial T_b}{\partial x} \right) \right) \right] \mathrm{d}y = 0, \quad k = 1, n-1. \tag{11}$$

For a ternary mixture, in the general case ($D_{kj} \neq 0$, $j \neq k = 1, 2$) we deduced:

$$\begin{cases} m_1 = \dfrac{5[FC_1((HU_P)^2 + 30(D_{22}^2 + D_{21} D_{12}) D_{T1} - 30 FC_2 D_{12} (D_{11} + D_{22}) D_{T2}](T_H - T_C) U_P}{(HU_P)^2 [(HU_P)^2 + 30(D_{11}^2 + 2D_{21} D_{12} + D_{22}^2)] + 900(D_{11} D_{22} - D_{21} D_{12})^2} \\ m_2 = \dfrac{5[FC_2((HU_P)^2 + 30(D_{11}^2 + D_{12} D_{21}) D_{T2} - 30 FC_1 (D_{21} (D_{11} + D_{22}) D_{T1})](T_H - T_C) U_P}{(HU_P)^2 [(HU_P)^2 + 30(D_{11}^2 + 2D_{21} D_{12} + D_{22}^2)] + 900(D_{11} D_{22} - D_{21} D_{12})^2}, \end{cases} \tag{12}$$

where: $FC_k = C_{k0}(1 - C_{k0})$, for $k = 1, 2$.

In the case where the cross-diffusion coefficients $D_{ij}(i \neq j)$ are negligible compared to D_{ii}, we obtained:

$$\begin{cases} m_1 = \dfrac{5FC_1D_{T1}(T_H - T_C)U_P}{(HU_P)^2 + 30D_{11}^2} \\ m_2 = \dfrac{5FC_2D_{T2}(T_H - T_C)U_P}{(HU_P)^2 + 30D_{22}^2}. \end{cases} \tag{13}$$

In the case of n components under the previous approximation, we found the following general results for $k = 1, n-1$:

$$m_k = \frac{5C_{k0}(1 - C_{k0})D_{Tk}(T_H - T_C)U_P}{(HU_P)^2 + 30D_{kk}^2} \tag{14}$$

and

$$C_{bk} = m_k x - \frac{m_k U_P \left[\frac{y^3}{3H} - \frac{y^2}{2} + \frac{H^2 - 6DL}{12}\right]}{D_{kk}} + \frac{D_{Tk}(T_H - T_C)C_{k0}(1 - C_{k0})\left(\frac{y}{H} + \frac{1}{2}\right)}{D_{kk}} + C_{k0}. \tag{15}$$

4. Optimization of the species separation

The species separation of the component k, $S_k = m_k L$ is defined as the difference in mass fraction of the component k between the two ends of the cell, $x = 0$ and $x = L$, with m_k obtained in Equation (14). For a given n-component mixture, the mass diffusion coefficient D_{kk}, the thermodiffusion coefficient D_{Tk} and the initial mass fraction of the denser component C_{k0}, for the component k, are known. The analysis of Equation (14) shows that the species separation decreases as the thickness, H, of the cavity increases. Moreover, the species separation, S_k, increases when the temperature difference $(T_H - T_C)$ increases. Then, only one independent control parameter remains, namely the velocity U_p imposed on the wall $y = 0$ and $-U_p$ imposed on the wall $y = H$. The optimum separation S_k is obtained solving equation:

$$\frac{\partial m_k}{\partial U_p} = 0. \tag{16}$$

The resolution of the algebraic equation (16) leads to:

$$U_{Pk\,\mathrm{Opt}} = \pm\sqrt{30}D_{kk}/H. \tag{17}$$

The optimal velocity $U_{Pk\,\mathrm{Opt}}$, with respect to the parameter U_p, depends only of the mass diffusion coefficient D_{kk} and the distance H. So, if the mass diffusivity of the component k is known, the experiments can be conducted with this optimal velocity. Replacing U_p by $U_{Pk\,\mathrm{Opt}}$ in Equation (14) leads to the expression of the maximum mass fraction gradient:

$$m_{k\,\mathrm{Opt}} = \frac{\sqrt{30}C_{k0}(1 - C_{k0})D_{Tk}(T_H - T_C)}{12HD_{kk}}. \tag{18}$$

Equation (18) can also be written in the following form:

$$m_{k\,\mathrm{Opt}} = \frac{\sqrt{30}C_{k0}(1 - C_{k0})S_{Tk}(T_H - T_C)}{12H}, \tag{19}$$

where $S_{Tk} = D_{Tk}/D_{kk}$ is the Soret coefficient of the component k of the mixture.

Thus, the optimum value of the mass fraction gradient (Equation (19)) depends only on the thermal gradient in the y direction, $(T_H - T_C)/H$, once the initial mass fraction C_{k0}, $k = 1, n-1$ and the Soret coefficient S_{Tk} are known. Equations (17) and (19) show that it possible to access

Table 1. Thermophysical properties of tetralin, isobutyl benzene, *n*-dodecane with respectively mass fraction 0.8–0.1–0.1 at 25 °C [11].

D_{11} (10^{-10} m^2·s^{-1})	D_{12}	D_{21}	D_{22}	D_{T1} (10^{-10} m^2·(s·K)$^{-1}$)	D_{T2}
5.96	0.15	1.1	6.79	0.0065	−0.0049

the indirect measurement of the Soret coefficient S_{Tk} by measuring the optimal mass fraction gradient $m_{k\mathrm{Opt}}$:

$$S_{Tk} = 12Hm_{k\mathrm{Opt}}/\sqrt{30}C_{k0}(1-C_{k0})(T_H - T_C). \tag{20}$$

To measure $m_{k\mathrm{Opt}}$, it is necessary that the walls be set in motion with the optimal velocity $U_{Pk\mathrm{Opt}}$. The determination of the optimal velocity requires the mass diffusivity D_{kk} of the component k.

In the following paragraph, we showed that it is also possible to measure of the mass diffusion coefficient D_{kk} using Equation (14). To do so, it is sufficient to carry out two experiments, one with a velocity U_{P1} and the other with different velocity U_{P2} for the same cell of thickness H subjected to the same temperature difference $\Delta T = T_H - T_C$.

We obtained:

$$m_{ki} = \frac{5C_{k0}(1-C_{k0})D_{Tk}(T_H - T_C)U_{Pi}}{(HU_{Pi})^2 + 30D_{kk}^2} \tag{21}$$

with $i = 1,2$. The ratio m_{k1}/m_{k2} leads to:

$$m_{k1}/m_{k2} = U_{P1}((HU_{P2})^2 + 30D_{kk}^2)/U_{P2}((HU_{P1})^2 + 30D_{kk}^2). \tag{22}$$

From Equation (22) we can deduce the mass diffusion coefficient D_{kk} after measuring the mass fraction gradients m_{k1} and m_{k2} obtained from two fixed wall velocities U_{P1} and U_{P2} respectively. We obtained:

$$D_{kk}^2 = U_{P1}U_{P2}(U_{P1}m_{k1} - U_{P2}m_{k2})H^2/30(U_{P1}m_{k2} - U_{P2}m_{k1}). \tag{23}$$

5. Application to the species separation of a tetralin, isobutyl benzene, *n*-dodecane with respectively 0.8–0.1–0.1 mass fractions

5.1. *Species separation under weightlessness conditions*

To illustrate the analytical results obtained in this study, we only considered the experimental values of the thermophysics parameters of tetralin, isobutyl benzene, *n*-dodecane with respectively 0.8–0.1–0.1 mass fractions studied experimentally in weightlessness [11].

The thermophysical properties of this ternary solution at the mean temperature 25 °C are presented in Table 1.

Using the values presented in Table 1 for a cavity of thickness $H = 2 \times 10^{-3}$ m, the optimum value of the velocity and the mass fraction gradient following the x axis for the component 1 namely tetralin and the component 2 namely isobutyl benzene were obtained as a function of the thermal gradient following the y axis, ΔT.

$$\begin{cases} U_{Pk\mathrm{Opt}} = \pm\dfrac{\sqrt{30}D_{kk}}{H} \\ m_{k\mathrm{Opt}} = \dfrac{\sqrt{30}C_{k0}(1-C_{k0})D_{Tk}(T_H - T_C)}{12HD_{kk}}. \end{cases} \tag{24}$$

For $\Delta T = 10$, we obtained:

$$\begin{cases} U_{P1\mathrm{Opt}} = \pm\dfrac{\sqrt{30}D_{11}}{H} = \pm 5.96\dfrac{10^{-7}\sqrt{30}}{2} = \pm 1.63 \times 10^{-6}\ \mathrm{m/s} \\ m_{1\mathrm{Opt}} = 0.597\ \mathrm{m}^{-1} \end{cases} \tag{25}$$

and

$$\begin{cases} U_{P2\,\mathrm{Opt}} = \pm\dfrac{\sqrt{30}D_{22}}{H} = \pm 6.79\dfrac{10^{-7}\sqrt{30}}{2} = \pm 1.86\times 10^{-6}\ \mathrm{m/s} \\ m_{2\,\mathrm{Opt}} = -0.222\ \mathrm{m}^{-1}. \end{cases} \tag{26}$$

Considering the low optimal velocity $U_{Pk\,\mathrm{Opt}}$ obtained, the time required to reach the stationary state of species separation would be around ten hours. The main interest here is given by Equation (24) which specifies that the measurement of the optimal mass fraction gradient $m_{k\,\mathrm{Opt}}$ allows access to the determination of the thermodiffusion coefficient D_{Tk}.

If the cross-diffusion coefficients D_{ij} $(i \neq j)$ are non-zero, the analytical expression leading to the optimal velocity is the solution of an algebraic equation of the 6th degree. We obtained this velocity using the values in Table 1.

$$\begin{cases} U_{P1\,\mathrm{Opt}} = \pm 1.61\times 10^{-6}\ \mathrm{m/s} \\ m_{1\,\mathrm{Opt}} = 0.605\ \mathrm{m}^{-1} \end{cases} \tag{27}$$

$$\begin{cases} U_{P2\,\mathrm{Opt}} = \pm 1.37\times 10^{-6}\ \mathrm{m/s} \\ m_{2\,\mathrm{Opt}} = -0.329\ \mathrm{m}^{-1}. \end{cases} \tag{28}$$

5.2. *Comparison with the species separation inside a vertical thermogravitation column under gravity conditions*

The theoretical study of the thermogravitational separation process of n-component mixture inside a vertical column, under gravity conditions, was the subject of a communication at the French Mechanical congress in 2017 [12]. This study focused on a bi-dimensional vertical thermogravitational column. The analytical study was based on the parallel flow approximation and the theory was developed by Furry Jones and Onsager. Using these hypotheses, the velocity, the mass-fraction of each component and the temperature at the stationary state were calculated. Knowing the different flowfields in the column, the separation of each component in the mixture was determinated. Analytical expressions of the separation and transport coefficients were obtained. The results obtained were in good agreement with the thermo-diffusion coefficients found in the literature. In the case where the cross-diffusion effect can be neglected, it is possible to obtain a formula that allows us to calculate the coefficients of thermo-diffusion D_{Tk} knowing the term D_{kk}, explicitly, from the measurements of the different mass fraction gradients m_k^c:

$$m_k^c = \frac{504H^2 g D_{Tk}\nu\beta_T(T_H - T_C)^2}{H^6(g\beta_T(T_H - T_C))^2 + 362880\nu^2 D_{kk}^2}. \tag{29}$$

It can be noticed that, from Equation (29), we find the classical relation giving the expression of the mass fraction gradient m_{col} in the case of binary solutions:

$$m_{\mathrm{col}} = \frac{504H^2 g D_T\nu\beta_T(T_H - T_C)^2}{H^6(g\beta_T(T_H - T_C))^2 + 362880\nu^2 D^2}. \tag{30}$$

Larrañaga *et al.* [13] determined the separation of each constituent of the ternary mixture tetralin, isobutylbenzene and n-dodecane in mass fraction (0.8–0.1–0.1). From the values of the mass fractions measured, these authors determined the values of the coefficients of thermodiffusion D_{Tk} of each component k. The mass fraction gradient m_1^c and m_2^c in the z direction for the vertical thermogravitational column and for a cavity with the same thickness $H = 2\times 10^{-3}$ m submitted of the same temperature difference $(T_H - T_C) = 10$ are respectively:

$$m_1^c = 0.00721\ \mathrm{m}^{-1} \quad \text{and} \quad m_2^c = 0.00544\ \mathrm{m}^{-1}. \tag{31}$$

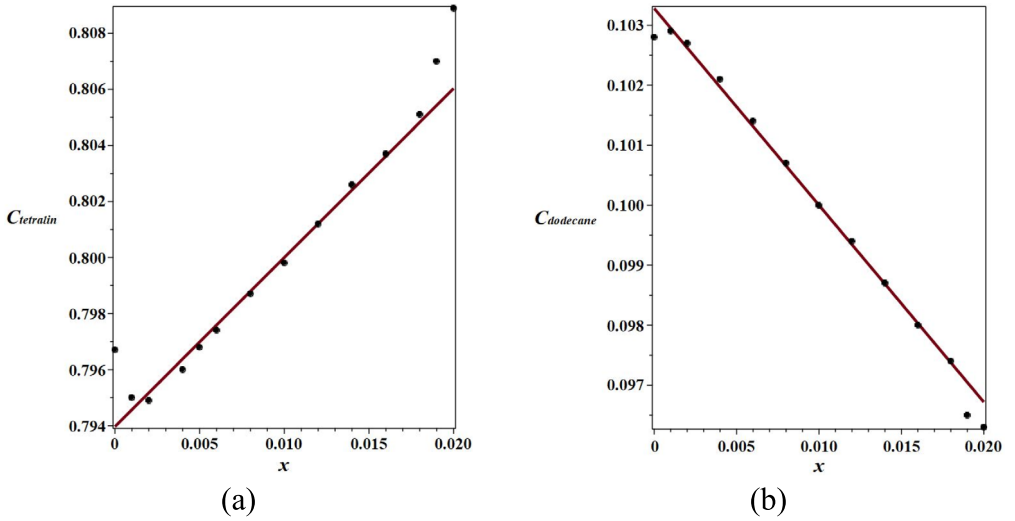

Figure 2. (a) Mass fraction of the tetralin and (b) mass fraction of the n-dodecane as a function of x for $y = H/2 = 1$ mm, for a cavity of $L = 20$ mm and $H = 2$ mm (analytical results — numerical solution •).

Thus, the mass fraction gradient $m_{1\,\mathrm{Opt}} = 0.597\ \mathrm{m}^{-1}$ obtained in microgravity is 82.8 times greater than $m_1^c = 0.00721\ \mathrm{m}^{-1}$. The mass fraction gradient $m_{2\,\mathrm{Opt}} = -0.222\ \mathrm{m}^{-1}$ obtained in microgravity is 40.84 times greater than $m_2^c = 0.00544\ \mathrm{m}^{-1}$.

6. 2D numerical simulations

The dimensional system (3) associated to boundary conditions (4) was solved numerically using a finite element code, Comsol Multiphysics, with rectangular mesh. The time-dependent solver and the set of equations (incompressible Navier–Stokes, energy equation and two conservation equations of chemical species, one for the tetralin and the other one for the n-dodecane) in transient form were used. The condition of conservation of the average mass fraction in the cavity was imposed for each iteration. Direct numerical simulations were performed for cavities of the same thickness $H = 2 \times 10^{-3}$ m and various lengths $L = 2 \times 10^{-2}$ m and 5×10^{-2} m, which correspond to aspect ratios of 10 and 25 respectively. We considered quadrangle spatial resolutions from 20–200 up to 30–700. The analytical calculations led to $m_{1\,\mathrm{Opt}} = 0.605\ \mathrm{m}^{-1}$ and $m_{2\,\mathrm{Opt}} = -0.329\ \mathrm{m}^{-1}$ for the tetralin and the n-dodecane respectively and the direct numerical simulations to $m_{1\,\mathrm{num}} = 0.590\ \mathrm{m}^{-1}$ and $m_{2\,\mathrm{num}} = -0.324\ \mathrm{m}^{-1}$. The numerical values obtained for $m_{1\,\mathrm{num}}$ and $m_{2\,\mathrm{num}}$ are in good agreement with the analytical values, except for the neighborhood of $x = 0$ and $x = L$. The reason for this is that our analytical solution assumes a fluid layer of very large extension along x and does not take into account the return flow of the fluid at $x = 0$ and from $x = L$.

The mass fraction C_{tetralin} and C_{dodecane} as a function of x for $y = H/2 = 1$ mm (Figure 2a) and (Figure 2b) for $L = 20$ mm show a very good agreement between the analytical calculations (red line) and the direct numerical simulation results (dark points).

The streamlines, iso-mass fraction lines and mass fraction field (in colour) for $\Delta T = 20$, $L = 50$ mm, $H = 2$ mm are presented in Figure 3 (n-dodecane) and Figure 4 (tetralin).

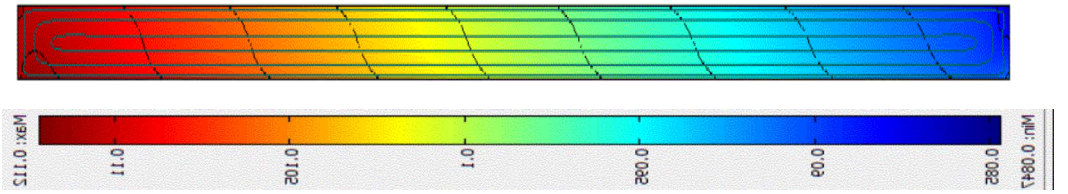

Figure 3. Streamlines, iso-mass fraction lines and mass fraction field (in colour) for n-dodecane and for $\Delta T = 20$, $L = 50$ mm, $H = 2$ mm.

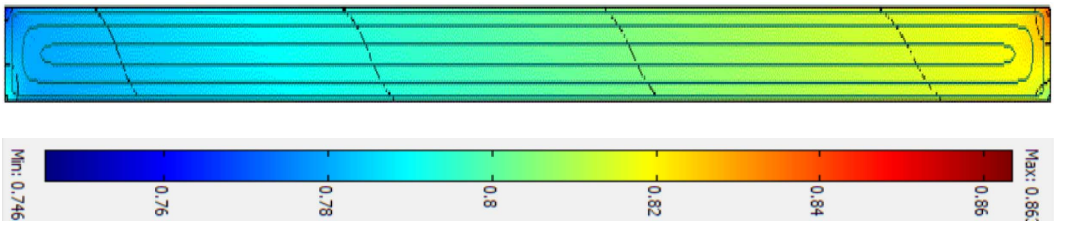

Figure 4. Streamlines, iso-mass fraction lines and mass fraction field (in colour) for tetralin and for $\Delta T = 20$, $L = 50$ mm, $H = 2$ mm.

7. Conclusion

In the vertical thermogravitation columns previously used in terrestrial applications to increase the species separation, the velocity of the flow depends on the temperature gradient imposed $(T_H - T_C)$ and its thickness H. However, for these columns, it was shown that there is no optimum of species separation according to these two independent parameters $(T_H - T_C)$ and H, [14]. For a given value of $(T_H - T_C)$ the separation is optimal for a very small thickness of the column $H < 1$ mm. Similarly, for fixed H, if we increase the value of $(T_H - T_C)$ to increase the separation, we increase the velocity of the flow which reduces the species separation. In microgravity, the temperature difference $(T_H - T_C)$ does not induce convective motion. The flow in the cell was obtained using a rectangular cavity with two opposite isothermal walls (T_H and T_C) of great length, moving with equal optimal velocities in opposite directions, $U_{Pk\,\mathrm{Opt}}$ and $-U_{Pk\,\mathrm{Opt}}$. The velocities of these two walls are independent of $(T_H - T_C)$. We can increase $(T_H - T_C)$ to increase the separation without modifying the velocity. We showed that the species separation in microgravity with $U_{P\,\mathrm{Opt}}$ is several orders of magnitude greater than the one obtained in a vertical thermogravitation column of same geometrical dimensions and submitted to the same temperature difference. These results, previously obtained in binary mixtures, were extended to multi-component mixtures with a detailed study on ternary tetralin, isobutyl benzene and n-dodecane with respectively 0.8–0.1–0.1 mass fractions. To obtain the coefficients of thermodiffusion D_{Tk} associated with each of the components of the mixture, the experiments must be carried out with the optimal velocity associated with the species considered $U_{Pk\,\mathrm{Opt}}$.

Conflicts of interest

Authors have no conflict of interest to declare.

Acknowledgements

The authors acknowledge the scientific support of CNES, the French National Space Agency. The authors thank Professor P. Costeseque for helpful discussion.

References

[1] W. H. Furry, R. C. Jones, L. Onsager, "On the theory of isotope separation by thermal diffusion", *Phys. Rev.* **55** (1939), p. 1083-1095.

[2] M. Lorenz, A. H. Emery, "The packed thermal diffusion column", *Chem. Eng. Sci.* **11** (1959), p. 16-23.

[3] J. K. Platten, M. M. Bou-Ali, J. F. Dutrieux, "Enhanced molecular separation in inclined thermogravitational columns", *J. Phys. Chem. B* **107** (2003), no. 42, p. 11763-11767.

[4] M. C. Charrier-Mojtabi, B. Elhajjar, A. Mojtabi, "Analytical and numerical stability analysis of Soret driven in a horizontal porous layer", *Phys. Fluids* **19** (2007), article no. 124104.

[5] A. Mojtabi, B. Ouattara, D. A. S. Rees, M. C. Charrier-Mojtabi, "The effect of conducting bounding horizontal plates on species separation in porous cavity saturated by a binary mixture", *Int. J. Heat Mass Transfer* **126** (2018), p. 479-488.

[6] V. Sechenyh, J. C. Legros, A. Mialdun, J. M. Ortiz De Zárate, V. Shevtsova, "Fickian diffusion in ternary mixtures composed by 1, 2, 3, 4-tetrahydronaphthalene, isobutylbenzene, and *n*-dodecane", *J. Phys. Chem. B* **120** (2016), no. 3, p. 535-548.

[7] A. Mialdun, V. Sechenyh, J. C. Legros, J. M. Ortiz De Zárate, V. Shevtsova, "Investigation of fickian diffusion in the ternary mixture of 1, 2, 3, 4-tetrahydronaphthalene, isobutylbenzene, and dodecane", *J. Chem. Phys.* **139** (2013), no. 10, article no. 104903.

[8] D. Mutschler, A. Mojtabi, "Theoretical and numerical analysis of Soret-driven convection in a horizontal porous layer saturated by an *n*-component mixture: application to ternary hydrocarbon mixture tetralin, isobutyl benzene, *n*-dodecane with mass fractions 0.8–0.1–0.1", *Int. J. Heat Mass Transfer* **162** (2020), article no. 120339.

[9] A. Mojtabi, "A new process for the determination of the Soret coefficient of a binary mixture under microgravity", *Int. J. Therm. Sci.* **146** (2020), article no. 106204.

[10] A. Mahidjiba, R. Bennacer, P. Vasseur, "Flows in a fluid layer induced by the combined action of a shear stress and the Soret effect", *Int. J. Heat Mass Transfer* **49** (2006), p. 1403-1411.

[11] M. M. Bou-Ali, A. Ahadi, D. Alonso de Mezquia, Q. Galand, M. Gebhardt, O. Khlybov, W. Köhler, M. Larrañaga, J. C. Legros, T. Lyubimova, A. Mialdun, I. Ryzhkov, M. Z. Saghir, V. Shevtsova, S. Van Vaerenbergh, "Benchmark values for the Soret, thermodiffusion and molecular diffusion coefficients of the ternary mixture tetralin, isobutyl benzene, *n*-dodecane with 0.8–0.1–0.1 mass fraction", *Eur. Phys. J. E* **38** (2015), article no. 30.

[12] D. Mutschler, M. A. Larabi, A. Mojtabi, "Couplage thermodiffusion-convection dans une colonne thermogravitationnelle en vue de la séparation des espèces d'un mélange multiconstituants", in *23ème Congrès Français de Mécanique, Lille, 28-1 Septembre*, 2017.

[13] M. Larrañaga, M. M. Bou-Ali, D. A. de Mezquia, D. A. S. Rees, J. A. Madariaga, C. Santamaría, J. K. Platten, "Contribution to the benchmark for ternary mixtures: determination of Soret coefficients by the thermogravitational and the sliding symmetric tubes techniques", *Eur. Phys. J. E* **38** (2015), no. 4, p. 1-7.

[14] A. Mojtabi, A. Khouzam, L. Yacine, M. C. Charrier-Mojtabi, "Analytical and numerical study of Soret mixed convection in two-sided lid-driven horizontal cavity: optimal species separation", *Int. J. Heat Mass Transfer* **139** (2019), p. 1037-1046.

Comptes Rendus
Mécanique
2023, Vol. 351, Special Issue S2, p. 273-287
https://doi.org/10.5802/crmeca.143

Physical Science in Microgravity within the Thematic Group Fundamental and Applied Microgravity / *Sciences physiques en microgravité au sein du GDR Micropesanteur Fondamentale et Appliquée*

Thermoelectric convection in a planar capacitor: theoretical studies and experiments in parabolic flights

Convection thermoélectrique dans un condensateur plan : études théoriques et expériences lors des vols paraboliques

Elhadj B. Barry [a], Harunori N. Yoshikawa [b], Changwoo Kang [c], Antoine Meyer [d], Martin Meier [d], Olivier Crumeyrolle [a], Christoph Egbers [d] and Innocent Mutabazi [*, a]

[a] Normandie Université, UNIHAVRE, LOMC, UMR CNRS 6294, 53, rue de Prony, 76058 Le Havre Cedex, France

[b] Université Côte d'Azur, INPHYNI, 06100 Nice Cedex, France

[c] Department of Mechanical Engineering, Jeonbuk National University, 567 Baekje-daero, Deokjin-gu, Jeonju-si, Jeollabuk-do, 54896, Republic of Korea

[d] Department of Aerodynamics and Fluid Mechanics, Brandenburg University of Technology Cottbus-Senftenberg, Siemens-Halske-Ring 15a, 03046 Cottbus, Germany

E-mails: elhadj-boubacar.barry@univ-lehavre.fr (E. B. Barry), Harunori.Yoshikawa@univ-cotedazur.fr (H. N. Yoshikawa), changwoo.kang@jbnu.ac.kr (C. Kang), meyer@b-tu.de (A. Meyer), meyer@b-tu.de (M. Meier), olivier.crumeyrolle@univ-lehavre.fr (O. Crumeyrolle), egbers@b-tu.de (C. Egbers), innocent.mutabazi@univ-lehavre.fr (I. Mutabazi)

Abstract. Thermoelectric convection in a plane capacitor is investigated in a microgravity environment and in the case of the thermal stable and unstable stratification in terrestrial conditions. Energetic analysis shows that in the thermal stable stratification, the thermoelectric convection is delayed while in the thermal unstable stratification, it is enhanced by the Archimedean buoyancy before the latter takes over the dielectrophoretic buoyancy and drives natural thermal convection. An experiment in parabolic flights shows the formation of thermoelectric convection at the end of the microgravity phase.

* Corresponding author.

Résumé. Nous avons étudié la convection thermoélectrique dans un condensateur plan placé dans un environnement de microgravité et dans des conditions terrestres avec une stratification thermique instable ou stable. L'analyse énergétique montre que dans le cas de stratification stable, la convection thermoélectrique est retardée alors que dans le cas de stratification thermique instable, elle est amplifiée par la poussée d'Archimède avant que cette dernière ne prenne le dessus et pilote la convection thermique naturelle. Une expérience réalisée lors des vols paraboliques illustre la formation de la convection thermoélectrique à la fin de la phase de microgravité.

Keywords. Thermoelectric convection, Dielectrophoretic force, Electric gravity, Zero-gravity, Convective patterns.

Mots-clés. Convection thermoélectrique, Force diélectrophorétique, Gravité électrique, Gravité zéro, Motifs de convection.

Published online: 8 February 2023

1. Introduction

The problem of heat transfer in microgravity conditions or in a low-gravity environment represents a scientific and technological issue to be addressed thoroughly with the development of long-term missions for space exploration. Heat transfer in fluids can be achieved through three well-identified mechanisms: heat conduction, thermal convection, and radiation. Among the three mechanisms, thermal convection represents the most efficient way to transfer heat from one surface to another through a given fluid. In many applications, thermal convection is forced by external mechanisms which are often cumbersome, especially in space devices where the weight and volume need to be optimized. In microgravity, natural convection cannot be achieved because of weak Archimedean buoyancy. Thus, to create natural-like convection, physicists have suggested using either electric force acting on dielectric liquids [1] or magnetic force acting on ferrofluids [2]. When an electric field acts on a dielectric liquid, it generates a dielectric force [1] which contains a conservative term and non-conservative component responsible for the vorticity generation. The last force called dielectrophoretic force generates thermoelectric convection when coupled with a temperature gradient in the liquid [3]. In the case of a magnetic field acting on a ferrofluid with a temperature gradient, a similar but thermomagnetic force is responsible for thermomagnetic convection generation [4].

Many studies have focused on the thermoelectric convection in spherical and cylindrical cavities because of the intense values of the dielectrophoretic force due to the inhomogeneity of the electric field induced by the curvature and because of its potential applications in the modeling of convection generation in planets [5–10]. Despite their simplicity, thermoelectric convection in rectangular cavities has been less investigated [11–13] in particular because the electric gravity is less effective than in curved configurations. However, because of the development of microfluidic systems, it is possible to achieve strong electric fields between two parallel plates distant of few microns for small values of the applied electric tension [14].

The present study addresses the linear stability analysis of the thermoelectric convection in a rectangular cavity in microgravity and thermally stable or unstable stratification. The choice of stable or unstable thermal stratification is motivated by the applications where it is either needed to evacuate heat or to enhance heat transfer between two surfaces separated by a dielectric liquid in Earth conditions. Both numerical simulations around the threshold and experiments under microgravity conditions have been performed to characterize flow patterns. The paper is organized as follows. The next section presents the physical system under investigation. Section 3 gives the base state and linearized equations near the base state. In Section 4, the linear stability results and the thermo-convective patterns are presented and discussed. Section 5

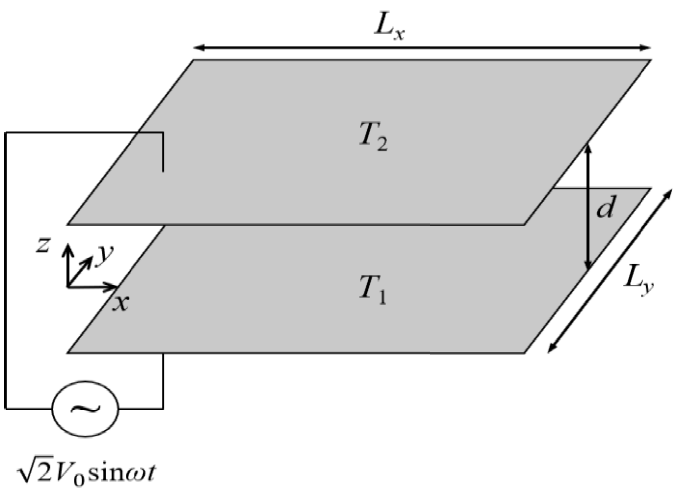

Figure 1. Dielectric liquid confined between two horizontal plates with dimensions (L_x, L_y) differentially heated $(T_1 \neq T_2)$ and with a fast alternating electric tension of frequency $f = \omega/2\pi$.

is dedicated to the experimental results. The last section contains discussions and concluding remarks.

2. Problem formulation

We consider a dielectric liquid confined between two horizontal plates differentially heated and subject to an alternating electric tension $V(t) = \sqrt{2}\,V_0 \sin\omega t$ as shown in Figure 1. The fluid is characterized by the density ρ, the kinematic viscosity ν, the thermal diffusivity κ and the electric permittivity ϵ.

The electric field $\vec{E}$ induces in the fluid a volume force called electrohydrodynamic force density which is given by [1]

$$\vec{f}_{\mathrm{EHD}} = \rho_e \vec{E} + \vec{\nabla}\left[\frac{\rho}{2}\left(\frac{\partial \epsilon}{\partial \rho}\right)_T \vec{E}^2\right] - \frac{\vec{E}^2}{2}\vec{\nabla}\epsilon \tag{1}$$

where ρ_e is the density of electric charges. The first term in (1) is the Coulomb force density, the second term is the electrostriction force density and the last term in (1) is the dielectrophoretic force $\vec{f}_{\mathrm{DEP}}$. If the frequency of the electric tension is chosen much larger than all the inverses of characteristic times of the dielectric fluid (charge relaxation, thermal diffusion and viscous times) i.e. $(\tau_e^{-1}, \tau_\kappa^{-1}, \tau_\nu^{-1}) = (\sigma_{el}/\epsilon, \kappa/d^2, \kappa/d^2) \ll f$, then it is possible to neglect the charge accumulation in the fluid so that the Coulomb force is negligible. Moreover, it is then possible to use the time-averaged electric potential instead of the alternating one. In addition to the physical phenomena described above, the displacement due to the polarization produces internal heating in the fluid when the frequency of the applied electric field is too large [15]. So, to highlight the effect of the dielectrophoretic force, we assume that the dielectric heating, arising from the dielectric loss, is negligible.

2.1. *Dielectrophoretic buoyancy and electric gravity*

We assume the electrohydrodynamic Boussinesq approximation i.e. $\rho(\theta) = \rho_0(1 - \alpha\theta)$; $\epsilon(\theta) = \epsilon_{\mathrm{ref}}(1 - e\theta)$ where $\theta = T - T_{\mathrm{ref}}$ is the deviation from the reference temperature, $\rho_0 = \rho(\theta =$

0), α is the thermal expansion coefficient and e is the thermal coefficient of the permittivity. The reference temperature is the average temperature of the two plates i.e. $T_{\text{ref}} = (T_1 + T_2)/2$. The density of the dielectrophoretic force in (1) becomes

$$\vec{f}_{\text{DEP}} = \vec{\nabla}\left[\left(\frac{\rho}{2}\left(\frac{\partial \epsilon}{\partial \rho}\right)_T + \epsilon - \epsilon_0 + \epsilon_{\text{ref}}\right)\vec{E}^2\right] - \alpha\rho_0\theta\vec{g}_e \tag{2}$$

ϵ_0 is the vacuum permittivity. The first term is a conservative force density, which represents the gradient of the electric contribution to the fluid pressure, the second term is a non-conservative force density and it is the source of the vorticity. It is written in analogy with the Archimedean buoyancy ($-\alpha\rho_0\theta\vec{g}$) and it will be called *dielectrophoretic buoyancy* with $\vec{g}_e = -\vec{\nabla}\Psi$ defined as the electric gravity where $\Psi = -e\epsilon_{\text{ref}}\vec{E}^2/2\rho_0\alpha$ is the analog of the gravitational potential and it is proportional to the electrostatic energy density stored in the capacitor. Values of properties of some dielectric liquids used in microgravity experiments are given in [13].

2.2. *Dimensionless governing equations*

We chose the characteristic scales d for lengths, ν/d for velocities, viscous diffusion time d^2/ν for time, $\Delta T = T_1 - T_2$ for temperature and V_0 for potential. The governing equations are the mass conservation equation, the momentum equation, the energy equation, and the Gauss law (charge conservation) which, in dimensionless form, read

$$\vec{\nabla}\cdot\vec{u} = 0, \tag{3a}$$

$$\frac{\partial \vec{u}}{\partial t} + (\vec{u}\cdot\vec{\nabla})\vec{u} = -\vec{\nabla}\pi + \Delta\vec{u} + Pr^{-1}\theta(Ra\vec{e}_z - L\vec{\hat{g}}_e), \tag{3b}$$

$$Pr\left[\frac{\partial \theta}{\partial t} + (\vec{u}\cdot\vec{\nabla})\theta\right] = \Delta\theta, \tag{3c}$$

$$\vec{\nabla}\cdot[(1-\gamma_e\theta)\vec{\nabla}\phi] = 0, \tag{3d}$$

where $\vec{u}$ represents the velocity field, $\gamma_e = e\Delta T$ is the thermoelectric coupling parameter, $\vec{\hat{g}}_e = \vec{g}_e/g_e$ and ϕ is the electrostatic potential i.e. $\vec{E} = -\vec{\nabla}\phi$. We have introduced the following dimensionless control parameters: the Prandtl number $Pr = \nu/\kappa$, the Rayleigh number $Ra = \alpha\Delta T g d^3/\nu\kappa$, the electric Rayleigh number $L = \alpha\Delta T\overline{g}_e d^3/\nu\kappa$ where the electric gravity $\overline{g}_e$ is computed at the central position $z = 0$ of the cavity. The quantity π represents the dimensionless hydraulic charge (Bernoulli function) [13].

The boundary conditions at the plates of the capacitor are given by:

$$u = v = w = 0, \quad \theta = \tfrac{1}{2}, \quad \phi = 1 \text{ at } z = -\tfrac{1}{2}, \tag{4a}$$

$$u = v = w = 0, \quad \theta = -\tfrac{1}{2}, \quad \phi = 0 \text{ at } z = +\tfrac{1}{2}. \tag{4b}$$

3. Base state and linear stability theory

In this section, we assume that the system has infinite extent both in the x and y directions i.e. $L_x \to \infty, L_y \to \infty$.

3.1. *Base state*

The base state is a quiescent state ($\vec{u} = 0$). The temperature, the electric potential, and the electric field depend only on the z coordinate as follows [12, 13]:

$$\theta_b(z) = -z \tag{5a}$$

$$\phi_b(z) = \ln\left(\frac{1+\gamma_e z}{1+\frac{\gamma_e}{2}}\right)\left[\ln\left(\frac{2-\gamma_e}{2+\gamma_e}\right)\right]^{-1} \tag{5b}$$

$$E_b(z) = -\frac{\gamma_e}{(1+\gamma_e z)\ln\left(\frac{2-\gamma_e}{2+\gamma_e}\right)} \tag{5c}$$

The characteristic gravity is chosen at the center of the cavity ($z = 0$) i.e.

$$\overline{g}_e = \frac{\varepsilon_{\text{ref}} e V_0^2 \gamma_e^3}{\alpha \rho_0 d^3}\left[\ln\left(\frac{1-\gamma_e/2}{1+\gamma_e/2}\right)\right]^{-2}$$

and the dimensionless electric gravity profile of the base state is given by

$$\hat{g}_{eb}(z) = -\left(1+\gamma_e z\right)^{-3} \tag{6}$$

3.2. *Linear stability analysis*

The linear stability theory consists of the superposition of infinitesimal perturbations to the base flow and then in the linearization of the resulting equations around the base state solution:

$$(u, v, w, \pi, \theta, \phi) = (0, 0, 0, \pi_b, \theta_b, \phi_b) + (u', v', w', \pi', \theta', \phi'), \tag{7}$$

where the prime denotes the perturbations. The horizontal cavity is assumed infinite in the horizontal directions so that the perturbations can be expanded into normal modes:

$$\begin{bmatrix} u'(x,y,z,t) \\ v'(x,y,z,t) \\ w'(x,y,z,t) \\ \pi'(x,y,z,t) \\ \theta'(x,y,z,t) \\ \phi'(x,y,z,t) \end{bmatrix} = \begin{bmatrix} U(z) \\ V(z) \\ W(z) \\ \Pi(z) \\ \Theta(z) \\ \Phi(z) \end{bmatrix} \exp[st + \mathrm{i}(k_x x + k_y y)] + \text{c.c.} \tag{8}$$

where $s = \sigma + \mathrm{i}\omega$ is the complex growth rate of the perturbations with σ the real growth rate and ω the frequency, k_x and k_y are the wavenumbers along the horizontal x and y directions respectively; c.c. represents the complex conjugate term. The perturbations in the temperature and the electric field induce a perturbation of the electric gravity $\vec{g}_e'$ (i.e. $\vec{g}_e = \vec{g}_{e_b} + \vec{g}_e'$) which can also be expanded into normal modes:

$$\vec{g}_e' = (G_{e_x}\vec{e}_x + G_{e_y}\vec{e}_y + G_{e_z}\vec{e}_z)\exp[st + \mathrm{i}(k_x x + k_y y)]. \tag{9}$$

The amplitudes of the normal mode of the electric gravity perturbation can be written as follows

$$\left.\begin{aligned} G_{ex} &= f(\gamma_e)(\mathrm{i}k_x D\phi_b D\Phi) \\ G_{e_y} &= f(\gamma_e)(\mathrm{i}k_y D\phi_b D\Phi) \\ G_{e_z} &= f(\gamma_e) D(D\phi_b D\Phi) \end{aligned}\right\} \tag{10}$$

where $f(\gamma_e) \equiv (1/\gamma_e^3)[\ln((1-\gamma_e/2)/(1+\gamma_e/2))]^2$. The continuity equation for the perturbation $\vec{u}'$ suggests introducing the quantity $l\hat{U} = k_x U + k_y V$ in order to reduce the problem to a 2-dimensional one.

Substitution into the linearized equation leads to

$$\left.\begin{aligned} \mathrm{i}l\hat{U} + DW &= 0 \\ sl\hat{U} &= -\mathrm{i}k^2\Pi + (D^2-k^2)l\hat{U} - \frac{L}{Pr}\theta_b(k_x G_{e_x} + k_y G_{e_y}) \\ sW &= -D\Pi + (D^2-k^2)W + \frac{1}{Pr}(Ra - L\hat{g}_{eb_0})\Theta - \frac{L}{Pr}\theta_b G_{e_z} \\ s\Theta &= W + \frac{1}{Pr}(D^2-k^2)\Theta \\ [(1+\gamma_e z)(D^2-k^2) + \gamma_e D]\Phi - \gamma_e(D^2\phi_b + D\phi_b D)\Theta &= 0 \end{aligned}\right\} \tag{11}$$

The elimination of the pressure and the use of relations (10) leads to the following system of coupled equations for W, Θ, and Φ:

$$(D^2-k^2-s)(D^2-k^2)W - \frac{k^2}{Pr}(Ra - L\hat{g}_{eb})\Theta + \frac{L}{Pr}f(\gamma_e)k^2 D\phi_b D\Phi = 0, \tag{12a}$$

$$(D^2-k^2-sPr)\Theta = -PrW, \tag{12b}$$

$$[(1+\gamma_e z)(D^2-k^2) + \gamma_e D]\Phi - \gamma_e(D^2\phi_b + D\phi_b D)\Theta = 0, \tag{12c}$$

where $k^2 = k_x^2 + k_y^2$. The axial velocity component can be eliminated to get a coupled system of equations for the perturbations of the temperature Θ and of the electric potential Φ:

$$[(D^2-k^2-s)(D^2-k^2-sPr)(D^2-k^2) + k^2(Ra - L\hat{g}_{eb})]\Theta - Lf(\gamma_e)k^2 D\phi_b D\Phi = 0, \tag{13a}$$

$$[(1+\gamma_e z)(D^2-k^2) + \gamma_e D]\Phi - \gamma_e D(D\phi_b\Theta) = 0. \tag{13b}$$

The system (13) contains the Rayleigh–Bénard convection as a limit case when $L = 0$ and $\Phi = 0$ [16]. From the system of Equations (13), one deduces immediately that stationary modes ($s = 0$) are independent of Pr as in the Rayleigh–Bénard convection [16]. This was confirmed by the works of Roberts [3] and Yoshikawa *et al.* [12]. From the system of Equations (13), we retrieve the equations solved by Roberts [3] and Stiles [11] if we neglect the perturbative gravity terms i.e. the last terms in Equations (13a), (13b). The system of Equations (12) or (13) shows that the perturbations wavenumber intervenes through its modulus.

The amplitudes of the perturbations described by the system of Equations (11) satisfy the eigenvalue problem

$$\overline{\overline{\mathrm{L}}}\vec{\Psi} = \mathrm{s}\overline{\overline{\mathrm{M}}}\vec{\Psi}, \tag{14}$$

where the vector $\vec{\Psi}$ represents the perturbation eigenvector,

$$\vec{\Psi}(z) = \left[\hat{U}\ W\ \Pi\ \Theta\ \Phi\right]^t \tag{15}$$

where the expressions of the operators $\overline{\overline{\mathrm{L}}}$ and $\overline{\overline{\mathrm{M}}}$ are obtained from the system (11).

The boundary conditions impose that perturbations vanish at the hot and the cold parallel plates:

$$\vec{\Psi}(z = \pm 1/2) = 0. \tag{16}$$

The eigenvalue problem allows for the determination of the complex growth rate (s) of the perturbations as a function of the wavenumber $\vec{k}$ and of the control parameters (Ra, L, Pr, γ_e). Thus, solving this eigenvalue problem is equivalent to finding the following characteristic equation:

$$F(Ra, L, Pr, \gamma_e, \sigma, \omega, k) = 0. \tag{17}$$

This problem is then solved by the spectral collocation method. All unknown functions are expanded into the Chebyshev polynomial series and equations are discretized at the Chebyshev–Gauss–Lobatto collocation points [7]. The highest order of the Chebyshev polynomials series is fixed to $N = 32$ to ensure the convergence of solutions. The discretized problem is then solved by the QZ-decomposition method.

Table 1. Critical parameters (L_c, k_c) for $Pr = 11.03$ and given values of Ra.

Ra	-1000	-500	0	500	1000
L_c	3370.08	2749.87	2128.70	1506.58	883.51
k_c	3.294	3.260	3.227	3.192	3.160

3.3. *Direct numerical simulation*

The system of Equations (3) together with the boundary conditions (4) have also been solved using direct numerical simulations (DNS) based on the finite volume method [17]. Periodic boundary conditions have been imposed in the horizontal plane:

$$\begin{aligned}\vec{u}(x,y,z) &= \vec{u}(x \pm L_x, y \pm L_y, z)\\ \theta(x,y,z) &= \theta(x \pm L_x, y \pm L_y, z)\\ \phi(x,y,z) &= \phi(x \pm L_x, y \pm L_y, z)\end{aligned}$$

The period of the computation box ($L_x = L_y = 10$) has been chosen in order to ensure the presence of sufficient enough convective structures. A regular mesh has been fixed to 256 points in the x and y directions while in the z-direction, the mesh size was adapted near the wall with $\Delta z = 0.005$. The flow structures were visualized using the plots of the iso-surfaces of the quantity $Q = -(1/2)\mathrm{tr}\left(\overline{\overline{S}}^2 + \overline{\overline{\Omega}}^2\right)$ where $\overline{\overline{S}}$ and $\overline{\overline{\Omega}}$ represent the symmetric and the antisymmetric parts of the velocity-gradient tensor $\vec{\nabla}\vec{u}$ respectively [9, 10].

4. Results

4.1. *Critical parameters*

Ignoring the perturbative gravity terms in (11), Roberts [3] has proved the validity of the exchange of stability which claims that the marginal states are stationary ($\omega = 0$). Keeping the perturbative gravity terms, we searched for the marginal stability curves which correspond to $\sigma = 0$ and we found that the marginal states remain stationary. The minimum point of the neutral curves ($\sigma = 0$) gives the critical stability point which characterizes the onset of the thermoelectric instability in the fluid between the two parallel plates.

In their studies, Yoshikawa *et al.* [12] have shown that the threshold of thermoelectric convection in a rectangular cavity is insensitive to the values γ_e of when $\gamma_e < 0.1$. In the problem under study $\gamma_e \ll 1$. We have determined the curves of marginal stability states in the (k, L) plane (Figure 2) for various fixed values of Pr and of $Ra \in \{-12000, 1700\}$. The critical modes are stationary and the threshold L_c is insensitive to the values of Pr. We fixed $Ra \in [-12000; 0[$ which corresponds to a thermally stable stratification, $Ra \in]0; 1700]$ to an unstable thermal stratification and $Ra = 0$ which corresponds to the zero-gravity environment. The thermal stable stratification delays the onset of thermoelectric convection; while the thermal unstable stratification accelerates the thermoelectric convection, i.e. $L_c(0 < Ra < Ra_c) < L_c(Ra = 0) < L_c(Ra < 0)$. Values of critical parameters are presented in Table 1 for few values of Ra.

We also present, in Figure 3 the eigenfunctions of the critical electric mode plotted in both vertical planes (x–z) and (y–z) under microgravity conditions ($Ra = 0$) for $Pr = 11.03$. The thermoelectric convection patterns are inclined in the horizontal (x–y) plane with two wavenumbers $k_x \neq k_y \neq 0$.

The variations of the critical parameters (L_c, k_c) with Ra are shown in Figure 4 and we confirm the results [3, 12] that the critical electric mode is not sensitive to the Pr regardless of heating

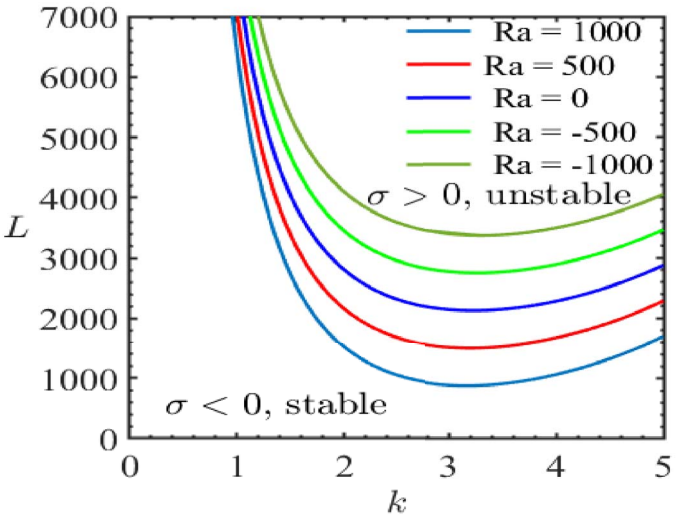

Figure 2. Marginal stability curves for $Pr = 11.03$ and $Ra \in \{-1000, -500, 0, 500, 1000\}$.

direction ($Ra < 0$ or $0 < Ra < 1708$). These variations can be approximated by linear relationships in the range of computed values of $Ra \in [-1.2 \times 10^4, 1.7 \times 10^3]$:

$$L_c = L_c^0 - C\,Ra, \quad \text{with } C = L_c^0/Ra_c^0; \quad k_c = 3.223 - 8 \times 10^{-5} Ra \tag{18}$$

here $L_c^0 = 2128.6$ is the critical electric Rayleigh number under microgravity conditions ($Ra = 0$) and $Ra_c^0 = 1708$ is the critical Rayleigh number in the classical Rayleigh–Bénard convection, so that with $C = L_c^0/Ra_c^0 = 1.247$. We recover the relationship (one obtained analytically by Stiles [11] who found $C = 1.246$ and $L_c^0 = 2128.695$. The threshold of thermoelectric convection in a thermal stable stratified liquid is larger than in microgravity while that of the thermal unstable stratified liquid is lower than that in microgravity. The size of convective structures increases with *Ra*.

4.2. *Energetic analysis near the TEHD threshold*

The equation of the kinetic energy of the perturbations is obtained by taking the scalar product of the velocity perturbation $\vec{u}'$ by the momentum equation and integrating over the volume to get

$$\frac{\mathrm{d}K}{\mathrm{d}t} = W_{\mathrm{BEG}} + W_{\mathrm{PEG}} + W_G - D_v, \tag{19}$$

where $K = \int (1/2)|\vec{u}|^2\,\mathrm{d}V$ is the kinetic energy, $W_{\mathrm{BEG}} = -(L_c/Pr)\int \theta \vec{u}' \cdot \vec{g}_{eb}\,\mathrm{d}V$ is the power of the dielectrophoretic buoyancy, $W_{\mathrm{PEG}} = -(L_c/Pr)\int (\overline{\theta}\vec{u}') \cdot \vec{g}_e'\,\mathrm{d}V$ is the power performed by the perturbation of the dielectrophoretic buoyancy, $W_G = \int \theta \vec{u}' \cdot \vec{g}\,\mathrm{d}V$ is the power performed by the Archimedean buoyancy, and $D_v = \int d_v\,\mathrm{d}V$ is the dissipation of perturbative vorticity by viscosity with

$$d_v = Re^2 \left\{ 2\left[\left(\frac{\partial u'}{\partial x}\right)^2 + \left(\frac{\partial v'}{\partial y}\right)^2 + \left(\frac{\partial w'}{\partial z}\right)^2 \right] + \left[\left(\frac{\partial v'}{\partial x} + \frac{\partial u'}{\partial y}\right)^2 + \left(\frac{\partial w'}{\partial y} + \frac{\partial v'}{\partial z}\right)^2 + \left(\frac{\partial u'}{\partial z} + \frac{\partial w'}{\partial x}\right)^2 \right] \right\}.$$

The terms of the energy equation of a flow in a system heated from the bottom are presented in Figure 5 for $Pr = 11.03$. All terms were computed for different values of $Ra < Ra_c = 1708$. The power W_G increases when increasing *Ra*; while the contribution of the basic electric gravity W_{BEG} decreases with *Ra*. In the stable thermal stratification, the Archimedean buoyancy has a negative power and the dielectrophoretic force furnishes a large power to trigger thermoelectric convection.

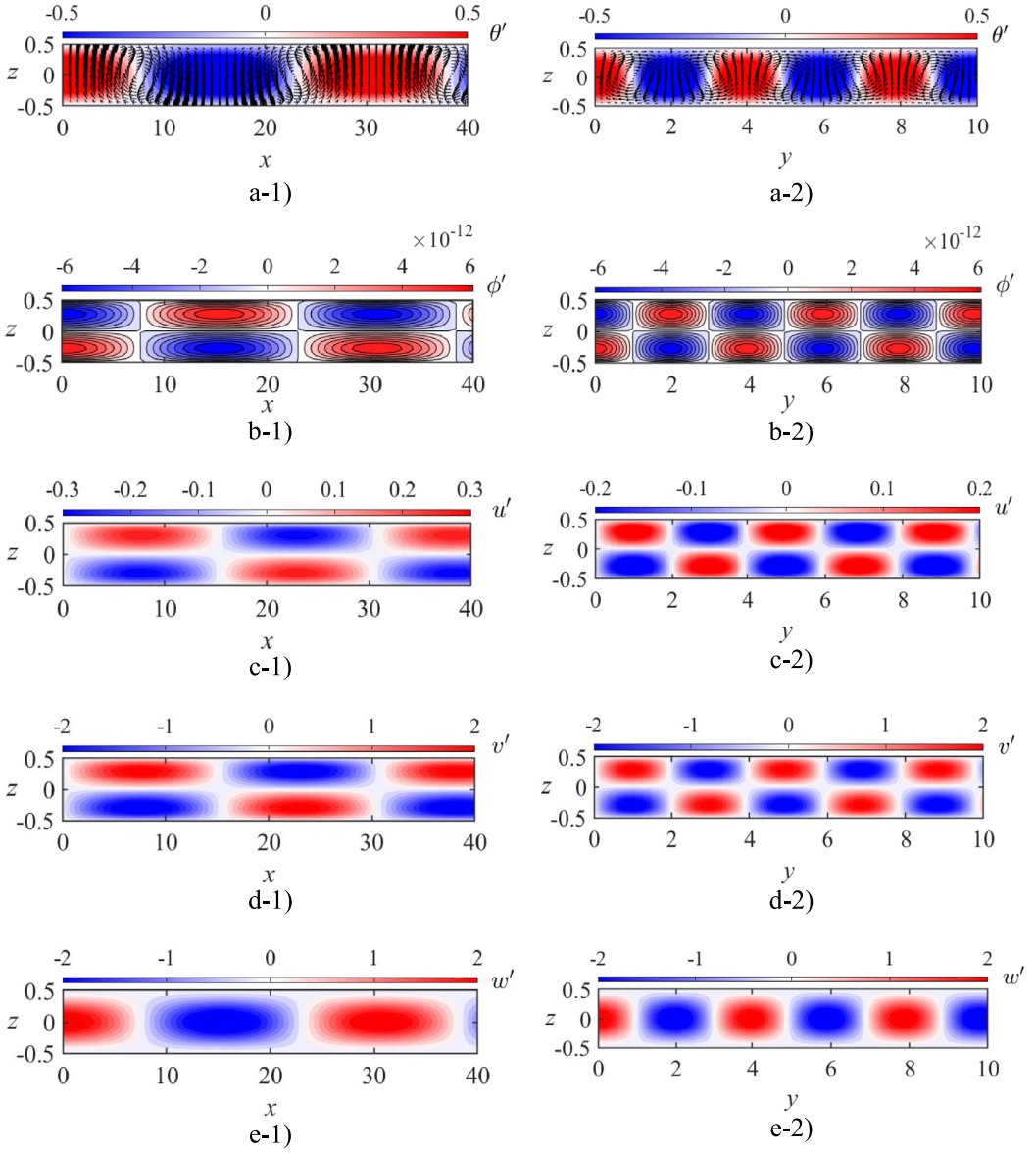

Figure 3. Eigenfunctions of the electric mode in the planes $y = 0$ and $x = 0$ for $Pr = 11.03$, $Ra = 0$, and $L_c = 2128.69$: (a) velocity fields and temperature levels, (b) electric potential ϕ', (c,d) the horizontal velocity components u' and v', and (e) the vertical velocity w'. We choose $L_x = 40$ in order to highlight the periodicity along the x-direction.

For unstable thermal stratification, Archimedean buoyancy contributes to the power of the dielectrophoretic buoyancy to induce thermoelectric convection. For $Ra^* \approx 954$, $W_G = W_{\mathrm{BEG}}$ so that for $Ra < Ra^*$, the thermoelectric convection is enhanced by the Archimedean buoyancy while for $Ra > Ra^*$, the Archimedean buoyancy furnishes the larger power in triggering thermal convection so that the dielectrophoretic force gives less power. Just below Ra_c, we obtain $W_{\mathrm{BEG}} \to 0$. So we can conclude that the thermoelectric convection occurs for $Ra < Ra^*$ while for $Ra > Ra^*$, we have Rayleigh–Bénard convection enhanced by dielectrophoretic buoyancy. The viscous

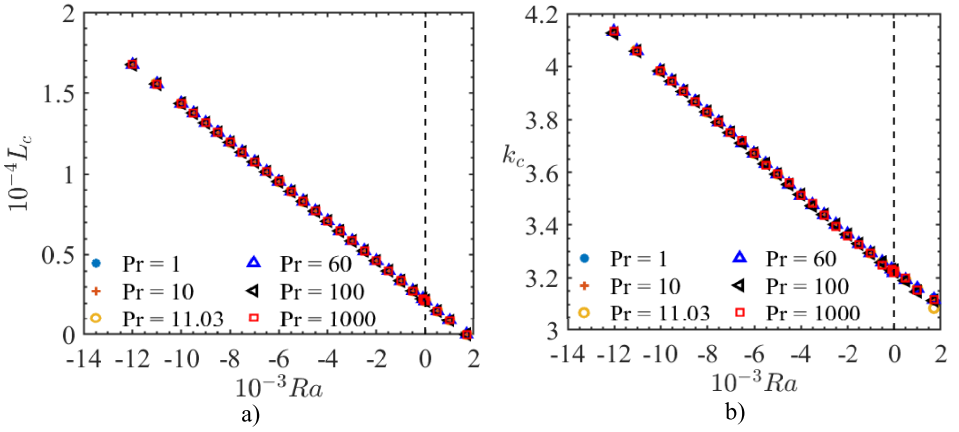

Figure 4. Variation of critical parameters against *Ra* for various values of *Pr*: (a) critical electric Rayleigh number L_c; (b) critical wavenumber k_c.

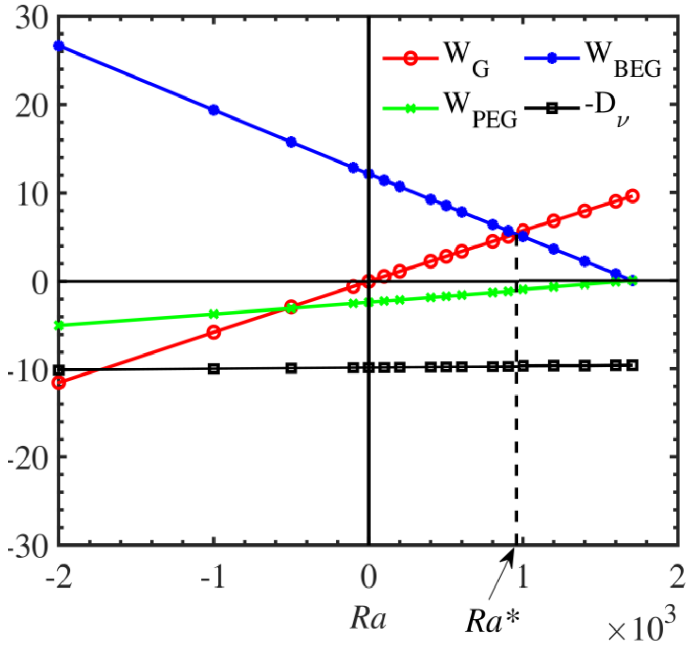

Figure 5. Different terms of the energy balance at the critical point (L_c, k_c) normalized by twice the kinetic energy plotted as a function of the Rayleigh number *Ra* (a) for *Pr* = 11.03 (Novec 7200) and $Ra \in]-2000; 1700]$.

dissipation does not change with *Ra*, while the absolute value of the power from the perturbative dielectrophoretic buoyancy decreases as *Ra* increases. This means that the power produced by the buoyancies in the fluid is tuned to balance the viscous dissipation which is independent of *Ra*.

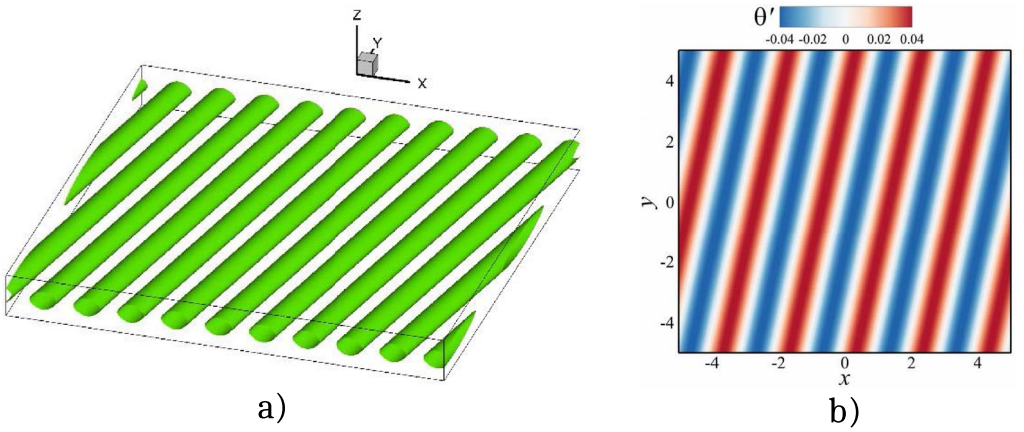

Figure 6. Flow vortical structures illustrated by (a) iso-surfaces of $Q = 4$, and (b) isotherms in the horizontal (x–y) plane for $Pr = 1$, $\gamma_e = 0.01$, $Ra = 0$ and $L = 2150$.

Table 2. Properties of the working fluid (Novec 7200 at $T = 298.15$ K).

ρ (kg·m^{-3})	α (10^{-3} K^{-1})	ν (10^{-7} m^2·s^{-1})	κ (10^{-8} m^2·s^{-1})	ϵ_r	e (10^{-3} K^{-1})	Pr	V_i (V)	V_b (kV)
1430	1.6	4.3	3.90	7.3	3.9	11.03	0.61	40

4.3. *Thermo-convective flow pattern around the threshold*

The results from DNS for $Pr = 1$ near the threshold ($\delta = (L - L_c)/L_c = 0.01$) in zero-gravity confirm the results from linear stability analysis on the inclination of convective structures in the (x–y) plane.

Figure 6a shows the iso-surfaces of Q and Figure 6b shows the isotherms of the thermo-convective patterns in the horizontal plane. Vertical cross-sections of the instantaneous fields are presented in Figure 7 and the vorticity components are illustrated in Figure 8.

5. Experimental results

We have performed experiments in a horizontal rectangular cavity of sizes ($L_x = 0.2$ m, $L_y = 0.04$ m, $d = 0.005$ m) during a parabolic flight aboard the zero-g Airbus of NOVESPACE-CNES. We fixed the value of the temperature difference ΔT between the upper and lower plates and varied the value of the applied effective electric potential V_0. The system has an accelerometer that detects the microgravity phase so that the control program can activate the high voltage at a specified instant of the parabola. The horizontally aligned cavity was heated from the top and cooled from the bottom so that the gravity phases always correspond to a thermal stable stratification. The high voltage is applied 5 s after the microgravity conditions started so the initial conditions favor the growth of thermoelectric instabilities [18].

For the given working fluid, we introduced an intrinsic electric potential $V_i = \sqrt{\rho \nu \kappa / \epsilon_{\text{ref}}}$ based on the properties of the fluid. The potential V_i is used in theoretical studies to scale the applied voltage [10]. The working dielectric liquid in the experiment was Novec 7200 ($C_4F_9OC_2H_5$), the properties of which are given in Table 2. The breakdown potential V_b of this dielectric liquid is also presented in Table 2.

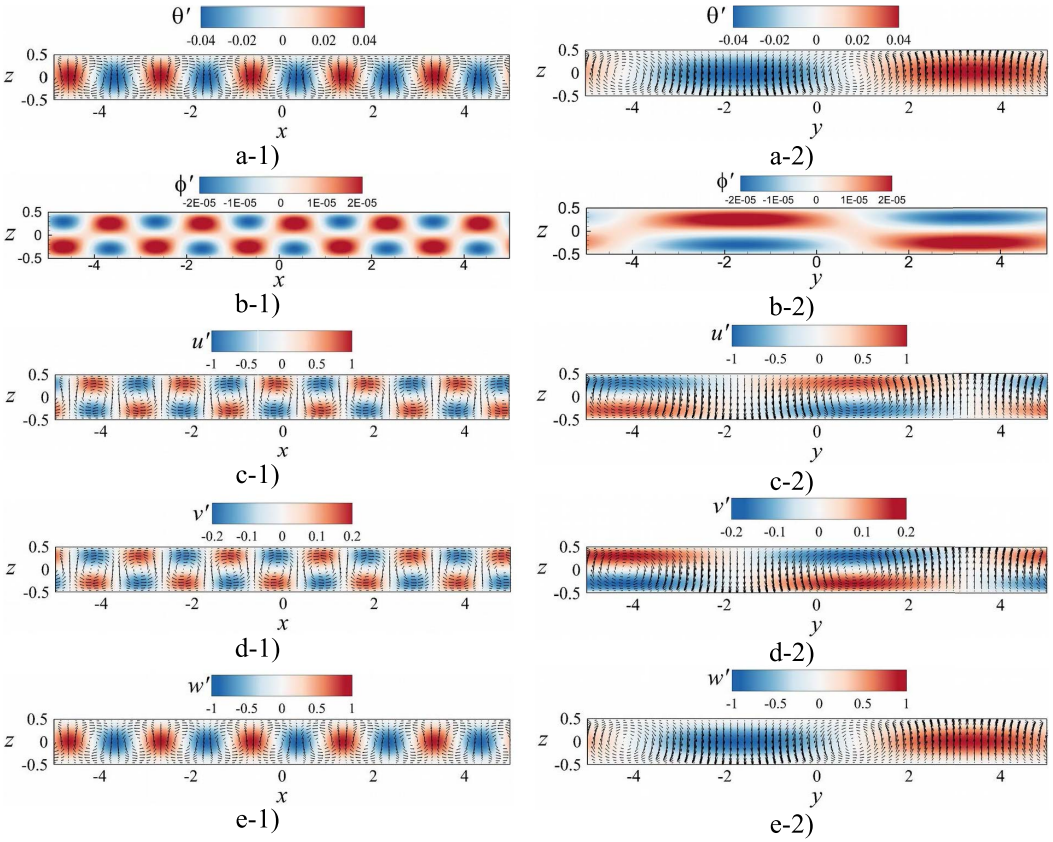

Figure 7. Instantaneous flows in the vertical planes $y = 0$ and $x = 0$ for $Ra = 0$, $Pr = 1$ and $L = 2150$. Vectors represent the velocity fields: (a) temperature distribution (color); (b) potential; (c,d) horizontal velocity component v (color); and (e) vertical velocity (color).

For flow visualization, we have used the background-oriented Schlieren technique (BOS) which is based on the variation of the refractive index of the fluid due to the density gradient [19–22]. A section of the horizontal gap is illuminated from the bottom to the top with an LED panel, to which is attached a background image composed of dots with random positions. On the other side of the gap, a camera takes pictures of the illuminated section. The density gradient can be correlated with the local optical displacement of that random pattern in the (x, y) plane compared to a reference case [20]. That reference image corresponds to the one with no applied temperature difference and no applied electric potential.

Figure 9 shows the divergence of the displacement field $(\vec{\nabla} \cdot \vec{d})$ for $\Delta T \approx 7$ K for two values of V_0. Pictures are taken at the end of the microgravity phase (0 g) so that the patterns had time to develop in the flow. The first image corresponds to the case without electric potential where the displacement field presents no particular divergence. The image is then completely correlated to the reference one, up to its homogeneous translation. However, when the potential $V_0 = 1.41$ kV is applied, and the divergence of the displacement field highlights the occurrence of alternated positive and negative areas. As the corresponding electric Rayleigh number $L = 4000$ is then nearly twice the critical value under microgravity conditions ($L_c \approx 2129$), this mode is interpreted as a result of the thermoelectric instability.

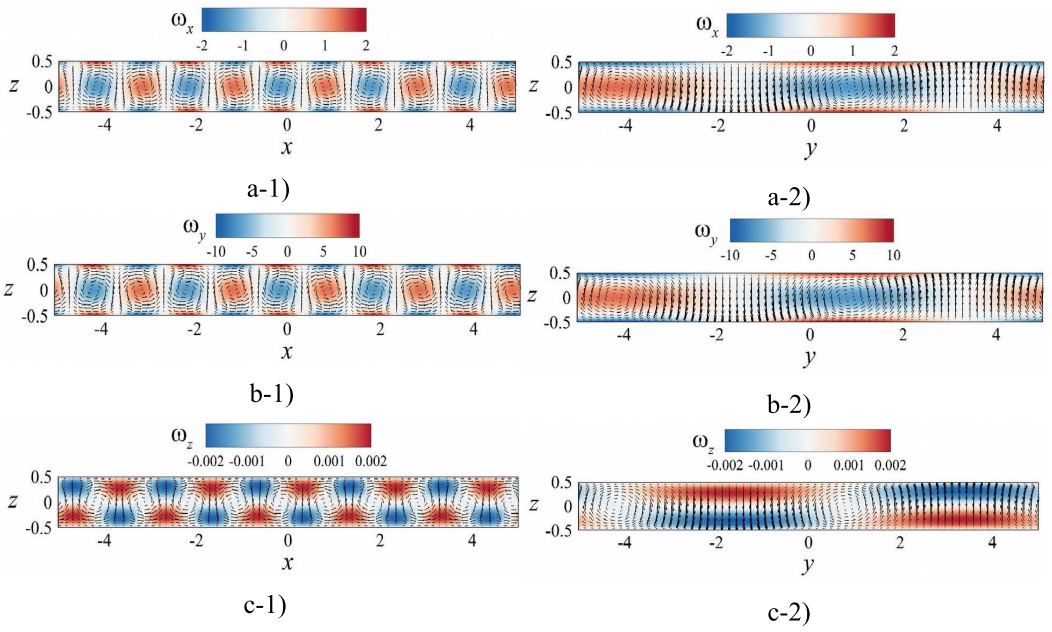

Figure 8. Vorticity components in the plane $y = 0$, and in the plane $x = 0$ for $Pr = 1$, $Ra = 0$, and $L = 2150$. Vectors represent the velocity fields: (a,b) horizontal vorticity components (color); and (c) vertical vorticity components (color).

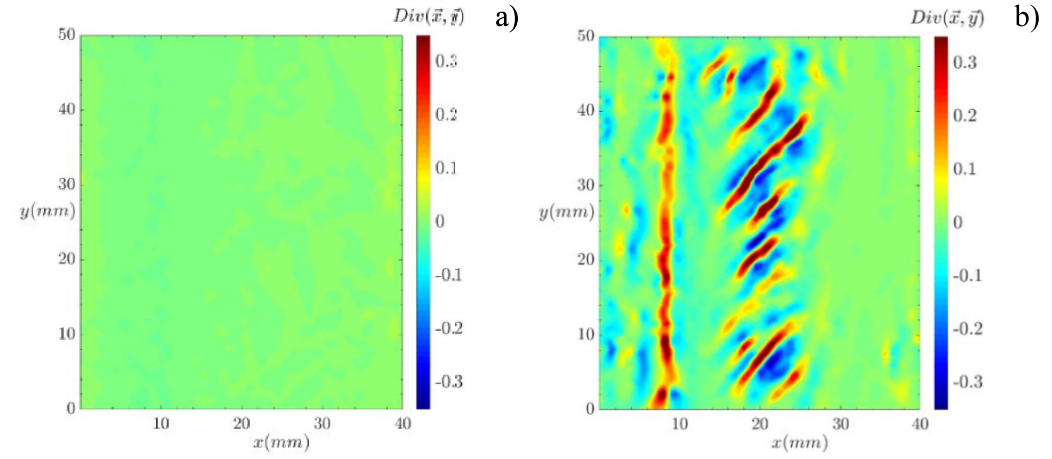

Figure 9. Patterns of the divergence of the displacement vector ($\vec{\nabla}\cdot\vec{d}$) corresponding to $\Delta T \approx 7$ K in the microgravity phase: (a) $V_0 = 0$, (b) $V_0 = 1.41$ kV.

6. Conclusion

We have performed a linear stability analysis of thermoelectric convection in a planar capacitor in microgravity and investigated the effect of the stable and unstable thermal stratification on the critical parameters. The results from zero-gravity are confirmed by the DNS. The experiment performed in parabolic flight aboard zero-g Airbus confirmed the existence of thermo-convective structures induced by the dielectric buoyancy in the microgravity phase.

Nomenclature

Symbols	Signification	Symbols	Signification
V_b	Breakdown potential	Ra	Rayleigh number
d	Cavity width	κ	Thermal diffusivity
$\vec{f}_{\mathrm{DEP}}$	Density of the dielectrophoretic force	ν	Kinematic viscosity
$\vec{E}$	Electric field	ρ	Fluid density
$\vec{g}_e$	Electric gravity	α	Thermal expansion coefficient
ϕ	Electric potential	ϵ	Permittivity
V_0	Effective electric tension	e	Thermal coefficient of the permittivity
L_x, L_y	Horizontal lengths of the cavity	γ_e	Thermoelectric coupling parameter
V_i	Intrinsic electric potential	σ_{el}	Electrical conductivity
π	Dimensionless pressure	k_x	Wavenumber along x direction
ΔT	Temperature difference	k_y	Wavenumber along y direction
T_{ref}	Reference temperature	k	Total wavenumber
θ	Temperature deviation	L	Electric Rayleigh number
s	Complex growth rate	Pr	Prandtl number

Conflicts of interest

Authors have no conflict of interest to declare.

Acknowledgments

The present work was supported partially by both the CNES (project INTEHLDI) and the DLR (Grant Nos 50WM1644 and 50WM1944), the CNRS LIA 1092 ISTROF, and the French National Research Agency (ANR) through the program "Investissements d'Avenir (Grant Nos ANR-10LABX-09-01)", LABEX EMC^3. EB benefitted from a PhD scholarship cofounded both by the CNES and the Région Normandie. CK was supported by the National Research Foundation of Korea (NRF) grant funded by the Korean Ministry of Science and ICT (MSIT) (NRF-2021K1A3A1A21039317). CK and IM acknowledge the support from the bilateral French-Korean exchange program STAR-PHC.

References

[1] L. D. Landau, E. M. Lifshitz, *Electrodynamics of Continuous Media*, Elsevier Buttherworth-Heinemann, Burlington, MA, 1984.

[2] R. E. Rosensweig, *Ferrohydrodynamics*, Cambridge University Press, Cambridge, MA, 1985.

[3] P. H. Roberts, "Electrohydrodynamic convection", *Q. J. Mech. Appl. Math.* **22** (1969), no. 2, p. 211-220.

[4] A. A. Bozhko, S. A. Suzlov, *Convection in Ferro-Nanofluids: Experiments and Theory*, Springer (eBook), 2018.

[5] J. E. Hart, G. A. Glatzmaier, J. Toomre, "Space-laboratory and numerical simulations of thermal convection in a rotating hemispherical shell with radial gravity", *J. Fluid Mech.* **173** (1986), p. 519-544.

[6] B. Futterer, A. Krebs, A.-C. Plesa, F. Zaussinger, R. Hollerbach, D. Breuer, C. Egbers, "Sheet-like and plume-like thermal flow in a spherical convection experiment performed under microgravity", *J. Fluid Mech.* **735** (2013), p. 647-683.

[7] H. N. Yoshikawa, O. Crumeyrolle, I. Mutabazi, "Dielectrophoretic force-driven thermal convection in annular geometry", *Phys. Fluids* **25** (2013), article no. 024106.

[8] V. Travnikov, O. Crumeyrolle, I. Mutabazi, "Influence of the thermo-electric coupling on the heat transfer in cylindrical annulus with a dielectric fluid under microgravity", *Acta Astronaut.* **129** (2016), p. 88-94.

[9] C. Kang, I. Mutabazi, "Dielectrophoretic buoyancy and heat transfer in a dielectric liquid contained in a cylindrical annular cavity", *J. Appl. Phys.* **125** (2019), article no. 184902.

[10] C. Kang, I. Mutabazi, "Columnar vortices induces by dielectrophoretic force in a stationary cylindrical annulus filled with a dielectric liquid", *J. Fluid Mech.* **908** (2021), article no. A26.

[11] P. J. Stiles, "Electro-thermal convection in dielectric liquids", *Chem. Phys. Lett.* **179** (1991), no. 3, p. 311-315.
[12] H. N. Yoshikawa, M. Tadie Fogaing, O. Crumeyrolle, I. Mutabazi, "Dielectrophoretic Rayleigh–Bénard convection under microgravity conditions", *Phys. Rev. E* **87** (2013), article no. 043003.
[13] M. Tadie Fogaing, H. N. Yoshikawa, O. Crumeyrolle, I. Mutabazi, "Heat transfer in the thermo-electro-hydrodynamic convection under microgravity conditions", *Eur. Phys. J. E* **37** (2014), article no. 35.
[14] Z. Liu, C. Li, B. Wang, "Flow structure and heat transfer of electro-thermo-convection in a dielectric liquid layer", *Phys. Fluids* **31** (2019), article no. 064103.
[15] H. Yoshikawa, C. Kang, I. Mutabazi, F. Zaussinger, P. Haun, C. Egbers, "Thermoelectrohydrodynamic convection in parallel plate capacitors under dielectric heating conditions", *Phys. Rev. Fluids* **5** (2020), article no. 113503.
[16] S. Chandrasekhar, *Hydrodynamic and Hydromagnetic Stability*, Dover Publications, New York, 1981.
[17] E. B. Barry, C. Kang, H. Yoshikawa, I. Mutabazi, "Transfert de chaleur par convection thermoelectrique dans des cavités rectangulaires horizontales", *Entropie* **2** (2021), no. 2, p. 1-11, ISTE Open Sciences.
[18] A. Meyer, M. Meier, M. Jongmanns, T. Seelig, C. Egbers, I. Mutabazi, "Effect of the initial conditions on the growth of thermoelectric instabilities during parabolic flights", *Microgravity Sci. Technol.* **31** (2019), p. 715-721.
[19] K. Hayasaka, Y. Tagawa, T. Liu, M. Kameda, "Optical-flow-based background-oriented Schlieren technique for measuring a laser-induced underwater shock wave", *Exp. Fluids* **57** (2016), article no. 179.
[20] G. Meier, "Computerized background-oriented Schlieren", *Exp. Fluids* **33** (2002), p. 181-187.
[21] L. Venkatakrishnan, G. E. A. Meier, "Density measurements using the background oriented Schlieren technique", *Exp. Fluids* **37** (2004), p. 237-247.
[22] M. Raffel, "Background-oriented Schlieren (BOS) techniques", *Exp. Fluids* **56** (2015), article no. 60.

Comptes Rendus

Mécanique

Objet de la revue

Les *Comptes Rendus Mécanique* sont une revue électronique évaluée par les pairs de niveau international, qui couvre l'ensemble des domaines de la discipline. Ils publient des articles originaux de recherche, des articles de revue, des mises en perspective historiques, des textes à visée pédagogique ou encore des actes de colloque, sans limite de longueur, en anglais ou en français. Les *Comptes Rendus Mécanique* sont diffusés selon une politique vertueuse de libre accès diamant, gratuit pour les auteurs (pas de frais de publication) comme pour les lecteurs (libre accès immédiat et pérenne).

À propos de la revue

Toutes les informations concernant la revue, y compris le texte des articles publiés qui est en accès libre intégral, figurent sur le site https://comptes-rendus.academie-sciences.fr/mecanique/.

Informations à l'attention des auteurs

Pour toute question relative à la soumission des articles, les auteurs peuvent consulter le site https://comptes-rendus.academie-sciences.fr/mecanique/.

Contact

Académie des sciences
23, quai de Conti, 75006 Paris, France
Tél. : (+33) (0)1 44 41 43 72
CR-Mecanique@academie-sciences.fr

Comptes Rendus
de l'Académie des sciences

Mécanique

Volume 351, nº S2, 2023

Special issue / *Numéro thématique*

Physical Science in Microgravity within the Thematic Group Fundamental and Applied Microgravity / *Sciences physiques en microgravité au sein du GDR Micropesanteur Fondamentale et Appliquée*

Guest editors / *Rédacteurs en chef invités*

Olga Budenkova (CNRS, Université Grenoble Alpes,Grenoble INP, SIMaP, 38000 Grenoble, France), Catherine Colin (IMFT, Université de Toulouse, CNRS, INPT, UPS et GDR 2799 Micropesanteur Fondamentale et Appliquée)

Guillaume Legros (ICARE, CNRS UPR 3021, Univ. Orléans et GDR 2799 Micropesanteur Fondamentale et Appliquée)

Cover illustration / *Illustration de couverture*

Deniz Kaya Eyice, Fabien Haltera, Ahmet Yozgatlıgil, Iskender Gökalp, and Christian Chauveau

1873-7234 (electronic)

Académie des sciences — Paris

COMPTES RENDUS
DE L'ACADÉMIE DES SCIENCES

Mécanique

Volume 351, nº S2, 2023